

REPORT NO.
UCB/EERC-86/10
DECEMBER 1986

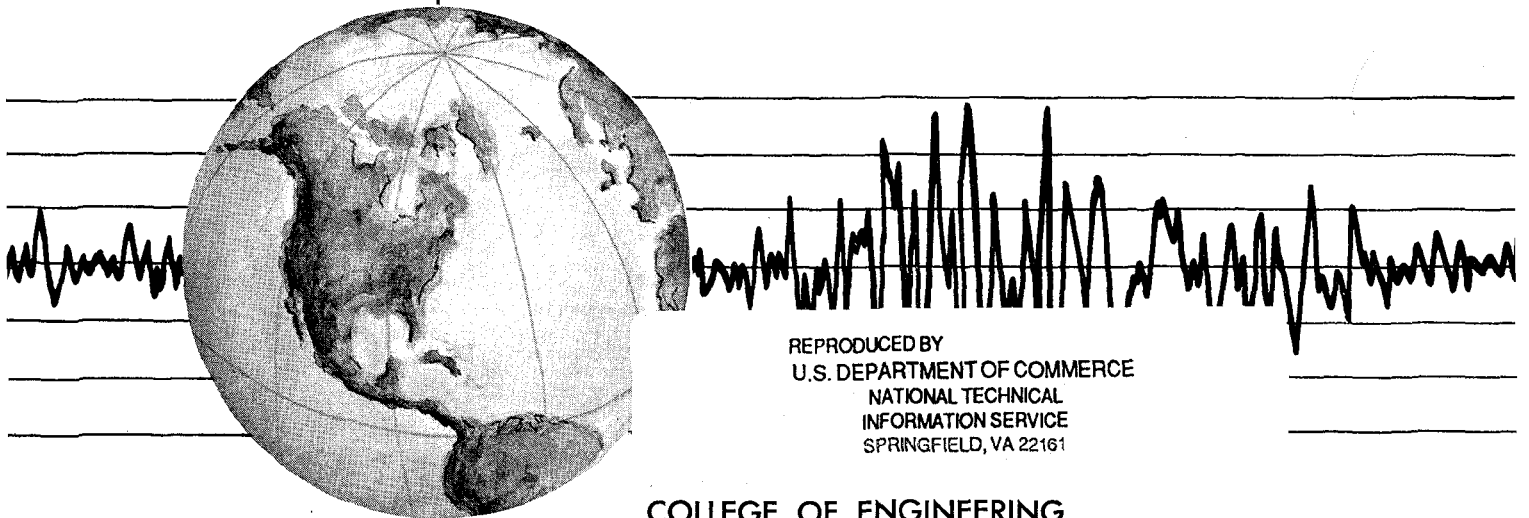
EARTHQUAKE ENGINEERING RESEARCH CENTER

EARTHQUAKE SIMULATION TESTS AND ASSOCIATED STUDIES OF A 0.3-SCALE MODEL OF A SIX-STORY CONCENTRICALLY BRACED STEEL STRUCTURE

by

CHIA-MING UANG
VITELMO V. BERTERO

Report to the National Science Foundation



REPRODUCED BY
U.S. DEPARTMENT OF COMMERCE
NATIONAL TECHNICAL
INFORMATION SERVICE
SPRINGFIELD, VA 22161

COLLEGE OF ENGINEERING

UNIVERSITY OF CALIFORNIA • Berkeley, California

For sale by the National Technical Information Service, U.S. Department of Commerce, Springfield, Virginia 22151

See back of report for up to date listing of EERC reports.

DISCLAIMER

Any opinions, findings, and conclusions or recommendations expressed in this publication are those of the authors and do not necessarily reflect the views of the National Science Foundation or the Earthquake Engineering Research Center, University of California, Berkeley

REPORT DOCUMENTATION PAGE		1. REPORT NO. NSF/ENG- 86017	2.	3. Recipient's Accession No. PBB7 1635647AS	
4. Title and Subtitle Earthquake Simulation Tests and Associated Studies of a 0.3 scale Model of a Six-Story Concentrically Braced Steel Structure				5. Report Date December 1986	
7. Author(s) Chia-Ming Uang and Vitelmo V. Bertero				8. Performing Organization Rept. No. UCB/EERC-86/10	
9. Performing Organization Name and Address Earthquake Engineering Research Center University of California, Berkeley 1301 So. 46th Street Richmond, Calif. 94804				10. Project/Task/Work Unit No.	
12. Sponsoring Organization Name and Address National Science Foundation 1800 G Street, N.W. Washington, D.C. 20550				11. Contract(C) or Grant(G) No. (C) (G) ECE 84-19739	
				13. Type of Report & Period Covered	
15. Supplementary Notes					
16. Abstract (Limit: 200 words) This report summarizes the University of California, Berkeley part of the Six-Story Concentrically K-braced Steel Structure Phase of the U.S.-Japan Cooperative Earthquake Research Program. The design of the full-scale test building is reviewed and its behavior predicted analytically. The scale of the largest model that could be tested on the U.C. Berkeley earthquake simulator is determined. The reduced-scale model is designed, fabricated, instrumented and, finally, tested on the earthquake simulator. The test results and their implications regarding earthquake-resistant design and construction of concentrically K-braced steel structures are evaluated. The reliability of computer programs to predict the seismic response of steel structures is also evaluated. Recommendations for improving the design and construction of such braced steel frames are formulated.					
17. Document Analysis a. Descriptors					
b. Identifiers/Open-Ended Terms					
c. CQSATI Field/Group					
18. Availability Statement: Release Unlimited			19. Security Class (This Report)		21. No. of Pages 387
			20. Security Class (This Page)		22. Price

i.a

U.S.-JAPAN COOPERATIVE EARTHQUAKE RESEARCH PROGRAM

**EARTHQUAKE SIMULATION TESTS AND ASSOCIATED STUDIES
OF A 0.3-SCALE MODEL OF A SIX-STORY
CONCENTRICALLY BRACED STEEL STRUCTURE**

by

Chia-Ming Uang

and

Vitelmo V. Bertero

A Report to Sponsor:

National Science Foundation

Report No. UCB/EERC-86/10

Earthquake Engineering Research Center

College of Engineering

University of California

Berkeley, California

December 1986

ABSTRACT

This report summarizes research conducted as part of the Six-Story Concentrically K-braced Steel Structure Phase of the U.S.-Japan Cooperative Earthquake Research Program. The U.C. Berkeley part of the research program had the following main objectives: (i) to review the design of the full-scale test building and to predict its behavior analytically; (ii) to design, fabricate and instrument the largest scale model that could be tested on the U.C. Berkeley earthquake simulator; (iii) to conduct earthquake simulator testing of the reduced scale model; (iv) to evaluate the test results and their implications regarding earthquake-resistant design and construction of concentrically K-braced steel structures; (v) to evaluate the reliability of computer programs to predict the seismic response of steel structures; and (vi) to formulate recommendations for improving the design and construction of such braced steel frames.

The following main conclusions have been drawn from these studies:

- (1) The full-scale test building represents a typical design based upon current practice.
- (2) Earthquake simulator testing of a reduced scale model can provide a better understanding of the dynamic response of the structure to earthquake ground motion because strain rate effect is implicitly accounted for and no stress relaxation problem exists. Good correlation can be expected between the test results of the full-scale and the reduced scale models if the difference in local behavior due to different detailing is recognized and taken into account.
- (3) Present computer programs (e.g., DRAIN-2D and ANSR-1) for linear or nonlinear dynamic analysis of multistory buildings can be used with sufficient practical accuracy. Good correlation is difficult to obtain once the bracing element ruptures; available mathematical brace elements fail to consider brace rupture. Shaking table pitching motions should be considered in an analytical correlation study.

- (4) Present UBC and ATC seismic design forces are unrealistically low when compared with those forces that develop in structures designed according to their minimum requirements; the ATC linear elastic design response spectra is not conservative. The UBC and ATC requirement of designing the ductile moment-resisting space frame for 25 percent of the design base shear is unrealistic in view of the forces that develop. Present UBC and ATC requirements for proportioning the bracing elements cannot prevent severe buckling and rupture of the brace.

It is recommended that:

- (1) Present UBC seismic regulations regarding the minimum seismic force should be increased to make it compatible with the actual supplied stiffness and strength that result from the present UBC computational procedures for estimating supplies.
- (2) A more rational design method should be based on a realistic inelastic design response spectra and the period of the dual system to estimate the structural demand. The structure should be designed using capacity design methods. Similarly, the ductile moment-resisting space frame should be checked based on realistic inelastic design response spectra and the period of the ductile moment-resisting space frame to estimate the structural demand.
- (3) On the basis of the test results, the brace compressive strength should be equal to at least 80 percent of the required tensile strength and the brace width-thickness ratio should be limited to 18 to avoid local buckling and rupture.
- (4) Moment connection should be used in the dual structural system with concentric bracing; use of bolted shear plates, copes and groove welding for the flanges should be avoided.

ACKNOWLEDGEMENTS

The research reported here was supported by the National Science Foundation Grant Number ECE 84-19739. The ongoing encouragement from Drs. S.C. Liu, J.B. Scalzi and M.P. Gaus of the NSF is greatly appreciated. Any opinions, discussions, findings, conclusions and recommendations are those of the authors and do not necessarily reflect the views of the sponsor.

The work described was carried out by Chia-Ming Uang in partial fulfillment of the requirements for the degree of Doctor of Philosophy in Engineering and was supervised by Professor V.V. Bertero. This report reproduces the dissertation submitted in November 1986 to the Graduate Division of the University of California, Berkeley. The assistance of Professor R.W. Clough in reviewing this report is appreciated.

A number of people have made significant contributions to this research and their assistance is greatly appreciated. Mr. C.R. Llopiz assisted with the construction of the model and Dr. K. Igarashi, a Research Engineer with the Kajima Co. in Japan, provided invaluable advice during the course of this project and assisted with the processing of the initial dynamic tests. The technical support of the staff of the Earthquake Engineering Research Center, especially Dr. J.S. Dimsdale, Messrs P. Quinn, D. Clyde, W. Neighbour and Dr. B. Bolt, is gratefully acknowledged. The considerable assistance of Mr. A.S. Whittaker throughout these studies and the writing of this report is also acknowledged.

TABLE OF CONTENTS

ABSTRACT	i
ACKNOWLEDGEMENTS	iii
TABLE OF CONTENTS	iv
LIST OF TABLES	ix
LIST OF FIGURES	xi
I. INTRODUCTION	1
1.1 Introductory Remarks	1
1.2 Objectives	3
1.3 Scope	4
II. PROTOTYPE DESIGN REVIEW	6
2.1 Introductory Remarks	6
2.2 Description of the Prototype Structure	6
2.2.1 Structural System	6
2.2.2 Member Sizes, Materials and Connections	7
2.3 Review of the Prototype Design	7
2.3.1 General	7
2.3.2 Design Loading	9
2.3.3 Mechanical Characteristics of the Structural Materials	10
2.3.4 Design Assumptions for the Composite Girder	11
2.3.5 UBC Lateral Load Analysis	12
2.3.6 Discussion of the UBC Results	12
2.3.7 Concluding Remarks	14
III. PROTOTYPE ANALYTICAL RESPONSE PREDICTION	15
3.1 Introductory Remarks	15
3.2 Prototype Flexibility, Natural Periods and Mode Shapes	15
3.3 Prototype Strength	17
3.3.1 Introductory Remarks	17
3.3.2 Step-by-Step Nonlinear Static Analysis	17
3.3.3 Limit Analysis Using Simple Plastic Theory	23
3.4 Prototype Seismic Response	25
3.4.1 Introductory Remarks	25
3.4.2 Serviceability Level Analysis	26
3.4.3 Damageability Level Analysis	26
3.4.4 Collapse Level Analysis	26
3.5 Prototype Strength Comparison	27

IV. MODEL DESIGN, CONSTRUCTION AND INSTRUMENTATION	30
4.1 Introductory Remarks	30
4.2 Selection of the Scale Factor	30
4.3 Model Design	31
4.3.1 Similitude Requirements	31
4.3.2 Aspects of the Model Construction	32
4.3.3 Materials and Mechanical Characteristics	34
4.3.4 Member Fabrication	38
4.4 Composite Girder Tests	39
4.4.1 Introductory Remarks	39
4.4.2 Composite Girder Test Specimens	39
4.4.3 Test Results	41
4.4.4 Evaluation of Results	44
4.5 Model Construction	46
4.5.1 Structural Steel Frames	46
4.5.2 Composite Floor System	46
4.6 Model Instrumentation	47
4.6.1 Shaking Table Motions	48
4.6.2 Model Global Responses	48
4.6.3 Model Local Responses	49
4.7 Data Acquisition	50
V. MECHANICAL CHARACTERISTICS OF THE MODEL	52
5.1 Introductory Remarks	52
5.2 Analytical Prediction of the Model Response	52
5.3 Dynamic Characteristics of the Model	53
5.3.1 Introductory Remarks	53
5.3.2 Test Procedures	54
5.3.3 Stage 1 Test - Unbraced Model without Composite Slab	56
5.3.4 Stage 2 Test - Braced Model without Composite Slab	57
5.3.5 Stage 3 Test - Model without Auxiliary Mass	58
5.3.6 Stage 4 Test - Model	60
5.4 Comparison of the Model and the Prototype Test Results	62
5.5 Comparison of the Model Analytical and Experimental Results	63
5.6 Concluding Remarks	64
VI. EARTHQUAKE SIMULATION TESTS OF THE MODEL: TEST PROGRAM AND PROCEDURES	66
6.1 Introductory Remarks	66
6.2 Analytical Response of the Model	66
6.2.1 Introductory Remarks	66
6.2.2 Prediction of the Model Strength	66
6.2.3 Prediction of the Model Seismic Response	67
6.2.4 Concluding Remarks	67

6.3 Shaking Table Input Motion	68
6.4 Test Program	68
6.5 Data Reduction	69
6.5.1 Data Noise	69
6.5.2 Sign Convention	71
6.5.3 Force Calculation	72
6.5.4 Member Designation	74
6.6 Energy Calculation	74
VII. MODEL EXPERIMENTAL RESULTS	77
7.1 Introductory Remarks	77
7.2 Global Response	78
7.2.1 Variation of Natural Periods and Damping Ratios	78
7.2.2 Response Envelopes	79
7.3 MO-6.3 Test	79
7.3.1 Response Time History	79
7.3.2 Inter-story Drift versus Story Shear Relationship	80
7.3.3 Maximum Response Envelopes	80
7.3.4 Column Axial Force - Bending Moment Interaction	81
7.3.5 Energy Distribution	81
7.4 MO-33 Test	82
7.4.1 Response Time History	82
7.4.2 Inter-story Drift versus Story Shear Relationship	82
7.4.3 Maximum Response Envelopes	83
7.4.4 Column Axial Force - Bending Moment Interaction	83
7.4.5 Energy Distribution	83
7.5 MO-65 Test	84
7.5.1 Response Time History	84
7.5.2 Inter-story Drift versus Story Shear Relationship	84
7.5.3 Maximum Response Envelopes	85
7.5.4 Brace Response	85
7.5.5 Column Axial Force - Bending Moment Interaction	87
7.5.6 Energy Distribution	87
7.5.7 Girder-Brace Joint Vertical Response	87
7.6 MO-post1 Test	88
7.6.1 Introductory Remarks	88
7.6.2 Response Time History	88
7.6.3 Inter-story Drift versus Story Shear Relationship	88
7.6.4 Maximum Response Envelopes	88
7.6.5 Energy Dissipation	89
7.6.6 Concrete Slab Crack Pattern	89
VIII. EVALUATION OF MODEL TEST RESULTS	90
8.1 Introductory Remarks	90

8.2 Inter-story Drift versus Story Shear Envelopes	90
8.3 Base Shear versus Roof and Critical Inter-story Drift Envelopes	91
8.3.1 Prototype Design Base Shear and the UBC Requirements	91
8.3.2 ATC Recommendations	91
8.3.3 Comparison of Model Results and Code Requirements	92
8.3.4 Comparison of Model Results and Analytical Results	94
8.3.5 Comparison of Model Results and Prototype Results	95
8.4 Base Shear versus Ground Excitation Intensity Relationship	97
8.5 Input Energy versus Base Excitation Intensity Relationship	98
8.5.1 Input Energy Test Results	98
8.5.2 Discussion of Input Energy	99
8.6 Viscous Damped Energy	102
8.6.1 Introductory Remarks	102
8.6.2 MO-6.3 Test	103
8.6.3 MO-33 Test	106
8.6.4 MO-65 Test	106
8.6.5 Concluding Remarks	106
8.7 Ductile Moment-Resisting Space Frame Response.....	107
8.8 Brace Behavior	108
8.8.1 Buckling Strength	108
8.8.2 Implications for Current Design Practice	109
8.9 Rational Design of the K-braced Dual System	110
IX. CORRELATION OF THE MODEL TEST RESULTS	112
9.1 Introductory Remarks	112
9.2 Prediction and Correlation of the Model Seismic Response	112
9.2.1 Introductory Remarks	112
9.2.2 Model 1 Correlation	114
9.2.3 Model 2 Correlation	121
9.2.4 Concluding Remarks	122
9.3 Correlation of the Model and the Prototype Test Results	123
9.3.1 Introductory Remarks	123
9.3.2 Serviceability Limit State Tests	124
9.3.3 Damageability Limit State Tests	124
9.3.4 Collapse Limit State Tests	125
9.3.5 Concluding Remarks	127
X. SUMMARY, CONCLUSIONS AND RECOMMENDATIONS	129
10.1 Summary	129
10.1.1 Prototype Design	129
10.1.2 Shaking Table Tests of the Model	129
10.1.3 Model and Prototype Response Comparison	132
10.1.4 Analytical Prediction	133
10.2 Conclusions	133

10.2.1 Soundness of the Prototype Design	134
10.2.2 Reliability of Earthquake Simulator Studies	134
10.2.3 Reliability of Current Analytical Prediction Methods	135
10.2.4 Seismic Resistant Design and Construction of Dual System	135
10.3 Recommendations	137
10.3.1 Areas of Future Research	137
10.3.2 Improvement in the Design of a Dual System	139
REFERENCES	141
APPENDIX A - List of Instrumentation	147
APPENDIX B - Derivation of Energy Equation	150
TABLES	153
FIGURES	176

LIST OF TABLES

TABLE 2.1	TEST STRUCTURE MEMBER SIZE
TABLE 2.2	PROTOTYPE DESIGN GRAVITY DEAD LOADS
TABLE 2.3	COMPARISON OF PROTOTYPE FLOOR WEIGHTS
TABLE 2.4	UBC LATERAL LOAD DISTRIBUTION FOR PROTOTYPE DESIGN
TABLE 2.5	PROTOTYPE MATERIAL STRENGTH
TABLE 3.1	PROTOTYPE FLEXIBILITY MATRIX
TABLE 3.2	PROTOTYPE PERIODS, MODE SHAPES AND DAMPING RATIOS
TABLE 4.1	SIMILITUDE LAW
TABLE 4.2	COMPARISON OF STEEL GIRDER SECTIONAL PROPERTIES (COMPOSITE GIRDER TESTS)
TABLE 4.3	DISTRIBUTION OF THE MODEL WEIGHT
TABLE 5.1	ANALYTICAL PREDICTION OF THE MODEL FLEXIBILITY AND STIFFNESS
TABLE 5.2	ANALYTICAL PREDICTION OF THE MODEL FREQUENCIES AND MODE SHAPES
TABLE 5.3	RESULTS OF FLEXIBILITY TEST OF FRAME A AND C (UNBRACED MODEL WITHOUT COMPOSITE SLAB)
TABLE 5.4	RESULTS OF FLEXIBILITY TEST OF FRAME B (UNBRACED MODEL WITHOUT COMPOSITE SLAB)
TABLE 5.5	RESULTS OF FLEXIBILITY TEST OF FRAME A AND C (BRACED MODEL WITHOUT COMPOSITE SLAB)
TABLE 5.6	RESULTS OF FLEXIBILITY TEST OF FRAME B (BRACED MODEL WITHOUT COMPOSITE SLAB)
TABLE 5.7	RESULTS OF FLEXIBILITY TEST OF THE MODEL WITHOUT AUXILIARY MASS
TABLE 5.8	RESULTS OF FLEXIBILITY TEST OF THE MODEL WITH AUXILIARY MASS
TABLE 5.9	COMPARISON OF PROTOTYPE AND MODEL PERIODS AND EQUIVALENT VISCOUS DAMPING RATIOS
TABLE 5.10	VARIATION OF NATURAL FREQUENCY OF THE MODEL BEFORE SHAKING TABLE TEST
TABLE 6.1	SHAKING TABLE TEST PROGRAM OF THE MODEL
TABLE 7.1	VARIATION OF MECHANICAL CHARACTERISTICS OF THE MODEL DURING SHAKING TABLE TESTS

TABLE 7.2	MODEL MO-6.3 TEST RESPONSE ENVELOPES
TABLE 7.3	MODEL MO-33 TEST RESPONSE ENVELOPES
TABLE 7.4	MODEL MO-65 TEST RESPONSE ENVELOPES
TABLE 7.5	MODEL MAXIMUM BRACE CURVATURES AND DOMINANT BUCKLING PLANE (MO-65 TEST)
TABLE 7.6	MODEL MO-POST1 TEST RESPONSE ENVELOPES
TABLE 8.1	COMPARISON OF MODEL BRACE BUCKLING LOADS
TABLE 8.2	MODEL BRACE P_{cr}/P_y AND B/t RATIOS
TABLE 9.1	PARTICIPATION FACTORS OF THE MODEL

LIST OF FIGURES

- FIG. 1.1 BRACED STEEL FRAMES
- FIG. 1.2 HYSTERESIS BEHAVIOR OF CONCENTRICALLY X-BRACED FRAME
- FIG. 2.1 TYPICAL PLAN AND ELEVATIONS OF THE PROTOTYPE
- FIG. 2.2 PROTOTYPE CONNECTION DETAILS IN THE BRACED BAY
- FIG. 2.3 COMPOSITE GIRDER CROSS SECTION(FRAME B)
- FIG. 2.4 EFFECTIVE WIDTH OF COMPOSITE GIRDER
- FIG. 2.5 UBC DESIGN STRESS RATIO
- FIG. 3.1 MATHEMATICAL MODEL OF THE PROTOTYPE STRUCTURE
- FIG. 3.2 PROTOTYPE FLEXIBILITY AND MODE SHAPES
- FIG. 3.3 MATHEMATICAL MODEL OF COLUMN
- FIG. 3.4 GIRDER-COLUMN JOINT PANEL ZONE
- FIG. 3.5 BRACE BUCKLING MODEL
- FIG. 3.6 ENVELOPES OF PROTOTYPE ROOF DRIFT INDEX VERSUS BASE SHEAR RATIO
- FIG. 3.7 STEP-BY-STEP ANALYSIS HINGE FORMATION SEQUENCE
- FIG. 3.8 POSSIBLE SWAY MECHANISMS
- FIG. 3.9 KINEMATICALLY ADMISSIBLE FIELDS
- FIG. 3.10 1978 MIYAGI-KEN-OKI EARTHQUAKE RECORD (N-S)
- FIG. 3.11 ELASTIC-3 TEST RELATIVE DISPLACEMENT TIME HISTORY
- FIG. 3.12 ELASTIC-3 TEST INTER-STORY DRIFT TIME HISTORY
- FIG. 3.13 ELASTIC-3 TEST STORY SHEAR TIME HISTORY
- FIG. 3.14 MODERATE TEST RELATIVE DISPLACEMENT TIME HISTORY
- FIG. 3.15 MODERATE TEST INTER-STORY DRIFT TIME HISTORY
- FIG. 3.16 MODERATE TEST STORY SHEAR TIME HISTORY
- FIG. 3.17 DAMAGE PATTERN AFTER MODERATE TEST
- FIG. 3.18 INTER-STORY DRIFT VERSUS STORY SHEAR CURVES DURING THE MODERATE TEST
- FIG. 3.19 FIRST STORY BRACE-GIRDER CONNECTING PANEL ZONE SHEAR DEFORMATION VERSUS SHEAR FORCE CURVE (MODERATE TEST)
- FIG. 3.20 FINAL TEST RELATIVE DISPLACEMENT TIME HISTORY
- FIG. 3.21 FINAL TEST INTER-STORY DRIFT TIME HISTORY
- FIG. 3.22 FINAL TEST STORY SHEAR TIME HISTORY

- FIG. 3.23 DAMAGE PATTERN AFTER MODERATE TEST
- FIG. 4.1 LIMITATION ON DYNAMIC PERFORMANCE OF THE SHAKING TABLE
- FIG. 4.2 TYPICAL CONNECTION DETAILS OF THE MODEL
- FIG. 4.3 MEAN STEEL STRESS-STRAIN RELATIONSHIPS
- FIG. 4.4 INDENTATION PATTERN IN THE PROTOTYPE METAL DECK
- FIG. 4.5 MODEL AND SCALED PROTOTYPE METAL DECK PROFILES
- FIG. 4.6 MODEL CONCRETE STRESS-STRAIN RELATIONSHIPS
- FIG. 4.7 DEFINITION OF RIB HEIGHT AND WIDTH FOR CALCULATING REDUCTION FACTOR
- FIG. 4.8 PORTION OF COMPOSITE GIRDER SIMULATED
- FIG. 4.9 COMPOSITE GIRDER TEST SETUP
- FIG. 4.10 INSTRUMENTATION OF COMPOSITE GIRDER
- FIG. 4.11 LOAD-TIP DEFLECTION CURVE OF STEEL GIRDER (SG)
- FIG. 4.12 LONGITUDINAL GIRDER-TO-COLUMN CONNECTION USED IN THE COMPOSITE GIRDER TESTS
- FIG. 4.13 LOAD-TIP DEFLECTION CURVE OF CG1 AND CG1R
- FIG. 4.14 LOAD-SLIP CURVE OF CG1R (LVDT8)
- FIG. 4.15 LOAD-TIP DEFLECTION CURVE OF CG3
- FIG. 4.16 LOAD-SLIP CURVE OF CG3 (LVDT8)
- FIG. 4.17 LOAD-BEAM FLANGE STRAIN CURVE OF CG3
- FIG. 4.18 PLASTIC HINGE ROTATION OF STEEL GIRDER AND COMPOSITE GIRDER
- FIG. 4.19 MOMENT-CURVATURE RELATIONSHIP
- FIG. 4.20 CONCRETE STRAIN DISTRIBUTION OF CG4 (4.5 INCHES FROM COLUMN FACE)
- FIG. 4.21 ACCUMULATED RESIDUAL DISPLACEMENT VERSUS ACCUMULATED ENERGY DISSIPATION CURVE
- FIG. 4.22 AUXILIARY LEAD BRICKS ATTACHED TO FLOORS
- FIG. 4.23 TEST STRUCTURE WITH REFERENCE FRAME
- FIG. 4.24 STRAIN GAGE INSTRUMENTATION OF THE COLUMNS
- FIG. 4.25 INSTRUMENTATION OF THE TEST MODEL
- FIG. 4.26 SHAKING TABLE SYSTEM BLOCK DIAGRAM
- FIG. 5.1 MODEL ANALYTICAL AND MEASURED MODE SHAPES
- FIG. 5.2 TEST SETUP - STATIC FLEXIBILITY TESTS
- FIG. 5.3 PROCEDURE FOR OBTAINING THE DAMPING COEFFICIENT AND NATURAL PERIOD FROM FREE VIBRATION TESTS

- FIG. 5.4 SHAKER FOR FORCED VIBRATION TEST
- FIG. 5.5 FREE VIBRATION FOURIER AMPLITUDE SPECTRA OF ROOF ACCELERATION (UNBRACED MODEL W/OUT SLAB)
- FIG. 5.6 FREE VIBRATION FOURIER AMPLITUDE SPECTRA OF ROOF ACCELERATION (BRACED MODEL W/OUT SLAB)
- FIG. 5.7 AMBIENT VIBRATION FOURIER AMPLITUDE SPECTRA OF ROOF VELOCITY (MODEL W/OUT AUXILIARY MASS)
- FIG. 5.8 FREE VIBRATION FOURIER AMPLITUDE SPECTRA OF ROOF ACCELERATION (MODEL W/OUT AUXILIARY MASS)
- FIG. 5.9 FORCED VIBRATION TESTS FREQUENCY RESPONSE CURVES (TEST MODEL WITH SLABS BUT W/OUT LEAD PIGS)
- FIG. 5.10 FLEXIBILITY TESTS DISPLACEMENT PROFILES (TEST MODEL WITH SLABS, WITH OR W/OUT LEAD PIGS)
- FIG. 5.11 AMBIENT VIBRATION FOURIER AMPLITUDE SPECTRA OF ROOF VELOCITY (MODEL WITH AUXILIARY MASS)
- FIG. 5.12 FREE VIBRATION FOURIER AMPLITUDE SPECTRA OF ROOF ACCELERATION (MODEL WITH AUXILIARY MASS)
- FIG. 5.13 FORCED VIBRATION TESTS FREQUENCY RESPONSE CURVES (TEST MODEL WITH SLABS AND LEAD PIGS)
- FIG. 5.14 COMPARISON OF PROTOTYPE AND MODEL FLEXIBILITY TESTS : DISPLACEMENT PROFILES
- FIG. 5.15 COMPARISON OF PROTOTYPE AND MODEL MEASURED MODE SHAPES
- FIG. 6.1 PREDICTED ROOF DRIFT INDEX VERSUS BASE SHEAR CURVES OF THE MODEL AND THE PROTOTYPE
- FIG. 6.2 STEP-BY-STEP ANALYSIS HINGE FORMATION OF BRACE BUCKLING/YIELDING SEQUENCE
- FIG. 6.3 SCALED SHAKING TABLE INPUT MOTION AND RESPONSE SPECTRA
- FIG. 6.4 PREDICTED MODEL SEISMIC RESPONSES (65 GAL M.O. EARTHQUAKE)
- FIG. 6.5 PREDICTED MODEL SEISMIC RESPONSES (250 GAL M. O. EARTHQUAKE)
- FIG. 6.6 PREDICTED MODEL SEISMIC RESPONSES (500 GAL M.O. EARTHQUAKE)
- FIG. 6.7 HIGH FREQUENCY NOISE FILTERING (ORMSBY FILTER)
- FIG. 6.8 LOW FREQUENCY NOISE FILTERING
- FIG. 6.9 SIGN CONVENTION

- FIG. 6.10 COMPARISON OF BASE SHEAR FROM TWO METHODS
- FIG. 6.11 FIRST STORY COLUMN END MOMENT EXTRAPOLATION
- FIG. 6.12 MEMBER DESIGNATION
- FIG. 7.1 VARIATION OF PERIODS AND DAMPING RATIOS THROUGHOUT THE SHAKING TABLE TESTS
- FIG. 7.2 MODEL BASE SHEAR AND OVERTURNING MOMENT VERSUS ROOF DRIFT INDEX ENVELOPES
- FIG. 7.3 MEASURED SHAKING TABLE HORIZONTAL MOTION AND RESPONSE SPECTRA (MO-6.3 TEST)
- FIG. 7.4 MO-6.3 TEST RELATIVE DISPLACEMENT TIME HISTORIES
- FIG. 7.5 MO-6.3 TEST INTER-STORY DRIFT TIME HISTORIES
- FIG. 7.6 STORY SHEAR (TOTAL AND BRACE COMPONENT) TIME HISTORIES OF MO-6.3 TEST
- FIG. 7.7 MO-6.3 TEST LATERAL INERTIA FORCE TIME HISTORIES
- FIG. 7.8 MO-6.3 TEST BASE OVERTURNING MOMENT TIME HISTORIES
- FIG. 7.9 COLUMN $1C_{Bl}$: CHANGE IN AXIAL FORCE AND END MOMENT TIME HISTORIES (MO-6.3 TEST)
- FIG. 7.10 MO-6.3 TEST INTER-STORY DRIFT VERSUS STORY SHEAR CURVES
- FIG. 7.11 MO-6.3 TEST RESPONSE ENVELOPES
- FIG. 7.12 MO-6.3 TEST RESPONSE PROFILES AT MAXIMUM RESPONSES
- FIG. 7.13 MO-6.3 TEST FIRST STORY COLUMN AXIAL FORCE VERSUS END MOMENT INTERACTION CURVES
- FIG. 7.14 MO-6.3 TEST ENERGY TIME HISTORIES
- FIG. 7.15 MEASURED SHAKING TABLE HORIZONTAL MOTIONS AND RESPONSE SPECTRA (MO-33 TEST)
- FIG. 7.16 MO-33 TEST RELATIVE DISPLACEMENT TIME HISTORIES
- FIG. 7.17 MO-33 TEST INTER-STORY DRIFT TIME HISTORIES
- FIG. 7.18 STORY SHEAR (TOTAL AND BRACE COMPONENT) TIME HISTORIES OF MO-33 TEST
- FIG. 7.19 MO-33 TEST LATERAL INERTIA FORCE TIME HISTORIES
- FIG. 7.20 MO-33 TEST $\frac{V^{BRACE}}{V^{TOTAL}}$ RATIO
- FIG. 7.21 MO-33 TEST BASE OVERTURNING MOMENT TIME HISTORIES
- FIG. 7.22 MO-33 TEST BRACE 9 AXIAL STRAIN TIME HISTORIES
- FIG. 7.23 MO-33 TEST INTER-STORY DRIFT VERSUS TOTAL STORY SHEAR CURVES

- FIG. 7.24 MO-33 TEST FIFTH STORY INTER-STORY DRIFT VERSUS STORY SHEAR CURVES
- FIG. 7.25 MO-33 TEST RESPONSE ENVELOPES
- FIG. 7.26 MO-33 TEST RESPONSE PROFILES AT MAXIMUM RESPONSES
- FIG. 7.27 MO-33 TEST FIRST STORY COLUMN AXIAL FORCE VERSUS END MOMENT INTERACTION CURVES
- FIG. 7.28 MO-33 TEST ENERGY TIME HISTORIES
- FIG. 7.29 MEASURED SHAKING TABLE HORIZONTAL MOTIONS AND RESPONSE SPECTRA (MO-65 TEST)
- FIG. 7.30 MO-65 TEST RELATIVE DISPLACEMENT TIME HISTORIES
- FIG. 7.31 MO-65 TEST INTER-STORY DRIFT TIME HISTORIES
- FIG. 7.32 STORY SHEAR (TOTAL AND BRACE COMPONENT) TIME HISTORIES OF MO-65 TEST
- FIG. 7.33 MO-65 TEST LATERAL INERTIA FORCE TIME HISTORIES
- FIG. 7.34 MO-65 TEST $\frac{V^{\text{BRACE}}}{V^{\text{TOTAL}}}$ RATIO
- FIG. 7.35 MO-65 TEST BRACE 9 AXIAL STRAIN TIME HISTORIES
- FIG. 7.36 MO-65 TEST BASE OVERTURNING MOMENT TIME HISTORIES
- FIG. 7.37 MO-65 TEST INTER-STORY DRIFT VERSUS TOTAL STORY SHEAR (V^{TOTAL}) CURVES
- FIG. 7.38 MO-65 TEST INTER-STORY DRIFT VERSUS STORY COLUMN SHEAR (V^{MRSF}) CURVES
- FIG. 7.39 MO-65 TEST INTER-STORY DRIFT VERSUS STORY BRACE SHEAR (V^{BRACE}) CURVES
- FIG. 7.40 MO-65 TEST RESPONSE ENVELOPES
- FIG. 7.41 MO-65 TEST RESPONSE PROFILES AT MAXIMUM RESPONSES
- FIG. 7.42 BRACE 2 P- Δ CURVE (MO-65 TEST)
- FIG. 7.43 BRACE 4 P- Δ CURVE (MO-65 TEST)
- FIG. 7.44 BRACE BRACE 6 P- Δ CURVE (MO-65 TEST)
- FIG. 7.45 BRACE BRACE 8 P- Δ CURVE (MO-65 TEST)
- FIG. 7.46 COMPARISON OF V^{BRACE} TIME HISTORIES (MO-65 TEST)
- FIG. 7.47 TYPICAL RESIDUAL STRESS DISTRIBUTION IN TUBE
- FIG. 7.48 BRACE 1 SECTIONAL CURVATURE TIME HISTORIES (MO-65 TEST)
- FIG. 7.49 TYPICAL MODEL BRACE SECTION
- FIG. 7.50 MO-65 TEST FIRST STORY COLUMN AXIAL FORCE VERSUS END MOMENT INTERACTION CURVES

- FIG. 7.51 MO-65 TEST ENERGY TIME HISTORIES
- FIG. 7.52 MO-TEST HYSTERETIC DISSIPATED ENERGY DISTRIBUTION
- FIG. 7.53 MO-65 TEST SECOND FLOOR BRACE-GIRDER JOINT VERTICAL DISPLACEMENT TIME HISTORY (MO-65 TEST)
- FIG. 7.54 MO-65 TEST SECOND FLOOR BRACE-GIRDER JOINT VERTICAL DISPLACEMENT-FIRST STORY SHEAR CURVE
- FIG. 7.55 MEASURED SHAKING TABLE HORIZONTAL MOTIONS AND RESPONSE SPECTRA (MO-POST1 TEST)
- FIG. 7.56 MO-POST1 TEST RELATIVE DISPLACEMENT TIME HISTORIES
- FIG. 7.57 MO-POST1 TEST INTER-STORY DRIFT TIME HISTORIES
- FIG. 7.58 STORY SHEAR (TOTAL AND BRACE COMPONENT) TIME HISTORIES OF MO-POST1 TEST
- FIG. 7.59 MO-POST1 TEST LATERAL INERTIA FORCE TIME HISTORIES
- FIG. 7.60 MO-POST1 TEST BASE OVERTURNING MOMENT TIME HISTORIES
- FIG. 7.61 MO-POST1 TEST INTER-STORY DRIFT VERSUS TOTAL STORY SHEAR (V^{TOTAL}) CURVES
- FIG. 7.62 MO-POST1 TEST INTER-STORY DRIFT VERSUS STORY COLUMN SHEAR (V^{MRSF}) CURVES
- FIG. 7.63 MO-POST1 TEST INTER-STORY DRIFT VERSUS STORY BRACE SHEAR (V^{BRACE}) CURVES
- FIG. 7.64 MO-POST1 TEST RESPONSE ENVELOPES
- FIG. 7.65 MO-POST1 TEST RESPONSE PROFILES AT MAXIMUM RESPONSES
- FIG. 7.66 MO-POST1 TEST ENERGY TIME HISTORIES
- FIG. 7.67 MO-POST1 TEST HYSTERETIC DISSIPATED ENERGY DISTRIBUTION
- FIG. 7.68 CONCRETE SLAB CRACK PATTERN AFTER SHAKING TABLE TESTS
- FIG. 8.1 ENVELOPES OF INTER-STORY DRIFT INDEX VERSUS STORY SHEAR
- FIG. 8.2 ENVELOPES OF ROOF DRIFT INDEX VERSUS BASE SHEAR RATIO
- FIG. 8.3 ENVELOPES OF CRITICAL INTER-STORY DRIFT INDEX VERSUS BASE SHEAR RATIO
- FIG. 8.4 COMPARISON OF 5% DAMPED LERS, ATC LEDRS AND MEASURED MODEL STRENGTH
- FIG. 8.5 COMPARISON OF LINEAR ELASTIC RESPONSE SPECTRA OF THE MO-65 TEST, 1985 MEXICO AND CHILEAN EARTHQUAKES AND THE ATC LINEAR ELASTIC DESIGN RESPONSE SPECTRA

- FIG. 8.6 STRAIN RATE EFFECT ON THE LOWER YIELD STRESS OF STRUCTURAL STEEL
- FIG. 8.7 ENVELOPES OF PSA/G VERSUS MAXIMUM BASE SHEAR AND MAXIMUM INPUT ENERGY
- FIG. 8.8 ENVELOPES OF PSV VERSUS INPUT ENERGY EQUIVALENT VELOCITY
- FIG. 8.9 NORMALIZED $\sum M_i \ddot{V}_i^T$ AND INPUT POWER TIME HISTORIES
- FIG. 8.10 TOTAL INPUT ENERGY SPECTRA FOR 2% DAMPED SINGLE-DEGREE-OF-FREEDOM SYSTEM SUBJECTED TO MEASURED MO-65 TEST TABLE HORIZONTAL ACCELERATION
- FIG. 8.11 INPUT ENERGY EQUIVALENT VELOCITY AND PSV SPECTRA FOR THE MEASURED MO-65 TEST TABLE HORIZONTAL ACCELERATION
- FIG. 8.12 MODAL DISPLACEMENT ($Y_i(T)$) TIME HISTORIES (MO-6.3 TEST)
- FIG. 8.13 COMPARISON OF VISCOUS DAMPED ENERGY (MO-6.3 TEST)
- FIG. 8.14 COMPARISON OF VISCOUS DAMPED ENERGY (MO-33 TEST)
- FIG. 8.15 MO-65 TEST STORY COLUMN SHEAR (V^{MRSF}) ENVELOPES
- FIG. 8.16 SHEAR FORCE DISTRIBUTION AT MAXIMUM V^{BRACE}
- FIG. 8.17 DAMAGED BRACES AFTER THE SHAKING TABLE TESTS
- FIG. 9.1 MATHEMATICAL MODELS OF THE TEST STRUCTURE (FRAME A AND FRAME C NOT SHOWN)
- FIG. 9.2 CORRECTION OF TABLE PITCHING RIGID BODY MOTION COMPONENT FROM THE LATERAL DISPLACEMENT
- FIG. 9.3 MEASURED TABLE PITCHING MOTION AND FOURIER AMPLITUDE SPECTRA OF MEASURED TABLE ACCELERATIONS (MO-6.3 TEST)
- FIG. 9.4 COMPARISON OF 0.3-SCALE MODEL TEST AND ANALYTICAL LATERAL DISPLACEMENT RESPONSES (MO-6.3 TEST)
- FIG. 9.5 COMPARISON OF 0.3-SCALE MODEL TEST AND ANALYTICAL STORY SHEAR RESPONSES (MO-6.3 TEST)
- FIG. 9.6 COMPARISON OF 0.3-SCALE MODEL TEST AND ANALYTICAL RESPONSE BY IGNORING TABLE PITCHING MOTION (MO-6.3 TEST)
- FIG. 9.7 MEASURED TABLE PITCHING MOTIONS (MO-33 TEST)
- FIG. 9.8 COMPARISON OF 0.3-SCALE MODEL TEST AND ANALYTICAL LATERAL DISPLACEMENT RESPONSES (MO-33 TEST)
- FIG. 9.9 COMPARISON OF 0.3-SCALE MODEL TEST AND ANALYTICAL STORY SHEAR RESPONSES (MO-33 TEST)

- FIG. 9.10 MEASURED FOUNDATION VERTICAL MOVEMENTS AT COLUMN 1C_{B2}
- FIG. 9.11 COLUMN 1C_{B2} BASE MOMENT AND FOUNDATION ROTATION (MO-33 TEST)
- FIG. 9.12 COLUMN 1C_{B2} : MEASURED FOUNDATION ROTATION VERSUS COLUMN END MOMENT CURVE (MO-33 TEST)
- FIG. 9.13 MEASURED TABLE PITCHING MOTIONS (MO-33 TEST)
- FIG. 9.14 COMPARISON OF 0.3-SCALE MODEL TEST AND ANALYTICAL LATERAL DISPLACEMENT RESPONSES (MO-65 TEST)
- FIG. 9.15 COMPARISON OF 0.3-SCALE MODEL TEST AND ANALYTICAL STORY SHEAR RESPONSES (MO-65 TEST)
- FIG. 9.16 COLUMN 1C_{B2} : MEASURED FOUNDATION ROTATION VERSUS COLUMN END MOMENT CURVE (MO-65 TEST)
- FIG. 9.17 MODEL 2 METHOD : COMPARISON OF MODEL TEST AND ANALYTICAL LATERAL DISPLACEMENT RESPONSE (MO-6.3 TEST)
- FIG. 9.18 MODEL 2 METHOD : COMPARISON OF MODEL TEST AND ANALYTICAL STORY SHEAR RESPONSE (MO-6.3 TEST)
- FIG. 9.19 MODEL 2 METHOD : COMPARISON OF MODEL TEST AND ANALYTICAL LATERAL DISPLACEMENT RESPONSE (MO-33 TEST)
- FIG. 9.20 MODEL 2 METHOD : COMPARISON OF MODEL TEST AND ANALYTICAL STORY SHEAR RESPONSE (MO-33 TEST)
- FIG. 9.21 MODEL 2 METHOD : COMPARISON OF MODEL TEST AND ANALYTICAL LATERAL DISPLACEMENT RESPONSE (MO-65 TEST)
- FIG. 9.22 MODEL 2 METHOD : COMPARISON OF MODEL TEST AND ANALYTICAL STORY SHEAR RESPONSE (MO-65 TEST)
- FIG. 9.23 PROTOTYPE AND MODEL COMPARISON OF GROUND MOTION USED IN SERVICEABILITY LIMIT STATE TESTS
- FIG. 9.24 COMPARISON OF PROTOTYPE AND MODEL LATERAL DISPLACEMENT RESPONSES IN SERVICEABILITY LIMIT STATE TESTS
- FIG. 9.25 COMPARISON OF PROTOTYPE AND MODEL STORY SHEAR RESPONSES IN SERVICEABILITY LIMIT STATE TESTS
- FIG. 9.26 PROTOTYPE ELASTIC-3 TEST SECOND FLOOR BRACE-GIRDER PANEL ZONE RESPONSE
- FIG. 9.27 PROTOTYPE AND MODEL COMPARISON OF GROUND MOTION USED IN DAMAGEABILITY LIMIT STATE TESTS
- FIG. 9.28 COMPARISON OF PROTOTYPE AND MODEL LATERAL DISPLACEMENT RESPONSES IN DAMAGEABILITY LIMIT STATE TESTS
- FIG. 9.29 COMPARISON OF PROTOTYPE AND MODEL INTER-STORY DRIFT RESPONSES IN DAMAGEABILITY LIMIT STATE TESTS

- FIG. 9.30 COMPARISON OF PROTOTYPE AND MODEL STORY SHEAR RESPONSES IN DAMAGEABILITY LIMIT STATE TESTS
- FIG. 9.31 DAMAGEABILITY LEVEL TEST INTER-STORY DRIFT VERSUS TOTAL STORY SHEAR CURVES
- FIG. 9.32 PROTOTYPE AND MODEL COMPARISON OF GROUND MOTION USED IN COLLAPSE LIMIT STATE TESTS
- FIG. 9.33 COMPARISON OF PROTOTYPE AND MODEL LATERAL DISPLACEMENT RESPONSES IN COLLAPSE LIMIT STATE TESTS
- FIG. 9.34 COMPARISON OF PROTOTYPE AND MODEL INTER-STORY DRIFT RESPONSES IN COLLAPSE LIMIT STATE TESTS
- FIG. 9.35 COMPARISON OF PROTOTYPE AND MODEL STORY SHEAR RESPONSES IN COLLAPSE LIMIT STATE TESTS
- FIG. 9.36 COMPARISON OF PROTOTYPE AND MODEL BRACE HYSTERETIC RESPONSES IN COLLAPSE LIMIT STATE TESTS
- FIG. 9.37 COMPARISON OF PROTOTYPE AND MODEL COLLAPSE LIMIT STATE TESTS INTER-STORY-DRIFT VERSUS TOTAL STORY SHEAR CURVES
- FIG. 9.38 COMPARISON OF PROTOTYPE AND MODEL COLLAPSE LIMIT STATE TESTS INTER-STORY-DRIFT VERSUS STORY COLUMN SHEAR CURVES
- FIG. 9.39 COMPARISON OF PROTOTYPE AND MODEL COLLAPSE LIMIT STATE TESTS HYSTERETIC ENERGY DISTRIBUTION

I. INTRODUCTION

1.1 Introductory Remarks

The research reported herein was conducted at the University of California, Berkeley, as part of the Steel Structure Phase of the U.S.-Japan Cooperative Research Program Utilizing Large-Scale Testing Facilities [1]. The overall objective of the program is to improve seismic safety practices through studies to determine the relation between full-scale tests, small-scale tests, component tests and analytical studies. In addition, the program has been designed to represent building structural systems as realistically as possible, to represent the best design and construction practice in current use in both countries and finally, to check the validity of newly developed earthquake-resistant design procedures.

It is commonly accepted in the earthquake-resistant design of buildings that the structure should remain elastic and that non-structural components should not be damaged during events which have a moderate to high frequency of occurrence. This is the serviceability requirement which is generally met by supplying the structure with sufficient strength to avoid yielding under service loads and sufficient initial stiffness to obtain acceptable (non-damaging) inter-story drifts. The moment-resisting space frame (MRSF) is known to exhibit large deformability and is thus too flexible for tall steel building construction. Therefore bracing, which provides considerable lateral stiffness to the structure, is used in conjunction with traditional MRSFs to prevent excessive deflection under the serviceability conditions; concentrically K-braced framing is a very popular structural system for tall steel buildings. The concentrically K-braced frame (CBF) offers a number of advantages with respect to the conventional X-braced frame, one of these is the added planning flexibility available to architects and interior

designers.

The other requirement of earthquake-resistant design is that the structure should not collapse during the most severe earthquake that is expected. In addition to supplying sufficient strength, the survival of the structure is strongly dependent upon the energy absorption and energy dissipation capacities of the critical structural members. It is well-known that concentrically braced frames do not exhibit good energy dissipation characteristics because of the buckling of the braces; this leads to pinched hysteresis loops. This undesirable behavior has been recognized by researchers and by the profession.

By virtue of their greater lateral rigidity, braced structures usually attract higher seismic forces than those of moment-resisting space frames [2]. Standard codes [3,4] specify higher lateral forces for the design of these braced systems than for MRSF as well as providing stringent requirements for the design of the bracing. As a result, several alternative braced frame designs have been proposed. Reference 5 summarizes a survey conducted to evaluate the performance of different steel braced frame structures under cyclic loading; the eccentrically braced frame (EBF) was shown to be a very promising and efficient structural system. The braces in the eccentrically braced frame are designed to avoid buckling, and the shear links behave like a 'structural fuse'. This system is characterized by its high lateral stiffness and significant, yet stable, energy dissipation capacity through its yielding in shear [6].

Figure 1.1 depicts the CBF and EBF framing systems. The standard codes [3,4], in addition to specifying higher lateral forces for braced frames, require that a secondary system consisting of moment-resisting frames resist the lateral forces once the braces have buckled and that the compressive strength of braces shall not be less than 50 percent of their required tensile strength [4]. This precludes the use of slender X-bracing in concentrically braced frames for resisting seismic loads. A typical load-deflection curve of a concentrically X-braced frame is shown in Fig 1.2 [2]. Loading in a given direction

elongates the tension diagonal; upon reapplication of the lateral load (following loading in the opposite direction), the elongated diagonal member offers no resistance to the lateral load until the residual strain is overcome and the member elongated further.

Many component (elements or subassemblages) tests have been conducted to study the cyclic responses of braces [7] and shear links [6]. Most of these studies have been performed in a quasi-static manner and very few tests have been undertaken on complete structures. In accordance with recommendations of the U.S.-Japan Cooperative Research Planning Group [1], a full-scale six-story braced steel test structure was designed, constructed and tested at the large-scale testing facilities of the Building Research Institute (BRI) at Tsukuba, Japan.

After analyzing the lateral resistance of the test structure and the capacity of the earthquake simulator facility at Richmond Field Station of the University of California, Berkeley, a length scale factor of 0.3048 was selected to construct the largest replica with artificial mass simulation of the prototype that could be tested.

In this report, the structure tested in the BRI is designated as the **prototype** and the structure tested at U.C. Berkeley is designated as the **model**.

The U.C. Berkeley research program was divided into two phases; the first involved the testing of a concentrically braced frame and the second involved the testing of an eccentrically braced frame. This report documents the results obtained in the first phase.

1.2 Objectives

The main objectives of the first phase studies reported herein were:

- (1) to review and improve, if necessary, the design of the test structure;
- (2) to determine the reliability of the experimental structural analysis based on tests conducted on the Berkeley earthquake simulator and to evaluate the correlation of the experimental results with the prototype test results;

- (3) to evaluate the reliability of the available linear and nonlinear structural analysis computer programs for predicting the seismic performance of buildings;
- (4) to evaluate the results as they pertain to the state-of-the-art and of current practice in earthquake-resistant design and construction of braced steel structures.

1.3 Scope

To achieve these objectives, the following integrated analytical studies and experimental tests have been conducted:

- (1) A review of the design of the prototype test structure based on the seismic provisions of the 1985 Uniform Building Code [3] (hereafter denoted as UBC).
- (2) Analytical studies using available linear and nonlinear computer programs to predict the prototype response to static and dynamic excitations. These studies provided the basis for the selection of the scale of the model. The analytical response of the model was then compared with the experimental response of the prototype.
- (3) Preliminary static and dynamic experiments to determine the dynamic characteristics of the model.
- (4) Earthquake simulator tests of the model under different intensities of ground motion.
- (5) Correlation studies of the experimental responses of the prototype and the model and of the experimental and analytically predicted responses.
- (6) Assessment of the implications of these results regarding the state-of-the-art, and particularly the current practice of earthquake-resistant design and construction of dual systems with concentrically braced steel frames.
- (7) Formulation of recommendations for the improvement of U.S. seismic codes and for research needs to advance the state-of-the-art in analysis and design of dual

systems with braced steel frames.

The soundness of the prototype design and its predicted dynamic behavior are discussed in Chapters 2 and 3. Selection of the scale factor, design, construction and instrumentation of the reduced scale model are described in Chapter 4. In Chapter 5, results of tests to determine the initial mechanical characteristics of the reduced scale model are presented and compared with the analytically predicted results.

Chapter 6 discusses the experimental program, earthquake simulator tests, data acquisition and processing. The results obtained in four of the tests are described in Chapter 7. Further evaluation of the test results and their implications regarding the states of the practice and art of earthquake-resistant design are discussed in Chapter 8. Correlation of the reduced scale model test results with the analytically predicted responses and results of the full-scale tests (the Japan part of the program) are discussed in Chapter 9.

In Chapter 10, the primary results are summarized and pertinent conclusions drawn. Recommendations for improving the state-of-the-art and current practice of earthquake-resistant design of concentrically K-braced structures are formulated; future research needs are outlined.

II. PROTOTYPE DESIGN REVIEW

2.1 Introductory Remarks

A six-story steel braced frame office building was recommended [1] for the purpose of comparing actual full-scale building behavior with scaled model behavior. The prototype test structure is described first; the soundness of the design will be reviewed in accordance with the 1985 UBC seismic design provisions.

2.2 Description of the Prototype Structure

2.2.1 Structural System

The prototype building was a six-story steel structure representing a portion of a typical office building. It consisted of a two bay by two bay structure with the following structural components (Fig. 2.1):

- (1) three frames in the longitudinal (testing) direction;
- (2) three frames in the transverse direction;
- (3) composite floor system.

In the longitudinal direction the two exterior frames, designated as Frame A and Frame C, were of ductile moment-resisting type. The central longitudinal frame, designated as Frame B, was braced in the 1-2 bay with concentric K-bracing. The two exterior frames, Frame 1 and Frame 3, were diagonally X-braced in the transverse direction to stiffen the structure against torsional motion.

The composite floor system comprised the following:

- (1) steel decking;

- (2) headed studs as shear connectors;
- (3) steel reinforcement in the form of wire mesh;
- (4) cast-in-place lightweight concrete.

2.2.2 Member Sizes, Materials and Connections

The structural member sizes are shown in Table 2.1. The structural steels used in the prototype were:

- (1) Girders, beams and columns: Wide flange shape ASTM-A36 steel. In Frames A, B and C, all girder to column connections were moment connections.
- (2) Longitudinal concentric K-braces: Square tube section ASTM A500 Grade B steel.
- (3) Transverse concentric X-braces: Double angles with equal legs ASTM A500 Grade B steel. The girders were connected to the columns by shear connections, i.e., AISC Type 2 Framing.

Typical details of the brace-girder joint connections are shown in Fig. 2.2.

2.3 Review of the Prototype Design

2.3.1 General

The prototype was designed [8] to satisfy the requirements of both the 1979 Uniform Building Code (U.S.A.) and the 1981 Japanese Aseismic Design Code. Since the design requirements in the two Codes are significantly different, a compromise had to be achieved. The primary differences between these two codes are: (i) the value of the seismic lateral load coefficient, C_s ; (ii) the manner of computing the reactive mass (the Japanese Aseismic Design Code includes live load); and (iii) the specified live load. It is the purpose of this section to ascertain whether the prototype design satisfies the 1985 UBC earthquake-resistant design provisions.

This structure in the loading direction is classified as a UBC Type 3 structure (building with a dual lateral resisting system consisting of a ductile moment-resisting

space frame and braced frames); the UBC specifies the following design criteria:

- (1) The moment frames and braced frames shall resist the total lateral force in accordance with their relative rigidities considering the interaction of the ductile moment-resisting space frame and the braced frames.
- (2) The braced frames acting independently of the ductile moment-resisting portions of the space frame shall resist the total lateral force.
- (3) The ductile moment-resisting space frame shall have the capacity to resist not less than 25 percent of the required lateral force.

Accordingly, the structural system factor (K) may be taken as 0.8. The UBC requires that buildings designed for a K factor equal to 0.8 include ductile moment-resisting space frames. The UBC requires that for braced frames in Seismic Zones No. 3 and No. 4, all members be designed for 1.25 times the total lateral design force (Section 2312(j)1G) and that connections be designed to develop the full capacity of the members or be based on the design forces without the one-third increase usually permitted for stresses resulting from earthquake forces. The UBC states "...necessary ductility for a ductile moment-resisting space frame shall be provided by a frame of structural steel with moment-resisting connections, which complies with Section 2722 for buildings in Seismic Zone No. 3 and No. 4..." For the structure to behave in a ductile manner, that is, to dissipate energy in a stable manner during an earthquake, each girder moment connection to a column must be capable of developing the full plastic capacity of that girder (Section 2722(d)). Therefore members in which hinges will form during inelastic deformation of the frames shall comply with the requirements for "Plastic Design" (Section 2721) [3].

2.3.2 Design Loading

2.3.2.1 Gravity Loads

Dead Load : The design gravity dead loads are summarized in Table 2.2. The exterior wall weight was included in the design for gravity loading. In order to avoid proportioning a structure too strong to be suitably damaged during testing, it was decided during the design stage to exclude the exterior wall mass from the reactive mass (i.e., the mass that can induce inertia force) calculation. The pseudo-dynamic test structure (i.e., the **prototype** designated in this report) did not include the partitions, fireproofing etc., that are listed in Table 2.2. Therefore the reactive mass used in the design process was different from the as-built mass of the prototype; this difference must be considered when interpreting the test results. Table 2.3 summarizes the weights of structure reactive masses noted above and a comparison of its second and the third columns shows that the reactive mass is increased by 28% if the exterior wall mass is included.

Live Load : 60 psf was used for the slab and floor beam design and 37 psf was used for the design of the frames (this accounts for the live load reduction permitted by the UBC). The UBC does not require that the weight (W) of the structure reactive mass, which was used in the design against seismic load, include the live load.

2.3.2.2 Equivalent Lateral Loads

The UBC suggests the following design procedure:

- (1) Estimate the total lateral force or total base shear V_b

$$V_b = C_s W = Z I K S C W . \quad (2.1)$$

The factors in this formula for the prototype structure are:

C_s = total base shear ratio = code seismic resistance coefficient,

W = weight of structure reactive mass,

Z = 1.0 for a building in Zone No. 4,

$I = 1.0$ for non-essential facilities,

$K = 0.8$ for a dual braced system,

$S = 1.5$ for T_s not properly established,

$$T = 0.05 \frac{h_n}{\sqrt{D}} = 0.05 \frac{70.5'}{\sqrt{49.2}} = 0.503 \text{ second,}$$

$$C = \frac{1}{15\sqrt{T}} = 0.094,$$

where the formula for the fundamental period T given by the UBC was used to determine the base shear; based upon these parameters:

$$V_b = 0.113 W . \quad (2.2)$$

(2) Lateral force distribution over the height.

As the concentrated lateral force F_t at the top of the structure may be considered to be zero when $T \leq 0.7$ second, the following expression was used to distribute the total lateral force over the height of the structure:

$$F_x = V_b \frac{W_x h_x}{\sum_{i=1}^n W_i h_i} \quad (2.3)$$

where F_x , W_x and h_x are the lateral force, the weight corresponding to the reactive mass of the structure and the height at level x , respectively, and W_i is the portion of W that is assigned to level i and h_i is the height above the base to level i .

2.3.3 Mechanical Characteristics of the Structural Materials

Structural Steel : ASTM A36 carbon steel was used for the columns, beams and girders and A500 Grade B steel was used for the tubular braces. The nominal and measured yield and ultimate tensile stresses of the beams, girders, columns and braces are shown in Table 2.5. The nominal yield stresses were used for the UBC design check.

Concrete Slab : The typical cross section of the floor system is shown in Fig. 2.3. The specified compressive strength of the lightweight concrete was 3.0 ksi; the 28-day compressive strength of the lightweight concrete was 4.17 ksi and the elastic modulus E_c was 2,170 ksi [9]. D6 (6 mm nominal diameter) wire mesh on a 4 inch (10 cm) pitch was used as steel reinforcement. The yield stress of the wire mesh was 57.7 ksi and the ultimate tensile stress was 79 ksi [9].

2.3.4 Design Assumptions for the Composite Girder

To check the composite girder design, the AISC Specification [10] was followed. In order to perform the analysis, the section properties of the composite section were computed in accordance with elastic theory (AISC Section 1.11.2.2). According to this Specification (Section 1.11.1), when the slab extends on both sides of the beam, the effective width of the concrete flange shall be taken as not more than 1/4 the span (L) of the beam, and its effective projection (b') beyond the edge of the beam shall not be taken as more than 1/2 the clear distance (b_o), nor more than 8 times the concrete slab thickness (t):

$$b_E \leq \begin{cases} L/4 \\ b_o + b_f \\ 16t + b_f \end{cases} \quad (2.4)$$

where the total slab thickness (t), including ribs, was used to determine the effective width of concrete flange (AISC Section 1.11.5.1). The Specification also specifies the effective width for the exterior beam. The composite slab overhung the exterior girders; the projection ($=b_{op} + b_f/2$) was 50 cm from the centerline of the columns. The slab effective widths suggested for an interior beam were believed to be reasonable for the exterior beams (Fig. 2.4). In the instance where the decking ribs ran perpendicular to the loading direction, the concrete below the top of the decking was neglected in determining the relevant section properties (AISC Section 1.11.5.2).

2.3.5 UBC Lateral Load Analysis

According to the UBC, the following loading combinations have to be checked:

- (1) D.L.+L.L. (Dual system)
- (2) D.L.+L.L. \pm E.Q. (Dual system)
- (3) D.L.+L.L. \pm 0.25 E.Q. (Ductile moment-resisting space frame)
- (4) D.L.+L.L. \pm 1.25 E.Q. (Braced frame only)

The UBC Section 2312.(e)4 also requires that the shear-resisting elements be capable of resisting a torsional moment assumed to be equivalent to the story shear acting with an eccentricity of not less than 5 percent of the maximum building dimension at that level. A 5 percent eccentricity was considered in the lateral load analyses. To perform the linear static analyses, the ETAB segment of the SAP-80 computer program [11] was used to analyze the response of the prototype. A three-dimensional elastic analysis was performed by idealizing the structure as six planar frames linked by rigid in-plane floor diaphragms. A one-third increase in the allowable stress under earthquake loading is permitted by the UBC and was used in these analyses. The member forces of each member were checked to the UBC Specification; the stress ratio, which is the ratio of the calculated extreme stress to the allowable stress, the factored lateral displacements and inter-story drifts are shown in Fig. 2.5. The nominal lateral displacements and inter-story drifts were multiplied by $\frac{1}{K}$ to calculate the factored lateral displacements and inter-story drifts (UBC Section 2312.(h)).

2.3.6 Discussion of the UBC Results

Case 1: Exterior wall weight and live load were included in the gravity loads but excluded from the design lateral loads.

The allowable stress ratios shown in Fig. 2.5 indicate that the column and the composite girder stresses satisfied the UBC requirements. The critical load case for the

braced frame was that which required the braced frame to resist 125% of the design lateral forces. Assuming that the braces were pin-connected (effective length factor equal to 1), the compression braces barely satisfied the UBC requirements (Fig. 2.5(c)). The braces were welded to the flanges of the steel girders and the columns, the true effective length factor was significantly less than one. Therefore, a realistic effective length factor k equal to 0.7 was used to check the brace stress ratios (Fig. 2.5(d)). All the brace stress ratios were satisfactory and the critical compression braces were located in the second and the fourth stories.

The factored lateral floor displacements and the inter-story drift indices are shown in Fig. 2.5(f). The maximum inter-story drift index ($=0.12\%$) is significantly less than the code specified limit of 0.5%.

A further analysis was performed to ascertain the contribution of the composite action to the lateral stiffness of the structure. When the composite action was ignored, the subsequent decrease in the lateral stiffness was of the order of 8%; this indicated that the lateral stiffness was dictated by the axial stiffness of the concentric braces.

Case 2: As for Case 1 except that the reactive weight included that of the exterior wall

Assuming an effective length factor equal to 0.7, all the member stresses satisfied the UBC requirements. The critical brace stress ratio was 0.93 (second story) and the maximum inter-story drift index was 0.15%.

Case 3: The structure was designed as a ductile moment-resisting space frame

The UBC design check was performed assuming that the braces had been removed. The exterior wall weight was included as a reactive weight and full composite action was assumed. As a result of its well-known ductile properties, the UBC assigns a smaller K factor ($=0.67$) to an MRSF; thus the base shear becomes

$$V_b = C_s W = 0.094W . \quad (2.5)$$

The two relevant loading conditions for this structure were gravity loads alone and

gravity loads in conjunction with lateral loads. Although the maximum stress ratio was 0.7 for the first loading condition, it reached 1.41 for the second loading condition and approximately half of the girders exceeded the allowable stress ratio. The roof lateral displacement was 2.75 inches, approximately three times the corresponding displacement of the dual system. The maximum factored inter-story drift index of 0.58% exceeded the UBC limit of 0.5%; the nominal lateral displacements were multiplied by $\frac{1}{K}$ ($K=0.67$) to calculate the factored inter-story drifts.

2.3.7 Concluding Remarks

The following conclusions are drawn from the UBC analyses:

- (1) Assuming an effective length factor of 0.7 for braces, the prototype design satisfied the 1985 UBC requirements even for the instance in which the reactive weight included that of the exterior wall.
- (2) A comparison of Case 1 and Case 3 shows that the concentric braces reduced the maximum inter-story drift index by nearly a factor of four.
- (3) The influence of composite action on the lateral stiffness of the structure was small (8%) and it was the axial stiffness of the concentric braces that dominated the elastic stiffness of the dual system.

III. PROTOTYPE ANALYTICAL RESPONSE PREDICTION

3.1 Introductory Remarks

In this chapter, the analytical strength and seismic response of the prototype are presented. In Section 3.2, the analytical dynamic characteristics of the prototype are described. The prototype strength was predicted using both simple plastic theory and a step-by-step nonlinear analysis computer program; these results are presented in Section 3.3. The analytical seismic response of the prototype to the 1978 Miyagi-Ken-Oki earthquake record is compared with the measured prototype response in Section 3.4 and the UBC in Section 3.5.

3.2 Prototype Flexibility, Natural Periods and Mode Shapes

The flexibility matrix was calculated by sequentially applying unit lateral loads at each floor level. The following assumptions were used to model the prototype:

- (1) An in-plane rigid floor diaphragm was assumed; that is, the horizontal joint displacements at a given floor level were constrained to be identical.
- (2) Center-line dimensions were used; the finite girder-to-column panel zone was considered to be flexible.
- (3) The reactive weights shown in the second and the fourth columns of Table 2.3, assumed to be lumped at each floor level, were considered separately.
- (4) The average flexural rigidities (EI) of the composite girders under positive and negative bending were used. Figure 3.1 shows the mathematical idealization of the prototype.

Flexibility : The predicted flexibility matrix is listed in Table 3.1 and shown in Fig. 3.2(a). The experimental results reported by the Japanese researchers [13] are also listed. A comparison of these two flexibilities in Fig. 3.2(a) shows that the correlation is good; the analytical model however is more flexible in the upper three stories.

Natural Periods and Mode Shapes : Using the predicted flexibility matrix and a lumped diagonal mass matrix, the following eigenvalue problem was solved to calculate the natural periods and mode shapes of the prototype:

$$\underline{K}\phi = \omega^2 \underline{m} \phi \quad (3.1)$$

where

$\underline{K} = \underline{F}^{-1}$ = stiffness matrix (6x6);

\underline{m} = diagonal mass matrix (6x6);

ϕ = mode shape vector;

ω = angular frequency.

The reactive masses used in the pseudo-dynamic test (the fourth column of Table 2.4) were used as the diagonal terms of \underline{m} ; the resulting natural periods and mode shapes are presented in Table 3.2. The predicted periods and the prototype forced vibration test results [14] correlate well; the difference in the fundamental periods is less than 0.5%. The analytical and measured mode shapes, shown in Fig. 3.2(b), also indicate that the correlation is good.

Table 3.2(b) presents the measured equivalent viscous damping ratios reported by the Japanese researchers; such low damping ratios rarely exist in real buildings due to partitions, exterior walls, cladding and so on.

When the design reactive masses listed in the second column of Table 2.4 were used as the diagonal terms of the mass matrix, the fundamental period increased by 22% to 0.743 second.

3.3 Prototype Strength

3.3.1 Introductory Remarks

The structure was subjected to fixed lateral load patterns to predict its ultimate strength. The two load patterns considered were an inverted-triangular load pattern and an uniform load pattern. The results of the step-by-step nonlinear analyses are presented in Section 3.3.2; the results of the limit analyses using simple plastic theory are presented in Section 3.3.3.

3.3.2 Step-by-Step Nonlinear Static Analysis

3.3.2.1 Mathematical Model

The mathematical idealization of the prototype is shown in Fig 3.1. The computer program ANSR-1 [15] was used to perform the nonlinear static analyses. The five element types used to model the structure are described below.

(1) Columns

A two-component model was used to simulate the bi-linear behavior of the columns; the column end moment-rotation relationship is shown in Fig. 3.3(a) and a strain-hardening ratio of 5 percent was assumed. The assumed column axial force-bending moment interaction surface is shown in Fig. 3.3(b). Note that due to the computational procedure used in ANSR-1, an axial force in excess of yield can be computed for zero moment. The interaction surfaces shown in Fig. 3.3(b) were based upon the recommendations of Reference 16.

(2) Girders

Since the shear connectors were designed to develop full composite action [17], the slab contribution was included in the analyses. One-quarter of the girder span was assumed as the slab effective width. The measured steel and concrete properties (Section 2.3.3) were used to calculate the flexural rigidity and the moment capacities of the composite girders. The slab reinforcement was included in the calculation of the moment

capacities under positive and negative bending (Fig. 2.3); a strain-hardening ratio of 5 percent was assumed in the analyses that follow. The finite size of the girder-column joint panel zones was considered in terms of rigid end offsets (Fig. 3.1).

(3) Joints

A joint panel zone yields earlier in composite construction because of the larger moment capacity of the composite section [18]. The girder-column joint panel zone was considered a flexible element with rotational flexibility. The semi-rigid element available in DRAIN-2D [19] was converted for ANSR-1. This element has a bi-linear moment-rotation relationship similar to that shown in Fig. 3.3(a). The semi-rigid joint behavior can be modeled in a tri-linear form [20] as follows:

(a) Elastic range:

$$0 < \gamma_p^{av} < \bar{\gamma}_y = \frac{1}{G} \frac{\sigma_y}{\sqrt{3}} \sqrt{1-(P_c/P_{cy})^2}$$

$$K_e = \frac{\Delta M}{\gamma_p^{av}} = \frac{G(d_c-t_c^f)t_c^w d_b}{1-\rho} \quad (3.2)$$

$$\rho = \frac{V_c d_b}{\Delta M}$$

where γ_p^{av} is the average panel zone shear distortion, G is the shear modulus of steel and the other terms are illustrated in Fig. 3.4. If the column axial load (P_c) is small and the beneficial effect of the column shear is ignored, the panel zone yielding moment may be approximated by:

$$\Delta M_y = \frac{\sigma_y}{\sqrt{3}} \sqrt{1-(P_c/P_{cy})^2} \left[\frac{(d_c-t_c^f)d_b t}{1-\rho} \right] \approx \frac{(d_c-t_c^f)d_b t}{\sqrt{3}} \sigma_y \quad (3.3)$$

(b) Post-elastic range:

$$\bar{\gamma}_y < \gamma_p^{av} \leq 4\bar{\gamma}_y$$

$$K_t = \frac{G}{1-\rho} \frac{62.4 I_{cf}}{5 t_c^f} \quad (3.4)$$

where I_{cf} is the moment of inertia of one column flange.

(c) Strain-hardening range:

$$\begin{aligned}\gamma_p^{av} &> 4\bar{\gamma}_y \\ K_S &= K_e \frac{E_{sh}}{E}\end{aligned}\tag{3.5}$$

where E_{sh} is the tangent modulus of steel at the onset of strain-hardening. These equations were used to evaluate the parameters for the semi-rigid element in the ANSR-1 analyses.

(4) Braces

Two elements are available in ANSR-1 to model brace behavior. The first brace model is shown in Fig. 3.5(a); in this instance, the brace retains its strength after buckling. It is well-known that brace strength will decrease drastically after buckling. Maison [21] proposed a 9 zone phenomenological buckling model to simulate the global behavior of a brace after buckling (Fig. 3.5(b)). There are two problems with the use of this element; firstly, the user must select suitable parameters to obtain reasonable brace behavior and secondly, the brace negative axial stiffness in zone 4 or 5 (Fig. 3.5(b)) causes numerical problems. The complicated behavior of the Maison model combined with the necessity for numerical iteration causes the brace to reload in zones 4 or 5 and subsequently the solution will diverge.

To simplify the problem, the first element (Fig. 3.5(a)) was modified to account for the brace buckling behavior shown in Fig. 3.5(d). The modified element was similar to that proposed by Jain [22] (Fig. 3.5(c)); the difference is that the buckled brace cannot reload, thus cannot change the sign of the brace stiffness during the iteration process. The horizontal distance between points O and B ($=5\Delta_y$ in Fig. 3.5(d)) recommended by Jain was adopted. The initial buckling load (P_{yn}) was calculated using the AISC formula [10] with the safety factor removed:

$$P_{yn} = \left[1 - \frac{(kl/r)^2}{2C_c^2} \right] F_y A \quad (3.6)$$

where $C_c = \sqrt{2\pi^2 E_s / F_y}$ and k , the effective length factor, was equal to 0.7. Experimental test results for tubular braces [22] showed that the compressive load at a displacement of $5\Delta_y$ remains relatively constant from cycle to cycle. The strength (P_{ync}) at this displacement level varies with the effective slenderness ratio and was estimated by Jain et al. [22] to be

$$\psi = \frac{P_{ync}}{P_{yn}} = \frac{18}{(kl/r)} \quad (3.7)$$

where ψ is the buckling load reduction factor, which varies from 0.23 to 0.35 for the braces used in the prototype.

(5) Generalized Spring Element

The computer program ANSR-1 uses a load control algorithm. Given the specified load patterns, the user has to specify in advance the load increments, either in the form of an increasing or decreasing load factor. If the strength of the structure drops due to the buckling of braces for example, the program cannot detect when the load must be decreased in order to follow the correct load path. The solution diverges and the post-buckling behavior cannot be traced. To overcome this problem, a generalized spring [23] was adopted; the formulation is presented below.

The problem to be solved at any load increment is

$$\underline{K}_T \Delta \underline{r} = \Delta \underline{R} = \Delta \alpha \underline{R} \quad (3.8)$$

where

\underline{K}_T = tangent structure stiffness;

$\Delta \underline{r}$ = incremental lateral displacement vector;

$\Delta \underline{R}$ = incremental force vector;

\underline{R} = force vector of specified load pattern;

$\Delta\alpha$ = incremental load factor.

A generalized spring with a stiffness equal to G in the direction of \underline{b} is added to the structure, where \underline{b} is the unit vector in the direction of \underline{R} :

$$\underline{b} = \frac{\underline{R}}{(\underline{R}^T \cdot \underline{R})^{1/2}}.$$

Applying a stiffness formulation to this one-dimensional element gives:

$$q = \underline{b}^T \underline{r}$$

$$Q = G q$$

$$\underline{R}_s = \underline{b} Q = \underline{b} G q = (\underline{b} G \underline{b}^T) \underline{r} \equiv \underline{K}_s \underline{r} \quad (3.9)$$

where

\underline{r} = displacement vector;

q = generalized spring deformation in the direction \underline{b} ;

Q = generalized spring force in the direction \underline{b} ;

G = generalized spring stiffness;

\underline{R}_s = force vector in global coordinates exerted by the generalized spring.

The global stiffness of the generalized spring is

$$\underline{K}_s \equiv \underline{b} G \underline{b}^T$$

and the modified structure stiffness (\underline{K}_m) incorporating the generalized spring may be expressed as

$$\underline{K}_m = \underline{K}_T + \underline{K}_s = \underline{K}_T + \underline{b} G \underline{b}^T. \quad (3.10)$$

Equation (3.7) is then modified as

$$(\underline{K}_T + \underline{b} G \underline{b}^T) \Delta \underline{r}_m = \Delta \underline{R}_m$$

$$\text{or} \quad \mathbf{K}_m \Delta \mathbf{r}_m = \Delta \mathbf{R}_m \quad (3.11)$$

where \mathbf{r}_m and \mathbf{R}_m are the structural displacement and load vectors after the generalized spring is added; with the force vector (\mathbf{R}_s) exerted by the generalized spring expressed by Eq. (3.9), the modified load vector (\mathbf{R}) is

$$\mathbf{R} = \mathbf{R}_m - \mathbf{R}_s = \mathbf{R}_m - (\mathbf{b} G \mathbf{b}^T) \mathbf{r}_m . \quad (3.12)$$

There are problems associated with this method; the value selected for the generalized spring constant (G) should be sufficiently large that the total stiffness in the direction of \mathbf{b} (i.e., the generalized spring direction) is positive. However, the constant G should not be so large that numerical problems are encountered. The generalized spring element based upon these concepts was written for ANSR-1 and was used in the following step-by-step analyses.

3.3.2.2 Predicted Structure Response

The roof drift index versus the base shear ratio (V_B/W) curves ($W=1154$ kips) for the inverted-triangular and uniform lateral load patterns are shown in Fig. 3.6. The plastic hinge formation and the brace buckling (or yielding) sequences are shown in Fig. 3.7; the majority of the beam-column joint panel zones yielded prior to the adjacent girders. This indicates the change in the hinging pattern as a consequence of composite action. The composite girders yielded under negative bending and under positive bending at the brace-girder joint because of the unbalanced vertical component of the brace force that existed after the adjacent brace buckled.

Figure 3.6 shows the increase of the structural strength after brace buckling; this was due to the contribution from the moment-resisting space frame. The rate of increase of the shear resisted by the moment-resisting space frames must be larger than the rate of decrease of the shear resisted by the braces to ensure that a drop in strength will not occur. The strength of the structure under a uniform lateral load was about 20% higher than that under an inverted-triangular lateral load.

3.3.3 Limit Analysis Using Simple Plastic Theory

3.3.3.1 Introductory Remarks

Simple plastic theory using a collapse mechanism approach was used to bound the strength of the structure [24]. The theory is based upon the following assumptions:

- (1) the material is rigid-perfectly plastic;
- (2) deformations are infinitesimally small;
- (3) local member instability (such as local buckling, lateral-torsional buckling) is prevented.

The first assumption can be applied to ductile steel members, such as beams, columns and tension braces but not to compression braces since they do not exhibit ductile behavior after buckling. The use of the initial buckling load as the brace strength in the simple plastic analysis will lead to an unrealistically high structure strength. To account for brace strength deterioration, it was assumed that the compression brace strength was equal to P_{ync} (Eq. 3.7) and that this strength was retained after buckling.

The plastic moments of the composite girders under positive and negative bending and the plastic moments of the columns were based on the measured material yield stresses; Equation 3.3 was used to calculate the plastic moment capacity of each joint panel zone.

Two types of mechanisms in the braced bay were considered. The Type 1 mechanism shown in Fig. 3.8 incorporates a yielding tension brace and a buckled compression brace. For a virtual displacement θ , the internal work done by the braces is

$$W_I = \theta h (P_y + P_{ync}) \cos\alpha \quad (3.13)$$

where P_y is the brace tensile yield load. The internal work done by the plastic hinges at the ends of the braces is negligibly small and can be ignored. The Type 2 mechanism shown in Fig. 3.8 incorporates a buckled compression brace in conjunction with plastic hinges at one end of each girder. The internal work done by the compression brace is

$$W_I = \theta l P_{ync} \cos\left(\frac{\pi}{2} - 2\alpha\right). \quad (3.14)$$

3.3.3.2 Analysis 1 : Inverted-Triangular Load Pattern

For the limit analysis different mechanisms were considered, the one shown in Fig. 3.9(a) gave the lowest base shear (=735 kips). The Type 2 mechanism resulted in a higher base shear (=766 kips).

Since the braces were likely to buckle or rupture during the test, the capacity of the unbraced structure was evaluated. Assuming individual soft story formations from story six to one, respectively, the structure strength was 805, 593, 547, 550, 578, and 565 kips. The critical structure strengths (735 kips, 547 kips) are shown in Fig. 3.6.

3.3.3.3 Analysis 2 : Uniform Load Pattern

In this instance, the mechanism shown in Fig. 3.9(b) gave the lowest base shear (=865 kips). Assuming individual soft story formations from story six to one, respectively, the unbraced structure strength was 1337, 908, 764, 696, 655, and 565 kips.

3.3.3.4 Conclusions

It is apparent from Figure 3.6 that the application of simple plastic theory provides a simple yet reliable method to estimate the strength of the structure. It must be noted however, that the lowest collapse load associated with a kinematically admissible field is still an upper bound on the structure strength. In order to verify that the collapse load associated with a kinematically admissible field is in fact the true collapse load, the corresponding statically admissible field must be evaluated. Unless the collapse mechanism is complete or over-complete, it is not a simple task to evaluate this statically admissible distribution of bending moments.

A judicious choice of collapse mechanisms will however provide a simple means by which to bound the structure strength.

3.4 Prototype Seismic Response

3.4.1 Introductory Remarks

The analytical response of the prototype under the 1978 (N-S) Miyagi-Ken-Oki Earthquake (hereafter M.O. Earthquake) excitation is evaluated in this section. The M.O. Earthquake record was used for the pseudo-dynamic tests in Tsukuba, Japan. The duration of the record is twenty seconds and the maximum acceleration is 0.26 g. The acceleration time history is shown in Fig. 3.10(a); the record has four major acceleration pulses occurring around the 3, 7, 10.5 and 14.5 second mark. The linear elastic response spectra is shown in Fig. 3.10(b).

The two-dimensional nonlinear dynamic analysis computer program DRAIN-2D [19] was used to predict the seismic response of the structure. The mathematical idealization of the structure was the same as that used for the strength prediction (Fig. 3.1) and the brace model (Fig. 3.5(c)) developed by Jain [22] was used in the analyses.

The DRAIN-2D program allows the user to specify Rayleigh-type viscous damping. The damping matrix \underline{C} is expressed as:

$$\underline{C} = \alpha \underline{M} + \beta \underline{K}_0 \quad (3.15)$$

where \underline{K}_0 and \underline{M} are the original stiffness and mass matrices, respectively. The constants α and β are chosen to reproduce any two modal damping ratios. The first two modal damping ratios reported by the Japanese researchers [14] were equal to 0.5%; these two damping ratios were used to determine the constants α and β .

The three cases corresponding to the major pseudo-dynamic tests conducted in Japan were analyzed. They are designated as **Elastic-3 Test** (65 gal), **Moderate Test** (250 gal) and **Final Test** (500 gal) in the following discussion. These three intensity levels were intended to simulate the serviceability, damageability and collapse limit states of the test structure.

3.4.2 Serviceability Level Analysis

The predicted lateral displacement, inter-story drift and story shear time histories are shown as dotted lines in Fig. 3.11 to Fig. 3.13. The pseudo-dynamic test results [12] are shown in solid lines; the pseudo-dynamic test was stopped after 11.98 seconds. The correlation between the analytical prediction and the test results is good.

3.4.3 Damageability Level Analysis

The predicted global responses are shown in Fig. 3.14 to Fig. 3.16; the pseudo-dynamic test results are shown in solid lines; the pseudo-dynamic test was stopped after 17.16 seconds. Although the predicted lateral displacement time histories are larger than the test results, the correlation is still satisfactory.

The damage pattern after the pseudo-dynamic Moderate Test is shown in Fig 3.17. In this test, four braces buckled (three out of plane) and the second floor brace-girder panel zone fractured. The inter-story drift versus story shear relationship for the lower two stories is shown in Fig 3.18. Although the braces in the first story did not buckle, a significant amount of energy was dissipated; this was due to the yielding of the second floor brace-girder panel zone (Fig. 3.19). The second floor brace-girder joint details are shown in Fig. 2.2. Although the concentric brace centerlines coincided at the steel girder mid-height, the central panel actually performed like a shear link. This failure mode emphasizes the importance of the proper detailing of brace connections to ensure that the brace forces are transmitted through the centroid of the brace members. The first story columns in the braced bay of the prototype also yielded in this test. The free vibration test that followed this test showed that the fundamental period had increased to 0.707 second (a 16% increase).

3.4.4 Collapse Level Analysis

The responses predicted by DRAIN-2D are shown in Fig. 3.20 to Fig. 3.22. DRAIN-2D predicted that all the braces except those in the sixth story would buckle.

Prior to the Final Test, the second floor brace-girder panel zone was repaired. The measured global responses of the prototype are also shown in Fig. 3.20 to Fig. 3.22.; the pseudo-dynamic test was terminated after 11.14 seconds. It is apparent from Fig. 3.22 that the story shear correlation is good; the permanent deformations in the lower three stories were not predicted by DRAIN-2D (Fig. 3.21). The post-test damage pattern is shown in Fig. 3.23; seven braces buckled and one ruptured. Yielding of columns, girders and joint panel zones was concentrated in the lower three stories.

3.5 Prototype Strength Comparison

The envelopes of roof drift index versus base shear ratio for the DRAIN-2D analyses and the pseudo-dynamic test results are shown in Fig. 3.6.

The strength-deformation envelopes from the DRAIN-2D analyses and pseudo-dynamic test results are reasonably well bounded by the curves obtained from the step-by-step analyses. The maximum strength from the pseudo-dynamic tests (=730 kips) is very close to that strength predicted using simple plastic theory (=735 kips). The one point from the pseudo-dynamic Final Test that falls out of the bounds of the step-by-step analyses corresponds to the maximum roof drift and a strength level of 610 kips; this is a consequence of severe brace buckling in several stories and in particular the rupture of one brace in the third story. The strength level of 610 kips is bounded by those predicted using simple plastic theory with an inverted-triangular load pattern (= 550 kips) and a uniform load pattern (= 696 kips) if the third story bracing is ignored in the analyses.

Prototype Strength and the Design Base Shear

The prototype was designed for a base shear [8] of

$$V_{B(\text{design})} = C_s W_{(\text{design})} = 0.197 (634.7 \text{ tons}) = 125 \text{ tons} = 276 \text{ kips}$$

where C_s (=0.197) is the design base shear coefficient according to the Japanese Aseismic

Code, and the weight of reactive mass $W_{(design)}=634.7$ tons (1400 kips) did not include the exterior wall weight. This base shear is used for a working stress design; extrapolating it to the yield stress level by assuming an allowable stress equal to $0.6F_y$ and accounting for the one-third increase in the allowable stresses permitted by the UBC, the yield base shear is

$$V_{B(yield)} = \frac{V_{B(design)}}{\left(0.6 \times \frac{4}{3}\right)} = 345 \text{ kips .}$$

The weight of reactive mass used in the prototype pseudo-dynamic test was 1154 kips (=523.6 tons). The true yield base shear coefficient is

$$C_y = \frac{V_{B(yield)}}{W_{(test)}} = \frac{345}{1154.3} = 0.30 . \quad (3.16)$$

This strength level (C_y) is shown in Fig. 3.6; a comparison of this level with the maximum strength developed in the pseudo-dynamic test indicates a significant **over-strength** of the order of 2.1 (=0.63/0.30).

Prototype Strength and UBC Minimum Requirements

According to the UBC, the design base shear coefficient at working stress level is 0.113 (Eq. 2.2). For a dual system with braces, the UBC requires that the braced frame alone should resist 125% and the ductile MRSF should resist 25% of the design base shear. An upper bound to the minimum required base shear coefficient at working stress levels is 0.17 (=0.113x(1.25+0.25)). At this load level, the UBC also requires that the maximum inter-story drift δ_{xe} be limited to

$$\frac{\delta_{xe}}{h_x} \leq 0.005K \quad (3.17)$$

where $K = 0.8$ for a dual system

h_x = story height

i.e.,
$$\frac{\delta_{xe}}{h_x} \leq 0.004 .$$

The yield base shear coefficient by extrapolation is

$$\frac{0.17F_y}{(0.6 \times \frac{4}{3})F_y} = 0.21 .$$

The corresponding yield level inter-story drift index is

$$\frac{\delta_{xy}}{h_x} = 0.004 \left(\frac{0.21}{0.17} \right) = 0.005 .$$

As noted above, the design reactive weight was 1400 kips as opposed to the as-built reactive weight of 1154 kips; the true UBC yield level is 0.25 ($=0.21 \times \frac{1400}{1154}$). The UBC Section 2312(j)D also requires that the maximum inter-story drift index be limited to that given by Eq. (3.17) multiplied by 3/K:

$$\frac{3}{K}(0.005K) = 0.015 . \quad (3.18)$$

Assuming a uniform inter-story drift over the height of the structure, the UBC requirements are shown in Fig. 3.6. A comparison of the true UBC yield level and the measured prototype strength shows that the **overstrength** of the UBC-designed concentric K-braced structure is of the order of 2.5 ($=0.63/0.25$).

The prototype strength-deformation envelope shows that the roof displacement ductility was about 2.3; this is less than the UBC implied ratio of 3 ($=0.015/0.005$). It demonstrates that, as a result of brace buckling and rupture, the concentric K-braced frame does not possess large displacement ductility.

IV. MODEL DESIGN, CONSTRUCTION AND INSTRUMENTATION

4.1 Introductory Remarks

The selection of the scale of the model to be tested at Berkeley is described in this chapter, together with a summary of the member fabrication and model construction. A detailed discussion of the fabrication of the members and the erection of the model is given in Reference 17. Prior to the construction of the model, a series of composite girder tests was conducted to study their cyclic behavior. These tests also supplied information necessary for the construction of the composite floor of the model [18]. The instrumentation and data acquisition used in the tests of the model are described in Section 4.7.

4.2 Selection of the Scale Factor

One of the primary objectives of the study at Berkeley was to design, construct and test the largest possible steel model of the prototype that could be accommodated on the earthquake simulator.

Figure 4.1 shows the plan and elevation of the shaking table [25]; the plan dimensions of the table are 20 feet square and it weighs 100 kips. The maximum height of a test structure is limited to 30 feet. In operation, the pit beneath the shaking table is pressurized so that the total dead weight of the table and the test structure is air supported. The 1 foot gap between the shaking table and the interior foundation walls is sealed by a 24 inch wide strip of vinyl covered nylon fabric. The maximum air pressure on nylon fabric is limited to 4 psi, and thus, the maximum weight on the table is limited to 130 kips. Assuming that the weight of the structure foundation and reference frame

is about 15 kips, the maximum weight of a test structure is 115 kips. The total weight of the prototype was 1178 kips (534.2 tons), therefore the maximum length factor that could be used was $\sqrt{115/1178}=0.312$ (see Section 4.3.1 for similitude law). A length scale factor of 0.3048 (hereafter noted as 0.3) was adopted for the design and construction of the model; this scale factor was selected to satisfy the weight limitations and to facilitate the unit conversion between prototype (metric) and model (U.S.) length dimensions (one meter in the prototype corresponds to one foot in the model). It was determined that with this scale factor and considering both the performance of the shaking table and the frequency content of the similitude scaled Miyagi-Ken-Oki earthquake, the response in the first three modes of the structure could be obtained.

4.3 Model Design

4.3.1 Similitude Requirements

The Berkeley model was designed to comply with the similitude requirements for a direct reduced-scale model of the prototype shown in Fig 2.1. Three types of models are suggested for small scale model studies [26], a true replica model; a model which uses materials with the same properties as materials in the prototype but with additional non-structural masses; and an identical model in which gravity forces are neglected. Table 4.1 [26] shows the similitude requirements for these three types of modeling. As the gravitational contributions to stress histories must be accounted for, the gravity force cannot be neglected. In a one-g field, the mass density similitude of the true replica model requires that

$$\left(\frac{E}{\rho} \right)_r = l_r \quad (4.1)$$

where the subscript r refers to the ratio of a physical quantity between the prototype and the model; E is the Young's modulus and ρ is the mass density. Equation (4.1) places a severe limitation on the choice of model materials; it requires either a small

material modulus or a large mass density or both. As such materials are difficult to obtain, it appears more suitable to augment the density of structurally effective material with additional material which is structurally ineffective. This is easily achieved in lumped mass systems, being the typical assumption for building structures with seismically effective masses concentrated at the floor levels. Equation (4.1) may be rewritten as

$$\left(\frac{E}{\rho l} \right)_r = \left(\frac{El^2}{\rho l^3} \right)_r = \left(\frac{El^2}{M} \right)_r = 1$$

or
$$M_r = E_r l_r^2 \quad (4.2)$$

where $M (= \rho l^3)$ is the lumped mass at the floor levels. Equation (4.2) is known as Cauchy's requirement for proper simulation of inertia forces and restoring forces.

The most suitable model was determined to be the second type, that is, an artificial mass simulation model which satisfied the true replica similitude laws, except for the requirement of the mass density relationship. To satisfy this requirement, lead ballast was added to the roof and floor slabs so that it did not affect the stiffness of the floor system and therefore the dynamic characteristics (periods, mode shapes) of the structure.

4.3.2 Aspects of the Model Construction

The similitude requirements were satisfied by designing and fabricating the model as a 0.3-scale replica of the prototype. However, several problems were encountered during the design process; these problems are discussed below.

(1) Structure Foundation: To enable proper attachment of the model to the shaking table, the design of the scale model foundation differed from that of the prototype. Although the foundation differed in shape, design, and detailing from the prototype, its stiffness was sufficiently large (as was the case of the prototype) to consider it as a rigid foundation.

(2) Structural Steel Members: The scaled steel sections were not commercially available, therefore all of the steel columns and girders were fabricated from steel plates. For the model, a number of the section properties had to be distorted because of the differences between the required flange and web thicknesses and commercially available plate thicknesses. The moment of inertia and the elastic and plastic section moduli with respect to the loading direction were considered to be the most important geometric properties and thus they were simulated as closely as possible. Attention was also focused on the width-thickness ratio in order to simulate the slenderness ratio and the degree of compactness that existed in the prototype girders and columns.

(3) Metal Deck: The profile of the corrugated metal deck used in the prototype was distorted because the desired shape was not commercially available. A series of composite girder tests were conducted to verify the performance of the composite girder with the selected metal deck [18].

(4) Brace Force Measurement: A load cell was included in each brace of the prototype. The installation of these load cells resulted in the undesirable misalignment of the braces and it triggered early nonlinear behavior in the braces. The load cells were not used in the braces of the model; the load cells were replaced by strain gages glued directly to each brace. The disadvantage of this approach was that the brace forces had to be calculated on the basis of the material strain-stress relationship from coupon tests and the measured strain readings.

(5) Brace-Girder Connection Details: Figure 2.2 shows the typical prototype brace-girder connection details. A construction joint existed at the girder midspan and continuity of the steel girder was provided by welding the flanges and connecting the webs with high strength bolts. To facilitate the construction of the model and to avoid the brace-girder connection failure of the prototype (Fig. 3.17), this construction joint was eliminated by providing a single steel girder in the braced bay. In addition, the brace-girder connection was modified to incorporate a full depth stiffener in lieu of the mid-

depth stiffener used in the prototype (Fig. 4.2).

(6) Girder-Column Connection Details: The prototype was constructed using a welded connection for steel girder flanges and a bolted connection in the webs (Fig. 2.2). To ensure continuity and to prevent slippage, the shear plate was fillet welded to the girder web (Fig. 4.2); the copes at the ends of the steel girders were also eliminated. The beam copes were eliminated so that the beam web could provide lateral support to the beam bottom flange at the column face.

(7) Column Splice: The column splices in the prototype used a shear plate connection in the web and a welded connection in the flange. The model column splice incorporated full bearing butt plates with continuous perimeter welding (Fig. 4.2).

4.3.3 Materials and Mechanical Characteristics

4.3.3.1 Steel Column, Girder and Brace

The most difficult step in attaining a reduced-scale model of the second type discussed in Section 4.3.1 was satisfying the requirements for the mechanical characteristics of the constituent materials. As one objective of the research program was to evaluate the reliability of experimental analysis of reduced-scale models in predicting the behavior of full scale models, the individual stress-strain relationships of the model materials had to be similar to those of the prototype materials over the expected strain range. ASTM A36 steel was used for the prototype columns and girders; A500 Grade B square section was used for the braces. Typical stress-strain curves are presented in Reference 9 and the average values are summarized in Table 2.5.

In order to find those steel plates which most closely matched the material properties of the prototype, a large number of coupon tests were conducted on commercially available products. In addition to the ASTM A36 steel, Grade 50 steel in two different supplier designations, X10 and COR10, was tested. Figure 4.3 gives the average stress-strain curves of the prototype and model materials. On the basis of the coupon tests of

the model materials with the prototype material characteristics [17], the following conclusions were drawn:

Columns and Girders: Grade 50-X10 was the best choice up to a range of 12 % strain and therefore this grade of steel was selected. A36 was below and COR10 was well above the required strength (Fig. 4.3). For gage No. 14 (0.0747 inch), X10 was unavailable, and COR10 was used in lieu.

Braces: Grade 50-COR10 was the best choice in the strain range under consideration. The test results showed a lower average yield stress (55 ksi versus 59 ksi) but a higher average tensile stress (74 ksi versus 68 ksi) than the required prototype material strength.

4.3.3.2 Composite Floor System

(1) Prototype Composite Floor Construction

The formed metal deck used in the floor system was oriented such that the ribs were perpendicular to the loading direction; Figure 2.3 shows a typical cross-section of the composite floor system. The prototype composite girder construction is summarized as follows [9]:

- (A) Metal deck - Figure 4.4 shows the indentation pattern and dimensions of the formed metal deck used in the prototype. It was designated as Kawa-Ken QL-99-1.6, which was equivalent to H.H. Robertson's QL-99 (conforming to ASTM-A-446-M-80 Grade B); the thickness is 0.063 inch (1.6mm).
- (B) Shear connectors - Headed studs 7/8 inch in diameter and 5.12 inches (13 cm) long were used; because of the layout of the metal deck, the studs on all the transverse frames and Frame B were welded directly to the girder flanges. For Frames A, C and the secondary beams, the connectors were welded through the metal deck to the flange of the girders. Accordingly, the centers on these studs were dictated by

the profile of the decking and its intermittent contact with the girder. The studs were installed as follows: (i) double rows on a 11.81 inch (30 cm) pitch in each girder of Frames A and C; (ii) a single row on a 11.81 inch pitch on the transverse girders and all the secondary beams; and (iii) a single row on a 5.91 inch (15 cm) pitch on each girder in Frame B.

- (C) Lightweight concrete - Coarse aggregate of a lightweight type combined with normal weight sands was used for the prototype floor slab. The specified compressive strength (f'_c) was 3 ksi. The Japanese researchers tested 12 cylinders (6 inches diameter by 12 inches high), 2 per floor approximately 28 days after casting to determine the mechanical characteristics of the concrete. The average compressive strength from these tests was 4.17 ksi and the average modulus of elasticity was 2,170 ksi; Figure 4.6(a) shows the typical stress-strain curve.
- (D) Reinforcement - A single layer of square welded wire mesh, 0.236 inch (6 mm) in diameter on a 3.94 inch (10 cm) pitch, was used to reinforce the concrete slab; the minimum cover was 1.14 inches (3 cm). Three samples of this reinforcement were tested, the average yield stress was 57.7 ksi and the tensile stress was 79 ksi.

(2) Model Composite Floor Construction

A description of the components of the model floor system follows and the differences with respect to the prototype are emphasized.

- (A) Metal deck - Figure 4.5 shows the similitude scaled metal deck profile and the profile of the corrugated metal sheet used in the model. The galvanized metal sheet used in the model corresponded to ASTM-A-446 grade A designation, gage 26 steel with a thickness of 0.018 inch (the required thickness was 0.0192 inch). The difference between the required and the adopted shapes was negligible and more important, the thickness of the concrete over the top of the deck was practically the same for the two cases. The main difference existed in the profile and size of

the ribs, but neither of these significantly affected the volume of concrete nor the effective cross-sectional area. The geometry discrepancy did affect the values of the reduction factors to be applied to the capacity of the studs [18] (see Eq. 4.3).

- (B) Stud - Shear connectors, 0.27 inch in diameter and 1.56 inches long were required to satisfy the similitude laws. The steel studs used in the model were designated as H-4L concrete anchors (ASTM-A-108-Grade 1010 with 55 ksi and 65 ksi as yield stress and tensile stress); the studs were 0.25 inch in diameter and 1.56 inches long. As for the connector distribution and spacing, the different geometry of the model deck imposed a severe limitation as to where the studs could be welded. The prototype studs were welded on a scaled pitch of 3.6 inches while the model corrugated steel sheet required a stud spacing of 3 inches (Fig. 4.5). As the prototype studs satisfied the AISC Specification for full composite action, this was the basic criterion used for the number and spacing of the shear connectors for the model. An AISC design check for full composite action for the model was conducted and the studs were concluded to be satisfactory [18].
- (C) Lightweight concrete slab - As for the prototype construction, lightweight coarse aggregate mixed with normal weight sand was used for the model. A special aggregate gradation to account for the 0.3-scale factor was prepared, resulting in a concrete with a maximum aggregate size of 0.25 inch. An extensive number of mix designs with differing water/cement ratios and aggregate proportions were prepared to find the mix that provided the closest stress-strain relationship to that of the prototype concrete. The fresh unit weight was 116 pcf and the dry unit weight after 28 days was 112 pcf; the water/cement ratio was 0.6. The desired slump was 4.5 inches and the measured average slump was 4.53 inches. Figure 4.6(a) shows the typical concrete stress-strain relationships for the model concrete. The 28-day average compressive strength of the concrete using 3 inch by 6 inch cylinders was 4.0 ksi, which was close to the desired strength of 4.17 ksi. The Young's moduli for

the prototype concrete and the model concrete were 2,170 ksi and 2,600 ksi, respectively. Therefore the model concrete was about 20% stiffer than the prototype concrete. The 28-day tensile strengths of the model concrete from the split tension tests and one-third point rupture tests of 3 inch by 6 inch cylinders were 0.55 ksi and 0.60 ksi, respectively. The compressive strength of the model concrete at the time of the shaking table tests was 5.32 ksi (Fig. 4.6(b)), 33% higher than the 28-day compressive strength.

- (D) Slab reinforcement - A square wire mesh with a 1.2 inch pitch and a 0.072 inch diameter was required for the model. The reinforcement used in the model was a square welded mesh with a 1 inch pitch and 0.0625 inch (gage 16) diameter. The difference between the prototype and the model steel reinforcement areas was 9.7%; the steel reinforcement ratio in the model was 0.31% as opposed to the required 0.34%. The yield stress and tensile stress from the coupon tests of the wire mesh were 79 ksi and 85 ksi, respectively; these were higher than the yield stress (57.7 ksi) and tensile stress (79 ksi) of the prototype wire mesh.

4.3.4 Member Fabrication

Although the selected scale factor was reasonably large for modeling, the model structural members (columns, girders and braces) were not commercially available. Therefore approximately 300 members were individually built up to simulate the prototype wide flange and square tube sections geometrically. For the girders, beams and columns, three hot rolled plates were welded to obtain the web and flange components of the scaled wide flange shapes [17]. For the concentric braces, two strips bent at 90 degrees were welded to conform to the scaled square sections for the model. In both cases an automatic self-propelled dual head welder, running on specially fabricated table, was utilized. During the welding process, the heat caused member camber. The cambered members were straightened by applying constant moment at their member ends to

meet the AISC Specification tolerance [10].

4.4 Composite Girder Tests

4.4.1 Introductory Remarks

As mentioned in Section 4.3.2, the composite floor for the model was distorted because of the difficulty in finding a suitable metal deck that was geometrically similar to that of the prototype. Therefore four composite girders and one bare steel girder were tested prior to the construction of the model with the following objectives:

- (1) to study in detail the composite girder cyclic behavior of the beam-column subassembly of the model;
- (2) to provide information for selecting the metal deck, slab reinforcement, shear connector and lightweight concrete for the model;
- (3) to foresee any problems during the composite floor construction of the model; and
- (4) to ascertain the adequacy of the composite girder-column connections.

4.4.2 Composite Girder Test Specimens

It was agreed by the U.S.-Japan Planning Group [1] that the floor system be designed to develop the full composite action. The AISC Specification (Section 1.11) [10] gives a series of requirements for full composite action.

One consequence of the difference in geometric shape was the different definition of the parameters used in the calculation of the shear stud capacity reduction factor ϕ :

$$\phi = \frac{0.85}{\sqrt{N_r}} \left(\frac{h_s - h_r}{h_r} \right) \left(\frac{w_r}{h_r} \right) \leq 1.0 \quad (4.3)$$

where w_r , h_r and h_s are illustrated in Fig. 4.7 and N_r is the number of stud connectors on a beam in one rib. A comparison of the number of required shear connectors was made in Reference 18; it was concluded that both the prototype and the model composite

girders satisfied the AISC requirements for full composite action.

Another difference between the two deckings was that the prototype metal deck had mechanical indentations to increase the bond between the concrete and the decking (Fig. 4.4). The model metal deck as purchased was zinc-coated without mechanical indentations. The four composite girders were prepared with different surface treatments:

- (1) First Composite Girder (**CG1**) - The metal deck of this composite girder was mechanically indented with a similar indentation pattern to that of prototype decking.
- (2) Second Composite Girder (**CG2**) - The metal deck was prepared by sand-blasting its surface to remove the zinc coat, painting it with an epoxy resin and then evenly spreading sand prior to the epoxy setting.
- (3) Third Composite Girder (**CG3**) - For this specimen the decking was sand-blasted only. The sand blasting was sufficient to remove the zinc, thus improving both the mechanical and chemical bond.
- (4) Fourth Composite Girder (**CG4**) - The metal sheet was used as supplied, that is, with no surface treatment.

A bare steel girder (SG) was tested first; this provided a basis for a comparison to be made with the composite girder test results.

The portion of the composite floor system simulated is shown in Fig. 4.8. At the time of this test, the model steel girder fabrication had not commenced; the closest commercially available steel section, M6x4.4, was used. A comparison of the sectional properties is listed in Table 4.2.

The test set-up is shown in Fig. 4.9; fifty channels of instrumentation (Fig. 4.10) were used to measure the global and local responses that included: (i) vertical deflection; (ii) strain profile along the depth of the steel beam (giving the curvatures); (iii) rotation

of the composite girder 4.5 inches from the column surface; (iv) concrete strain profiles across the slab in the transverse direction to determine the slab effective width; and (v) slip between the concrete slab and the steel girder (LVDT6, LVDT7, LVDT8 in Fig. 4.10).

4.4.3 Test Results

4.4.3.1 Bare Steel Girder Test

The experimental program consisted of: (i) five tests at the working load level, and (ii) seven loading cycles inducing plastic deformation. The test was terminated when the connection failed. Figure 4.11 shows the load-tip deflection curve; the specimen failed prematurely during the first significant yielding reversal deformation (point A in Fig. 4.11) due to the poor welding of the column face to the bottom flange. Fracture occurred in the grooved weld of the beam bottom flange to the column face because of insufficient penetration through the thickness of the flange [18].

4.4.3.2 CG1 and CG2 Tests

CG1 and CG2 were cast at the same time using the same lightweight concrete mix. The average concrete strength of the 3x6 inches cylinder tests at 28 days was 4.6 ksi. The two girder tests had a premature failure similar to the bare steel girder test in the first half cycle. The specimens were repaired as follows:

- (1) the weld size was increased;
- (2) the welds were checked to ensure penetration into the flange;
- (3) the girder web connection was modified by welding the bolt-connected shear plate.

The modified connection details are shown in Fig. 4.12. The first two steps were taken to guard against weld failure. The analytical studies showed that under positive bending, the neutral axis would be close to the top flange, thus highly stressing the web. Bolted connections have been shown to produce pinched hysteresis loops due to bolt

slippage [27] and therefore it was decided to weld the shear plate to the beam web. Figure 4.13 shows the repaired CG1 (designated as **CG1R**) load-deflection curve, which resulted in a total deflection ductility of 9.5. Reversing the loading direction, the maximum resistance was controlled by severe local buckling in the bottom flange and web; this caused the gradual drop in the load-carrying capacity. The load versus slip (between the concrete slab and the steel girder) curve shown in Fig. 4.14 indicates a large slip near the peak load. The simple plastic moment (M_p) was exceeded despite the occurrence of large slip.

4.4.3.3 CG3 and CG4 Tests

CG3 and CG4 were cast at the same time with the 28-day average compressive strength of the 3x6 inch cylinders being 3.4 ksi. Based upon the previous tests, the beam-to-column connections were modified as shown in Fig. 4.12 (and noted in Section 4.4.3.2) to prevent premature connection failure.

Specimen CG3: Cyclic loading was applied to specimen CG3 once the displacement ductility ratio reached 10.4 (Fig. 4.15). The hysteresis loops were fairly stable and reproducible although the ultimate capacity decreased as the number of cycles at the same displacement level was increased. Unlike the bare steel girder (Fig. 4.11), the stiffness of the reloading curves under positive bending moment in the subsequent cycles decreased drastically; this is attributed to the fact that the concrete cracks which developed in the previous negative bending cycle did not close.

The load versus slip (between the concrete slab and the steel girder) relationship is shown in Fig. 4.16; the figure shows that the interaction between the concrete slab and the steel beam deteriorated as the number of cycles increased. Severe local buckling of the bottom flange occurred in every cycle. The bottom flange did not fracture despite its severe local buckling during eight complete cycles. The load versus strain relationship at the top and the bottom flanges of the steel girder (located 1.5 inches from the

column face) are shown in Fig. 4.17. Under positive bending, very large strains were induced in the bottom flange as a consequence of composite action.

It is known that the plastic hinge rotation (θ_p) capacity of a steel girder is limited by the local buckling of its flanges [28]. Figure 4.18(a) shows the method of calculation of plastic hinge rotation ($\theta_p=0.0152$) upon local buckling. The plastic hinge rotation capacity of the composite girder under positive bending, however, was not limited by the top flange local buckling because of the lateral support provided by the concrete slab. Figure 4.18(b) shows the curvature distribution at the time of maximum applied load. The θ_p ($= 0.0358$) was significantly larger than the θ_p ($= 0.0152$) of the steel girder alone [18].

CG3 had sufficient bond between the concrete slab and the metal sheet to prevent their separation.

Specimen CG4: This specimen was subjected to a similar cyclic loading to that of the previous test; the behavior was similar to that of CG3. Figure 4.19 shows the moment-curvature curves of the composite girders. The moment capacities of the four specimens are marked in Fig. 4.19. Assuming an effective width equal to the full slab width, the simple plastic moment (M_p) of the composite girder under positive bending and the plastic moment of the steel girder (M_{ps}) are also shown in Fig. 4.19(a); this figure shows that full composite action increased the moment capacity by a factor of more than two. It was observed that under positive bending, in spite of large slip, the theoretical simple plastic moment (M_p) can be exceeded. This is attributed to the strain-hardening effect in the bottom flange and in the web of the steel beam. Assuming the reinforcement (wire mesh) in the entire slab width to be effective under negative bending, the simple plastic moment was increased by 50% (Fig. 4.19(b)). Nevertheless, this simple plastic moment was not exceeded, although the test results were very close to it. The local buckling of the bottom, laterally unsupported, steel flange caused the deterioration of the negative moment capacity. As expected, of all the girders tested the separation of

the concrete from the metal deck for CG4 was the largest for which no surface treatment was applied.

4.4.4 Evaluation of Results

Detailed evaluation of the test results was reported in Reference 18. A summary of the important conclusions is as follows:

- (1) The steel girder should be fully welded to the column. Use of bolted-web connection and large beam copes can lead to early flange or weld failure in the surrounding region.
- (2) If the galvanized metal sheet is sand-blasted before casting the concrete, there is sufficient bond to avoid separation; this type of treatment was adopted for the 0.3-scale model structure.
- (3) Measurements showed that when the composite girder was subjected to positive bending, the concrete strain distribution across the width of the concrete slab varied with the level of displacement. The effective width was practically uniform and was close to but slightly larger than $16t+b_f$ at working load levels (Fig. 4.20). The effective width decreased at higher load level. The effective width corresponding to the maximum measured concrete strain (0.0021) was only 65% of the slab width for CG4 at the maximum applied positive moment.
- (4) Beam-column joint panel zone deformation contributes significantly to composite girder deflections. The two to three fold increase in the positive bending moment due to composite action causes the panel zone to yield in preference to the beam. The flexible joint panel zone should be considered in predicting the response of structures incorporating composite construction.
- (5) The simple plastic moment of a composite girder under positive bending can be exceeded because of strain-hardening of the steel girder. The neutral axis of the

steel girder is close to the top flange because of the composite action, the bottom flange and the web are highly strained.

- (6) The simple plastic moment of a composite girder under negative bending cannot be exceeded because of local buckling of the laterally unsupported (bottom) compression flange. However with the steel section satisfying the proportion requirements for plastic design (see Table 4.2 and AISC Specification Section 2.7), the simple plastic moment still gives a very good estimate of the negative ultimate moment capacity.
- (7) Although the plastic hinge rotation capacity ($\theta_p=0.0152$) of the steel girder was limited by flange local buckling, the θ_p of the composite girder under positive bending was greatly increased since the concrete slab could laterally support the compression flange. The total θ_p ($= 0.0358$) reached by the composite girder CG3 at point 153 in Fig. 4.15 was approximately two to three times that of the steel girder alone.
- (8) The girder hysteresis loops under load reversal were fairly stable. The resistance at the same level of deformation decreased as the number of cycles increased. The decrease in the positive bending capacity was due to the deterioration of the composite action and the cracking of the concrete slab. The decrease in the negative bending capacity was due to the local buckling of the steel flanges under load reversal. Compared with that of the bare steel girder, the energy dissipation capacity of the composite girder increased by thirty to fifty percent for the same accumulated plastic deflection (Fig. 4.21). The use of a composite girder floor system can be of great benefit provided that increases in stiffness and strength are considered in the design of joints, connections and columns.

4.5 Model Construction

4.5.1 Structural Steel Frames

First the structural elements of the model were fabricated, then the bare steel structure was erected on the floor beside the shaking table. The model foundation was designed and constructed so that it was stiff and strong enough to transport the model onto the shaking table to facilitate the tie-down and prestressing to the shaking table, and also to provide a fixed-base condition for the first story columns.

The bare steel structure was assembled in a two story sequence. All the columns and beams were set in position with erection bolts and tack welded. The geometry was then checked by two transits located in two perpendicular directions to ensure that the construction was within the erection tolerances specified by the AISC. After the overall dimensions were carefully checked, final tightening of all the bolts and final welding followed. Once the whole bare steel structure was constructed, static and free vibration tests were conducted in order to determine the mechanical characteristics of the model (Chapter 5).

4.5.2 Composite Floor System

- (1) **Steel decking:** Following the construction of the bare steel structure, the corrugated metal decking was sand-blasted before it was placed in position. One hundred and twenty holes per floor were drilled in the metal deck in order to install the fixtures required for the attachment of the auxiliary mass (lead pigs).
- (2) **Studs:** For Frames B, 1, 2 and 3 (Fig 2.1), the studs were welded directly to the steel girder top flange. This was done before the assembly of the bare steel frame. The remaining studs were welded through the corrugated deck.
- (3) **Wire mesh:** The wire mesh was welded at the head of the studs to maintain the required cover.

The steel frame was then transported onto the shaking table with rollers beneath the foundation. After leveling the foundation with hydrostone, the model was prestressed to the shaking table slab through the foundation girders at twenty five locations using high strength steel rods, 1.25 inches in diameter.

- (4) **Casting concrete:** Starting from the roof, two floors per day were cast, each requiring three batches of concrete. After casting, the floors were covered by plastic sheets to prevent moisture loss; the curing process lasted 28 days. The control cylinders were maintained in a similar condition. Three weeks after casting, the model structure was subjected to static flexibility tests and a series of free, ambient and forced vibration tests.
- (5) **Adding auxiliary mass:** After these tests, the auxiliary mass was placed in position (Fig. 4.22). To calculate the amount of lead required for each floor, the average concrete slab thickness was measured at 36 locations per floor in order to calculate the slab weight. About 900 lead bricks (weighing approximately 92 lb each), contributing 71% of the total reactive mass, were attached to the slabs. Table 4.3 lists the distribution of the model floor weight. The lead bricks were distributed and fastened to the floor with steel angles and threaded bolts. Steel shims and rubber pads were laid beneath the ends of each lead brick. The rubber pad was used on one end only so that the flexural stiffness of the slab would not be increased by the attachment of lead bricks.

4.6 Model Instrumentation

One hundred and seventy-six channels were available for data acquisition at the time of testing. The instrumentation was designed to measure the table motions and the main global and local responses of the model.

4.6.1 Shaking Table Motions

Ten channels were reserved to monitor the shaking table motion: horizontal and vertical displacements and accelerations as well as pitch, roll and twist accelerations.

4.6.2 Model Global Responses

The main parameters for measuring overall structural responses were: (i) lateral displacement; (ii) inter-story drift; (iii) floor acceleration; (iv) story shear; and (v) story overturning moment. The instrumentation was designed to obtain sufficient data to compute the time histories of these parameters.

- (1) Absolute horizontal displacements and accelerations at each floor level were measured using direct current linear voltage differential transducers (DCDT), linear potentiometers (LP) and accelerometers installed on each floor at Frames A and B. The relative horizontal displacements of each floor were then calculated by subtracting the horizontal table displacement from the absolute horizontal displacements. The inertia force at each floor was calculated by multiplying the floor reactive mass (Table 4.3) by the corresponding absolute horizontal acceleration.
- (2) The relative vertical displacements of the test structure were measured at the roof level through the use of a truss reference frame mounted on the structure foundation (Fig 4.23). The reference frame was essentially rigid and very light; its fundamental period is very small. Six DCDTs were mounted on this reference frame to measure the relative vertical displacements at the roof level.
- (3) The relative transverse displacements of the test structure were measured at the roof level. Two DCDTs were mounted on the reference frame to measure the transverse displacements of Frames 1 and 3. The difference between these two measurements provided information on the structure torsional deformation.

4.6.3 Model Local Responses

4.6.3.1 Braces

- (1) **Brace force:** Four strain gages were installed at the quarter point, adjacent its upper end, of each of the bottom four story braces. Assuming that plane sections remain plane, the four strain readings permit calculation of the axial force and bending moment about the two major axes. Two strain gages only were installed on the fifth and sixth story braces due to the limited number of available data acquisition channels. To calculate the brace forces, the brace material properties had to be known, these were established from a series of coupon tests.
- (2) **Brace axial deformation:** After buckling, it is impossible to calculate the brace axial deformations from the strain gage readings; DCDTs were installed on the bottom four story braces to measure the total axial deformation.

4.6.3.2 Columns

- (1) **Column shear:** The columns were instrumented to determine the story shear distribution. Two rosettes, one glued on each side of the column web (for major-axis bending) or the column flange (for minor-axis bending), were combined into one channel to increase the accuracy of the reading (Fig. 4.24); these gages were located at the column mid-height. Except for the first story, where all the nine columns were instrumented, only those columns in Frames A and B were instrumented. Frame C response was assumed to be the same as that of Frame A, a reasonable assumption because the X-brace in the transverse direction (Frames 1, 3) effectively restrained the torsional response of the structure. The column rosettes were calibrated by a special loading set-up so that the channels gave the column shear directly.
- (2) **Column axial force and bending moment:** Four strain gages, with two combined into one channel on each column flange, were installed at mid-height of all

the columns in the first story. These strain readings enabled the column axial force and bending moment time histories to be calculated (Section 6.5.3.3).

- (3) **Column axial deformation:** Since large column axial forces existed in the braced bay, LVDTs were installed in the columns of the first two stories to ascertain the influence of column deformations on the inter-story drifts.
- (4) **Column end rotation:** The column ends in the first two stories were instrumented by a pair of DCDTs to measure the column end rotation (Fig. 4.25).

Limited by the available number of data acquisition channels, it was impossible to instrument the composite girders and beam-column panel zones comprehensively. The steel structure was painted with a special type of whitewash, which bubbles and peels upon yielding, to facilitate visual inspection of the structure.

Figure 4.25 shows the instrumentation scheme; Appendix A lists the associated transducers.

4.7 Data Acquisition

The data acquisition system of the Earthquake Simulation Laboratory functions in the following manner:

- (1) The individual transducer (strain gages, DCDTs, accelerometers etc.) output is passed through a *Pacific* Signal Conditioner which provides the excitation voltage for the transducer, amplifies its output and filters that output to eliminate frequencies above 100 Hz.
- (2) The *Preston* Multiplexer scans the signal conditioners and sequentially reads each channel at a burst rate of 0.5MHz, that is, for two adjacent channels, the true read time difference is two microseconds. The scanning rate (i.e., number of times per second each channel is sampled) is specified in the data acquisition software.

- (3) The analog signal from the Multiplexer is then passed through a *Preston* A/D Converter which converts the signal to a digital form. The digitized record is stored on hard disk on the in-house VAX 11-750. Figure 4.26 shows the shaking table system block diagram.

The first 128 channels of the 176 channels were processed by this data acquisition system. The remaining 49 channels used amplifiers without filters; this raw data was disturbed by high frequency noise. A numerical Ormsby filter was used to filter out the undesirable noise. For low level shaking table tests (peak acceleration $< 10\%$ g), the scanning rate of the data acquisition system was set at 100 Hz; the scanning rate was set to 200 Hz for all other shaking table tests.

The statistical software package S [29] was used to process the raw data. New functions, such as numerical filters, response spectra evaluation, numerical integration and differentiation, energy calculation and so on, were written and added to the S package during this project to aid the processing of the acquired data.

V. MECHANICAL CHARACTERISTICS OF THE MODEL

5.1 Introductory Remarks

Throughout the construction phase and shaking table tests of the model, tests were conducted to determine the static and dynamic characteristics of the test model. These tests included static flexibility, free vibration, forced vibration and ambient vibration tests. The characteristics to be determined were the structural flexibility, natural frequencies and equivalent viscous damping ratios. The objectives of these tests were to assess the variation of these mechanical characteristics throughout the construction stage and the shaking table tests, and, to evaluate the reliability of the analytical predictions using commonly applied analytical modeling schemes.

5.2 Analytical Prediction of the Model Response

The initial mechanical characteristics of the model were evaluated after the composite floor had been cast and then prior to the shaking table tests. On the basis of the coupon tests of the steel members, the modulus of elasticity (E_s) was chosen as 29,000 ksi. The lightweight concrete modulus of elasticity (E_c), determined from the 28 day compression tests of 3 by 6 inch cylinders, was 2,400 ksi. The analytical assumptions were the same as those noted in Section 3.2.

Flexibility: By applying unit loads at each floor level, the flexibility matrix of the model was calculated; the resultant matrix is shown in Table 5.1(a). The corresponding stiffness matrix was obtained by inverting the flexibility matrix (Table 5.1(b)).

Periods and Mode Shapes: Using this flexibility matrix and the lumped diagonal mass matrix with and without the auxiliary lead (Table 4.3), the periods and mode shapes were calculated (Table 5.2(a), Table 5.2(b)). The mode shapes, together with their

respective natural periods, are shown in Fig. 5.1.

Note that the terms outside the tri-diagonal band of the calculated stiffness matrix (Table 5.1(b)) are non-zero; these terms will be zero only for the pure shear type of building structure. Assuming that the test model was a pure shear type of structure, the flexibility and stiffness matrices and the natural frequencies were re-evaluated (Table 5.1(c), Table 5.1(d) and Table 5.2(c)). The fundamental frequency changed from 3.0 Hz to 4.0 Hz, implying that the lateral stiffness was increased by a factor of 1.7 ($= (4.0/3.0)^2$). The assumption of a pure shear type of structure is inappropriate for this concentrically braced steel frame.

5.3 Dynamic Characteristics of the Model

5.3.1 Introductory Remarks

The dynamic characteristics of the model were determined at various stages of the construction as follows:

- (1) unbraced model without composite slab;
- (2) braced model without composite slab;
- (3) model without auxiliary mass (lead pigs);
- (4) model with auxiliary mass, i.e., the model as it would be tested in the shaking table experiments.

The objectives of these tests were as follows:

- (1) to quantify the increase in lateral stiffness when Frame B was braced;
- (2) to quantify the increase in lateral stiffness and change in damping ratio when the composite floor system was incorporated into the model.
- (3) to ascertain the effect of the auxiliary mass on the lateral flexibility and the lateral stiffness of the model.

The model's dynamic characteristics after the shaking table tests commenced are described in Section 7.2.1.

5.3.2 Test Procedures

A description of the test procedures for the static flexibility, free vibration, ambient vibration and forced vibration tests follows.

5.3.2.1 Static Flexibility Tests (Unit Loading Test)

The objectives of the static flexibility test were: (i) to compare the flexibility characteristics of the test structure with those predicted analytically; (ii) to compute the natural frequencies of the test structure assuming a lumped mass system and to compare the results with those obtained from the vibration tests; and (iii) to compare the results at different stages of the construction of the test structure and to discuss the contribution of the braces, the composite slab and the auxiliary mass to the flexibility of the test structure.

The test structure was loaded sequentially at each floor level by a rigid steel beam (Fig. 5.2). Two cables were extended to the laboratory floor from the steel loading beam and anchored to the floor; a load cell and turnbuckle were inserted in each cable. The load was applied by tightening the turnbuckle of each cable simultaneously to maintain equal load levels in both cables. The vertical component of the cable force was resisted by two tubular steel columns fixed to the laboratory floor; steel angles were welded to these tubular columns at each floor level to support the steel loading beam.

For the first two groups of tests, the model foundation was clamped to the laboratory floor by anchor bolts and by placing piles of lead pigs on the foundation to prevent its horizontal and vertical movement. After moving the model onto the locked shaking table, its foundation was prestressed to the shaking table with high strength steel rods.

5.3.2.2 Free Vibration Tests

The test structure was subjected to a small lateral displacement by applying a load at the roof level via two cables. The two cables attached to the roof level were then connected to a single cable and anchored to the laboratory floor. Two turnbuckles, one in each cable, were inserted to equalize the displacement. A 3/8 inch threaded rod was attached to the end of the cable close to the floor. When the appropriate displacement level was induced at the roof level, the threaded rod was cut. The structure then responded in free vibration and its motions were recorded by the data acquisition system.

The recorded displacement and acceleration response time histories contained a number of modes of vibration; the simple application of the logarithmic decrement method would not give a good estimate of the damping ratio. The following procedure was used to estimate the modal damping ratios and natural periods (Fig. 5.3):

- (1) The recorded lateral acceleration (or displacement) time history was transformed into the frequency domain using the Fast Fourier Transform (FFT).
- (2) The appropriate cut-off frequencies around the frequency of interest were selected and then band-pass filtered; the filtered response was then transformed back into the time domain using the Inverse Fast Fourier Transform (IFFT).
- (3) The modal time histories obtained in Step (2) were treated as the free vibration decay wave of a single degree of freedom system. The natural period was calculated by the zero crossing method and damping ratio was obtained using the conventional logarithmic decrement method.
- (4) Steps (2) and (3) were repeated with a variety of cut-off frequencies in order to minimize the variation and error in the natural period and the damping ratio.

5.3.2.3 Ambient Vibration Tests

Ambient vibration tests were carried out by placing two seismometers, calibrated to measure velocity, on the two exterior frames at the roof level of the test structure (Fig. 4.22). The outputs of the two seismometers were averaged or subtracted to produce the translational or torsional ambient velocity responses. The velocity response was input to a FFT analyzer to calculate its Fourier amplitude spectrum and to detect the dominant frequencies. These calculations were repeated more than 100 times and averaged to increase the S/N (Signal/Noise) ratio. The frequencies at which significant power was indicated in the Fourier amplitude spectrum were considered as the natural frequencies of the test structure.

5.3.2.4 Forced Vibration Tests

Forced vibration tests were performed using harmonic excitation to obtain the dynamic characteristics of the test structure. A small shaking table was used as a force generator on the roof level (Fig. 5.4); this maintained a constant force amplitude during the forced vibration test. This small shaking table was an electro-dynamic force generator and was used primarily to calibrate instruments and to test small models. The shaking table was air-supported and could produce a constant acceleration of up to 0.6 g in the frequency range of 2 to 20 Hz. A maximum force amplitude of 30 lb could be generated with 50 lb of weight installed on the shaking table. During the forced vibration tests, the lateral displacement time histories at different exciting frequencies were recorded by the data acquisition system and analyzed to construct the frequency response curves. The forced vibration tests were performed only for the test model with the cast concrete slab.

5.3.3 Stage 1 Test - Unbraced Model without Composite Slab

(1) Static Flexibility Tests

Each frame of the test structure was expected to behave independently because of both the lack of a concrete slab and the fact that the transverse beams were shear-connected. The maximum load applied to the test structure ranged from 5 kips on the roof level to 10 kips on the second floor. For a test at a given floor level, the load was applied in several increments; the data were then processed using a least squares method to check the linearity of the response and to improve the reliability of the flexibility matrix coefficients. The resulting flexibility matrices of Frame A (C) and Frame B are shown in Tables 5.3 and 5.4, respectively. The corresponding stiffness matrices were calculated by inverting the symmetric flexibility matrix, which was obtained from the measured flexibility matrix by averaging its off-diagonal terms ($f'_{ij} = (f_{ij} + f_{ji})/2$). The periods were calculated by solving the eigen-value problem (Eq. 3.1) with the diagonal mass matrix.

(2) Free Vibration Tests

As expected, many peaks appeared in the Fourier amplitude spectra of the measured roof accelerations as Frames A (C) and B behaved practically independently (Fig. 5.5). The mode shapes associated with each peak were distinguished by evaluating the amplitude of the Fourier spectra and relative phase angles at each floor level in each frame. The first dominant frequency was 8.43 Hz for Frame A and 5.35 Hz for Frame B. Although the flexibility test showed that Frame B was stiffer, its natural frequency was smaller than that of Frame A because of the larger structural weight shared by Frame B. The first mode equivalent viscous damping ratios were 0.78% for Frame A and 0.40% for Frame B.

5.3.4 Stage 2 Test - Braced Model without Composite Slab

In the second stage of the model construction, the concentric braces were installed in Frame B between Frames 1 and 2 (Fig. 5.2).

(1) Static Flexibility Tests

The maximum applied load ranged from 10 kips on the roof level to 20 kips on the second floor. The resulting flexibility and stiffness matrices and natural frequencies of Frames A (C) and B are listed in Tables 5.5 and 5.6, respectively. The stiffness of Frame B increased tenfold with the addition of the bracing. The stiffness of Frame A (C) was not expected to change; however there was a reduction of the order of 10 percent. As a result of increased loads being applied to the frames, uplift of the structure foundation occurred with the subsequent reduction in frame stiffness.

(2) Free Vibration Tests

Because of the large difference in the lateral stiffnesses of Frame A (C) and Frame B, the predominant frequencies of each frame were easily distinguished. These were 6.73 Hz, 23.37 Hz and 36.71 Hz for the first three modes of Frame A (C) and 13.77 Hz for the first mode of Frame B (Fig. 5.6). The first modal damping ratios were 1.23% for Frame A (C) and 2.4% for Frame B; these damping ratios are much higher than those found in the Stage 1 tests. The large difference in the stiffnesses of Frames A (C) and B resulted in significantly different lateral displacements of these frames leading to increased interactions of the elements in their connections, and consequently the damping ratios increased.

5.3.5 Stage 3 Test - Model without Auxiliary Mass

Prior to casting the concrete slab, the structure was moved onto the shaking table and its foundation was prestressed to the shaking table. The shaking table was assumed to have sufficient rigidity to be considered as a rigid base. The following tests were carried out 14 days after the casting of the concrete slab.

(1) Static Flexibility Tests

At this stage, the displacements of Frame A (C) and B were expected to be identical because of the in-plane rigidity of the floor system. In addition, the vertical and

horizontal displacements of the shaking table relative to the laboratory floor were measured to remove the effect of the rotation and lateral movement of the shaking table on the lateral displacements of the test structure.

The maximum applied lateral loads ranged from 6 kips on the roof level to 11 kips on the second floor. The flexibility and stiffness matrices and the calculated natural frequencies are presented in Table 5.7. The symmetry of the flexibility matrix was improved slightly with respect to the previous test results.

(2) Ambient Vibration Tests

The Fourier amplitude spectrum indicated that the first five frequencies in the loading direction were 5.57 Hz, 15.63 Hz, 25.93 Hz, 37.01 Hz and 48.05 Hz (Fig. 5.7).

(3) Free Vibration Tests

The Fourier amplitude spectrum of the roof level acceleration response showed four clear peaks (Fig. 5.8) at 5.37 Hz, 15.47 Hz, 28.19 Hz and 36.87 Hz; these peaks corresponded to the first four modes of vibration in the loading direction. The first mode damping ratio was 1.63%.

(4) Forced Vibration Tests

The test structure was excited with harmonic input at and around the natural frequencies determined from the previous tests. The frequency response curves for each mode were constructed (Fig. 5.9); the resonant frequencies evaluated from these curves were 5.38 Hz, 15.55 Hz and 28.11 Hz. The equivalent viscous damping ratios, obtained using the half power band-width method [30], were 1.57%, 1.01% and 1.19% for the first three modes.

A comparison of the analytically predicted periods (Table 5.2) with the test results shows that the correlation is very good. The difference in the fundamental periods is about 4%. The measured mode shapes are plotted in Fig. 5.1(b). A comparison of these measured mode shapes with the analytically predicted mode shapes shows excellent

correlation.

5.3.6 Stage 4 Test - Model

(1) Static Flexibility Tests

The same loading levels used in the previous tests were applied to the model in order to investigate the change in the flexibility caused by the addition of the auxiliary mass. The flexibility and stiffness matrices and the calculated natural frequencies are listed in Table 5.8. The difference resulting from the unsymmetric nature of the flexibility matrix was less than 5 percent. The coefficients of the flexibility matrix decreased slightly when compared with the flexibility matrix of the model without the lead pigs. The displacement profiles of the model with and without the auxiliary mass are shown in Fig. 5.10. The difference between the two measured flexibilities was less than 10% for the upper four floors, 15% for the third floor and 25% for the second floor.

The increase in structure stiffness can be attributed to the method of attachment of the auxiliary mass. Ideally, each lead brick should be simply supported at both ends and the tightening force should pass through these frictionless supports, thus avoiding its stiffening effect. The lead bricks were supported at one end by a steel pad and at the other end by a rubber pad. Although the rubber pad was deformable, it could not prevent some increase in stiffness of the slabs by the lead bricks; the stiffness of the model increased after the addition of the auxiliary mass. To improve the accuracy of the measured lateral displacements, larger lateral loads, which resulted in greater flexural deformation in the floor elements, were applied to the lower stories. The increased restraint due to the attachment of lead pigs caused a significant difference in the measured lateral displacements upon loading the lower floors. Other effects such as the axial force on the column stiffnesses may also contribute to the increased stiffness.

It was also observed that loading the upper stories of the test structure led to a flexural mode of deformation while loading the lower stories led to a shear mode of deformation. The analytically predicted flexibility profiles are shown in Fig. 5.10; their

correlation with the test results is satisfactory.

(2) Ambient Vibration Tests

The four peaks observed in the Fourier amplitude spectrum of the roof velocity (Fig. 5.11) corresponded to frequencies of 2.98 Hz, 8.5 Hz, 14.45 Hz and 19 Hz; these were the natural frequencies of the first four modes of vibration. The first mode frequency in the transverse direction was 3.03 Hz.

(3) Free Vibration Tests

From the Fourier amplitude spectrum of the roof velocity, the first four natural frequencies were 2.92 Hz, 8.42 Hz, 14.53 Hz and 18.85 Hz (Fig. 5.12). The corresponding damping ratios in the first three modes were 1.29%, 0.67% and 0.54%. A comparison of the analytically predicted first mode natural frequency (3.03 Hz from Table 5.2(b)) with the measured first mode natural frequency shows that the difference is 4%; however, the analytically predicted first mode natural frequency assuming pure shear type structure (3.97 Hz from Table 5.2(c)) is 33% higher than the measured first mode natural frequency.

(4) Forced Vibration Test

The frequency response curves based upon the roof acceleration response indicated that the natural frequencies of the first three modes were 2.90 Hz, 8.39 Hz and 14.59 Hz (Fig. 5.13). The damping ratios were 1.56%, 0.72% and 0.63%, respectively.

The fundamental periods from the ambient test (2.98 Hz), the free vibration test (2.92 Hz), the forced vibration test (2.90 Hz) and that predicted analytically (3.03 Hz) are very close.

The free and forced vibration tests had similar vibration amplitudes, therefore, the measured periods were close. The ambient vibration test had a much smaller vibration amplitude; it resulted in a higher natural frequency because the initial Young's modulus of the concrete associated with the small vibration amplitude was larger and the

concrete cracks, due to gravity load (say), had not yet been initiated.

5.4 Comparison of the Model and the Prototype Test Results

The model was designed and constructed as a true replica of the prototype. The accuracy of the modeling was evaluated by comparing the fundamental mechanical characteristics of the model with those of the prototype.

(1) Flexibility Matrix

A comparison of the flexibility profiles is shown in Fig. 5.14. The model was more flexible when loaded from the roof and stiffer when loaded from the fifth floor than the prototype; the correlation in general is very good. The difference in the coefficients of the flexibility matrices of both structures is less than 5 percent.

(2) Periods and Mode Shapes

The natural periods of the model and the prototype obtained from the free and forced vibration tests are shown in Table 5.9; the periods of the model were time scaled to the prototype level. The difference in their fundamental periods was 3% from the free vibration tests and 2% from the forced vibration tests. The forced vibration tests yielded differences in the second and the third mode periods of 1% and 5%, respectively. The measured model mode shapes, shown in Fig. 5.15, are very similar to those of the prototype.

(3) Damping

According to similitude laws, the nondimensional damping ratios should be the same for both the prototype and the model. Despite the good correlation of the flexibility, natural periods and mode shapes, the damping ratios are dissimilar. The equivalent viscous damping ratios for the first three modes from the forced vibration tests were 1.56%, 0.72% and 0.63% for the model and 0.49%, 0.48%, 0.50% for the prototype. It is believed that, as a result of the reduced floor slab thickness, the model had more

shrinkage cracking, which resulted in higher equivalent viscous damping ratios. The significant difference between the first mode damping ratios must be considered when comparing the model shaking table test responses with the prototype pseudo-dynamic test results.

5.5 Comparison of the Model Analytical and Experimental Results

The natural frequencies predicted analytically and measured experimentally are summarized in Table 5.10. The semi-analytical predictions using the measured flexibility matrix and a lumped mass matrix are also presented.

(1) Unbraced Model without the Composite Slab

The weight of the test structure at this stage was only 6.85 kips; this corresponded to 6.4% of the total weight of the model. In the analytical and semi-analytical predictions, the ratio of the mass distributed to each frame was 25% for Frame A (or C) and 50% for Frame B. The analytical and semi-analytical methods used the same diagonal mass matrix and they agreed well. These natural frequencies were significantly lower than the free vibration test results. The assumption of lumped masses at each floor is not reasonable prior to the casting of the composite slab; the analytical and semi-analytical methods were only approximate in this case.

(2) Braced Model without the Composite Slab

The stiffness of Frame B increased significantly upon the addition of the concentric braces, as a consequence, approximately 80% of the total lateral load was resisted by Frame B and significant vertical movement in the foundation was observed. The natural frequencies of Frame B from the free vibration test and the semi-analytical method were 10 percent lower than those predicted analytically. The measured fundamental frequency of Frame A from the free vibration tests changed from 8.43 Hz to 6.73 Hz; this was due in part to foundation uplift.

(3) Model Structure without the Auxiliary Mass

The test structure was moved and fastened tightly to the shaking table, the rigidity of the structure foundation was therefore improved. The weight of the test structure at this stage was 27% of that of the model.

The correlation of the natural frequencies between the analytical, semi-analytical and test results is excellent. Because the test structure foundation was not perfectly rigid, the analytically predicted fundamental frequency (5.60 Hz) was 5% higher than the measured frequency (5.37 Hz).

(4) Model

The degree of correlation between the analytical, semi-analytical and test results was similar to that obtained in the previous stage. The results show that the analytical model could predict the first four natural frequencies and mode shapes.

5.6 Concluding Remarks

Different vibration tests were carried out to ascertain the variation in the dynamic characteristics of the test structure as its construction proceeded. The conclusions of these studies are as follows:

- (1) The damping ratios of the unbraced test structure were very small. After the braces were installed in Frame B, the stiffness of Frame B increased almost tenfold. The natural frequency of Frame A (C) was about half that of the unbraced Frame B; its damping ratios increased after the concentric braces were installed in Frame B.
- (2) After casting the concrete slab, the damping ratios of the test structure increased. The natural frequencies determined by the different testing techniques were very close; the maximum differences between them were 4%, 1% and 8% for the first three modes.

- (3) The natural frequencies decreased after the auxiliary mass was added to the structure. The natural frequencies evaluated by the different vibration testing techniques were in good agreement; the maximum differences between the three methods were 3%, 1% and 1% for the first three modes.
- (4) The analytically predicted flexibility, natural periods and mode shapes correlated reasonably well with the test results. The difference between the predicted and measured fundamental periods after adding the auxiliary mass to the model was 4%. If a pure shear type of building structure were assumed, the analytical fundamental natural frequency of this concentrically braced frame would be overestimated by 30%.
- (5) The model was carefully designed and constructed; therefore the similitude scaled flexibility and natural periods and the mode shapes were close to those of the prototype. The only significant difference between the two structures was in their first mode viscous damping ratios ($\xi_{1(\text{model})}=1.56\%$, $\xi_{1(\text{prototype})}=0.49\%$). The shrinkage cracking in the model slabs was more pronounced than in the prototype slabs; this resulted in higher damping ratios in the model.
- (6) The analytical model was able to predict the first four natural periods and their respective mode shapes reliably. Thus, since the linear elastic response of a structure to earthquake ground motion in a given direction is a function of only the first few participating modes, the analytical model is satisfactory.

VI. EARTHQUAKE SIMULATION TESTS OF THE MODEL: TEST PROGRAM AND PROCEDURES

6.1 Introductory Remarks

After the initial mechanical characteristics of the model were determined (Chapter 5), it was subjected to a series of simulated ground motion excitations. To facilitate the execution of the test program, the analytical response of the model to selected shaking table motions was predicted prior to testing. The nonlinear static analyses and limit analyses of the model are described in this chapter.

The test program is described in Section 6.4; the data reduction procedure is discussed in Section 6.5, emphasizing the noise elimination techniques used on the recorded responses.

6.2 Analytical Response of the Model

6.2.1 Introductory Remarks

The procedures described in Sections 3.3 and 3.4 were applied to the model to predict its behavior. These analyses were conducted using the same assumptions as those used for the prototype; the element properties were based on the measured sectional properties and material characteristics.

6.2.2 Prediction of the Model Strength

(1) Step-by-Step Static Nonlinear Analysis

The computer program ANSR-1 was used to predict the strength of the model under monotonically increasing proportional lateral load. Two lateral load patterns, inverted-triangular and uniform, were considered. The roof drift index versus the base

shear ratio curves for these two cases are shown in Fig. 6.1; the hinge formation sequence is shown in Fig. 6.2.

(2) Limit Analysis Using Simple Plastic Theory

The base shear corresponding to the collapse mechanism shown in Fig. 3.9(a) was 69.8 kips ($V_B/W=0.65$) for inverted-triangular lateral loading; for a uniform lateral loading the base shear was 81.0 kips ($V_B/W=0.76$) based on the mechanism shown in Fig. 3.9(b).

6.2.3 Prediction of the Model Seismic Response

The computer program DRAIN-2D was applied to the model to predict its seismic response. The earthquake ground motion selected was the same as that used for the testing of the prototype (Fig. 3.10). The ground motion was time scaled by a factor of $1/\sqrt{0.3048}$ ($=1.811$) to satisfy the similitude law. The scaled acceleration and displacement time histories are shown in Fig. 6.3. The measured first two mode damping ratios ($\xi_1=1.29\%$, $\xi_2=0.67\%$) were used to calculate the Rayleigh damping constants (Eq. 3.15); this would overestimate the measured third mode damping ratio by 18%. The roof lateral displacement and base shear time histories of the model subjected to 65 gal, 250 gal and 500 gal ground motions are shown in Fig. 6.4 to Fig. 6.6.

6.2.4 Concluding Remarks

The envelope of roof drift index versus base shear ratio extracted from the dynamic analyses is shown in Fig. 6.1. The predicted nonlinear behavior of the prototype (from Fig. 3.6) is also shown in Fig. 6.1; the figure indicates that the strength of the model, after scaling it to the prototype level, was about 4% higher than that of the prototype. This is attributed to the higher strength of the material used for fabrication of the model members (Figs. 4.2 and 4.5).

6.3 Shaking Table Input Motion

The scaled displacement time history of the Miyagi-Ken-Oki Earthquake (Fig. 6.3) was used as the input signal to the earthquake simulator; the corresponding linear elastic response spectra are shown in Fig. 6.3(c).

During the shaking table test, the span setting of the the table displacement was adjusted to obtain the desired intensity of the table motion. The span is directly proportional to the displacement and approximately proportional to the acceleration for low intensity table motion. Under high intensity motion the relationship with the acceleration is distorted significantly by the table-structure interaction.

6.4 Test Program

The model was subjected to the sequence of tests listed in Table 6.1. As indicated in this table, the earthquake simulator tests were classified into four categories. The first series of tests were of a diagnostic nature, that is, low amplitude tests conducted to confirm the operation of the earthquake simulator, the instrumentation, the data acquisition system as well as to generate the **serviceability** limit state response.

The second series of tests consisted of table motions of increasing intensity to simulate the **damageability** limit state of the model response. These tests were designed to introduce moderate structural damage in the form of brace buckling and minor yielding in some of the critical regions in the moment-resisting space frames.

In the third series of tests, the model was subjected to severe input motion with the objective of reaching the **collapse** limit state of the model. Severe brace buckling or rupture was expected; the moment-resisting space frame was also expected to yield significantly.

The fourth series of tests were designed to investigate the effects of **aftershocks** on the model. The intensities selected were similar to those used for the damageability

limit state testing.

To evaluate the variation of the mechanical characteristics of the test model with the degree of damage, free vibration tests were carried out at the beginning and the end of most of the earthquake simulator tests. Unlike the free vibration test procedure described in Chapter 5, where the model was excited by cutting the pretensioned cable connecting the roof level to the laboratory floor, the model was excited by inputting a displacement pulse of a small intensity to the shaking table. The free decay vibrations were then recorded and analyzed to determine the natural frequencies and damping ratios of the model. There are two advantages to this type of free vibration test:

- (1) It is easier to conduct during shaking table testing as the table does not have to be lowered and locked to use the pull-and-release procedure described in the previous chapter.
- (2) The frequencies and damping ratios measured under this condition reflect the true characteristics of the model on the "soft" foundation provided by the shaking table.

The natural frequencies measured in this fashion will be lower than those in the locked foundation condition. The damping will be higher because of the presence of the hydraulic actuators and passive stabilizers.

6.5 Data Reduction

6.5.1 Data Noise

Recorded data containing noise is an inevitable phenomenon in the use of an electronic data acquisition system. Of the 176 channels used, the signal conditioners of the first 128 channels were equipped with an electronic filter. Significant noise was mixed with the true signals for the remaining 49 channels. Two kinds of undesirable noises were encountered during the tests:

(1) High Frequency Noise - The high frequency noise arising in an electronic data acquisition system can be easily identified. A numerical filtering technique was used throughout the data reduction procedure. The Ormsby lowpass filter, used by researchers at the California Institute of Technology to process earthquake records [31], was adopted and implemented into the S computer program [29] to remove the high frequency noise. A cut-off frequency (f_c) equal to 20 Hz was selected for the following reasons: (i) the filtered data contained the first four modes of vibration (see Table 5.8); the contribution of the modes higher than the fourth was negligible; (ii) the Fourier amplitude spectrum of the time scaled input signal showed little energy associated with those frequencies higher than 20 Hz; and (iii) the oil column resonant phenomenon of the shaking table drastically distorts input frequency content higher than 16 Hz (Fig. 4.1) [25]. A typical example of the response time histories before and after applying the Ormsby lowpass filter is shown in Fig. 6.7.

(2) Low Frequency Noise - Low frequency noise was generally not filtered out of the response unless significant evidence showed that it had to be. The need to remove low frequency noise arose from the permanent non-zero readings of a number of the recorded channels. Permanent offsets were observed in both displacement measurements (DCDTs or LPs) and axial strain gage readings; this reflected either permanent deformation or plastic strain. Filtering low frequency noise in this instance would have been dangerous as it would have distorted the true response. A permanent offset was not allowed for acceleration (from accelerometers) and force transducer measurements (column shears from rosettes) in the calibrated range as the response must decay to zero following the test. The recorded accelerations were of very good quality in this respect; however, a number of rosettes installed at the column mid-height showed a certain degree of permanent offset. These errors increased monotonically over the duration of the test (see Fig. 6.8(a)). A simple procedure was used to remove the low frequency noise:

- (1) The mean (A) of the last two seconds of the recorded free vibration response following the base excitation was calculated.
- (2) The response was corrected by subtracting the noise function $e(t)$ from the recorded time history, where

$$e(t) = \frac{A}{2} \left(1 - \cos \frac{\pi t}{t_d} \right) \quad (6.1)$$

A = permanent offset at the end of duration;

t_d = recorded duration = 18 seconds.

Note that Eq. (6.1) assumes that the low frequency noise had a period equal to twice the duration of data acquisition.

This method, illustrated in Fig. 6.8, was used to process all column shear data.

Twelve seconds duration (from 1 to 13 seconds) of seismic response will be presented in the following chapters; this duration encompasses the Miyagi-Ken-Oki Earthquake signal (the subsequent free vibration response was insignificant).

6.5.2 Sign Convention

The following sign convention is used throughout this report:

- (1) lateral displacement, inter-story drift, acceleration: positive to the right (west) side and upward in the vertical direction;
- (2) brace axial strain, axial deformation and force: positive for elongation and tension;
- (3) column shear force, story shear force: positive shear force induced by positive inter-story drift.

This sign convention is shown in Fig. 6.9.

6.5.3 Force Calculation

(1) Brace Force

To calculate the axial force in the unbuckled braces, the average axial strains were multiplied by the measured Young's modulus ($E_s=29,000$ ksi). Upon brace buckling, either in-plane or out-of-plane, the axial force and the bi-axial bending moments at the measured section were calculated from the strain readings on its four sides. Although the strain gages were installed at the quarter point of the brace length, close to the analytical inflection point, the strain gages measured significant yielding excursions once the brace buckled. The measured strain time history together with the tubular brace material properties from coupon tests were used to trace the corresponding stress state.

A modified version of the computer program UNCOLA [32] was used to calculate the axial force and moments of an arbitrary section subjected to axial force and biaxial bending. The actual stress-strain relationship was idealized by a Ramberg-Osgood constitutive relationship. The four strain gage time histories, one from each side of the tubular brace, were used as input data. Assuming plane sections remained plane, strain readings at three different locations at one section would be sufficient to define the orientation of the section plane (or the strain profile of the whole section). Least-squares fitting was performed on the four strain readings in order to minimize the errors; the corresponding axial force and bending moments in both directions were then calculated. Only two strain gages were installed in the braces of the two top stories; in this instance in-plane bending was assumed and only the axial force and in-plane bending moments were estimated.

(2) Story Shear

Two methods were used to calculate the story shear:

- (a) The story shear was calculated by summing the individual floor inertia forces at each floor above that story; these inertia forces were calculated by multiplying the measured absolute acceleration by the floor weight listed in Table 4.3. The

advantage of this method is that the calculation is simple and dependable if the measured accelerations are accurate and the floor weight is precisely measured. The disadvantage is that the damping force is also included in the calculation. The following equation of equilibrium explains this problem:

$$f_I + f_D + f_S = 0$$

or
$$f_I = -(f_S + f_D) . \quad (6.2)$$

Therefore this method is reliable when the damping is small; this was the case for the model for which the first modal damping ratio was about 1.3%.

- (b) The story shear was calculated by summing the column shears from the strain rosette measurements and the horizontal components of the concentric brace forces; this is the correct way to calculate the story shear. However, the brace axial forces were not measured directly but were calculated by the method discussed in the previous section. These calculated brace forces were less reliable, especially upon brace buckling, because the brace material properties from coupon tests had to be assumed and brace residual stresses were ignored.

The two methods were compared for the low intensity level test of 6.3% g peak acceleration (Table 6.1). Figure 6.10 shows that the difference between the two methods is trivial and the correlation coefficient is almost 1. The inertia force method was therefore used for the story shear calculation when the tests induced buckling in some braces.

The total story shear (V_i^{TOTAL}) can be subdivided into two components:

$$V_i^{\text{TOTAL}} = V_i^{\text{BRACE}} + V_i^{\text{MRSF}} \quad (6.3)$$

where V_i^{TOTAL} = total shear in story i

V_i^{MRSF} = shear resisted by moment-resisting space frame in story i

= summation of column shears in story i

V_i^{BRACE} = shear resisted by braces in story i

= sum of horizontal components of brace forces in story i.

Subtracting the column shears from the total story shear gives the story shear resisted by the braces; namely,

$$V_i^{\text{BRACE}} = V_i^{\text{TOTAL}} - V_i^{\text{MRSF}} . \quad (6.4)$$

(3) Column Axial Force and Bending Moment

The first story columns were instrumented at the column mid-height, with shear transducers (rosettes) installed on the web and axial strain gages on both sides of the flanges (Fig. 4.22). With the recorded axial strain time histories, UNCOLA was used to calculate the axial force and bending moment at the measured section. This moment together with the measured column shear force can be used to extrapolate the column end moments.

6.5.4 Member Designation

The member designation for the subsequent discussion of the model response is shown in Fig. 6.12.

6.6 Energy Calculation

Analysis of structural behavior by energy methods is exceedingly useful. The ground excitation together with the foundation response generate the input energy (E_I) to the structure; the structure responds to the input energy as follows:

- (i) Kinetic energy (E_K) proportional to the absolute velocity squared;
- (ii) Strain energy (E_S) stored in the structure by elastic deformation;
- (iii) Viscous damping energy (E_μ) dissipated by structural damping mechanisms such as joint friction, material internal friction etc.; viscous damping is generally assumed for building structures and is proportional to relative velocity;

(iv) Hysteretic energy (E_H) dissipated by the inelastic behavior of the structure.

The energy equation can be expressed as:

$$E_K + E_A + E_\mu = E_I \quad (6.5)$$

where $E_A (= E_S + E_H)$ is the absorbed energy. Details of its derivation are given in Appendix B. Assuming a six-degree of freedom lumped mass system, each term of Eq. 6.5 is expressed below in vector form:

(1) **Kinetic Energy (E_K)**

$$E_K = \frac{1}{2} \dot{\mathbf{v}}^t T \underline{\mathbf{m}} \dot{\mathbf{v}}^t = \frac{1}{2} \sum_{i=1}^6 m_i (\dot{v}_i^t)^2 \quad (6.6)$$

where $m_i =$ *ith* floor lumped mass (Table 4.3)

$\dot{v}_i^t =$ absolute lateral velocity at the *ith* floor level.

The \dot{v}_i^t are calculated by differentiating the measured absolute horizontal displacements.

(2) **Absorbed Energy (E_A)**

$$E_A = \int_0^t \mathbf{f}_S^T d\mathbf{v} = \sum_{i=1}^6 \int_0^t f_{S_i} dv_i = \text{absorbed energy} \quad (6.7)$$

$=$ strain energy (E_S) + hysteretic energy (E_H)

where $f_{S_i} =$ restoring force acting at the *ith* floor

$=$ difference of story shears above and below the *ith* floor

$v_i =$ *ith* floor relative lateral displacement.

Then, from Eq. (6.7), by means of a simple transformation (see Appendix B), E_A can be expressed in terms of the story shear and the inter-story drift.

$$E_A = \int_0^t \underline{\mathbf{V}}^T d\underline{\boldsymbol{\delta}} = \sum_{i=1}^6 \int_0^t V_i d\delta_i \quad (6.8)$$

where V_i = story shear in the i th story

δ_i = inter-story drift in the i th story

Thus the absorbed energy is obtained by integrating the story shear with respect to inter-story drift. The absorbed energy can be subdivided into the recoverable elastic strain energy (E_S) and the irrecoverable hysteretic energy (E_H). The elastic strain energy is calculated as follows:

$$E_S = \sum_{i=1}^6 \frac{V_i^2}{2K_i} \quad (6.9)$$

where K_i is the unloading stiffness of the δ_i versus V_i curve, assumed equal to the initial tangent stiffness. The hysteretic energy is calculated as follows:

$$E_H = E_A - E_S = \sum_{i=1}^6 \int_0^t V_i d\delta_i - \sum_{i=1}^6 \frac{V_i^2}{2K_i} \quad (6.10)$$

(3) Viscous damping Energy (E_μ)

The viscous damping energy is calculated as follows:

$$\begin{aligned} E_\mu &= \int_0^t \mathbf{f}_D^T d\mathbf{y} = \sum_{i=1}^6 \int_0^t \mathbf{f}_{Di} dv_i \\ &= \int_0^t \mathbf{q}^T d\mathbf{\delta} = \sum_{i=1}^6 \int_0^t q_i d\delta_i \end{aligned} \quad (6.11)$$

where q_i is the story damping force. Viscous damping energy is difficult to measure; the calculation of E_μ based upon the measured structural characteristics and responses is discussed in Section 8.6.

VII. MODEL EXPERIMENTAL RESULTS

7.1 Introductory Remarks

For the prototype tests at the BRI, Japan, three levels of ground motion were simulated: (i) 65 gal to simulate the serviceability limit state; (ii) 250 gal for the damageability limit state; and (iii) 500 gal for the collapse limit state test. For the model, a total of twenty shaking table tests were conducted (Table 6.1). However, because of obvious restrictions on the length of this report, only the results of the following tests are presented in detail and compared directly with the prototype test results.

- (1) Serviceability limit state test: 6.3% g (Test No. 7) was the closest test for direct comparison with the prototype 65 gal test.
- (2) Damageability limit state test: 250 gal peak ground acceleration was used in the prototype test to induce moderate brace buckling and frame yielding at several locations. A peak table acceleration of 28% g was produced in Test No. 25; however, no brace buckling was observed in this test and therefore the table intensity was increased to about 30% g. The test resulted in 33% g peak acceleration (Test No. 27) and the fifth story brace buckled. This test represented the damageability limit state of the model.
- (3) Collapse limit state test: 50% g was the target peak table acceleration. As a result of shaking table-structure interaction, the measured peak table acceleration in Test No. 29 was 65% g. This test represented the collapse limit state of the model.
- (4) After-shock test: Three moderate intensity tests, ranging from 26% g to 30% g table peak acceleration, were conducted after the collapse level test (65% g). Only the first test (30% g, Test No. 32) is described in this report.

These four tests are designated as **MO-6.3**, **MO-33**, **MO-65**, **MO-post1 Tests**, respectively, in the following discussion.

7.2 Global Response

7.2.1 Variation of Natural Periods and Damping Ratios

The natural period and damping ratio variations for the first three modes are listed in Table 7.1. The last row of the table corresponds to the model with all the concentric braces removed, that is, a ductile MRSF. Figure 7.1 shows the variation of periods and damping ratios with the sequence of testing. The following observations may be drawn from Table 7.1 and Fig. 7.1:

- (1) The fundamental periods of the first row and the last row of Table 7.1 show that the ratio of the stiffnesses of the dual system and the moment-resisting space frame is

$$\frac{K_{\text{DUAL}}}{K_{\text{MRSF}}} = \left(\frac{0.672}{0.342} \right)^2 = 3.9 . \quad (7.1)$$

The effectiveness of the concentric braces in increasing the lateral stiffness in the elastic range is quite apparent.

- (2) The variations in the natural periods and equivalent viscous damping ratios were relatively small (fundamental period changed from 0.361 second before shaking table tests to 0.392 second after the collapse limit state test). These variations were significantly smaller than those observed in studies conducted on the reinforced concrete frame-wall structure test [33].
- (3) The natural frequencies and damping ratios listed in Table 7.1 are characteristics of the floating shaking table-structure system. The equivalent viscous damping ratio is also dependent upon the shaking table hydraulic system.

- (4) Variations in the higher mode natural frequencies and damping ratios are less sensitive to structural damage.

7.2.2 Response Envelopes

The envelopes of base shear and base overturning moment versus roof drift are shown in Fig. 7.2, where the response corresponding to the largest cycle of roof drift in each test is plotted. The cycle of the MO-65 Test in Fig. 7.2(a) indicates that the maximum strength of the model was reached. As the excitation intensity increased, the deterioration in stiffness and strength is clearly shown.

7.3 MO-6.3 Test

7.3.1 Response Time History

The measured table horizontal acceleration and the corresponding response spectra are shown in Fig. 7.3. The ATC [4] introduced the concept of effective peak acceleration (EPA), which was obtained by the following procedure: (i) the 5% linear elastic pseudo-acceleration spectrum is drawn for the actual given motion; (ii) a straight line is fitted to the spectral shape for the structural fundamental period in the range of 0.1 to 0.5 second; and (iii) the ordinate of the straight line is divided by 2.5 to obtain the EPA. After scaling the period range by $\sqrt{T_r}$, the ATC procedure gave an EPA of 0.044g for this test. The relative lateral displacement, inter-story drift, story shear and lateral inertia force time histories at each floor level are shown in Fig. 7.4 to Fig. 7.7. It is clear that the first mode dominates the lateral displacement response of the model. The story shear time histories shown in Fig. 7.6 were calculated by summing the column shears and the horizontal components of the brace forces; the component resisted by the braces is also shown in this figure. Higher mode contributions can be detected for the bottom two floor lateral inertia forces. The total overturning moment time history at the base of the model, calculated by summing the product of the inertia force and floor height at

each floor level, is shown in Fig. 7.8. The component of the overturning moment resisted by the braces is also shown.

Based upon the procedure described in Section 6.5.3.3, the time histories of the change of column axial force and end moments in the first story column were calculated. The response time history of column 1C_{B1} is shown in Fig. 7.9. This figure shows that the first story column base moment is about twice the moment at the column upper end; this implies that the column inflection point is located about two-thirds of the story height above the column base. The calculated column responses were used to construct the column axial force versus bending moment interaction curves in Section 7.3.4.

7.3.2 Inter-story Drift versus Story Shear Relationship

The inter-story drift was calculated by subtracting the lateral displacements of two adjacent floor levels. The inter-story drift versus the story shear curves in each story are presented in Fig. 7.10. The response is primarily linear with minor deviations in the first story; the discrepancy is due to the lack of sensitivity of the transducers at this low excitation level test.

7.3.3 Maximum Response Envelopes

The envelopes of the maximum response of relative displacements, inter-story drifts, story shears, inertia forces and overturning moments over the height of the model are shown in Fig. 7.11 and summarized in Table 7.2. The lateral displacement and the lateral inertia force profiles over the height of the model at the time of maximum base shear and maximum roof displacement are shown in Fig. 7.12. Unlike the UBC lateral force distribution (Table 2.4), which is close to an inverted-triangular load pattern, the lateral force distributions in Fig. 7.12 are closer to a parabolic load pattern. The maximum inter-story drift index, which occurred in the fourth story, is 0.15%. The maximum base shear coefficient (V_b/W) of 0.14 exceeds the UBC design base shear coefficient of 0.113.

7.3.4 Column Axial Force - Bending Moment Interaction

As all of the channels were initialized at the beginning of each test, the gravity load effect and residual strains were not reflected in the recorded column axial strain time histories. To calculate the gravity load effect on the axial force in the bottom story columns, the gravity loads were considered to be uniformly distributed over the floor and the tributary area assumption was used. The end moment (M) and modified axial force (N) interaction curves of the first story columns were generated for columns in Frames A and B (Fig. 7.13). The AISC [16] column sectional yield surface, based upon the assumption of linear elastic-perfectly plastic material properties, is also shown in these figures. Comparing the plots for columns $1C_{B1}$ and $1C_{B2}$ (braced bay) with the plots of the remaining columns, the potentially large demand on the braced-bay columns in the higher intensity ground motion excitation is apparent. The other columns, including $1C_{A3}$ subjected to weak-axis bending, were significantly less stressed. As expected, the concentric braces induced significant stress increases in the columns to which the braces are connected.

7.3.5 Energy Distribution

On the basis of the method described in Section 6.6, the input energy, the kinetic energy and the strain energy time histories were calculated. As viscous damping is the only mechanism to dissipate energy in this low intensity test, the E_{μ} is calculated as

$$E_{\mu} = E_I - E_K - E_S . \quad (7.2)$$

Figure 7.14 shows the energy distribution of each of these components; the maximum lateral displacement does not necessarily occur at the time of maximum input energy because of the viscous damping effect.

7.4 MO-33 Test

7.4.1 Response Time History

The measured table horizontal acceleration and its response spectra are shown in Fig. 7.15; the EPA is 0.21g. The brace in the fifth story buckled during this test. The relative lateral displacement, inter-story drift, story shear and lateral inertia force time histories at each floor level are shown in Fig. 7.16 to Fig. 7.19. The story shear brace component in the fifth story, where the braces buckled, was calculated by subtracting the column shears from the total story shear (Eq. 6.7). In the other stories, the brace shear component was calculated from the elastic brace forces. The ratio of brace shear component to total story shear is shown in Fig. 7.20. Except in the fifth story, where a slight drop due to the brace buckling was observed, the ratio remained constant. The predicted brace component yield story shear that will cause initial brace buckling is calculated as

$$V_y^{\text{brace}} = 2 P_{cr} \cos\theta \quad (7.3)$$

where P_{cr} is the brace buckling load. The V_y^{brace} in each story is marked in Fig. 7.18; this figure also shows that the fifth story brace buckled. The bottom four story braces have reached at least 85% of their buckling loads. Figure 7.21 shows the time history of the base overturning moment. The axial strain time histories of brace #9 in the fifth story (Fig. 6.12) are shown in Fig. 7.22. The deviation of the strain readings (at about 4.3 seconds) on opposite sides of this brace indicates buckling. As brace axial deformation was not measured in the fifth story, the brace axial deformation versus brace axial force hysteretic curve is not available.

7.4.2 Inter-story Drift versus Story Shear Relationship

The inter-story drift versus story shear curves for each story are presented in Fig. 7.23. In the first story, where the braces remained elastic, a minor degree of yielding is apparent. This yielding resulted from column yielding, composite girder yielding and

slab cracking or column-girder joint panel zone yielding. The fifth story inter-story drift versus story brace shear is shown in two second increments in Fig. 7.24. The initial brace buckling is clear in the 4 to 6 second increment.

7.4.3 Maximum Response Envelopes

The envelopes of the maximum response of the relative displacements, inter-story drifts, story shears, inertia forces and overturning moments over the height of the model are shown in Fig. 7.25 and summarized in Table 7.3. The lateral displacement and the lateral inertia force profiles over the height of the model at the time of maximum base shear and maximum roof displacement are shown in Fig. 7.26. The maximum inter-story drift index, which occurred in the fifth story, was 0.69%. The maximum base shear coefficient developed was 0.56.

7.4.4 Column Axial Force - Bending Moment Interaction

Using a procedure similar to that described in Section 7.3.4, the axial force (N) and end moment (M) time histories were calculated for the first story columns; the N-M interaction curves are shown in Fig. 7.27. This figure shows that the column 1C_{B1} in the braced bay yielded; it partly explains the hysteretic behavior of the first story inter-story drift versus story shear curve (Fig. 7.23).

7.4.5 Energy Distribution

The input energy, kinetic energy and strain energy time histories are shown in Fig. 7.28. There were three high bursts of energy input (4-5 seconds, 6-7 seconds and 8-9 seconds); the brace buckling was initiated by the first energy burst. Subtracting the kinetic energy and strain energy from the input energy gives the hysteretic energy and viscous damped energy. It is important to identify the mechanisms of energy dissipation in a structure. If the different mechanisms can be identified, emphasis can be placed on improving those mechanisms that dissipate the bulk of the input energy. Separation of the two dissipated energies using a semi-analytical procedure will be discussed in Section 8.6.3.

7.5 MO-65 Test

7.5.1 Response Time History

The measured table horizontal acceleration and its corresponding response spectra are shown in Fig. 7.29; the EPA is 0.4g, comparable to the maximum EPA recommended by ATC [4]. The braces in the bottom five stories buckled during this test. The relative lateral displacement, inter-story drift, story shear and lateral inertia force time histories at each floor level are shown in Fig. 7.30 to Fig. 7.33. Although the lateral displacement responses show that the first mode dominates the model behavior, by comparing these with the displacement responses of the MO-6.3 test (Fig. 7.3) significant phase lag is apparent. This is attributed to the severe brace buckling which in turn caused the elongation of the period of the structure. The component of story shear resisted by braces is also shown in Fig. 7.32; the ratio of the brace shear component to total story shear is shown in Fig. 7.34. The brace component yield story shear (V_y^{brace}) estimated by using Eq. (7.3) is marked in Fig. 7.32; the actual story shear resisted by braces is well predicted by the analytical value of V_y^{brace} . The two braces in the fifth story ruptured during this test, therefore the fifth story shear ratio vanished at about 9 seconds. Figure 7.35 shows the fifth story brace # 10 axial strain time histories; it indicates the brace rupture at 9 seconds. Figure 7.36 shows the base overturning moment time histories.

7.5.2 Inter-story Drift versus Story Shear Relationship

The inter-story drift (δ) versus total story shear (V^{TOTAL}), the story shear resisted by columns (V^{MRSF}), the story shear resisted by braces (V^{BRACE}) curves for the six stories are presented in Fig. 7.37 to Fig. 7.39. The fifth story became a soft story as a consequence of brace rupture; the moment-resisting space frame in that story was highly stressed (Fig. 7.38). Figure 7.39 clearly shows the undesirable post-buckling behavior of a concentrically braced system upon brace buckling. The strength deterioration of the braces in the fifth story indicates the inefficiency of dissipating energy by brace buckling.

7.5.3 Maximum Response Envelopes

The envelopes of the maximum responses of the relative displacements, inter-story drifts, story shears, inertia forces and overturning moments over the height of the model are shown in Fig. 7.40 and summarized in Table 7.4. The lateral displacement and the lateral inertia force profiles over the height of the model at the time of maximum base shear and maximum roof displacement (also the maximum inter-story drift) are shown in Fig. 7.41. The UBC inter-story drift limit at yield level is 0.5% (Fig. 3.6); this level is marked in Fig. 7.31. This figure indicates that the inter-story drift limit was exceeded in every story. The maximum inter-story drift index, which occurred in the fifth story, was 1.9%; this index is larger than the UBC and ATC maximum value of 1.5%. The maximum base shear coefficient was 0.73. A further discussion of these results is presented in Section 8.3.

7.5.4 Brace Response

Using the procedure described in Section 6.5.3, the resulting axial force, bending moments and curvatures in the two mutually perpendicular directions were calculated. The calculated axial force is plotted against the measured brace axial deformation (measured by DCDTs' installed on the bottom four story braces) in Fig. 7.42 to Fig. 7.45.

The accuracy of the brace force calculation, especially that for the buckled brace subjected to significant yielding reversal, was evaluated as follows:

- (1) In each story, the story shear resisted by braces was calculated by summing the horizontal components of the two calculated brace axial forces.
- (2) The story shear resisted by braces was calculated from Eq. (6.4) where V^{TOTAL} is calculated from inertia forces.

These shear two time histories will be very close if the assumed material properties of the tubes for brace force calculation are correct, the assumed Ramberg-Osgood type of steel hysteretic behavior is valid and if plane sections remain plane. Figure 7.46 shows

such a comparison for the bottom four stories. Although there is good agreement in general, there are some differences in the peak values. The major source of error is due to the assumed material properties which ignore the residual stresses. Residual stresses are a significant factor in tracing the correct stress level for a given strain time history. A typical residual stress distribution for a hot-rolled tubular section is shown in Fig. 7.47 [34]. The residual stress distribution of the model brace was unsymmetric as the brace was fabricated from two angles, each angle being bent from a plate section. The subsequent welding process introduced significant residual stresses; better correlation than that in Fig. 7.46 would be achieved if the residual stress distributions in the braces of the model were incorporated into the analysis.

Despite these errors, the global behavior of braces shown in Fig. 7.42 to Fig. 7.45 is acceptable for the purpose of studying brace response. Typical brace curvature time histories at the measured section are shown in Fig. 7.48. Comparing the magnitudes of in-plane and out of plane curvatures indicates the dominant plane of buckling. For each brace, the maximum curvatures in both directions are summarized in Table 7.5. As only two strain gages were installed in the top two story braces, only in-plane bending and curvature could be detected. The following observations are made regarding the buckling directions (Table 7.5):

- (1) Approximately half of the braces buckled primarily in-plane and the remaining braces buckled out of plane.
- (2) Figure 7.49 shows the cross section of a brace; the brace was not symmetric with respect to either the X-X or the Y-Y axis. Buckling in the positive (negative) X direction was always accompanied by minor buckling in the positive (negative) Y direction and vice versa; this phenomenon was due to the presence of the rounded corners.

7.5.5 Column Axial Force - Bending Moment Interaction

The calculated column axial force versus end moment interaction curves of Frames A and B are shown in Fig. 7.50. Plastic hinge formation occurred only in the braced-bay columns ($1C_{B1}$, $1C_{B2}$); the remaining columns remained elastic. Figure 7.50 shows that the N-M yield surface was exceeded for the braced-bay columns; this was due to strain-hardening effect in the steel columns.

7.5.6 Energy Distribution

The total input energy, kinetic energy, strain energy, viscous damped energy and hysteretic energy time histories were shown in Fig. 7.51. Only a small portion of the input energy was stored as recoverable strain energy and kinetic energy, both of which built up alternately and were limited by the inelastic response. The hysteretic energy was the most significant component and only a small portion of the input energy was dissipated as viscous damped energy. The distribution of the total hysteretic energy in each story is shown in Fig. 7.52; it indicates that the hysteretic energy is fairly uniformly distributed in the bottom five stories. The first story dissipated more energy than the fifth story, where the brace buckling commenced; this was due to the larger strength and stable hysteretic behavior of the first story braces (Fig. 7.39).

7.5.7 Girder-Brace Joint Vertical Response

One DCDT was installed to measure the second floor girder-brace joint vertical displacement response; this displacement time history is shown in Fig. 7.53. The permanent downward vertical displacement was associated with the unbalanced vertical component of the brace forces at this joint once one of the braces buckled. The base shear versus this vertical displacement is shown in Fig. 7.54. The point corresponding to brace buckling can be clearly identified; the permanent vertical displacement also implies that the plastic hinges formed at braced bay composite girder ends.

7.6 MO-post1 Test

7.6.1 Introductory Remarks

After most of the braces had buckled and the fifth story braces had ruptured, the model was subjected to three consecutive tests (Test No. 32, 33 and 35 in Table 6.1) with table peak accelerations in the range of 25% to 30% g (Table 6.1). The story stiffness distribution of the model was highly irregular because of the soft story formation in the fifth story. The first of these three tests is presented herein with the objective of studying the response of a damaged structure subjected to an aftershock of moderate intensity.

7.6.2 Response Time History

The measured table horizontal acceleration and its corresponding response spectra are shown in Fig. 7.55; the EPA is 0.2g. The relative lateral displacement, inter-story drift, story shear, lateral inertia force and the story shear time histories at each floor level are shown in Fig. 7.56 to Fig. 7.59. The large inter-story drift in the fifth story is apparent in Fig. 7.57. The lateral displacements at the six floors remain in phase. The story shear resisted by the braces is also shown in Fig. 7.58; the braces in the fifth story resisted almost no shear force. The brace component yield story shear (V_y^{brace}) estimated by using Eq. (7.3) is marked in Fig. 7.58; the actual story shear resisted by braces was less than the predicted value of V_y^{brace} . This was due to the fact that the braces had already buckled in the MO-65 Test and the subsequent buckling load was less than the initial buckling load. The two braces in the fifth story ruptured during this test, Figure 7.60 shows the time history of the base overturning moment.

7.6.3 Inter-story Drift versus Story Shear Relationship

The inter-story drift versus the total story shear (V^{TOTAL}), the story brace shear (V^{BRACE}) and the column story shear (V^{MRSF}) are shown in Fig. 7.61 to Fig. 7.63, respectively. Figure 7.63 shows again that the fifth story braces did not resist shear force. The fourth story braces exhibited stable hysteretic behavior. The inter-story drift versus

total story shear curve shows no global strength deterioration resulting from the brace buckling. Although the fifth story columns underwent the largest inter-story drift, they were capable of developing sufficient shear resistance and they worked with the other stories to ensure a satisfactory response.

7.6.4 Maximum Response Envelopes

The envelopes of the maximum response of relative displacements, inter-story drifts, story shear, inertia forces and overturning moment over the height of the model are shown in Fig. 7.64 and summarized in Table 7.6. The lateral displacement and the lateral inertia force profiles over the height of the model at the time of maximum base shear and maximum roof displacement are presented in Fig. 7.65. The maximum inter-story drift index, which occurred in the fifth story, was 1.47%. The maximum base shear coefficient was 0.54.

7.6.5 Energy Dissipation

The total input energy, kinetic energy, strain energy and hysteretic energy time histories are shown in Fig. 7.66. The distribution of hysteretic energy in each story is shown in Fig. 7.67; the MRSF in the fifth story dissipated a significant amount of input energy.

7.6.6 Concrete Slab Crack Pattern

The crack patterns of the composite floor in the bottom two stories are shown in Fig. 7.68. This pattern was recorded upon the completion of all the shaking table tests. The maximum crack width is about 0.015 inch; extrapolating it to the prototype unit, the crack width is 0.049 inch. Note that longitudinal cracks appeared along the shear stud line in the braced bay (Frame B). This crack pattern is consistent with observations from the subassembly tests of four composite girders [18]. The unbalanced vertical component of brace forces introduced high bending moments in the composite girders; longitudinal cracks formed along the stud line to develop the composite action.

VIII. EVALUATION OF MODEL TEST RESULTS

8.1 Introductory Remarks

In Chapter 7, four representative tests conducted on the model were described in detail; in this chapter, the most important results will be summarized and evaluated. The global behavior of the concentrically K-braced steel frame, as well as a comparison of the test results with the code requirements, the analytically predicted response and the test results obtained from the prototype are discussed in this chapter. The structural responses from the energy point of view are then described. The role of the ductile moment-resisting space frame in dual systems is emphasized and the rationale of code requirements regarding the ductile moment-resisting space frame is studied.

8.2 Inter-story Drift versus Story Shear Envelopes

The envelopes of inter-story drift index versus the corresponding total story shear (V^{TOTAL}), the story shear resisted by the braces (V^{BRACE}) and the story shear resisted by the MRSF (V^{MRSF}) for the MO-6.3, MO-16, MO-33 and MO-65 tests are shown in Fig. 8.1. The MO-16 test, not described in the previous chapter, represents Test No. 15 in Table 6.1. The shear force brace components in the fourth and fifth stories did show the strength deterioration resulting from severe brace buckling. As a result of the beneficial contribution of the ductile MRSF, the global strength (V^{TOTAL}) showed stable response. As the inter-story drift increased, the rate of strength increase of the MRSF was higher than the rate of strength deterioration of the braces; this ensured that the total response envelope was stable. For the bottom three stories, the brace contribution showed stable behavior under dynamic excitations, even though they underwent moderate buckling.

8.3 Base Shear versus Roof and Critical Inter-story Drift Envelopes

In order to compare the test results with the code minimum requirements, the envelopes of maximum base shear ratio (V_B/W) versus the roof drift index and the critical (fifth) inter-story drift index are shown in Fig. 8.2 and Fig. 8.3.

8.3.1 Prototype Design Base Shear and the UBC Requirements

The prototype design base shear and the UBC requirements were described in Section 3.5; the UBC minimum requirements, assuming a uniform inter-story drift index in each story, are shown in Fig. 8.2 and Fig. 8.3.

8.3.2 ATC Recommendations

In order to evaluate the test results in terms of the ATC Recommendations [4], the ATC requirements are presented and calculated for Zone 4 values. The minimum base shear coefficient (C_s) at first **significant yield** level is

$$C_s = \frac{1.2A_v S}{RT^{2/3}} \quad (8.1)$$

Then, for

$$A_v = 0.4 = \text{effective peak acceleration}$$

$$A_a = 0.4 = \text{effective velocity-related peak acceleration}$$

$$R = \text{response modification factor} = 6 \text{ for dual system} \quad (8.2)$$

$$S = 1.5 \text{ (soil type } S_3, \text{ soft soil)}$$

$$T = \frac{0.05h_n}{\sqrt{L}} = 0.503 \text{ sec. (fundamental period of building)}$$

$$C_s = 0.190$$

In practice, ATC specifies that C_s need not be taken greater than $\frac{2.5A_a}{R}$ ($=0.167$), so that in this case C_s is equal to 0.167. ATC also requires the following inter-story drift limit at yield level:

$$C_d \delta_{xe} \leq 0.015 h_{sx} \quad (8.3)$$

where C_d = deflection amplification factor = 5

δ_{xe} = inter-story drift determined by elastic analysis;

or,
$$\frac{\delta_{xe}}{h_{sx}} \leq 0.003 . \quad (8.4)$$

The ATC requirements are shown in Fig. 8.3; it is clear that, in this instance, the ATC requires a lower base shear coefficient, but the inter-story drift limit is smaller.

8.3.3 Comparison of Model Results and Code Requirements

Figure 8.3 shows that the actual model strength is much higher than the code minimum required strength. Although the maximum inter-story drift indices under the serviceability and the damageability level tests are satisfactory, this index exceeds the maximum value (=1.5%) allowed by the current codes during the most severe test (MO-65 test). This was primarily a consequence of brace rupture and the subsequent soft story formation in the fifth story.

Assuming the test model as a single degree of freedom system with 5% viscous damping and considering this model is to remain in the elastic range during the MO-65 test, the linear elastic response spectra in Fig. 7.29(c) indicate that the pseudo-acceleration would have been about 1g. It is economically not feasible to design a building with the base shear equal to the total reactive weight. In earthquake-resistant design the structure linear elastic strength demand can be reduced if the ductile behavior of the structural components is stable. ATC establishes a linear elastic design response spectrum (LEDRS) for a 5% viscous damping ratio; this spectrum is equal to $C_s R$, where C_s is given by Eq. (8.1). Figure 8.4 shows the LEDRS for soil types 1 and 3. ATC then uses a "response modification factor" R to reduce the LEDRS to the minimum required design base shear coefficient (C_s). According to Chapter 3 of the Commentary [4], "The response modification factor, R , and ... have been established considering that structures

generally have additional **overstrength** capacity above that whereby the design loads cause significant yield." In Chapter 4 of the Commentary, it also states that R "... is an empirical response reduction factor intended to account for both damping and the **ductility** inherent in the structural system at displacements great enough to surpass initial yield and approach the ultimate load displacements of the structural system..." The rationale in selecting R equal to 6 for the dual system is difficult to justify because of the lack of available information about the overstrength and ductility of the dual braced frame structure [35]. In fact, very little information is available for the actual behavior of concentrically K-braced steel frames subjected to ground motion excitation, either from laboratory testing or from field investigations after earthquakes [36].

Based upon the test results, Fig. 8.3 shows that the observed overstrength calculated from the maximum strength and the true yield base shear (Eq. 3.16) is 2.4 ($=0.73/0.3$). In order to estimate the reduction of strength due to ductility, the pseudo-acceleration linear elastic response spectrum (LERS) based on the recorded MO-65 test table horizontal acceleration was generated (Fig. 8.4). The spectrum of the 50% g M.O. earthquake record is also shown; this was the excitation level used in the prototype pseudo-dynamic test in Japan.

The effective peak acceleration (EPA) of the 50% g M.O. earthquake record, estimated and scaled from Fig. 6.3(c), is 0.3g; this value is smaller than the EPA (0.40g) of the measured table horizontal acceleration (Section 7.5). By considering the fundamental period variation before and after the MO-65 test, the actual table motion (65% g peak table acceleration) is less effective than the desired 50% g peak base acceleration. The linear elastic response spectra of the shaking table input and output motion (Fig. 8.4) indicate that peak acceleration is not a good index by which to express the intensity of the table motion.

Figure 8.4 shows that, within the experimental range of the structural fundamental period, the average strength reduction due to ductility (R_{μ}) is about 1.5. Therefore the

total reduction from the LERS to the test structure true design yield level (Fig. 8.3), with an overstrength of 2.4 and a ductility reduction effect of 1.5, is 3.6. The overstrength plays a more important role than ductility in interpreting the R factor.

The ATC LEDRS based on Eq. (8.1) is shown in Fig. 8.4. From analysis of the results presented in this figure, the following observations can be made:

- (1) Although the EPA of the measured MO-65 Test horizontal acceleration is the same as that assumed by ATC, the ATC LEDRS is low in comparison with the LERS of the measured MO-65 Test base excitation, during which the maximum model strength was developed. Considering the linear elastic response spectra of the recorded ground motions of the Chilean and Mexico City earthquake in 1985 [35], the use of the MO-65 table motion to test the 0.3-scale model is justified (Fig. 8.5). The period of the structure was 0.62 second (Table 5.9); for this period, the linear elastic spectral accelerations of MO-65 and ATC are similar, the ATC spectra however, are nonconservative with respect to the MO-65 spectra in the period range of 0.7 to 2.0 seconds.
- (2) For a dual system with a concentrically K-braced steel frame $R=6$ is too high in comparison with the actual total strength reduction factor from test results; the actual reduction factor due to ductility and overstrength was 3.6.

8.3.4 Comparison of Model Results and Analytical Results

The analytically predicted strengths of the model from Fig. 6.1 are included in Fig. 8.2 for comparison with the test results. Up to the MO-33 Test, the model test results are close to the predicted curve using the inverted-triangular lateral load pattern. Because the foundation was not perfectly rigid, the test results show slightly less elastic stiffness. The two data points of the MO-65 Test in Fig. 8.2 correspond to the responses at the time of maximum base shear and maximum roof drift index. The point corresponding to the maximum test strength of the model is very close to the predicted response curve for a uniform lateral load pattern.

8.3.5 Comparison of Model Results and Prototype Results

The prototype roof drift index and the critical inter-story drift index versus base shear ratio envelopes (Fig. 3.6) from the pseudo-dynamic test are also shown in Fig. 8.2 and Fig. 8.3. The maximum base shear ratio of the model ($=0.73$) is about 16% higher than that of the prototype ($=0.63$). The limit analysis discussed in Section 6.2.4 concluded that the model strength is about 4% higher than the prototype strength. The main reason for the 16% difference between the model and the prototype test strengths is the strain rate effect. In the pseudo-dynamic test, this effect was nonexistent because the lateral forces were applied quasi-statically. Because of similitude, the strain rate for the model was increased (see Table 4.1):

$$\dot{\epsilon}_r = \frac{\epsilon_r}{t_r} = \frac{1}{\sqrt{0.3048}} = 1.81 .$$

The effects of increasing rate of strain can be summarized as follows [37]:

- (1) The yield stress (σ_y) increases.
- (2) The modulus of elasticity (E_s) remains constant.
- (3) The strain at which strain hardening begins (ϵ_{st}) increases.
- (4) The ultimate strength only increases slightly.

Figure 8.6 shows the typical strain rate versus yield stress curve, which was based on 24 coupon tests of A36 steel under constant strain rate [26].

In order to quantify the strain rate effect on the model, the following procedures were used to calculate the "**mean strain rate**" of the model. First, note that the strain rate varied with each member of the model and that the concentric braces dominated the structure responses, only the recorded brace axial strain readings were used to calculate the strain rate. There were 40 recorded brace axial strain readings: four for each brace on the bottom four stories and two for each brace on the top two stories.

- (1) Differentiate numerically each brace axial strain time history to calculate the strain rate time history:

$$\dot{\epsilon}_i = \frac{d\epsilon_i(t)}{dt} \quad (8.5)$$

where ϵ_i represents the *ith* axial strain time history.

- (2) Calculate the root-mean-square of each strain rate time history:

$$\dot{\epsilon}_{i(\text{rms})} = \sqrt{\frac{\sum_{j=1}^n \dot{\epsilon}_{ij}^2}{n}} \quad (8.6)$$

where ϵ_{ij} = the *jth* point of the *ith* axial strain time history

n = total number of points of each time history.

- (3) Calculate the mean value of all the $\dot{\epsilon}_{i(\text{rms})}$:

$$\dot{\epsilon}_{(\text{mean})} = \frac{\sum_{i=1}^{40} \dot{\epsilon}_{i(\text{rms})}}{40} \quad (8.7)$$

The calculated $\dot{\epsilon}_{(\text{mean})}$ represents the mean strain rate of the model. For the MO-65 test, $\dot{\epsilon}_{(\text{mean})}$ is equal to 0.0116 in/in/sec. By virtue of the quasi-static method of the pseudo-dynamic technique, the strain rate of the prototype was of the order of 100 times smaller than that of the model. The strain rate of the prototype was therefore assumed to be zero. It was estimated from Fig. 8.6 that the yield stress ratio between the model and the prototype was

$$\frac{\sigma_{y(\text{model})}}{\sigma_{y(\text{prototype})}} = \frac{0.973 + 0.45(0.0116)^{0.33}}{0.973} = \frac{1.076}{0.973} = 1.11 \quad (8.8)$$

This value together with the previously mentioned 4% increase from the limit analysis may explain why the maximum strength of the model (from shaking table test) was 16% higher than the maximum strength of the prototype (from pseudo-dynamic test).

Although the higher strength of the model can be explained by the strain rate effect in this study, conflicting conclusions have been drawn by previous researchers. For example, the forced vibration tests performed by Hanson [38] on tubular steel columns showed that the dynamic force-deflection curves were very close to the static curves when the fundamental periods were about 0.3 second and that the maximum deflections were about twice the yield deflections. The correlation study on an X-braced tubular steel frame reported in Reference 39 also concluded that the strain rate has an insignificant effect on the global behavior of steel structures. A study of shaking table and pseudo-dynamic tests on twin two-story unbraced steel frames and twin two-story X-braced steel frames [40] showed: (i) that a 10% increase in base shear of the unbraced steel frame in the shaking table tests was attributed to the strain rate effect; (ii) that no significant strain rate effect of the braced frame was observed in the shaking table tests. An experimental study of the strain rate effect on five steel beams and five composite beams was reported in Reference 41. It was concluded that the maximum moment capacity of a steel beam is increased by 16% under monotonic loading and by 11% under cyclic loading. The maximum positive bending moment capacity of a composite girder is increased by 20% under monotonic loading; the negative bending moment capacity is increased by 5 to 8% under cyclic loading. More research is necessary to clarify the strain rate effect in shaking table tests and pseudo-dynamic tests.

8.4 Base Shear versus Ground Excitation Intensity Relationship

The peak acceleration of the base motion has been shown in Section 8.3.3 to be a poor index by which to express the damage potential of an earthquake ground motion. This is especially true for shaking table tests because of the table-structure interaction. Instead, the linear elastic response spectral values (pseudo-acceleration PSA or pseudo-velocity PSV) of the measured table motion will be used to quantify the intensity of the base excitation. As the model response was primarily a first mode response, it is

reasonable to use the measured fundamental period and the equivalent viscous damping ratio of the model before each test to define the spectral values. The equivalent viscous damping ratio was taken as 2% of critical, very close to the measured values shown in Table 7.1.

The PSA/g versus measured base shear ratio (V_B/W) is shown in Fig. 8.7. The base shear did not increase linearly as the PSA of the base excitation increased; the base shear was reduced by the ductility of the model. This figure shows again that the strength reduction due to the inelastic deformation was about 1.4.

8.5 Input Energy versus Base Excitation Intensity Relationship

8.5.1 Input Energy Test Results

The base excitation intensity, expressed by PSA/g, versus the maximum input energy (E_I) curve is shown in Fig. 8.7. While the rate of increase in the maximum base shear decreases with increasing excitation intensity, the maximum input energy increases significantly with the increase in base excitation intensity. This input energy curve is replotted with $\sqrt{2E_I/(W/g)}$ as the ordinate in Fig. 8.8. The quantity $\sqrt{2E_I/(W/g)}$, which is defined as the equivalent velocity (V_I) of the E_I , has the units of velocity. Therefore it is more convenient to use PSV as the abscissa in Fig. 8.8. For a linear elastic system, the input energy is proportional to the excitation intensity squared; that is, the equivalent velocity is linearly proportional to the excitation intensity.

The total input energy is either dissipated in the form of viscous damping energy (E_μ) and hysteretic damping energy (E_H) or stored as kinetic energy (E_K) and recoverable elastic strain energy (E_S). The portion of the total input energy that contributes to the **damage** of the structure is defined as E_D and can be expressed as

$$E_D = E_H + E_S + E_K = E_A + E_K \quad (8.9)$$

where E_A is the absorbed energy. Since the maximum values of E_S and E_K occur

alternatively, it is reasonable to ignore the last term in Eq. 8.9 when estimating the maximum values of E_D ; that is,

$$E_{D(\max)} \approx E_{A(\max)}.$$

The equivalent velocity of E_D is

$$V_D = \sqrt{\frac{2E_D}{(W/g)}} \quad (8.10)$$

The E_I and E_D differ by E_μ ; E_μ is typically small for a structure with low damping which undergoes significant inelastic deformation. The PSV versus V_D curve from the model test results is also shown in Fig. 8.8

Housner [42] proposed a limit design method based on energy considerations and suggested that the input energy contributing to structural damage be estimated by

$$E_D = \frac{1}{2}kS_d^2 = \frac{1}{2}k\left(\frac{PSV}{\omega}\right)^2 = \frac{1}{2}m(PSV)^2 = \frac{1}{2}\left(\frac{W}{g}\right)(PSV)^2$$

or

$$V_D = \sqrt{\frac{2E_D}{(W/g)}} = PSV \quad (8.11)$$

where $S_d (= PSV/\omega)$ is the spectral displacement. Equation (8.11) is valid for linear elastic systems. Housner assumed that this equation provided an upper bound for E_D for an inelastic system. A structure should then be designed such that its design hysteretic energy dissipation capacity is greater than $(E_D - E_S)$, where E_S is the maximum strain energy that can be stored in the structure. For a linear elastic-perfectly plastic single degree of freedom system with yield force R_y , E_S is equal to $\frac{1}{2}R_y\delta_y$. The straight line according to Housner's assumption is shown in Fig. 8.8; this assumption significantly underestimates the E_D of the MO-33 and the MO-65 Test results.

8.5.2 Discussion of Input Energy

Recall that the input energy is calculated by

$$E_I = \int_0^t \left(\sum_{i=1}^6 m_i \ddot{v}_i^t \right) dv_g = \int_0^t \left(\sum_{i=1}^6 m_i \ddot{v}_i^t \right) \dot{v}_g dt = \int_0^t P_I dt \quad (8.12)$$

where $P_I = \left(\sum_{i=1}^6 m_i \ddot{v}_i^t \right) \dot{v}_g \equiv \text{input power (kip-inch/sec)} . \quad (8.13)$

Shaking table velocity \dot{v}_g is approximately proportional to the base excitation intensity. $\sum m_i \ddot{v}_i^t$ is the sum of the lateral inertia forces on each floor; it is approximately equal to the base shear time history. The rate of increase of this quantity decreases with increasing base excitation intensity (Fig. 8.6). One reason for increasing the input energy is that the elongation of the response period of the time history of $\sum m_i \ddot{v}_i^t$ produces more "positive" input power (P_I). The normalized $\sum m_i \ddot{v}_i^t$ time histories for the MO-6.3 and the MO-65 Tests are shown in Fig. 8.9(a). The elongation of the response period is clearly shown during the MO-65 Test. The normalized input power time histories are shown in Fig. 8.9(b).

In order to study whether the input energy in the inelastic system will always be larger than in the elastic system and to find a simple analytical method to predict the input energy in the inelastic range, input energy response spectra for linear and non-linear systems were constructed; the computer program NONSPEC [43] was used for this purpose. The model was idealized as an elastic-perfectly plastic single degree of freedom system with yield force R_y equal to $0.6W$, the measured table horizontal motion of the MO-65 Test being used as input. Figure 8.10 shows the calculated energy spectra. It indicates that when the predominant period of the ground motion agreed with the period of the structure, the linear elastic system had a larger input energy. For a short period structure ($T < 0.5$ seconds), the inelastic E_I may be either larger or smaller than the elastic E_I , depending upon the period considered. This phenomenon was more critical in the range of 0.35 to 0.55 second. The fundamental period range of the model before and

after the MO-65 Test is shown in Fig. 8.10; the MO-65 Test E_I level (435 kip-inch) is also indicated. This level was approximately equal to the average value of the inelastic E_I in the period range considered; in this instance the linear elastic-perfectly plastic energy response spectra of a single degree of freedom system with 2% damping provided a good estimate of the inelastic input energy.

Akiyama [44] proposed that the total input energy spectrum of an undamped linear elastic-perfectly plastic system be approximated by a linear elastic input energy spectrum with 10% viscous damping. This was based upon the observation that the hysteretic damped energy of a structure with moderate inelastic deformation capacity is similar to the energy damped by a linear elastic system with equivalent viscous damping ratio of 10%. Based upon a parametric study, Akiyama also derived the following empirical equation in the form of equivalent velocity to consider the viscous damping effect,

$$\frac{V_D}{V_I} = \frac{1}{1 + 3\xi + 1.2\sqrt{\xi}} \quad (8.14)$$

where V_I is the equivalent velocity of a linear elastic system with 10% viscous damping ratio and V_D is the equivalent velocity of a damped linear elastic-perfectly plastic system with viscous damping ratio ξ . The calculated V_I and V_D spectra are shown in Fig. 8.11. The pseudo-velocity spectrum for 2% damping is also shown; this spectrum was assumed by Housner to be V_D for an inelastic system. The following observations can be made:

- (1) Housner's assumption that a linear elastic pseudo-velocity response spectrum be used to estimate the inelastic system input energy that contributes to structural damage significantly underestimates the test results for the model.
- (2) Akiyama's approach, that is to estimate the total input energy of an inelastic system by using the elastic system with ξ equal to 10%, is reasonable for estimating the input energy of the MO-65 test. However the test shows that Eq. (8.14) overestimates the viscous damping effect.

- (3) Using a single value of the period to define the spectral value is unreliable. This is especially true when the energy spectrum has sharp variation near the elastic period considered. A reasonable band in which the fundamental period may vary during the earthquake should be used to estimate the input energy. For this bare steel structure, a period range of 0.3 to 0.4 second is reasonable; the maximum spectral ordinate in this range should then be used to estimate the input energy.
- (4) The input energy (E_D) or the equivalent velocity (V_D) that contributes to the damage of the structure should be used in an energy-based limit design method. Figure 8.8 shows that for a lightly damped structure ($\xi = 2.40\%$ for the model), the equivalent velocity (V_D) of the input energy that contributes to the damage may be assumed to be given by the equivalent velocity (V_I) of the total input energy of a linear elastic system with 10% viscous damping for design purposes.

8.6 Viscous Damped Energy

8.6.1 Introductory Remarks

The energy equation from Appendix B is

$$\frac{1}{2} \dot{\mathbf{y}}^T \mathbf{m} \dot{\mathbf{y}} + \int_0^t \mathbf{f}_D^T d\mathbf{y} + \int_0^t \mathbf{f}_S^T d\mathbf{y} = \int_0^t \left(\sum_{i=1}^N m_i \ddot{v}_i \right) dv_g \quad (8.15)$$

i.e.,
$$E_K + E_\mu + E_H + E_S = E_I \quad (8.16)$$

where E_μ and E_H are the two energy dissipation mechanisms. For the model response in the linear elastic range (MO-6.3 test), equivalent viscous damping was the only source of energy dissipation. Once the structure has undergone "minor" inelasticity (MO-33 test), the viscous and hysteretic dissipated energies both become important. During the severe base excitation, the structure had significant member yielding and brace buckling (MO-65 test); the input energy is dissipated predominantly as hysteretic energy in the inelastic responses (Fig. 7.51).

As the damping mechanism is complicated and the damping force is difficult to measure, the damping energy E_μ dissipated in the tests is calculated indirectly. An attempt is also made to estimate E_μ analytically and to correlate the analytical E_μ with the indirectly measured E_μ .

8.6.2 MO-6.3 Test

8.6.2.1 Test Results

The model remained elastic during this low intensity test. Therefore, the E_H term in Eq. (8.16) vanishes and the viscous damped energy is calculated as

$$E_{\mu(\text{test})} = E_I - E_K - E_S . \quad (8.17)$$

The E_K and E_S are evaluated by Eq. (B.5) and Eq. (B.16), where k_i is the linearized slope of the i th story inter-story drift versus story shear curve.

8.6.2.2 Analytical Prediction of Viscous Damped Energy

The E_μ from Eq. (B.14) is

$$E_\mu = \int_0^t \underline{f}_D^T d\underline{v} . \quad (8.18)$$

A viscous damping mechanism is assumed in the following discussion to simplify the derivation. For a viscous damping mechanism, \underline{f}_D is written as

$$\underline{f}_D = \underline{C}\dot{\underline{v}} \quad (8.19)$$

where \underline{C} is the damping matrix. The most commonly used form for the damping matrix \underline{C} is Rayleigh damping:

$$\underline{C} = \alpha \underline{m} + \beta \underline{K} . \quad (8.20)$$

The significant advantage of Rayleigh damping is that it enables the equations of motion to be decoupled into the modal coordinates for the linear elastic system. This type of damping is also widely adopted in the linear and non-linear response analysis computer programs [15,19] for its mathematical convenience. Equation (8.18) is then reduced as

follows:

$$\begin{aligned}
 E_{\mu} &= \int_0^t (\alpha \dot{\underline{v}}^T \underline{m} + \beta \dot{\underline{v}}^T \underline{k}) d\underline{v} \\
 &= \int_0^t (\alpha \dot{\underline{v}}^T \underline{m} + \beta \dot{\underline{v}}^T \underline{k}) \dot{\underline{v}} dt \\
 &= \alpha \int_0^t \left(\sum_{i=1}^N \phi_i \dot{Y}_i \right) \underline{m} \left(\sum_{j=1}^N \phi_j \dot{Y}_j \right) dt + \beta \int_0^t \left(\sum_{i=1}^N \phi_i \dot{Y}_i \right) \underline{k} \left(\sum_{j=1}^N \phi_j \dot{Y}_j \right) dt \quad (8.21)
 \end{aligned}$$

where \underline{v} is expressed in the modal coordinates:

$$\underline{v}(t) = \sum_{i=1}^N \phi_i Y_i(t) \quad (8.22)$$

By normalizing ϕ_i such that

$$\phi_i^T \underline{m} \phi_i = M_i = 1 \quad (8.23a)$$

$$\phi_i^T \underline{k} \phi_i = K_i = \omega_i^2 M_i = \omega_i^2 \quad (8.23b)$$

and using the orthogonality properties

$$\phi_i^T \underline{m} \phi_j = 0 \quad i \neq j \quad (8.24a)$$

$$\phi_i^T \underline{k} \phi_j = 0 \quad i \neq j \quad (8.24b)$$

Eq. (8.21) is simplified as

$$E_{\mu} = \alpha \int_0^t \sum_{i=1}^N \dot{Y}_i^2 dt + \beta \int_0^t \sum_{i=1}^N \omega_i^2 \dot{Y}_i^2 dt = \sum_{i=1}^N [(\alpha + \beta \omega_i^2) \int_0^t \dot{Y}_i^2 dt] \quad (8.25)$$

The coefficients α , β can be evaluated from the measured periods and damping ratios of the first two modes [30]. Equation (8.25) shows that Rayleigh damping implies implicitly higher weighting factors ($=\alpha + \beta \omega_i^2$) in the higher modes. The weighting factors for the model were 0.71, 1.85, 4.40, respectively, for the first three modes.

To evaluate the modal displacement time history $Y_i(t)$, the following equation is used [30]

$$Y_i(t) = \frac{\phi_i^T \underline{m} \underline{v}}{\phi_i^T \underline{m} \phi_i} = \phi_i^T \underline{m} \underline{v} \quad (8.26)$$

where \underline{m} is assumed to be diagonal and the components of \underline{v} are the measured relative displacement time histories. The mode shapes obtained from the free vibration test with the shaking table locked were used. Note that during the shaking table test, the table was floated by air pressure and the structural period increased (Table 7.1). It is believed that the mode shape changes were minor and were thus ignored in this study. The $Y_1(t)$ calculated using Eq. (8.26) is shown in Fig. 8.12(a). The same procedure was used to calculate $Y_2(t)$; however, the result was greatly affected by the first mode component. It was realized that: (i) the structural response is predominantly controlled by the first mode; (ii) the actual mode shape during the shaking table test deviated slightly from the ϕ_i obtained from the free vibration test with the table locked; (iii) small deviation of the ϕ_i introduces a nonzero component of the predominant first mode response in the ϕ_2 direction, this "residual" being significantly larger than the real $Y_2(t)$ component.

The revised procedure used to evaluate $Y_2(t)$ follows. To project \underline{v} onto the ϕ_2 direction in order to calculate $Y_2(t)$, \underline{v} was band-pass filtered before applying Eq. (8.26). Since the natural frequencies of the first three modes, which were widely separated (Table 7.1), were known from the free vibration tests, a frequency window that passed only the frequency content between 6 and 12 Hz for the second mode was selected. The first mode component is thus filtered already. The $Y_2(t)$ calculated by this procedure is shown in Fig. 8.12(b); $Y_3(t)$ was also calculated by band-pass filtering \underline{v} through a window between 12 and 18 Hz (Fig. 8.12(c)). A comparison of the magnitudes of $Y_1(t)$, $Y_2(t)$ and $Y_3(t)$ shows the dominance of the first mode.

Numerical differentiation was used to compute $\dot{Y}_i(t)$ from the calculated $Y_i(t)$. E_μ was then evaluated from Eq. (8.25). The E_μ at the end of the time histories for the first three modes were 1.479, 0.032 and 0.004 kip-inches, respectively, implying that very little energy was dissipated in the higher modes. The resulting E_μ time history including

the first three modes is shown in Fig. 8.13; it shows that the predicted E_{μ} is about 15% smaller than the experimental result. The difference results from the assumption of Rayleigh viscous damping. The real damping mechanism is complicated and is due to connection friction, material internal friction and so on. In spite of this difference, the analytical method still gave a good estimate of E_{μ} .

8.6.3 MO-33 Test

During this test, the braces in the fifth story buckled; the structure response was therefore no longer linear. The DCDTs were not installed in the fifth story braces to measure the brace axial deformation, hence hysteretic dissipated energy due to brace buckling could not be calculated. As the fundamental period measured after this test showed little change (Table 7.1), it is believed that the mode shapes also varied little because the brace suffered just minor buckling during the test. The same analytical procedure was used to predict the E_{μ} ; the portion of viscous damped energy was then separated from the hysteretic energy. Figure 8.14 shows that for the model subjected to moderate intensity base excitation, the mechanism of viscous damping is still significant; it decreases the structural hysteretic energy dissipation demand, thus reducing the inelastic deformation.

8.6.4 MO-65 Test

Figure 7.51 shows the $E_{\mu(\text{test})}$ time history, it was calculated by applying the following equation:

$$E_{\mu(\text{test})} = E_I - E_K - E_S - E_H = E_I - E_K - E_A . \quad (8.27)$$

During this test, the input energy is increased significantly; the major part of the input energy is dissipated as hysteretic energy. The model experienced large inelastic deformation, which changed the fundamental period from 0.361 second to 0.392 second; the analytical estimation of E_{μ} could not be applied in this highly nonlinear system.

8.6.5 Concluding Remarks

The analytical prediction of E_μ assuming a Rayleigh viscous damping gave a good estimate of the viscous damped energy in the elastic range. The higher modal displacements can be calculated with the help of a numerical band-pass filter before applying Eq. (8.26). The analytically predicted E_μ indicated that almost all of the E_μ was dissipated in the first mode. This analytical prediction still gave a reasonable estimate of E_μ for the model with minor inelastic deformation, that is, if the fundamental period and mode shape deviate only slightly from the elastic system.

8.7 Ductile Moment-Resisting Space Frame Response

Present codes emphasize the provision of a secondary system in the form of a ductile MRSF. Recognizing the strength deterioration of the concentric braces after buckling, the UBC and the ATC Recommendations require that 25% of the minimum design base shear be resisted by the ductile MRSF. This is to supply a second line of defense after brace buckling. The rationale of this requirement is studied in this section.

Figure 8.1 shows very high demand for the MRSF in the fifth story during the MO-65 test. This is attributed to the braces buckling and, finally, rupture in that story. The envelope of the story shear resisted by the MRSF is shown in Fig. 8.15; the UBC minimum required story shear for the MRSF is also shown. A comparison of the two curves shows that the demanded strength from the MRSF columns significantly exceeded the code demanded strength. Fortunately the MRSF had a significant **overstrength**; the survival of the MRSF (or the whole structure) after brace buckling is due to this overstrength, which resulted from the over-sizing of the column sections in the original design (Fig. 2.5).

A soft story formed in the fifth story once the braces buckled. Figure 7.38 shows that the MRSF in the fifth story yielded; the MRSF **strength** was sufficient in this story, although excessive inter-story drift occurred (1.8% versus the UBC maximum

limit 1.5%). This implies that the MRSF **stiffness** has to be increased if the code maximum inter-story drift index limitation is to be satisfied. Assuming a soft story in each story, the shear capacities of the MRSF were calculated based upon linear elastic-perfectly plastic behavior and are shown in Fig. 8.15. The maximum shear developed in the fifth story during the MO-65 Test exceeded the calculated shear capacity; this was due to the strain-hardening of the columns.

The envelopes of the inter-story drift index versus the story shear resisted by the MRSF of the four representative tests are shown in Fig. 8.1. The MRSF provided not only the vertical carrying capacity but also the required lateral strength after brace buckling. The ductility of the MRSF was not mobilized (Fig. 7.38) because of its large deformability; its ductility can seldom be used because of the excessive inter-story drift associated with it. Excessive inter-story drift will cause non-structural component damage.

8.8 Brace Behavior

8.8.1 Buckling Strength

The brace force calculation method is described in Section 6.5.3. As discussed in Section 7.5.4, the calculated brace force is not very reliable because of the significant residual stresses and the fact that the material properties have to be obtained from coupon tests. In order to compare the experimental buckling load with the analytically predicted value, the following procedure was used to estimate indirectly the average buckling load of the braces in each story.

- (1) The extreme value of V_i^{BRACE} in each story was identified; first brace buckling was assumed to occur at this time.

- (2) On the basis of the results obtained from the tests of the model, it can be assumed that braces shared the same story shear up to first buckling (Fig. 8.16). The average buckling load $P_{cr(test)}$ was calculated as

$$P_{cr(test)} = \frac{V_{max}^{BRACE}}{2\cos\theta} \quad (8.28)$$

The calculated result is listed in Table 8.1. The analytical prediction using the AISC formulation [10] with the safety factor removed is

$$P_{cr(predicted)} = \left[1 - \frac{(kl/r)^2}{2C_c^2} \right] F_y A \quad (8.29)$$

where $C_c (= \sqrt{2\pi^2 E_s / F_y})$ is the limiting effective slenderness ratio above which the brace will buckle elastically and the effective length factor k was assumed to be 0.7 for the connections used. The predicted P_{cr} is also shown in Table 8.1. A comparison of the results indicates that Eq. (8.29) can give a good estimate of P_{cr} and that the assumed effective length factor (0.7) is reasonable for a brace with connection fixity similar to that used in the model.

Figure 8.17 shows the damaged braces cut from the model upon completion of the shaking table test program. Both braces in the fifth story and brace 7 in the fourth story ruptured at midspan; brace 8 ruptured at brace bottom end with significant residual bend.

8.8.2 Implications for Current Design Practice

The UBC does not have any special requirements for the selection of brace proportions in seismic design. ATC precludes the use of brace design using the tension-only concept by recommending that the brace have a compressive strength equal to at least 50 percent of the required tensile strength [4]. No further recommendations are made for braced frames that are designed to carry both tension and compression because "... there are insufficient data on the non-linear behavior of braced systems with which to develop

definite guidelines for adequate performance...." (Commentary Section 10.5.2).

It was observed in this test program that the braces in the bottom four stories performed satisfactorily. The theoretical P_{cr}/P_y ratio of these braces falls in the range 0.83 to 0.90 (Table 8.2). The fifth story braces, which buckled first and then ruptured after a few cycles of deformation reversal, had a P_{cr}/P_y ratio equal to 0.78. The brace compactness B/t ratio (width-thickness ratio) is also shown in Table 8.2. The maximum B/t ratio allowed in the AISC Specification Section 2.7 [10] is 26 ($=190/\sqrt{F_y}$) for a compressed flange plate in a box section. Although the braces used in the model satisfied this requirement, their local stability under load reversal is not guaranteed. The B/t ratios indicate that the fifth and the fourth story braces were critical regarding local buckling once the brace buckled globally; this is consistent with the observed damage of brace rupture in the fourth and the fifth stories (Fig. 8.17).

On the basis of the observation of local buckling and rupture of the braces, it seems necessary that the P_{cr}/P_y and B/t ratios be limited to prevent such undesirable behavior. The ATC recommendation that the brace shall have a compressive strength equal to at least 50 percent of the required tensile strength is apparently not sufficient to prevent significant brace strength deterioration. It is suggested from the limited data in Table 8.2 that for tubular braces the B/t ratio should be less than 18 and the P_{cr}/P_y should be greater than 0.8:

$$\frac{P_{cr}}{P_y} = \left[1 - \frac{(kl/r)^2}{2C_c^2} \right] \geq 0.8$$

i.e.,
$$\frac{kl}{r} \leq 0.63 C_c . \quad (8.30)$$

Further analytical and experimental research needs to be conducted to verify this recommendation. A method to improve brace performance is discussed in Section 10.3.

8.9 Rational Design of the K-braced Dual System

A rational method for earthquake-resistant design of building structures is proposed in Reference 35. The preliminary design is performed considering safety against collapse as the controlling limit state. The design base shear should be based upon a reliable inelastic design response spectra; this design base shear is much higher than the current design code requirements. To bound the demand on the capacity of individual elements, both an inverted-triangular and a uniform load pattern should be considered. The required structural element demands are then estimated by performing an elastic analysis of the structure. The capacity or plastic design methods can then be applied to proportion the braces, columns, girders, connections and joint panel zones. Global and local member stability must be considered and assured. The limits on the brace kl/r and B/t ratios discussed in the previous section may be incorporated at this stage of the design.

The role of the ductile moment-resisting space frame as a second line of defense should be thoroughly reviewed. By assuming soft story formation in each story, the shear capacity of the MRSF can be calculated by simple plastic theory. This shear capacity should be larger than the total story shear that would be demanded by the maximum credible earthquake; this is the force level estimated from the inelastic design response spectrum corresponding to the period of the MRSF.

When the building structure has more than two bays, the braced bays should be symmetrically located so that the center of rigidity is located very close to the center of mass. The braced bays should be located so as to maximize the **torsional rigidity** of the structure. Because of the significant increase in torsional eccentricity that can occur due to premature buckling of one of the braced bays, it is desirable to use more than two braced bays in a given direction so as to increase the **torsional redundancy** of the structural system.

IX. CORRELATION OF THE MODEL TEST RESULTS

9.1 Introductory Remarks

One of the main objectives of the research program was to evaluate the reliability of using available computer programs to predict the response of structures under seismic excitation. In this chapter, the analytical predictions of the seismic response using the measured shaking table motion as input are described. The correlation of the test results and the analytical predictions is discussed in Section 9.2 and used to judge the reliability of the analytical prediction.

Another main objective of this research program was to evaluate the reliability of using scaled models and different testing techniques to study the seismic response of structures. The results of the shaking table testing of the model and pseudo-dynamic testing of the prototype are compared and the reliability of using earthquake simulators for the testing of moderate-scale models is assessed.

9.2 Prediction and Correlation of the Model Seismic Response

9.2.1 Introductory Remarks

Previous researchers [45,46] have pointed out the significance of shaking table-structure interaction. The four vertical actuators and four vertical passive stabilizers beneath the table cannot fully constrain the induced overturning moment. The model was the heaviest tested so far on the shaking table; significant table pitching was observed and measured during the tests. To formulate an analytical model capable of predicting the experimental results, the table-structure interaction must be taken into account.

Two analytical models are described in Reference 45; a brief description of both models follows:

Model 1

The test structure is fixed at the column base; the horizontal and the pitching motions of the shaking table are included as input in the analysis (Fig. 9.1(a)). It has been pointed out [45] that, although this approach seems simple in principle, it has the basic shortcoming that most available computer programs are only capable of dealing with translational input ground motions.

Model 2

The complete table-structure system is modeled in the analysis and the measured table horizontal motion is used as input signal (Fig. 9.1(b)). The table is modeled as a rigid beam. Two vertical springs are used under the table to simulate the oil column and feed-back loop flexibility of the vertical hydraulic actuators, giving a pitching degree of freedom to the table-structure system. Generally the springs are assumed to be linear elastic and the stiffnesses are selected by a trial-and-error procedure so that the period of the complete table-structure system is consistent with the measured period of the complete table-structure system. Table 7.1 shows the increase in the fundamental period and the equivalent viscous damping ratios when the table is floated and controlled by the vertical actuators.

Figure 8.12 shows the contribution of the first three modes to the structural response. It is apparent that the contribution of the third mode is negligible; therefore, Rayleigh damping that reflected the first two modal damping ratios was used in DRAIN-2D. If Model 1 is used, the measured equivalent viscous damping ratios with the table locked should be used; the equivalent viscous damping ratios measured with the table floated should be used in the Model 2 analysis. For example, to predict the seismic response of the model to the MO-6.3 Test, the following damping ratios have to be used (Table 7.1):

(1) $\xi_1=1.29\%$, $\xi_2=0.67\%$ in the Model 1 analysis;

(2) $\xi_1=2.04\%$, $\xi_2=1.78\%$ in the Model 2 analysis.

Note also that the experimental lateral displacement time histories presented in Chapter 7 were calculated by subtracting the measured horizontal table displacement from the measured total lateral displacements at each floor level; the rigid body component due to table pitching is included in the results presented in Chapter 7. These lateral displacements should be used to correlate the Model 2 predicted lateral displacements. On the other hand, considering the nature of Model 1, the rigid body component due to pitching motion should be removed from the experimental lateral displacements to correlate with the analytically predicted lateral displacements. Figure 9.2 shows a typical example of the roof relative lateral displacement time history of the MO-65 Test presented in Fig. 7.30; the rigid body component due to table pitching motion is also shown.

These two models were studied and an approximate method was developed to overcome the basic shortcoming of Model 1.

9.2.2 Model 1 Correlation

9.2.2.1 Equivalent Base Horizontal Excitation Concept

The computer program DRAIN-2D allows the user to input horizontal and/or vertical ground accelerations. Independent vertical and horizontal ground motions can be specified in terms of acceleration time histories; multiple support excitation cannot be considered. Using the equation of motion for the linear elastic system and considering the horizontal excitation only, Eq. (B.1) in Appendix B can be written as

$$\underline{m}\ddot{\underline{v}} + \underline{c}\dot{\underline{v}} + \underline{k}\underline{v} = -\underline{m}\underline{r}_x\ddot{v}_{gx} \quad (9.1)$$

where the following expression is substituted into Eq. (B.1):

$$\underline{v}^t = \underline{v} + \underline{r}_x v_{gx} = \text{total lateral displacement vector}$$

\underline{v} = relative lateral displacement vector

$$\underline{r}_x^T = [1 \ 1 \ 1 \ 1 \ 1 \ 1]$$

v_{gx} = table horizontal displacement.

To consider the table pitching motion, the equations of motion have to be modified as follows:

$$\underline{v}^t = \underline{v} + \underline{r}_x v_{gx} - \underline{r}_\theta v_{g\theta} = \text{total lateral displacement vector}$$

where $\underline{r}_\theta^T = [h_1 \ h_2 \ h_3 \ h_4 \ h_5 \ h_6]$

h_i = height above column base to floor level i

$v_{g\theta}$ = table pitching angular displacement (radian).

Therefore,
$$\underline{m}\ddot{\underline{v}} + \underline{c}\dot{\underline{v}} + \underline{k}\underline{v} = -\underline{m}\underline{r}_x\ddot{v}_{gx} + \underline{m}\underline{r}_\theta\ddot{v}_{g\theta} \equiv \underline{P}_{equ}(t). \quad (9.2)$$

Given the table horizontal acceleration (\ddot{v}_{gx}) and pitching acceleration ($\ddot{v}_{g\theta}$), the equivalent lateral excitation force (\underline{P}_{equ}) is determined irrespective of whether the structure will experience inelastic deformation.

For the linear elastic system, Eq. (9.2) can be decomposed into the modal coordinate system using the following transformation,

$$\underline{v} = \sum_{i=1}^N \phi_i Y_i \quad (9.3)$$

where N is the number of degrees of freedom. Equation (9.2) can then be written as

$$\underline{m} \sum_{i=1}^N \phi_i \ddot{Y}_i + \underline{c} \sum_{i=1}^N \phi_i \dot{Y}_i + \underline{k} \sum_{i=1}^N \phi_i Y_i = -\underline{m}\underline{r}_x\ddot{v}_{gx} + \underline{m}\underline{r}_\theta\ddot{v}_{g\theta}.$$

This equation can be simplified by premultiplying both sides by ϕ_i^T , using the orthogonality properties of the mode shapes (Eq. 8.24), and dividing by M_i :

$$\ddot{Y}_i + 2\xi_i\omega_i\dot{Y}_i + \omega_i^2 Y_i = -\frac{\phi_i^T \underline{m}\underline{r}_x}{M_i} \ddot{v}_{gx} + \frac{\phi_i^T \underline{m}\underline{r}_\theta}{M_i} \ddot{v}_{g\theta} \quad (9.4)$$

where

$$\frac{\phi_i^T \underline{m} \underline{r}_x}{M_i} \equiv L_{xi} = \text{the participation factor for base horizontal} \quad (9.5a)$$

excitation in the i th mode

$$\frac{\phi_i^T \underline{m} \underline{r}_\theta}{M_i} \equiv L_{\theta i} = \text{the participation factor for base pitching} \quad (9.5b)$$

excitation in the i th mode

On the basis of a lumped mass matrix and the mode shapes measured from the free vibration test conducted prior to the shaking table tests, the participation factors for the first three modes were calculated (Table 9.1). One significant observation from this Table is that the pitching motion will excite predominantly the first mode response of the structure. This phenomenon is attributed to the similarity of \underline{r}_θ , which has the inverted-triangular shape, and the first mode shape, which is also very close to the inverted-triangular shape. Considering the limitation of the DRAIN-2D computer program, which is only capable of dealing with translational input ground motion, an approximate method that reproduced the same first mode pitching response is described below.

Equation (9.2) is approximated by the following:

$$\begin{aligned} \underline{m} \ddot{\underline{v}} + \underline{c} \dot{\underline{v}} + \underline{k} \underline{v} &= - \underline{m} \underline{r}_x \ddot{v}_{gx} + \underline{m} \underline{r}_x (\alpha \ddot{v}_{g\theta}) = - \underline{m} \underline{r}_x (\ddot{v}_{gx} - \alpha \ddot{v}_{g\theta}) \\ &\equiv - \underline{m} \underline{r}_x \ddot{v}_{gx(\text{equ})} \end{aligned} \quad (9.6)$$

where the term $\underline{m} \underline{r}_\theta \ddot{v}_{g\theta}$ in Eq. (9.2) is replaced by $\underline{m} \underline{r}_x (\alpha \ddot{v}_{g\theta})$ in Eq. (9.6). A constant α is introduced; it is determined such that the first mode participation factor due to $\ddot{v}_{g\theta}$ in both equations will be identical:

$$\frac{\phi_1^T \underline{m} \underline{r}_\theta}{M_1} = \alpha \frac{\phi_1^T \underline{m} \underline{r}_x}{M_1} \quad (9.7)$$

or

$$\alpha = \frac{\phi_1^T \underline{m} \underline{r}_\theta}{\phi_1^T \underline{m} \underline{r}_x} \quad (9.8)$$

The equivalent base horizontal acceleration $\ddot{v}_{gx(equ)}$ is given by

$$\ddot{v}_{gx(equ)} = \ddot{v}_{gx} - \alpha \ddot{v}_{g\theta} = \ddot{v}_{gx} - \left(\frac{\phi_1^T \underline{m} \Gamma_\theta}{\phi_1^T \underline{m} \Gamma_x} \right) \ddot{v}_{g\theta}. \quad (9.9)$$

The value of α is 185 inches; the calculated $\ddot{v}_{gx(equ)}$ is used as uni-directional horizontal acceleration input to the DRAIN-2D computer program.

Strictly, this technique can only be applied to linear elastic systems. To estimate the maximum error of this approach applied to a structure with a highly nonlinear response, let

$$\phi_1^* = [1 \ 1 \ 1 \ 1 \ 1 \ 1]^T,$$

which approximates the fundamental mode shape for a structure with a soft story in the first level; then the calculated α is 152 inches. In the extreme, the use of Eq. (9.9) overestimates the pitching motion effect by 17%. Since the model formed a soft story in the fifth level in the MO-65 Test, the error in the α value is insignificant.

9.2.2.2 Prediction and Correlation of MO-6.3 Test

The measured table horizontal acceleration and displacement time histories are shown in Fig. 7.3. The table pitching acceleration (displacement) was obtained from the shaking table vertical acceleration (displacement) time histories. The measured pitching acceleration and displacement time histories are shown in Fig. 9.3. The normalized Fourier amplitude spectra of the horizontal and pitching accelerations are also shown; it indicates that the pitching motion frequency content is concentrated around the fundamental natural frequency (2.8 Hz) of the test model. This results from the fact that the table pitching motion is driven by the base overturning moment, which in turn is governed by the first mode response.

Rayleigh damping was assumed for correlation purposes. Since Fig. 8.12 shows that the third mode contributed little to the response, the damping ratios ($\xi_1 = 1.29\%$, $\xi_2 = 0.67\%$) corresponding to the first two modes were used to calculate the Rayleigh

damping constants (Eq. 3.15). Applying $\ddot{v}_{gx(equ)}$ as the horizontal acceleration input, the calculated relative lateral displacement and story shear time histories are shown as dotted lines in Fig. 9.4 and Fig. 9.5; the test results are shown as solid lines. In general, the correlation is very good. The predicted lateral displacements are smaller than the test results; the largest difference occurs in the second floor. This is partially attributed to the fact that the model foundation was not perfectly fixed to the shaking table. This effect was more significant for the higher intensity tests; the foundation movement is described in detail in the following two sections. Figures 9.4 and 9.5 show that the predicted story shear time histories correlate better than the lateral displacement time histories. The good correlation of the story shear time histories indicates that the calculation of the effective excitation force (P_{equ}) by applying the equivalent base horizontal acceleration concept, is reliable.

In order to check the effect of table pitching motion on the seismic response, the measured table horizontal acceleration (\ddot{v}_{gx}) was used as input to DRAIN-2D. The predicted roof lateral displacement and base shear time histories are shown in Fig. 9.6. The correlation is poor; a significant phase difference is observed between the predicted and test responses. By including and excluding the table pitching motion effect, the base shear time history correlation coefficients are 0.94 (from Fig. 9.5) and 0.59 (from Fig. 9.6), respectively. This comparison shows that the equivalent base horizontal acceleration effectively considers the table pitching motion and that it gives significantly better correlation with the test results.

9.2.2.3 Prediction and Correlation of MO-33 Test

The measured table horizontal and pitching motions are shown in Fig. 7.5 and Fig. 9.7, respectively. The responses calculated by applying the equivalent horizontal acceleration are shown in Fig. 9.8 and Fig. 9.9. The story shear time histories correlate well with the test results; nevertheless, the calculated relative lateral displacements are

smaller than the test results. The largest discrepancy occurs on the second floor, where the predicted displacement is about half of the measured displacement at the time of maximum response; this can be attributed in part to foundation movement during the test. Two DCDTs were installed on both sides of the column $1C_{B1}$ and $1C_{B2}$ (Fig. 4.25) to measure the foundation girder vertical movement. The foundation vertical movement time histories of the central column $1C_{B2}$ are shown in Fig. 9.10. The corresponding foundation rotation and the column base moment time histories of column $1C_{B2}$ are shown in Fig. 9.11. The plot of foundation rotation versus column end moment in Fig. 9.12 indicates the nonlinear behavior. The plot, approximated by two straight lines, indicates the different foundation rotational stiffness under opposite bending directions. For positive bending moment at the column base, the concentric brace connected to the column under consideration was in compression. The foundation girder was, in addition to being tightened to the shaking table by the prestressed rods, compressed further by the brace; this increased the rotational stiffness of the foundation girder. When the column end moment was negative, the tensile brace force reduced the precompression in the foundation girder, thus reducing the rotational stiffness. The flexibility in the model foundation was not considered in the analytical model; this may explain why the calculated lateral displacements are smaller than the test results.

9.2.2.4 Prediction and Correlation of MO-65 Test

The measured table horizontal and pitching motions are shown in Fig. 7.29 and Fig. 9.13. Note that as a result of the reduced overturning moment in the MO-65 Test, the intensity of the pitching acceleration with respect to the horizontal acceleration is relatively small compared with those of the previous tests (MO-6.3, MO-33 Tests). The responses calculated by applying equivalent base horizontal acceleration are shown in Fig. 9.14 and Fig. 9.15. The story shear time histories correlate very well with the test results in the first 9 seconds; after that a phase shift between the test and predicted

responses is observed. This discrepancy is attributed to the rupture of the brace in the fifth story after 9.2 seconds (Fig. 7.35); this feature could not be adequately modeled in DRAIN-2D. The effect is more pronounced in the lateral displacement time histories, particularly at the second floor level. Significant foundation rotation was also observed for this test (Fig. 9.16); this may explain the large difference in the predicted and the test responses of the second floor lateral displacements. Good correlation of the response time histories in the first 9 seconds confirms the suitability of applying the equivalent horizontal acceleration concept to this model for nonlinear response.

9.2.2.5 Concluding Remarks

Based upon the above study, the following conclusions can be drawn regarding the correlation between the experimental responses and those predicted analytically:

- (1) The shortcoming of Model 1 mentioned in Section 9.2.1 can be overcome by using the concept of equivalent base horizontal acceleration derived in Section 9.2.2.1; this satisfactorily accounts for the base pitching motion.
- (2) The analytical prediction of the seismic responses of a concentrically braced frame using the computer program DRAIN-2D gave satisfactory correlation with the shaking table test results. Better correlation can be expected if the brace hysteretic behavior is properly modeled and the foundation condition is taken into account.
- (3) The available brace models, such as the model proposed in Reference 22 and used in the present study, cannot reflect brace rupture. Therefore the analytically predicted responses, especially lateral displacements, are not reliable once brace rupture occurs.
- (4) The two-dimensional idealization of the model in the DRAIN-2D analysis is reasonable. No significant relative vertical displacement between the interior braced frame (Frame B) and the exterior moment frame (Frame A) was measured. For the MO-65 Test, the peak relative vertical displacement of Frames A and B at the roof

level was less than 1 percent of the individual frame vertical displacements. The X-bracing in the transverse frames (Frames 1 and 3) effectively restrained the torsional motion of the structure.

9.2.3 Model 2 Correlation

9.2.3.1 General

Only the measured horizontal table acceleration was used as input signal to the complete shaking table-structure system. The table itself, with a rotational mass of 1,245 kips-sec-inch, was modeled as a rigid beam (Fig. 9.1(b)).

A trial-and-error procedure was used to evaluate the pitching spring constants. This procedure involves the solution of a seven degrees of freedom eigen-value problem. The first six degrees of freedom are associated with the lateral displacement of the six floors of the model structure (Sections 3.2 and 5.2); the seventh degree of freedom is associated with the pitching of the shaking table (Fig. 9.1(b)). The pitching spring constant was varied until the fundamental period of the table-structure system matched that measured in free vibration tests.

9.2.3.2 Prediction and Correlation of MO-6.3 Test

The pitching spring constant (k_p) was selected as 900 kips/inch on the basis of a fundamental period of 0.361 seconds. Rayleigh damping was used to reflect the measured damping ($\xi_1=2.04\%$ and $\xi_2=1.78\%$). A comparison of the analytically predicted lateral displacement and story shear time histories is shown in Fig. 9.17 and Fig. 9.18. The correlation is excellent; the analysis using Model 2 correlates better than that using Model 1. Using the roof lateral displacement time histories as an example, the correlation coefficients for Model 1 (Fig. 9.4) and Model 2 (Fig. 9.17) are 0.92 and 0.98, respectively.

9.2.3.3 Prediction and Correlation of MO-33 Test

The pitching spring constant was selected as 750 kips/inch on the basis of a fundamental period of 0.367 second. Rayleigh damping was used to reflect the measured damping ($\xi_1=2.04\%$ and $\xi_2=2.13\%$). Figures 9.19 and 9.20 show the lateral displacement and story shear time histories. Compared with the Model 1 method, the correlation of response time histories is improved, especially in the range between 5 and 6 seconds. The base shear time history correlation coefficients for Model 1 and Model 2 are 0.91 and 0.98, respectively.

9.2.3.4 Prediction and Correlation of MO-65 Test

The pitching spring constant was selected as 750 kips/inch on the basis of a fundamental period of 0.367 second. The measured damping ratios ($\xi_1=2.4\%$, $\xi_2=2.6\%$) were used in the analysis; Figures 9.21 and 9.22 show the lateral displacement and story shear time histories. As for the Model 1 analysis, the correlation is poor after 9 seconds. The Model 2 analysis gives an insignificant improvement in correlation. The base shear time history correlation coefficients for Model 1 and Model 2 are 0.91 and 0.95, respectively.

9.2.4 Concluding Remarks

Two mathematical models suitable for predicting shaking table test response have been evaluated; both models correlate well with the test results. The equivalent horizontal table acceleration concept simplifies the mathematical modeling because only the superstructure (i.e., test structure) is considered.

Model 2 is the conceptually correct method as the table pitching motion is treated as a **response quantity** and not as the **input excitation**. The difficulty with this method is that the pitching spring stiffness is indeterminate; it varies from test to test and a trial-and-error procedure must be used to select the suitable spring stiffness. Good correlation can be achieved if the pitching spring is selected such that the fundamental

period of the complete shaking table-structure system is consistent with the measured fundamental period of this complete system. If this period is not available, Model 1 using the equivalent horizontal table acceleration should be applied. A non-linear pitching spring has been used for correlation purposes by previous researchers [46].

9.3 Correlation of the Model and the Prototype Test Results

9.3.1 Introductory Remarks

One of the main objectives of this cooperative research program is to study the reliability of testing scaled models using different testing techniques in earthquake engineering research. A newly developed test technique, known as the computer-actuator on-line test technique or pseudo-dynamic test technique [39,47], was used in the BRI, Japan, for the prototype testing.

A global comparison of the prototype and the model results was discussed in Section 8.3.5. The maximum strength of the model was 16% higher than that of the prototype and it was concluded that the strain rate effect played an important role in interpreting the higher strength of the model. It is the purpose of this section to compare the seismic response time histories of the prototype and the model; both test structures were subjected to the same earthquake input signals with different intensities. Three tests, Elastic-3 Test (65 gal), Moderate Test (250 gal) and Final Test (500 gal), were conducted in the BRI to represent the serviceability, damageability and collapse limit states of the prototype. Three comparable shaking table tests, MO-6.3 Test, MO-33 Test and MO-65 Test discussed in Chapter 7, were selected to represent the three limit states of the model. In this comparison, the lateral displacement components due to the rigid body pitching motion of the shaking table were subtracted from the measured lateral displacements. Unless otherwise noted, the model response quantities have been scaled to the prototype level according to the similitude law.

9.3.2 Serviceability Limit State Tests

Figure 9.23 shows the horizontal acceleration time histories, Fourier amplitude spectra and linear elastic response spectra of the ground motions used in both test structures; it is observed from the frequency content and the linear elastic response spectra (LERS) that the prototype Elastic-3 Test had higher intensity. The relative lateral displacement and story shear time histories of the two test structures are shown in Fig. 9.24 and Fig. 9.25. The prototype Elastic-3 Test stopped at 11.98 seconds. The lateral displacement responses in Fig. 9.24 show that the model period ($0.620 \text{ second} = 0.342/\sqrt{T_r}$) was somewhat longer than that of the prototype (0.610 second). In addition to having higher ground motion intensity in the prototype Elastic-3 Test, the main difference in the responses of the two test structures results from the large difference in the damping ratios (Section 5.4). The first modal damping ratio was 0.49% for the prototype and 1.56% for the model. The importance of viscous damping in the linear elastic range of response has been shown in Fig. 8.12 from the energy point of view. The larger prototype lateral displacement is also partially attributed to the shear yielding of the second floor brace-girder joint panel zone (Fig. 9.26). The story shear time histories in Fig. 9.25 similarly show larger prototype response.

9.3.3 Damageability Limit State Tests

A comparison of the ground motions used in both tests is shown in Fig. 9.27; although the peak accelerations are quite different (0.26g versus 0.33g), the frequency content and the LERS indicate that both structures were subjected to similar intensity of input motion. The lateral displacement, inter-story drift and story shear time histories are shown in Fig. 9.28 to Fig. 9.30, where the prototype test stopped at 17.16 seconds because of the second floor brace-girder joint panel-zone failure. The model shows larger lateral displacements; this is due in some degree to the flexibility of the model foundation and the table pitching motion (Fig. 9.12). Local movement of the column foundation had greater influence on the first story inter-story drift. The second

floor brace-girder joint panel-zone ruptured during the prototype test; the period elongation of the prototype can be identified in the last two cycles of response. In general, the degree of correlation between the two test structures for the damageability level test is better than that for the serviceability level test; the correlation however is still poor around 9 seconds.

The inter-story drift versus story shear plot of each story is shown in Fig. 9.31; the prototype first story curve shows significant inelastic deformation. This is attributed to shear yielding in the second floor brace-girder joint panel zone (Fig. 3.19) which started at about 3 seconds. The out-of-plane buckling of two braces in the second story and the in-plane buckling of one brace in the third story (Fig. 3.17) produce the hysteretic behavior in these stories. As a consequence of inserting load cells in the prototype braces, the induced initial imperfection caused additional brace buckling in the prototype.

9.3.4 Collapse Limit State Tests

A comparison of the ground motions used in both tests is shown in Fig. 9.32. Although the MO-65 Test had significantly higher peak acceleration (0.50g versus 0.65g), the frequency content and the LERS indicate that the prototype Final Test had a higher intensity. Figure 9.33 to Fig. 9.35 show the relative lateral displacement, inter-story drift and story shear time histories for both the model and the prototype; the prototype test stopped at 11.135 seconds. Significant inter-story drift and permanent deformation can be observed in the bottom four stories of the prototype, particularly in the second and third stories (Fig. 9.34). The damage pattern is shown in Fig. 3.30. Although all stories except the sixth of the model experienced brace buckling, significant inter-story drift and permanent deformation were observed only in the fifth story; this was due to the rupture of braces in that story. A large elongation of the period of the prototype after 8 seconds was also observed as a consequence of severe brace damage. The response time histories of the model did not show a similarly large period elongation. The story shear time histories of the two test structures correlate well for the first 8

seconds (Fig. 9.35).

A comparison of typical hysteretic responses of the bottom four story braces is shown in Fig. 9.36. The prototype brace responses show a severe deterioration in the post-buckling strength; the braces of the model show a more stable hysteretic response. It is believed that this phenomenon is due to some initial misalignment of the load cells in the prototype braces as well as the difference in testing techniques. The pseudo-dynamic test technique is a quasi-static test method. Brace buckling is an unstable phenomenon; stress relaxation during the long time hold between time steps in the pseudo-dynamic test caused rapid brace strength deterioration.

The inter-story drift versus total story shear plot of each story is shown in Fig. 9.37. The damage and energy dissipation of the prototype are concentrated in the bottom three stories. The model has more damage concentrated in the fourth and the fifth stories. A comparison of the inter-story drift versus column story shear in each story is shown in Fig. 9.38, the high strength demanded in the second and the third story of the prototype as well as in the fifth story of the model were consistent with the observed severe brace buckling or rupture in those stories. Figure 9.39 shows that the distribution of hysteretic energy dissipation varies significantly between the model and the prototype. The differences in the distribution of energy dissipation are entirely consistent with the distribution of story shear forces and the observed damage in the two structures.

Correlation studies of shaking table and pseudo-dynamic tests have been conducted by other researchers [39,40] and reasonable correlation reported. In these studies, two identical structures were fabricated for the shaking table and pseudo-dynamic tests; the shaking table test was always conducted first and then the measured horizontal table acceleration was used as input to the pseudo-dynamic test. Input signal distortion was non-existent and variation in the test structure material properties was minimized. These two key factors made it difficult to correlate the response of the model and the prototype in the tests reported herein.

9.3.5 Concluding Remarks

Following conclusions may be drawn regarding the correlation of the test results of the model and the prototype:

- (1) A comparison of the model and the prototype ground motion frequency contents shows that peak table horizontal acceleration is a poor index to specify the intensity of the ground motion in shaking table tests. Use of an effective peak acceleration or the spectral quantities (pseudo-acceleration or pseudo-velocity) is preferable to that of peak acceleration.
- (2) Because the equivalent viscous damping ratios measured in the prototype are much less than those observed in the model, their responses are quite different in the serviceability level test. The larger lateral displacements in the prototype are partially attributed to the shear yielding of the second floor brace-girder joint panel zone; this behavior is undesirable in serviceability level tests.
- (3) Initial imperfections in the prototype braces resulting from the insertion of load cells caused premature nonlinear behavior and buckling in the damageability limit state test. Following the re-detailing of the second floor brace-girder joint panel zone, the shear yielding and rupture of this panel zone was prevented in the model structure.
- (4) The effects of strain rate and stress relaxation are significantly different in shaking table testing and pseudo-dynamic testing. It was concluded in Section 8.3.5 that the strain rate effect leads to an 11% increase of the model strength above that of the prototype. As a consequence of the initial imperfections of the brace and the stress relaxation problem in the pseudo-dynamic test, the brace hysteretic behavior for the prototype was quite different from those of the model. The difference in the locations of severe brace buckling or rupture caused different ductile MRSF response; high strength demand was associated with soft story formation. The subsequent difference in the brace hysteretic behavior at the collapse limit state tests

made it difficult to correlate the responses of the two structures.

X. SUMMARY, CONCLUSIONS AND RECOMMENDATIONS

10.1 Summary

10.1.1 Prototype Design

The design of the original prototype structure was based upon the 1979 UBC and the 1981 Japanese seismic code. A review of the design in accordance with the 1985 UBC concluded that the critical load case was that which required the braced frame alone to resist 125% of the design base shear. The original design satisfies the 1985 UBC requirements as a dual system provided that the effective length factor for the braces is taken as 0.7, consistent with the connection type used in the prototype. The requirement that the ductile moment-resisting space frame resist 25% of the design base shear is also satisfied. If the exterior wall weight is included in the weight of the reactive mass, the prototype just satisfies the UBC requirements. The design review indicated that the critical braces are in the second story.

10.1.2 Shaking Table Tests of the Model

(1) Mechanical Characteristics of the Model Materials

The model concrete mix design matched the prototype 28-day compressive strength (f'_c), but the corresponding value of Young's modulus (E_c) was 20% higher. The structural steel stress-strain characteristics of the model differed slightly from those of the prototype (Fig. 4.3).

As a result of the difference in the material characteristics, limit analysis shows that the strength of the model is 4% higher than that of the prototype. Compliance with the similitude laws up to failure level strains for the mechanical characteristics of the model material is a very important and difficult task.

(2) Design and Construction of the Model

All the member steel sections were carefully designed to satisfy the similitude laws. Connection detailing was the most difficult stage in the design of the model. Because the prototype brace-girder joint at the second floor level failed during the damageability limit state test, the joint was improved in the design and detailing of the model. The stiffener plates at both ends of the concentric braces were modified to simplify the model construction and to prevent joint failure. The copes and the bolted web connections at the ends of the model steel girders were eliminated by welding the girder webs to the shear plates (Fig. 4.2). The oversizing of the model structure's welds was unavoidable because of their small scaled size. In order to minimize brace misalignment, load cells were not installed in the model braces; instead, strain gages were glued to the model braces to measure the brace axial strains.

(3) Dynamic Characteristics of the Model

The measured flexibility matrices of the model show that the stiffness of Frame B increased tenfold with the addition of the bracing. After casting the concrete slab, the stiffness increased 30 percent and the damping remained constant. The measured flexibility indicates that the lateral stiffness was increased by 8 percent with the addition of the auxiliary mass (Section 5.3). The first mode damping ratio ($\xi_1=1.56\%$) of the model was significantly higher than that of the prototype ($\xi_1=0.49\%$); this can be attributed to the reduced slab thickness and consequent increased shrinkage cracking in the model.

(4) Performance of Shaking Table

Because of the interaction of the shaking table and the model, the table input signal was not well reproduced, particularly for high intensity tests. The model is the heaviest yet tested on the shaking table. Table pitching motion contributes up to 25 percent of the lateral displacement response of the structure. To correlate the analytically predicted response with the test results, the table pitching motion must be taken into account. The table pitching effect is similar in principle to soil-structure interaction In

certain instances, the entire soil-foundation-superstructure system must be analyzed to obtain realistic estimates of the structure response quantities.

As a result of table-structure interaction, use of measured peak horizontal acceleration to quantify the intensity of the base excitation is unreliable. The recommended approach is to compute the linear elastic response spectra from the measured table horizontal acceleration and compare the measured and theoretical spectral values. The effective peak acceleration, based upon the calculated pseudo-acceleration response spectra, is a good index for comparing shaking table test data.

The control and stabilizing system of the shaking table should be improved to minimize table-structure interaction. Furthermore, it is desirable to increase the capacity of the data acquisition system significantly to be able to collect additional data.

(5) Shaking Table Test Results of the Model

The concentric braces control the inter-story drifts at the service load level; the braces resist approximately 80% of the total story shear. During the damageability level test, a brace in the fifth story buckled; this brace was severely damaged and ruptured during the subsequent collapse level test. A soft story formed in the fifth story after brace rupture; it resulted in a high strength demand in the moment-resisting space frame at this level. All the braces in the bottom four stories buckled; the brace hysteresis loops are more stable than those obtained for the prototype. In the MO-33 test, the braces resisted between 60 and 80 percent of the story shear force (Fig. 7.20). In the MO-65 test, the braces in the first four stories and in the sixth story resisted between 60 and 80 percent of the story shear force (Fig. 7.34); the braces in the fifth story did not resist story shear force upon their rupture.

The maximum strength (or base shear) developed in the model is five times higher than the UBC minimum design base shear. The total input energy in the collapse level test is three times the energy that would be input to the model remaining in the elastic range. The hysteretic dissipated energy is uniformly distributed in the bottom five

stories during the collapse level test.

Full composite construction contributes significantly to the stiffness and strength of the girder. Composite construction increased the stiffness of the girder (positive flexure) by a factor of 3.5 and the strength of the girder (positive flexure) by a factor of 2.4. Subassemblage testing of four composite girders showed that their energy dissipation capacity under cyclic loading is increased by composite construction and thus, this type of construction is suitable for buildings in regions of high seismic risk.

10.1.3 Model and Prototype Response Comparison

- (1) The measured flexibility matrices, natural periods and mode shapes of the similitude scaled model and the prototype correlate very well ($T_{I(\text{model})}=0.625$ second, $T_{I(\text{prototype})}=0.610$ second); their viscous damping ratios, however, differed significantly ($\xi_{I(\text{model})}=1.56\%$, $\xi_{I(\text{prototype})}=0.49\%$).
- (2) The global responses of the two structures correlate reasonably well, especially in term of their strengths. The model strength is 16% higher than that of the prototype; the study in Section 8.3 indicates that this is primarily due to the strain rate effect.
- (3) No good correlation was found in the time history responses, particularly regarding displacements (lateral displacements and inter-story drifts) and the story hysteretic behavior.
- (4) The poor correlation of the brace behaviors is attributed to the differences in initial imperfections, residual stresses and testing techniques. In addition to the strain rate effect, stress relaxation phenomenon in the pseudo-dynamic testing affects the prototype brace hysteretic behavior.
- (5) The story hysteretic behavior is very sensitive to the detailing of the critical connections. The failure of the prototype brace-girder joint panel zone caused its hysteretic behavior to deviate significantly from that of the model.

10.1.4 Analytical Prediction

- (1) The analytically predicted flexibility matrices, natural periods and mode shapes of the model correlate well with the test results. The difference between the predicted and the measured fundamental periods is 4%.
- (2) The step-by-step static non-linear analyses, performed using an inverted-triangular and a uniform lateral load pattern bound the structural response. Up to the level of damageability limit state, the model strength-deformation envelope is close to that predicted using a inverted-triangular load pattern; the measured result above this level is close to that predicted using a uniform load pattern.
- (3) Limit analyses using simple plastic theory can predict the strength of a concentrically K-braced frame if reasonable assumptions are made regarding the brace post-buckling strength.
- (4) Dynamic analyses using the computer program DRAIN-2D predict well the model seismic response at the serviceability and damageability levels of earthquake ground motion. The prediction is less reliable for the high intensity tests as the mathematical brace model cannot simulate brace rupture.
- (5) The concept of an equivalent base horizontal acceleration, derived in Chapter 9, successfully accounts for the effect of table pitching motion on structure response.

10.2 Conclusions

A summary of the main conclusions relating to the original objectives of the U.S.-Japan Cooperative Research Program are presented in this section. These conclusions are, strictly speaking, valid only for the test model and for the type of excitation to which it was subjected. A number of the limitations should be carefully studied before extrapolating the conclusions to other K-braced structures. These limitations include:

- (i) that the test model was a bare steel structure and the effects of non-structural components could not be considered;
- (ii) the reactive mass considered was unrealistically low (34% less than the true reactive mass).
- (iii) the model was subjected to one horizontal component of the 1978 Miyagi-Ken-Okii Earthquake parallel to the concentrically braced frame; and
- (iv) the model was symmetric with respect to the ground excitation and the torsional rigidity of the model was increased significantly by using concentric X-bracing in the transverse frames.

10.2.1 Soundness of the Prototype Design

The prototype represents a typical design based upon current practice. The model connections were modified to prevent a brace-girder joint failure similar to that which occurred in the prototype.

10.2.2 Reliability of Earthquake Simulator Studies

Previous researchers [26] have pointed out that the dynamic response of structural building systems can be simulated quite accurately at model scales; the results obtained led to the following conclusions: (i) that the reliability of the response prediction depends upon the accuracy of the material simulation, fabrication techniques, the accuracy in simulating details at critical regions, the reproducibility of the dynamic input, and the accuracy of the instrumentation and capacity of the data acquisition system; and (ii) that moderate and small scale model tests may be unable to predict the behavior of the full scale structures when failure is initiated by localized phenomena such as weld fracture.

Traditionally, confidence in the results of experimental model studies lies in the selected scale factor. Model tests with a scale factor of 0.2 or smaller are viewed with skepticism [26]; few doubts have been raised regarding the reliability of experimental

results of 0.5 to 0.3 scale model tests.

Good correlation of the prototype and the model test results can be expected if localized phenomena can be taken into account.

Earthquake simulator testing of a model has the following advantages over subassemblage or pseudo-dynamic testing: (i) the model is subjected to realistic earthquake excitation, and (ii) the strain rate effect is implicitly accounted for and the problems associated with stress relaxation are nonexistent. The results obtained from shaking table tests are of great importance to the earthquake engineering profession as the results provide a profound insight into the response of full scale structures to earthquake excitation.

10.2.3 Reliability of Current Analytical Prediction Methods

- (1) Step-by-step static analyses using an inverted-triangular or a uniform lateral loading pattern can efficiently bound the strength of braced steel structures.
- (2) Limit analysis provides a simple means by which to bound the strength of a braced steel structure.
- (3) Current available computer programs for linear dynamic analysis of multistory buildings are suitable for response prediction in the serviceability limit state range. The computer program DRAIN-2D can predict the seismic response of structures in the damageability and collapse limit state ranges provided that the hysteretic behavior of the critical structural elements is accurately modeled.

10.2.4 Seismic Resistant Design and Construction of Dual System

- (1) Current (1985) UBC seismic design regulations are based on seismic forces that are unrealistically low when compared with those forces that develop in structures designed in accordance with their regulations. The ATC Recommendations require an even smaller base shear coefficient than that required by the UBC.

- (2) The measured horizontal acceleration in the model collapse level test has an effective peak acceleration of 0.40g, equivalent to the ATC effective peak acceleration in a region of high seismic risk. A comparison of the ATC linear elastic design response spectrum and the linear elastic response spectrum of the MO-65 Test shows that the ATC is nonconservative. If the linear elastic response spectra of the ground motions of the Chilean and Mexico City earthquakes of 1985 [35] are compared with the MO-65 Test ground motion, it is apparent that the MO-65 ground motion is a realistic ground motion for design, analysis and research purposes in the U.S.A.
- (3) The UBC and ATC requirement for designing a ductile MRSF for 25% of the design base shear is unrealistic in view of the forces and lateral displacements that were developed during the MO-65 Test. Significantly higher story shear forces were developed in the MRSF during this test, especially in the fifth story where the braces ruptured; however, the maximum inter-story drifts exceeded the 1.5 percent considered as acceptable.
- (4) The fundamental period (T) of the model varied between 0.34 and 0.43 second (0.62 to 0.78 second when scaled to the prototype units). The UBC allows the fundamental period to be estimated by the formula $0.05h_n/\sqrt{D}$; this results in T equal to 0.5 second. This formula is designed to give the period of an entire building; that is, it considers the interaction of the non-structural components with the structural system. As the measured period (0.62 second) represents the value corresponding to the bare structure, it cannot be compared directly with the period calculated using the simplified UBC formula; the difference between these two periods is 24 percent.
- (5) ATC precludes the use of bracing that resists only tension by recommending that the brace shall have a compressive strength equal to at least 50% of the required tensile strength. There are no provisions in the UBC for the effective slenderness

ratio of bracing elements. Although the model brace compactness ratio, that is, the width-thickness ratio, satisfied the UBC requirements, severe local buckling of the braces led to their rupture.

- (6) The bare steel structure would have easily survived the 1985 Mexico City earthquake due to the fact that the frequency content of this earthquake was centered around 0.5 Hz (or 2 seconds) and the scaled fundamental period of the model varied from 0.62 second to 0.78 second (Fig. 8.5). The bare steel structure would have survived the 1985 Chilean earthquake but with severe structural and non-structural damage because this earthquake and the MO-65 Test base horizontal motion have similar levels of spectral values within the model period range (Fig. 8.5).

10.3 Recommendations

Further research must be conducted to obtain a better understanding of the behavior of concentrically K-braced structures and to improve the experimental and analytical techniques used to predict structural response.

10.3.1 Areas of Future Research

- (1) The minimum seismic forces specified by the UBC and ATC are unrealistically low when compared with those forces developed in structures designed in accordance with these codes. Current code minimum seismic forces must be increased to a level whereby an optimally designed structure can survive a major earthquake (MO-65 for example) with maximum drift levels less than or equal to the current limits of 1.5%. Realistic linear elastic design response spectra and the response reduction factor R should be further investigated in order to develop realistic inelastic design response spectra.
- (2) Design methods based upon energy considerations are an important addition to the inelastic earthquake-resistant design of structures. Techniques to estimate the

energy input to structures and the energy dissipation capacity of different structural systems should be developed and verified.

- (3) The interaction of braced frames and moment-resisting space frames requires further study. Special emphasis should be focused upon the demand on moment-resisting space frames upon brace buckling and the relationship between the relative lateral stiffness, deformability, ductility ratio and yielding strength of the moment-resisting space frame and the braced frame.
- (4) The stiffness and strength of the joint panel zone in structures using composite construction requires further study as the girder-column joint panel zone can profoundly influence the stiffness and strength of the entire structure.
- (5) Brace hysteretic behavior is very sensitive to the effective slenderness ratio, brace compactness ratio, fabrication methods and residual stresses. Premature rupture and significant deterioration of the brace hysteretic behavior must be precluded. It is of paramount importance to study, experimentally and analytically, the effect of the slenderness and compactness ratio on the cyclic behavior of tubular steel members.
- (6) The tubular brace is susceptible to severe local buckling upon global buckling; the local buckling causes a concentration of curvature that the material may be unable to supply. A promising alternative is to use circular hollow sections as bracing elements and to fill them with expansive lightweight concrete. Local buckling should then be avoided or at least delayed on account of the restraint supplied by the concrete; the failure mode changes from one of local buckling to that of hoop buckling, which is not likely to occur because of the presence of tensile hoop stresses. Experimental and analytical studies should be conducted to study the cyclic behavior of the concrete-infilled circular hollow section braces.
- (7) Another type of braced steel frame, known as the friction damped braced frame [47], has been proposed. The advantage of this structural system is that the input

energy is dissipated mechanically by friction, rather than by the inelastic behavior of the structural members. Use of the friction damped device in concentrically K-braced steel frames appears very promising as undesirable brace buckling can be prevented.

10.3.2 Improvement in the Design of a Dual System

- (1) There is an urgent need to develop a rational design method [35]. The rationale behind the method is to satisfy the serviceability limit state for minor, frequent earthquakes and the collapse limit state for major, infrequent earthquakes. As the philosophy in the serviceability limit state is to preclude any form of damage, a design method similar to that proposed by ATC should be used to design the structure for minor earthquake shaking. The design method in the collapse limit state should be based upon realistic inelastic design response spectra; the availability of an increased number of strong motion earthquake records should facilitate the construction of these spectra. The inelastic design response spectra and the period of the dual system would be used to estimate the structural demand; the structure would be designed using capacity design methods. As the ductile MRSF is primarily a secondary or a redundant structural system, its design would be based upon the inelastic design response spectra noted above and the period of the ductile MRSF (that is, ignoring the braces). Currently, the UBC and ATC require that the ductile MRSF resist 25% of the design base shear, this has no rational basis and thus this clause would be deleted from the design method noted above.
- (2) Prior to implementing the rational method, a compromise method [35] is suggested. This method uses the ATC linear elastic design response spectra and a reliable value of the response modification factor R to estimate the story shear demand. The structural strength capacity may then be estimated by simple plastic theory. The maximum strength demand in the critical regions or elements (braces, panel zones etc) should be determined and then these regions can be designed and

detailed by the capacity design method. A detailed discussion of this design method is presented in Reference 35.

- (3) On the basis of the test results, the study in Section 8.8 suggests that the brace compressive strength should be equal to at least 80% of the required tensile strength and the brace width-thickness ratio should be limited to 18 to avoid local buckling and rupture.
- (4) Construction joints should be located well away from the critical regions. The use of bolted shear plates, copes and groove welding for the flanges should be avoided.
- (5) The following guidelines should be used for selecting the optimum framing layout of dual braced systems: (i) the layout of the braced bays should be symmetric so that the center of rigidity is located as close as possible to the center of mass; (ii) the braced bays should be located so as to maximize the torsional rigidity of the structure; (iii) three or more braced bays should be supplied in a structure in a given direction to enhance its torsional redundancy.

REFERENCES

- [1] U.S.-Japan Planning Group, Cooperative Research Program Utilizing Large-Scale Testing Facilities, "Recommendations for a US-Japan Cooperative Research Program Utilizing Large Scale Facilities," Report No. UCB/EERC-79/26, EERC, University of California, Berkeley, 1979.
- [2] Popov, E.P., and Bertero, V.V., "Seismic Analysis of Some Steel Building Frames," Journal of the Engineering Mechanics Division, ASCE, Vol. 106, No. EM1, Proc. Paper 15194, February 1980.
- [3] *Uniform Building Code*, 1979 Edition, International Conference of Building Officials, Whittier, California.
- [4] Applied Technology Council, "Tentative Provisions for the Development of Seismic Regulations for Buildings," U.S. National Bureau of Standards, Special Publication 510, 1978.
- [5] Popov, E.P., Takanashi, K., and Roeder, C.W., "Structural Steel Bracing Systems: Behavior under Cyclic Loading," Report No. UCB/EERC-76/17, Earthquake Engineering Research Center, University of California, 1976.
- [6] Hjelmstad, K.D., and Popov, E.P., "Seismic Behavior of Active Beam Links in Eccentrically Braced Frames," Report No. UCB/EERC-83/24, Earthquake Engineering Research Center, University of California, 1983.
- [7] Blacks, R.G., Wagner, W.A., and Popov, E.P., "Inelastic Buckling of Steel Struts under Load Reversals," Report No. UCB/EERC-80/40, Earthquake Engineering Research Center, University of California, August 1980.
- [8] Yamanouchi, H., and Midorikawa, M., "Design of the Full-Scale Six-Story Steel Building," The Third Joint Technical Coordinating Committee, U.S.-Japan Cooperative Research Program Utilizing Large Scale Test Facilities, July 1982, Tsukuba, Japan.

- [9] Foutch, D.A., Yamanouchi, H., Midorikawa, M., and Nishiyama, I., "Construction of Full-Scale Six-Story Steel Test Structure," The Fourth Joint Technical Coordinating Committee, U.S.-Japan Cooperative Research Program Utilizing Large Scale Test Facilities, June 1983, Tsukuba, Japan.
- [10] Specification for the Design, Fabrication and Erection of Structural Steel for Buildings, American Institute of Steel Construction, New York, N.Y., 1980.
- [11] Wilson, E.L., "The SAP-80 Series of Structural Analysis Programs for CP/M-80 Microcomputer Systems," February 1984.
- [12] B.R.I. Steel Group, "An Interim Report on Phase 1 Test Results," The Fifth Joint Technical Coordinating Committee, U.S.-Japan Cooperative Research Program Utilizing Large Scale Test Facilities, February 1984, Tsukuba, Japan.
- [13] Yamanouchi, H., Midorikawa, M., and Nishiyama, I., "Test Results of Full-Scale Six-Story Steel Building: 1. Unit Loading Test. 2. Pseudo-Dynamic Test (Elastic)," The Fourth Joint Technical Coordinating Committee, U.S.-Japan Cooperative Research Program Utilizing Large Scale Test Facilities, June 1983, Tsukuba, Japan.
- [14] Okada, H., and Sakai, H., "Vibration Test on Full-Scale Steel Building," The Fourth Joint Technical Coordinating Committee, U.S.-Japan Cooperative Research Program Utilizing Large Scale Test Facilities, June 1983, Tsukuba, Japan.
- [15] Mondkar, D.P., and Powell, G.H., "ANSR-1, General Purpose Computer Program for Analysis of Non-linear Structure Response," Report No. UCB/EERC-75/17, University of California, Berkeley, 1975.
- [16] ASCE-WRC, "Plastic Design in Steel - A guide and Commentary," ASCE Manual 41, 2nd ed., Welding Research Council - American Society of Civil Engineering Joint Committee, New York, 1971.
- [17] Bertero, V.V., and Llopiz, C.R., "Design and Construction of a 0.3-Scale Six-Story Steel Structure," UCB/EERC Report in preparation.

- [18] Uang, C.M., "Experimental and Analytical Study of the Hysteretic Behavior of Steel Composite Girders," CE299 Report, Berkeley, University of California, May 1985
- [19] Kannan, A.E., and Powell, G.H., "DRAIN-2D, A General Purpose Computer Program for Dynamic Analysis of Inelastic Plane Structures," Report No. UCB/EERC-73/6, University of California, Berkeley, 1973.
- [20] Krawinkler, H., Bertero, V.V., and Popov, E.P., "Shear Behavior of Steel Frame Joints," *Journal of the Structural Division, ASCE*, Vol. 101, No. ST11, Proc. Paper 11717, November 1975.
- [21] Maison, B.F., and Popov, E.P., "Cyclic Response Prediction for Braced Steel Frames," *Journal of the Structural Division, ASCE*, Vol. 106, No. ST7, Proc. Paper 15534, July 1980.
- [22] Jain, A.K., Goel, S.C. and Hanson, R.D., "Hysteresis Behavior for Bracing Members and Seismic Response of Braced Frames with Different Proportions," Report No. UMEE-78R3, University of Michigan, Ann Arbor, Michigan, July 1978.
- [23] Simons, J.W., and Powell, G.H., "Solution Strategies for Statically Loaded Non-linear Structures," University of California, Berkeley, Report No. UCB/EERC-82/22, November 1982.
- [24] Hodge, P.G., "Plastic Analysis of Structures," McGraw-Hill Book Company Inc., New York, 1959.
- [25] Rea, D. and Penzien, J., "Dynamic Response of a 20 ft x 20 ft Shaking Table," *Proceedings, Fifth World Conference on Earthquake Engineering*, Vol. 2, Rome, Italy, 1974.
- [26] Moncarz, P.D., and Krawinkler, H., "Theory and Application of Experimental Model Analysis in Earthquake Engineering," Report No 50, John A. Blume Earthquake Engineering Center, Department of Civil Engineering, Stanford University,

Stanford, California, June 1981.

- [27] Popov, E.P., and Bertero, V.V., "Cyclic Loading of Steel Beams and Connections," Journal of the Structural Division, ASCE, Vol. 99, No. ST6, Proc. Paper 9790, June, 1973.
- [28] Lay, M.G., "Flange Local Buckling in Wide-Flange Shapes," Journal of the Structural Division, ASCE, Vol. 91, No. ST6, December 1965.
- [29] Becker, R.A., and Chambers, J.M., "S - An Interactive Environment for Data Analysis and Graphics," The Wadsworth Statistics/Probability Series, 1984.
- [30] Clough, R.W. and Penzien, J., "Dynamics of Structures," McGraw-Hill, New York, 1975.
- [31] Trifunac, M.D., and Lee, V., "Routine Computer Processing of Strong-Motion Accelerograms," Earthquake Engineering Research Laboratory Report No. 73-03, California Institute of Technology, Pasadena, 1973.
- [32] Kaba, S.A. and Mahin, S.A., "Interactive Computer Analysis Methods for Predicting the Inelastic Cyclic Behavior of Structural Sections," Report No. UCB/EERC-83/18 July 1983.
- [33] Aktan, A.E., Bertero, V.V., Chowdhury, A.A. and Nagashima, T., "Experimental and Analytical Prediction of the Mechanical Characteristics of a 7-story R/C Frame-wall Building Structure," Report No. UCB/EERC-83/13, University of California, Berkeley, June 1983
- [34] Ballio, G. and Mazzolani, F.M., "Theory and Design of Steel Structures," Chapman and Hall, New York, 1983.
- [35] Bertero, V.V., "Implications of Recent Earthquakes and Research on Earthquake-Resistant Design and Construction of Buildings," University of California, Berkeley, Report No. UCB/EERC-86/03, University of California, Berkeley, March 1986.

- [36] SEAONC Research Committee, "Earthquake Resistant Design of Concentric and K-Braced Frames," San Francisco, July 1982.
- [37] Sabins, G.M., Harris, H.G., White, R.N., and Saeed Mirza, M., "Structural Modeling and Experimental Techniques," Prentice Hall, Inc., New Jersey, 1983.
- [38] Hanson, R.D., "Comparison of Static and Dynamic Hysteretic Curves," Journal of the Engineering Mechanics Division, ASCE, Vol. 106, No. EM5, Vol. 92, May 1966.
- [39] Shing, P.-S. and Mahin, S.A., "Pseudodynamic Test Method for Seismic Performance Evaluation: Theory and Implementation," Report No. UCB/EERC-84/01, University of California, Berkeley, January 1984.
- [40] Yamazaki, Y., Nakashima, M., and Kaminosono, T., "Correlation between Shaking Table Test and Pseudo Dynamic Test on Steel Structural Models," U.S.-Japan Cooperative Research Program Utilizing Large Scale Test Facilities, BRI, March 1986, Tsukuba, Japan.
- [41] Udagawa, K., Takanashi, K, and Kato, B., "Effects of Displacement Rates on the Behavior of Steel Beams and Composite Beams," Proceedings, Eighth World Conference on Earthquake Engineering, San Francisco, 1984.
- [42] Housner, G.W., "Limit Design of Structures to Resist Earthquakes," Proceedings of the World Conference on Earthquake Engineering, Berkeley, California, 1956.
- [43] Mahin, S and Lin, J., "Construction of Inelastic Response Spectra for Single-Degree-of-Freedom System," Report No. UCB/EERC-83/17, University of California, Berkeley, March 1983.
- [44] Akiyama, H., "Earthquake Resistant Limit-State Design for Buildings," University of Tokyo Press, 1985.
- [45] Ghanaat, Y. and Clough, R.W., "Shaking Table Tests of a Tubular Steel Frame Model," Report No. UCB/EERC-82/02, University of California, Berkeley, January 1982.

- [46] Yang, M., "Seismic Behavior of an Eccentrically X-Braced Steel Structure," Report No. UCB/EERC-82/14, University of California, Berkeley, September 1982.
- [47] Takanashi, K.; et al., "Pseudo-Dynamic Tests on a 2-Story Steel Frame by Computer-Load Test Apparatus Hybrid System,' Proceedings of the Seventh World Conference on Earthquake Engineering, Istanbul, 1981
- [48] Pall, A.S. and Marsh, C., "Seismic Response of Friction Damped Braced Frames," Journal of the Structural Division, ASCE, Vol. 108, No. ST6, Proc. Paper 17175 June 1982.

**Appendix A -
List of Instrumentation**

Channel	Explanation		
1	Table h1 Displacement	31	Vert. Displ. at Foundation B2L
2	Table h2 Displacement	32	Vert. Displ. at Foundation B2R
3	Table Horizontal Acceleration	33	Horizontal Displacement A6
4	Table Vertical Acceleration	34	Horizontal Displacement A5
5	Table Pitch Acceleration	35	Horizontal Displacement A4
6	Table Roll Acceleration	36	Horizontal Displacement A3
7	Table Twist Acceleration	37	Horizontal Displacement A2
8	Table v2 Displacement	38	Horizontal Displacement A1
9	Table v3 Displacement	39	Column Axial Strain 1-B1L
10	Table V4 Displacement	40	Column Axial Strain 1-B1R
11	Horizontal Acceleration B6	41	Column Axial Strain 1-B2L
12	Horizontal Acceleration B5	42	Column Axial Strain 1-B2R
13	Horizontal Acceleration B4	43	Column Axial Strain 1-B3L
14	Horizontal Acceleration B3	44	Column Axial Strain 1-B3R
15	Horizontal Acceleration B2	45	Column Axial Strain 1-A1L
16	Horizontal Acceleration B1	46	Column Axial Strain 1-A1R
17	Horizontal Acceleration A6	47	Column Axial Strain 1-A2L
18	Horizontal Acceleration A5	48	Column Axial Strain 1-A2R
19	Horizontal Acceleration A4	49	Column Axial Strain 1-A3L
20	Horizontal Acceleration A3	50	Column Axial Strain 1-A3R
21	Horizontal Acceleration A2	51	Brace 6-2 Strain
22	Horizontal Acceleration A1	52	Brace 6-4 Strain
23	Horizontal Displacement B6	53	Brace 8-1 Strain
24	Horizontal Displacement B5	54	Brace 8-3 Strain
25	Horizontal Displacement B4	55	Brace 8-2 Strain
26	Horizontal Displacement B3	56	Brace 8-4 Strain
27	Horizontal Displacement B2	57	Brace 10-1 Strain
28	Horizontal Displacement B1	58	Brace 10-2 Strain
29	Column Shear 6-A1	59	Brace 12-1 Strain
30	Vert. Displ. at Foundation B1R	60	Brace 12-2 Strain
		61	Column Shear 1-B3
		62	Column Shear 1-B2
		63	Column Shear 1-B1
		64	Column Shear 1-A3
		65	Column Shear 1-A2
		66	Column Shear 1-A1

67	Column Shear 1-C3	103	Brace 3-2 Strain
68	Column Shear 1-C2	104	Brace 3-4 Strain
69	Column Shear 1-C1	105	Brace 3-3 Strain
70	Column Shear 2-B3	106	Brace 3-1 Strain
71	Column Shear 2-B2	107	Brace 5-1 Strain
72	Column Shear 2-B1	108	Brace 5-3 Strain
73	Column Shear 2-A3	109	Brace 5-2 Strain
74	Column Shear 2-A2	110	Brace 5-4 Strain
75	Column Shear 2-A1	111	Brace 7-2 Strain
76	Column Shear 3-B3	112	Brace 7-4 Strain
77	Column Shear 3-B2	113	Brace 7-3 Strain
78	Column Shear 3-B1	114	Brace 7-1 Strain
79	Column Shear 3-A3	115	Brace 9-2 Strain
80	Column Shear 3-A2	116	Brace 9-1 Strain
81	Column Shear 3-A1	117	Brace 11-2 Strain
82	Column Shear 4-B3	118	Brace 11-1 Strain
83	Column Shear 4-B2	119	Brace 2-2 Strain
84	Column Shear 4-B1	120	Brace 2-4 Strain
85	Column Shear 4-A3	121	Brace 2-3 Strain
86	Column Shear 4-A2	122	Brace 2-1 Strain
87	Column Shear 4-A1	123	Brace 4-4 Strain
88	Column Shear 5-B3	124	Brace 4-2 Strain
89	Column Shear 5-B2	125	Brace 4-1 Strain
90	Column Shear 5-B1	126	Brace 4-3 Strain
91	Column Shear 5-A3	127	Brace 6-1 Strain
92	Column Shear 5-A2	128	Brace 6-3 Strain
93	Column Shear 5-A1	129	Vert. Displ. at Foundation B1L
94	Column Shear 6-B3	130	Vert. Displ. of Brace 1&2 Joint
95	Column Shear 6-B2	131	Brace 1 Axial Deformation
96	Column Shear 6-B1	132	Brace 2 Axial Deformation
97	Column Shear 6-A3	133	Brace 3 Axial Deformation
98	Column Shear 6-A2	134	Brace 4 Axial Deformation
99	Brace 1-1 Strain	135	Brace 5 Axial Deformation
100	Brace 1-3 Strain	136	Brace 6 Axial Deformation
101	Brace 1-2 Strain	137	Column 1-B1 Deformation
102	Brace 1-4 Strain	138	Column 1-B2 Deformation

139	Column 1-B3 Deformation	175	Beam Yielding Strain - Bottom
140	Column 2-B1 Deformation	176	Beam Yielding Strain - Top
141	Column 2-B2 Deformation		
142	Column 2-B3 Deformation		
143	Vertical Displacement 6-B1		
144	Vertical Displacement 6-B1		
145	Vertical Displacement 6-B2		
146	Vertical Displacement 6-B3		
147	Vertical Displacement 6-A1		
148	Vertical Displacement 6-A2		
149	Transverse Displacement 6-1A		
150	Transverse Displacement 6-3A		
151	Vertical Acceleration 6-B1		
152	Vertical Acceleration 6-B2		
153	Vertical Acceleration 6-B3		
154	Transverse Acceleration 6-1A		
155	Transverse Acceleration 6-3A		
156	Lead Acceleration at Roof Level		
157	Rotational Deformation 1-B1L		
158	Rotational Deformation 1-B1R		
159	Rotational Deformation 1-B2L		
160	Rotational Deformation 1-B2R		
161	Rotational Deformation 2-B1L		
162	Rotational Deformation 2-B1R		
163	Rotational Deformation 2-B2L		
164	Rotational Deformation 2-B2R		
165	Rotational Deformation 3-B1L		
166	Rotational Deformation 3-B1R		
167	Rotational Deformation 3-B2L		
168	Rotational Deformation 3-B2R		
169	Brace 7 Axial Deformation		
170	Brace 8 Axial Deformation		
171	Column Yielding Strain 1-B1		
172	Column Yielding Strain 1-B2		
173	Column Yielding Strain 1-A1		
174	Column Yielding Strain 1-A2		

Appendix B - Derivation of Energy Equation

For a typical N story building structure, the story weight is assumed to be lumped at each floor level. The equation of motion for this system with N lateral degrees of freedom is

$$\underline{f}_I + \underline{f}_D + \underline{f}_S = 0$$

or
$$\underline{m}\ddot{\underline{v}}^t + \underline{f}_D + \underline{f}_S = 0 \quad (B.1)$$

where $\underline{f}_I = \underline{m}\ddot{\underline{v}}^t =$ inertia force vector;

$\underline{f}_D =$ damping force vector;

$\underline{f}_S =$ restoring force vector;

$\underline{m} =$ diagonal mass matrix;

$\underline{v}^t =$ absolute lateral displacement vector $= \underline{v} + \underline{r}v_g$;

$\underline{v} =$ relative lateral displacement;

$v_g =$ base motion displacement;

$\underline{r} =$ Nx1 unity column vector.

Equation (B.1) is valid for linear and nonlinear response. Transpose above equation and integrate with respect to \underline{v} :

$$\int \ddot{\underline{v}}^tT \underline{m} d\underline{v} + \int \underline{f}_D^T d\underline{v} + \int \underline{f}_S^T d\underline{v} = 0 \quad (B.2)$$

where

$$\begin{aligned} \int \ddot{\underline{v}}^tT \underline{m} d\underline{v} &= \int \ddot{\underline{v}}^tT \underline{m} (d\underline{v}^t - \underline{r}dv_g) = \int \frac{d\underline{v}^tT}{dt} \underline{m} d\underline{v}^t - \int \ddot{\underline{v}}^tT \underline{m} r dv_g \\ &= \int d\underline{v}^tT \underline{m} \underline{v}^t - \int \ddot{\underline{v}}^tT \underline{m} r dv_g = \int \sum_{i=1}^N m_i \dot{v}_i^t d\dot{v}_i^t - \int (\sum_{i=1}^N m_i \ddot{v}_i^t) dv_g \end{aligned}$$

$$= \sum_{i=1}^N \frac{1}{2} m_i \dot{v}_i^2 - \int (\sum_{i=1}^N m_i \ddot{v}_i^t) dv_g = \frac{1}{2} \dot{\mathbf{v}}^t \mathbf{M} \dot{\mathbf{v}}^t - \int (\sum_{i=1}^N m_i \ddot{v}_i^t) dv_g . \quad (\text{B.3})$$

Substitute Eq. (B.3) into Eq. (B.2),

$$\frac{1}{2} \dot{\mathbf{v}}^t \mathbf{M} \dot{\mathbf{v}}^t + \int \mathbf{f}_D^T d\mathbf{v} + \int \mathbf{f}_S^T d\mathbf{v} = \int (\sum_{i=1}^N m_i \ddot{v}_i^t) dv_g \quad (\text{B.4})$$

where

$$\frac{1}{2} \dot{\mathbf{v}}^t \mathbf{M} \dot{\mathbf{v}}^t = \frac{1}{2} \sum_{i=1}^N m_i (\dot{v}_i^t)^2 = \text{kinetic energy} \equiv E_K \quad (\text{B.5})$$

$$\int \mathbf{f}_D^T d\mathbf{v} = \text{energy dissipated by viscous force} \equiv E_\mu \quad (\text{B.6})$$

$$\begin{aligned} \int \mathbf{f}_S^T d\mathbf{v} &= \int \sum_{i=1}^N f_{Si} dv_i = \sum_{i=1}^N \int f_{Si} dv_i \\ &= \text{energy absorbed by restoring forces} \equiv E_A . \end{aligned} \quad (\text{B.7})$$

$$\int (\sum_{i=1}^N m_i \ddot{v}_i^t) dv_g = \text{ground motion input energy} \equiv E_I \quad (\text{B.8})$$

i.e., $E_K + E_\mu + E_A = E_I . \quad (\text{B.9})$

Equation (B.7) may be rewritten by using the following transformation:

$$\underline{\delta} = \underline{\mathbf{a}} \underline{\mathbf{v}} \quad (\text{B.10})$$

where $\delta =$ interstory drift vector

$$\underline{\mathbf{a}} = \text{displacement transformation matrix} = \begin{bmatrix} 1 & -1 & & & & \\ & 1 & -1 & & & \\ & & & \ddots & & \\ & & & & -1 & \\ & & & & & 1 & -1 \\ & & & & & & 1 \end{bmatrix} .$$

By the principle of contragradience,

$$\mathbf{f}_S = \underline{\mathbf{a}}^T \mathbf{V} \quad (\text{B.11})$$

$$\mathbf{f}_D = \underline{\mathbf{a}}^T \mathbf{q} \quad (\text{B.12})$$

where \underline{V} = story shear vector

\underline{q} = story damping force vector .

Since \underline{V} , not \underline{f}_S , is commonly measured, Eq. (B.7) may be more conveniently expressed by

$$E_A = \int \underline{f}_S^T d\underline{v} = \int \underline{V}^T \underline{a}(\underline{a}^{-1} d\underline{\delta}) = \int \underline{V}^T d\underline{\delta} . \quad (\text{B.13})$$

Similarly, Eq. (B.6) may be rewritten as

$$E_\mu = \int \underline{f}_D^T d\underline{v} = \int \underline{q}^T \underline{a}(\underline{a}^{-1} d\underline{\delta}) = \int \underline{q}^T d\underline{\delta} . \quad (\text{B.14})$$

E_μ is difficult to measure experimentally. For a lightly damped structure subjected to severe inelastic deformation, E_μ is small and an energy dissipation mechanism through inelastic behavior of the structural members is desirable. The absorbed energy (Eq. B.12) consists of two parts:

$$E_A = \int \underline{f}_S^T d\underline{v} = E_S + E_H \quad (\text{B.15})$$

where E_S = recoverable elastic strain energy = $\sum_{i=1}^N \frac{V_i^2}{2K_i}$ (B.16)

E_H = irrecoverable hysteretic energy = $E_A - E_S$

$$= \sum_{i=1}^N \int V_i d\delta_i - \sum_{i=1}^N \frac{V_i^2}{2K_i} . \quad (\text{B.17})$$

The K_i in Eq. (B.16) is the unloading stiffness of the δ_i versus V_i curve; it may be assumed to be the initial stiffness, for simplicity. This assumption is reasonable if the δ_i versus V_i hysteresis loop is not severely pinched.

Floor	G1	G2	G3	G4
R	16W31	16W31		
6	16W31	16W31		
5	16W31	18W35	18W35	21W50
4	18W35	18W35		
3	18W35	18W40		
2	18W40	18W40		

(a) Size of Girders

Story	C1	C2	C3	C4	C5
6-5	10W33	10W33	10W49	10W33	12W40
4-3	10W39	12W53	12W65	10W60	12W72
2	12W50	12W65	12W79	12W79	12W106
1	12W65	12W87	12W87	12W106	12W136

(b) Size of Columns

Story	Brace
6	Tube 4x4x1/5.56
5	Tube 5x5x1/5.56
4	Tube 6x6x1/4
3	Tube 6x6x1/4
2	Tube 6x6x1/4
1	Tube 6x6x1/2

(c) Size of Braces

TABLE 2.1 TEST STRUCTURE MEMBER SIZE

	Floor (psf)	Roof (psf)
Metal Deck	6	6
3.5 inches Lightweight Concrete	39	39
Ceiling, Floor Finishes	10	20
Partitions	20	-
Structural Steel, Fire-Proofing	15	-
Total	90	75

Exterior Wall weight = 30 psf of wall surface.

TABLE 2.2 PROTOTYPE DESIGN GRAVITY DEAD LOADS

Floor	Actual Design Bldg. with Exterior Wall (k)	Designed Bldg. without Exterior Wall (k)	Pseudo-Dynamic Test Building (k)
Roof	227.7*	193.7	166.9
6th	300.6**	232.5	195.5
5th	300.6	232.5	195.5
4th	300.6	232.5	195.5
3rd	300.6	232.5	195.5
2nd	311.7	232.5	205.2
Total	1742	1356	1154

* roof weight in Table 2.2 multiplied by floor area (=49.2 ft. by 52.5 ft.)

** floor weight in Table 2.2 multiplied by floor area (=49.2 ft. by 52.5 ft.)

TABLE 2.3 COMPARISON OF PROTOTYPE FLOOR WEIGHTS

Floor	Design Wt. W_i (k)	Height h_i (ft.)	Lateral Load F_x (k)	Pseudo-dynamic Test Actual Weight (k)[13]
Roof	193.7	70.54	36.9	166.9
6th	232.5	59.38	37.3	195.5
5th	232.5	48.23	30.3	195.5
4th	232.5	37.07	23.3	195.5
3rd	232.5	25.92	16.3	195.5
2nd	232.5	14.76	9.3	205.2
Total	1356	--	153.4	1154

TABLE 2.4 UBC LATERAL LOAD DISTRIBUTION FOR PROTOTYPE DESIGN

Member Type		Nominal Stress	Sample Min Stress	Sample Max Stress	Sample Mean Stress	No. of Samples
Column	f_y	36	37	54	43	26
	f_u	58	63	71	66	
Girder	f_y	36	40	53	46	8
	f_u	58	63	71	67	
Brace	f_y	46	56	63	59	8
	f_u	58	66	72	68	

f_y = yield stress; f_u = tensile stress. (unit=ksi)

TABLE 2.5 PROTOTYPE MATERIAL STRENGTH

	Roof	6th	5th	4th	3rd	2nd
Roof	9.023	6.691	4.676	3.085	1.807	0.746
6th	6.691	6.206	4.460	2.975	1.770	0.744
5th	4.676	4.460	4.135	2.868	1.731	0.743
4th	3.085	2.975	2.868	2.684	1.698	0.741
3rd	1.807	1.770	1.731	1.698	1.581	0.743
2nd	0.746	0.744	0.743	0.741	0.743	0.678

(a) Predicted Flexibility Matrix ($\times 10^{-3}$ inch/kip)

	Roof	6th	5th	4th	3rd	2nd
Roof	7.713	6.122	4.443	3.014	1.864	0.791
6th	5.827	5.727	4.320	3.047	1.797	0.804
5th	4.097	4.163	4.018	2.891	1.730	0.770
4th	2.757	2.836	2.802	2.747	1.686	0.782
3rd	1.618	1.686	1.697	1.707	1.586	0.748
2nd	0.714	0.759	0.759	0.782	0.759	0.738

* maximum applied load is less than 8 tons.

(b) Experimental Flexibility Matrix ($\times 10^{-3}$ inch/kip) [13]

TABLE 3.1 PROTOTYPE FLEXIBILITY MATRIX

Mode	1st	2nd	3rd	4th	5th	6th
Period (sec)	0.612	0.222	0.131	0.097	0.077	0.061
Mode Shapes						
Roof	1.000	1.000	-0.979	-0.489	0.190	-0.026
6th	0.931	0.263	0.775	1.000	-0.611	0.124
5th	0.729	-0.547	1.000	-0.378	1.000	-0.366
4th	0.522	-0.937	-0.089	-0.729	-0.699	0.758
3rd	0.325	-0.877	-0.933	0.306	-0.338	-1.000
2nd	0.145	-0.503	-0.836	0.785	0.860	0.743

(a) Predicted Periods and Mode Shapes

Mode	1st	2nd	3rd	4th	5th	6th
Period (sec) ^{*1}	0.599	-	-	-	-	-
Period (sec) ^{*2}	0.610	0.217	0.131	-	-	-
Damping ratio (%) ^{*2}	0.49	0.48	0.50	-	-	-

*1 From free vibration test

*2 From forced vibration test

(b) Experimental Periods and Damping Ratios [14]

TABLE 3.2 PROTOTYPE PERIODS, MODE SHAPES AND DAMPING RATIOS

Model Type		True Replica Simulation	Artificial Mass (Prototype Material)	Gravity Forces Neglected
length	l_r	l_r	l_r	l_r
time	t_r	$l_r^{1/2}$	$l_r^{1/2}$	l_r
frequency	ω_r	$l_r^{-1/2}$	$l_r^{-1/2}$	l_r^{-1}
velocity	v_r	$l_r^{1/2}$	$l_r^{1/2}$	1
acceleration	a_r	1	1	l_r^{-1}
mass density	ρ_r	E_r/l_r	-	1
strain	ϵ_r	1	1	1
stress	σ_r	E_r	E_r	1
elasticity modulus	E_r	E_r	E_r	1
specific stiffness	$(E/\rho)_r$	l_r	-	1
displacement	δ_r	l_r	l_r	l_r
force	F_r	$E_r l_r^2$	$E_r l_r^2$	l_r^2
energy	$(EN)_r$	$E_r l_r^3$	$E_r l_r^3$	l_r^3

TABLE 4.1 SIMILITUDE LAW [26]

	Scaled W18x40	M6x4.4	AISC Plastic Design Requirements [16]
Areas (in ²)	$11.8 \times l_r^2 = 1.098^*$	1.29	
d (in)	$17.9 \times l_r = 5.46$	6.00	
I_x (in ²)	$612 \times l_r^4 = 5.30$	7.20	
I_y (in ²)	$19.1 \times l_r^4 = 0.165$	0.165	
Z_x (in ³)	$678.4 l_r^3 = 2.22$	2.80	
$(b_f)/(2t_f)$	5.7	10.8	<17 for plastic design
$(d_w)/(t_w)$	53.5	49.6	<70 for plastic design

* $l_r = 0.3048$

TABLE 4.2 COMPARISON OF STEEL GIRDER SECTIONAL PROPERTIES (COMPOSITE GIRDER TESTS)

	without Slab (kip)	without Lead (kip)	Added Weight (kip)	Total Weight (kip)	Required* ¹ (kip)	Ratio* ² (%)
Roof	1.00	4.64	10.88	15.52	15.50	100.1
6F	1.01	4.64	13.52	18.16	18.17	99.9
5F	1.14	4.74	13.40	18.14	18.17	99.8
4F	1.12	4.75	13.33	18.08	18.17	99.5
3F	1.25	5.08	13.02	18.10	18.17	99.6
2F	1.33	4.99	14.09	19.08	19.07	100.1
Total	6.85	28.84	78.24	107.08	107.25	99.8

*1 Prototype weight used in the Pseudo-dynamic Test

*2 (Total Weight)/(Required Weight)

TABLE 4.3 DISTRIBUTION OF THE 0.3-SCALE MODEL WEIGHT

	Roof	6th	5th	4th	3rd	2nd
Roof	28.443	21.212	14.519	9.64	5.753	2.486
6th	21.212	19.677	13.831	9.288	5.629	2.476
5th	14.519	13.831	12.762	8.940	5.495	2.467
4th	9.640	9.288	8.940	8.351	5.382	2.455
3rd	5.753	5.630	5.496	5.382	5.010	2.461
2nd	2.486	2.476	2.467	2.455	2.461	2.243

(a) Flexibility Matrix ($\times 10^{-3}$ inch/kip)

	Roof	6th	5th	4th	3rd	2nd
Roof	181.16	-211.10	19.54	-0.44	5.86	4.81
6th	-211.10	462.98	-286.71	39.38	-7.04	2.86
5th	19.54	-286.71	641.08	-422.82	54.10	-6.83
4th	-0.44	39.38	-422.82	844.95	-522.04	70.02
3rd	5.86	-7.04	54.10	-522.04	976.43	-558.17
2nd	4.81	2.86	-6.83	70.02	-558.17	980.64

(b) Stiffness Matrix (kip/inch)

	Roof	6th	5th	4th	3rd	2nd
Roof	15.486	11.354	7.906	5.627	3.759	2.070
6th	11.354	11.354	7.906	5.627	3.759	2.070
5th	7.906	7.906	7.906	5.627	3.759	2.070
4th	5.627	5.627	5.627	5.627	3.759	2.070
3rd	3.759	3.759	3.759	3.759	3.759	2.070
2nd	2.070	2.070	2.070	2.070	2.070	2.070

(c) Flexibility Matrix Assuming Pure Shear Type Structure ($\times 10^{-3}$ inch/kip)

	Roof	6th	5th	4th	3rd	2nd
Roof	242.01	-242.01	0.00	0.00	0.00	0.00
6th	-242.01	532.04	-290.01	0.00	0.00	0.00
5th	0.00	-290.01	728.86	-438.83	0.00	0.00
4th	0.00	0.00	-438.83	974.12	-535.28	0.00
3rd	0.00	0.00	0.00	-535.28	1127.34	-592.03
2nd	0.00	0.00	0.00	0.00	-592.03	1075.05

(d) Stiffness Matrix Assuming Pure Shear Type Structure (kip/inch)

TABLE 5.1 ANALYTICAL PREDICTION OF THE 0.3-SCALE MODEL FLEXIBILITY AND STIFFNESS

Mode	1st	2nd	3rd	4th	5th	6th
Frequency (Hz)	5.596	15.173	26.564	35.833	45.714	57.891
Mode Shapes						
Roof	1.000	1.000	-0.923	-0.457	0.159	0.025
6th	0.855	0.221	0.814	1.000	-0.564	-0.130
5th	0.663	-0.587	1.000	-0.407	1.000	0.403
4th	0.477	-0.934	-0.053	-0.661	-0.736	-0.818
3rd	0.312	-0.902	-0.936	0.283	-0.391	1.000
2nd	0.140	-0.516	-0.846	0.708	0.944	-0.732

(a) Test Structure without Auxiliary Lead

Mode	1st	2nd	3rd	4th	5th	6th
Frequency (Hz)	3.026	8.247	14.314	18.988	24.301	31.065
Mode Shapes						
Roof	1.000	1.000	-0.971	-0.506	0.170	0.023
6th	0.932	0.288	0.763	1.000	-0.553	-0.113
5th	0.717	-0.571	1.000	-0.405	1.000	0.367
4th	0.515	-0.945	-0.050	-0.652	-0.750	-0.777
3rd	0.327	-0.889	-0.910	0.274	-0.378	1.000
2nd	0.153	-0.533	-0.873	0.724	0.910	-0.702

(b) Test Structure with Auxiliary Lead

Mode	1st	2nd	3rd	4th	5th	6th
Frequency (Hz)	3.973	10.096	16.345	20.901	25.989	31.999
Mode Shapes						
Roof	1.000	1.000	-0.996	-0.496	0.120	0.010
6th	0.970	0.359	0.809	1.000	-0.446	-0.063
5th	0.778	-0.478	1.000	-0.512	1.000	0.286
4th	0.599	-0.824	-0.001	-0.565	-0.896	-0.720
3rd	0.421	-0.819	-0.820	0.242	-0.361	1.000
2nd	0.245	-0.568	-0.900	0.659	0.908	-0.660

(c) Test Structure with Auxiliary Lead (Assuming Pure Shear Type Structure)

**TABLE 5.2 ANALYTICAL PREDICTION OF THE 0.3-SCALE MODEL
NATURAL FREQUENCIES AND MODE SHAPES**

	6 th	5 th	4 th	3 rd	2 nd	1 st
6 th	49.118	40.397	30.995	22.080	14.658	7.464
5 th	39.121	37.929	29.717	21.780	14.528	7.450
4 th	30.450	30.666	27.450	21.455	14.315	7.246
3 rd	21.726	21.655	20.667	19.652	14.203	7.296
2 nd	13.615	13.894	14.414	13.683	12.344	6.764
1 st	6.967	7.408	7.769	7.483	7.390	5.685

(a) Flexibility Matrix ($\times 10^{-2}$ inch/kip)

	6 th	5 th	4 th	3 rd	2 nd	1 st
6 th	13.97	-17.89	4.65	-0.78	-0.80	1.53
5 th	-17.89	47.60	-40.47	7.61	6.50	-4.04
4 th	4.65	-40.47	70.90	-35.68	-2.72	3.12
3 rd	-0.78	7.61	-35.68	61.50	-41.46	9.85
2 nd	-0.80	6.50	-2.73	-41.46	79.87	-49.42
1 st	1.53	-4.04	3.12	9.85	-49.42	65.54

(b) Stiffness Matrix (kip/inch)

	1 st	2 nd	3 rd	4 th	5 th	6 th
F (Hz)	6.207	17.424	33.570	45.926	72.839	78.581
T (sec)	0.161	0.057	0.030	0.022	0.014	0.013

(c) Natural Frequencies and Periods

**TABLE 5.3 RESULTS OF FLEXIBILITY TEST OF FRAME A AND C
(UNBRACED MODEL WITHOUT COMPOSITE SLAB)**

	Roof	6 th	5 th	4 th	3 rd	2 nd
Roof	39.138	31.489	23.065	15.884	9.576	4.538
6th	30.255	29.160	22.331	15.668	9.502	4.444
5th	22.262	22.351	20.574	15.348	9.252	4.408
4th	15.023	15.510	15.193	13.745	8.871	4.264
3rd	9.478	9.714	9.592	9.312	7.601	4.146
2nd	3.927	4.576	4.848	4.647	3.843	2.742

(a) Flexibility Matrix ($\times 10^{-2}$ inch/kip)

	Roof	6 th	5 th	4 th	3 rd	2 nd
Roof	16.38	-20.46	3.25	2.10	-3.96	5.25
6th	-20.46	48.59	-37.19	11.79	-5.51	3.30
5th	3.25	-37.20	78.67	-63.33	31.36	-19.39
4th	2.10	11.79	-63.33	107.13	-85.14	34.19
3rd	-3.96	-5.51	31.36	-85.14	150.06	-118.01
2nd	5.25	3.30	-19.39	34.19	-118.01	172.04

(b) Stiffness Matrix (kip/inch)

	1 st	2 nd	3 rd	4 th	5 th	6 th
F (Hz)	5.123	14.253	26.908	40.281	54.508	81.885
T (sec)	0.195	0.070	0.037	0.025	0.018	0.012

(c) Natural Frequencies and Periods

**TABLE 5.4 RESULTS OF FLEXIBILITY TEST OF FRAME B
(UNBRACED MODEL WITHOUT COMPOSITE SLAB)**

	Roof	6 th	5 th	4 th	3 rd	2 nd
Roof	54.243	43.344	29.500	20.976	15.294	7.825
6th	43.254	40.661	28.667	20.691	15.114	7.809
5th	33.450	32.159	26.656	20.229	14.531	7.492
4th	23.948	23.609	20.468	19.548	14.735	7.750
3rd	15.093	15.609	13.751	13.125	12.231	6.854
2nd	8.074	8.005	7.422	7.103	7.213	5.906

(a) Flexibility Matrix ($\times 10^{-2}$ inch/kip)

	Roof	6 th	5 th	4 th	3 rd	2 nd
Roof	12.80	-15.80	2.44	-1.07	3.44	-1.90
6th	-15.80	37.18	-26.80	6.69	-6.13	4.21
5th	2.44	-26.80	50.94	-28.69	6.05	-2.88
4th	-1.07	6.69	-28.69	54.77	-41.83	9.66
3rd	3.44	-6.13	6.05	-41.83	77.21	-43.41
2nd	-1.90	4.21	-2.85	9.66	-43.41	57.00

(b) Stiffness Matrix (kip/inch)

	1 st	2 nd	3 rd	4 th	5 th	6 th
F (Hz)	6.086	17.268	32.562	45.098	58.678	76.938
T (sec)	0.164	0.058	0.031	0.022	0.017	0.013

(c) Natural Frequencies and Periods

**TABLE 5.5 RESULTS OF FLEXIBILITY TEST OF FRAME A AND C
(BRACED MODEL WITHOUT COMPOSITE SLAB)**

	Roof	6 th	5 th	4 th	3 rd	2 nd
Roof	44.724	36.454	25.879	18.729	11.316	5.822
6th	34.963	32.237	24.027	17.229	10.659	5.416
5th	22.744	22.075	18.489	13.947	8.752	4.422
4th	16.592	16.851	14.614	12.161	8.225	4.299
3rd	10.580	10.660	9.349	8.615	7.258	4.087
2nd	4.939	5.484	4.379	4.344	3.604	2.680

(a) Flexibility Matrix ($\times 10^{-3}$ inch/kip)

	Roof	6 th	5 th	4 th	3 rd	2 nd
Roof	240.29	-399.65	242.99	-91.78	-58.95	164.03
6th	-399.65	1050.62	-1186.28	619.42	103.22	-533.65
5th	242.99	-1186.28	2677.57	-2363.27	287.37	927.02
4th	-91.78	619.43	-2363.27	3094.75	-1070.60	-649.32
3rd	-58.95	103.22	287.38	-1070.60	1430.47	-890.12
2nd	164.03	-533.65	927.01	-649.32	-890.12	1932.03

(b) Stiffness Matrix (kip/inch)

	1 st	2 nd	3 rd	4 th	5 th	6 th
F (Hz)	15.585	50.414	93.329	154.897	239.149	373.666
T (sec)	0.064	0.020	0.011	0.007	0.004	0.003

(c) Natural Frequencies and Periods

**TABLE 5.8 RESULTS OF FLEXIBILITY TEST OF FRAME B
(BRACED MODEL WITHOUT COMPOSITE SLAB)**

	Roof	6 th	5 th	4 th	3 rd	2 nd
Roof	27.610	21.164	15.068	10.186	7.257	3.914
6th	21.179	19.693	14.292	9.737	7.099	3.856
5th	15.236	14.672	13.578	9.522	6.806	3.640
4th	10.333	10.099	9.800	8.857	6.384	3.485
3rd	6.494	6.790	6.427	5.971	5.660	3.416
2nd	3.425	3.702	3.541	3.256	3.267	2.978

(a) Flexibility Matrix ($\times 10^{-3}$ inch/kip)

	Roof	6 th	5 th	4 th	3 rd	2 nd
Roof	212.41	-252.13	29.18	-31.29	49.94	2.38
6th	-252.13	540.30	-326.36	107.75	-93.81	1.87
5th	29.18	-326.36	687.14	-470.62	79.18	-6.45
4th	-31.29	107.75	-470.62	955.25	-667.57	1.37
3rd	49.94	-93.81	79.18	-667.57	1313.62	-7.56
2nd	2.38	1.87	-6.45	137.09	-756.23	1031.49

(b) Stiffness Matrix (kip/inch)

	1 st	2 nd	3 rd	4 th	5 th	6 th
F (Hz)	5.658	15.747	29.097	36.917	49.800	67.420
T (sec)	0.177	0.064	0.034	0.027	0.020	0.015

(c) Natural Frequencies and Periods

TABLE 5.7 RESULTS OF FLEXIBILITY TEST OF THE 0.3-SCALE MODEL WITHOUT AUXILIARY MASS

	Roof	6 th	5 th	4 th	3 rd	2 nd
Roof	27.022	19.953	14.269	10.945	6.097	2.887
6th	20.080	18.622	13.266	9.750	5.974	2.609
5th	14.555	13.130	12.627	9.242	5.856	2.741
4th	9.884	9.539	9.153	8.684	5.586	2.619
3rd	6.150	6.074	5.944	5.634	5.142	2.632
2nd	3.041	2.924	2.774	2.911	2.763	2.327

(a) Flexibility Matrix ($\times 10^{-3}$ inch/kip)

	Roof	6 th	5 th	4 th	3 rd	2 nd
Roof	188.04	-192.83	-46.94	30.26	45.65	-43.54
6th	-192.83	405.72	-166.18	-49.04	-28.48	51.47
5th	-46.94	-166.18	582.05	-361.36	-54.81	60.59
4th	30.26	-49.04	-361.36	798.51	-439.90	9.15
3rd	45.65	-28.48	-54.81	-439.90	1073.66	-681.36
2nd	-43.54	51.47	60.59	9.15	-681.36	1131.22

(b) Stiffness Matrix (kip/inch)

	1 st	2 nd	3 rd	4 th	5 th	6 th
F (Hz)	3.051	8.556	15.158	18.453	24.336	31.561
T (sec)	0.328	0.117	0.066	0.054	0.041	0.032

(c) Natural Frequencies and Periods

TABLE 5.8 RESULTS OF FLEXIBILITY TEST OF THE MODEL WITH AUXILIARY MASS

Mode		Free Vibration			Forced Vibration		
		1st	2nd	3rd	1st	2nd	3rd
Prototype*	T_i (sec)	0.599	-	-	0.610	0.217	0.131
	ξ_i (%)	0.40	-	-	0.49	0.48	0.50
0.3-Scale Model	T_i (sec)	0.619	0.215	0.125	0.625	0.216	0.124
	ξ_i (%)	1.29	0.67	0.54	1.56	0.72	0.63

* Reference 14

TABLE 5.9 COMPARISON OF PROTOTYPE AND MODEL PERIODS AND EQUIVALENT VISCOUS DAMPING RATIOS

			Natural Frequency (Hz)					
Mode			1st	2nd	3rd	4th	5th	6th
Unbraced Frame B	Frame A	Analysis* ¹	5.38	15.20	27.81	42.57	60.84	81.70
		Flex* ²	5.32	15.06	27.95	39.73	61.41	65.18
		Free* ³	8.43	27.45	42.43	---	---	---
Unbraced Frame B	Frame B	Analysis	4.36	12.49	23.12	36.70	53.46	75.01
		Flex	4.39	12.32	22.64	34.63	47.03	69.96
		Free	5.35	21.00	33.68	---	---	---
Braced Frame B	Frame A	Analysis	5.38	15.20	27.80	42.57	60.84	81.70
		Flex	5.15	14.90	27.90	38.67	50.22	66.28
		Free	6.73	23.37	36.71	45.25	---	---
Braced Frame B	Frame B	Analysis	15.08	40.41	71.37	97.91	123.97	159.68
		Flex	13.12	43.52	75.28	131.24	184.96	276.66
		Free	13.77	42.99	---	---	---	---
Test Model	without Lead	Analysis	5.60	15.17	26.56	35.83	45.71	57.89
		Flex	5.66	15.75	29.10	36.92	49.80	67.42
		Ambient* ⁴	5.57	15.63	25.93	37.01	48.05	---
		Free	5.37	15.47	26.19	36.87	46.05	---
		Forced* ⁵	5.38	15.55	28.11	---	---	---
Test Model	with Lead	Analysis	3.03	8.25	14.31	18.99	24.30	31.07
		Flex	3.05	8.56	15.16	18.45	24.34	31.56
		Ambient	2.98	8.50	14.45	19.00	---	---
		Free	2.92	8.42	14.53	18.85	---	---
		Forced	2.90	8.39	14.59	---	---	---

*1 Analytical Method Using ANSR-1

*2 Semi-Analytical Method Using Experimental Flexibility Matrix and Lumped Mass Matrix

*3 Pull and Release Method

*4 High Performance Seismometers Installed on the Model Roof Level

*5 Small Shaking Table Installed on the Model Roof Level

TABLE 5.10 VARIATION OF NATURAL FREQUENCY OF THE MODEL BEFORE SHAKING TABLE TEST

Series	Test No.	Input Signal	Peak Amplitude (%g)
1 Diagnostic and Serviceability Level Tests	1	MO* ¹	0.46
	2	MO	0.71
	3	MO	1.02
	4	MO	2.15
	5	MO	2.43
	6	MO	4.45
	7	MO	6.34
	8	FV* ²	
	9	MO	6.17
	10	FV	
	11	FV	
	12	MO	8.50
	13	MO	9.90
	14	FV	
	15	MO	16.01
	16	FV	
	17	MO	14.68
	18	FV	
	19	FV	
	20	MO	14.68
	21	FV	
	22	MO	19.89
	23	FV	
2 Damageability Level Tests	24	FV	
	25	MO	27.63
	26	FV	
	27	MO	33.49
3 Collapse Level Tests	28	FV	
	29	MO	64.92
	30	FV	
4 After Main Shock Tests	31	FV	
	32	MO	30.07
	33	MO	27.64
	34	FV	
	35	MO	26.53
	36	FV	

*1 Miyagi-Ken-Oki Earthquake motion

*2 Free Vibration by pulse

(The shaking table was floated by differential air pressure)

TABLE 8.1 SHAKING TABLE TEST PROGRAM OF THE 0.3-SCALE MODEL

	Natural Period (sec)			Damping Factor (%) *1		
	1 st	2 nd	3 rd	1 st	2 nd	3 rd
Before Test *2	0.342	0.119	0.069	1.29	0.67	0.54
Before Test *3	0.361	0.121	0.070	2.04	1.78	---
After MO 6.3%g	0.366	0.122	0.070	2.04	2.70	----
Before MO 9.9%g	0.354	0.121	0.070	2.41	2.70	----
After MO 9.9%g	0.359	0.121	0.070	1.99	1.52	----
After MO 16.0%g	0.360	0.121	0.071	1.57	1.42	----
After MO 14.7%g	0.361	0.121	0.070	1.87	1.30	----
After MO 14.7%g	0.366	0.122	0.071	2.00	1.90	----
Before MO 19.9%g	0.367	0.123	0.071	1.98	2.59	----
After MO 19.9%g	0.368	0.123	0.071	2.51	2.60	----
Before MO 27.6%g	0.367	0.123	0.071	2.16	1.96	----
Before MO 33.5%g	0.371	0.123	0.071	2.04	2.13	----
Before MO 64.9%g	0.367	0.124	0.071	2.40	2.60	----
After MO 64.9%g	0.392	0.150	0.073	1.66	1.71	----
Before MO 30.1%g	0.394	0.150	0.074	1.53	1.90	----
After 2 MO 27.6%g	0.412	0.160	0.074	1.73	2.75	----
After MO 26.5%g	0.434	0.162	0.085	1.95	2.15	----
After Removing Braces *2	0.672	0.240	0.139	0.73	0.40	0.33

*1 Obtained from Free-decay Time History

*2 Shaking Table was Locked by Screw Jacks

*3 Shaking Table was floated by Differential Air Pressure (below this row)

**TABLE 7.1 VARIATION OF MECHANICAL CHARACTERISTICS
OF THE MODEL DURING SHAKING TABLE TESTS**

Floor/Story	6	5	4	3	2	1
Lateral Displ (in.)	-0.28	-0.23	-0.22	-0.15	-0.11	-0.06
Time (sec)	4.32	4.33	4.33	4.33	4.33	4.34
Inter-story Drift (in.)	-0.056	0.045	-0.060	-0.048	-0.043	-0.062
Inter-story Drift Index (%)	0.14	0.11	0.15	-0.12	-0.11	-0.11
Time (sec)	4.31	4.50	4.32	4.32	4.33	4.34
Story Shear (k)	-3.4	-6.0	-8.7	-11.2	-13.1	-14.8
Story Shear/Total Wt.(%)	3.1	5.6	8.2	10.5	12.3	13.9
Time (sec)	4.30	4.31	4.31	4.32	4.33	4.33
Inertia Force (k)	3.3	3.3	2.8	2.6	2.1	1.6
Time (sec)	4.30	4.31	4.35	4.34	4.34	4.33
Overturn. Moment (k-in)	136.5	408.8	788.2	1245.1	1763.4	2538.8
Time (sec)	4.30	4.31	4.31	4.31	4.32	4.32

TABLE 7.2 MODEL MO-6.3 TEST RESPONSE ENVELOPES

Floor/Story	6	5	4	3	2	1
Lateral Displ (in.)	-1.41	-1.21	-0.95	-0.70	-0.51	-0.29
Time (sec)	4.35	4.35	4.35	8.54	8.55	8.55
Inter-story Drift(in.)	-0.20	-0.28	0.25	-0.23	-0.21	-0.28
Inter-story Drift Index (%)	0.50	0.69	0.61	0.56	0.39	0.51
Time (sec)	4.34	8.99	4.56	8.54	4.36	8.55
Story Shear (k)	-16.8	-30.8	-41.0	-49.4	-55.6	-60.1
Story Shear/Total Wt. (%)	15.7	28.8	38.3	46.2	51.9	56.1
Time (sec)	4.34	4.35	4.34	4.35	4.35	8.54
Inertia Force (k)	16.8	16.7	12.9	10.0	8.5	7.9
Time (sec)	4.34	4.37	8.52	8.52	4.29	4.28
Overturn. Moment (k-in)	684.7	1926.9	3604.0	5620.7	7887.2	11058.2
Time (sec)	4.34	4.35	4.35	4.35	4.35	4.35

TABLE 7.3 MODEL MO-33 TEST RESPONSE ENVELOPES

Floor/Story	6	5	4	3	2	1
Lateral Displ (in.)	-2.37	-2.12	-1.55	-1.13	-0.83	-0.47
Time (sec)	8.61	8.61	8.61	4.36	4.37	4.37
Inter-story Drift (in.)	-0.27	0.77	0.49	-0.33	-0.34	-0.47
Inter-story Drift Index (%)	0.66	1.89	1.20	0.81	0.83	0.87
Time (sec)	8.59	8.87	8.86	4.36	4.36	4.37
Story Shear (k)	-20.5	-42.4	-54.4	-65.8	73.8	-78.6
Story Shear/Total Wt. (%)	19.2	39.6	50.8	61.5	69.0	73.4
Time (sec)	8.59	4.38	8.61	4.35	4.34	4.34
Inertia Force (k)	20.49	22.44	18.30	-16.63	13.62	13.97
Time (sec)	8.59	4.38	4.33	8.79	4.30	4.29
Overturn. Moment (k-in)	836.1	2543.5	4713.5	7255.6	10227.3	14344.2
Time (sec)	8.59	4.38	8.60	4.36	4.36	4.35

TABLE 7.4 MODEL MO-65 TEST RESPONSE ENVELOPES

Brace No.	In-Plane ϕ_x ($\times 10^{-3}$)	Out-of-Plane ϕ_y ($\times 10^{-3}$)	Dominant Buckling Plane
1	0.5628	0.1405	in-plane
2	0.2466	0.7411	out-of-plane
3	0.1268	0.6616	out-of-plane
4	0.3805	0.2628	in-plane
5	0.5177	0.5796	out-of-plane
6	0.2816	0.0566	in-plane
7	0.3567	0.9387	out-of-plane
8	0.5937	0.2571	in-plane
9	1.4998	not measured	not available
10	2.5755	not measured	not available
11	0.4791	not measured	not available
12	0.2859	not measured	not available

Section measured at one quarter of brace length. (unit:radian/inch)

**TABLE 7.5 MODEL MAXIMUM BRACE CURVATURES AND
DOMINANT BUCKLING PLANE (MO-65 TEST)**

Floor/Story	6	5	4	3	2	1
Lateral Displ (in)	1.78	1.61	1.02	0.67	-0.48	0.27
Time (sec)	6.76	6.76	6.75	6.74	6.98	6.73
Inter-story Drift (in)	-0.20	0.60	0.37	-0.22	0.19	-0.27
Inter-story Drift Index (%)	0.49	1.47	0.91	0.54	0.47	0.50
Time (sec)	4.37	6.78	6.77	6.98	6.73	6.97
Story Shear (k)	16.50	33.20	41.77	46.57	52.02	57.78
Story Shear/Total Wt.(%)	15.4	31.0	39.0	43.5	48.6	54.0
Time (sec)	6.77	6.77	6.76	6.75	6.73	6.72
Inertia Force (k)	-16.50	-16.70	12.42	-11.58	-9.26	-7.70
Time (sec)	6.77	6.77	6.96	6.70	6.69	6.20
Overturn. Moment (k-in)	673.2	2027.9	3735.6	5577.8	7558.0	10378.6
Time (sec)	6.77	6.77	6.77	6.76	6.75	6.74

TABLE 7.8 MODEL MO-POST1 TEST RESPONSE ENVELOPES

Story	1st	2nd	3rd	4th	5th	6th
kl/r	61	48	48	59	70	78
P_y^{*1}	48.8	30.2	30.2	24.9	15.9	14.3
P_{cr} (predicted)*2 (kip)	40.7	27.1	27.1	24.9	12.4	10.4
P_{cr}^{*3} (test) (kip)	45.0	30.2	29.5	24.3	11.4	-*4

*1 $P_y = F_y A$

*2 $P_{cr(\text{predicted})} = \left[1 - \frac{(kl/r)^2}{2C_c^2} \right] F_y A$; $C_c = \sqrt{2\pi^2 E_s / F_y}$

*3 $P_{cr(\text{test})} = V_{\text{max}}^{\text{BRACE}} / 2\cos\theta$

*4 did not buckle

TABLE 8.1 COMPARISON OF MODEL BRACE BUCKLING LOADS

Story	P_{cr}/P_y *1	B/t *2	Observed Damage
1	0.83	12.7	Buckled
2	0.90	17.4	Buckled
3	0.90	17.4	Buckled
4	0.84	20.5	Buckled and ruptured at bottom end
5	0.78	20.0	Buckled and ruptured at mid-span
6	0.73	18.0	Unbuckled

*1 $P_{cr(\text{predicted})}/P_y = 1 - \frac{(kl/r)^2}{2C_c^2}$

*2 B = tube width; t = tube thickness

TABLE 8.2 MODEL BRACE P_{cr}/P_y AND B/t RATIOS

Participation Factor	Horizontal L_{xi}	Pitching $L_{\theta i}$
First Mode	0.476	87.929
Second Mode	-0.188	-0.260
Third Mode	0.088	0.877

TABLE 9.1 PARTICIPATION FACTORS OF THE MODEL

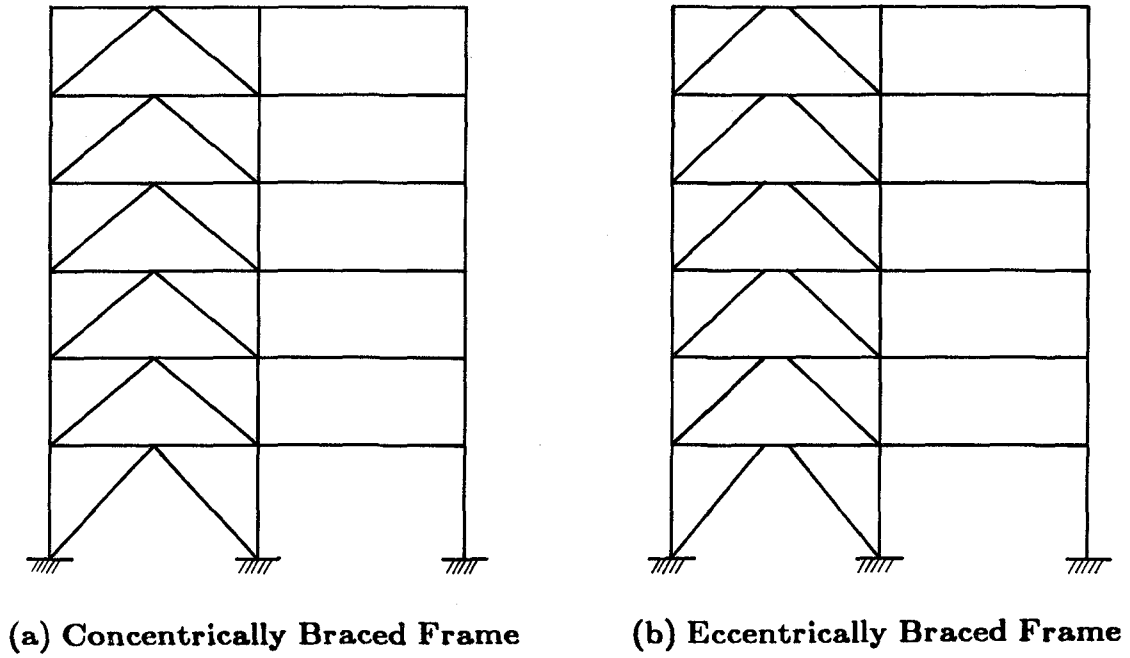


FIG. 1.1 BRACED STEEL FRAMES

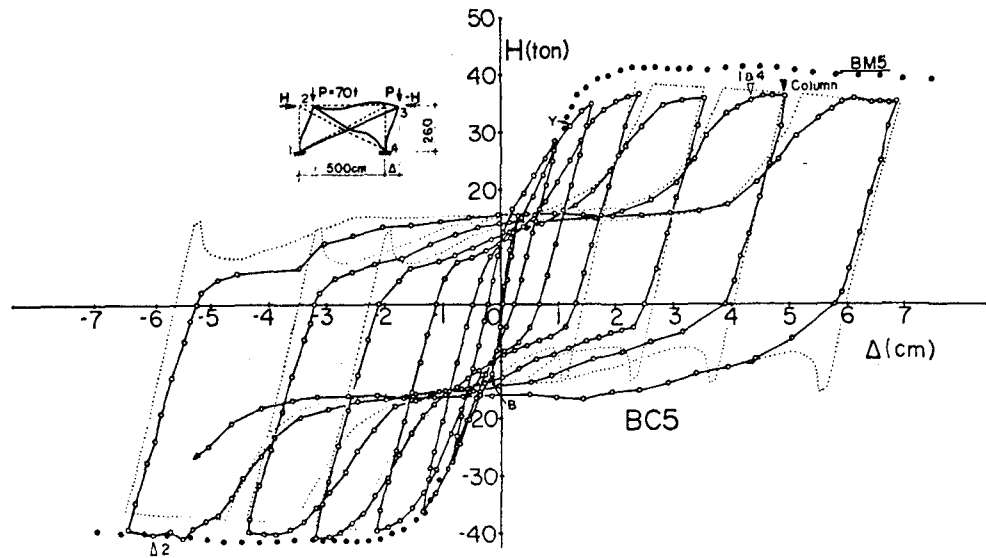
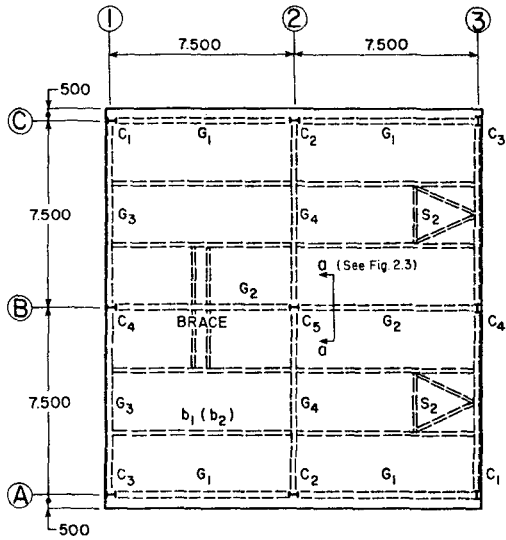
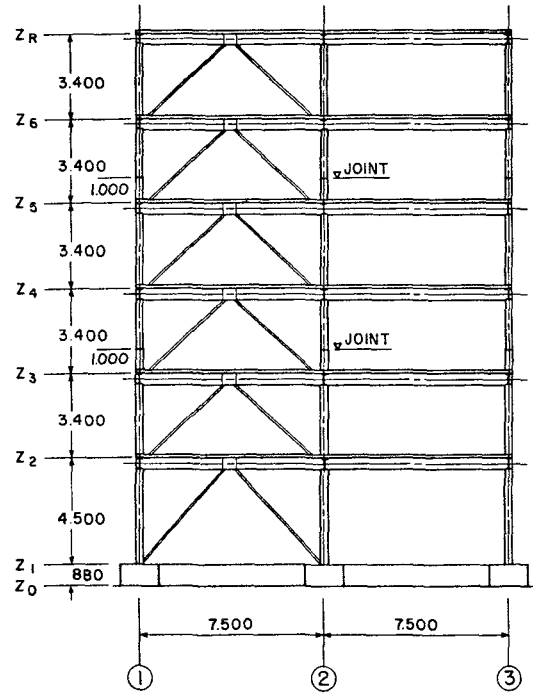


FIG. 1.2 HYSTERESIS BEHAVIOR OF CONCENTRICALLY X-BRACED FRAME [2]

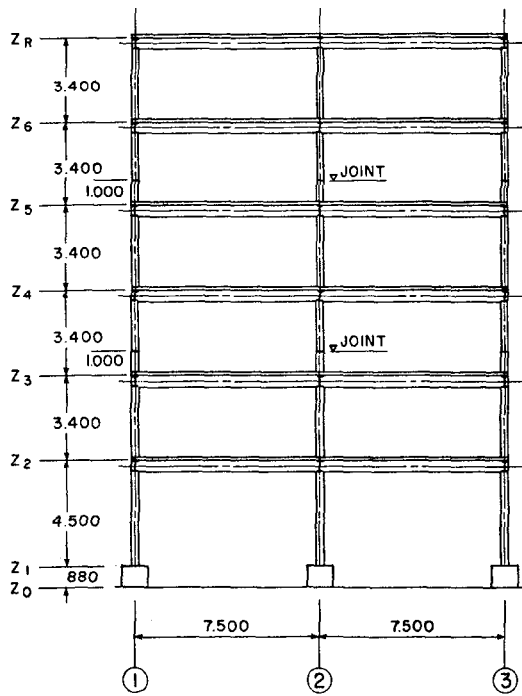
Unit : mm (1mm=0.03937 inch)



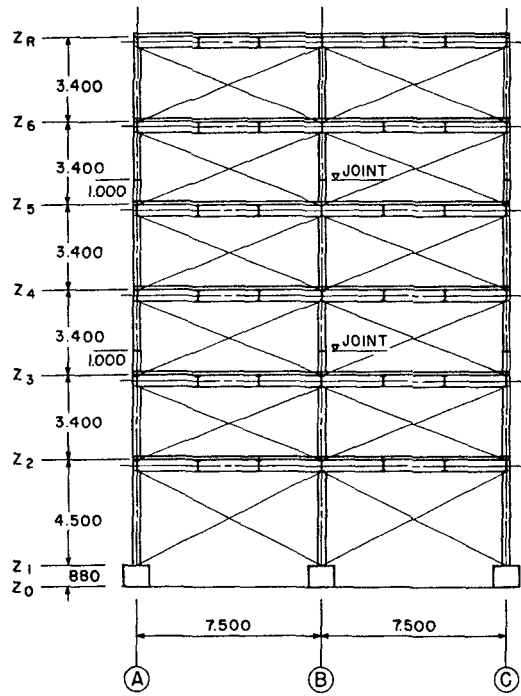
(a) Typical Floor Plan



(b) Elevation Frame B



(c) Elevation Frame A, C



(d) Elevation Frame 1, 3

FIG. 2.1 TYPICAL PLAN AND ELEVATIONS OF THE PROTOTYPE

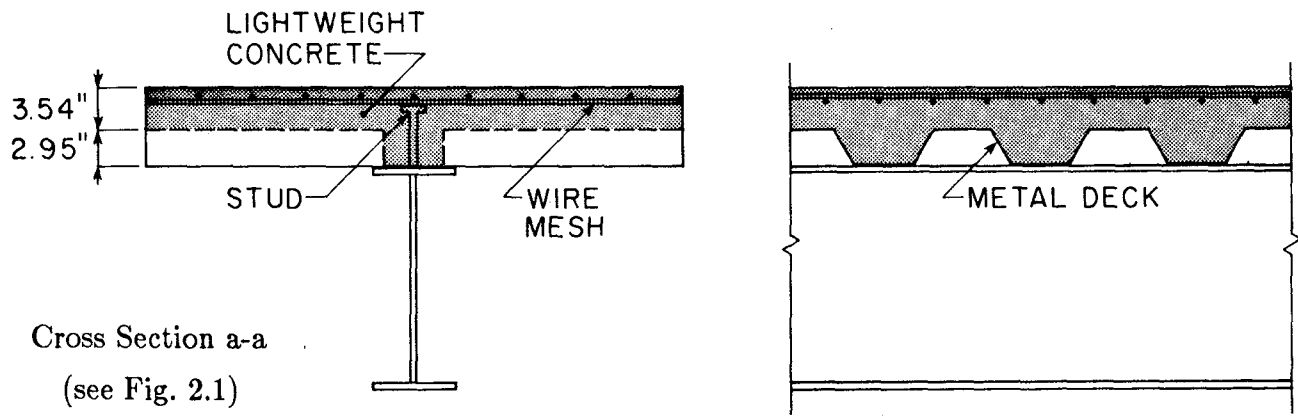


FIG. 2.3 COMPOSITE GIRDER CROSS SECTION (FRAME B)

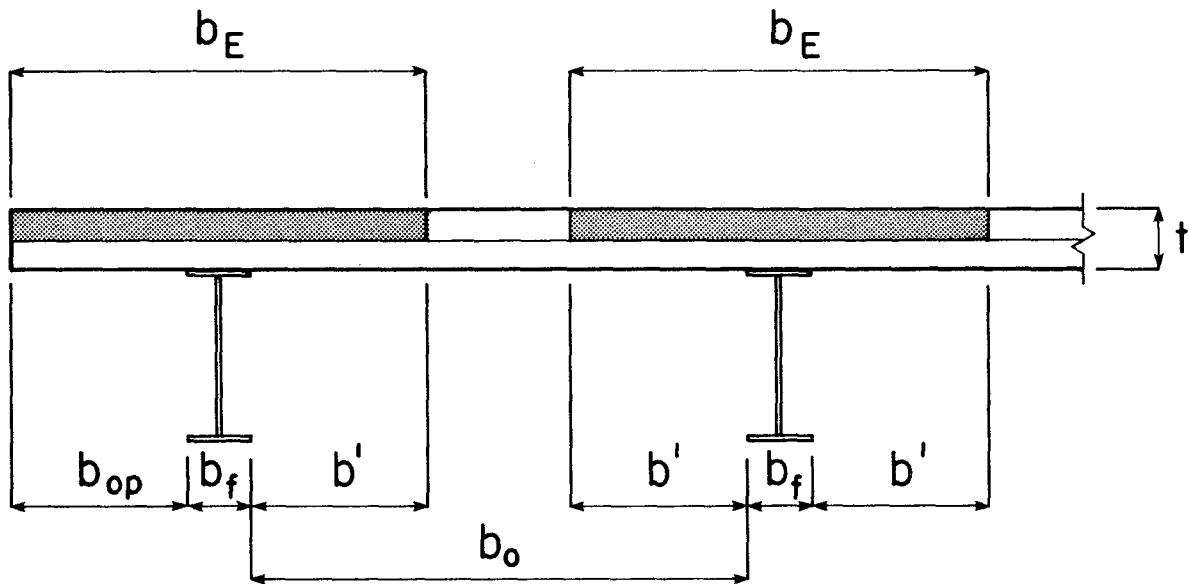
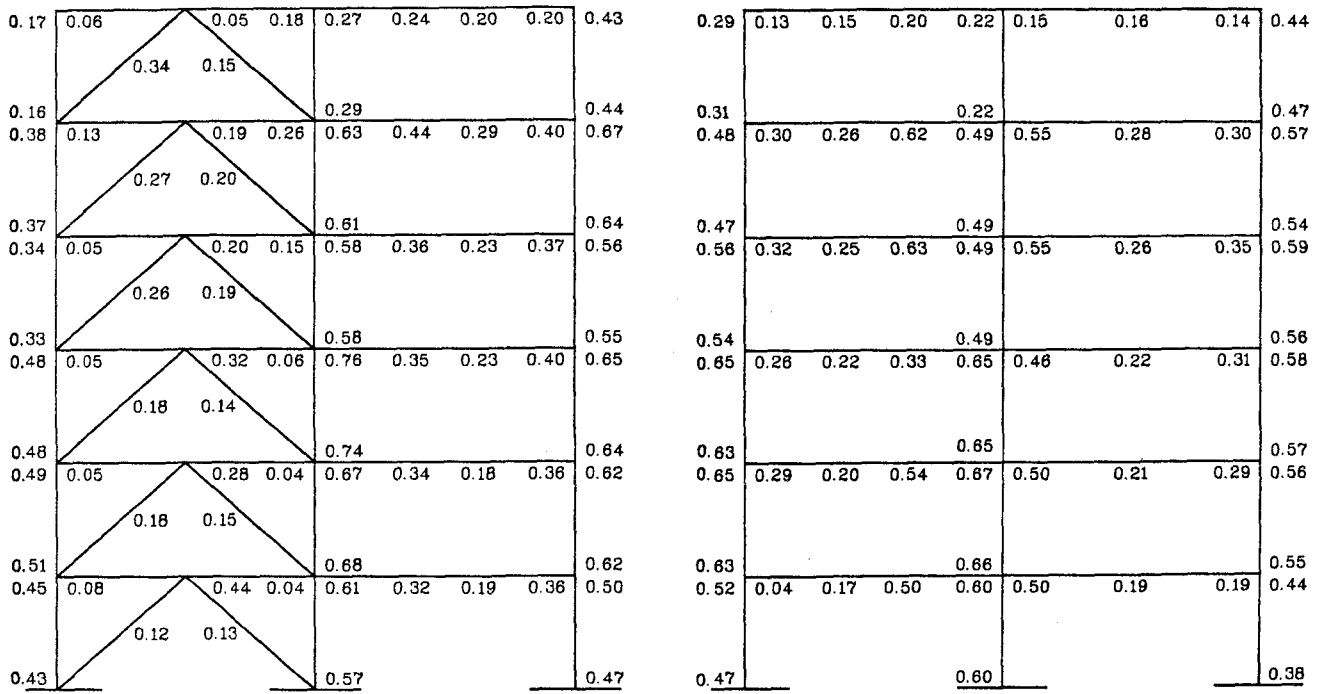
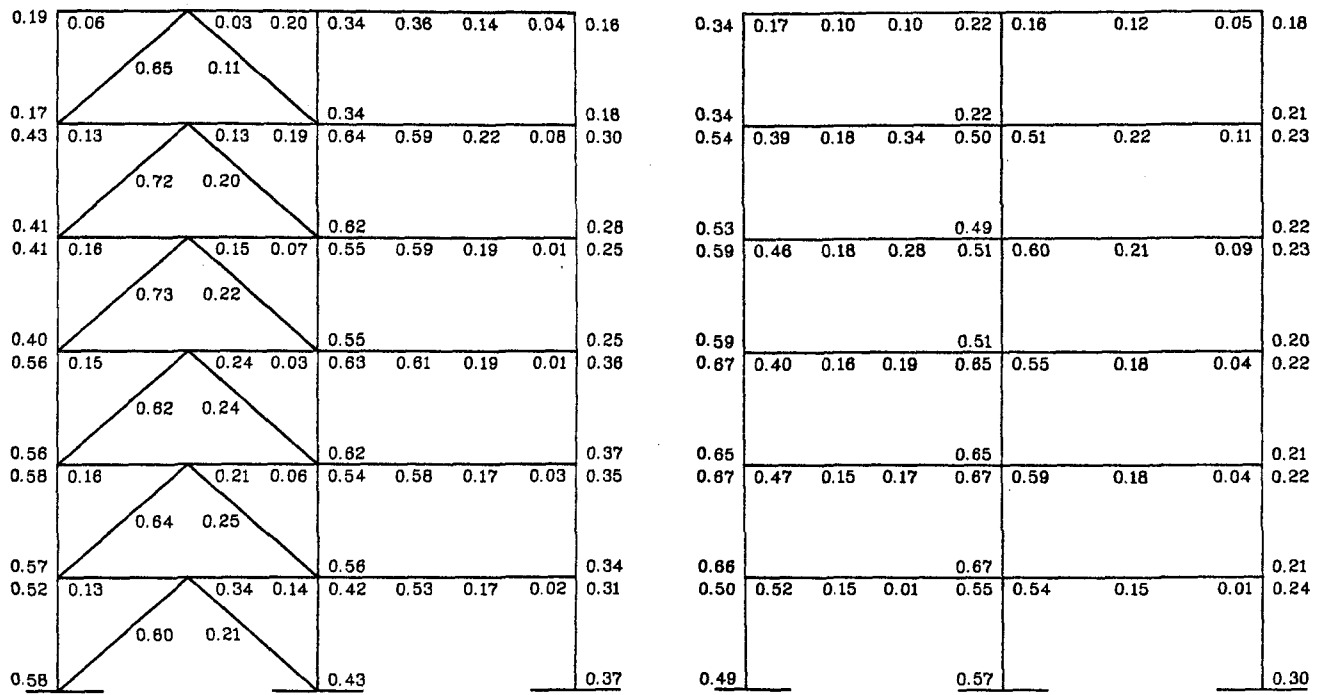


FIG. 2.4 EFFECTIVE WIDTH OF COMPOSITE GIRDER

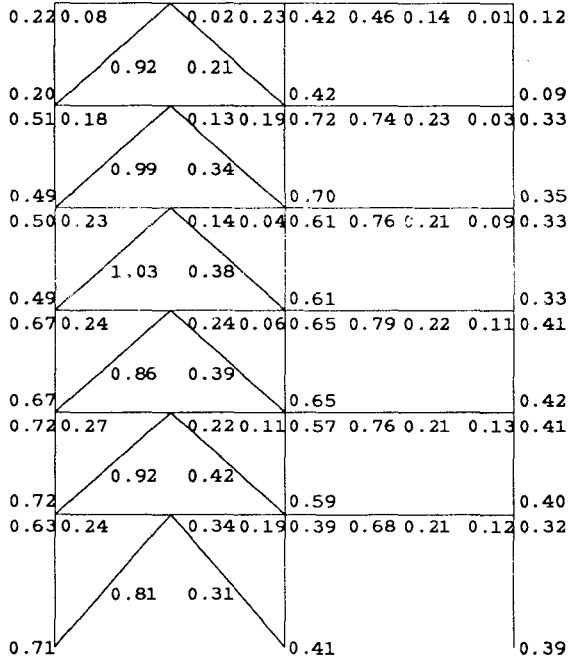


(a) D.L. + L.L.

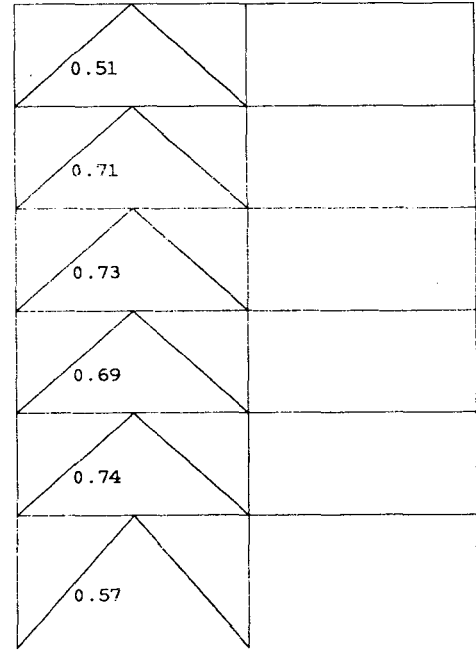


(b) D.L. + L.L. + E.Q.

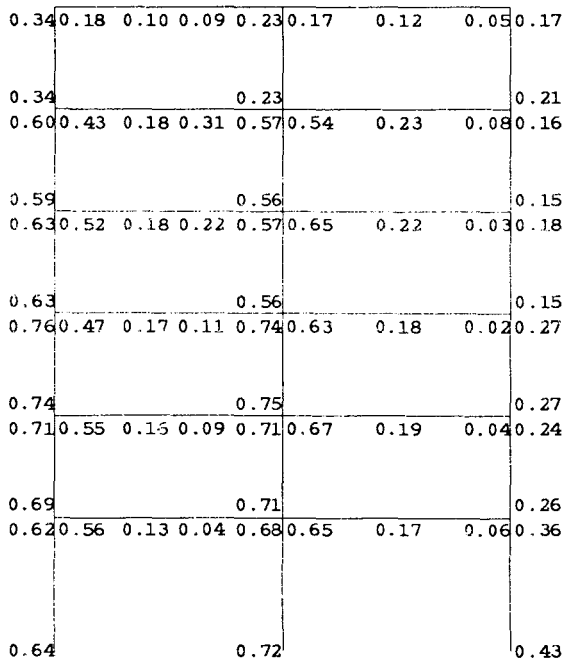
FIG. 2.5 UBC DESIGN STRESS RATIO



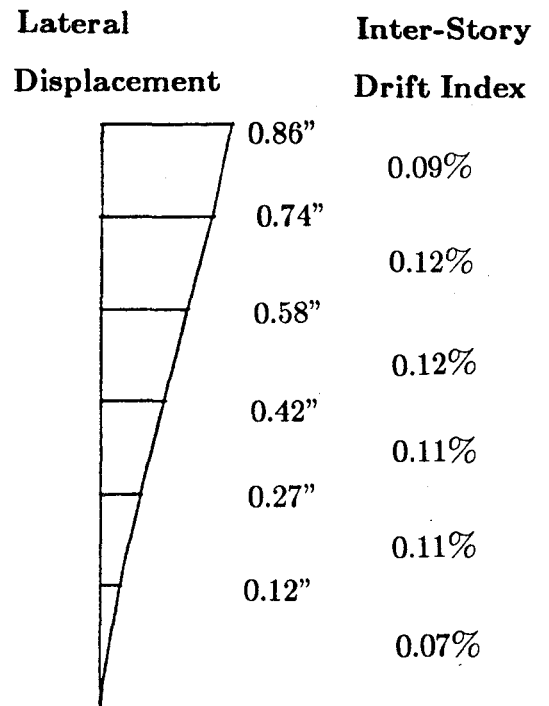
(c) D.L. + L.L. + 1.25E.Q. (k=1.0)



(d) D.L. + L.L. + 1.25E.Q. (k=0.7)

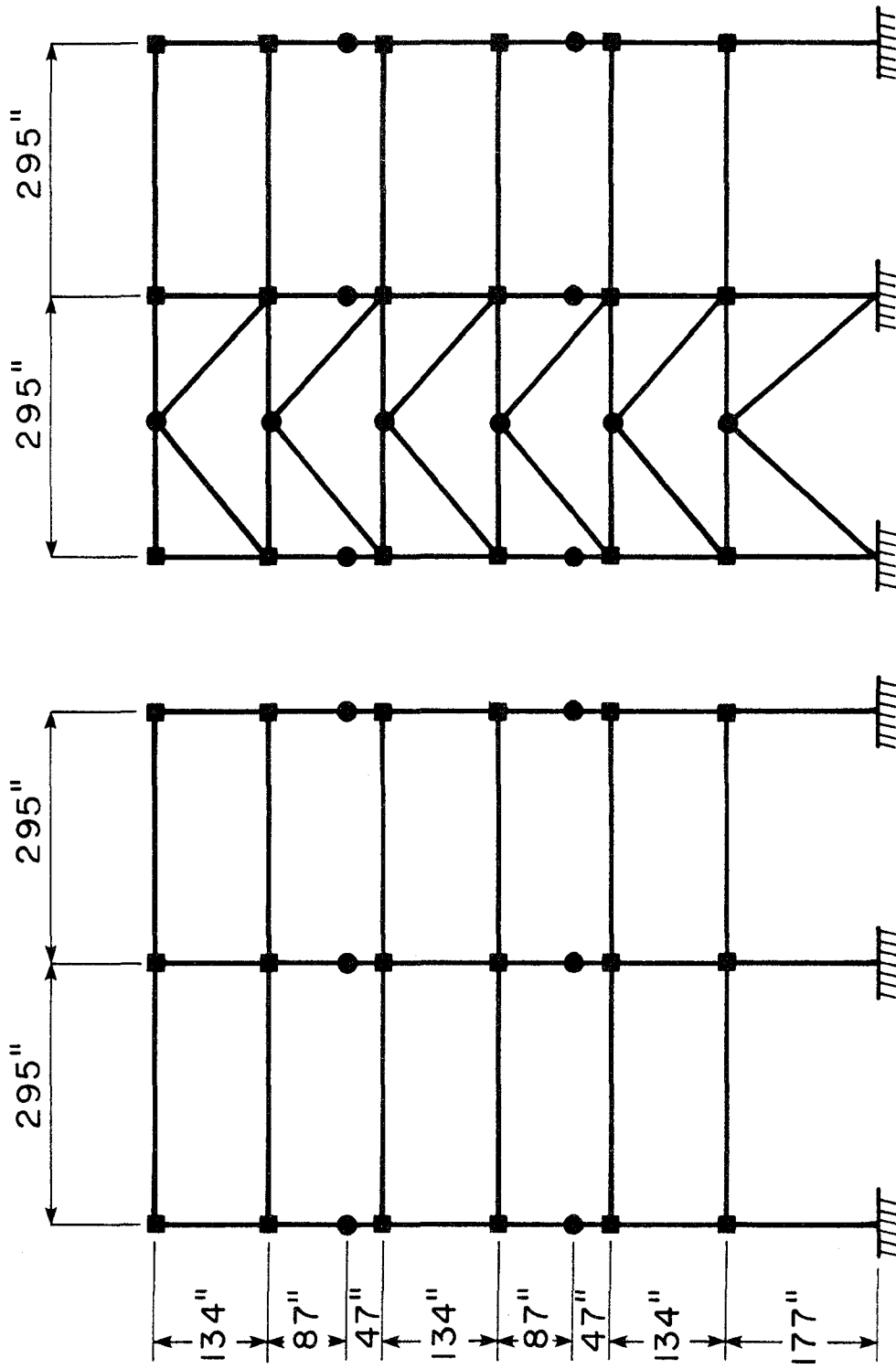


(e) D.L. + L.L. + 0.25E.Q.



(f) Lateral Displacement and Inter-story Drift Index

FIG. 2.5 UBC DESIGN STRESS RATIO (CONTINUED)

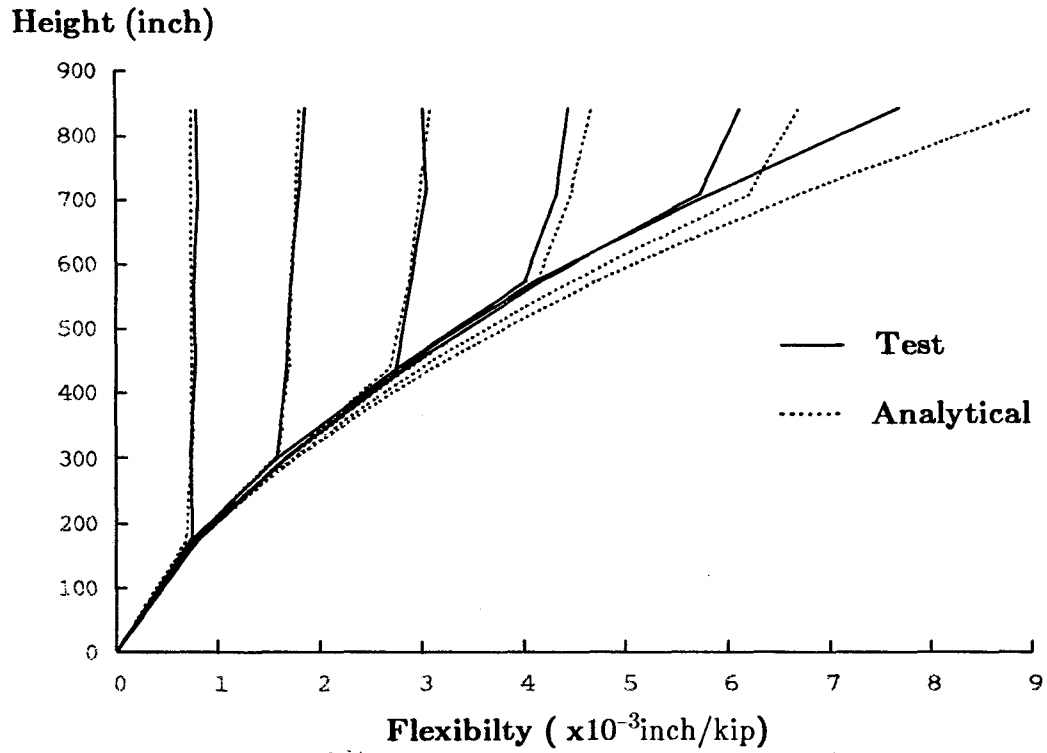


(a) Frame A & C

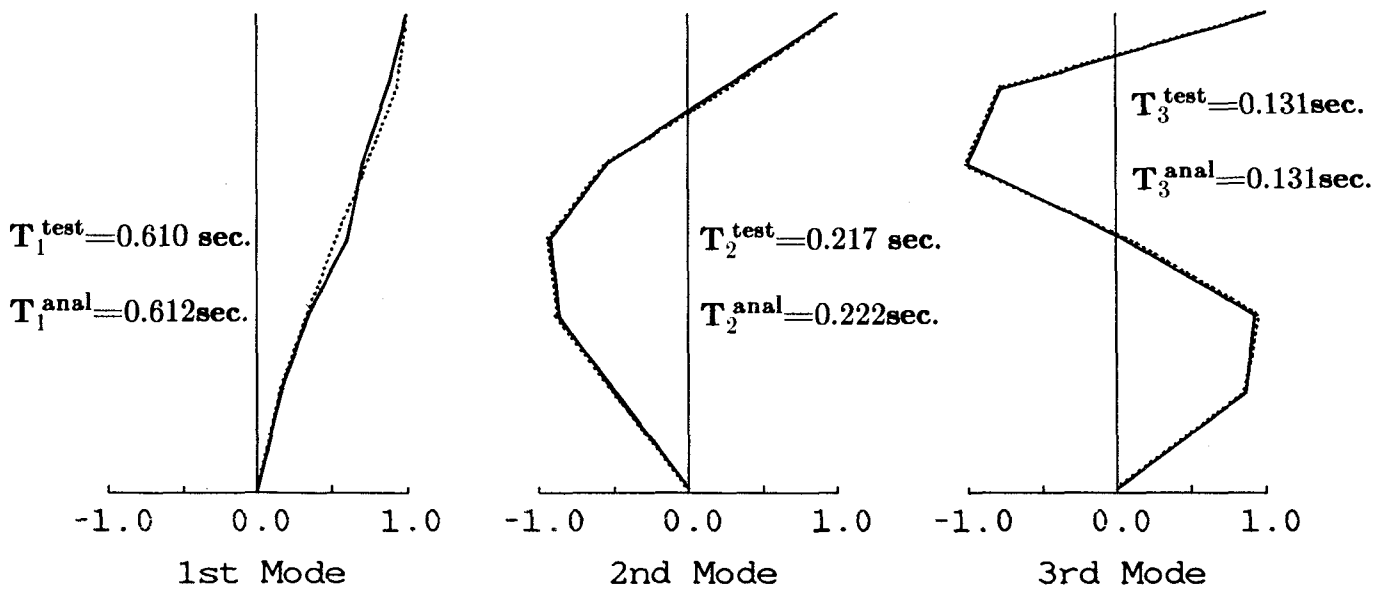
(b) Frame

- Nodal Point
- Nodal Point with Finite Size

FIG. 3.1 MATHEMATICAL MODEL OF THE PROTOTYPE STRUCTURE



(a) Flexibility Profiles



(b) Mode Shapes

FIG. 3.2 PROTOTYPE FLEXIBILITY AND MODE SHAPES

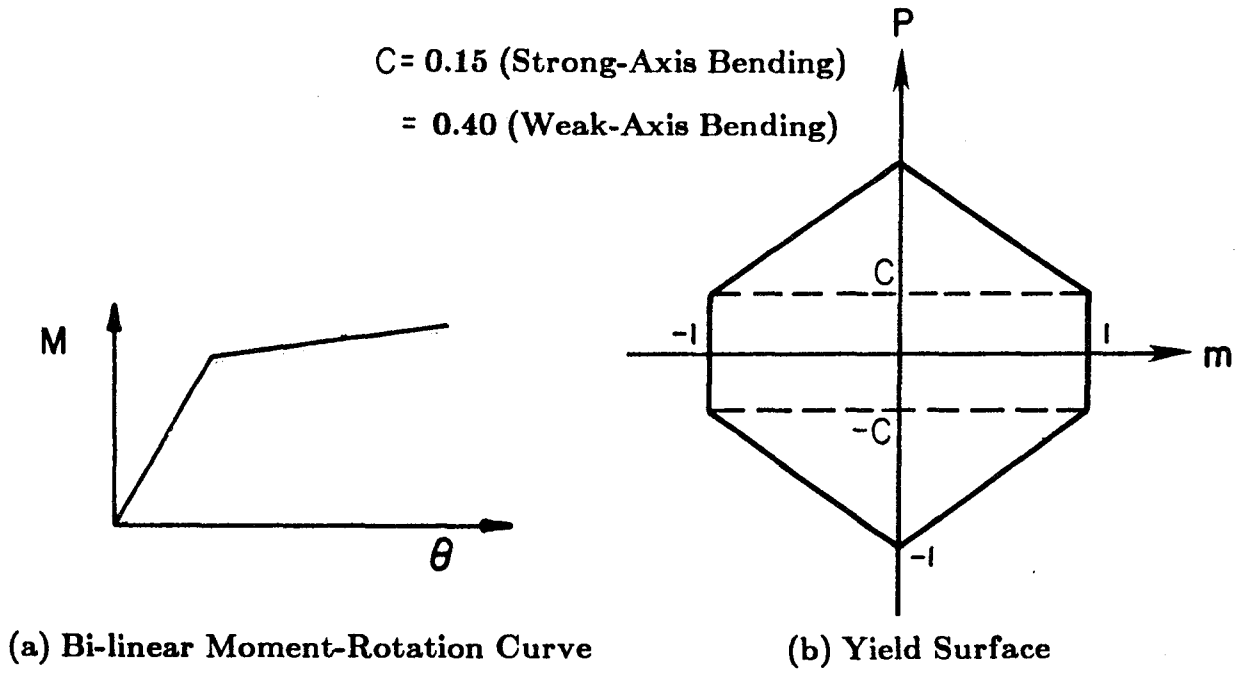


FIG. 3.3 MATHEMATICAL MODEL OF COLUMN

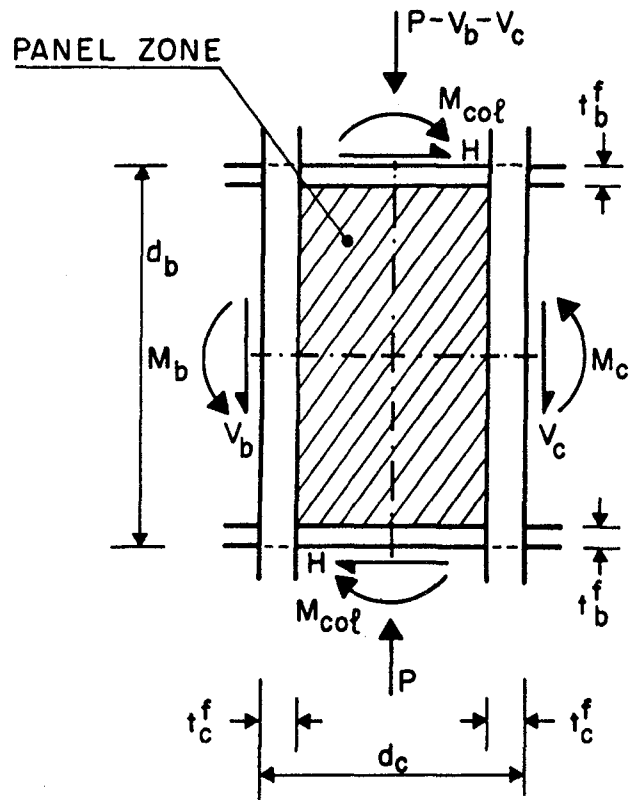
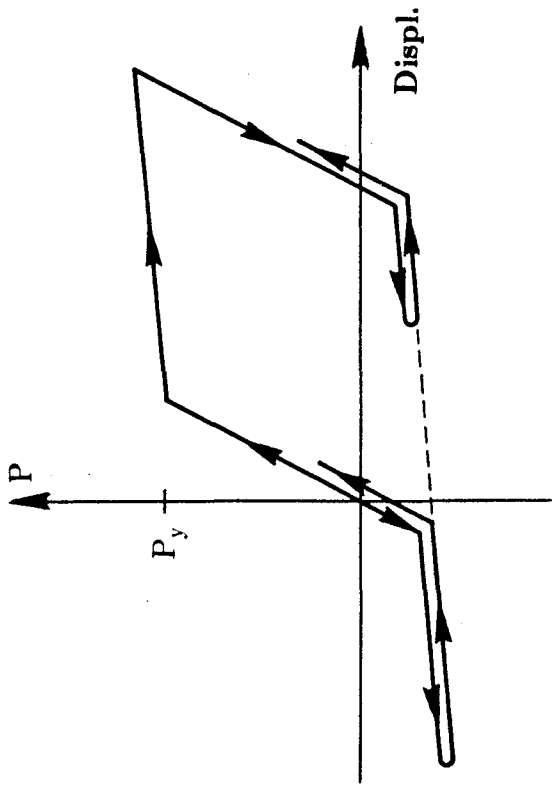
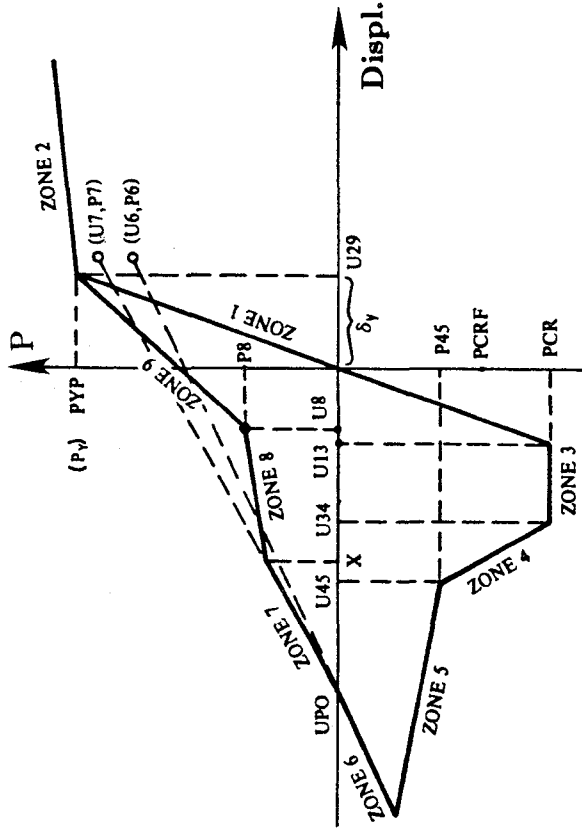


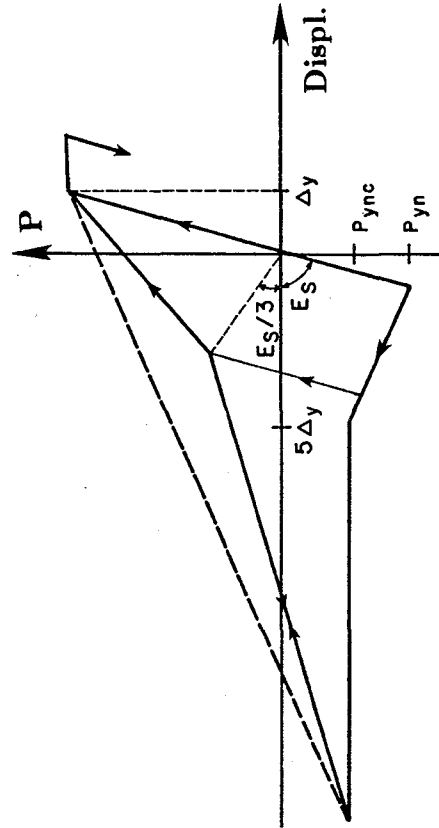
FIG. 3.4 GIRDER-COLUMN JOINT PANEL ZONE



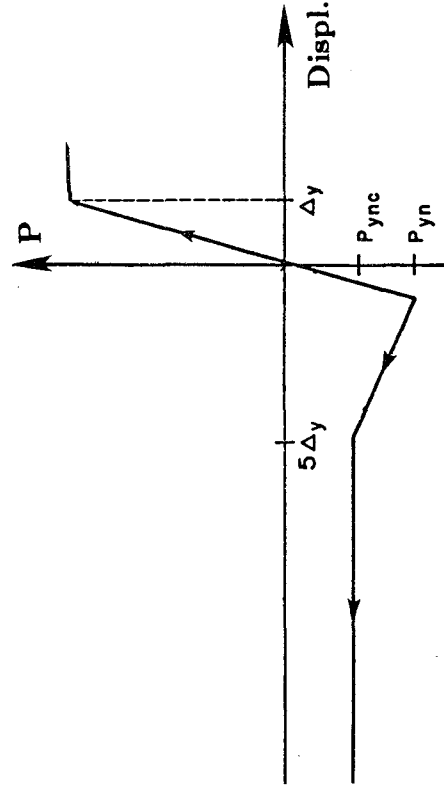
(a) Yield in Tension, Buckling in Compression



(b) Maison's Model



(c) Jain's Model



(d) Simplified Model for Step-by-Step Analysis

FIG. 3.5 BRACE BUCKLING MODEL

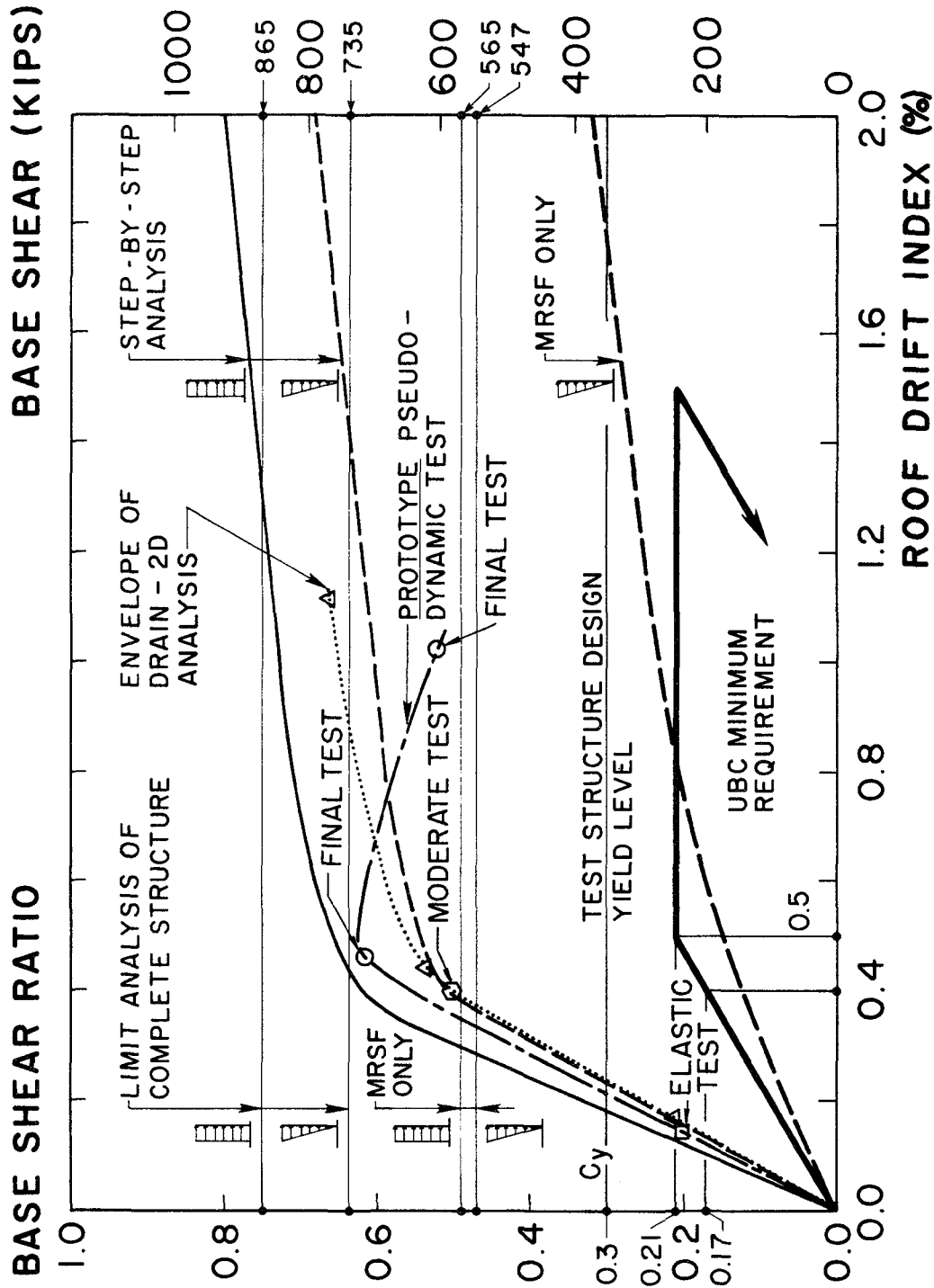
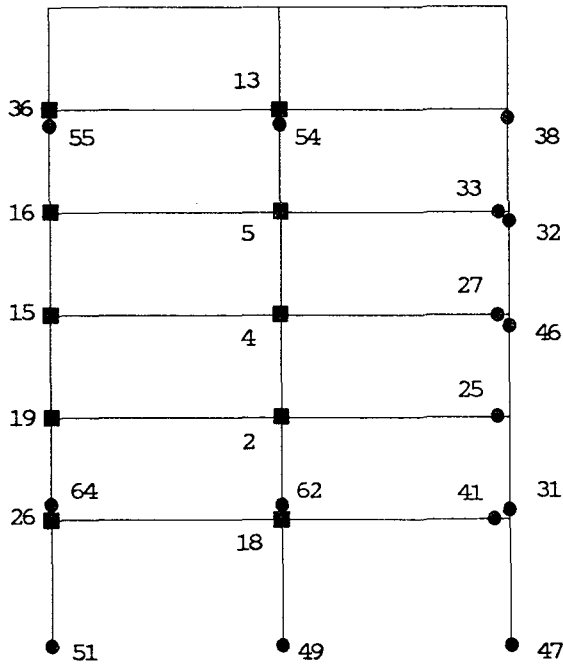
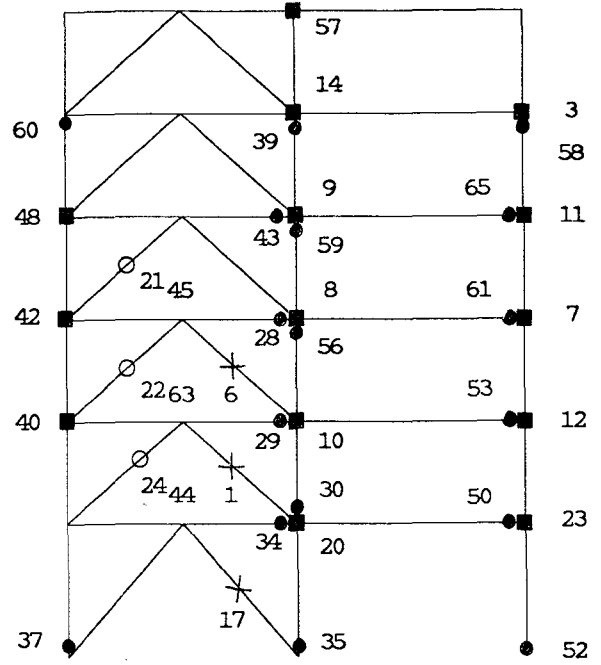


FIG. 3.6 ENVELOPES OF PROTOTYPE ROOF DRIFT INDEX VERSUS
BASE SHEAR RATIO

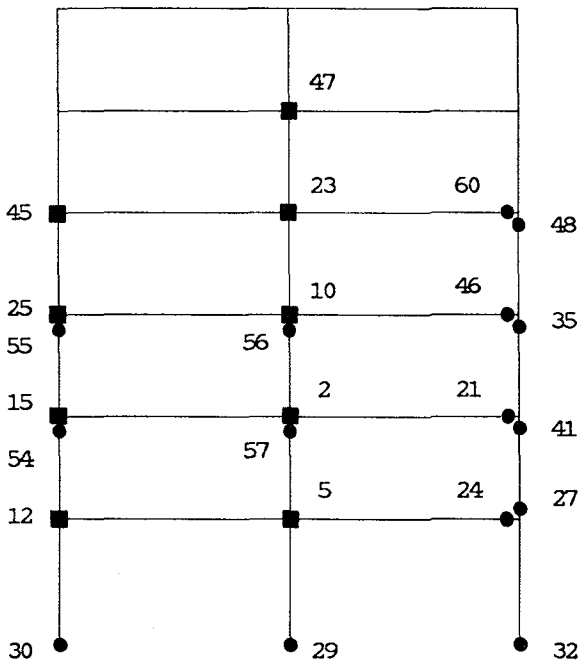


Frame A or C

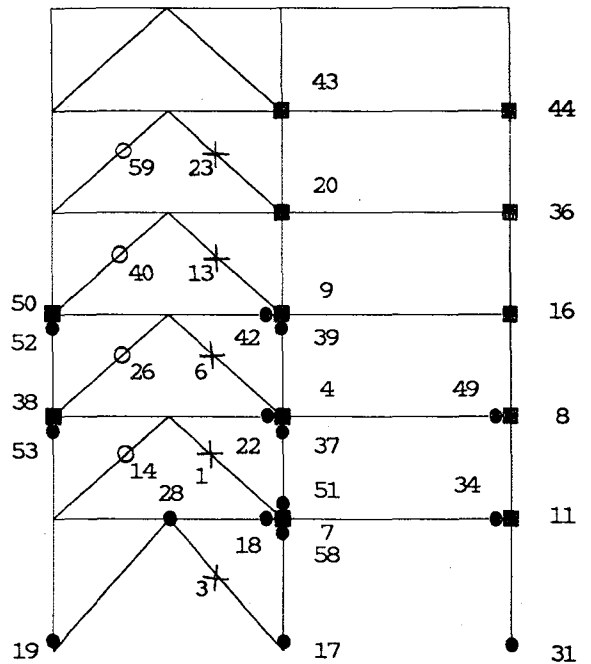


Frame B

(a) Triangular Load Pattern



Frame A or C



Frame B

(b) Uniform Load Pattern

● flexural member plastic hinge

○ brace yielding

■ panel zone plastic hinge

× brace buckling

FIG. 3.7 STEP-BY-STEP ANALYSIS HINGE FORMATION SEQUENCE

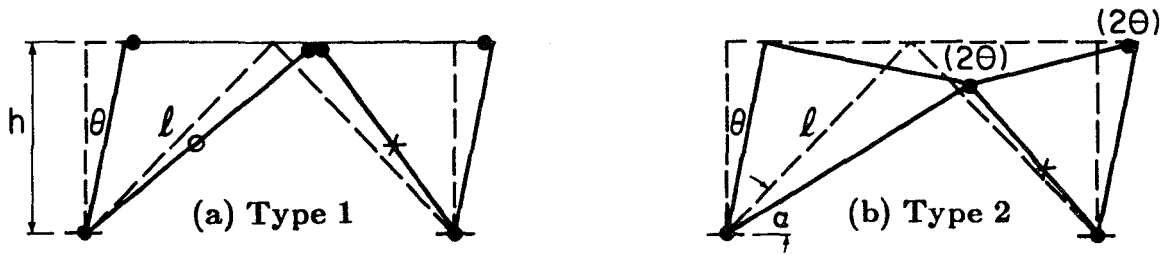


FIG. 3.8 POSSIBLE SWAY MECHANISMS

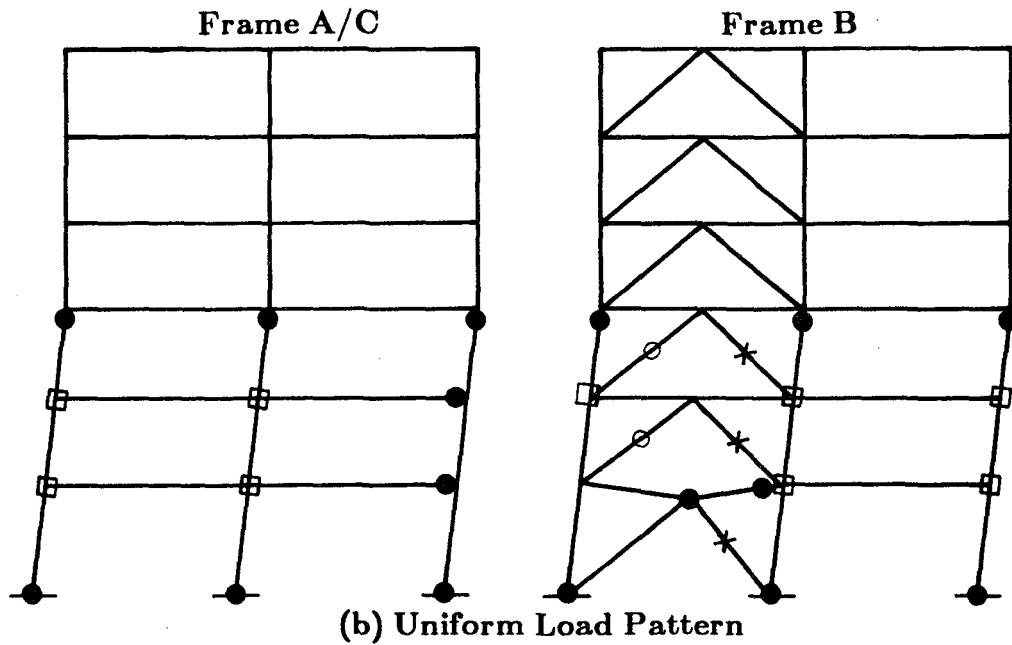
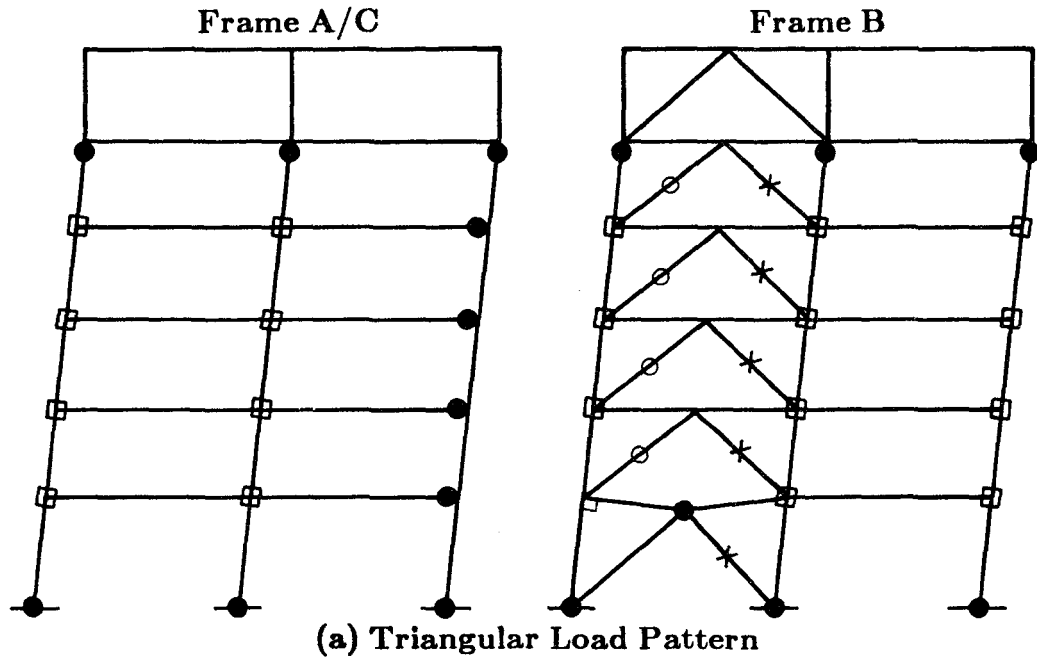
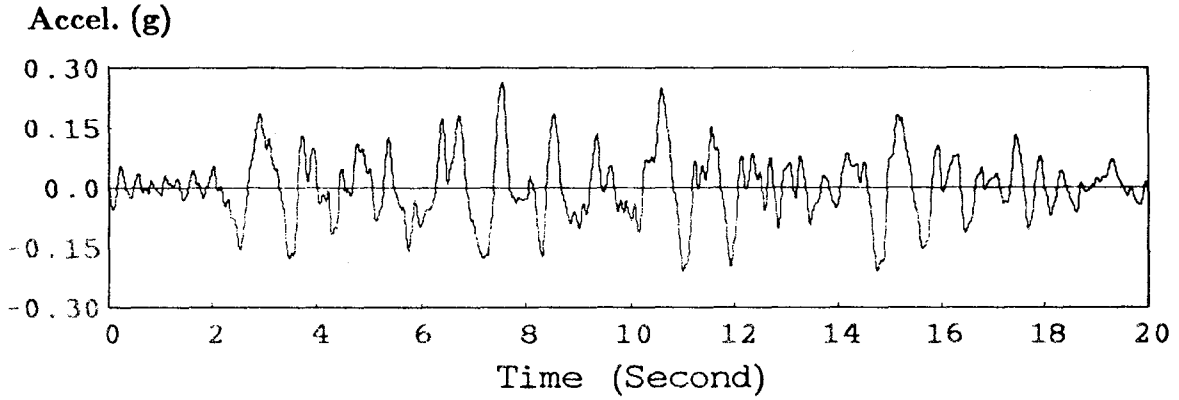
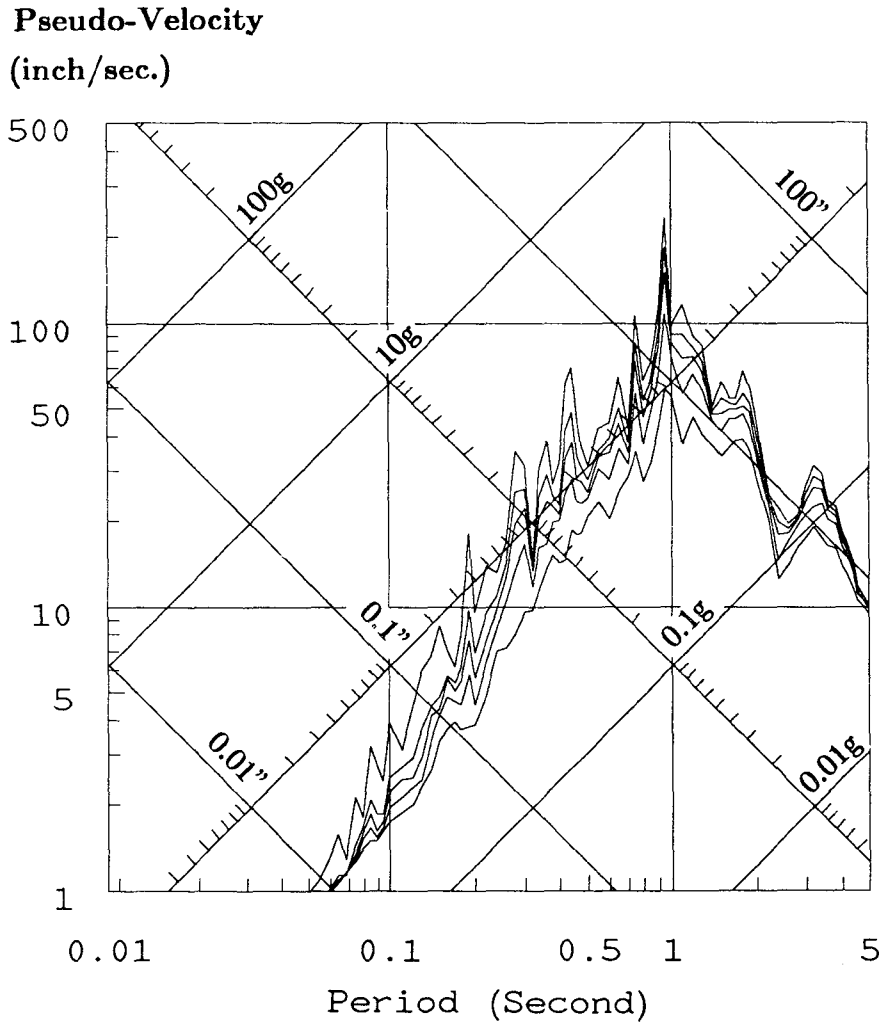


FIG. 3.9 KINEMATICALLY ADMISSIBLE FIELDS



(a) Acceleration Time History



(b) Linear Elastic Response Spectra (0,0.5,1,2,5 Percent Damping)

FIG. 3.10 1978 MIYAGI-KEN-OKI EARTHQUAKE RECORD (N-S)

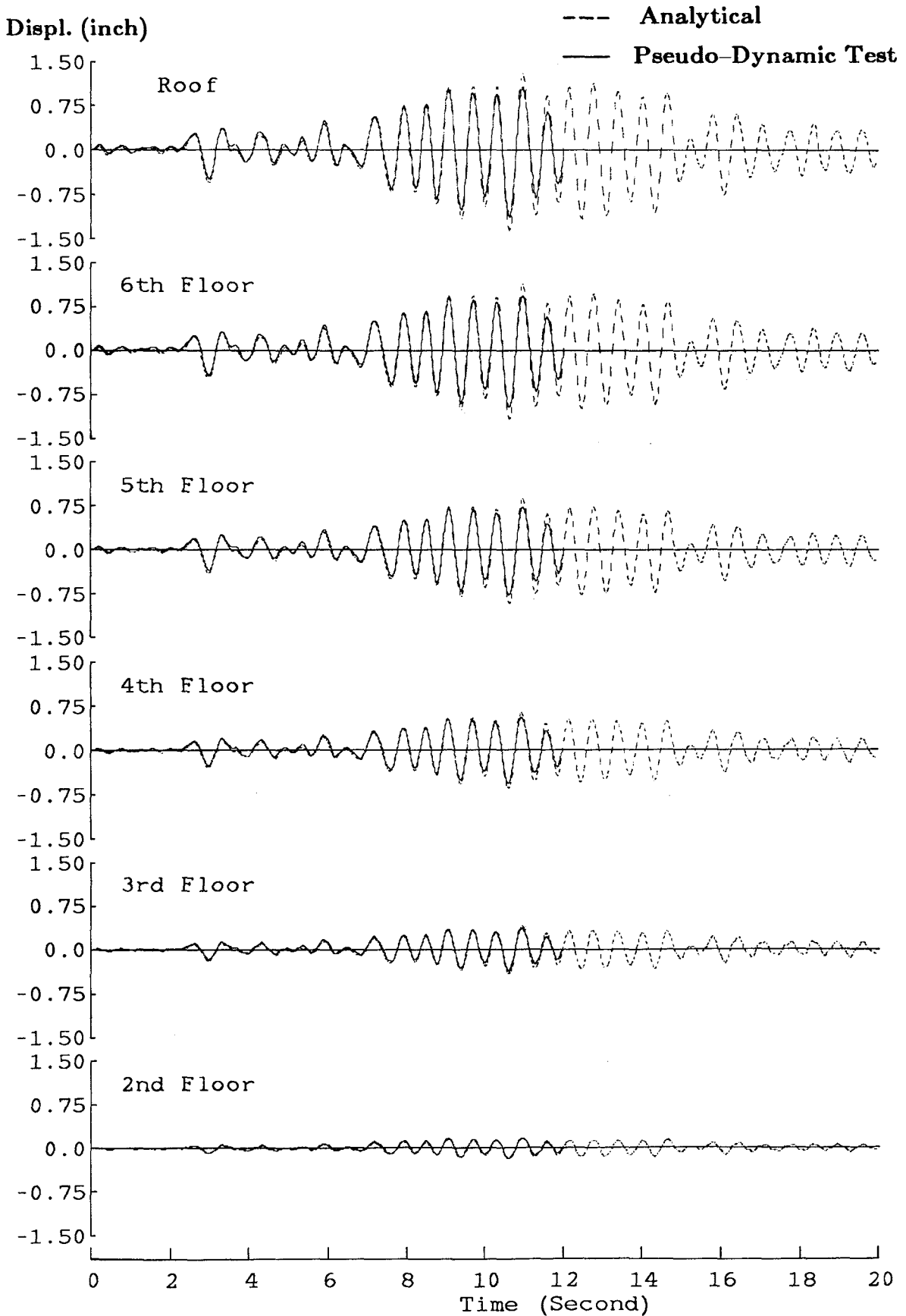


FIG. 3.11 ELASTIC-3 TEST RELATIVE DISPLACEMENT TIME HISTORY

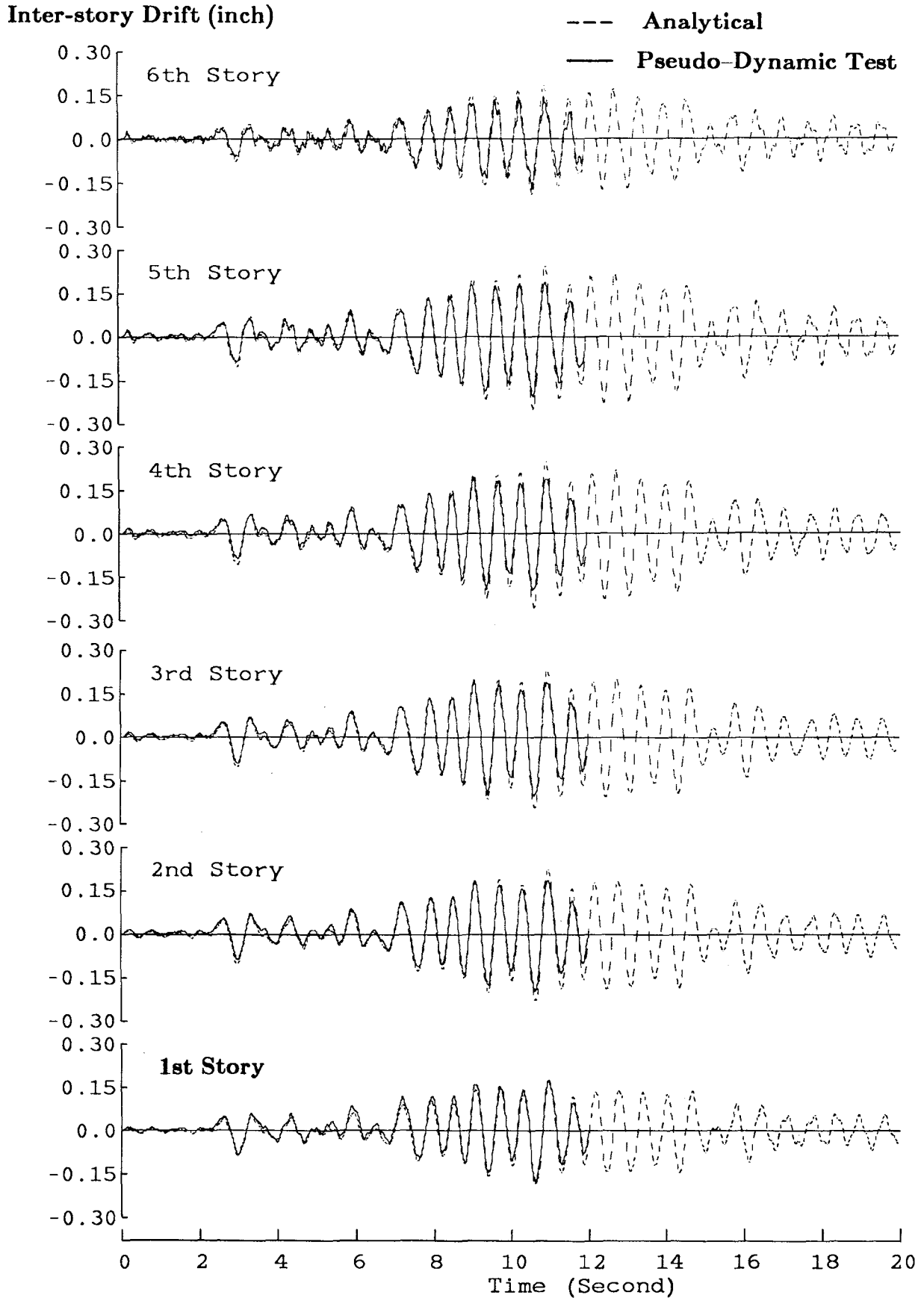


FIG. 3.12 ELASTIC-3 TEST INTER-STORY DRIFT TIME HISTORY

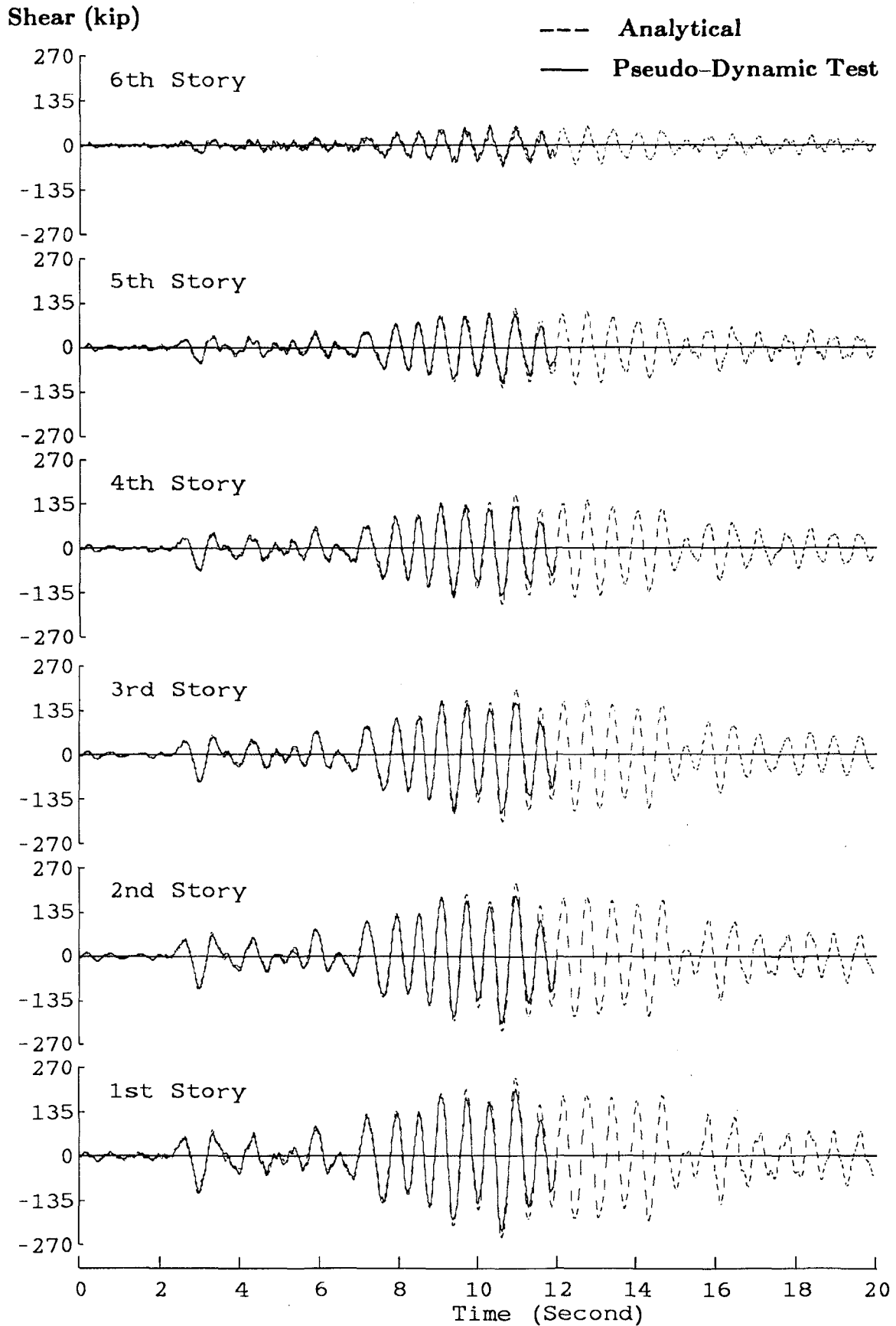


FIG. 3.13 ELASTIC-3 TEST STORY SHEAR TIME HISTORY

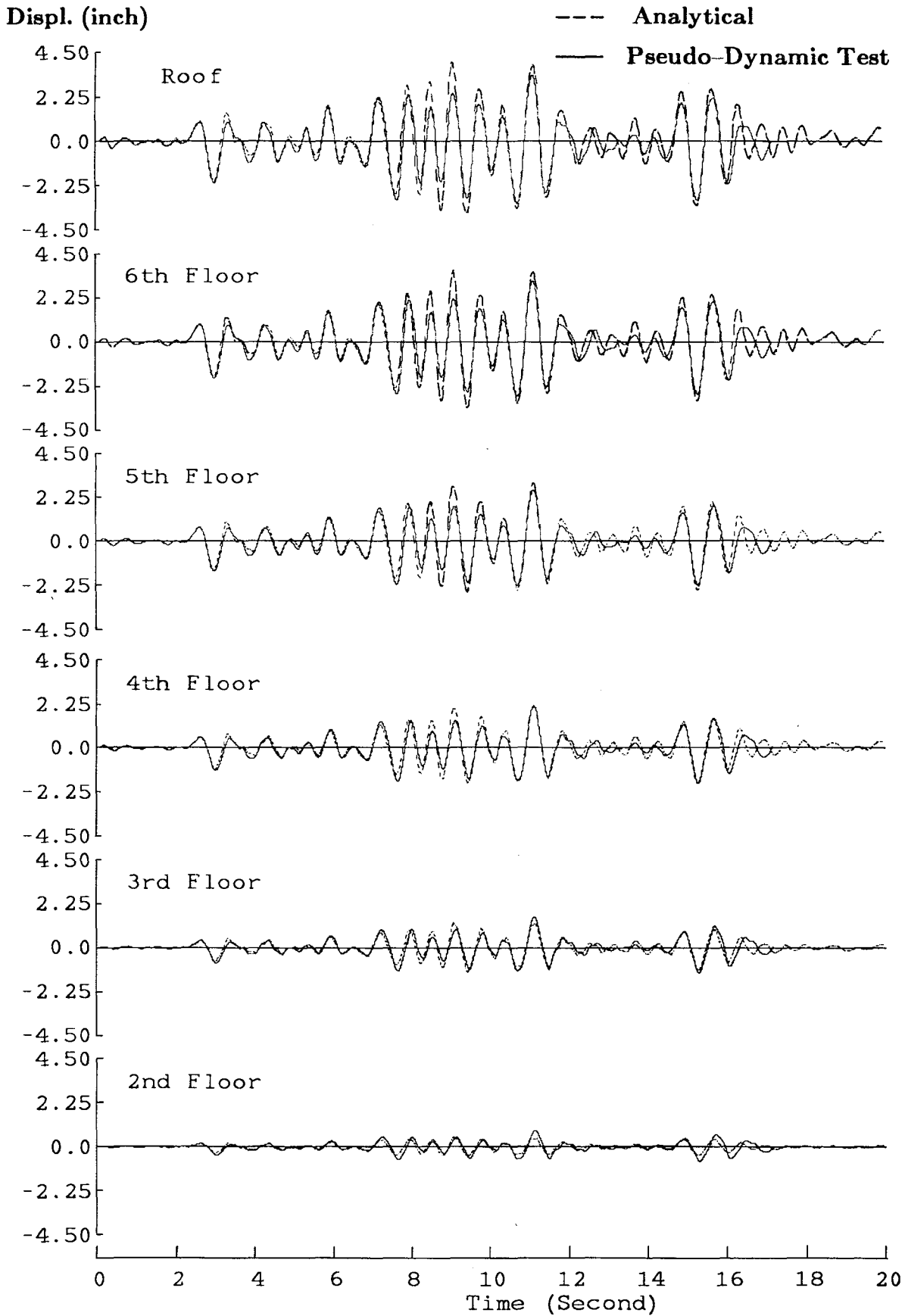


FIG. 3.14 MODERATE TEST RELATIVE DISPLACEMENT TIME HISTORY

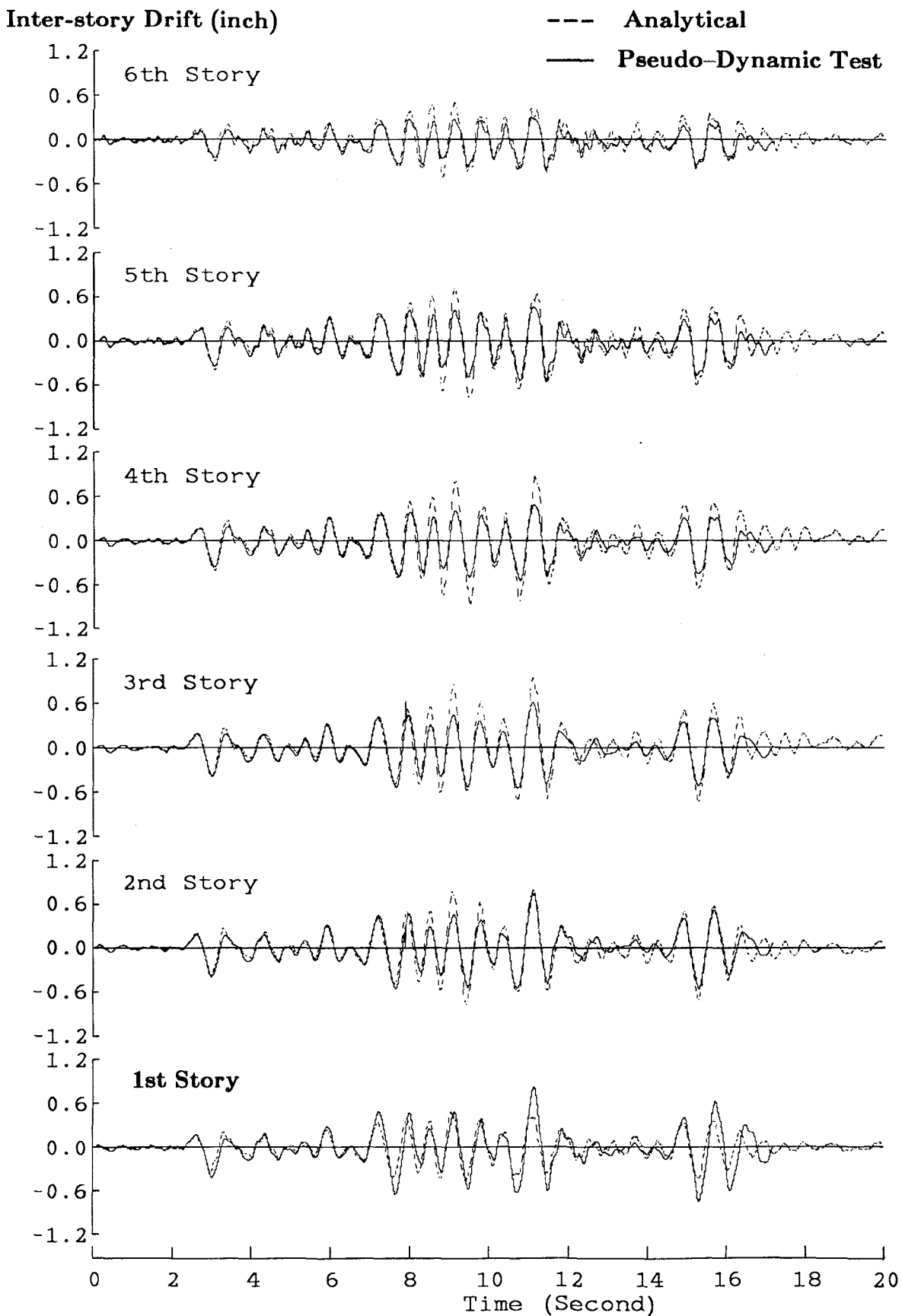


FIG. 3.15 MODERATE TEST INTER-STORY DRIFT TIME HISTORY

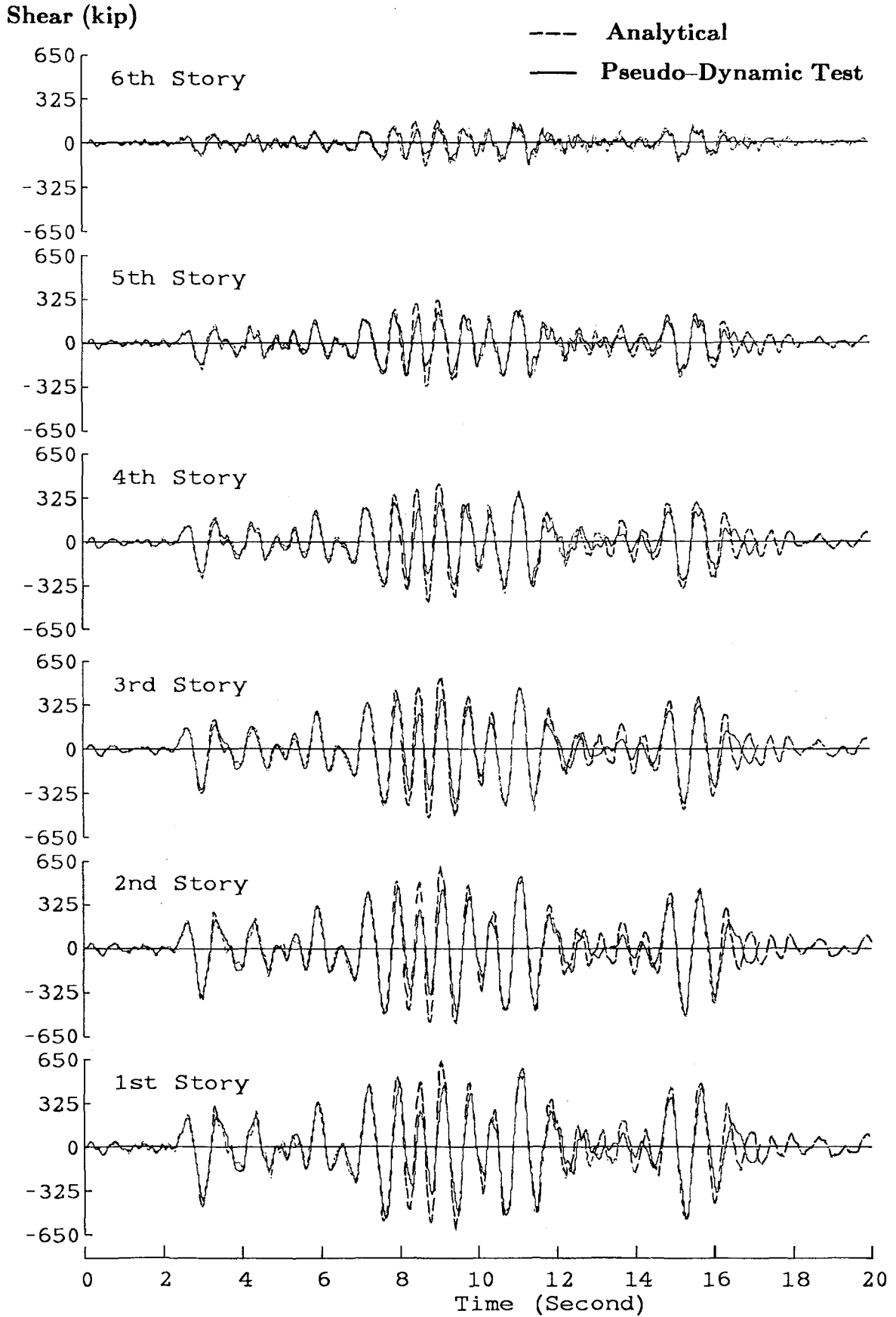
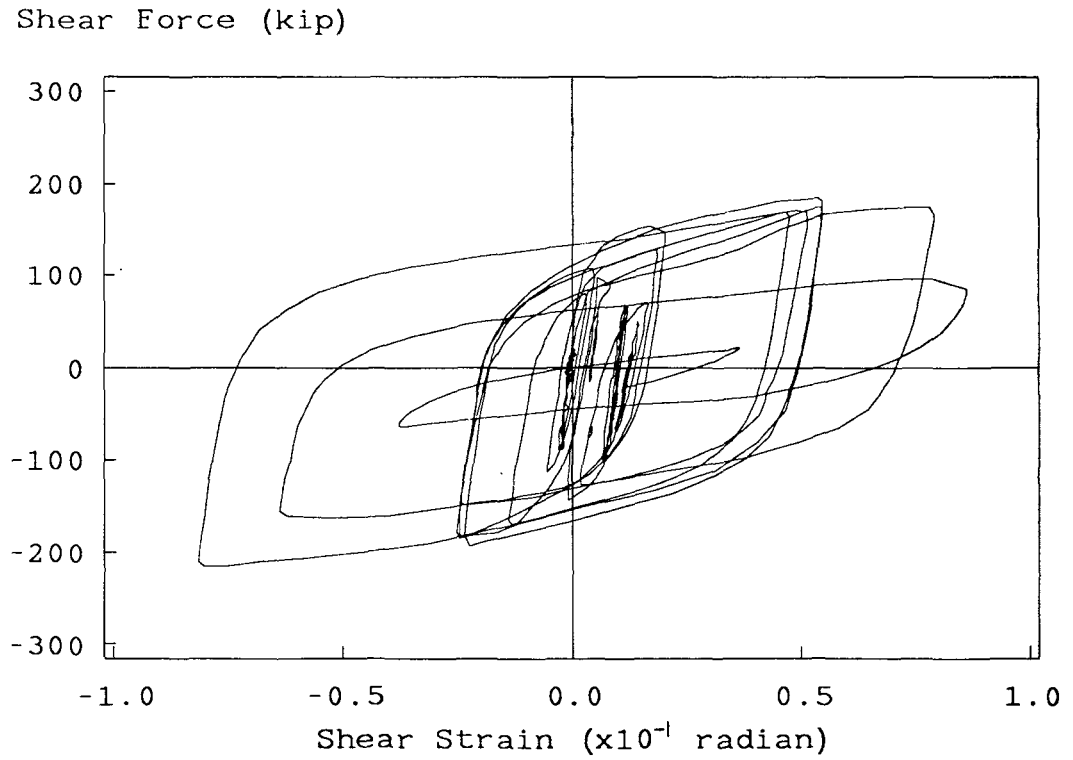


FIG. 3.16 MODERATE TEST STORY SHEAR TIME HISTORY



**FIG. 3.19 FIRST STORY BRACE-GIRDER CONNECTING PANEL
ZONE SHEAR DEFORMATION VERSUS SHEAR FORCE CURVE
(MODERATE TEST) [12]**

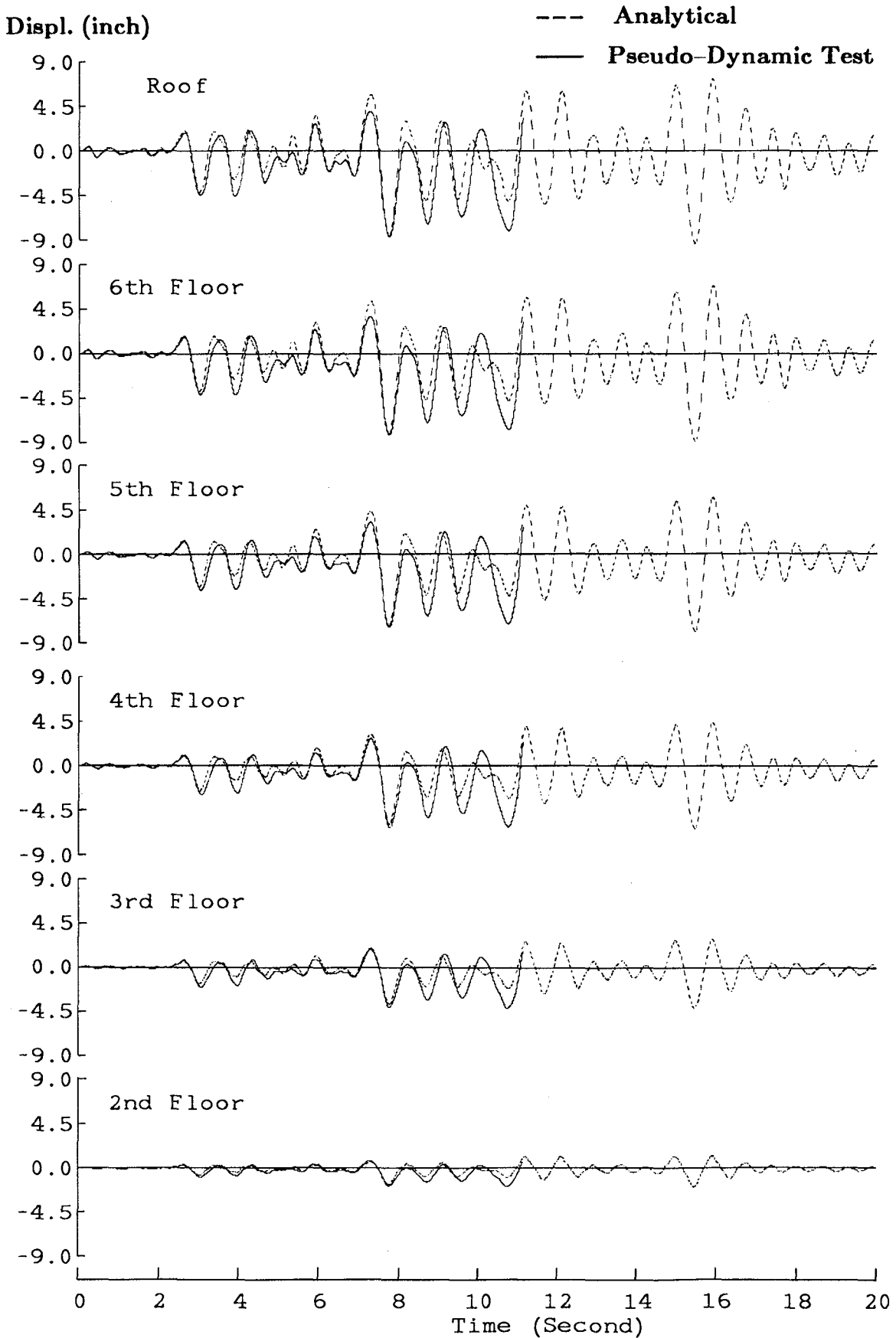


FIG. 3.20 FINAL TEST RELATIVE DISPLACEMENT TIME HISTORY

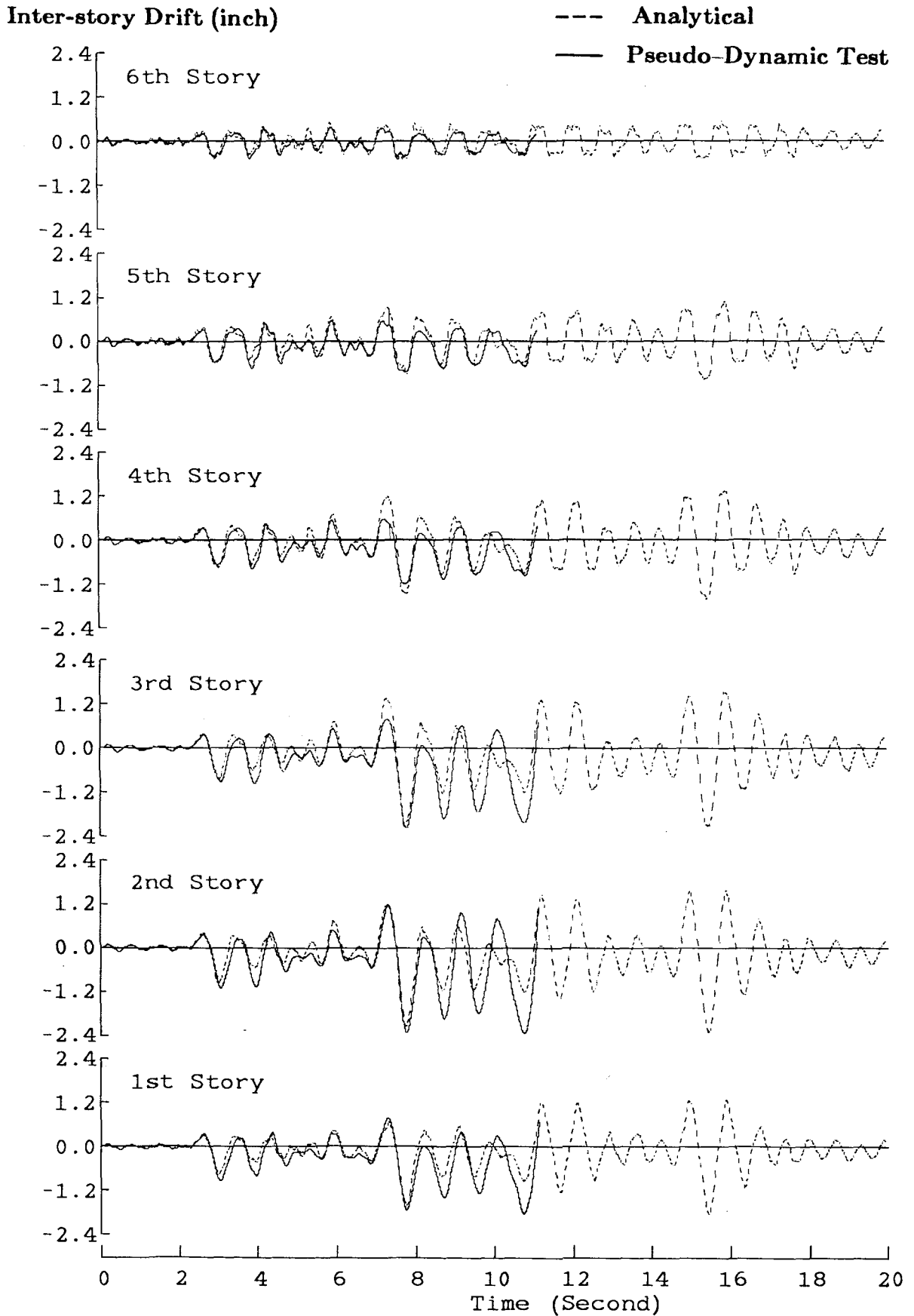


FIG. 3.21 FINAL TEST INTER-STORY DRIFT TIME HISTORY

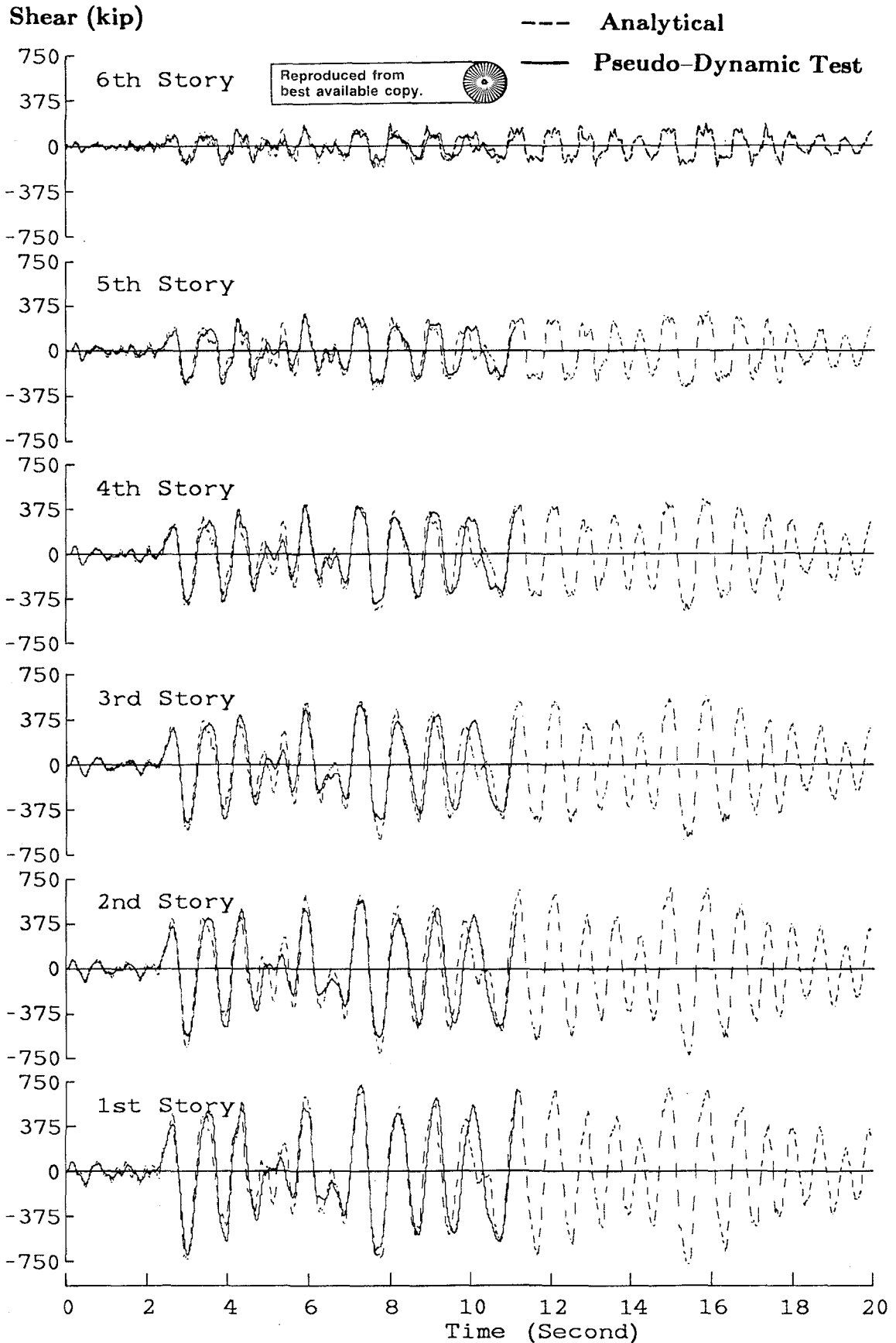


FIG. 3.22 FINAL TEST STORY SHEAR TIME HISTORY

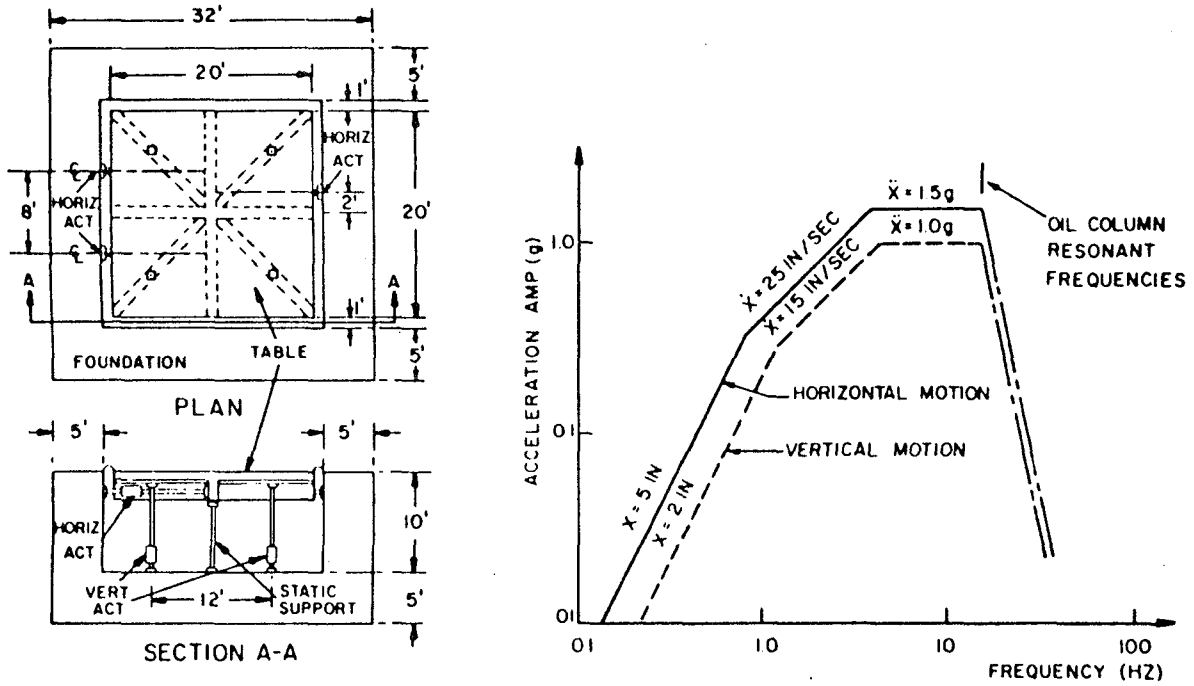


FIG. 4.1 LIMITATION ON DYNAMIC PERFORMANCE OF THE SHAKING TABLE [25]

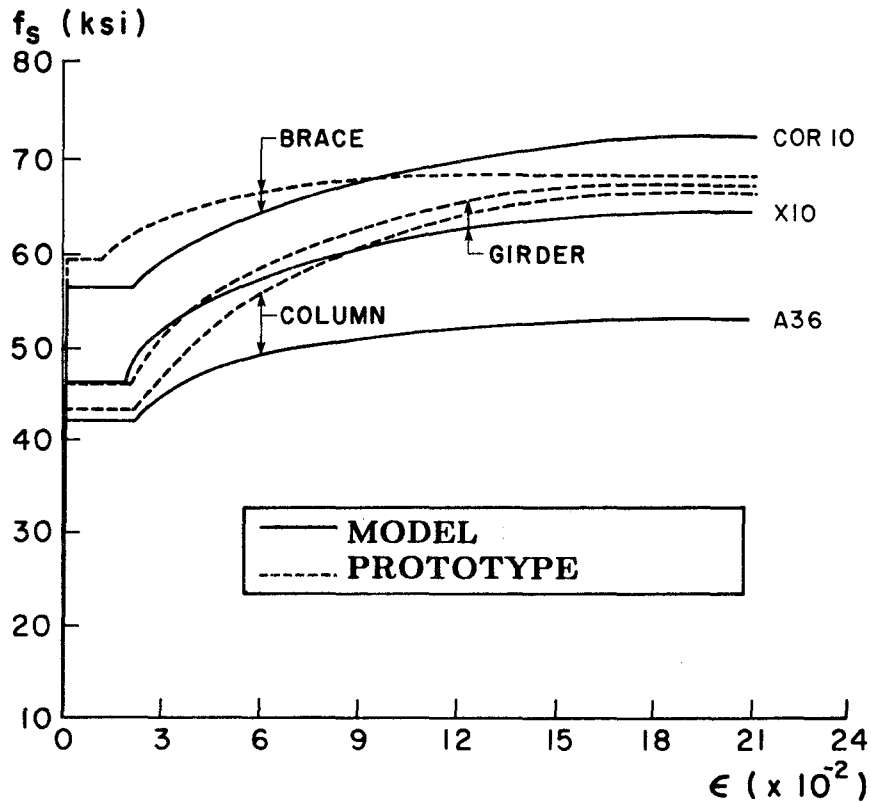


FIG. 4.3 MEAN STEEL STRESS-STRAIN RELATIONSHIPS

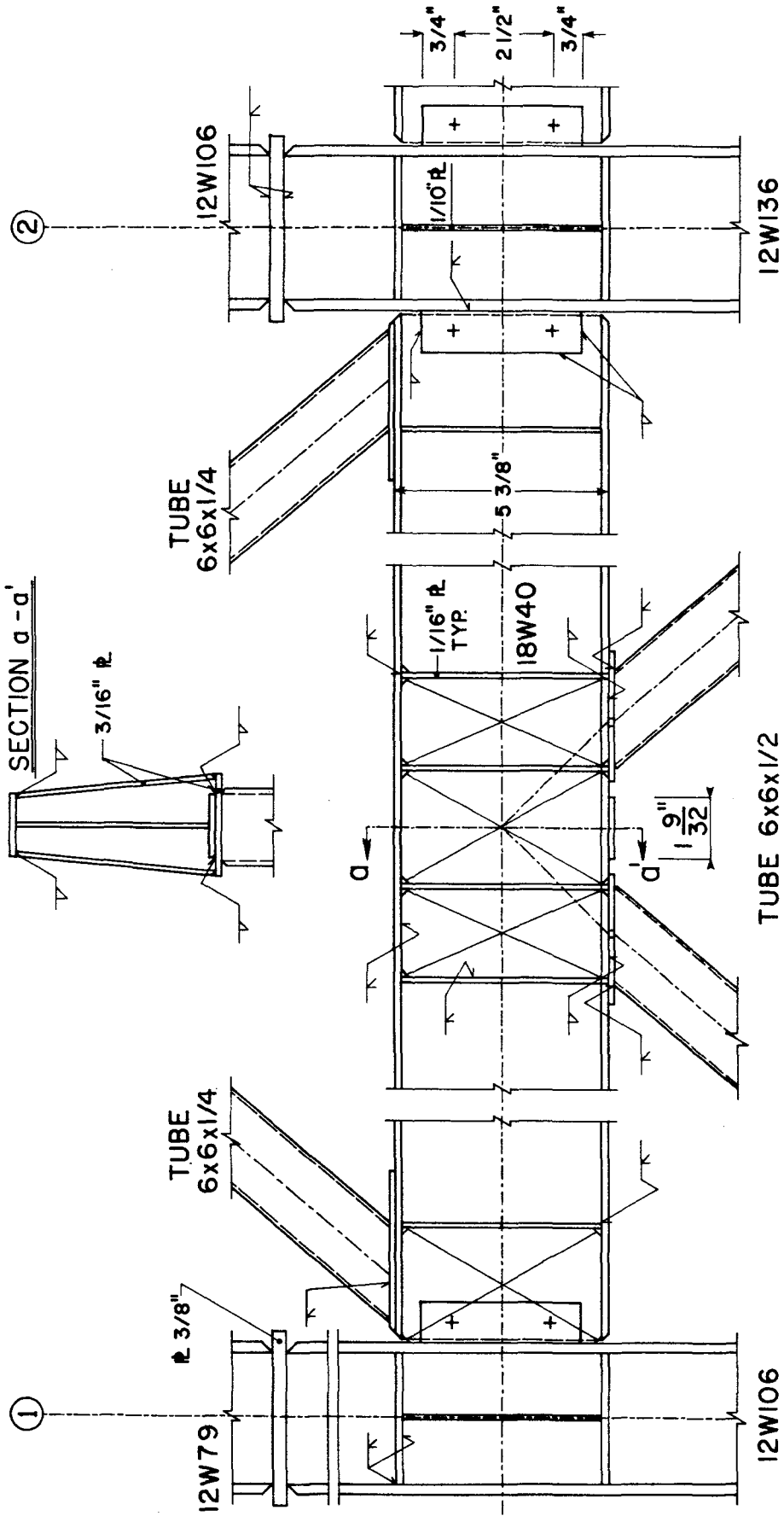


FIG. 4.2 TYPICAL CONNECTION DETAILS OF THE MODEL

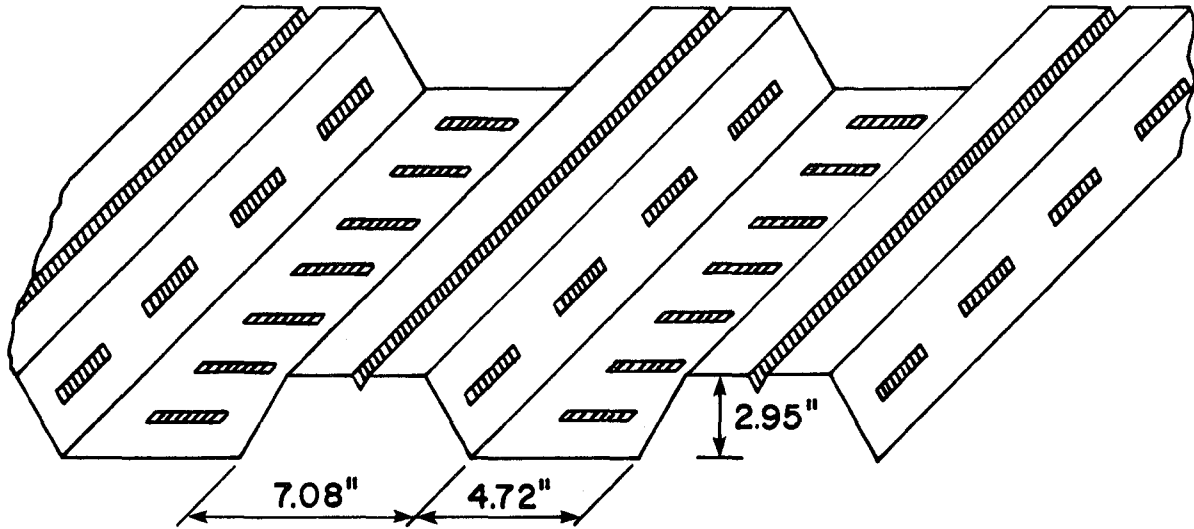


FIG. 4.4 INDENTATION PATTERN IF THE PROTOTYPE METAL DECK

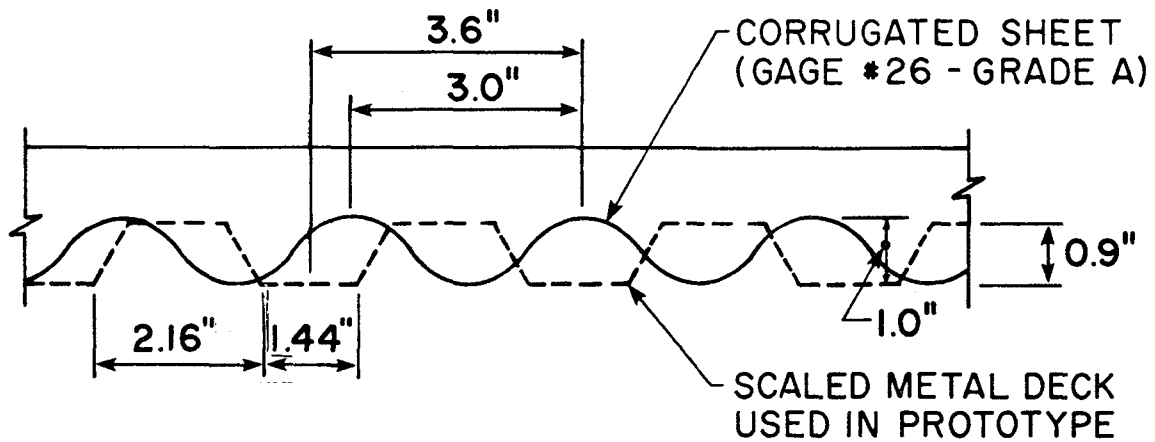
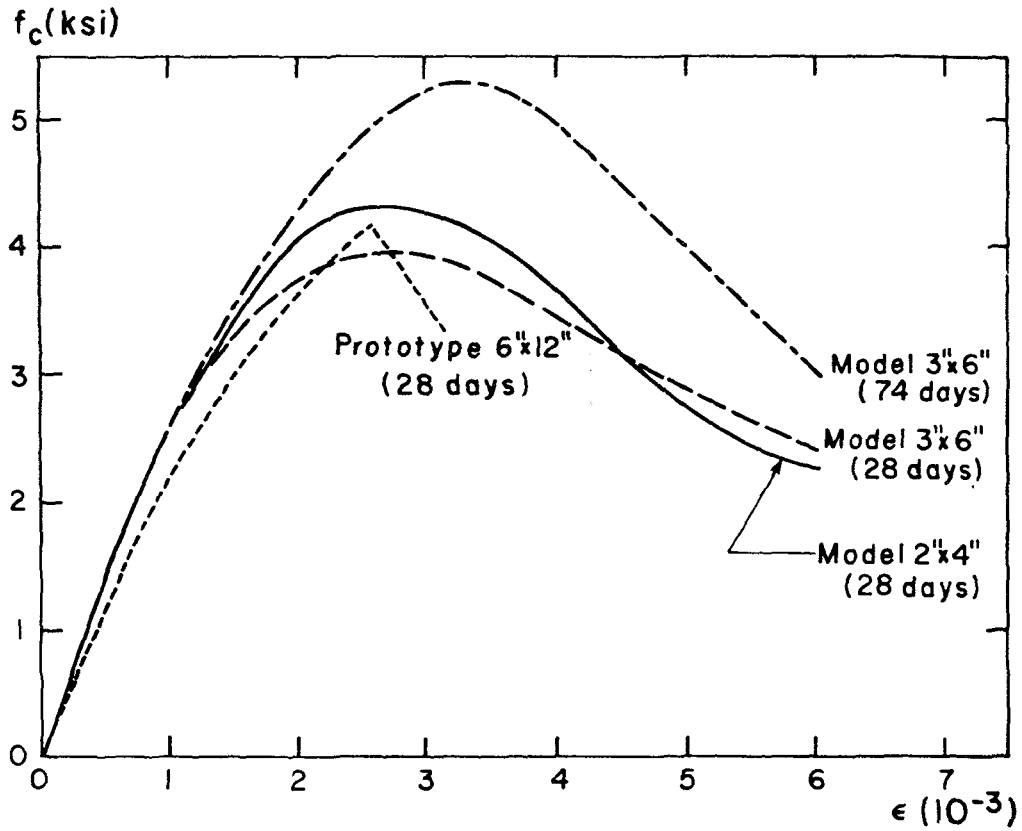
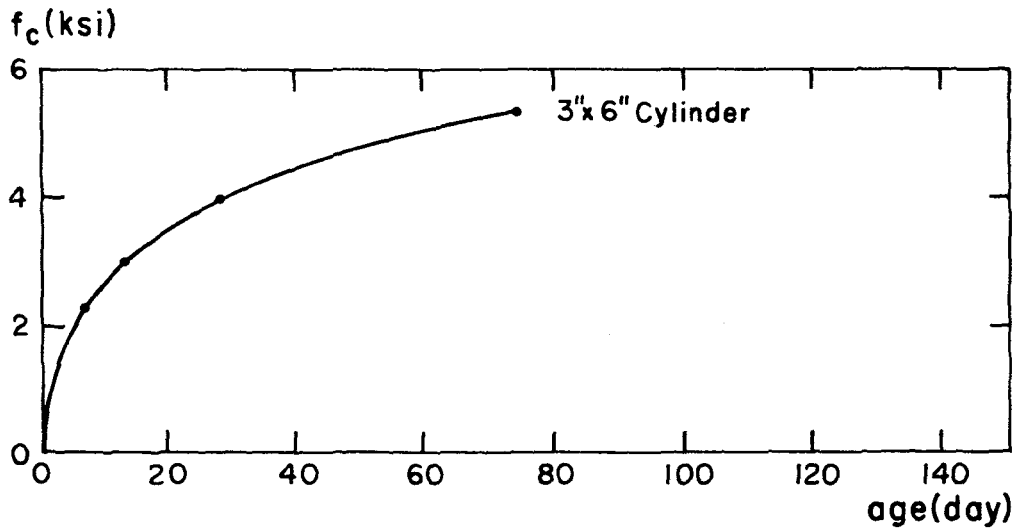


FIG. 4.5 MODEL AND SCALED PROTOTYPE METAL DECK PROFILES



(a) Typical Stress Versus Strain Curves



(b) Variation of Concrete Compressive Strength with Age

FIG. 4.6 MODEL CONCRETE STRESS-STRAIN RELATIONSHIPS

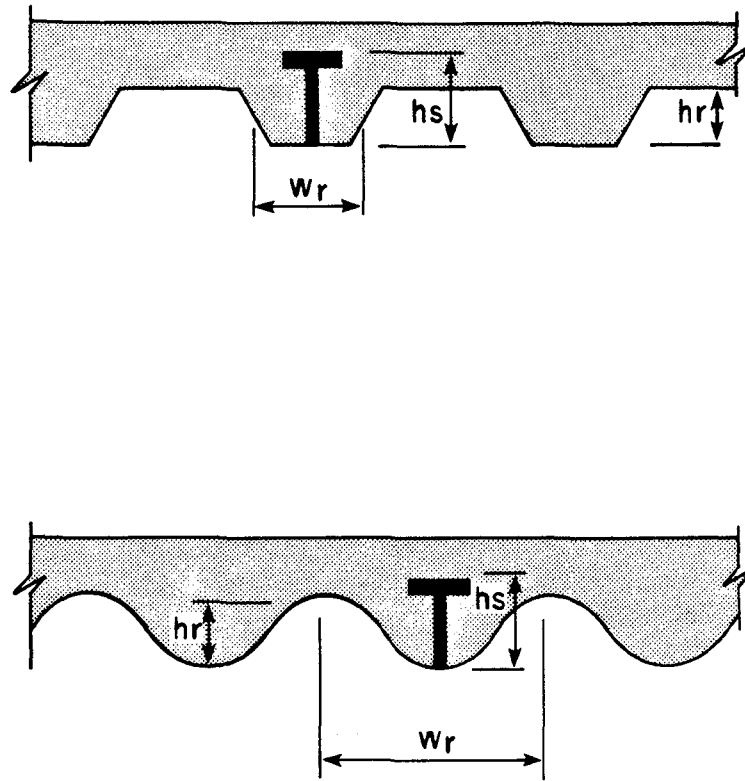
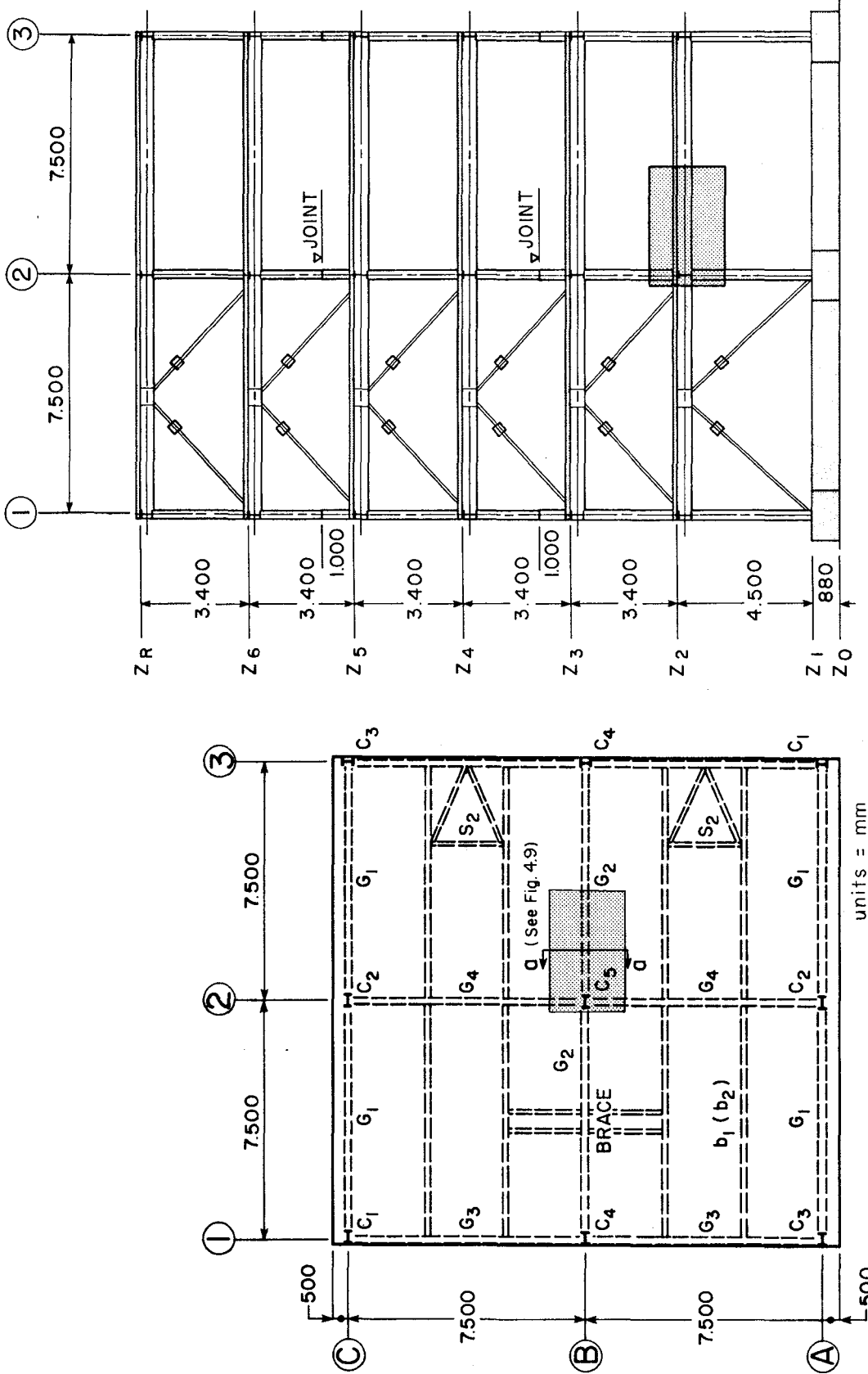


**FIG. 4.7 DEFINITION OF RIB HEIGHT AND WIDTH FOR
CALCULATING REDUCTION FACTOR**



(a) Steel Test Building Plan

(b) Steel Test Building Elevation

FIG. 4.8 PORTION OF COMPOSITE GIRDER SIMULATED

units = mm

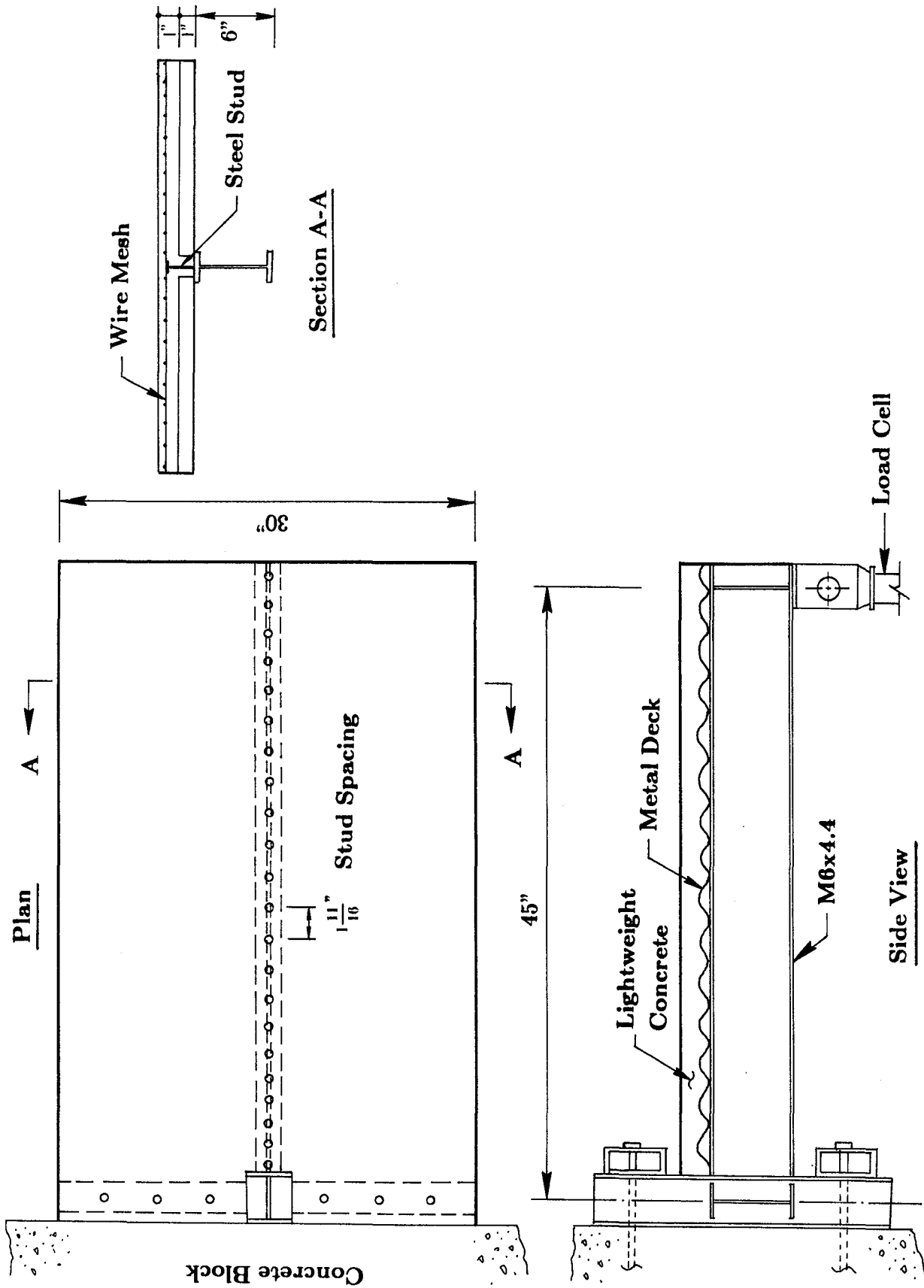


FIG. 4.9 COMPOSITE GIRDER TEST SET-UP

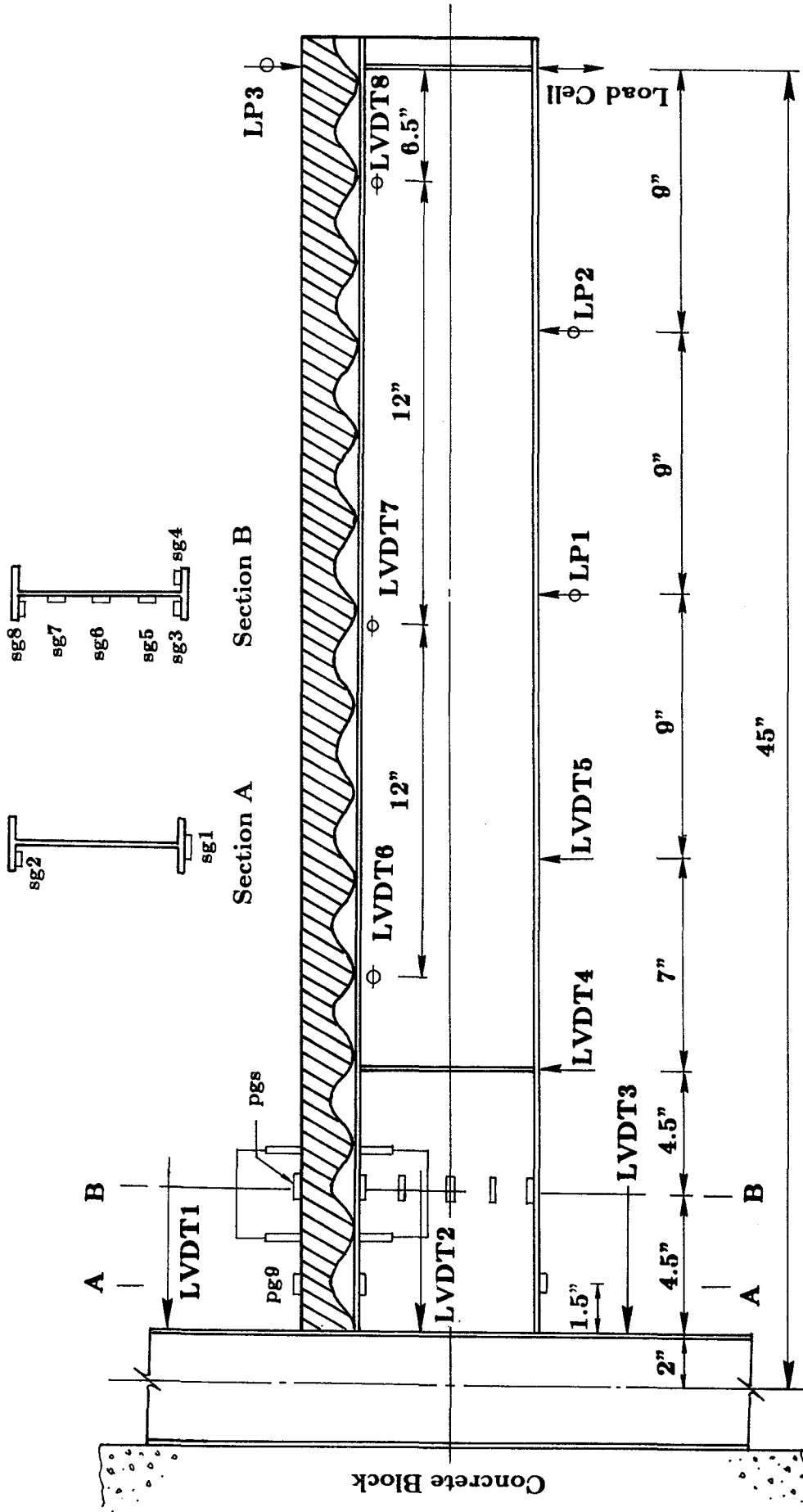


FIG. 4.10 INSTRUMENTATION OF COMPOSITE GIRDER

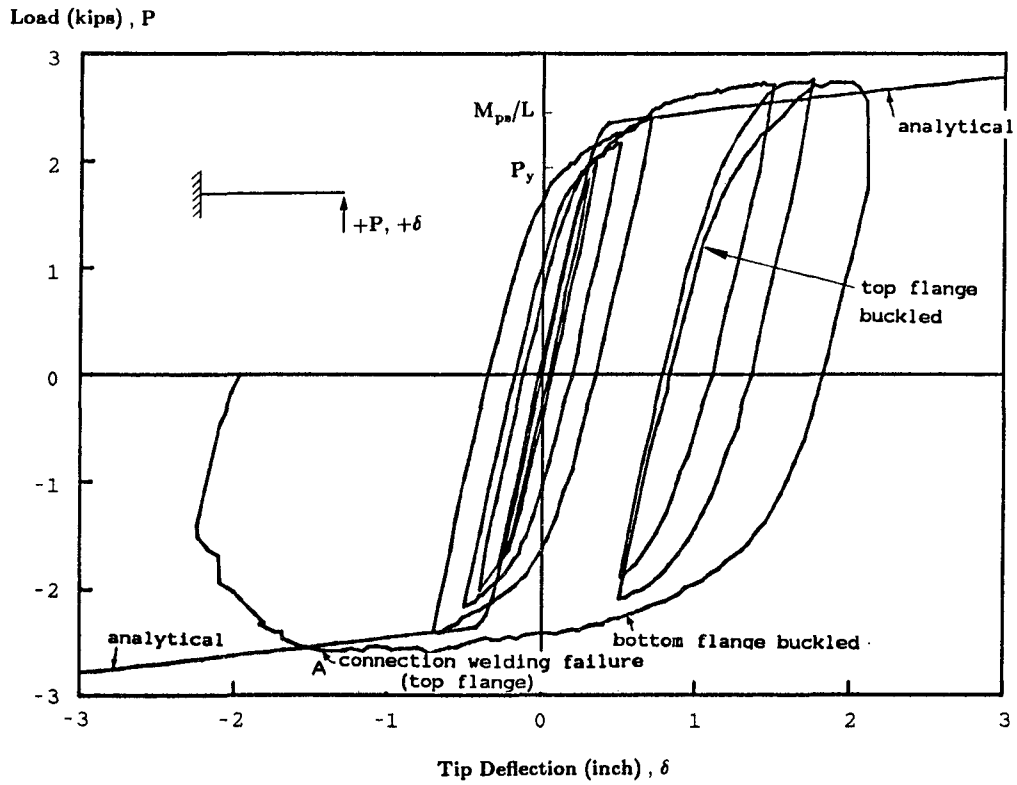


FIG. 4.11 LOAD-TIP DEFLECTION CURVE OF STEEL GIRDER (SG)

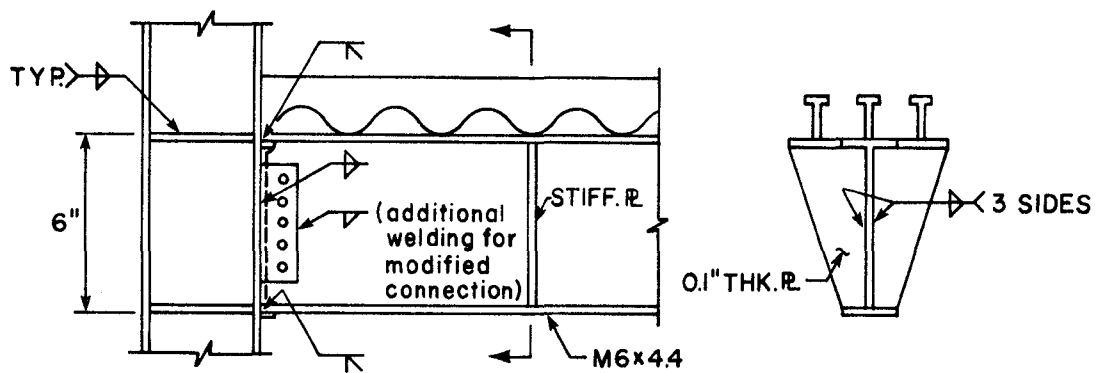


FIG. 4.12 LONGITUDINAL GIRDER-TO-COLUMN CONNECTION
USED IN THE COMPOSITE GIRDER TESTS

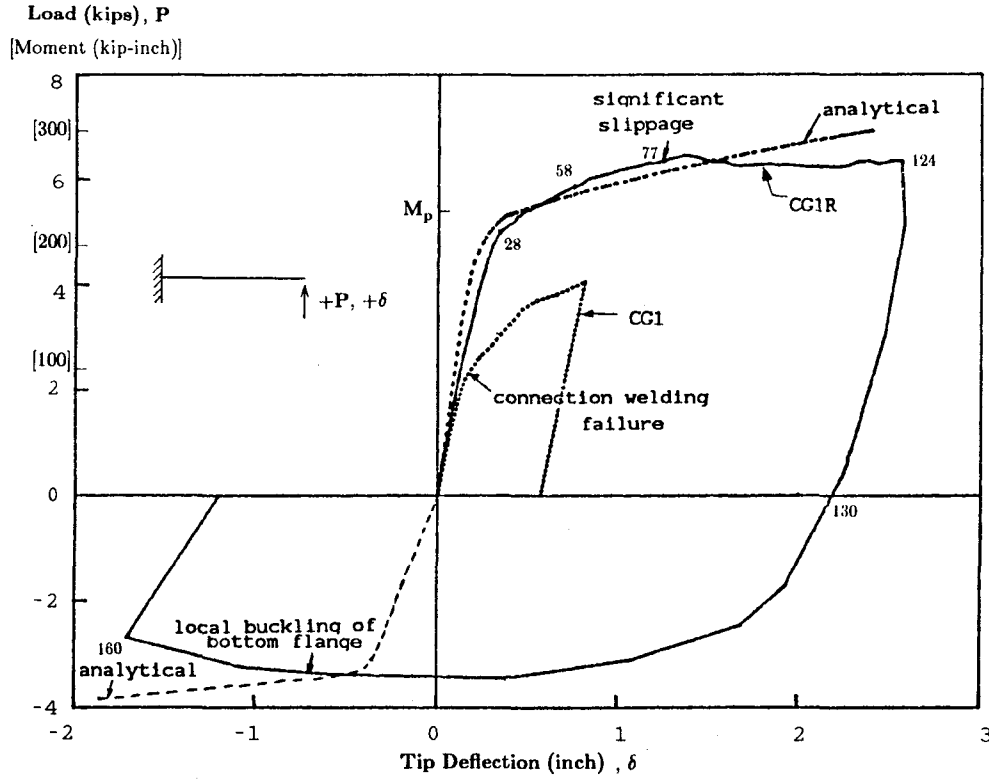


FIG. 4.13 LOAD-TIP DEFLECTION CURVE OF CG1 AND CG1R

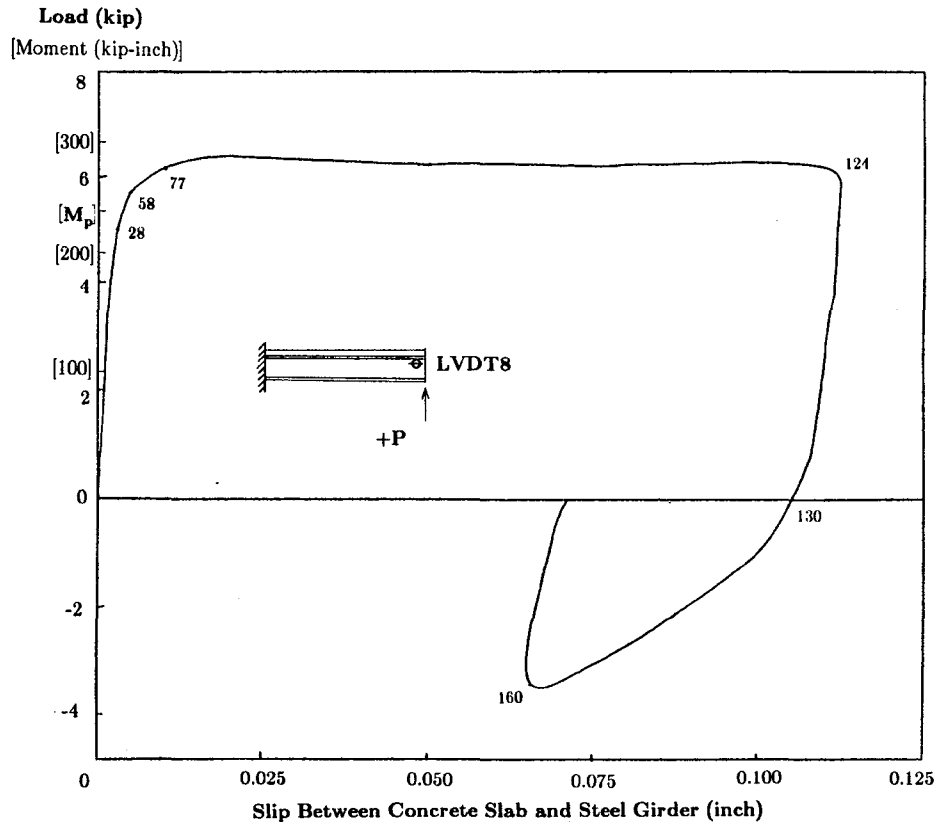


FIG. 4.14 LOAD-SLIP CURVE OF CG1R (LVDT8)

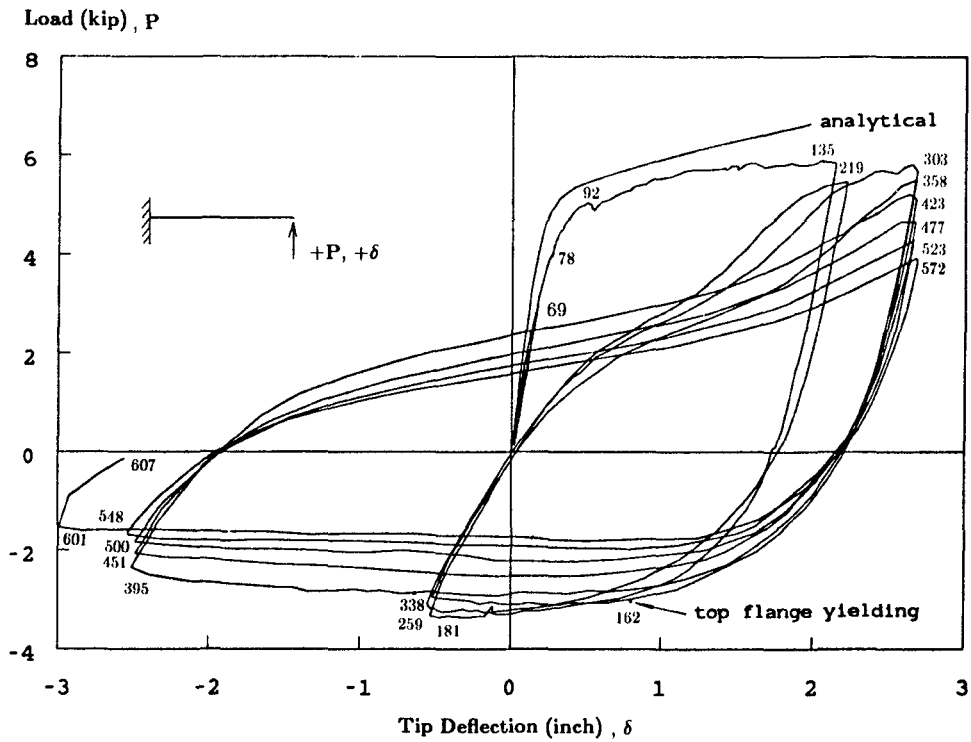


FIG. 4.15 LOAD-TIP DEFLECTION CURVE OF CG3

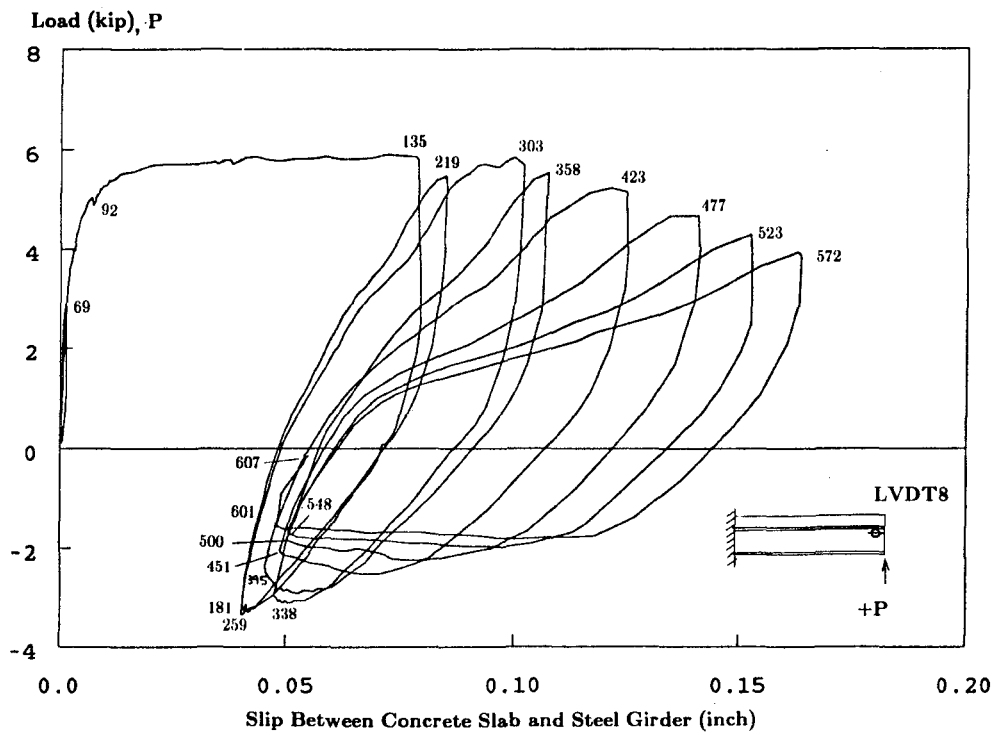
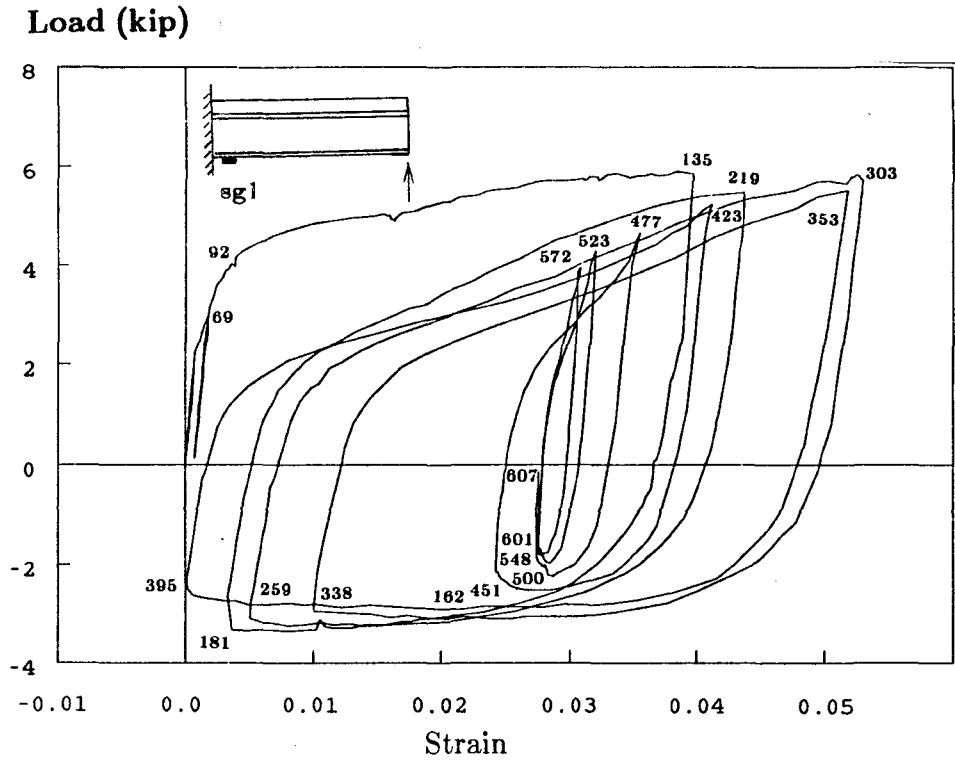
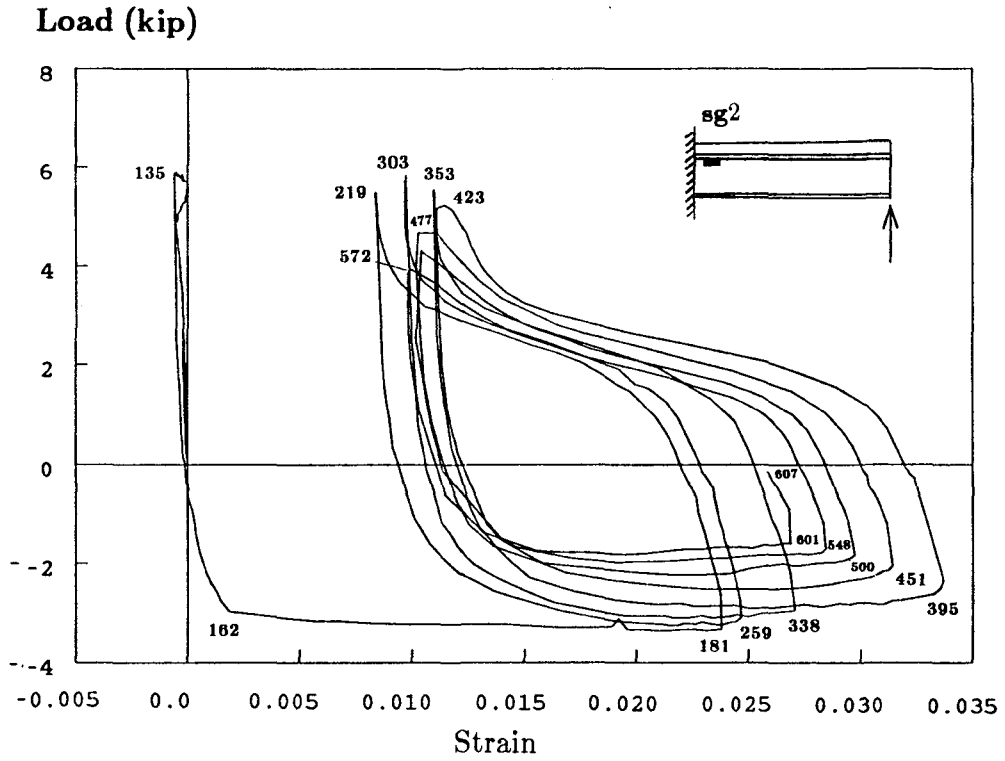


FIG. 4.16 LOAD-SLIP CURVE OF CG3 (LVDT8)

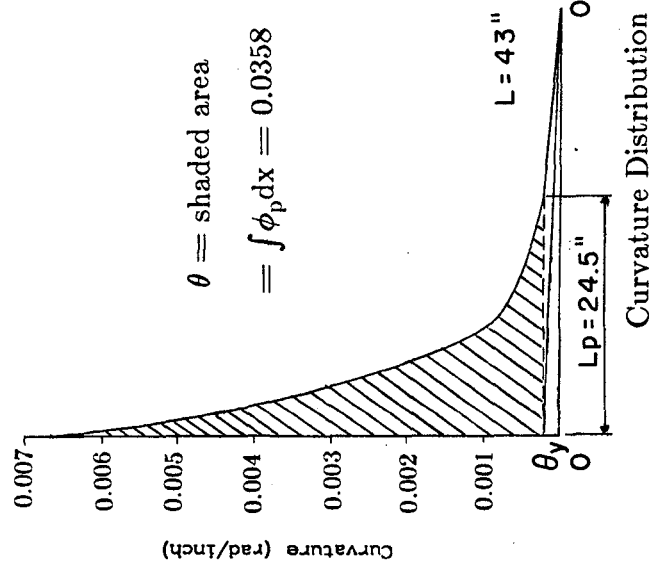
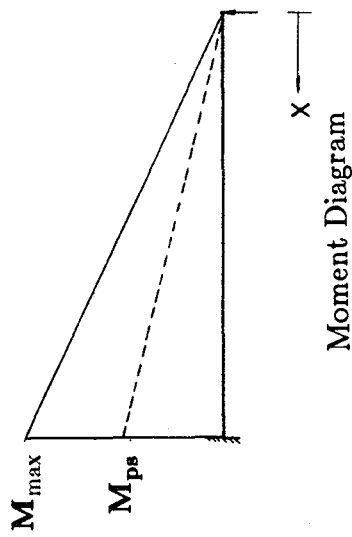


(a) Bottom Flange Strain (sg1) at Section A

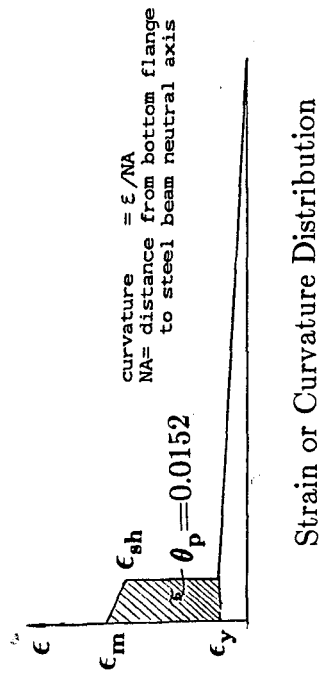
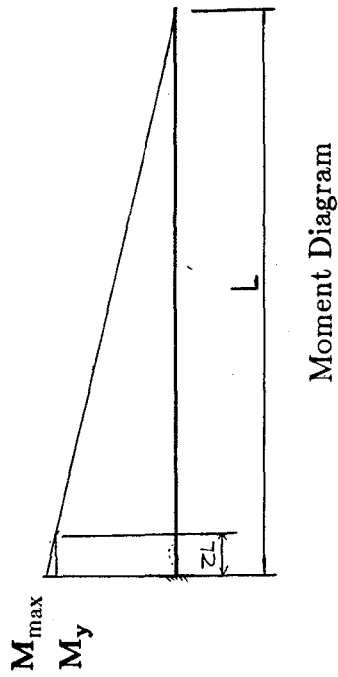


(b) Top Flange Strain (sg2) at Section A

FIG. 4.17 LOAD-BEAM FLANGE STRAIN CURVE OF CG3



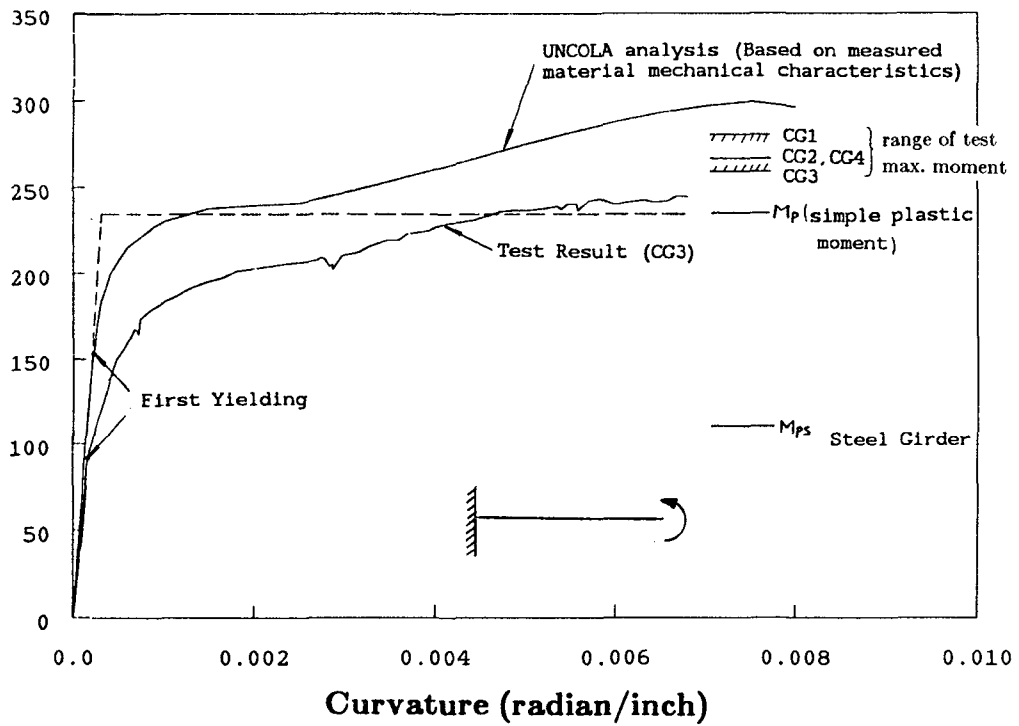
(b) Composite Girder (CG3)



(a) Steel Girder

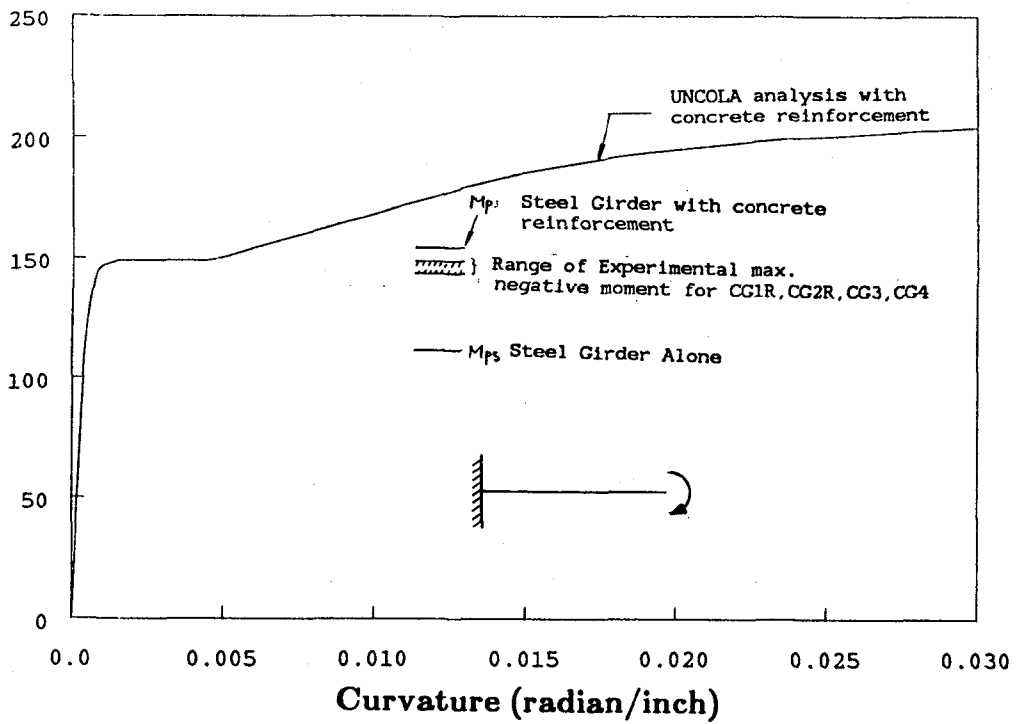
FIG. 4.18 PLASTIC HINGE ROTATION OF STEEL GIRDER AND COMPOSITE GIRDER

Moment (kip-inch)



(a) Positive Bending

Moment (kip-inch)



(b) Negative Bending

FIG. 4.19 MOMENT-CURVATURE RELATIONSHIP

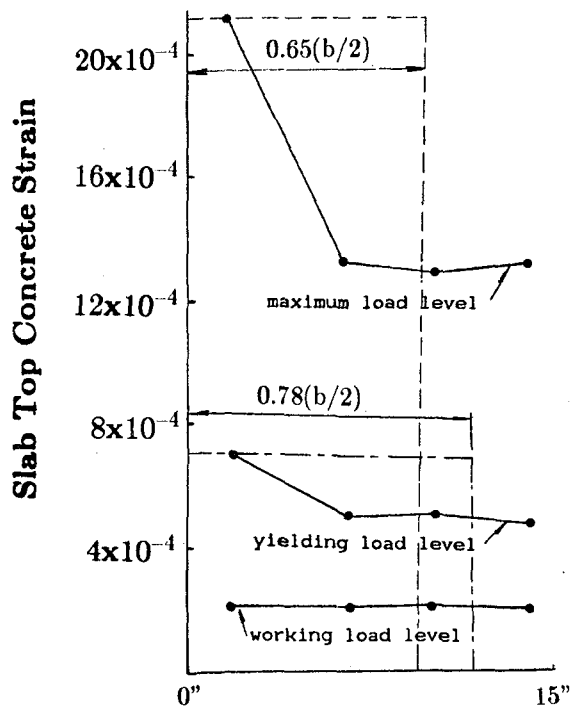
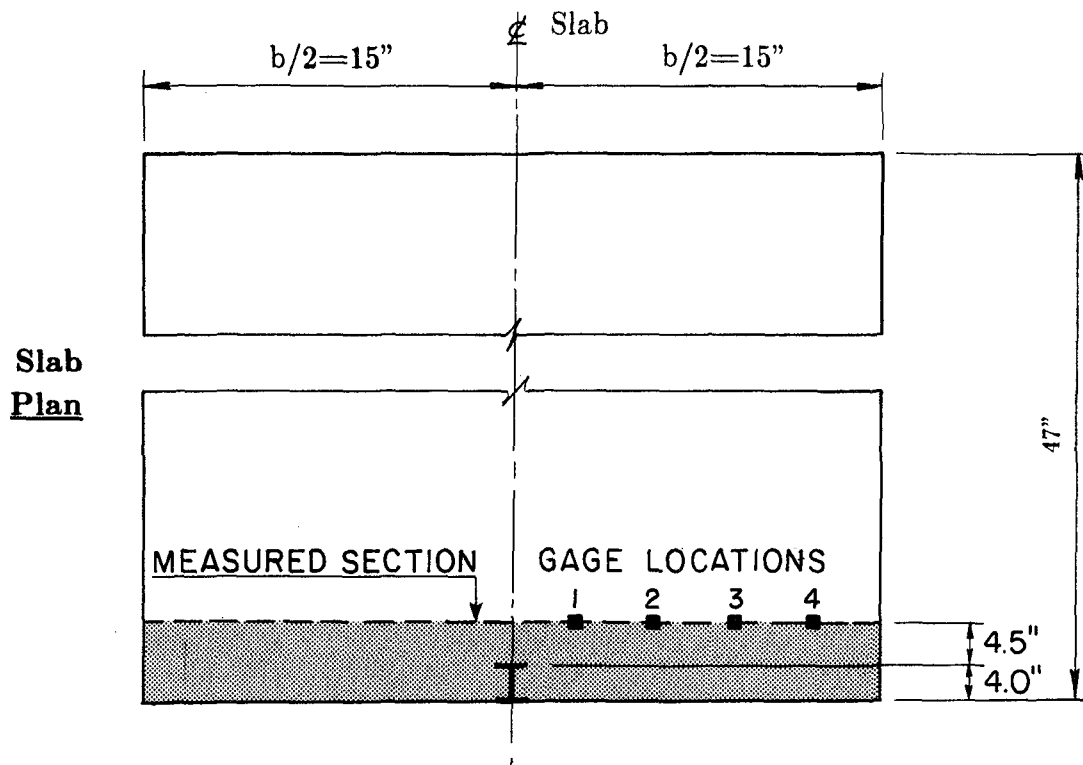


**FIG. 4.20 CONCRETE STRAIN DISTRIBUTION OF CG4
(4.5 INCHES FROM COLUMN FACE)**

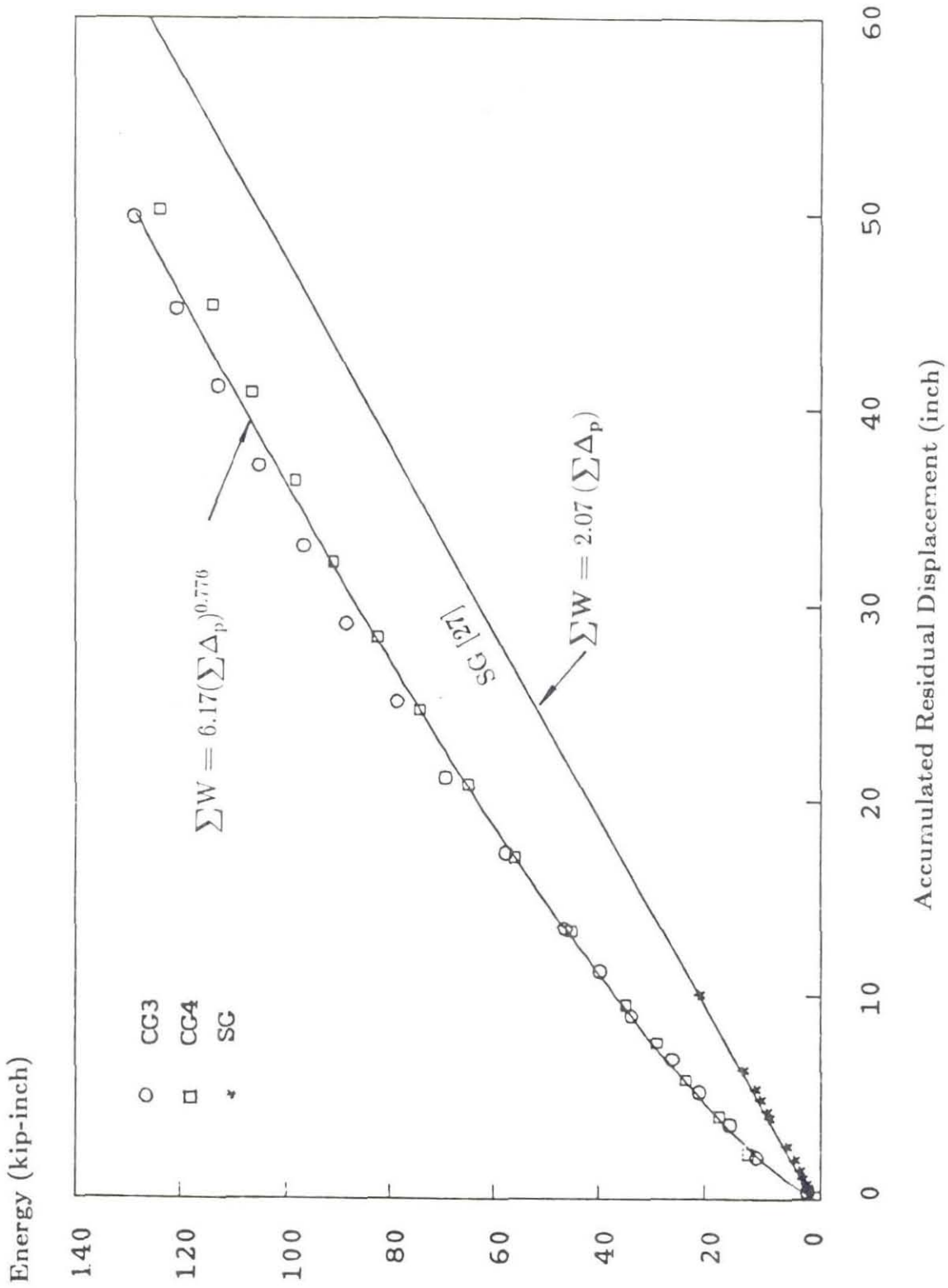


FIG. 4.21 ACCUMULATED RESIDUAL DISPLACEMENT VERSUS ACCUMULATED ENERGY DISSIPATION CURVE

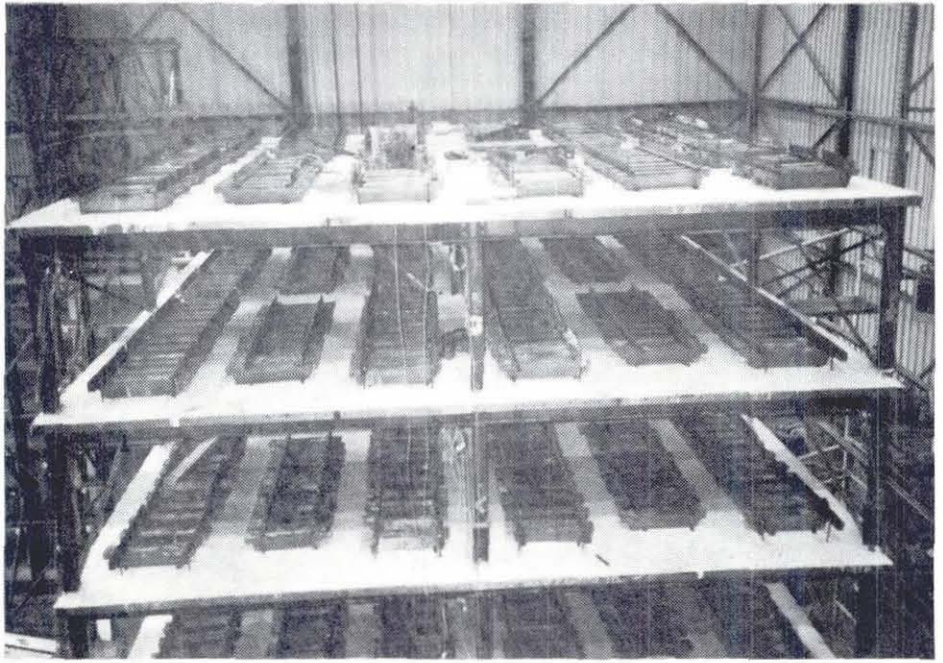


FIG. 4.22 AUXILIARY LEAD BRICKS ATTACHED TO FLOORS

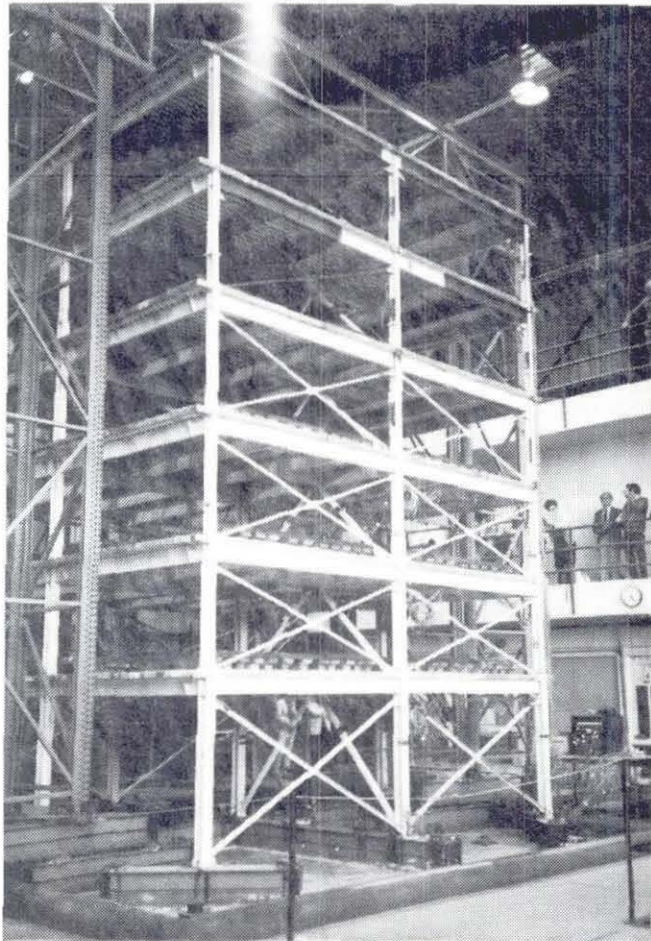
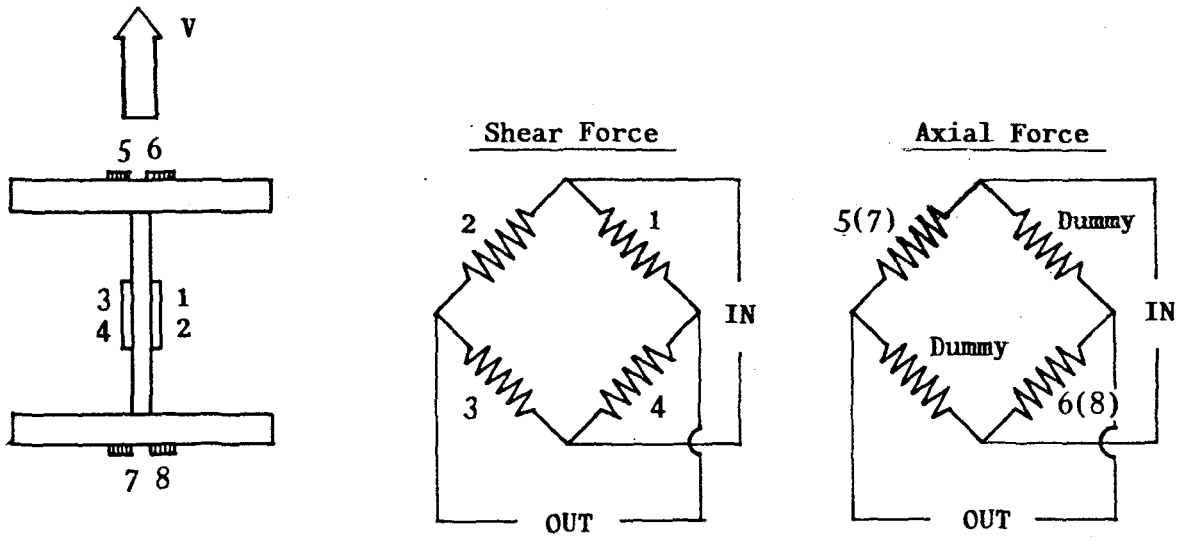
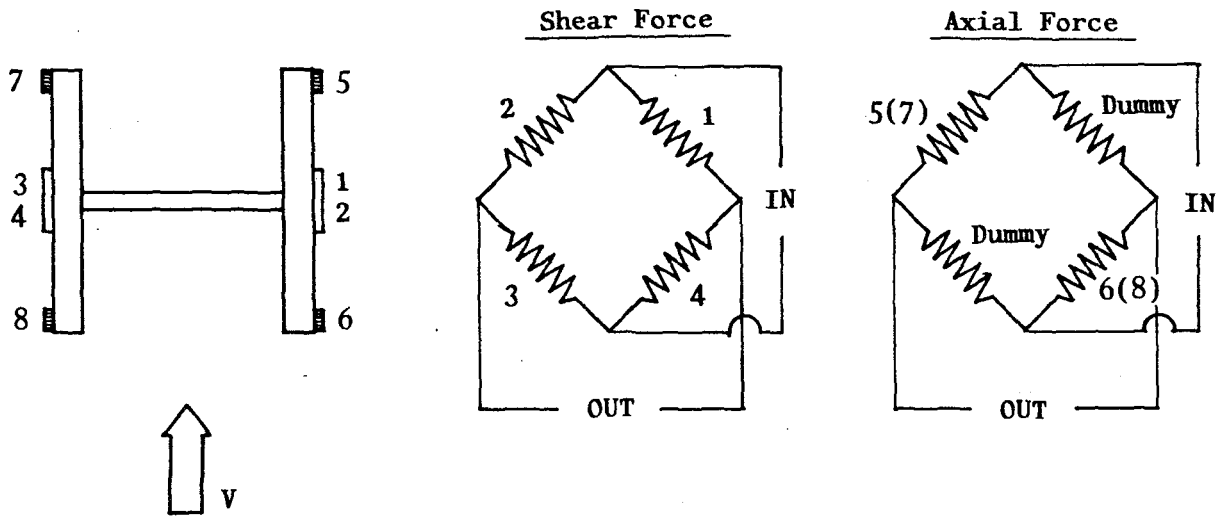


FIG. 4.23 TEST STRUCTURE WITH REFERENCE FRAME

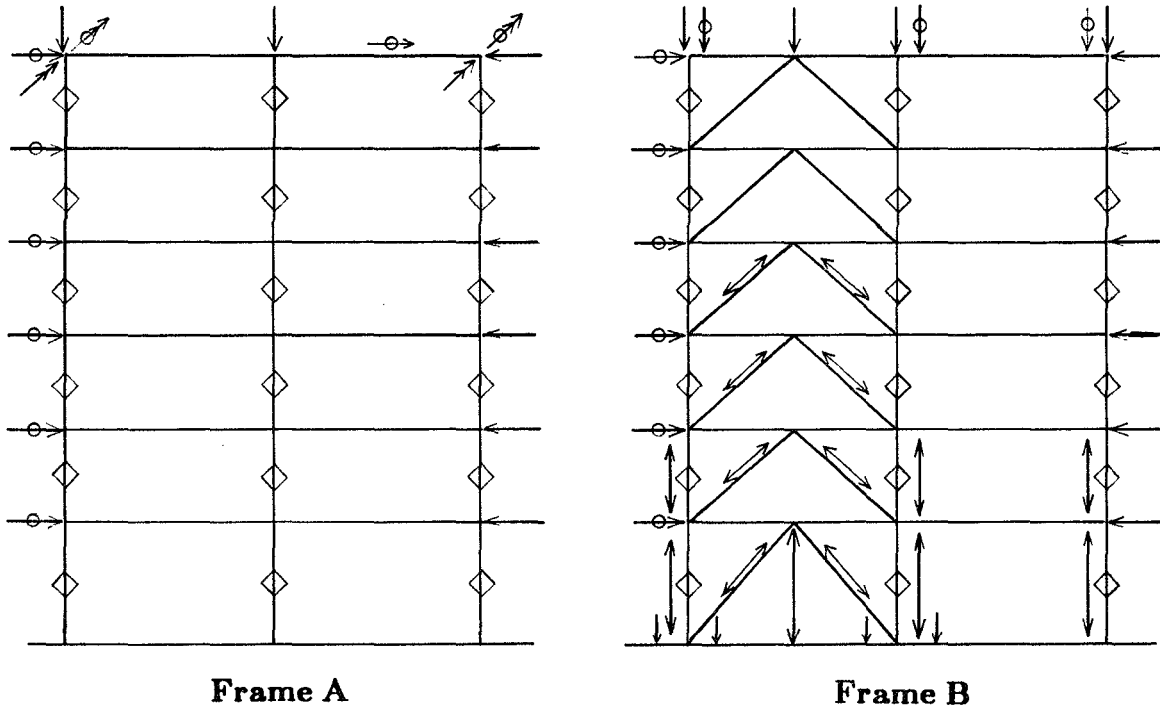


(a) Strong Axis bending



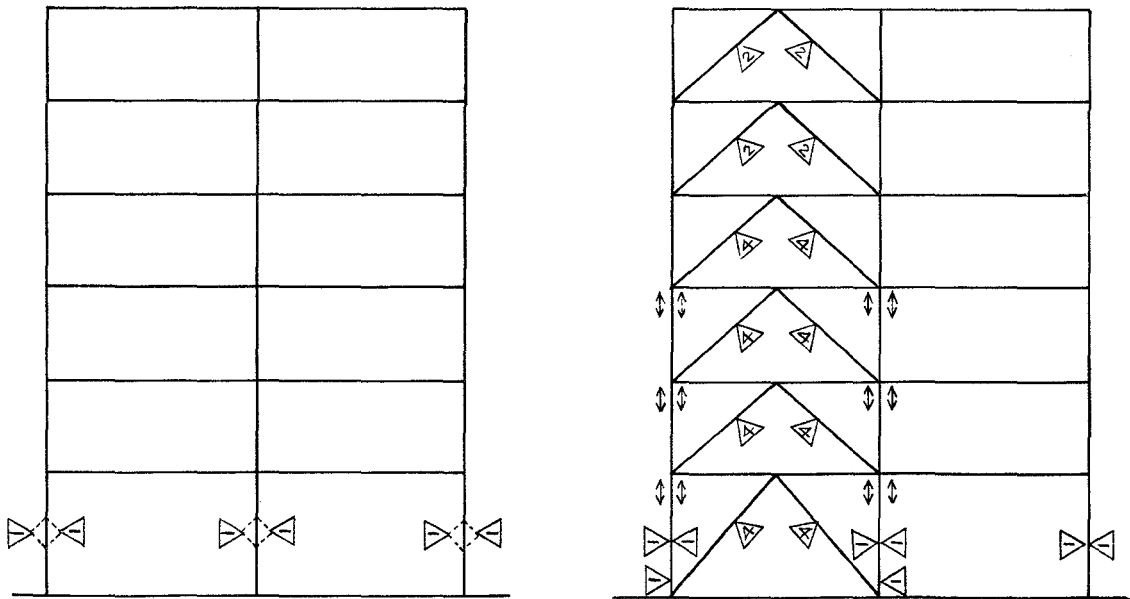
(b) Weak Axis bending

FIG. 4.24 STRAIN GAGE INSTRUMENTATION OF THE COLUMNS



Frame A

Frame B



Frame A (C)

Frame B

- ⊖→ transverse accel.
- ↔ axial deformation
- △ axial strain with N gages
- ◇ column shear force (Frame A or B)
- ◇ column shear force (Frame C)

- horizontal displ.
- ↑ vertical displ.
- transverse displ.
- ⊖→ horizontal accel.
- ⊕ vertical accel.

FIG. 4.25 INSTRUMENTATION OF THE MODEL

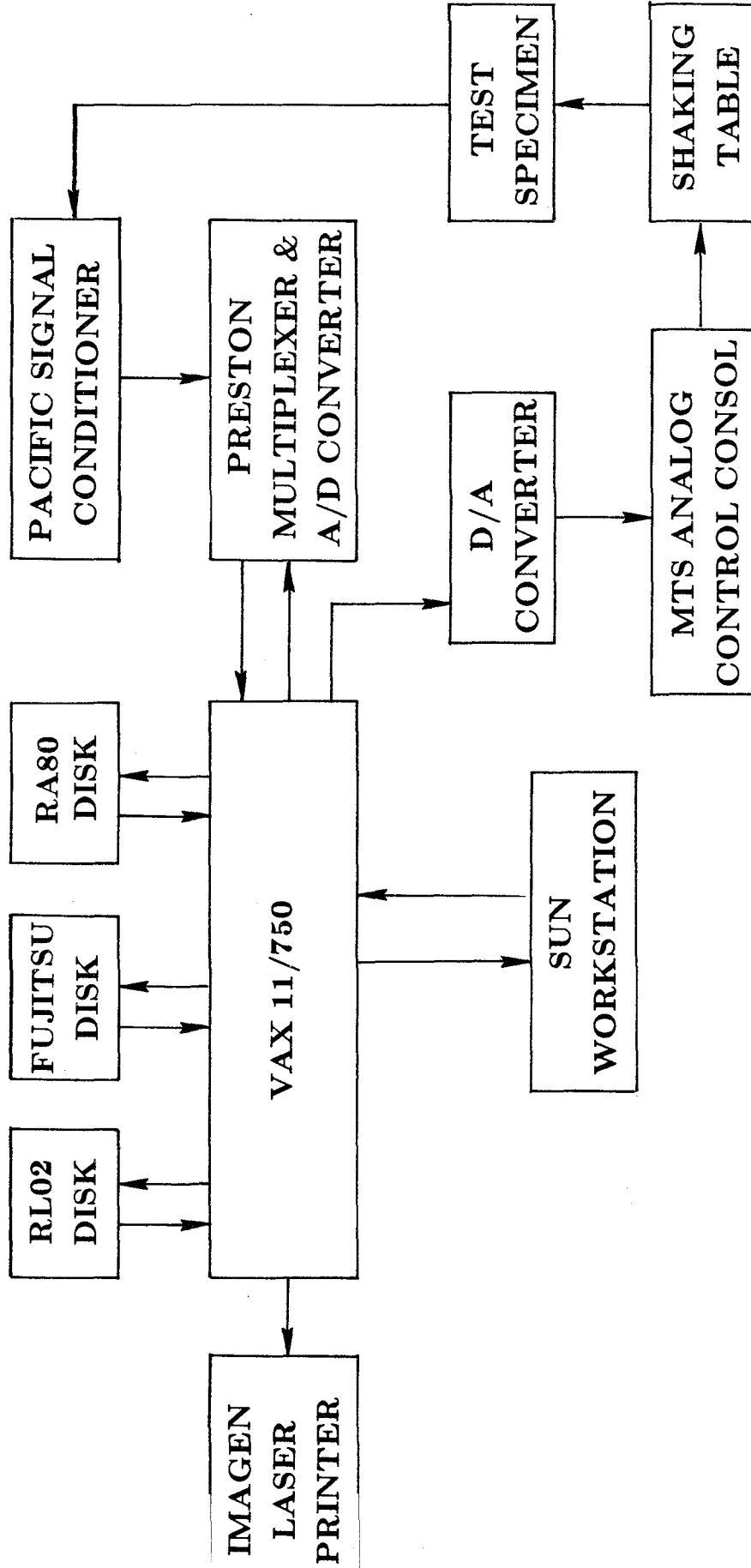
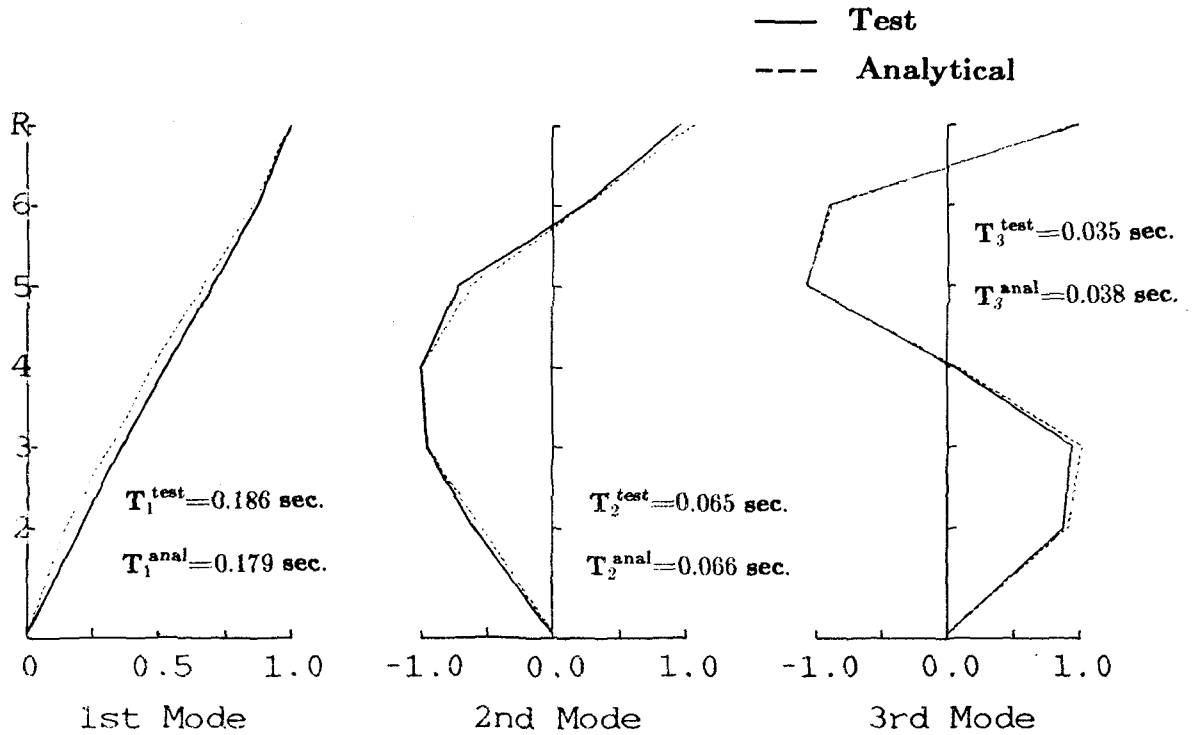
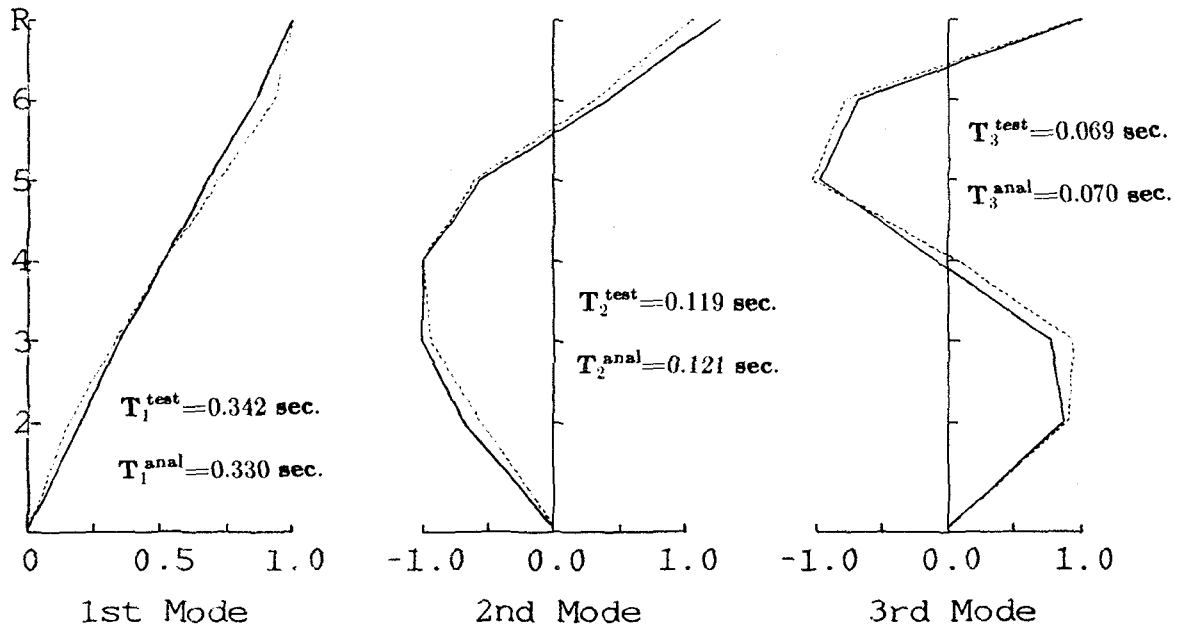


FIG. 4.26 SHAKING TABLE SYSTEM BLOCK DIAGRAM

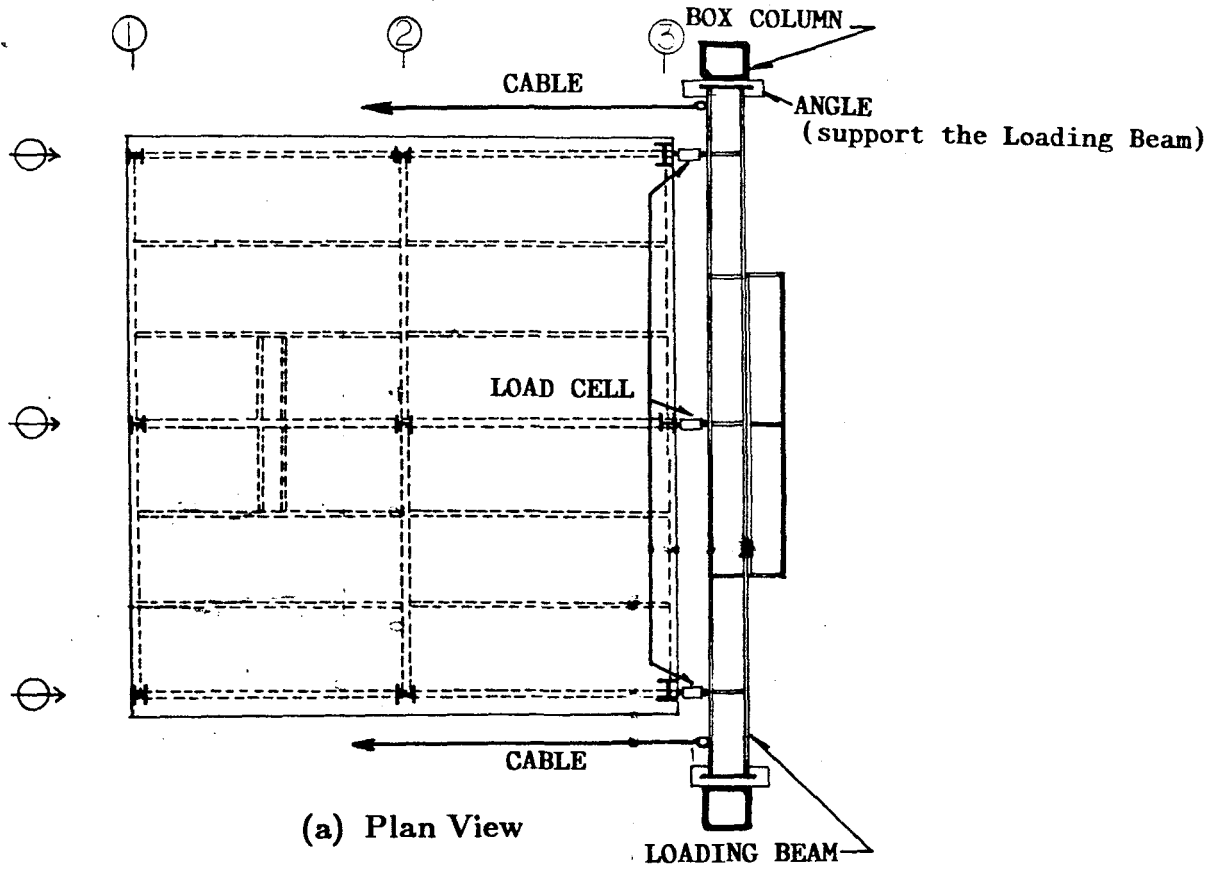


(a) Test Model with Slabs but without Lead Pigs



(b) Test Model with Slabs and Lead Pigs

FIG. 5.1 MODEL ANALYTICAL AND MEASURED MODE SHAPES



\oplus = DCDT
(Displacement Transducer)

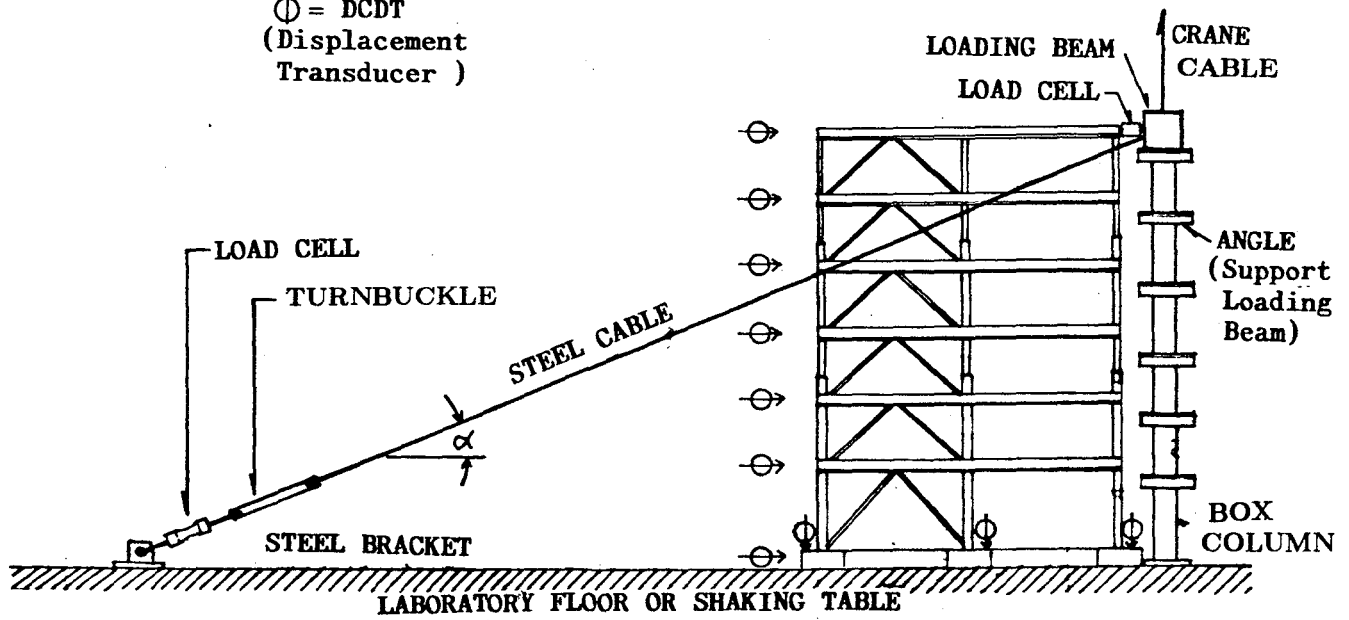


FIG. 5.2 TEST SETUP - STATIC FLEXIBILITY TESTS

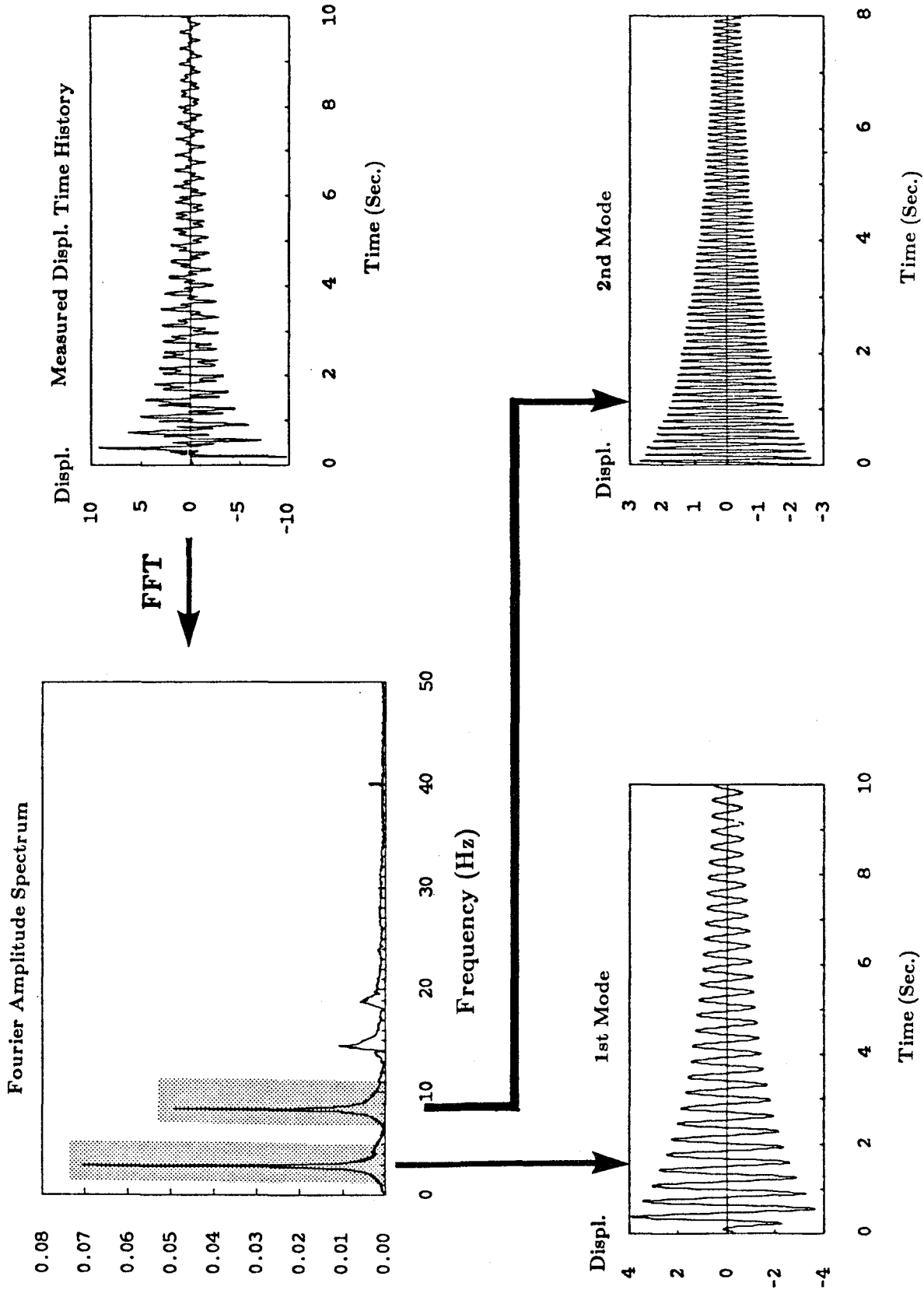


FIG. 5.3 PROCEDURE FOR OBTAINING THE DAMPING COEFFICIENT AND NATURAL PERIOD FROM FREE VIBRATION TESTS

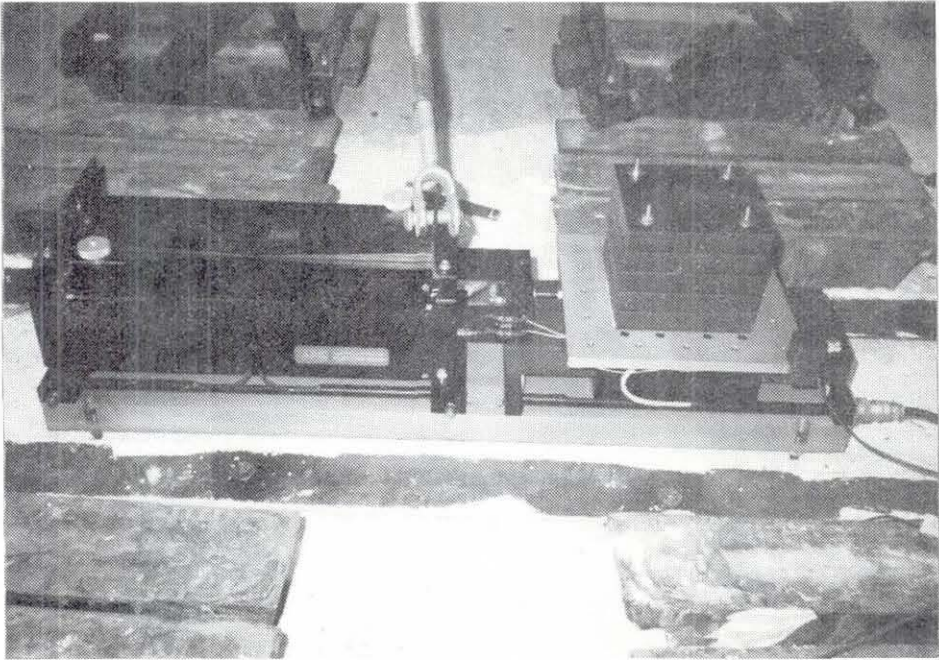


FIG. 5.4 SHAKER FOR FORCED VIBRATION TEST

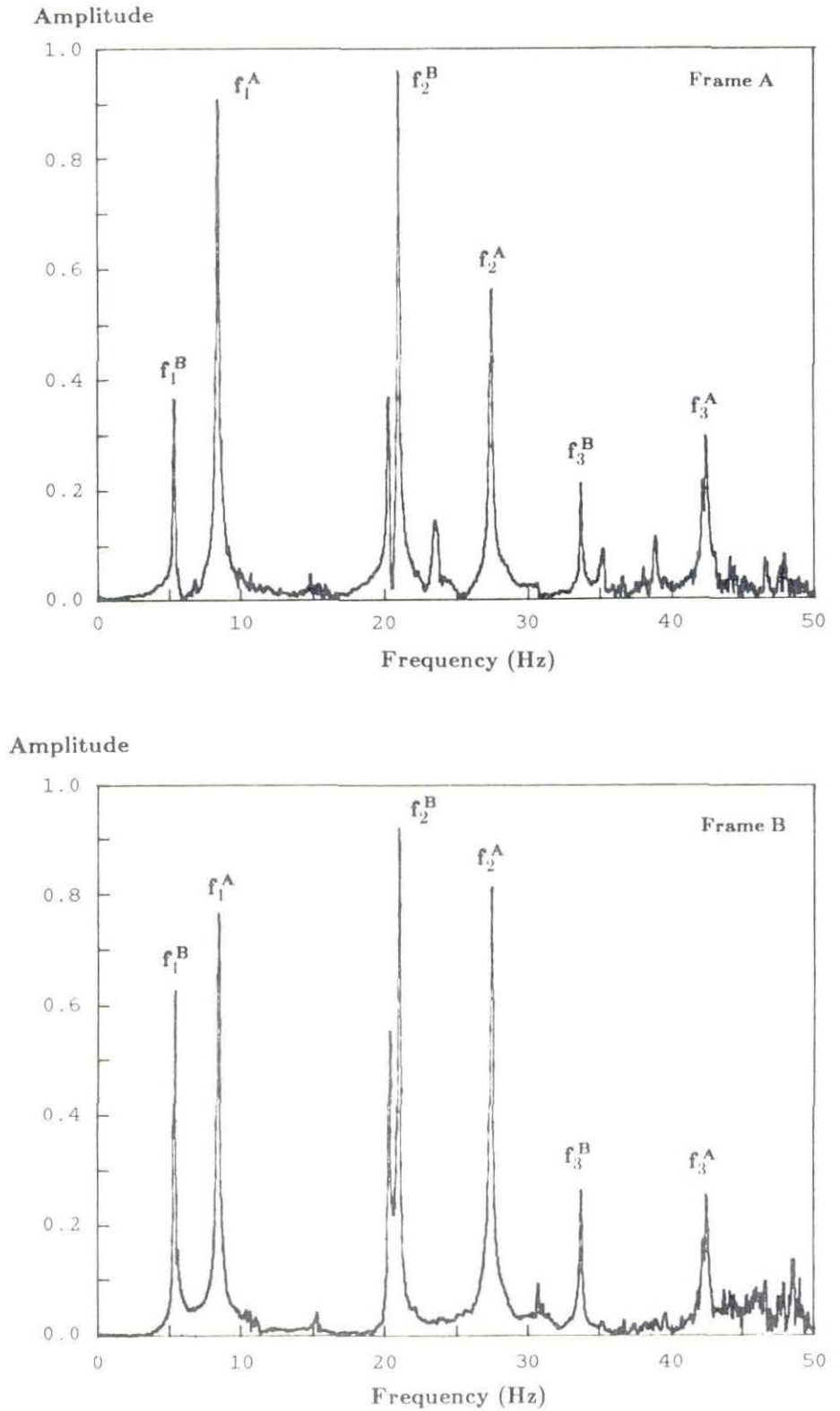


FIG. 5.5 FREE VIBRATION FOURIER AMPLITUDE SPECTRA OF ROOF ACCELERATION (UNBRACED MODEL W/OUT SLAB)

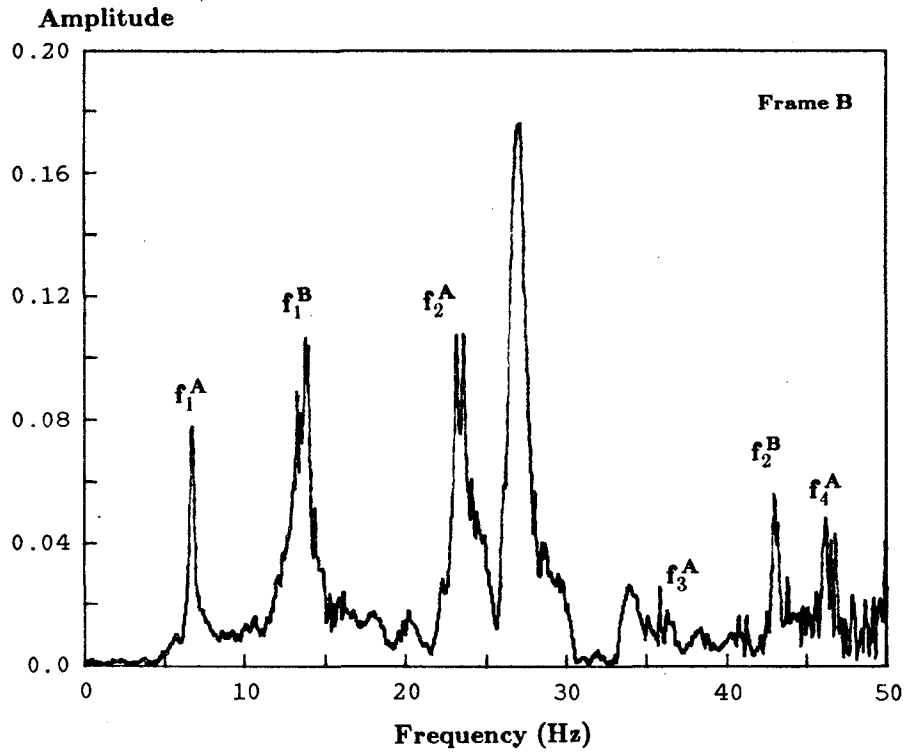
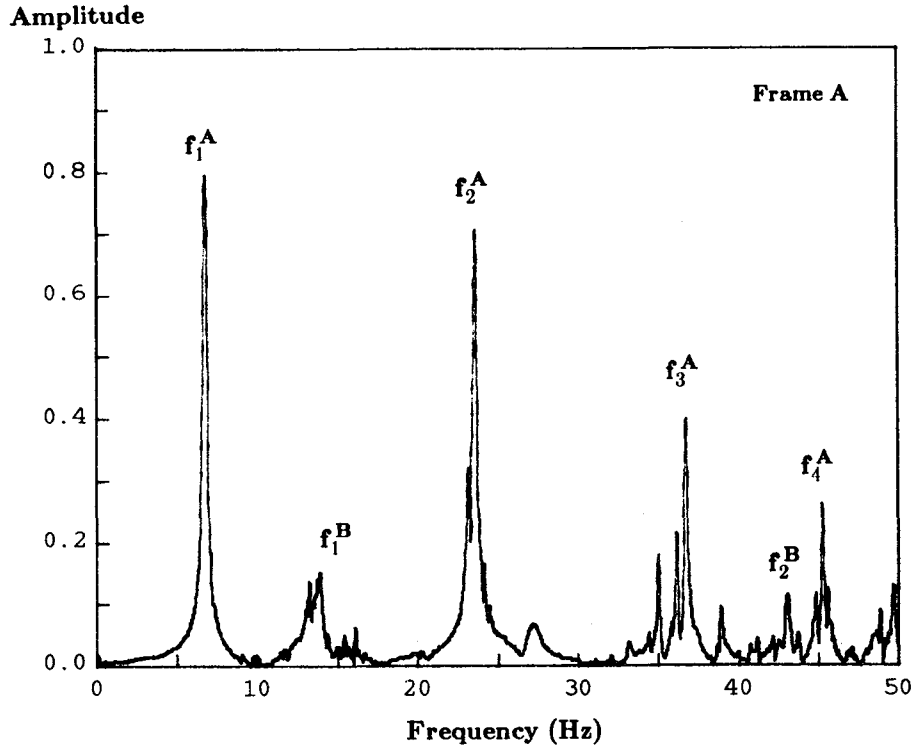


FIG. 5.6 FREE VIBRATION FOURIER AMPLITUDE SPECTRA OF ROOF ACCELERATION (BRACED MODEL W/OUT SLAB)

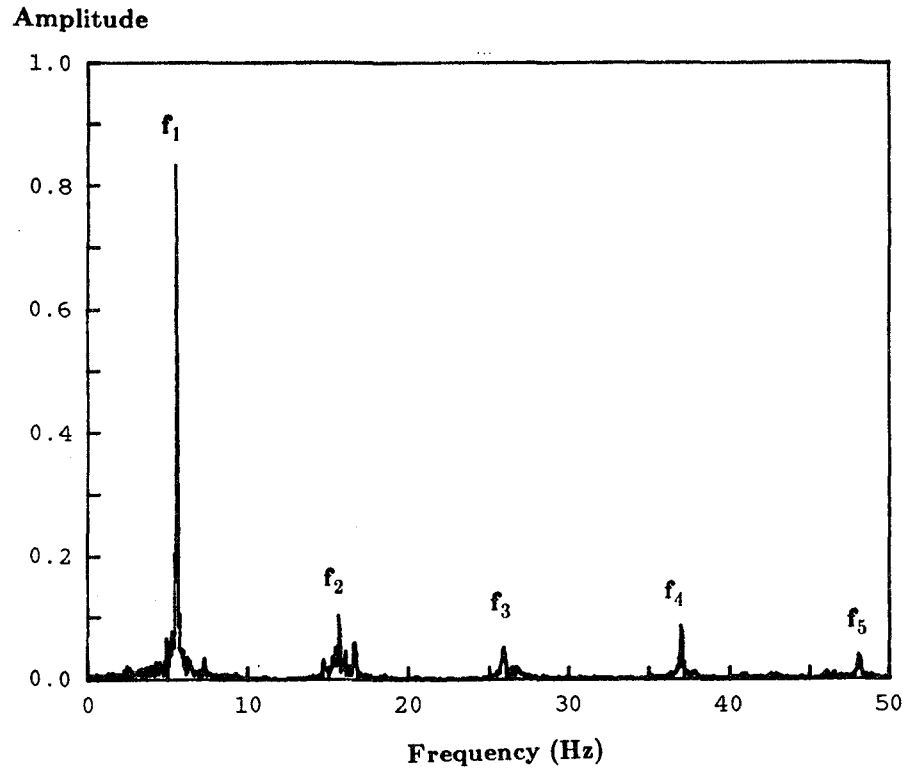


FIG. 5.7 AMBIENT VIBRATION FOURIER AMPLITUDE SPECTRA OF ROOF VELOCITY (MODEL W/OUT AUXILIARY MASS)

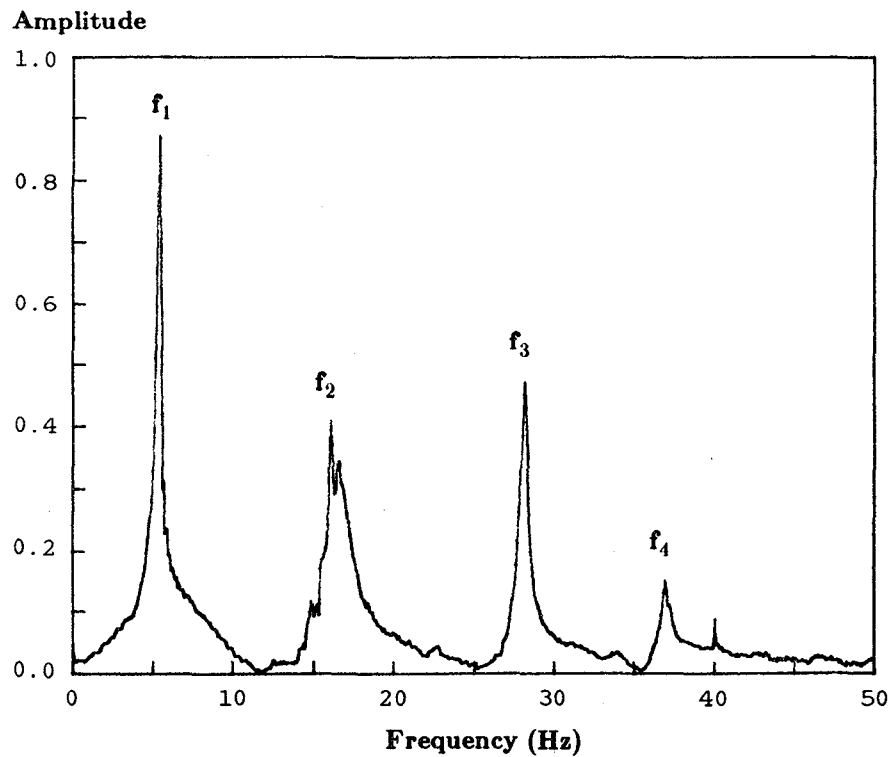
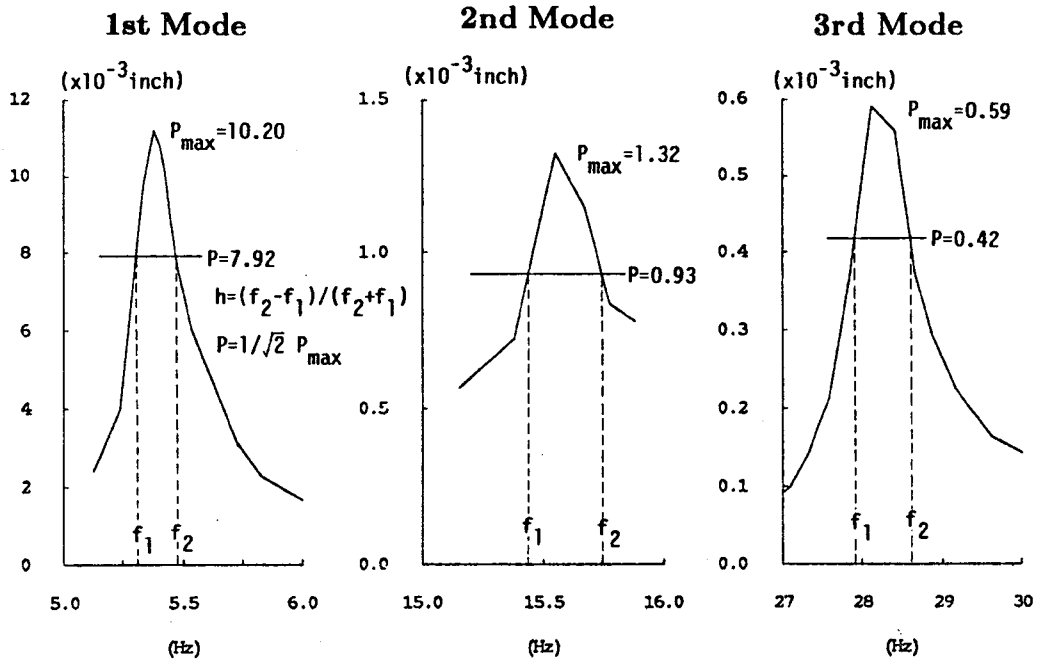
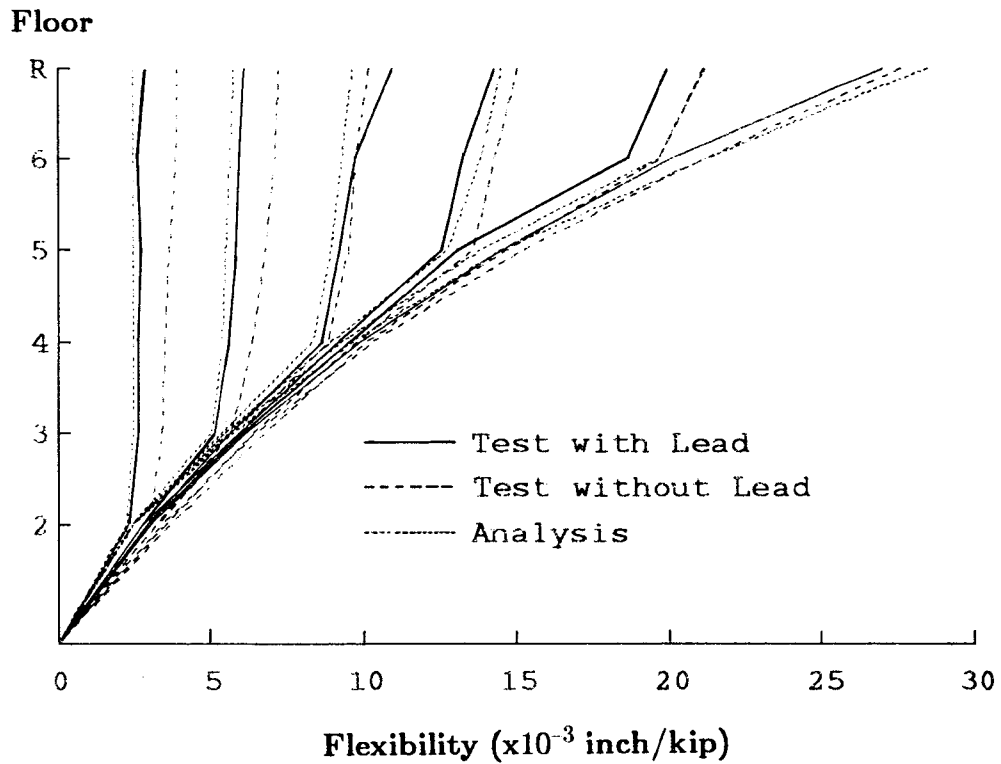


FIG. 5.8 FREE VIBRATION FOURIER AMPLITUDE SPECTRA OF ROOF ACCELERATION (MODEL W/OUT AUXILIARY MASS)



**FIG. 5.9 FORCED VIBRATION TESTS FREQUENCY RESPONSE CURVES
(TEST MODEL WITH SLABS BUT W/OUT LEAD PIGS)**



**FIG. 5.10 FLEXIBILITY TESTS DISPLACEMENT PROFILES
(TEST MODEL WITH SLABS, WITH OR W/OUT LEAD PIGS)**

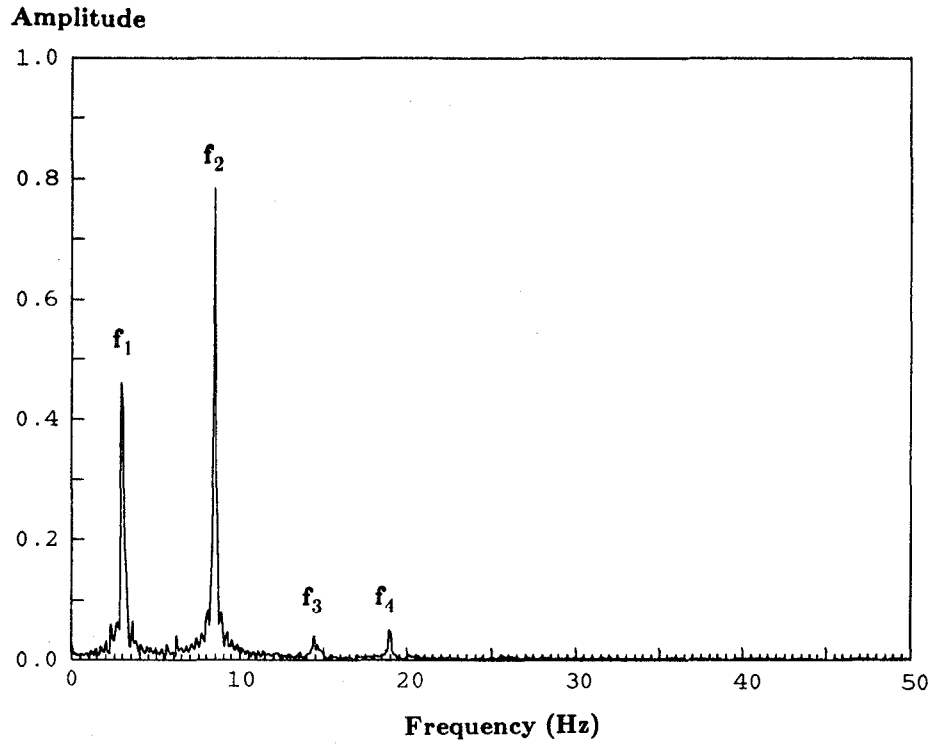


FIG. 5.11 AMBIENT VIBRATION FOURIER AMPLITUDE SPECTRA OF ROOF VELOCITY (MODEL WITH AUXILIARY MASS)

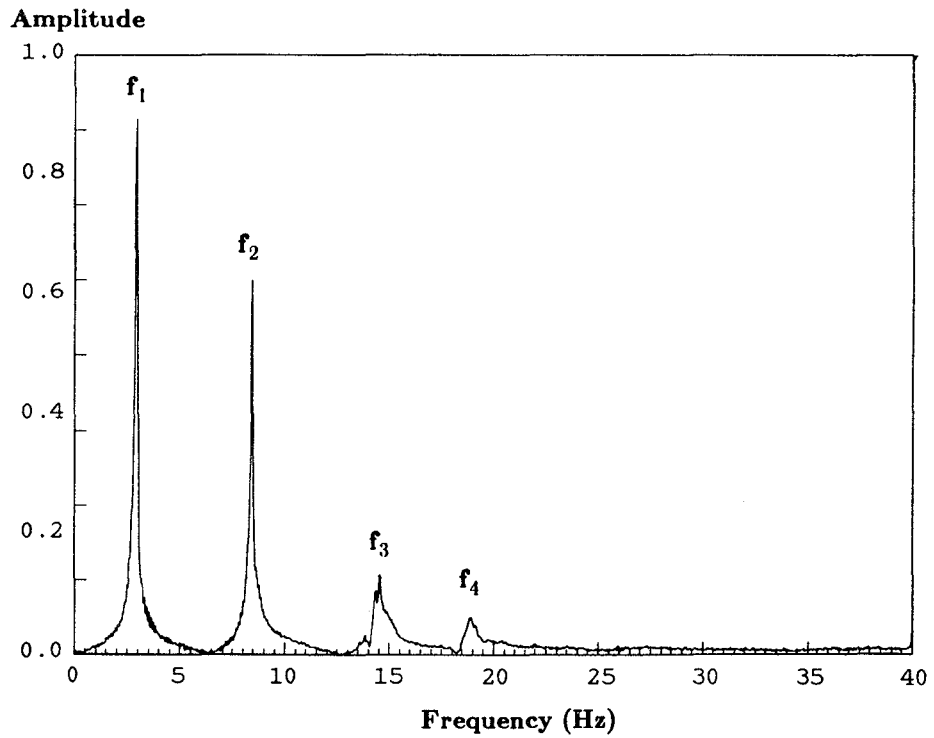
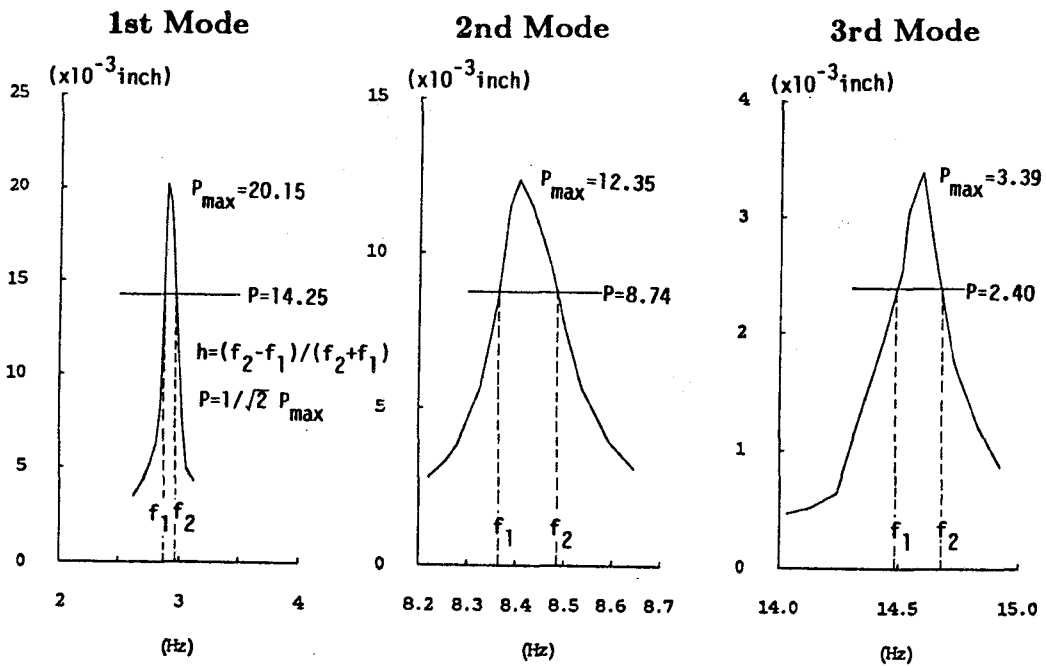
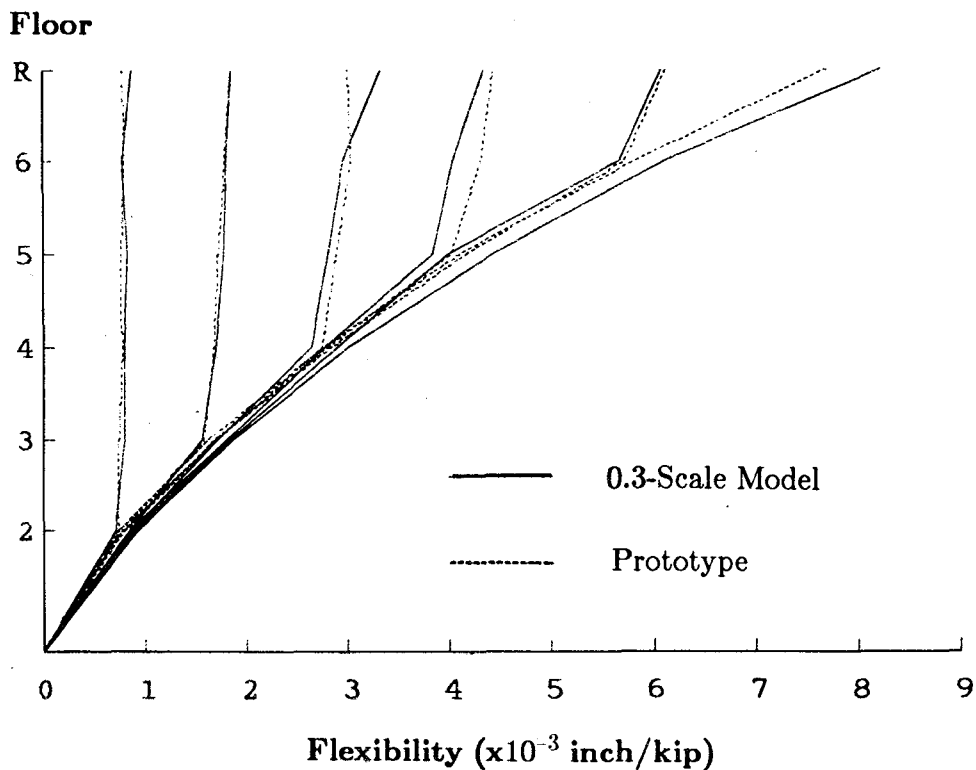


FIG. 5.12 FREE VIBRATION FOURIER AMPLITUDE SPECTRA OF ROOF ACCELERATION (MODEL WITH AUXILIARY MASS)



**FIG. 5.13 FORCED VIBRATION TESTS FREQUENCY RESPONSE CURVES
(TEST MODEL WITH SLABS AND LEAD PIGS)**



**FIG. 5.14 COMPARISON OF PROTOTYPE AND MODEL FLEXIBILITY
TEST DISPLACEMENT PROFILES**

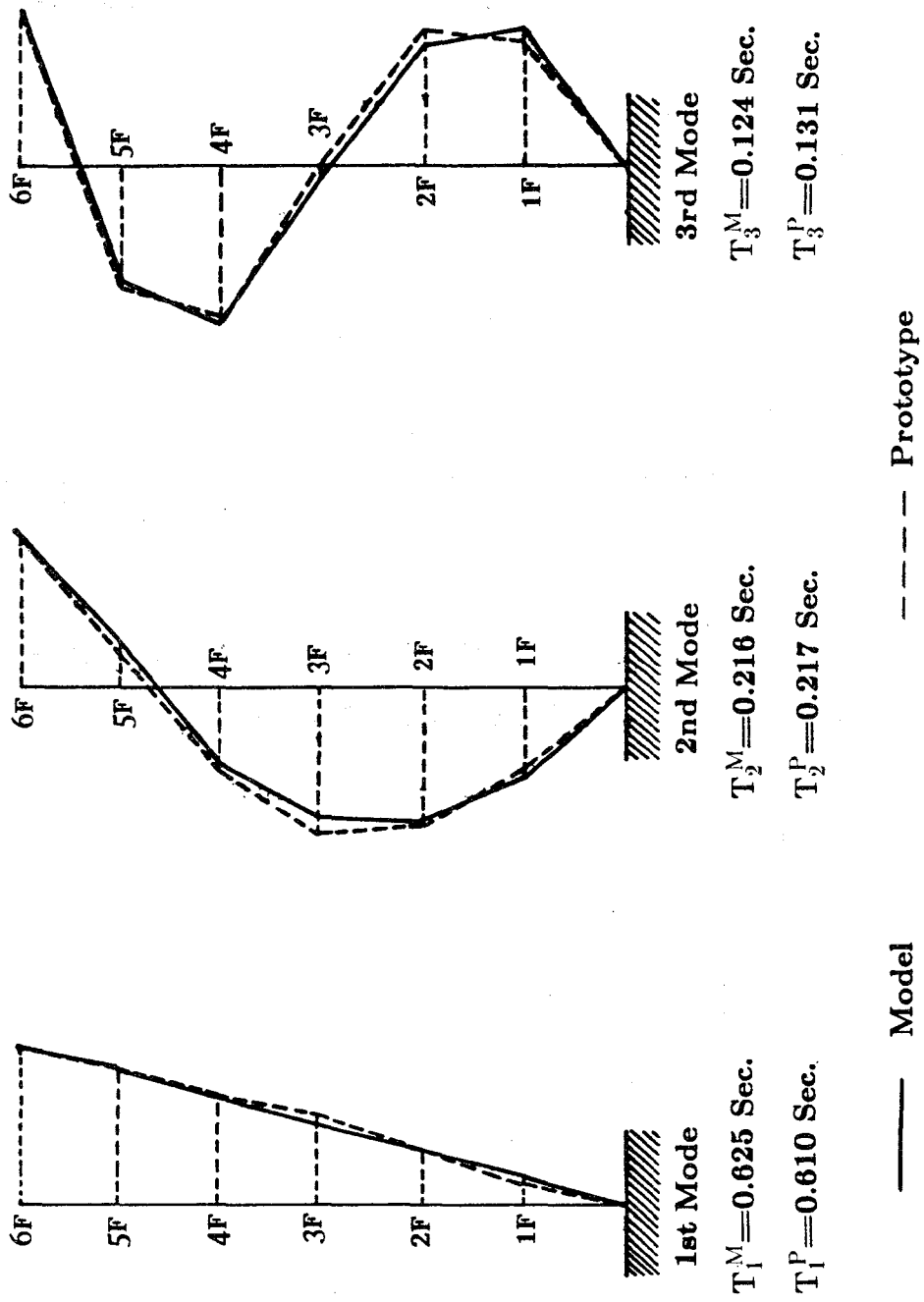


FIG. 5.15 COMPARISON OF PROTOTYPE AND MODEL
MEASURED MODE SHAPES

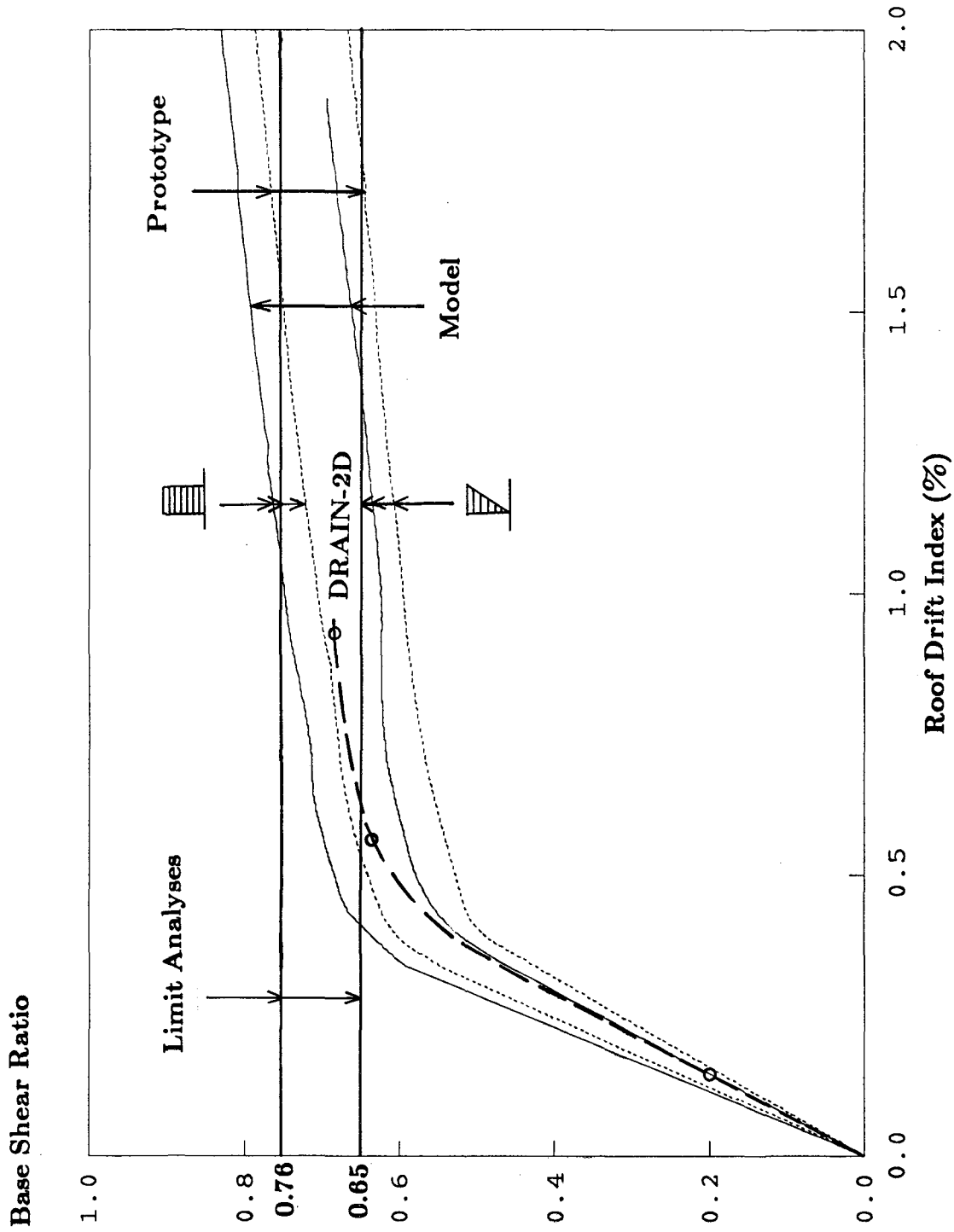
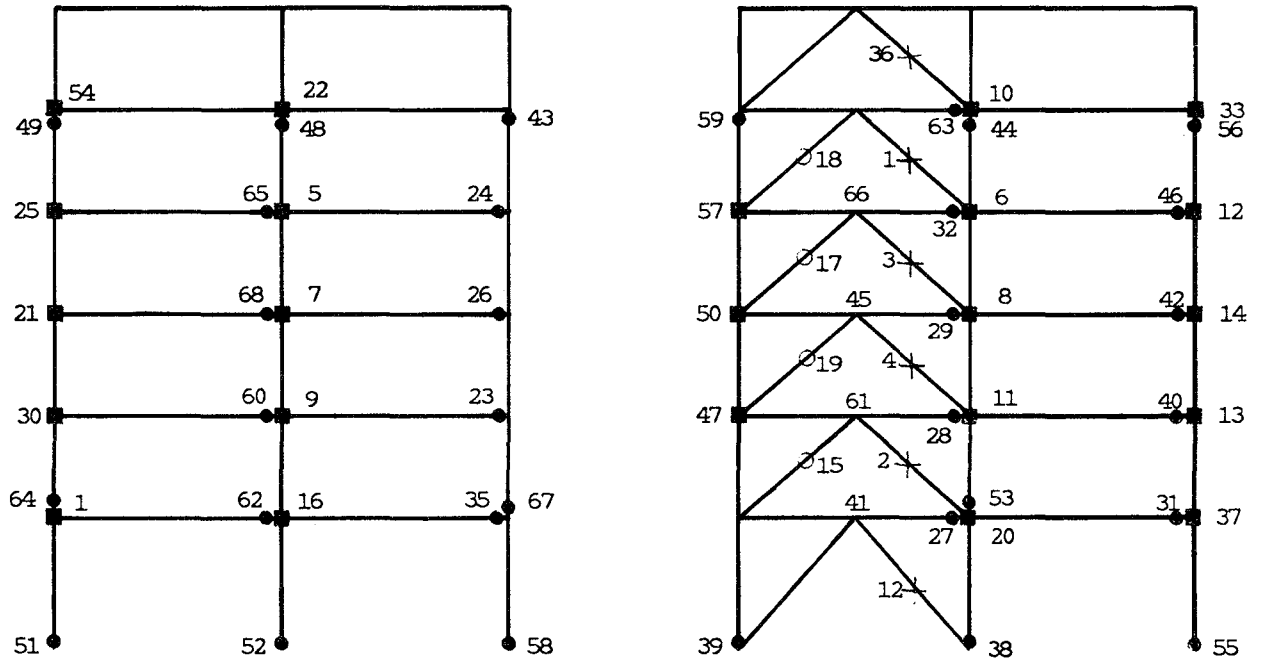
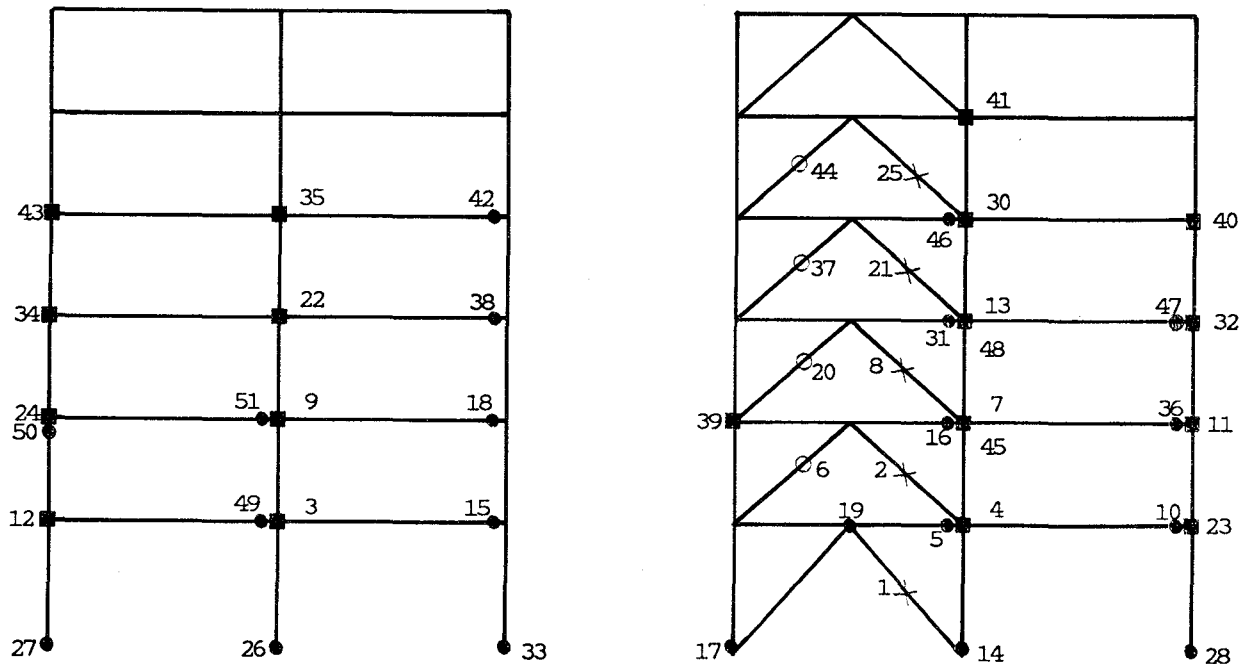


FIG. 6.1 PREDICTED ROOF DRIFT INDEX VERSUS BASE SHEAR CURVES OF THE MODEL AND THE PROTOTYPE

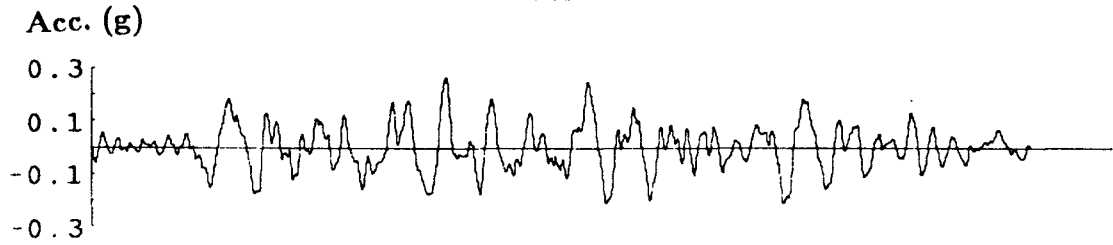


(a) Triangular Load Pattern

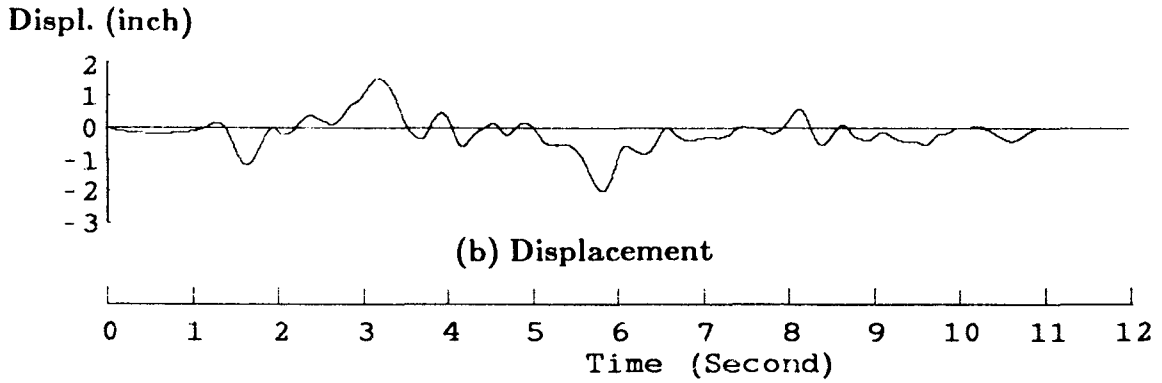


(b) Uniform Load Pattern

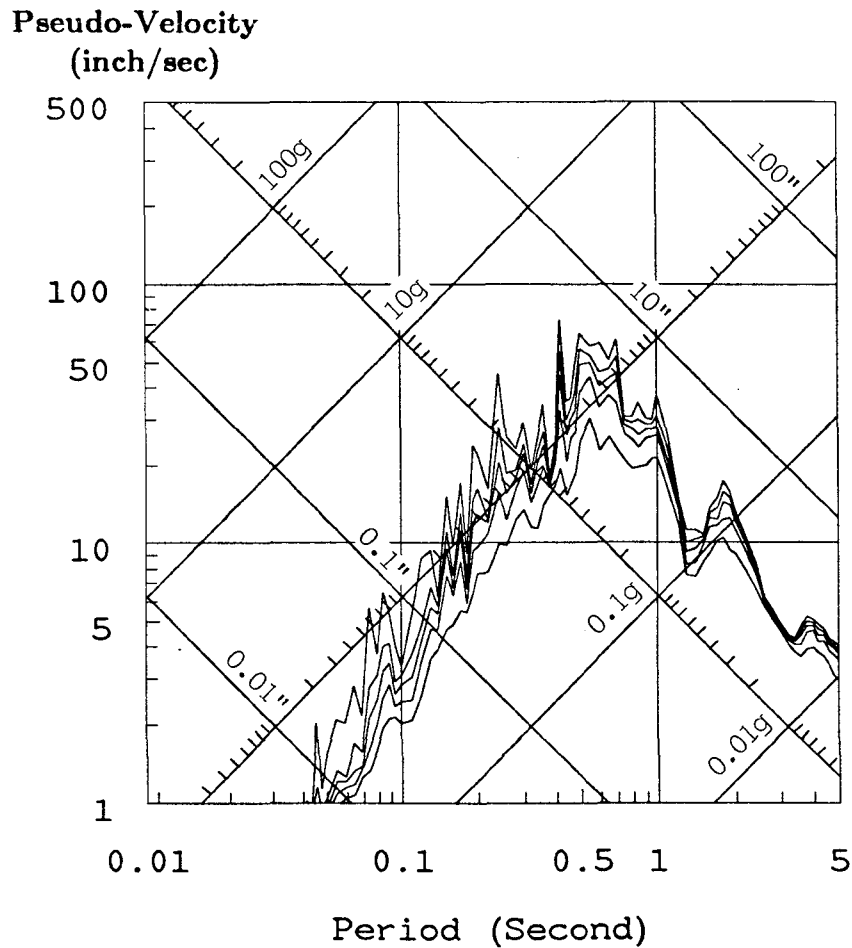
FIG. 6.2 STEP-BY-STEP ANALYSIS HINGE FORMATION
OR BRACE BUCKLING/YIELDING SEQUENCE



(a) Acceleration



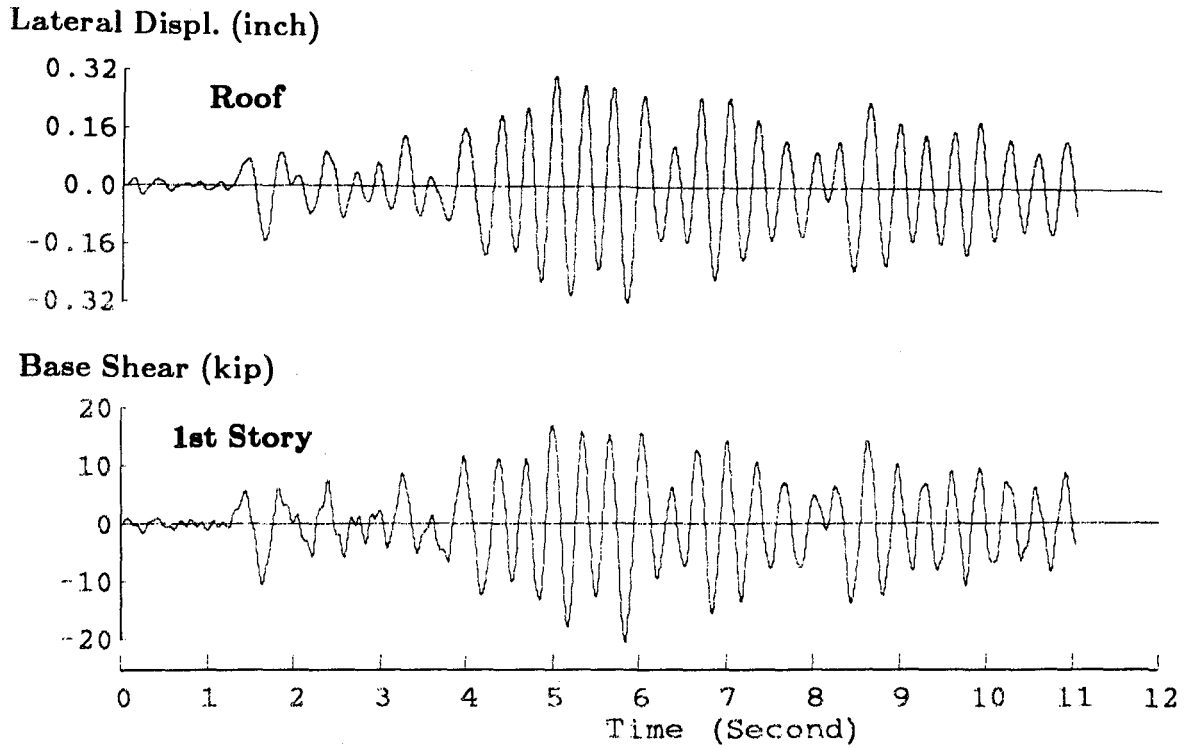
(b) Displacement



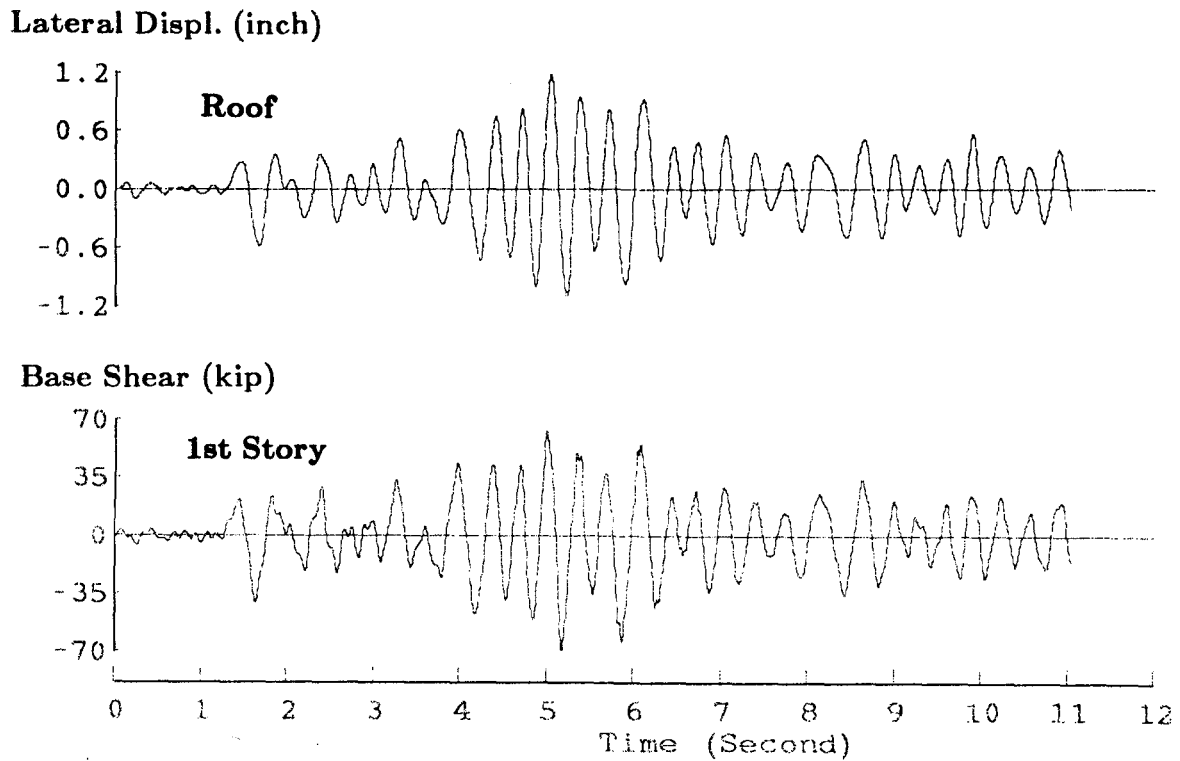
(c) Linear Elastic Response Spectra (0,0.5,1,2,5% Damping)

FIG. 6.3 SCALED SHAKING TABLE INPUT MOTION

AND RESPONSE SPECTRA

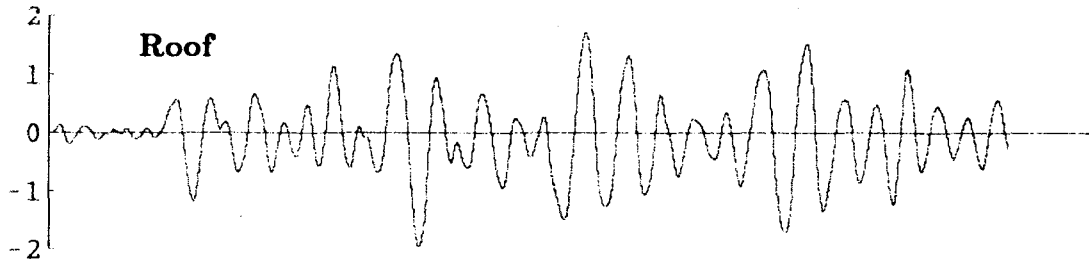


**FIG. 6.4 PREDICTED MODEL SEISMIC RESPONSES
(65 GAL M.O. EARTHQUAKE)**



**FIG. 6.5 PREDICTED MODEL SEISMIC RESPONSES
(250 GAL M.O. EARTHQUAKE)**

Lateral Displ. (inch)



Base Shear (kip)

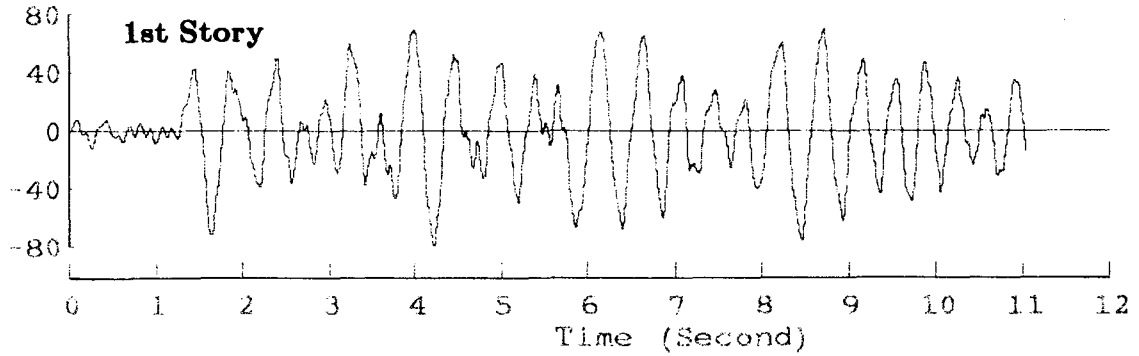
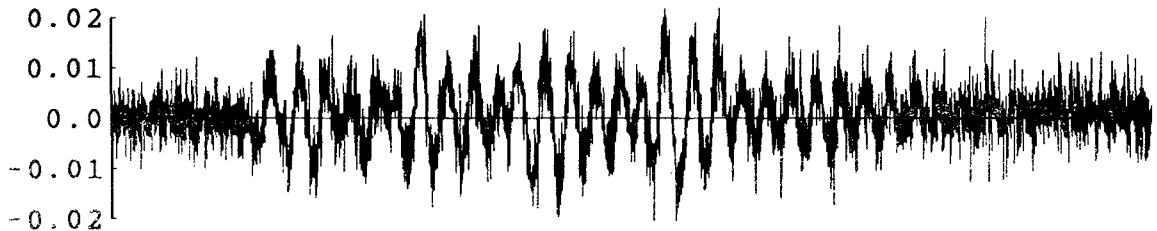


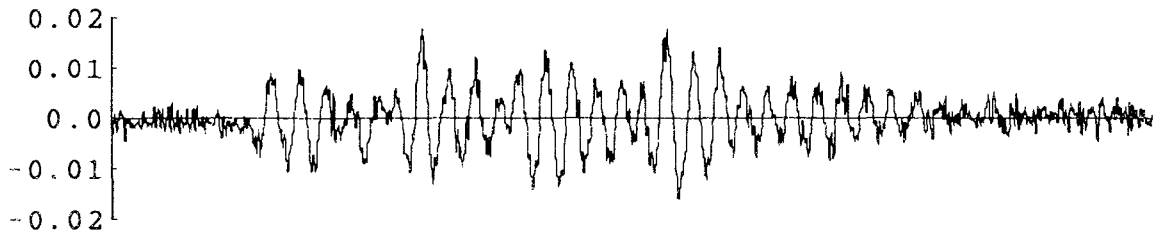
**FIG. 6.6 PREDICTED MODEL SEISMIC RESPONSES
(500 GAL M.O. EARTHQUAKE)**

Deformation (inch)



(a) Unfiltered Column 1C_{B3} Axial Deformation

Deformation (inch)



(b) Filtered Column 1C_{B3} Axial Deformation

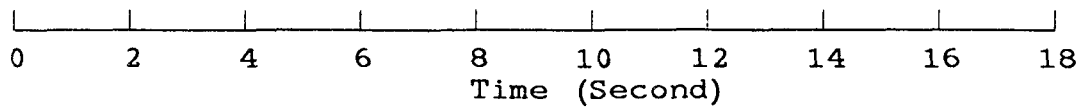
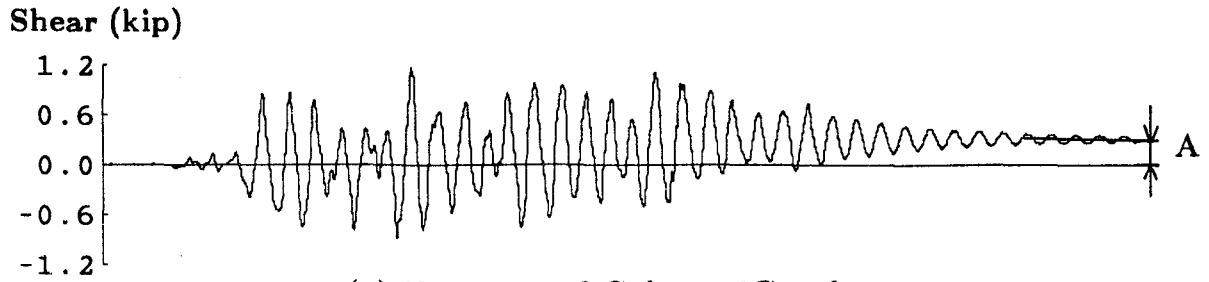
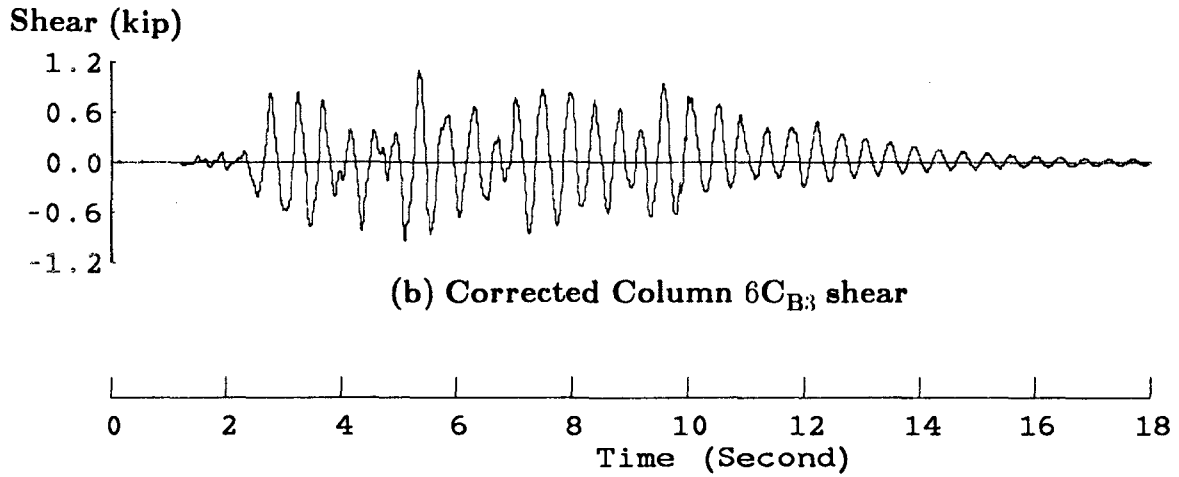


FIG. 6.7 HIGH FREQUENCY NOISE FILTERING (ORMSBY FILTER)



(a) Uncorrected Column 6C_{B3} shear



(b) Corrected Column 6C_{B3} shear

FIG. 6.8 LOW FREQUENCY NOISE FILTERING

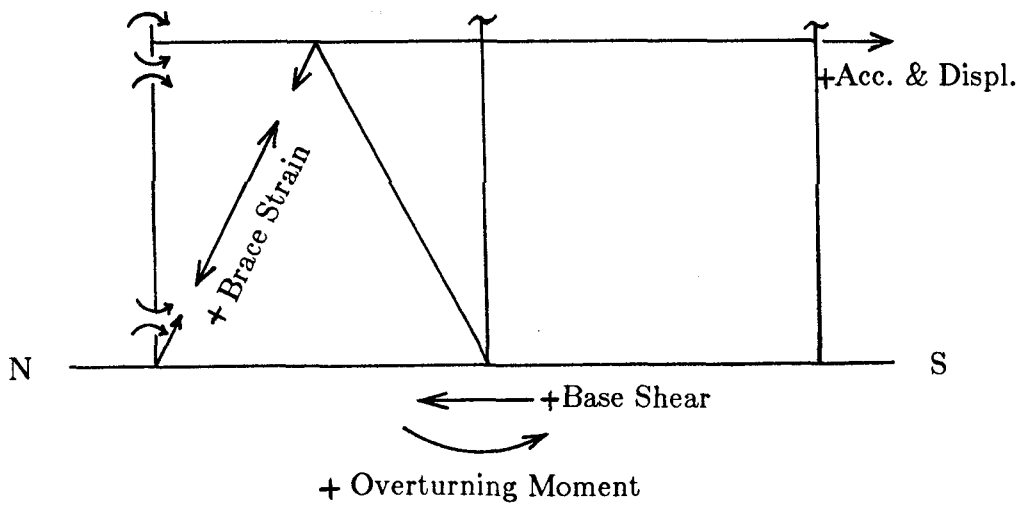


FIG. 6.9 SIGN CONVENTION

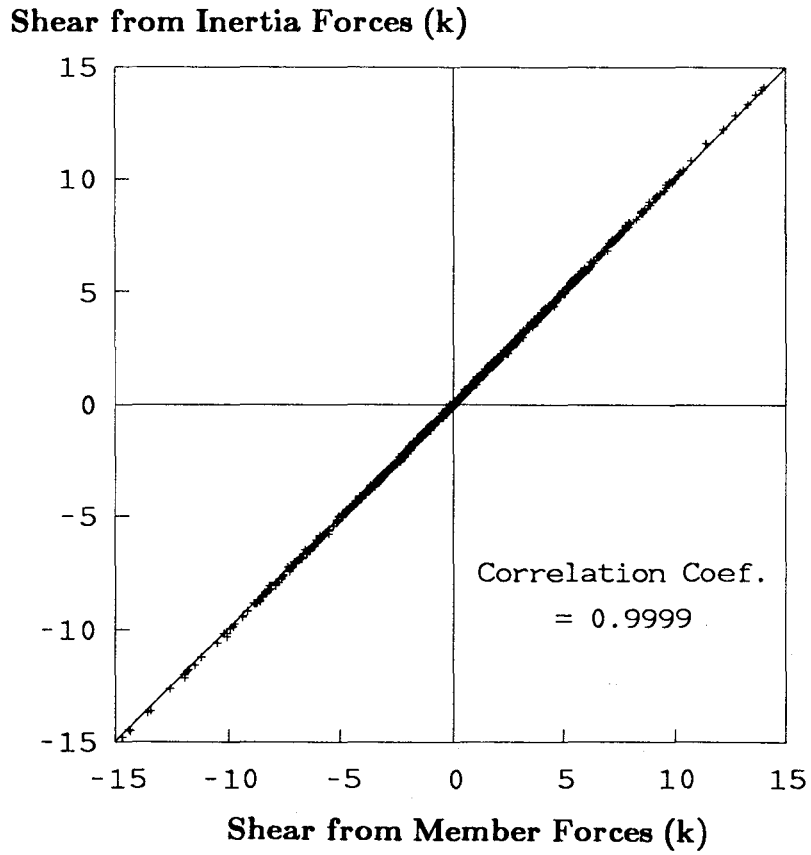


FIG. 6.10 COMPARISON OF BASE SHEAR FROM TWO METHODS

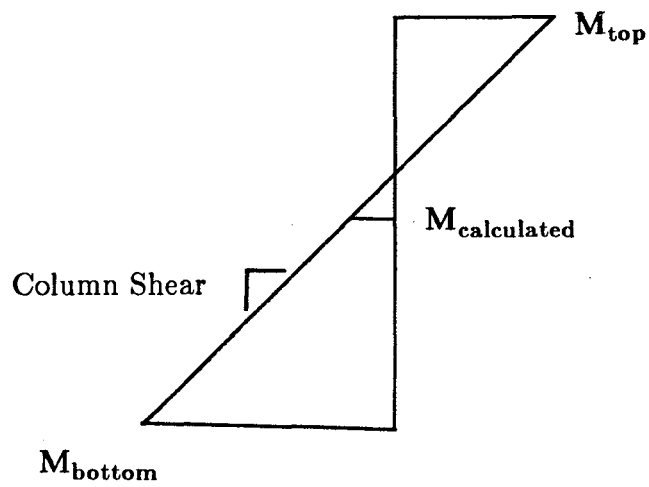
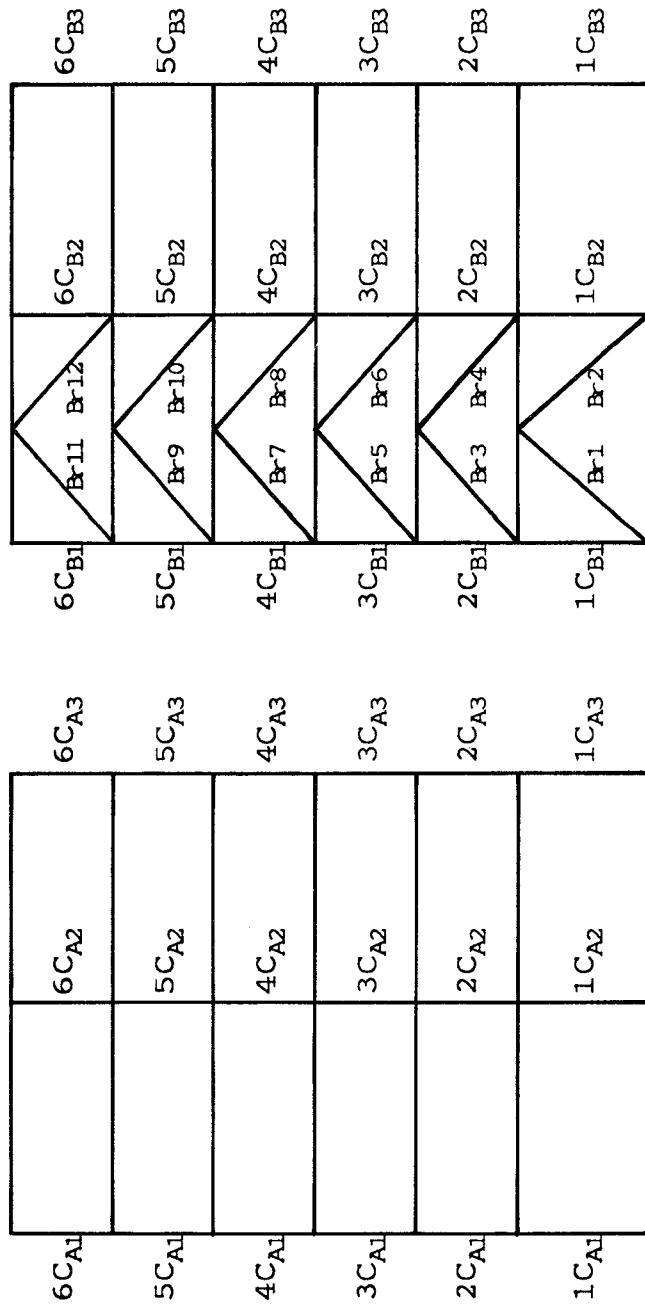


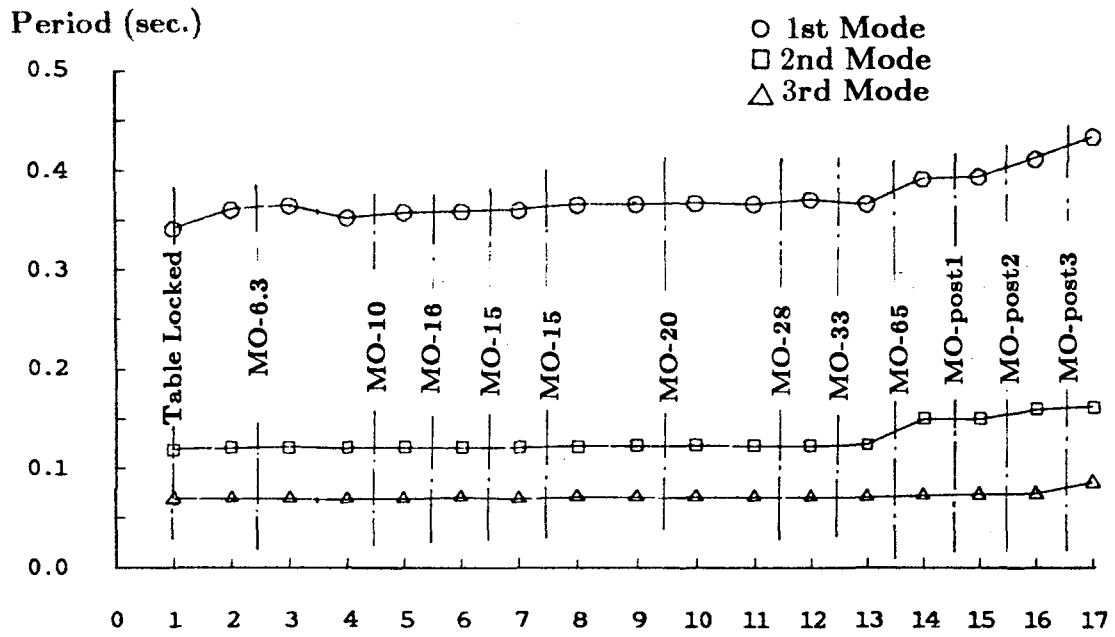
FIG. 6.11 FIRST STORY COLUMN END MOMENT EXTRAPOLATION



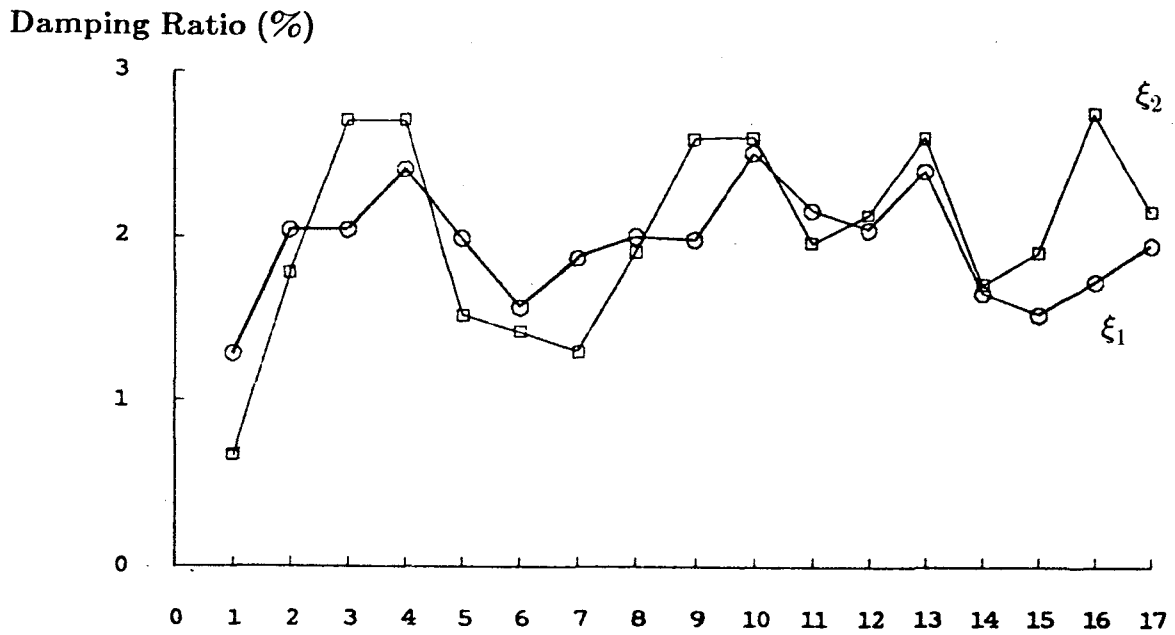
Frame A

Frame B

FIG. 6.12 MEMBER DESIGNATION

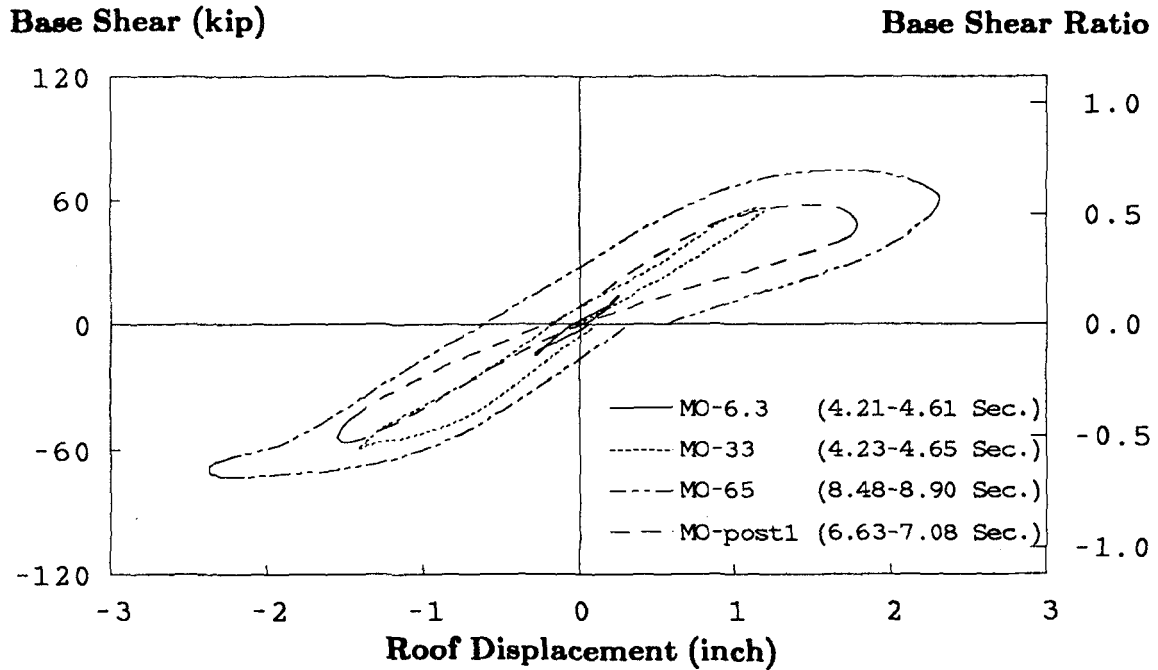


(a) Natural Periods

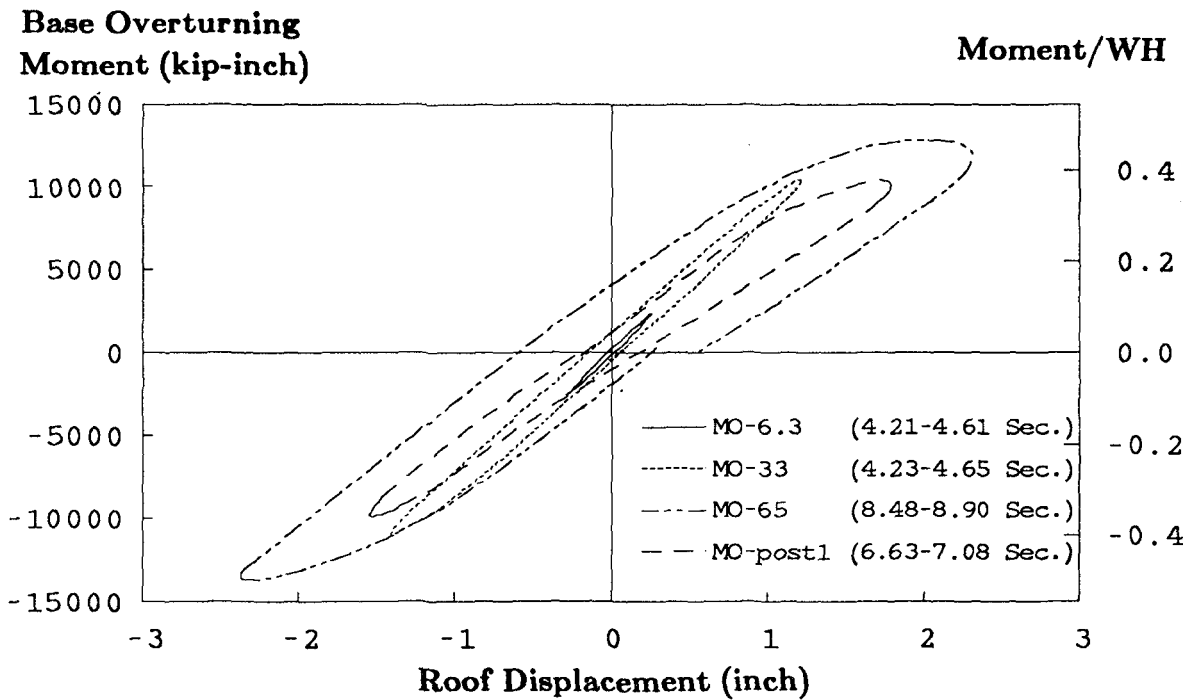


(b) Damping Ratios

FIG. 7.1 VARIATION OF MODEL PERIODS AND DAMPING RATIOS THROUGHOUT THE SHAKING TABLE TESTS

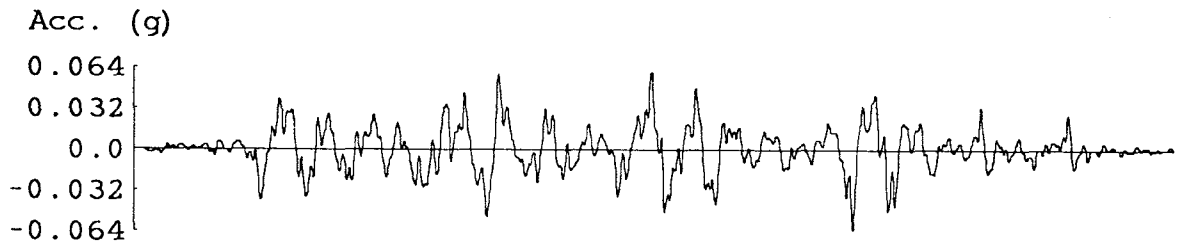


(a) Composite of Largest Cycles of Roof Drift versus Base Shear Curves

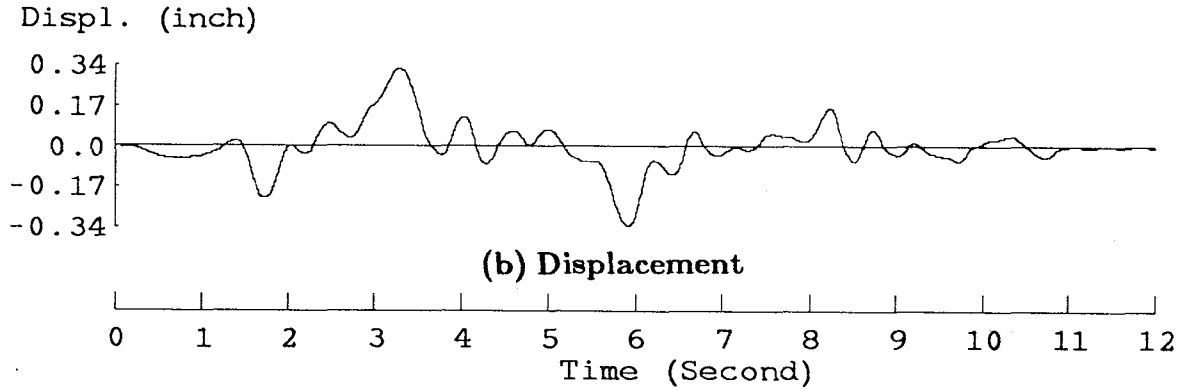


(b) Composite of Largest Cycles of Roof Drift versus Base Overturning Moment Curves

FIG. 7.2 MODEL BASE SHEAR AND OVERTURNING MOMENT VERSUS ROOF DRIFT INDEX ENVELOPES

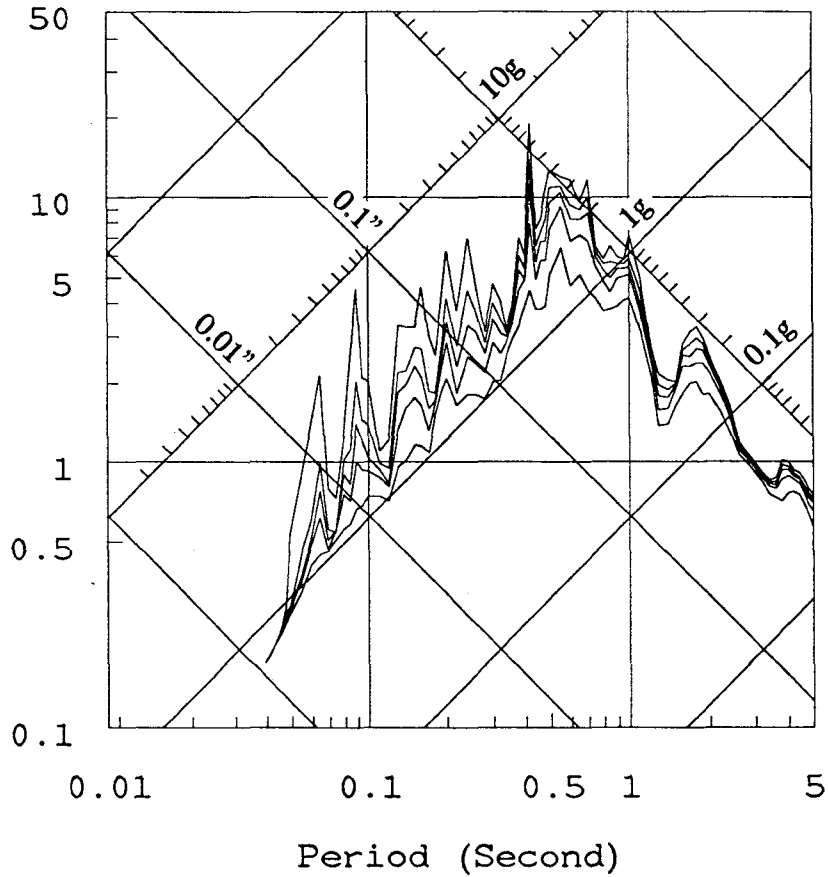


(a) Acceleration



(b) Displacement

Pseudo-Velocity (in/sec)



(c) Linear Elastic Response Spectra (0,0.5,1,2,5% Damping)

FIG. 7.3 MEASURED SHAKING TABLE HORIZONTAL MOTION
AND RESPONSE SPECTRA (MO-6.3 TEST)

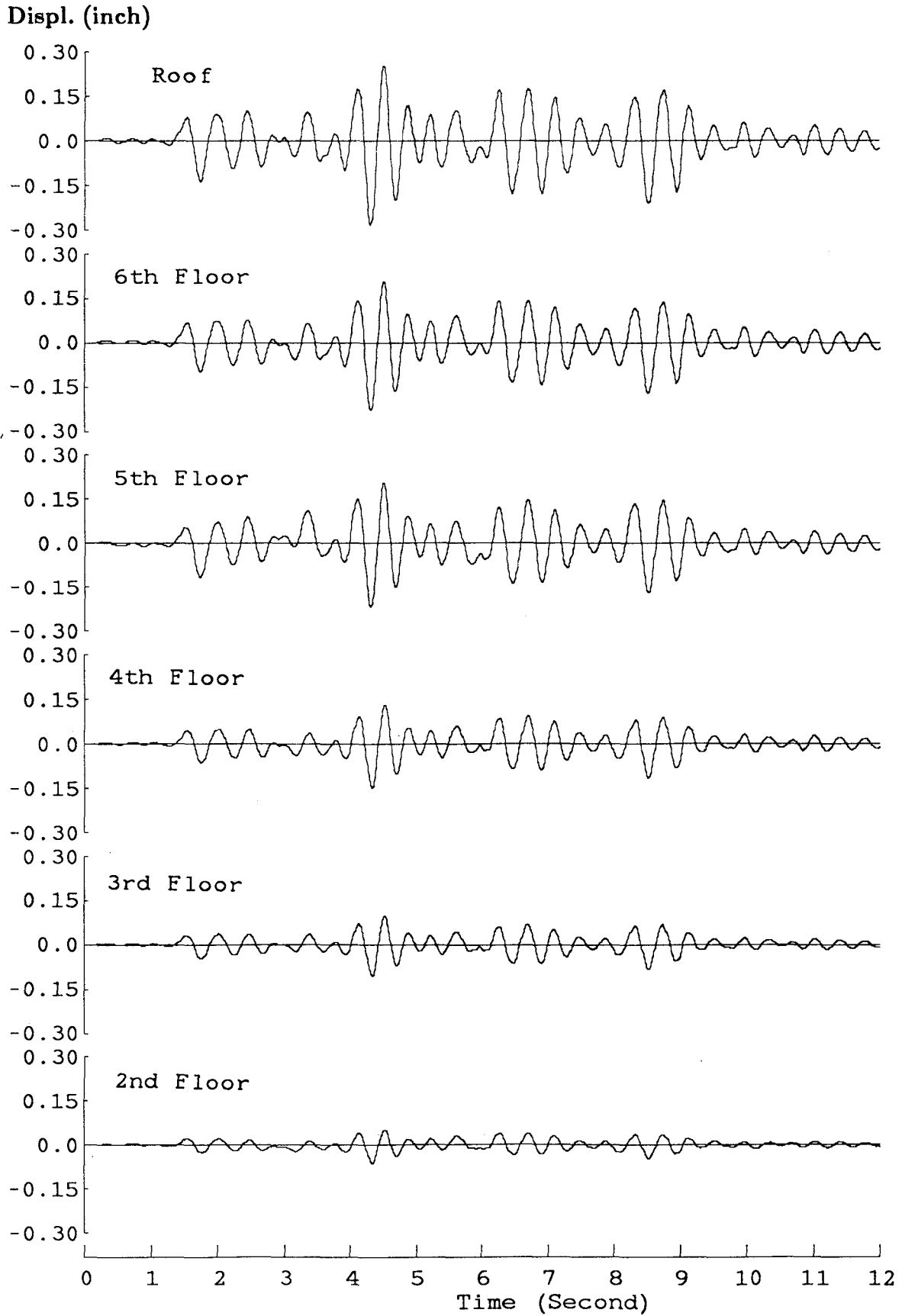


FIG. 7.4 MO-6.3 TEST RELATIVE DISPLACEMENT TIME HISTORIES

Inter-story drift (inch)

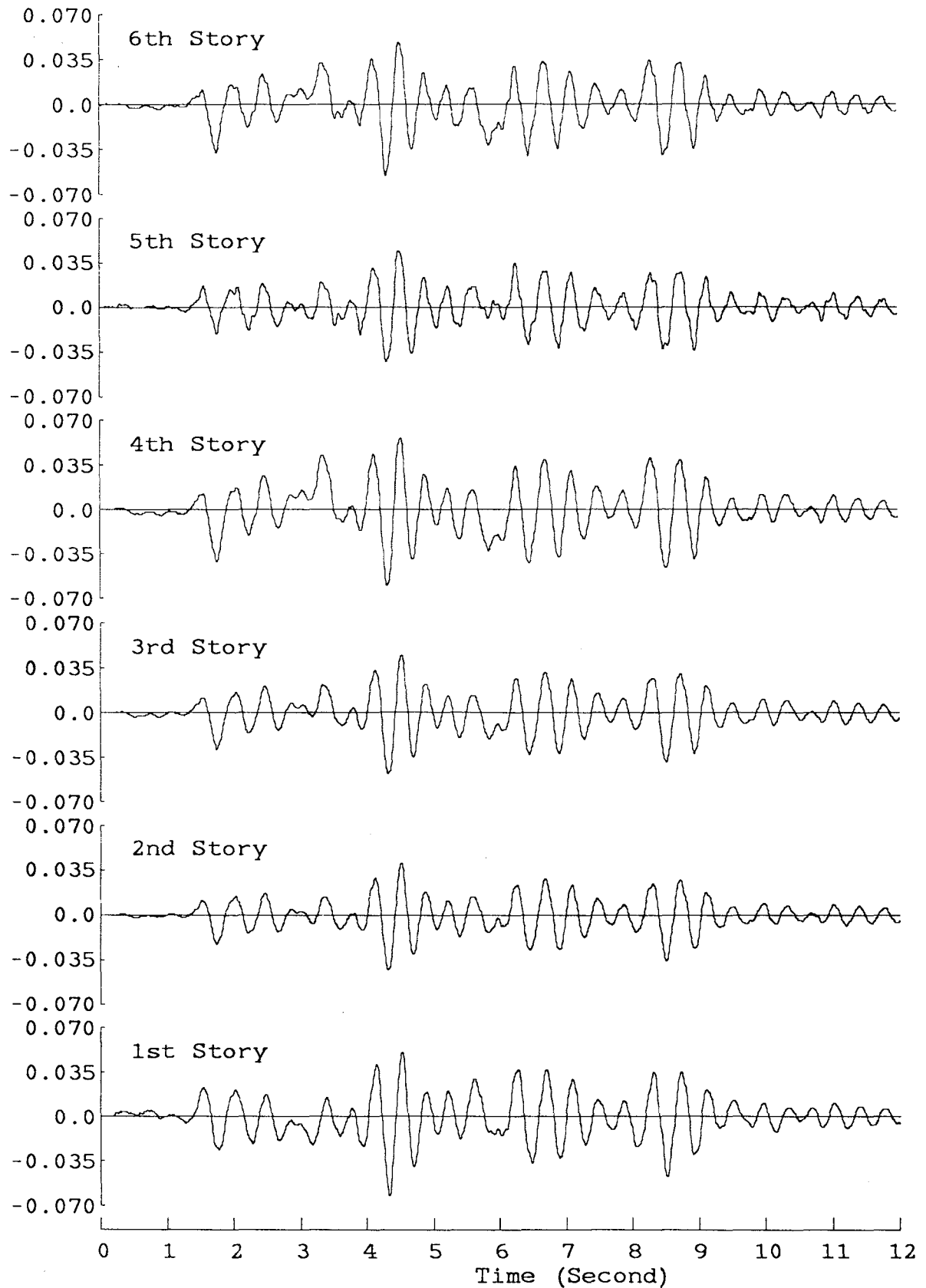
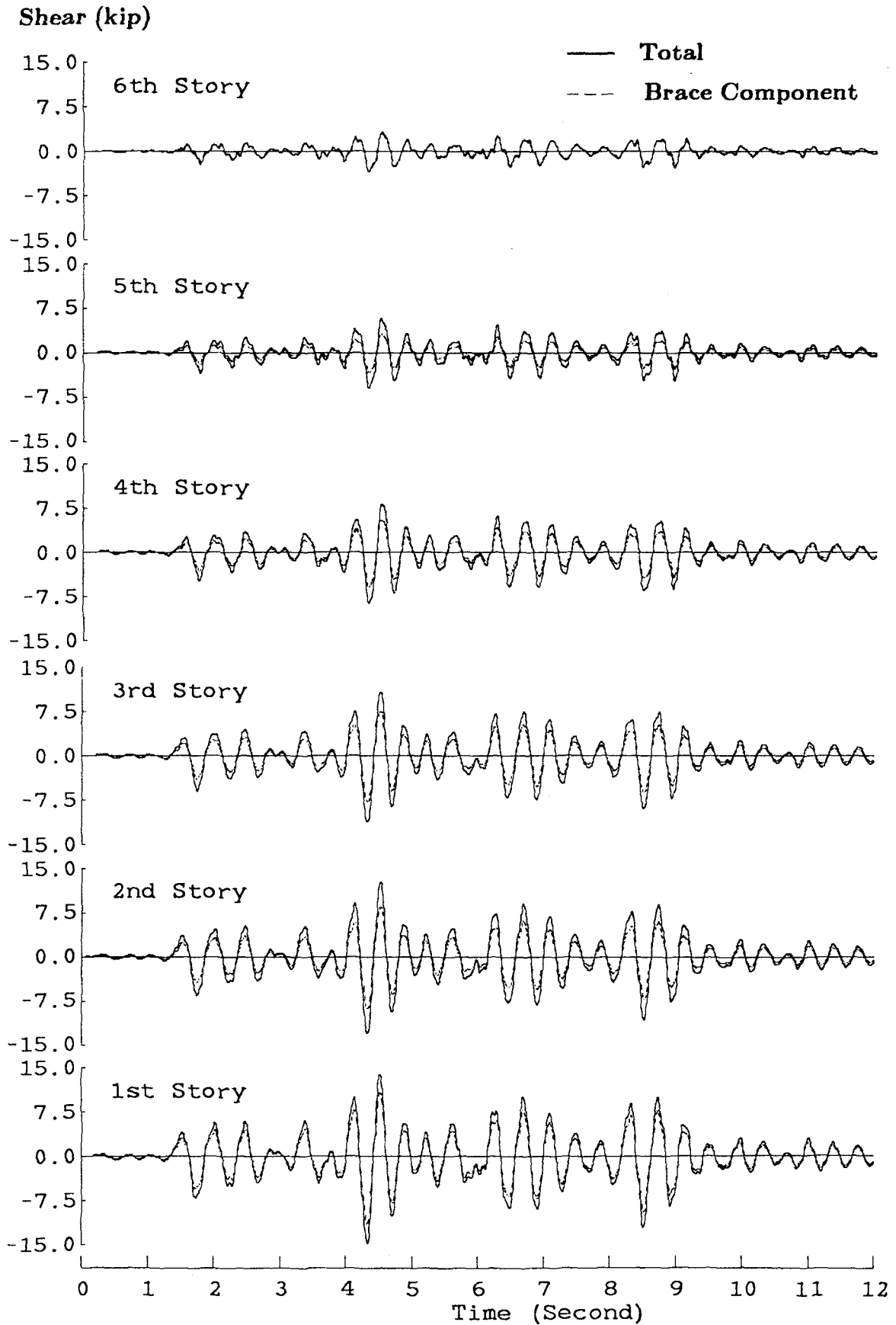


FIG. 7.5 MO-6.3 TEST INTER-STORY DRIFT TIME HISTORIES



**FIG. 7.6 STORY SHEAR (TOTAL AND BRACE COMPONENT)
TIME HISTORIES OF MO-6.3 TEST**

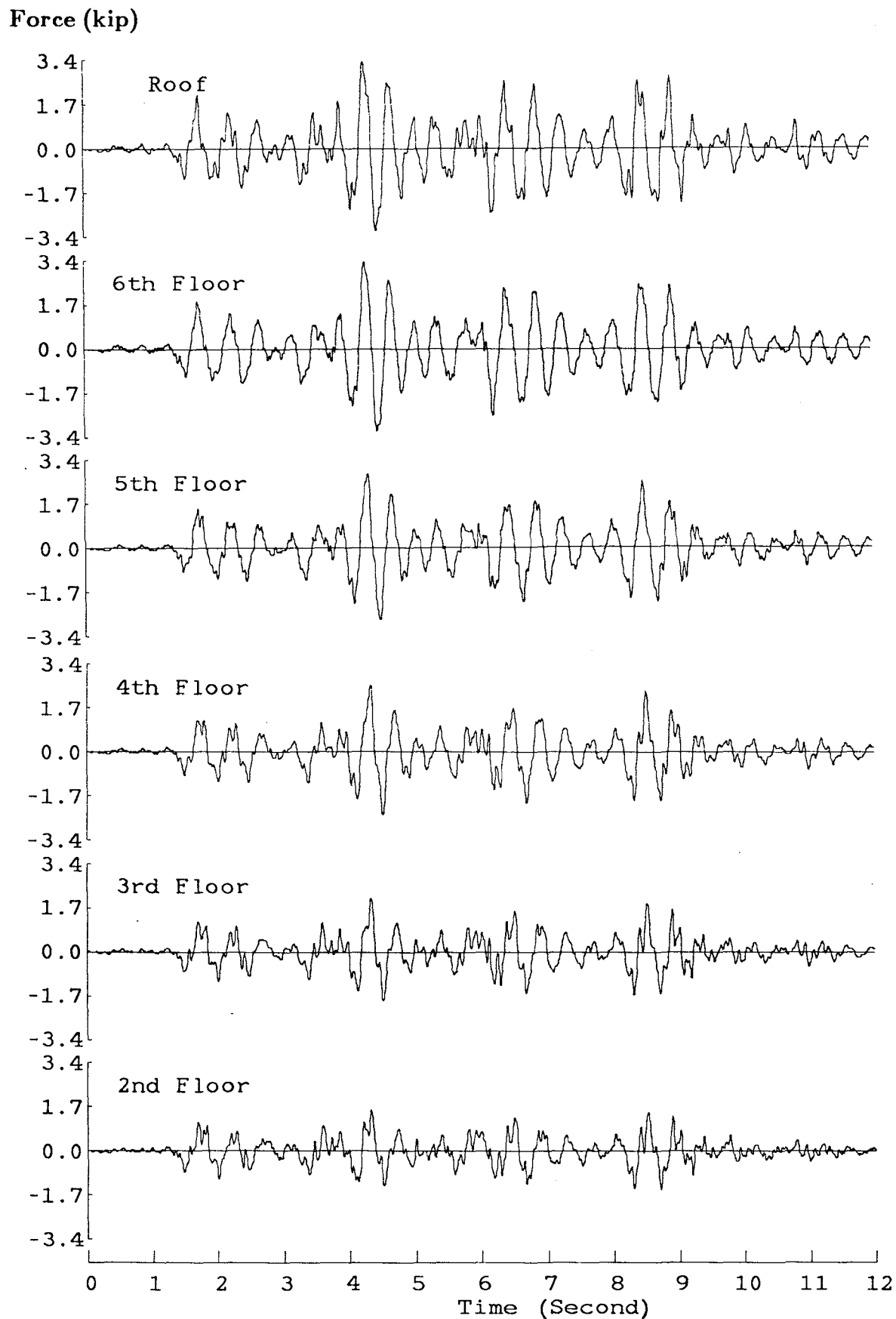


FIG. 7.7 MO-6.3 TEST LATERAL INERTIA FORCE TIME HISTORIES

Base Overturning

Moment (kip-inch)

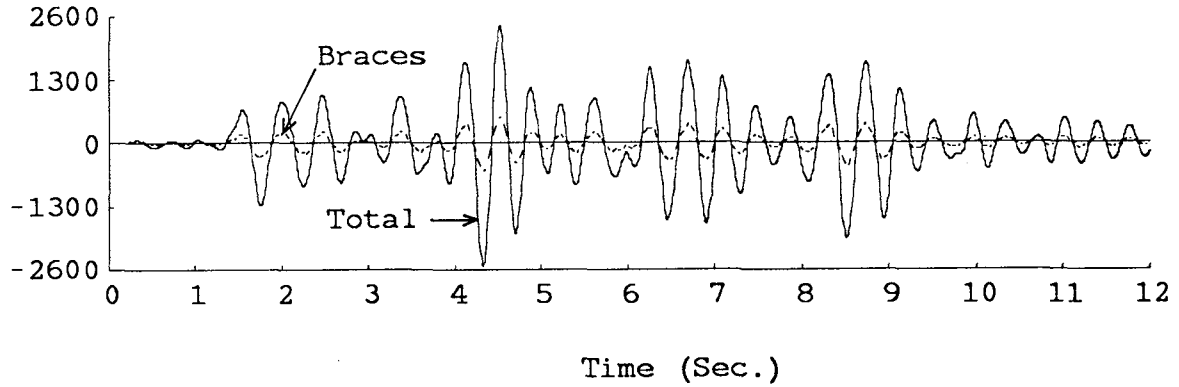
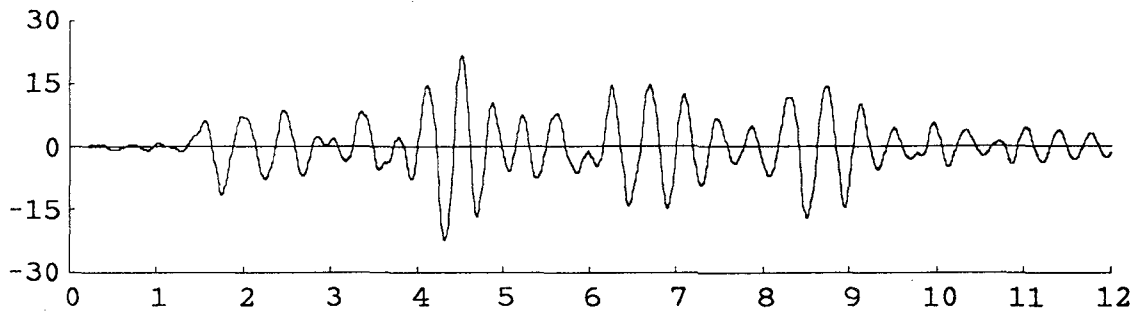
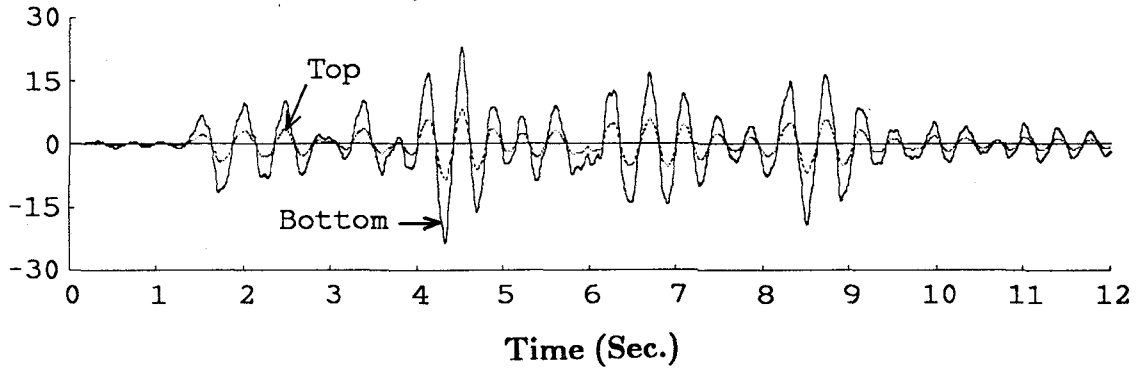


FIG. 7.8 MO-6.3 TEST BASE OVERTURNING MOMENT TIME HISTORIES

Change in Axial Force (kip)



Change in Moment (kip-inch)



**FIG 7.9 COLUMN 1C_{B1}: CHANGE IN AXIAL FORCE AND
END MOMENT TIME HISTORIES (MO-6.3 TEST)**

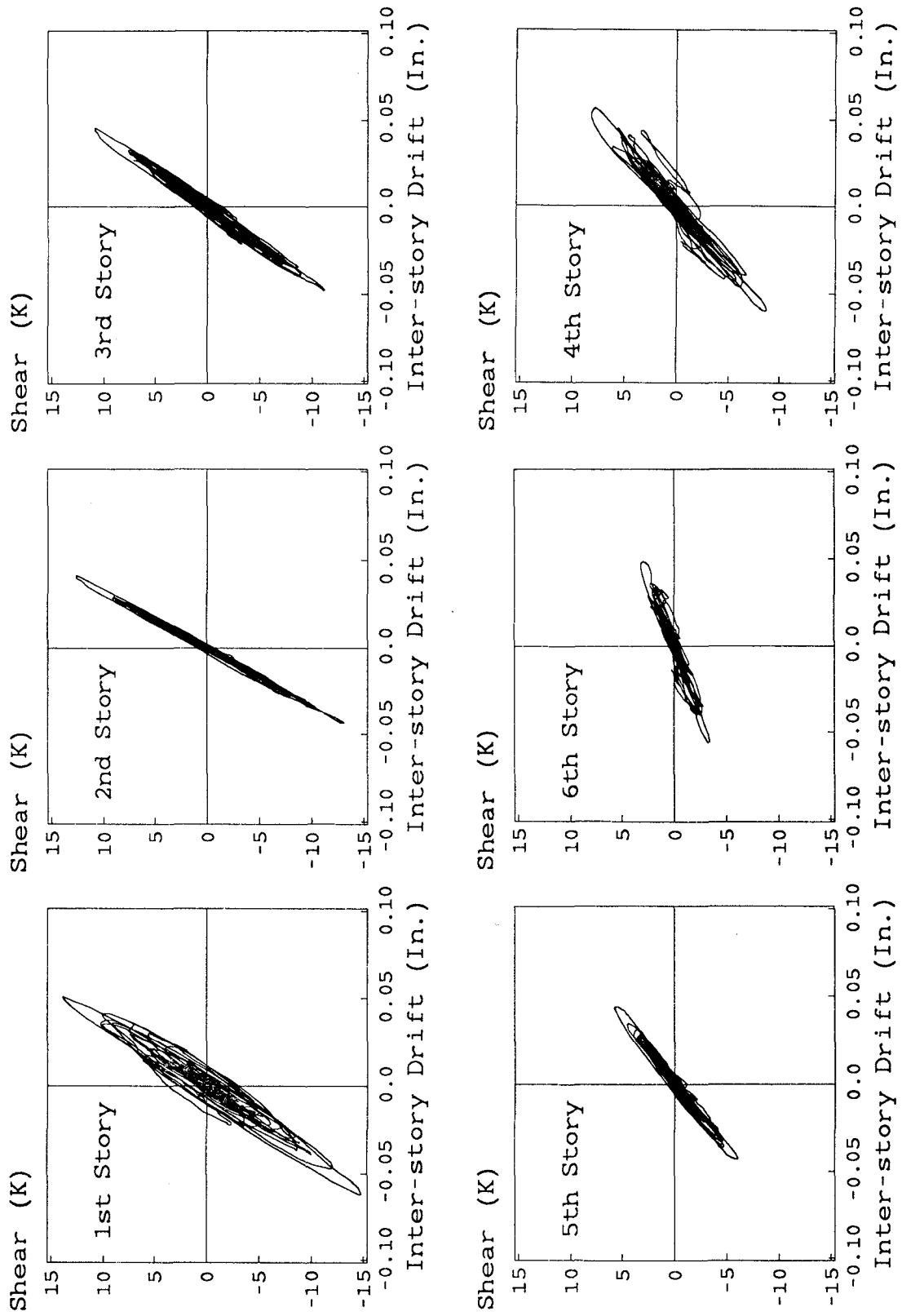


FIG. 7.10 MO-6.3 TEST INTER-STORY DRIFT VERSUS STORY SHEAR CURVES

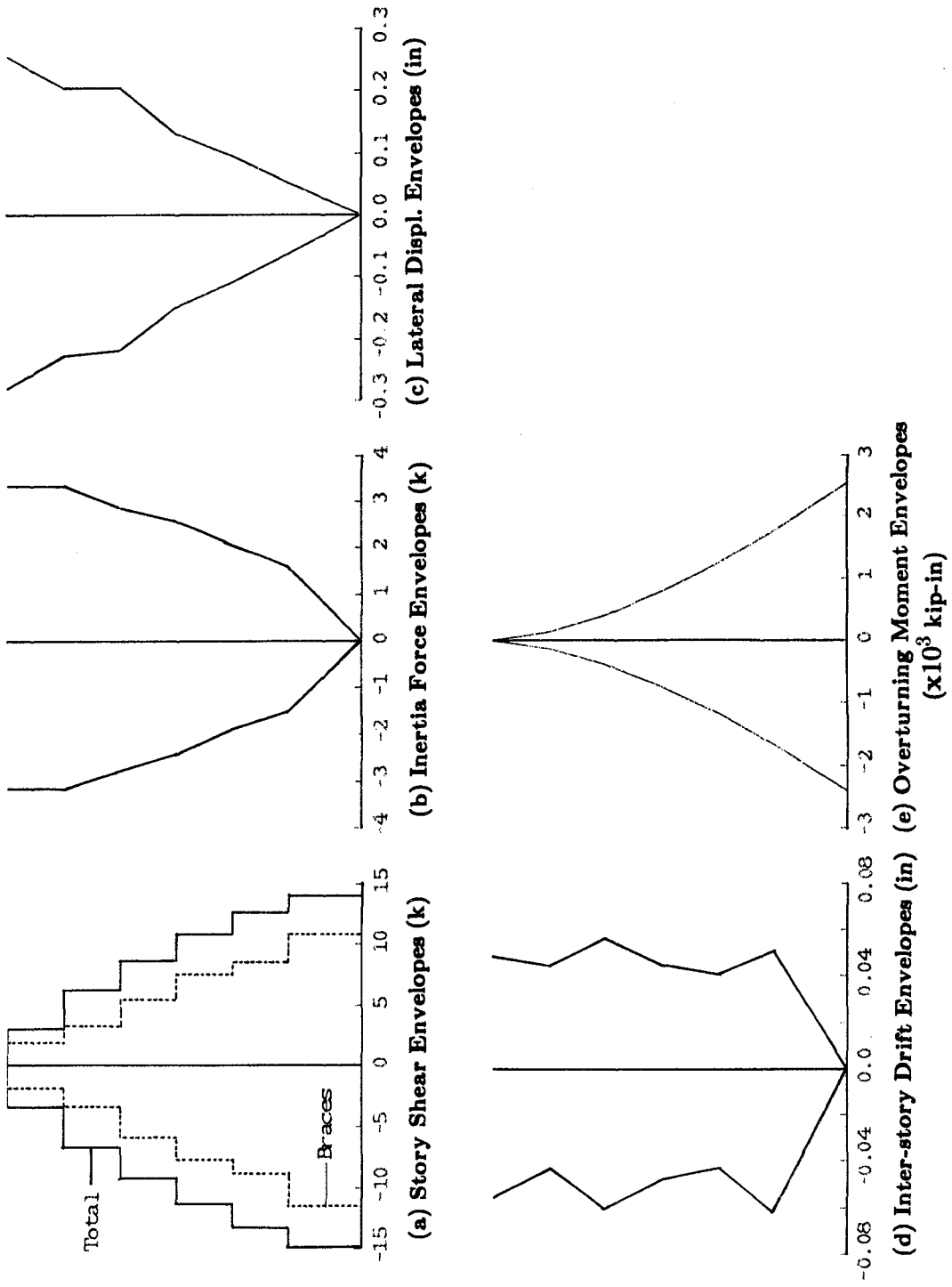


FIG. 7.11 MO-6.3 TEST RESPONSE ENVELOPES

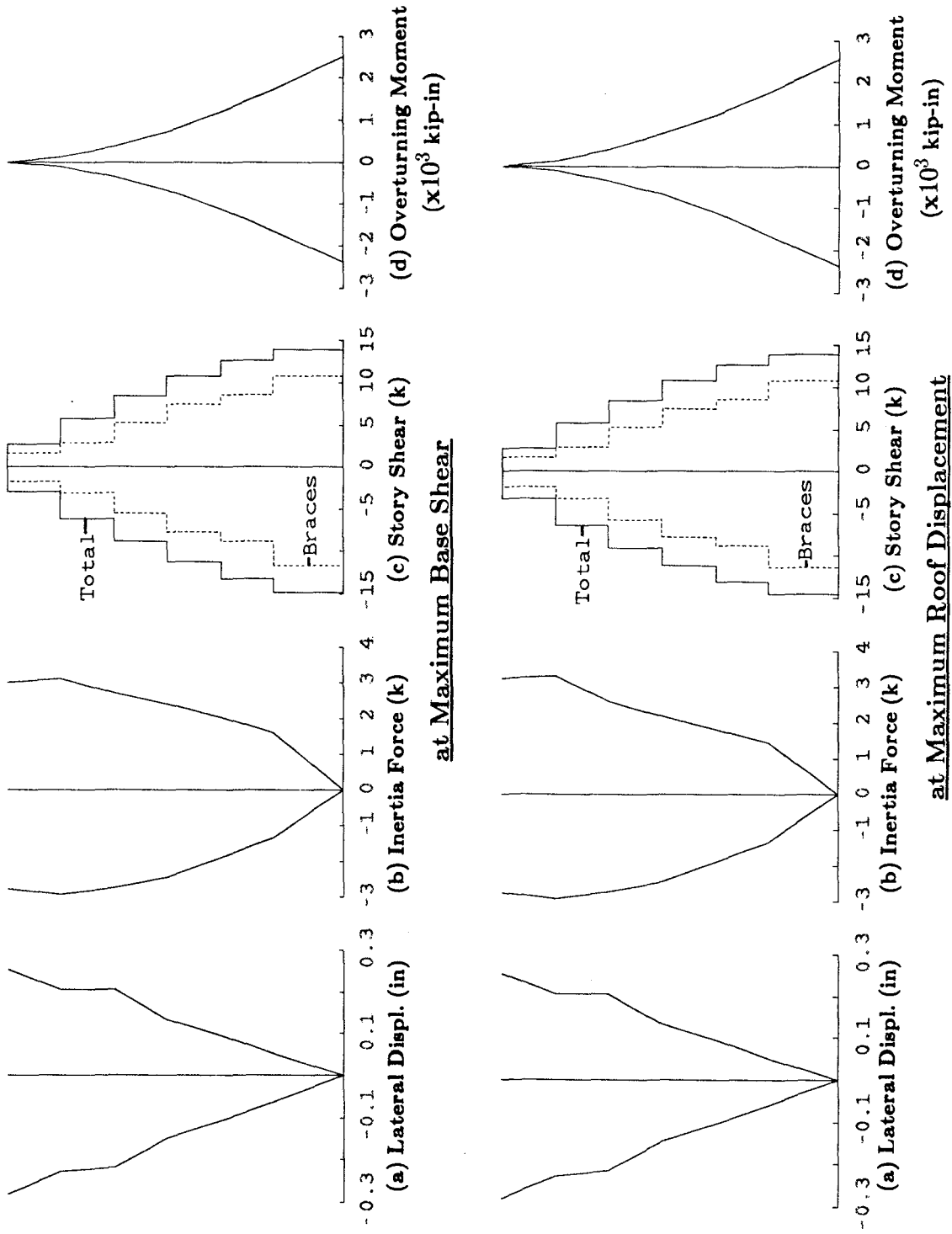


FIG. 7.12 MO-6.3 TEST RESPONSE PROFILES AT MAXIMUM RESPONSES

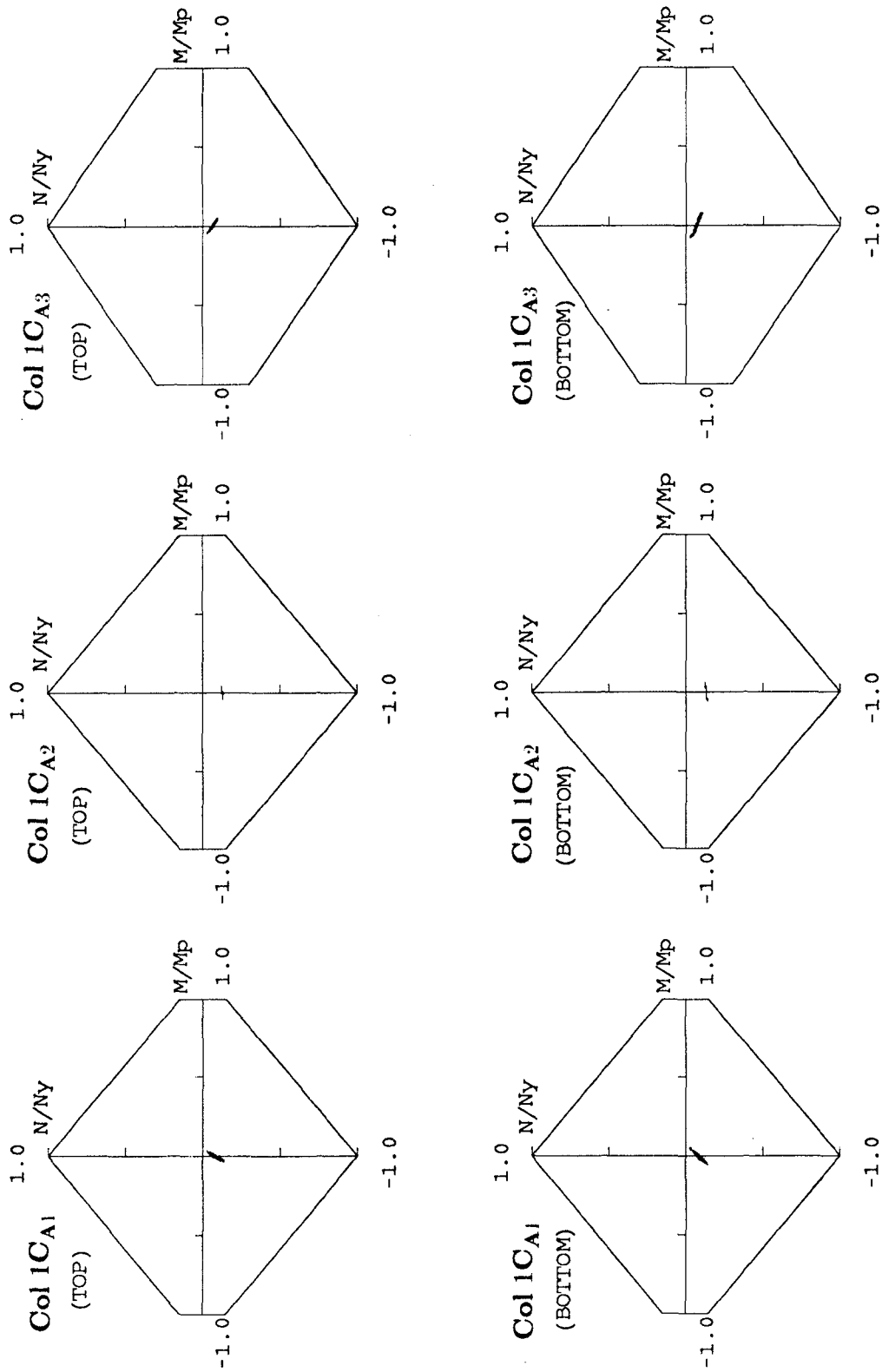


FIG. 7.13(a) MO-6.3 TEST FIRST STORY COLUMN AXIAL FORCE
VERSUS END MOMENT INTERACTION CURVES (FRAME A)

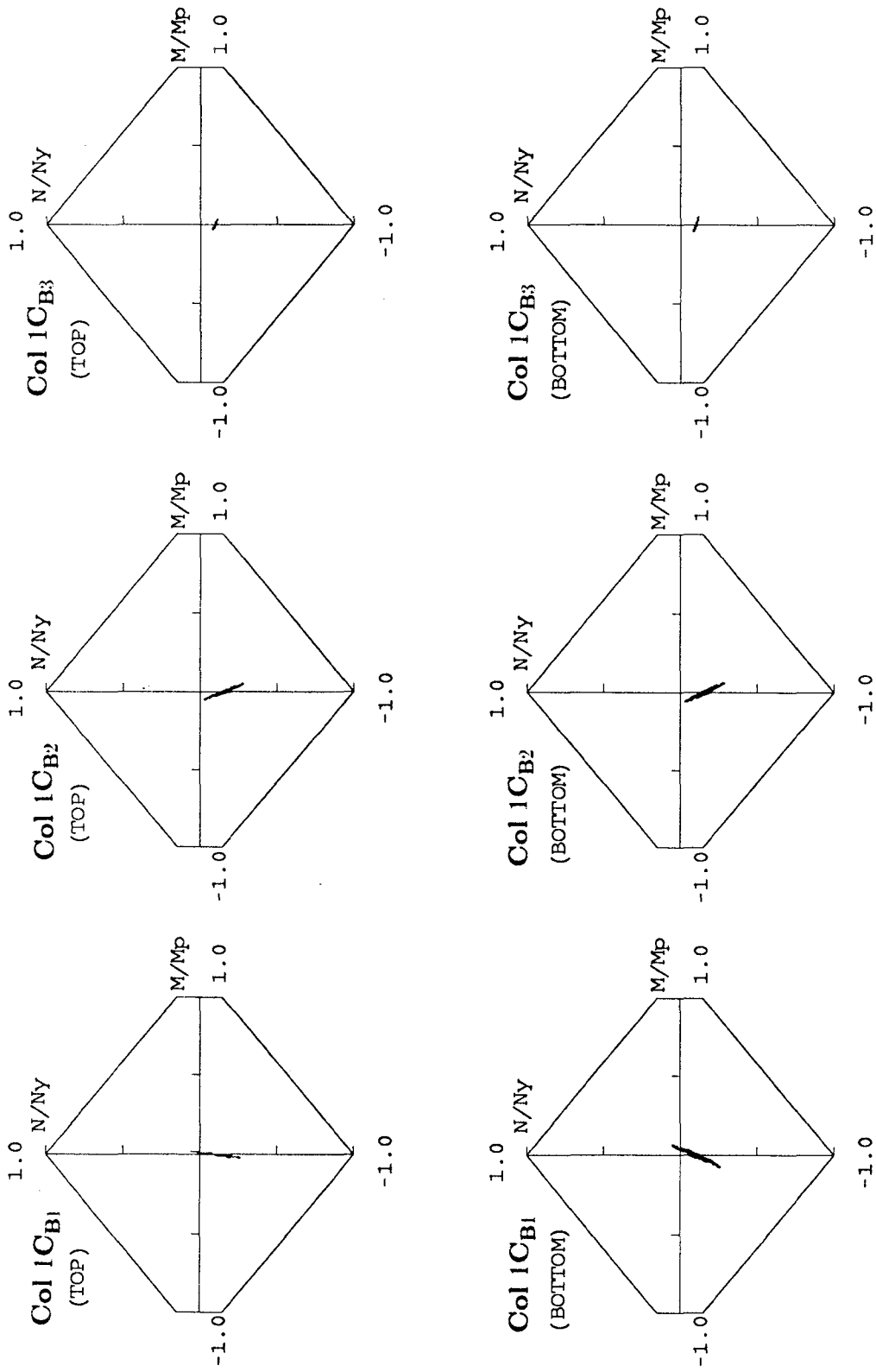


FIG. 7.13(b) MO-6.3 TEST FIRST STORY COLUMN AXIAL FORCE VERSUS END MOMENT INTERACTION CURVES (FRAME B)

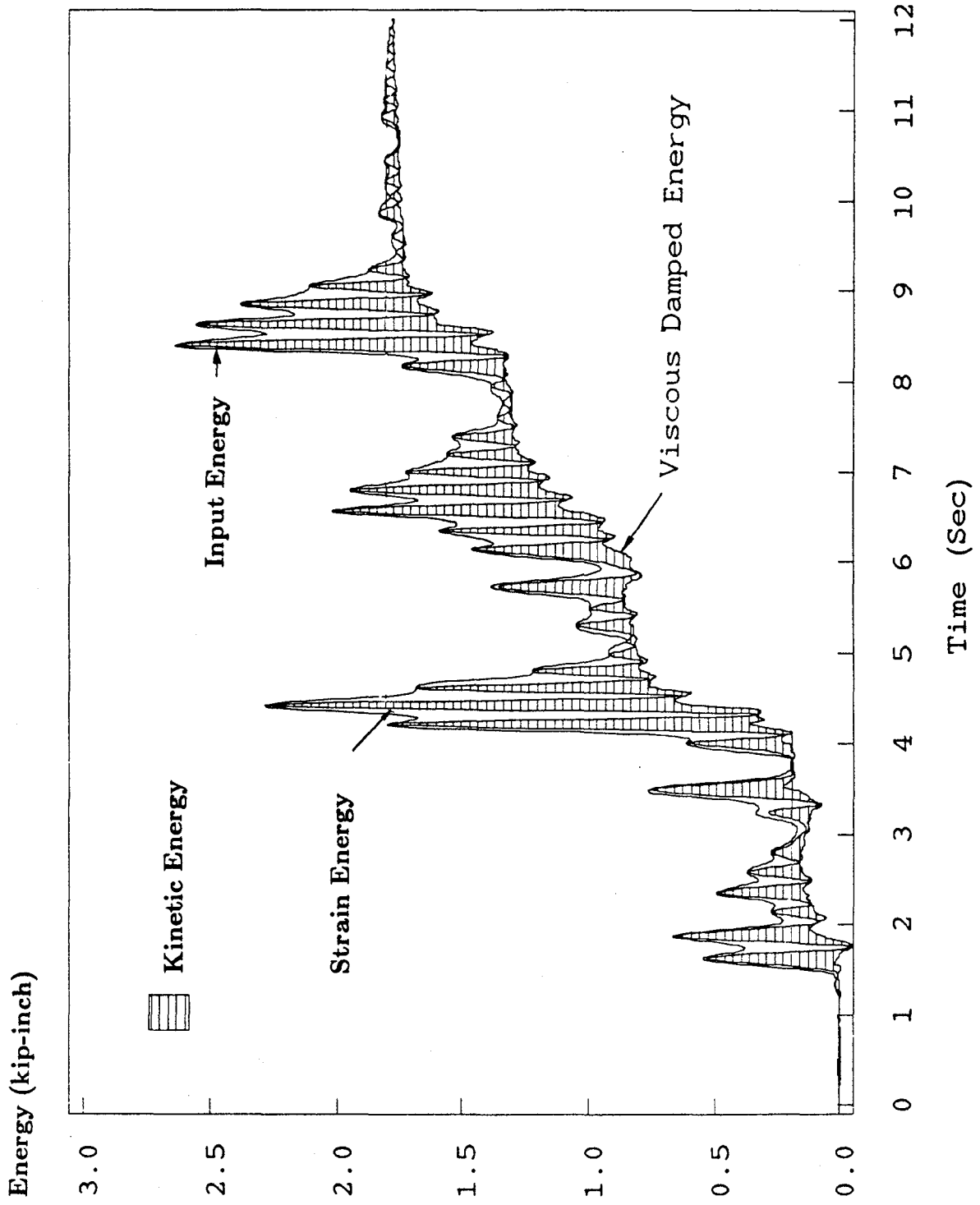
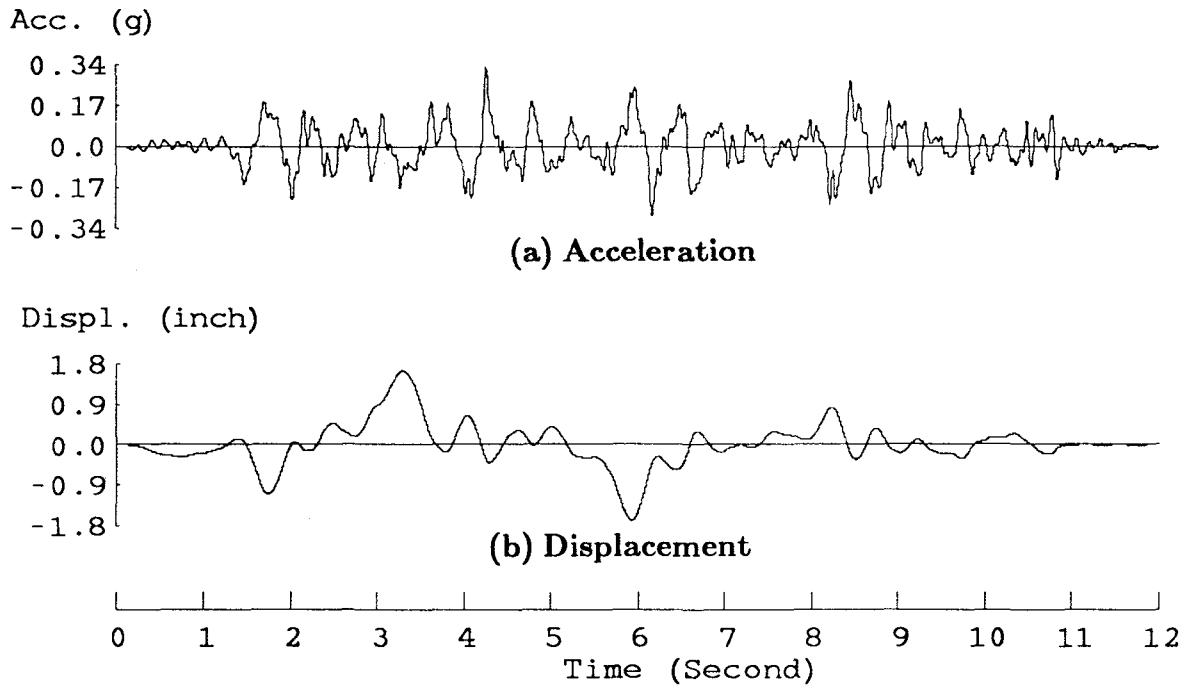
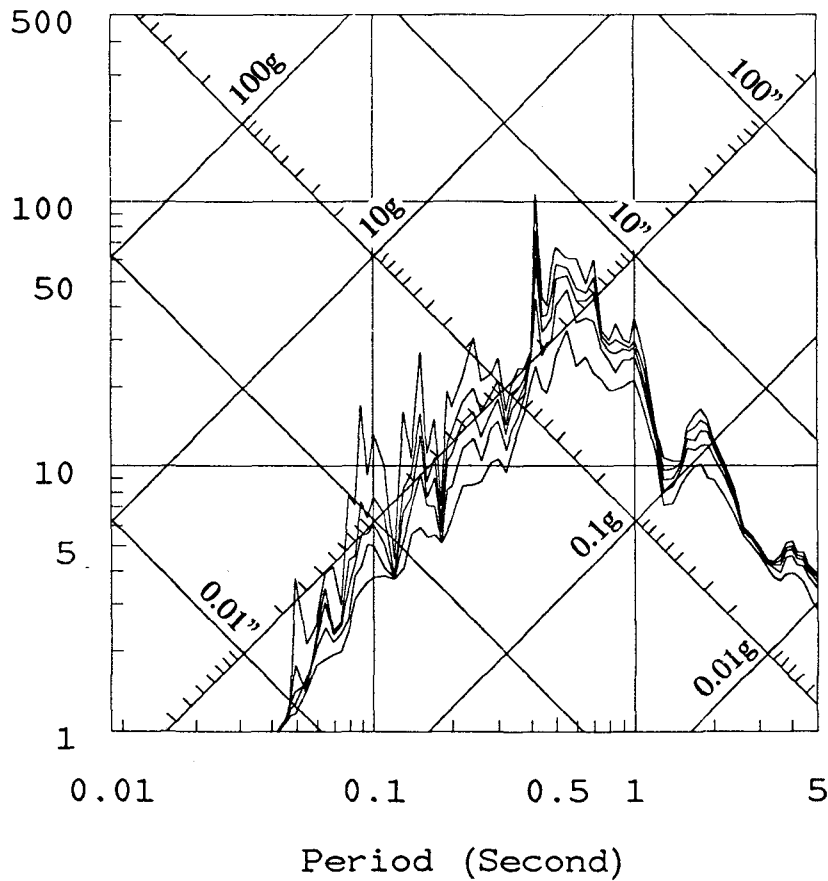


FIG. 7.14 MO-6.3 TEST ENERGY TIME HISTORIES



Pseudo-Velocity (in/sec)



(c) Linear Elastic Response Spectra (0,0.5,1,2,5% Damping)

FIG. 7.15 MEASURED SHAKING TABLE HORIZONTAL MOTIONS AND RESPONSE SPECTRA (MO-33 TEST)

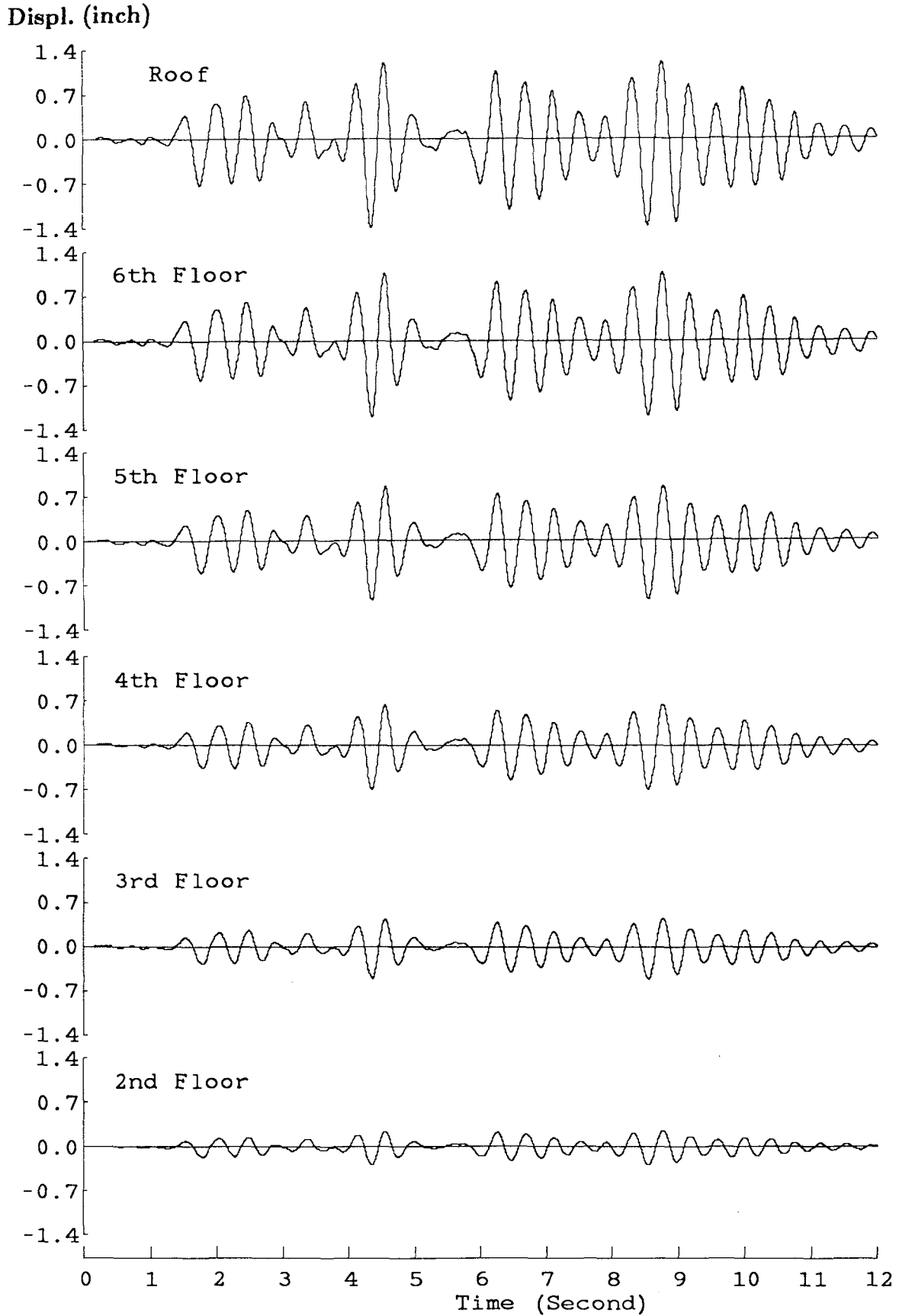


FIG. 7.16 MO-33 TEST RELATIVE DISPLACEMENT TIME HISTORIES

Inter-story drift (inch)

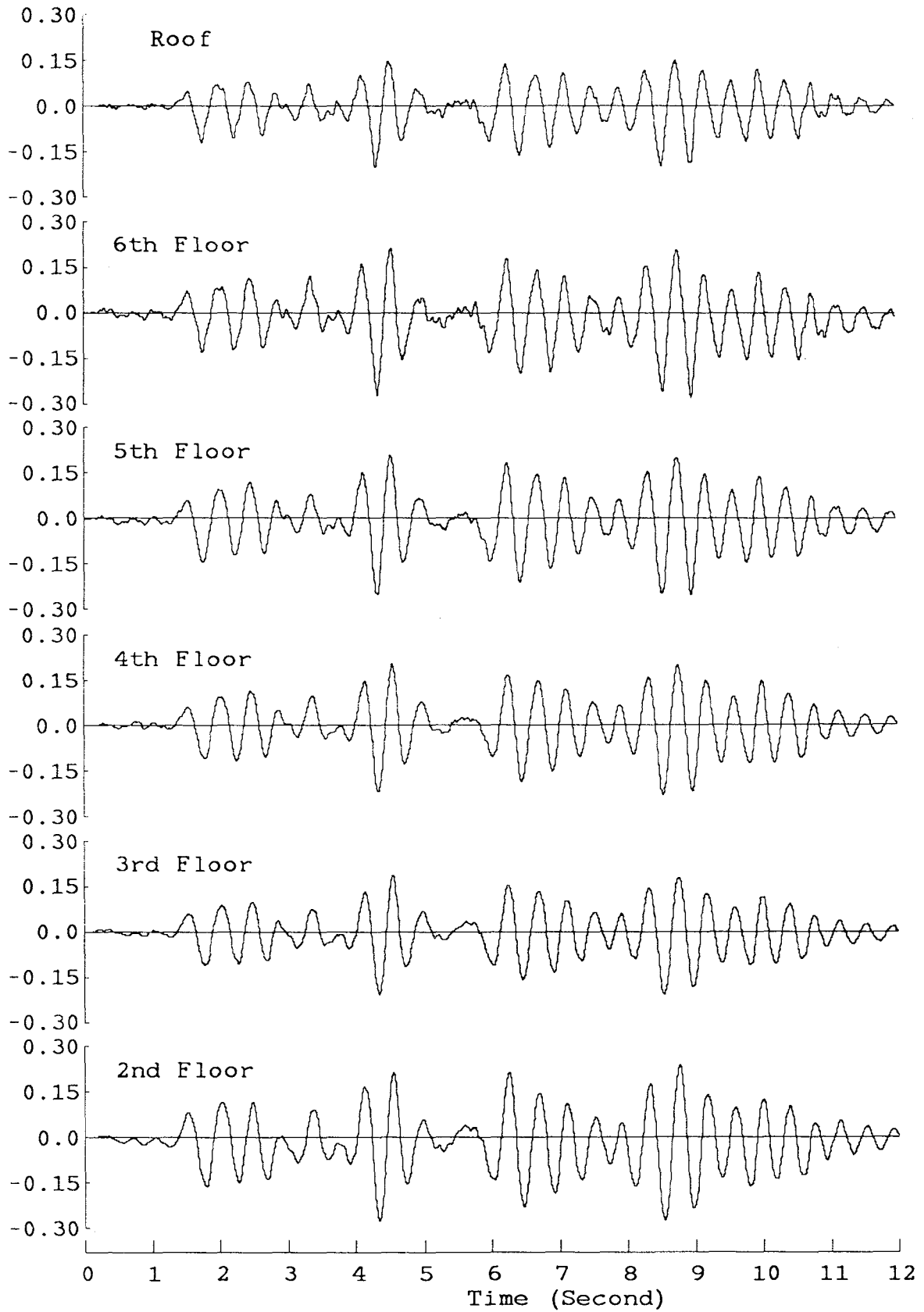
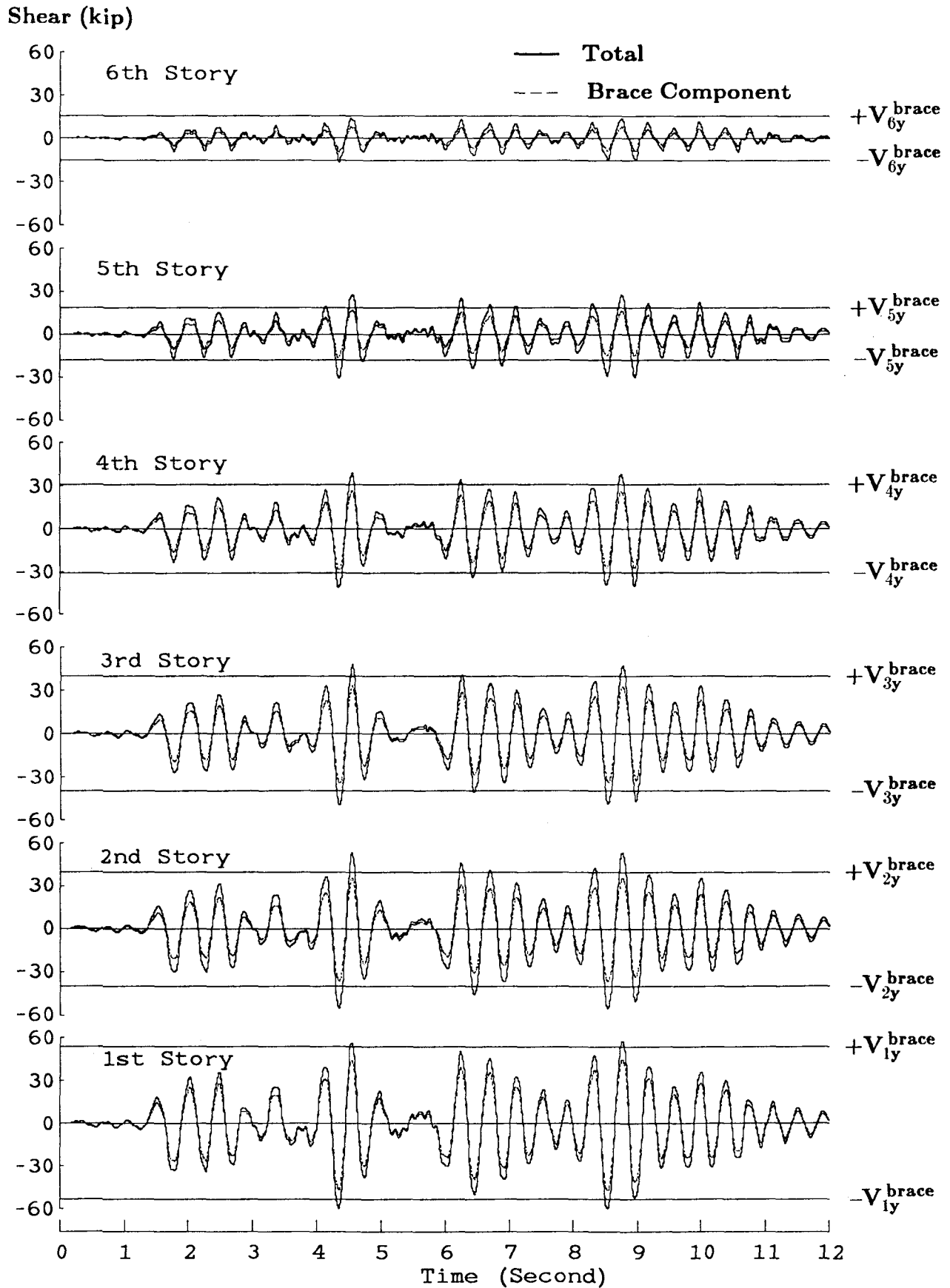


FIG. 7.17 MO-33 TEST INTER-STORY DRIFT TIME HISTORIES



**FIG. 7.18 STORY SHEAR (TOTAL AND BRACE COMPONENT)
TIME HISTORIES OF MO-33 TEST**

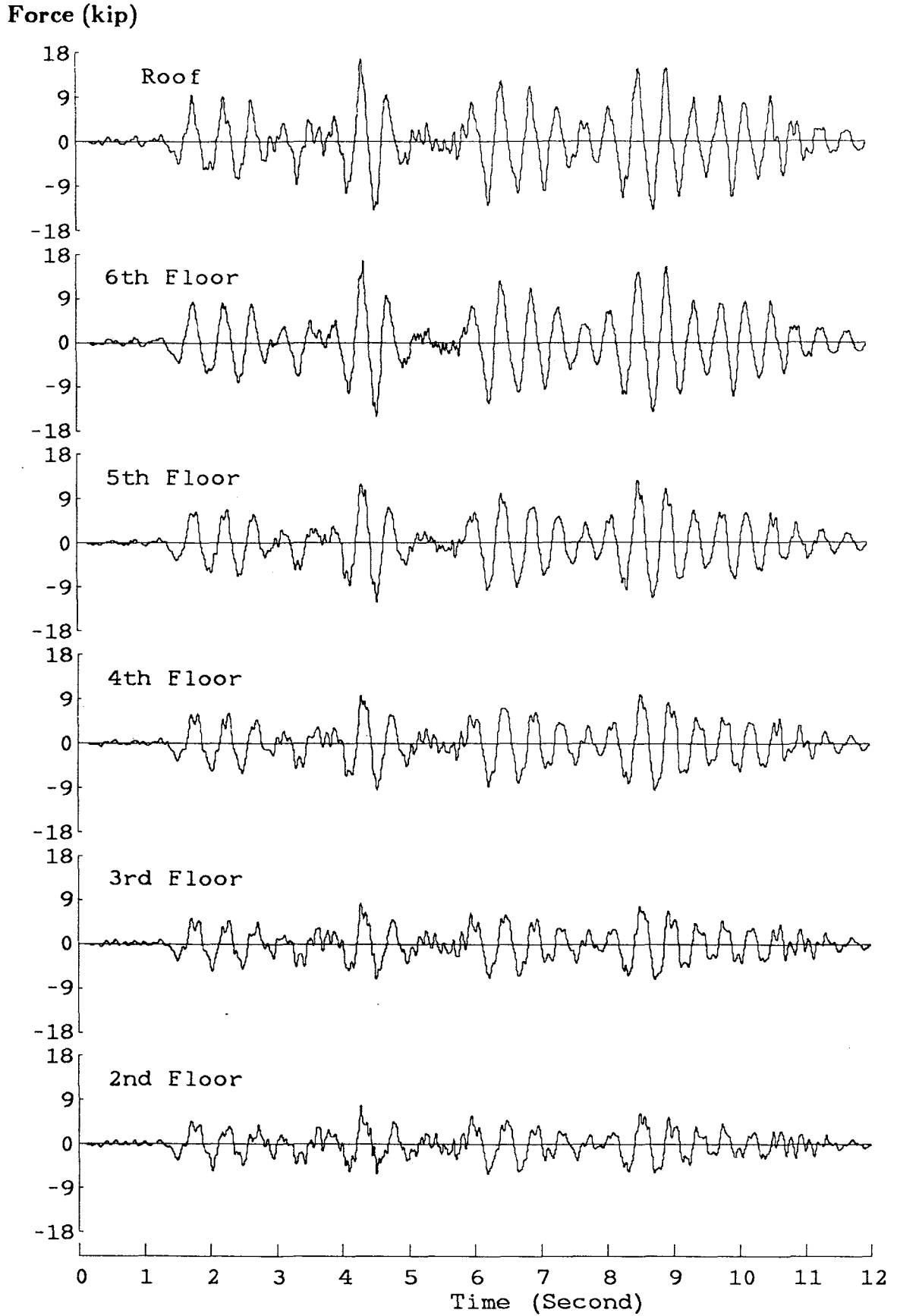


FIG. 7.19 MO-33 TEST LATERAL INERTIA FORCE TIME HISTORIES

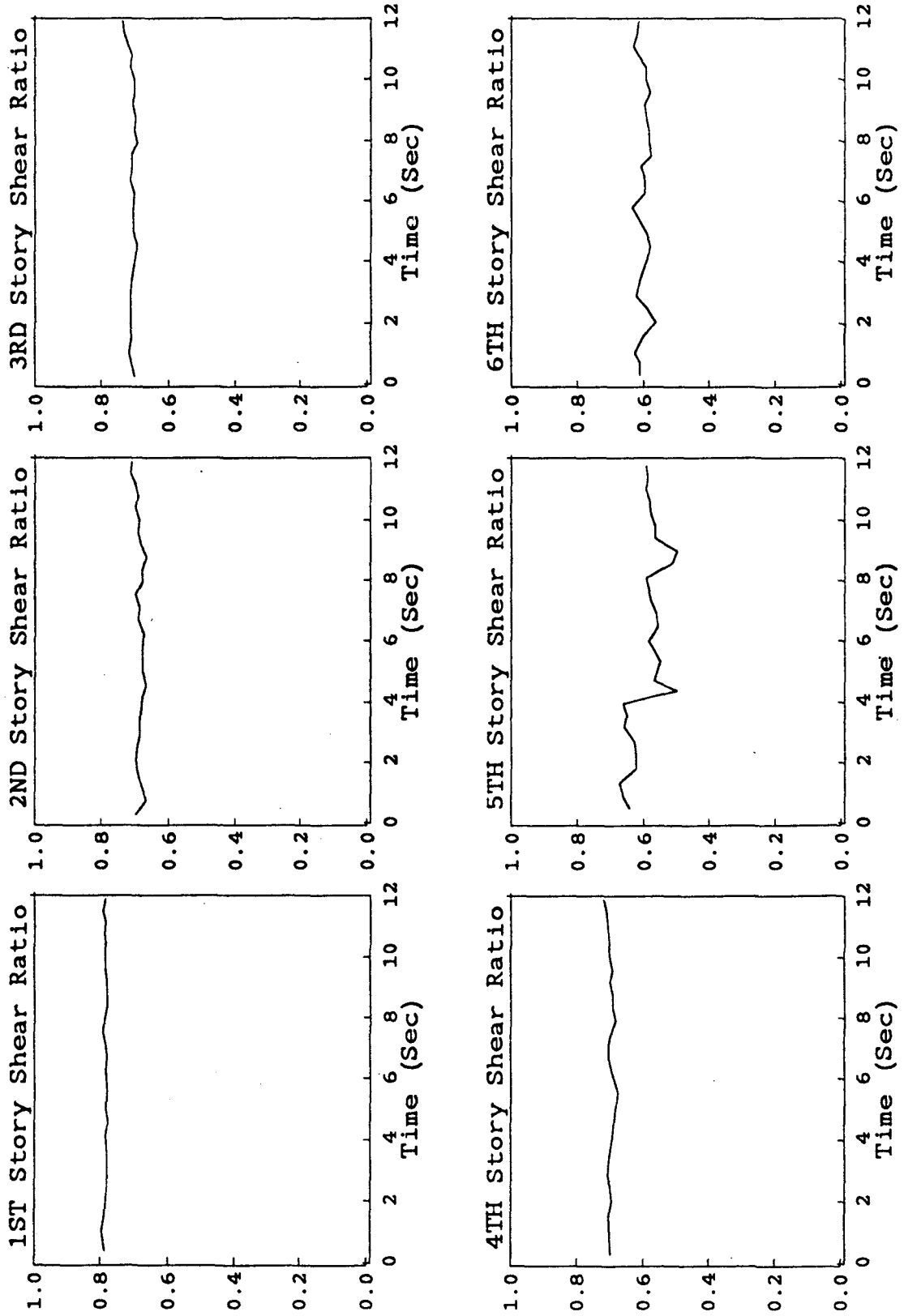


FIG. 7.20 MO-33 TEST $\frac{V_{BRACE}}{V_{TOTAL}}$ RATIO

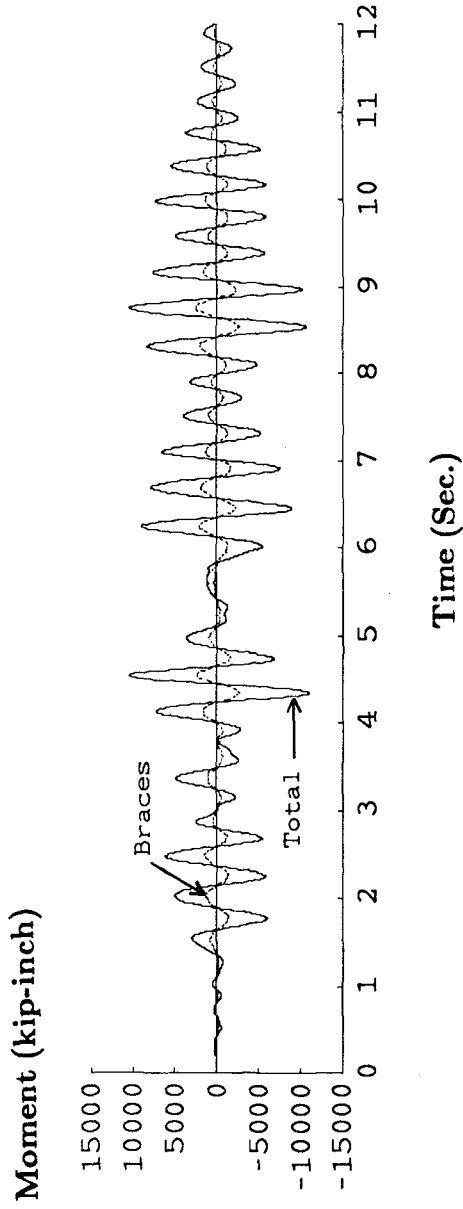


FIG. 7.21 MO-33 TEST BASE OVERTURNING MOMENT TIME HISTORIES

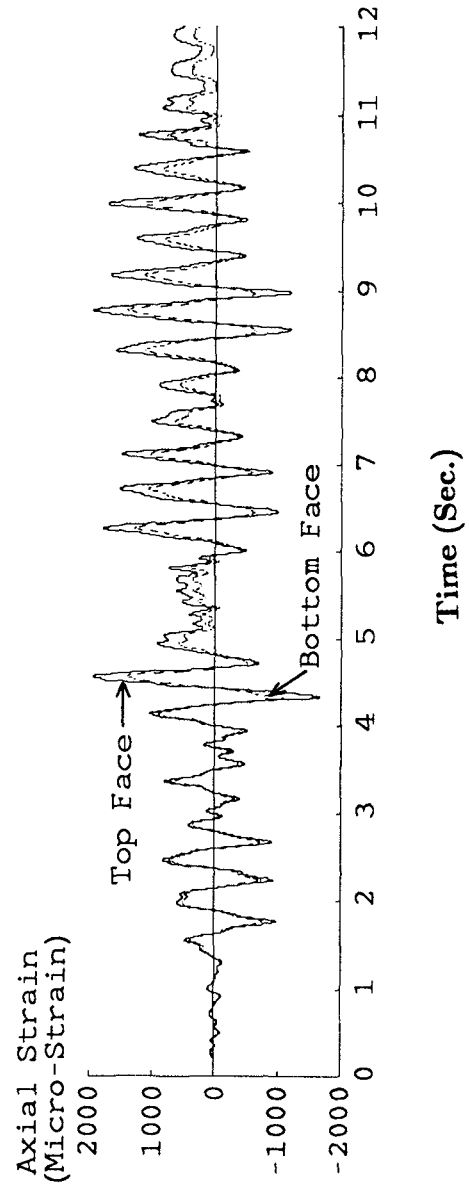


FIG. 7.22 MO-33 TEST BRACE 9 AXIAL STRAIN TIME HISTORIES

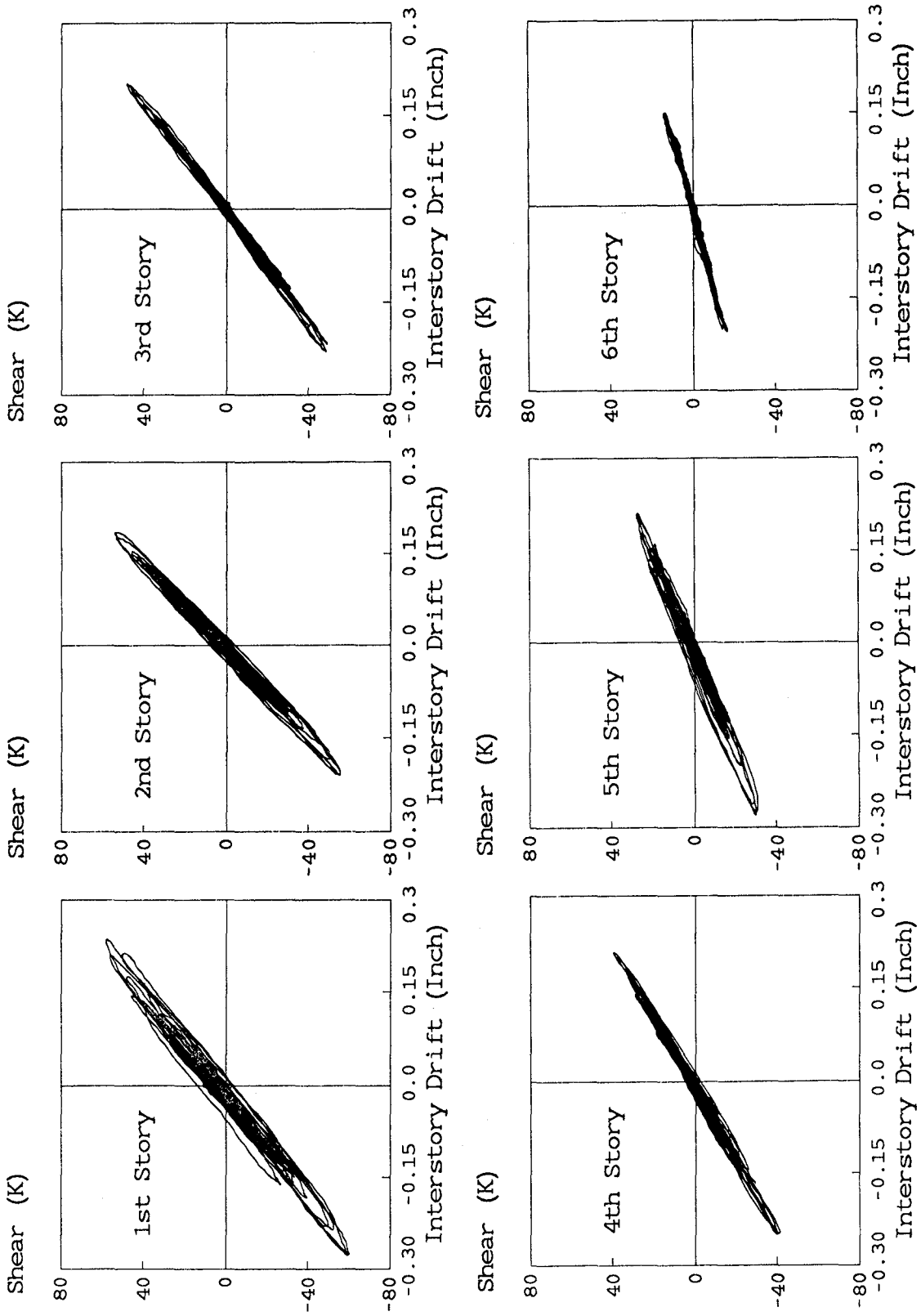


FIG. 7.23 MO-33 TEST INTER-STORY DRIFT VERSUS TOTAL STORY SHEAR CURVES

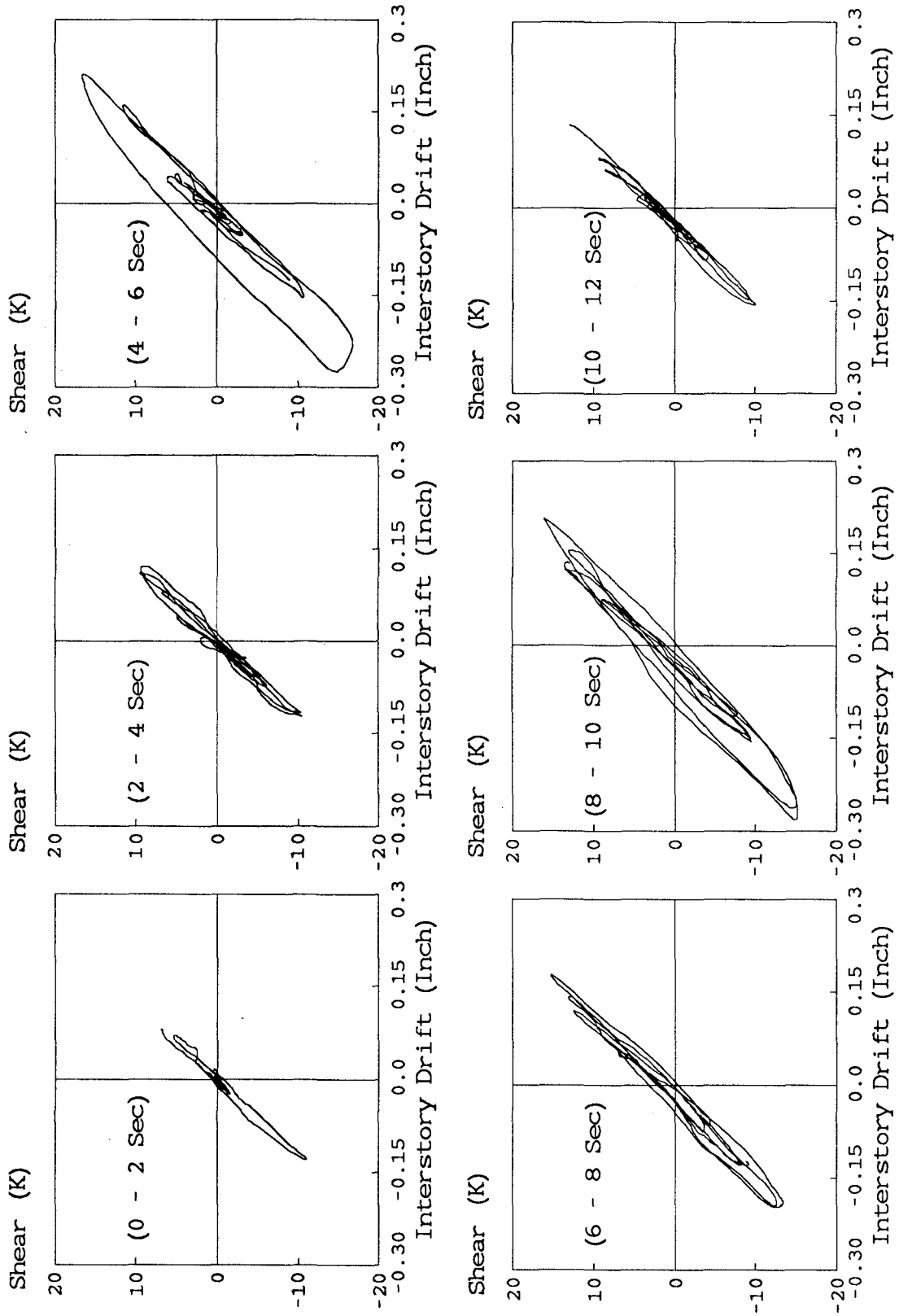


FIG. 7.24 MO-33 TEST FIFTH STORY INTER-STORY DRIFT VERSUS STORY SHEAR CURVES

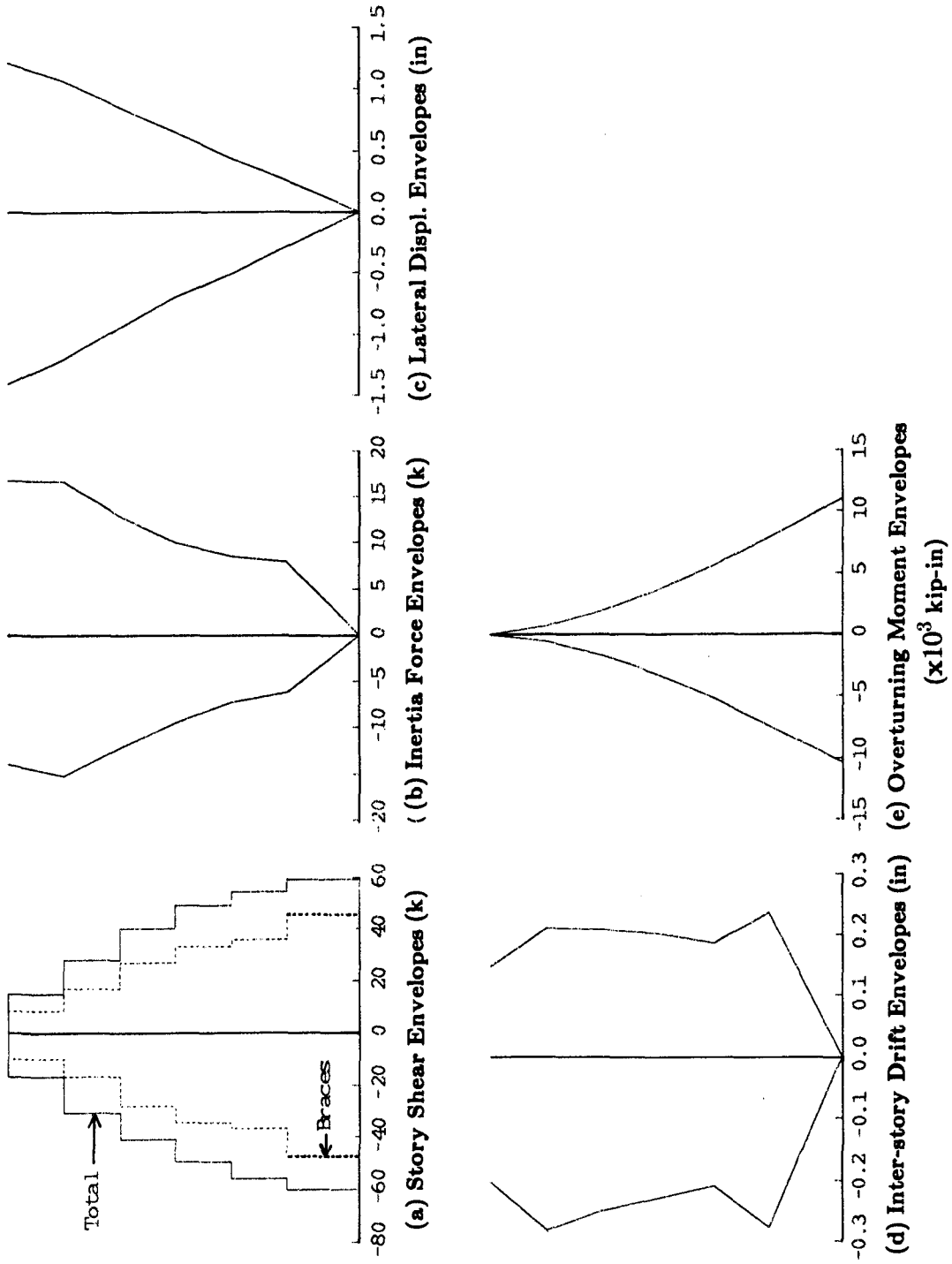


FIG. 7.25 MO-33 TEST RESPONSE ENVELOPES

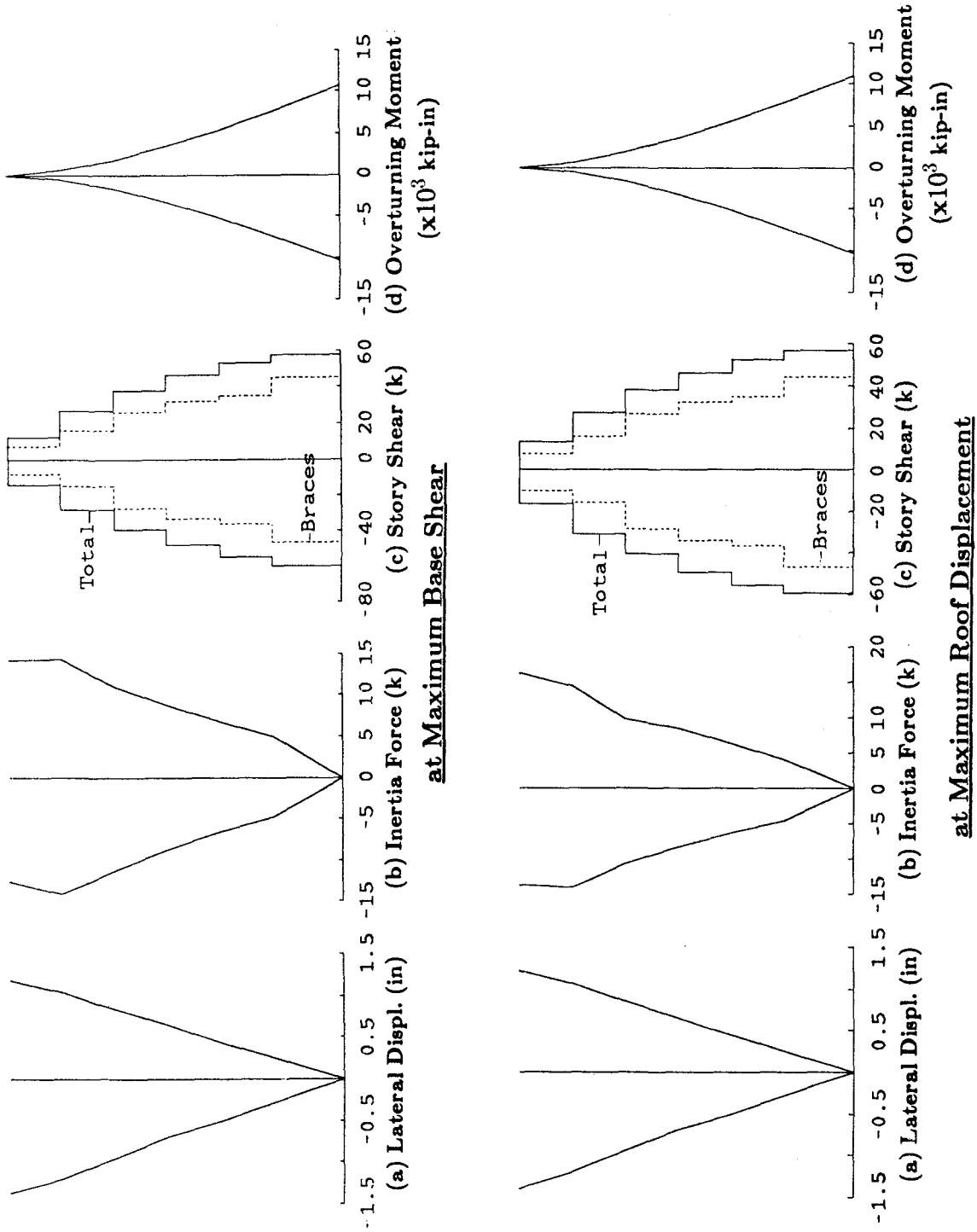


FIG. 7.26 MO-33 TEST RESPONSE PROFILES AT MAXIMUM RESPONSES

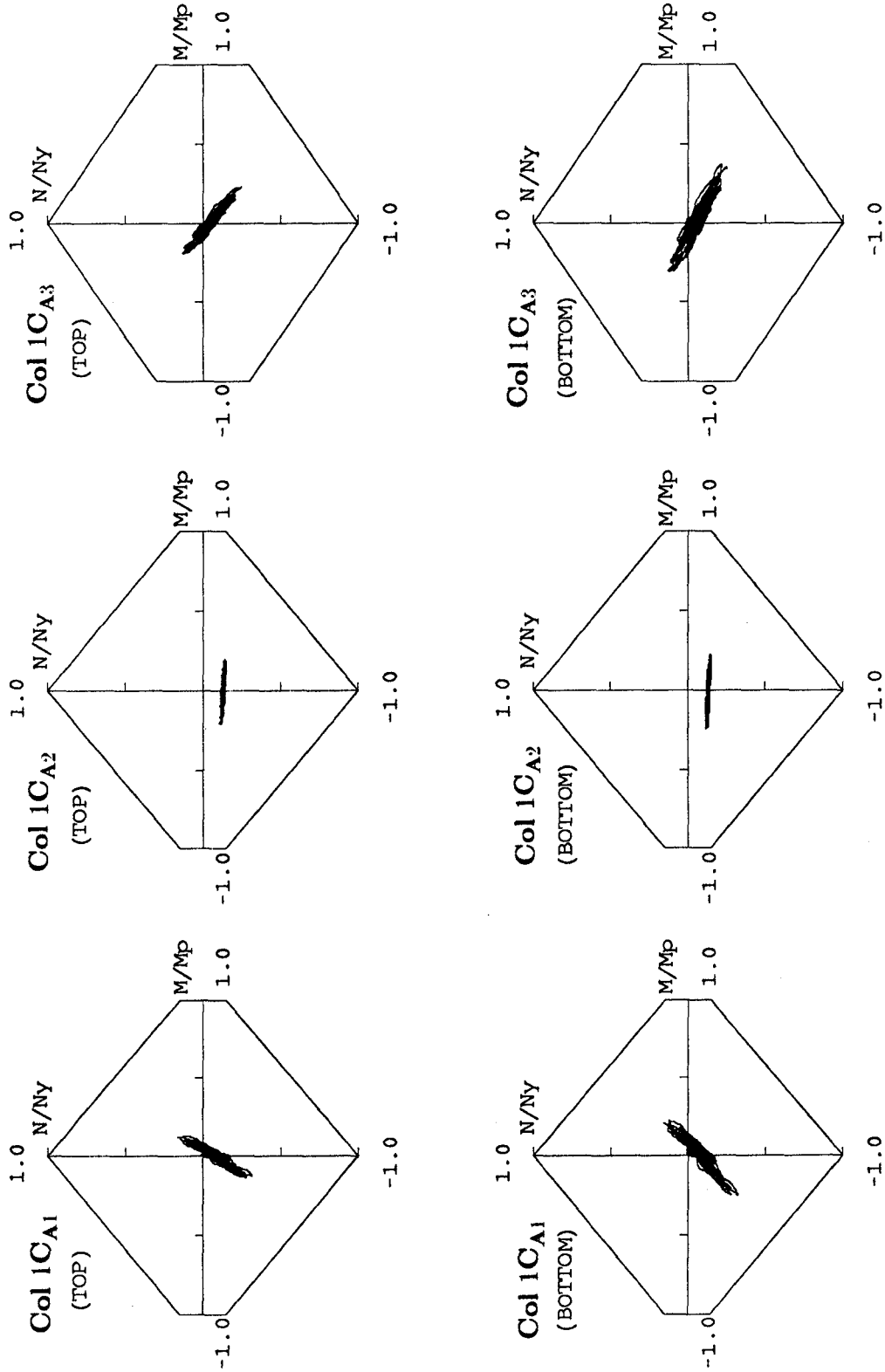


FIG. 7.27(a) MO-33 TEST FIRST STORY COLUMN AXIAL FORCE
VERSUS END MOMENT INTERACTION CURVES (FRAME A)

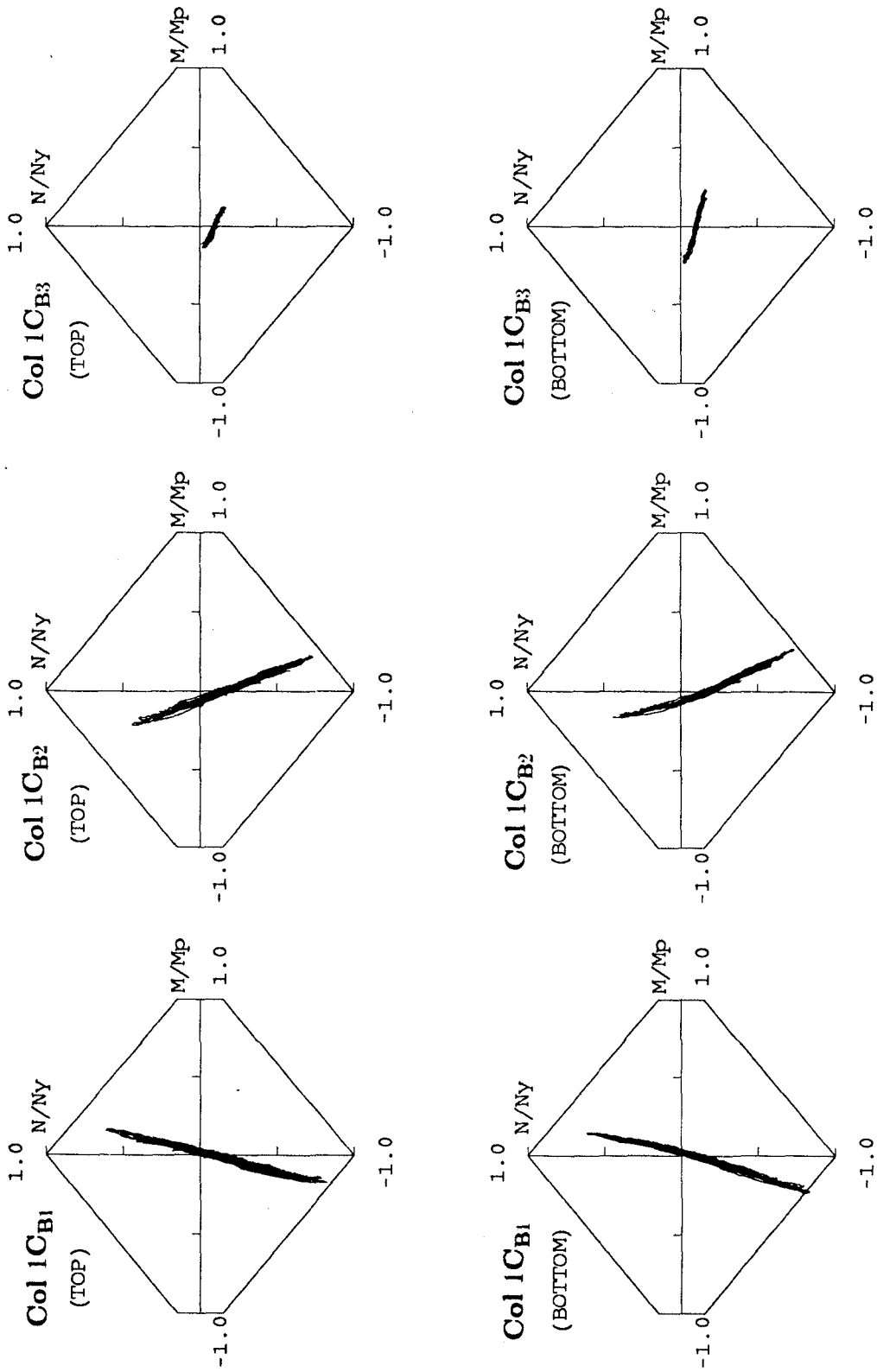


FIG. 7.27(b) MO-33 TEST FIRST STORY COLUMN AXIAL FORCE
VERSUS END MOMENT INTERACTION CURVES (FRAME B)

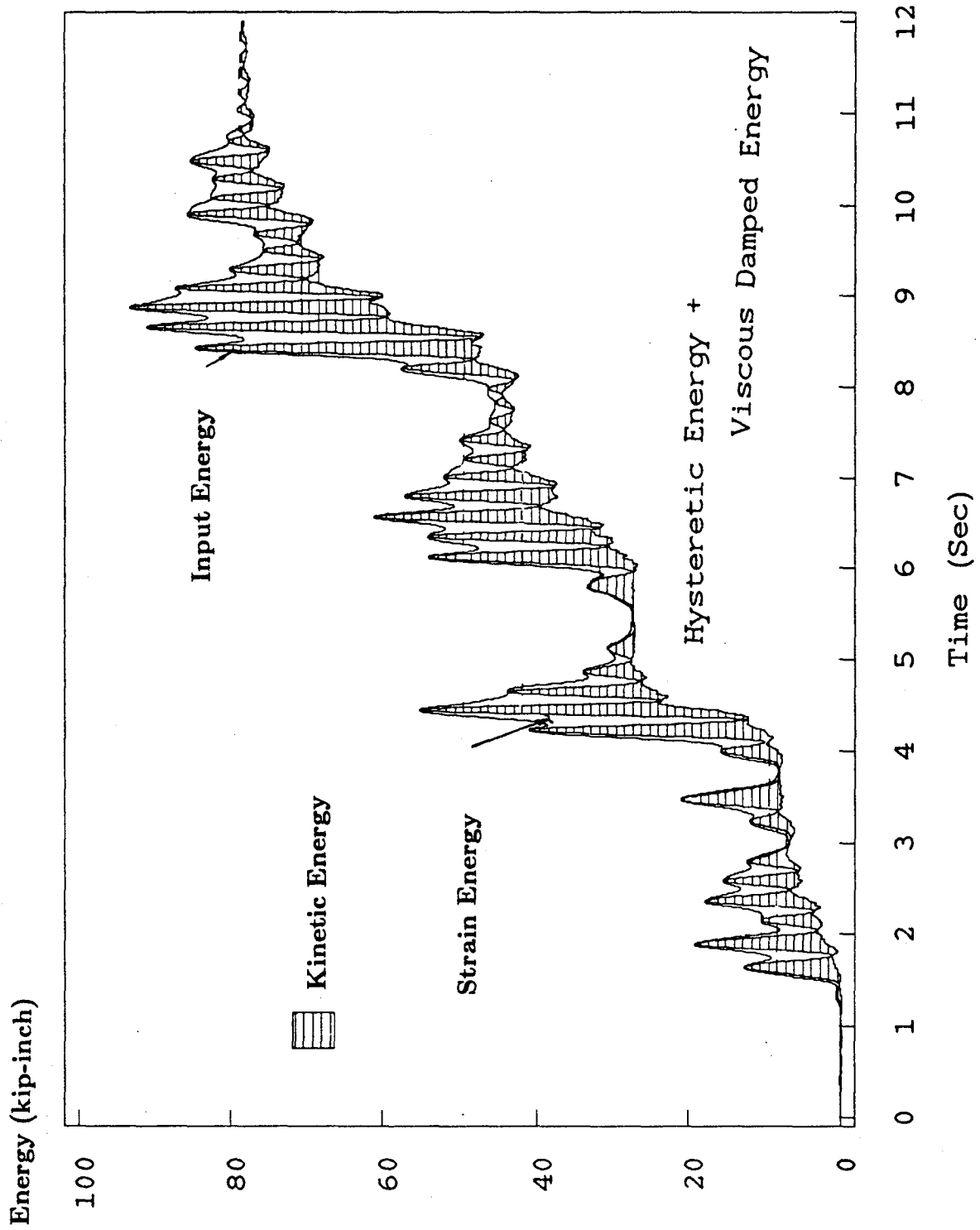
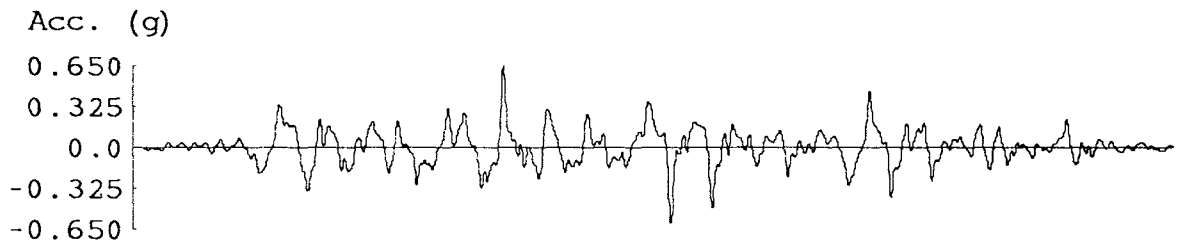
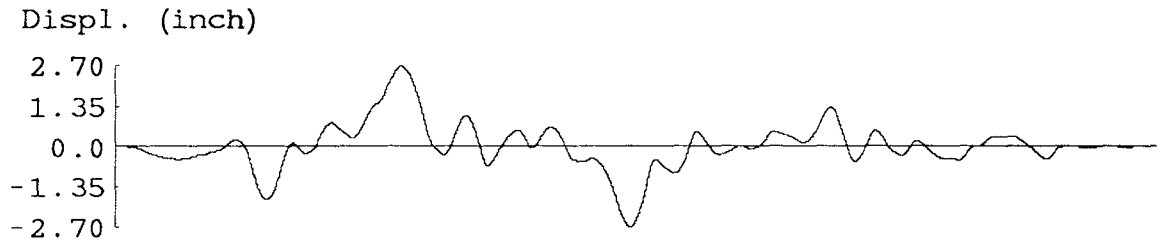


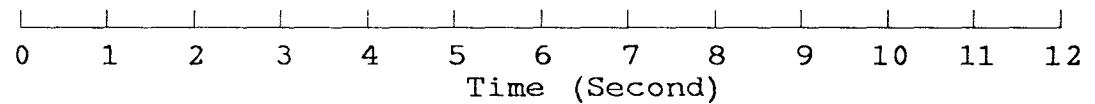
FIG. 7.28 MO-33 TEST ENERGY TIME HISTORIES



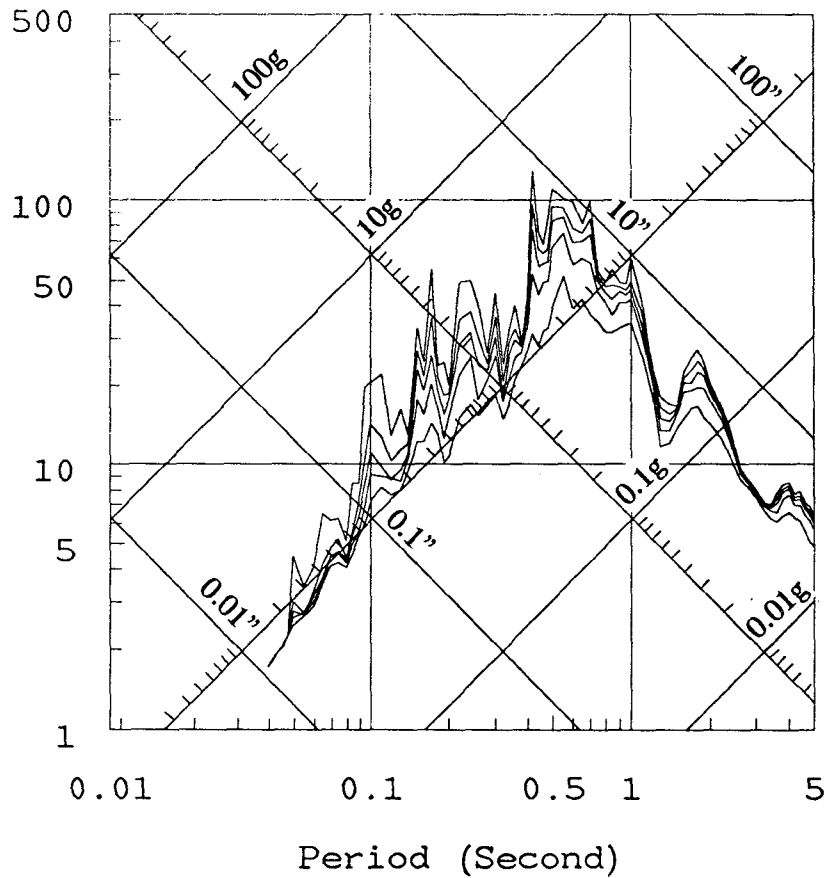
(a) Acceleration



(b) Displacement



Pseudo-Velocity (in/sec)



(c) Linear Elastic Response Spectra (0,0.5,1,2,5% Damping)

FIG. 7.29 MEASURED SHAKING TABLE HORIZONTAL MOTIONS AND RESPONSE SPECTRA (MO-65 TEST)

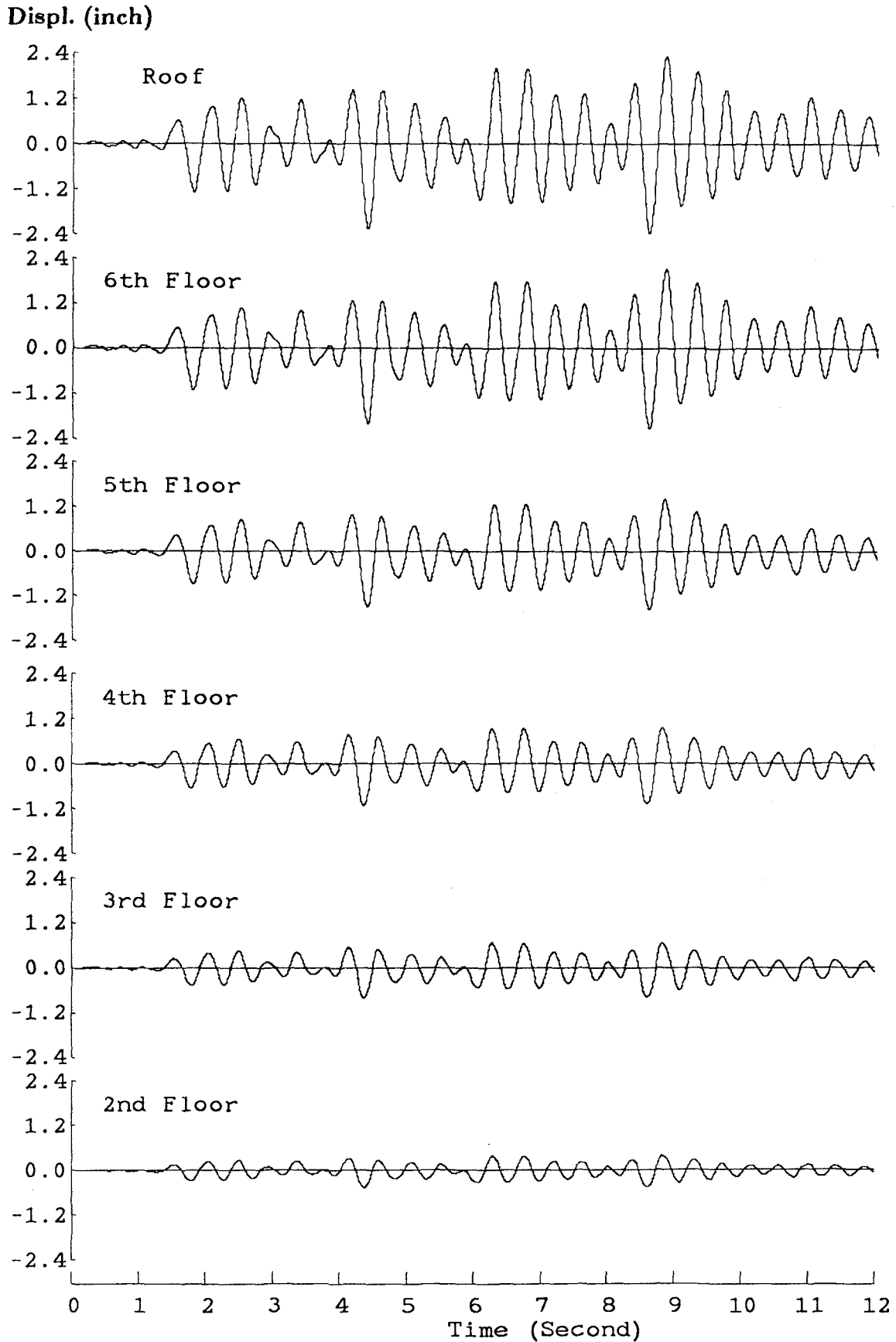


FIG. 7.30 MO-65 TEST RELATIVE DISPLACEMENT TIME HISTORIES

Inter-story drift (inch)

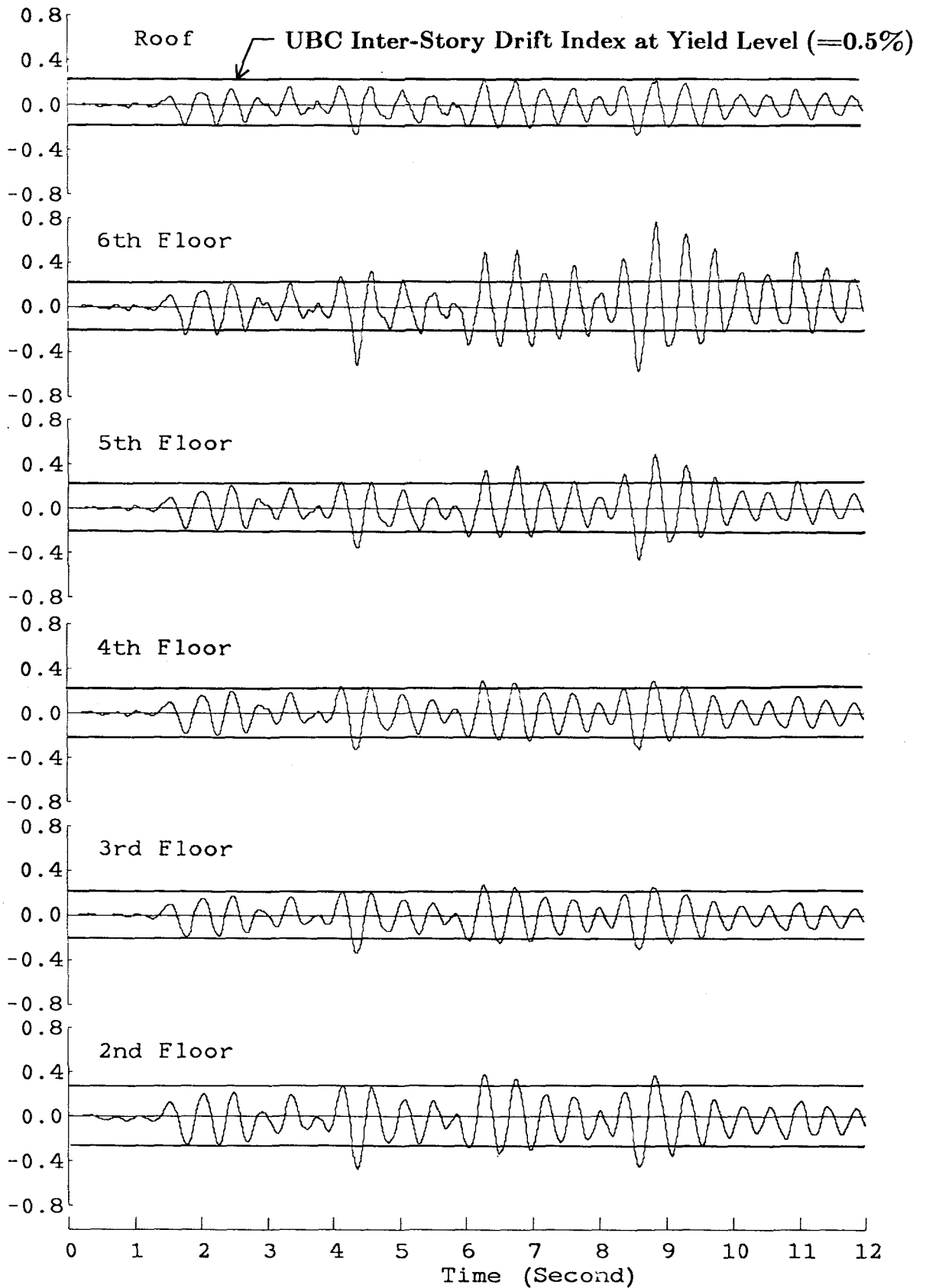


FIG. 7.31 MO-65 TEST INTER-STORY DRIFT TIME HISTORIES

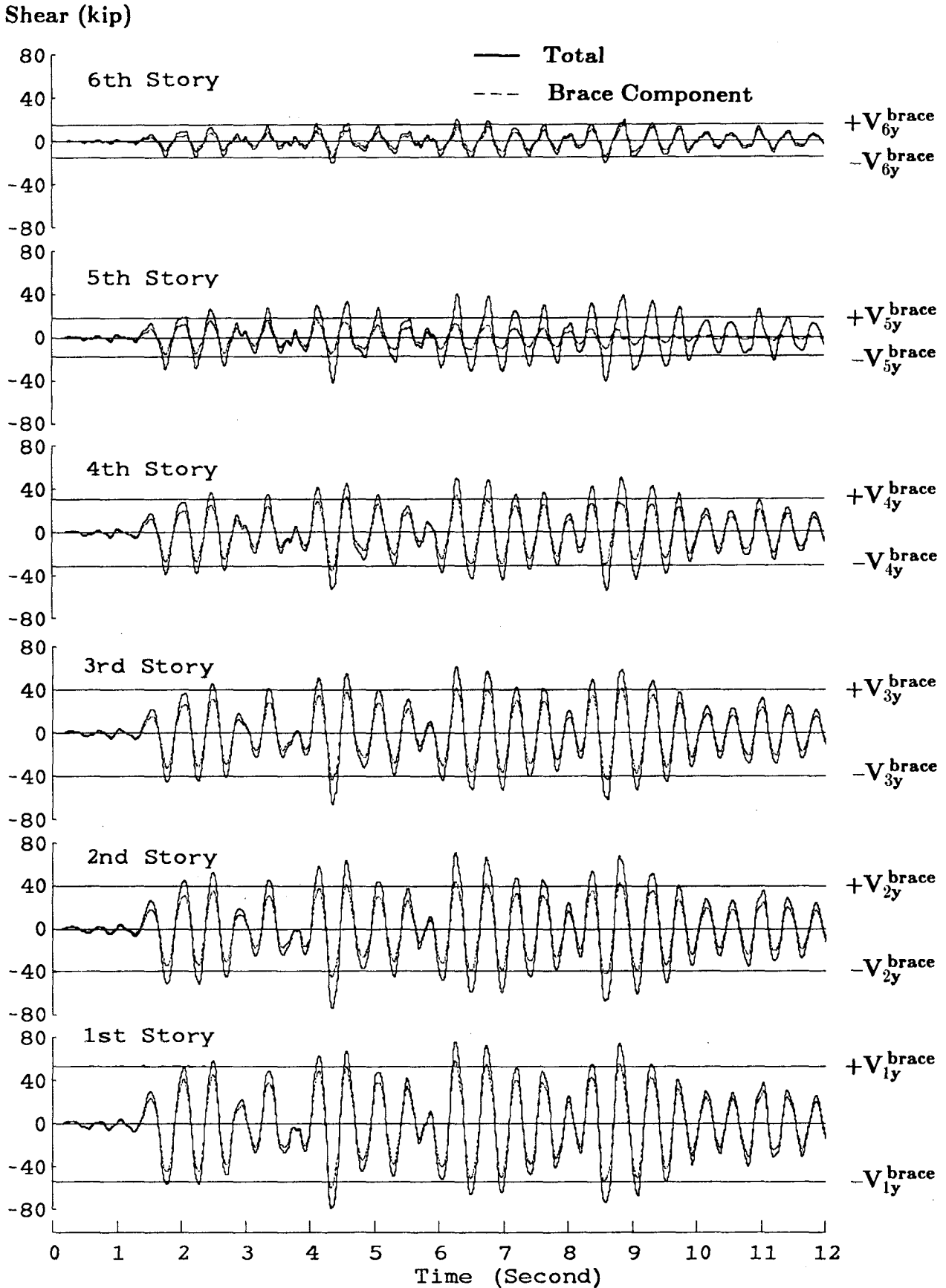


FIG. 7.32 STORY SHEAR (TOTAL AND BRACE COMPONENT)
TIME HISTORIES OF MO-65 TEST

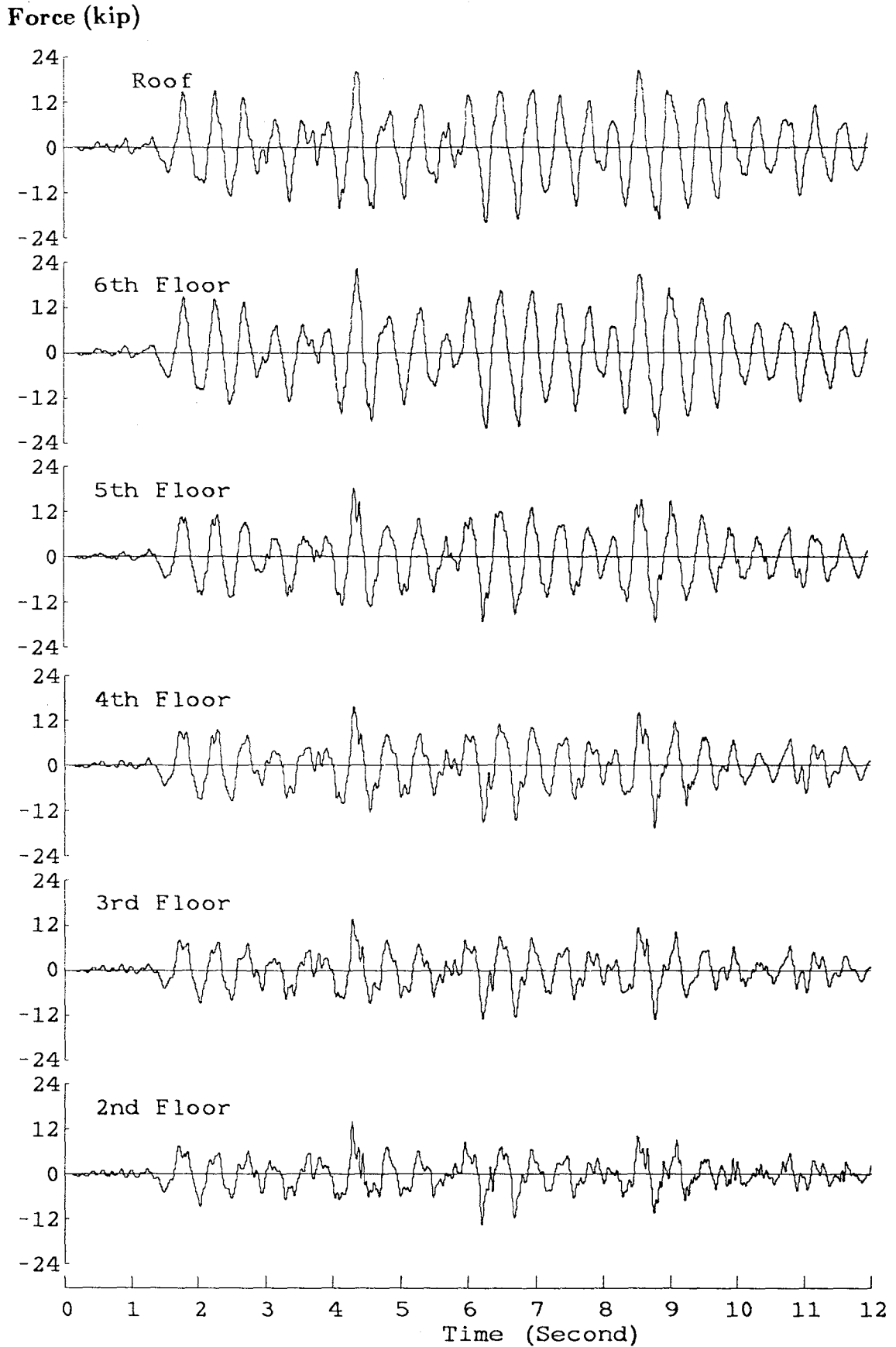


FIG. 7.33 MO-65 TEST LATERAL INERTIA FORCE TIME HISTORIES

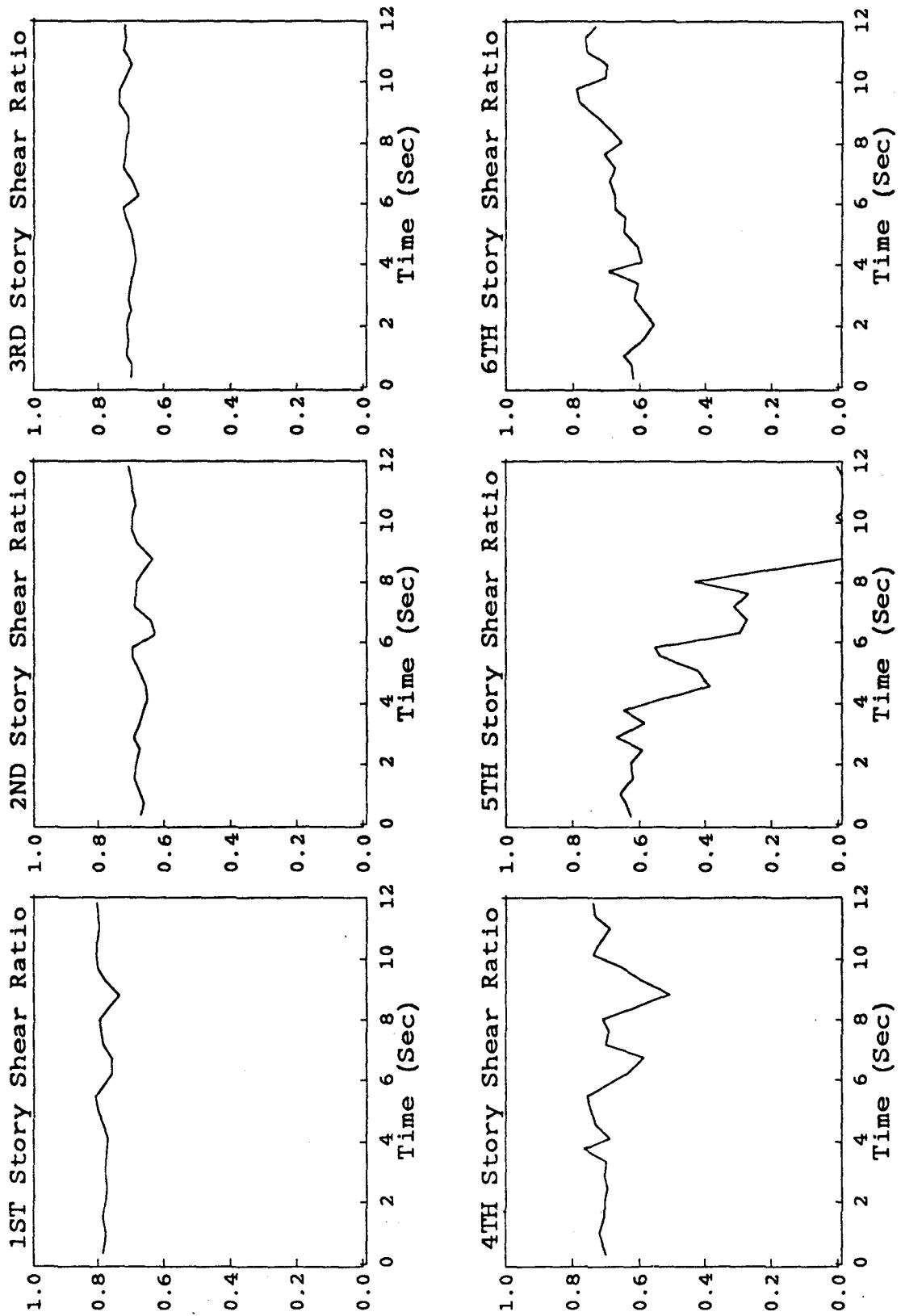
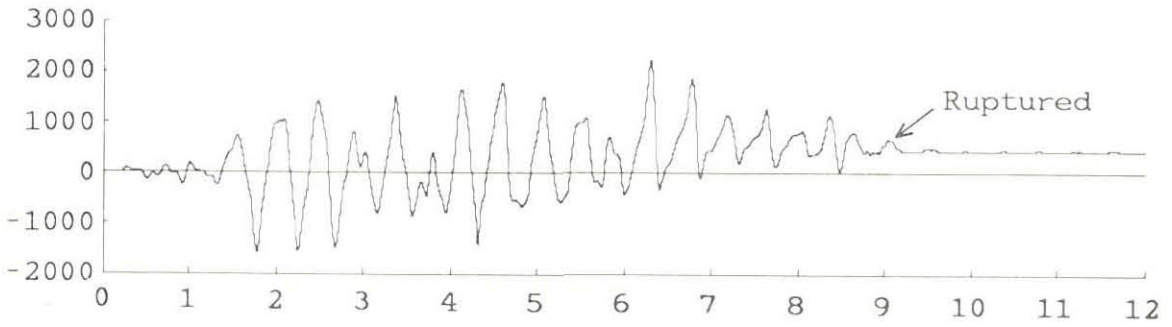


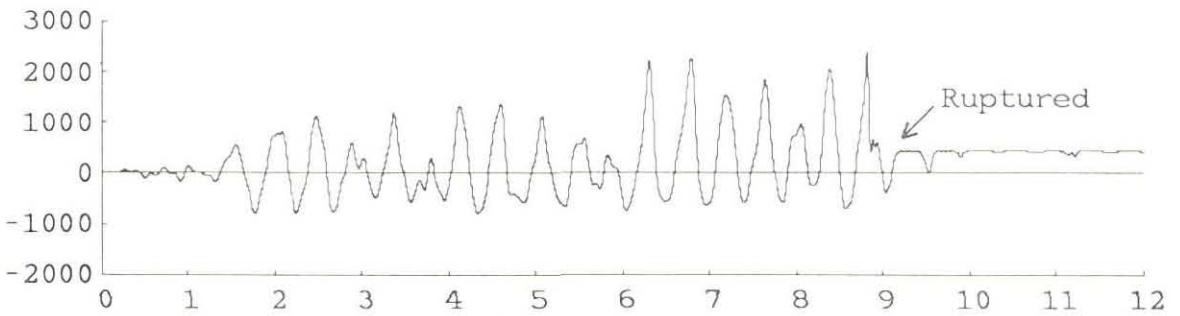
FIG. 7.34 MO-65 TEST $\frac{V_{BRACE}}{V_{TOTAL}}$ RATIO

Axial Strain ($\times 10^{-6}$)

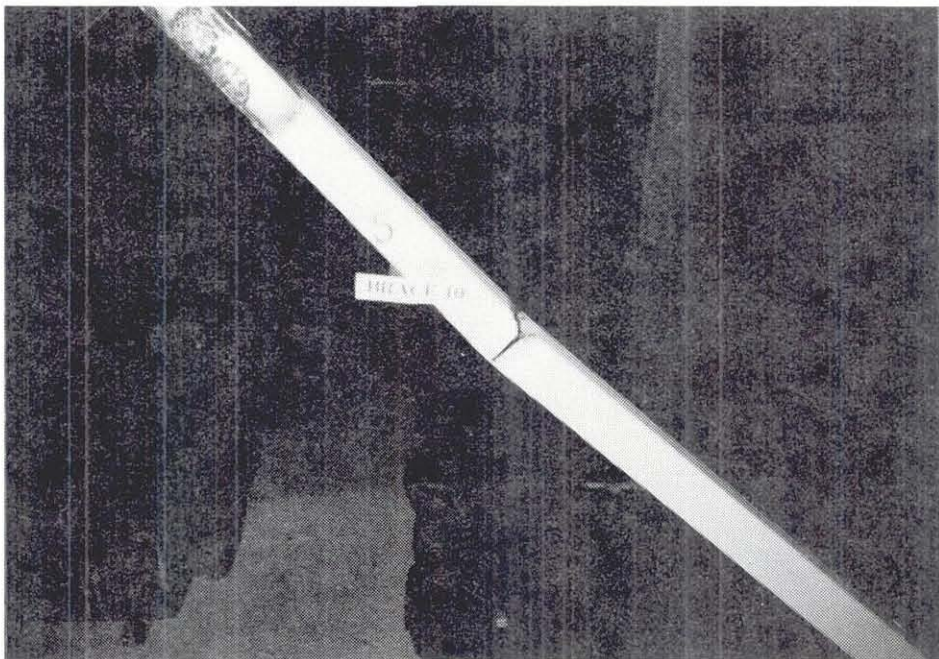


(a) Top Face Axial Strain

Axial Strain ($\times 10^{-6}$)



(b) Bottom Face Axial Strain



(c) Damaged Brace after MO-65 test

FIG. 7.35 MO-65 TEST BRACE 10 AXIAL STRAIN TIME HISTORIES

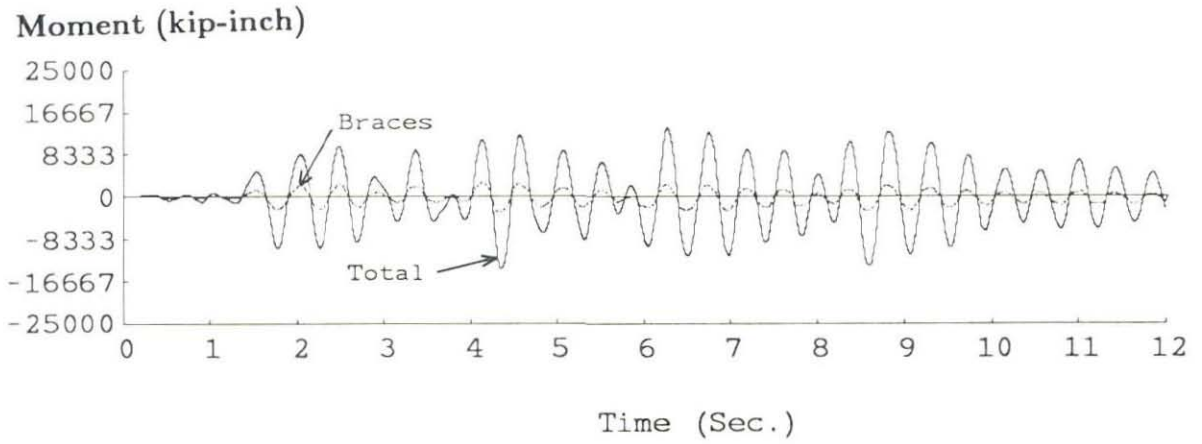


FIG. 7.36 MO-65 TEST BASE OVERTURNING MOMENT TIME HISTORIES

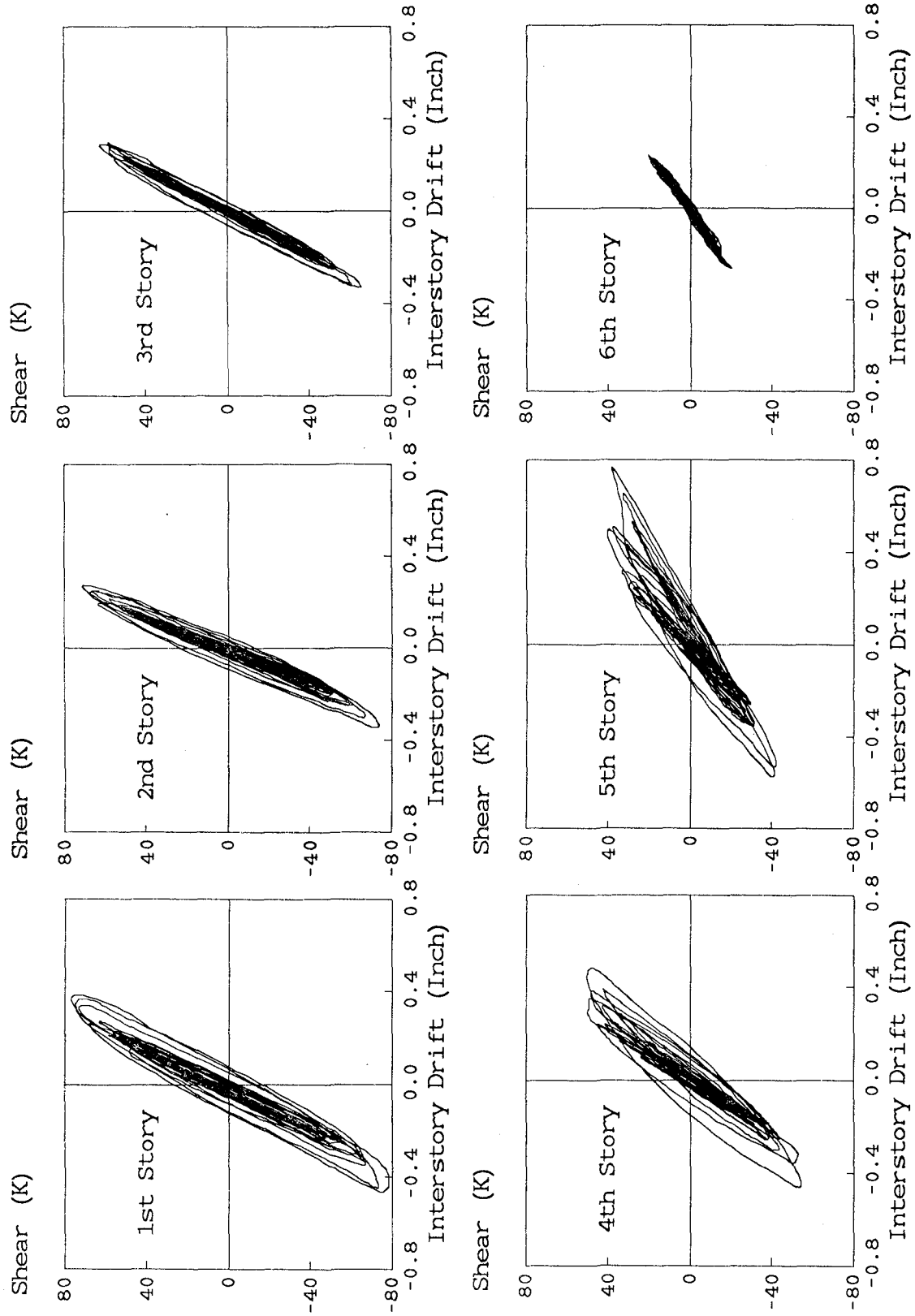


FIG. 7.37 MO-65 TEST INTER-STORY DRIFT VERSUS TOTAL STORY SHEAR (V^{TOTAL}) CURVES

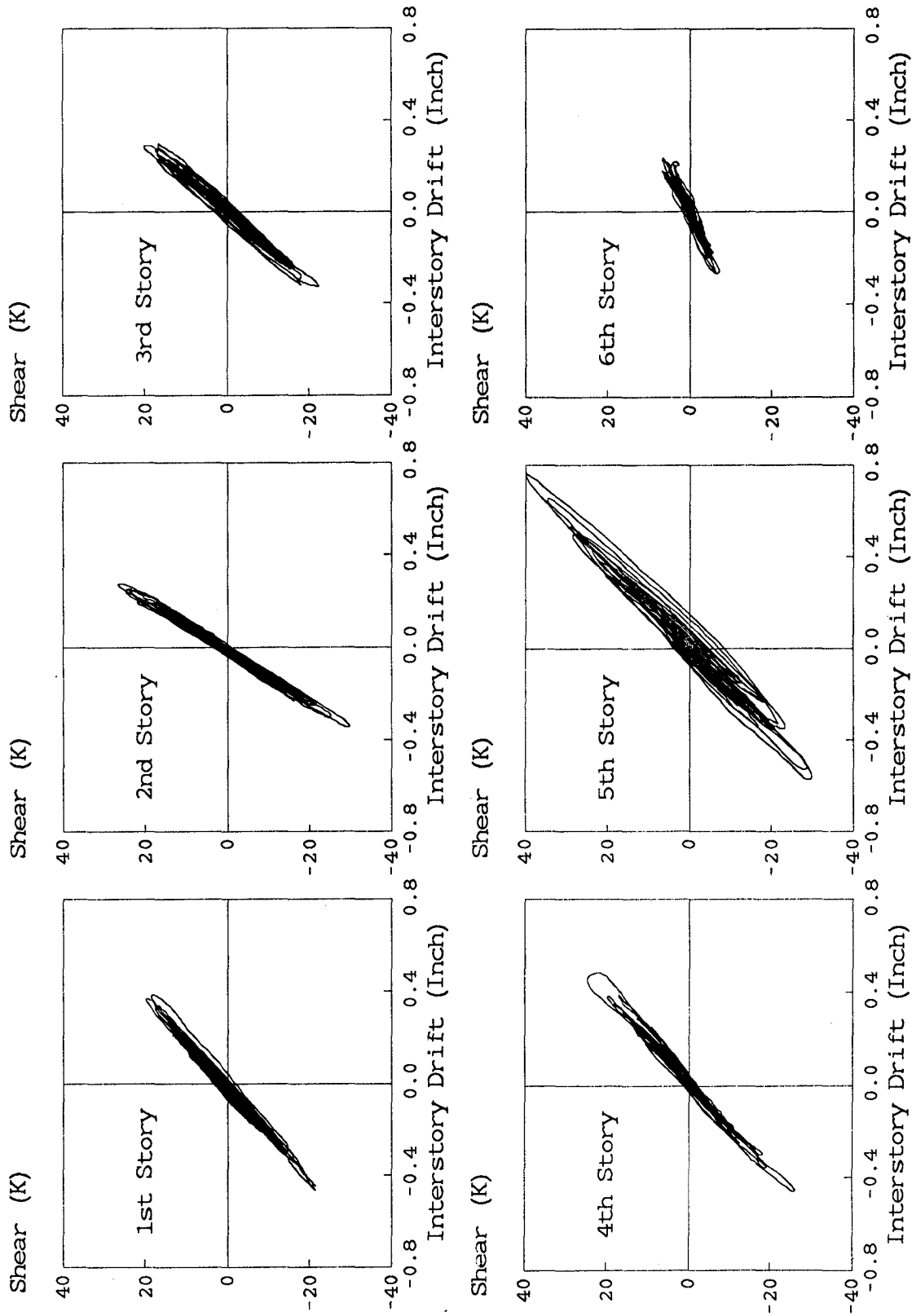


FIG. 7.38 MO-65 TEST INTER-STORY DRIFT VERSUS STORY COLUMN SHEAR (V^{MRSF}) CURVES

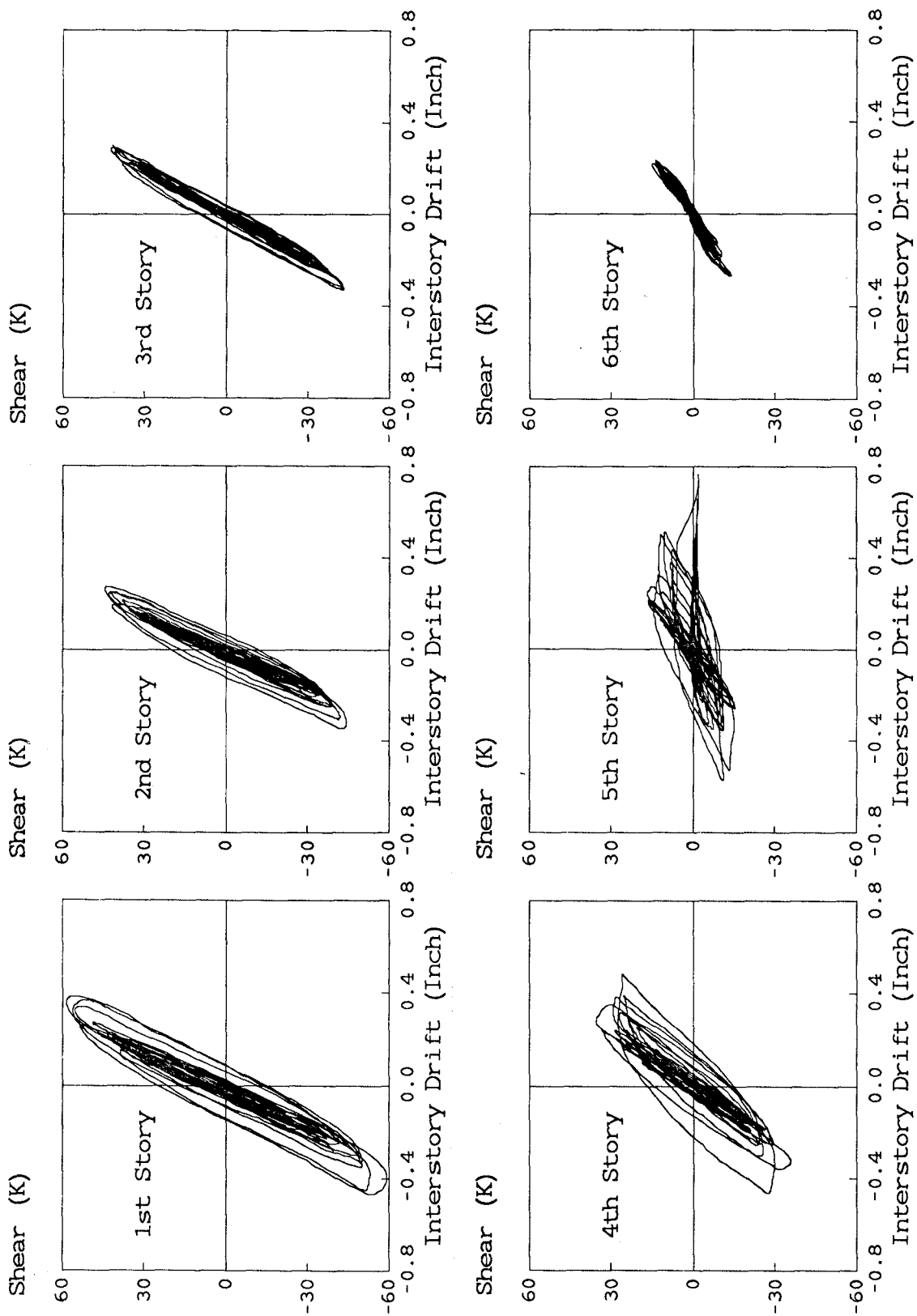


FIG. 7.39 MO-65 TEST INTER-STORY DRIFT VERSUS STORY BRACE SHEAR (V_{BRACE}) CURVES

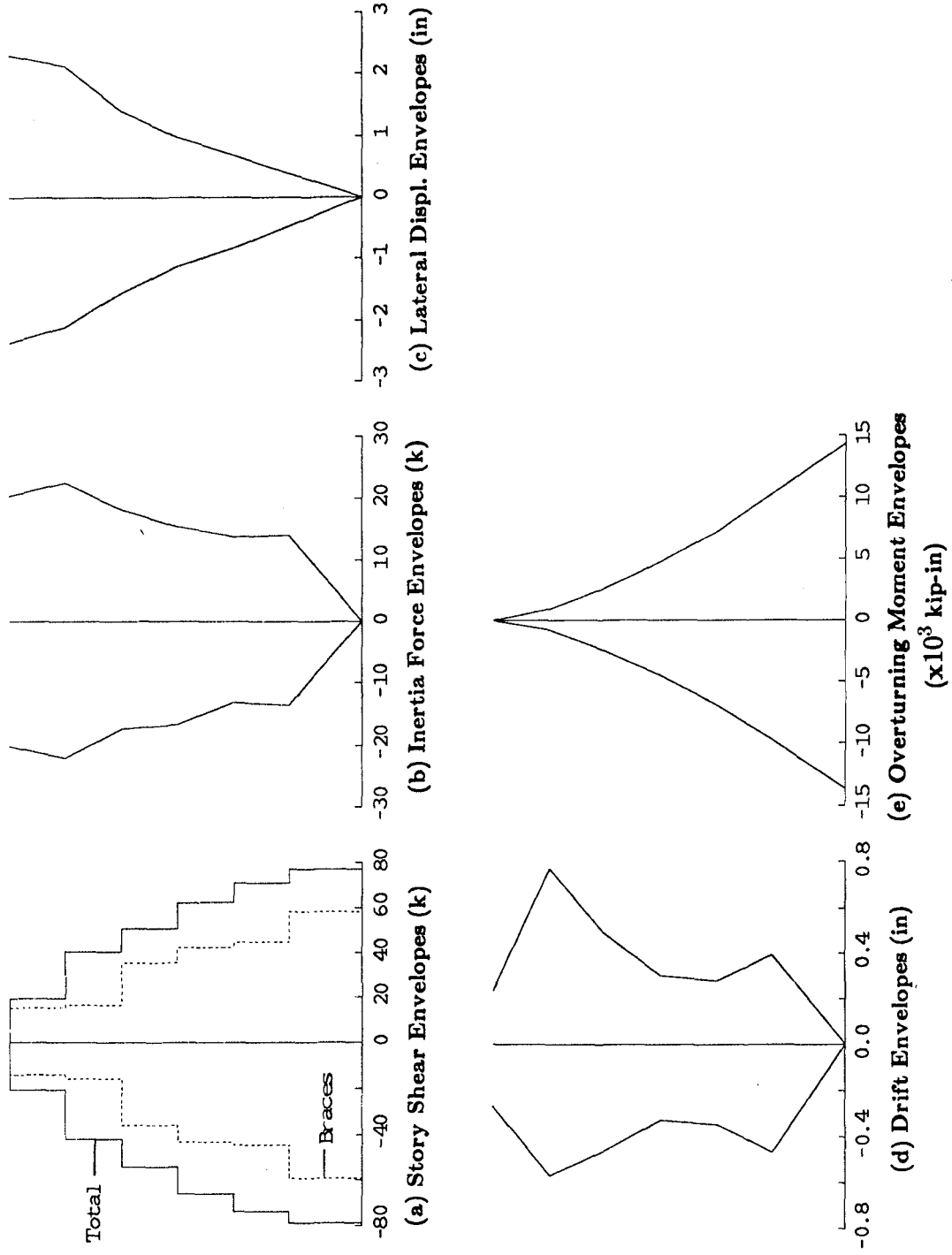


FIG. 7.40 MO-65 TEST RESPONSE ENVELOPES

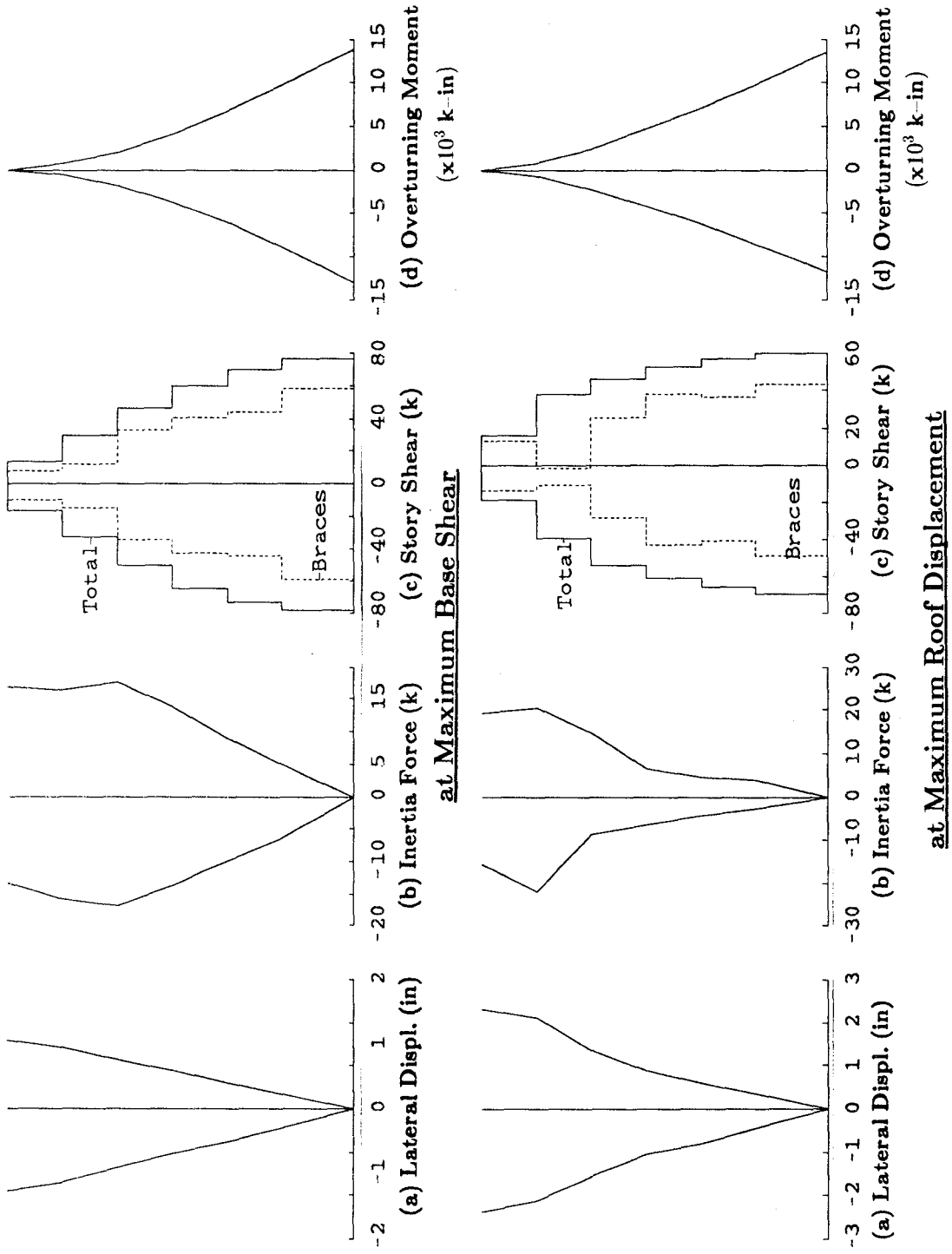


FIG. 7.41 MO-65 TEST RESPONSE PROFILES AT MAXIMUM RESPONSES

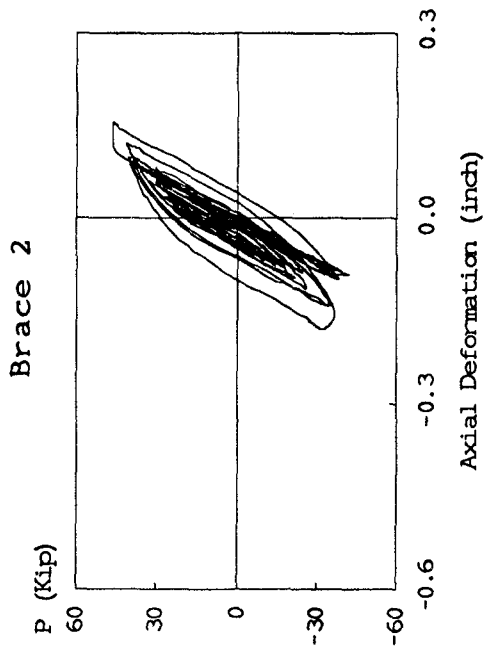


FIG. 7.42 BRACE 2 P - Δ CURVE (MO-65 TEST)

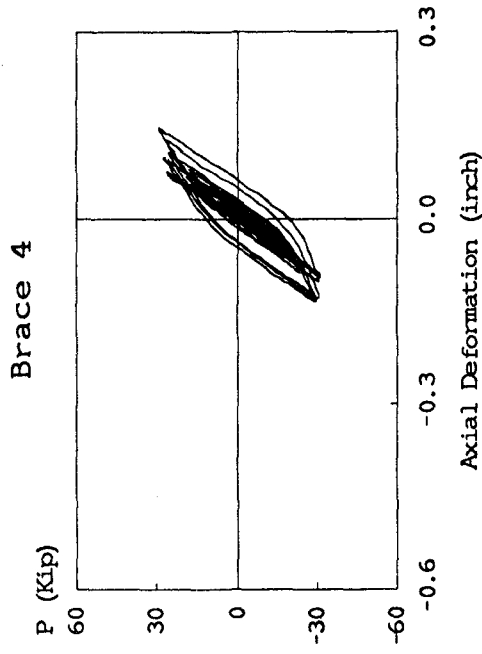


FIG. 7.43 BRACE 4 P - Δ CURVE (MO-65 TEST)

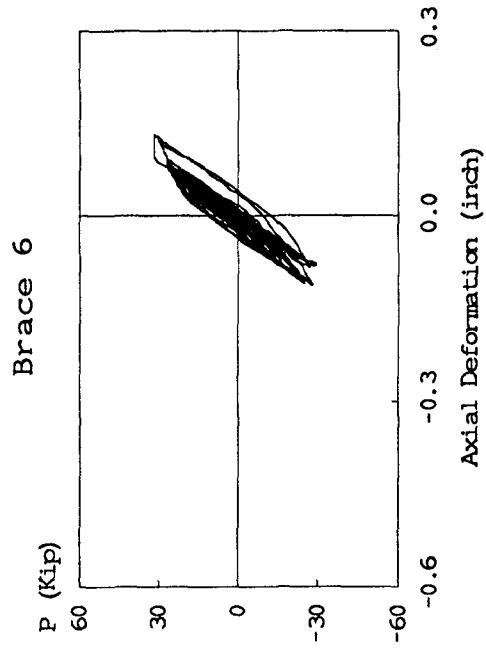


FIG. 7.44 BRACE 6 P - Δ CURVE (MO-65 TEST)

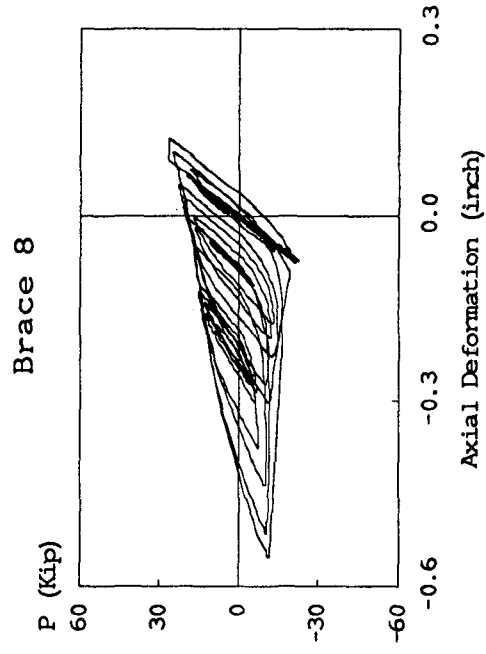


FIG. 7.45 BRACE 8 P - Δ CURVE (MO-65 TEST)

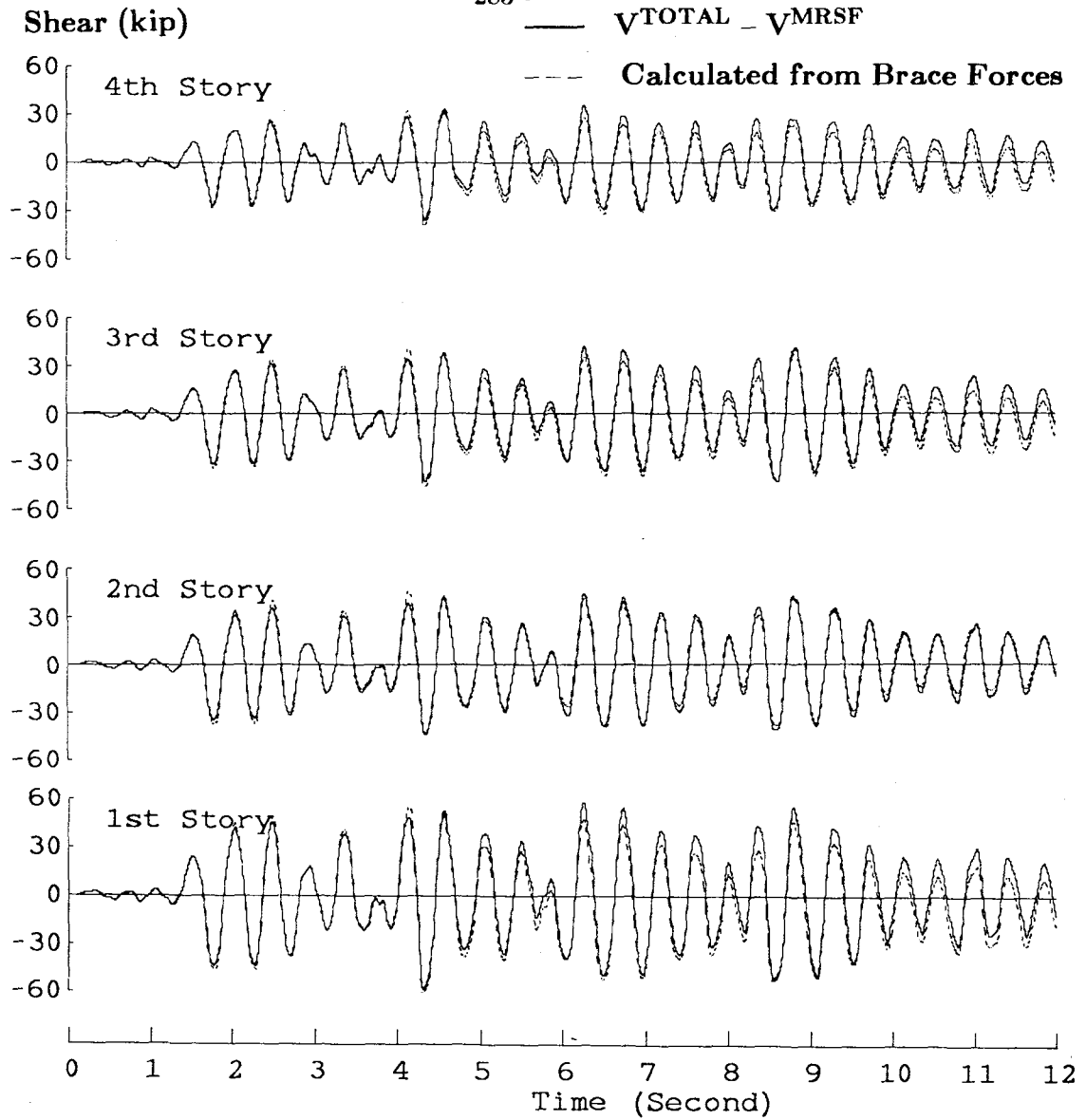


FIG. 7.46 COMPARISON OF V^{BRACE} TIME HISTORIES (MO-65 TEST)

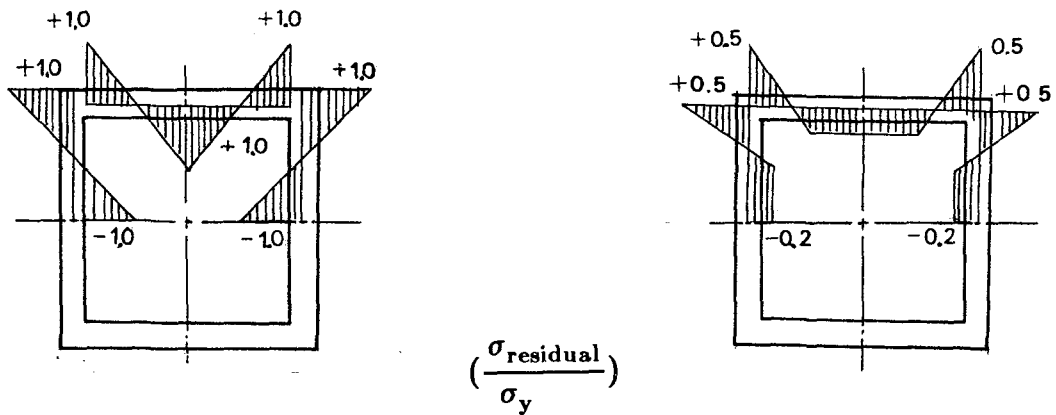
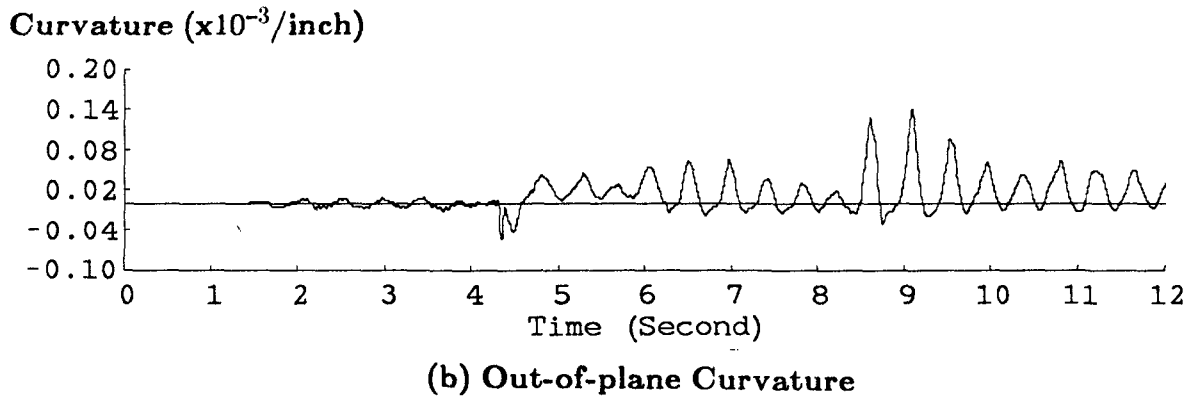
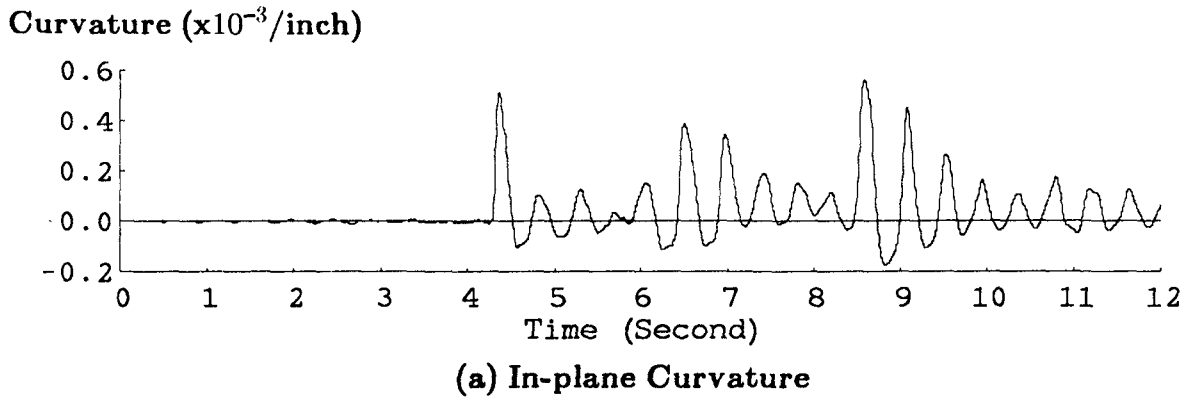


FIG. 7.47 TYPICAL RESIDUAL STRESS DISTRIBUTION IN TUBE [34]



**FIG. 7.48 BRACE 1 SECTIONAL CURVATURE TIME HISTORIES
(MO-65 TEST)**

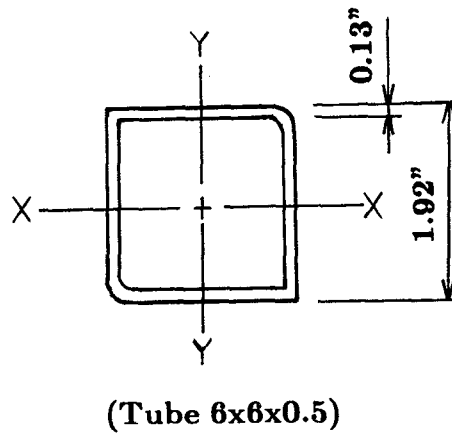


FIG. 7.49 TYPICAL MODEL BRACE SECTION

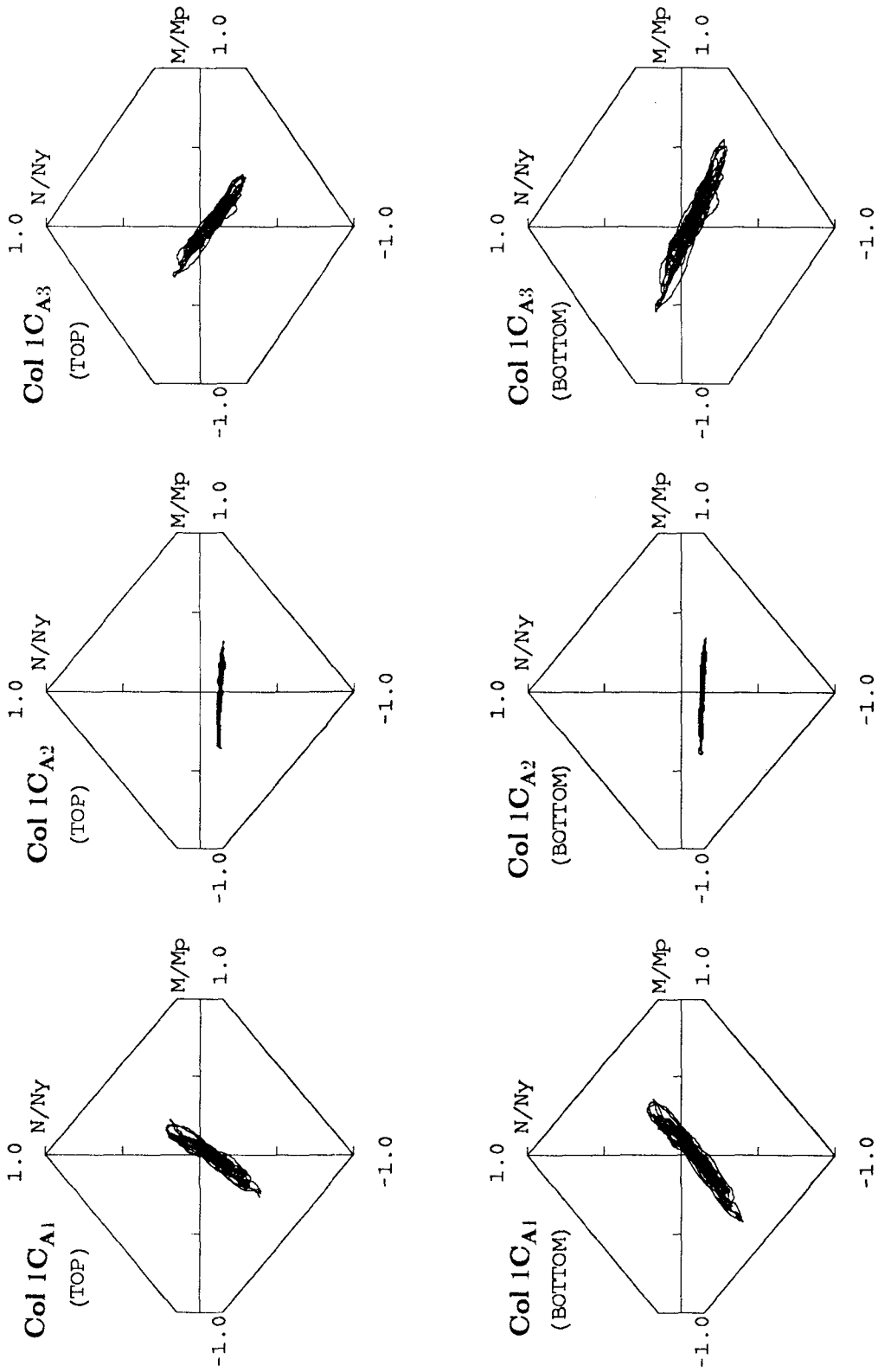


FIG. 7.50(a) MO-65 TEST FIRST STORY COLUMN AXIAL FORCE
VERSUS END MOMENT INTERACTION CURVES (FRAME A)

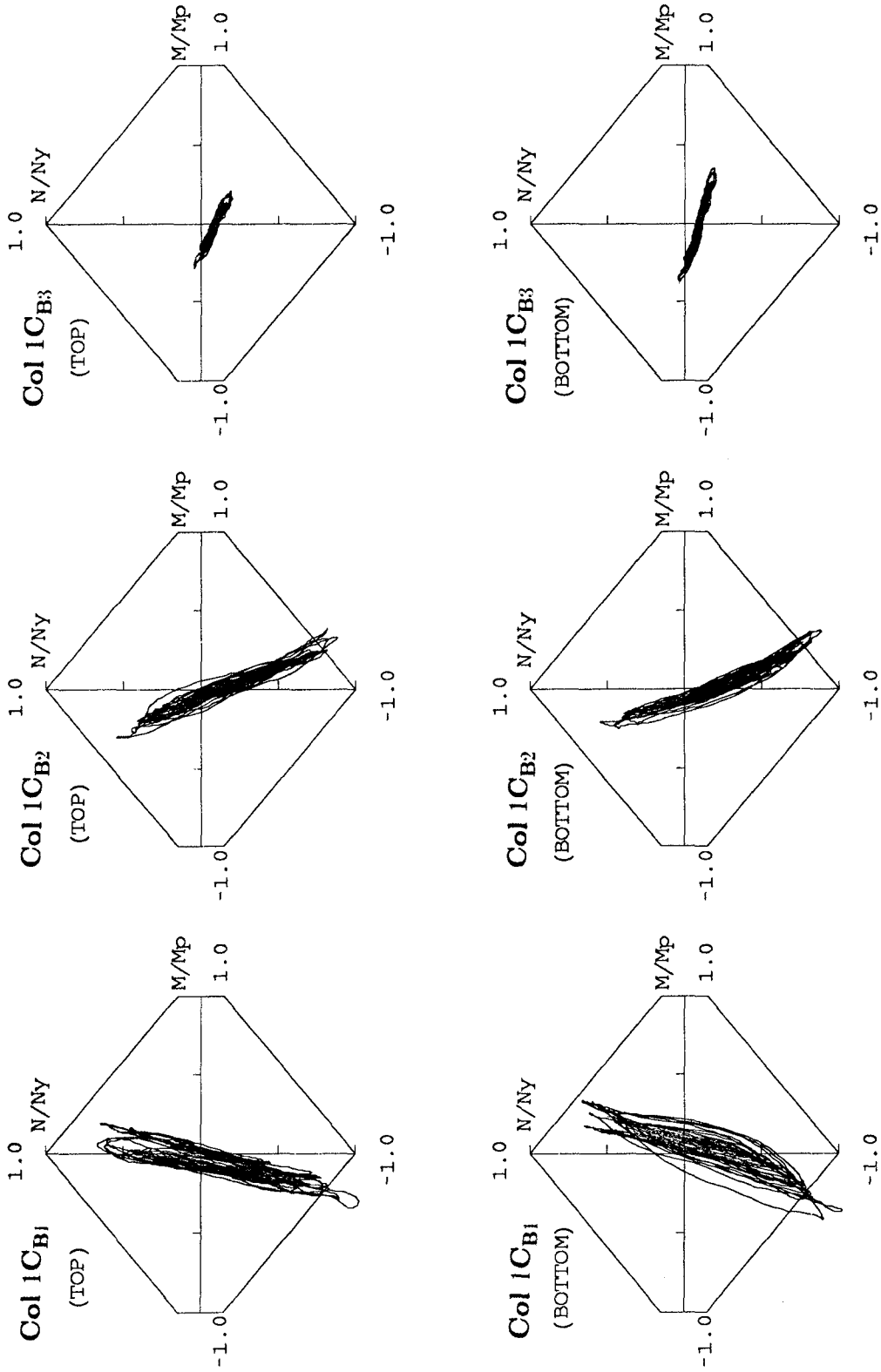


FIG. 7.50(b) MO-65 TEST FIRST STORY COLUMN AXIAL FORCE
VERSUS END MOMENT INTERACTION CURVES (FRAME B)

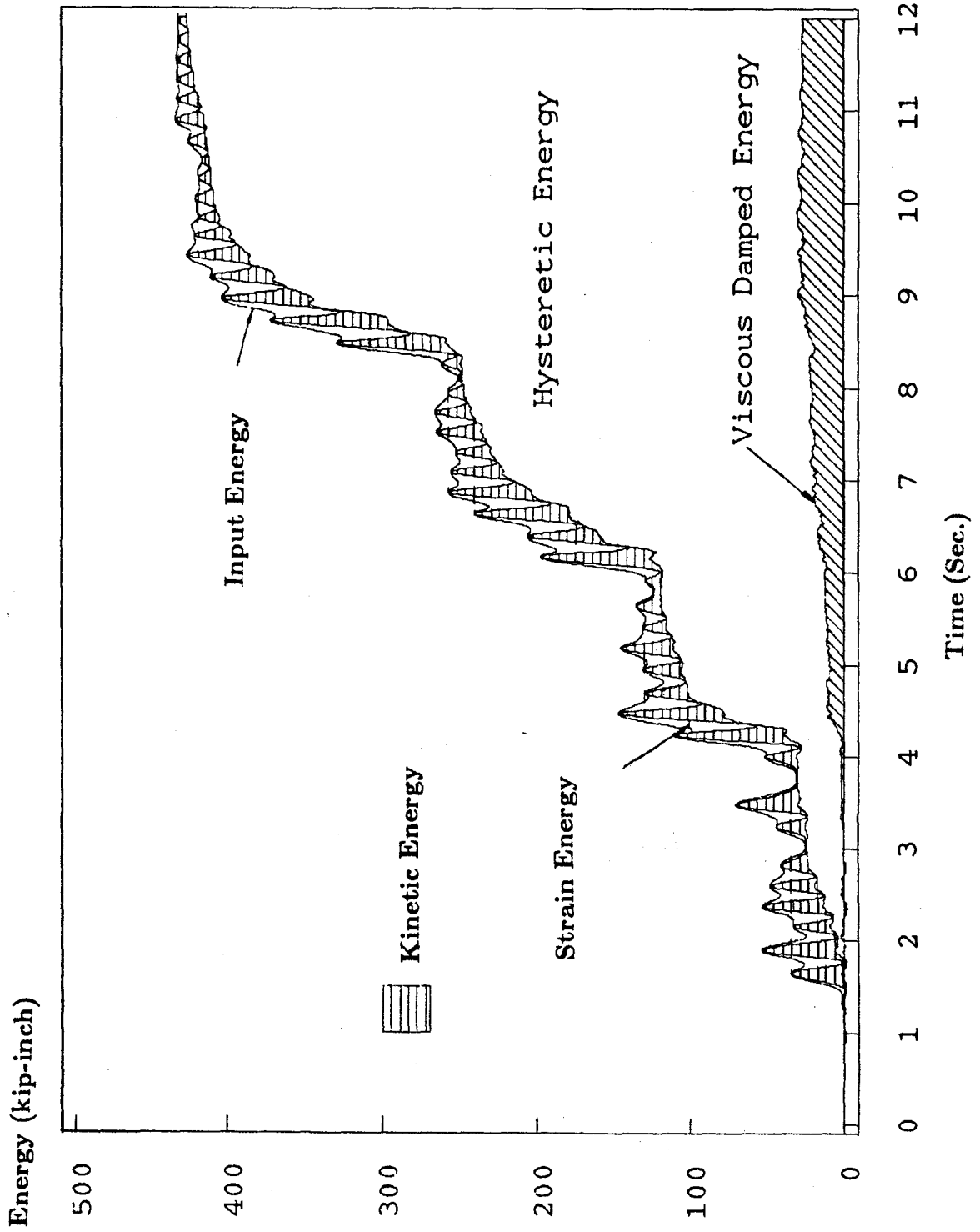


FIG. 7.51 MO-65 TEST ENERGY TIME HISTORIES

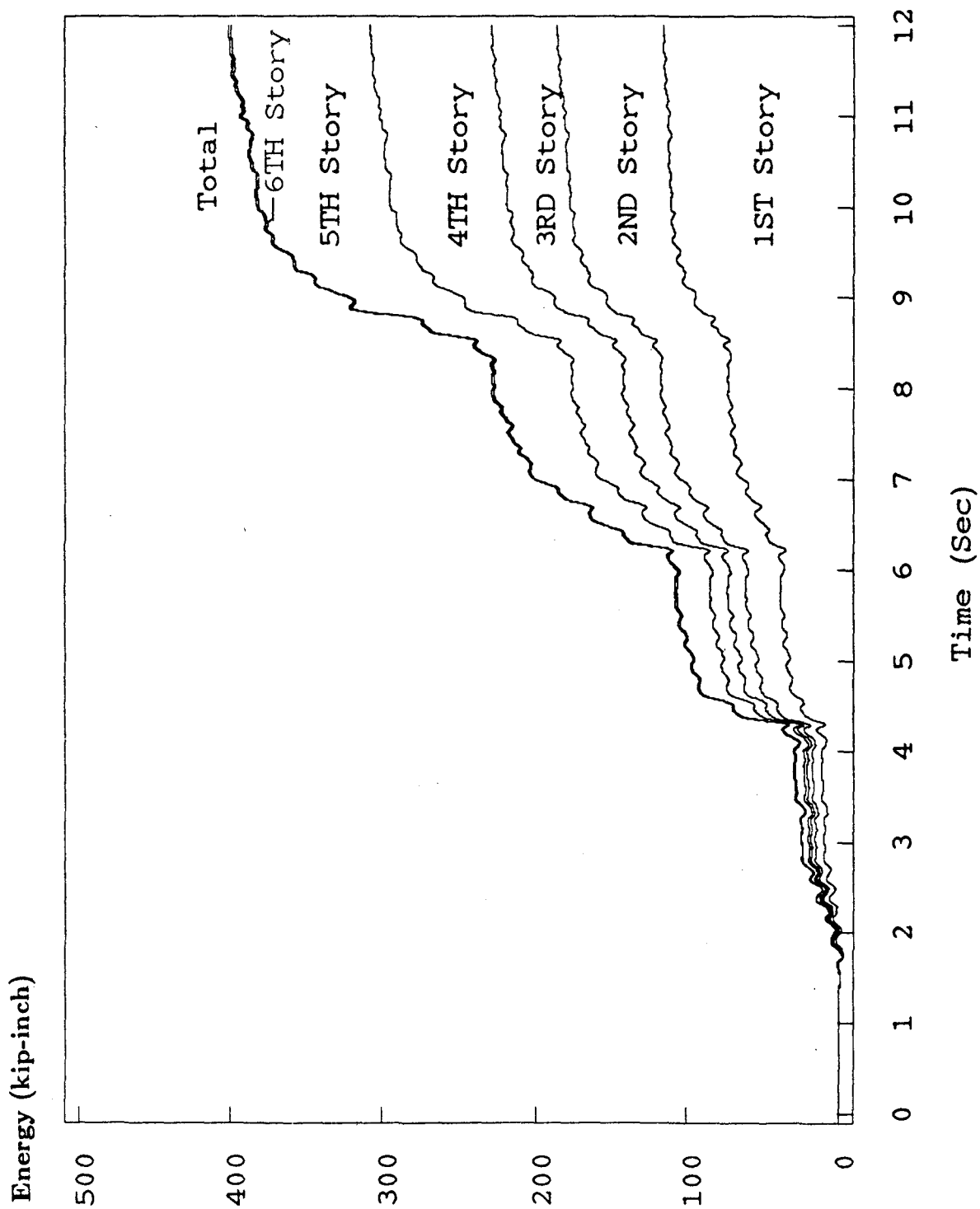
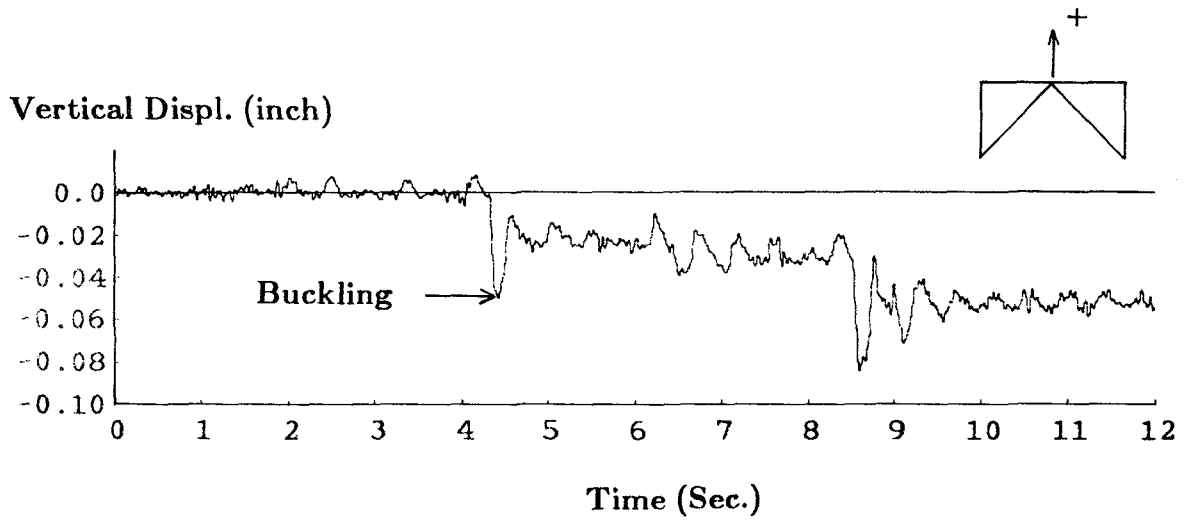
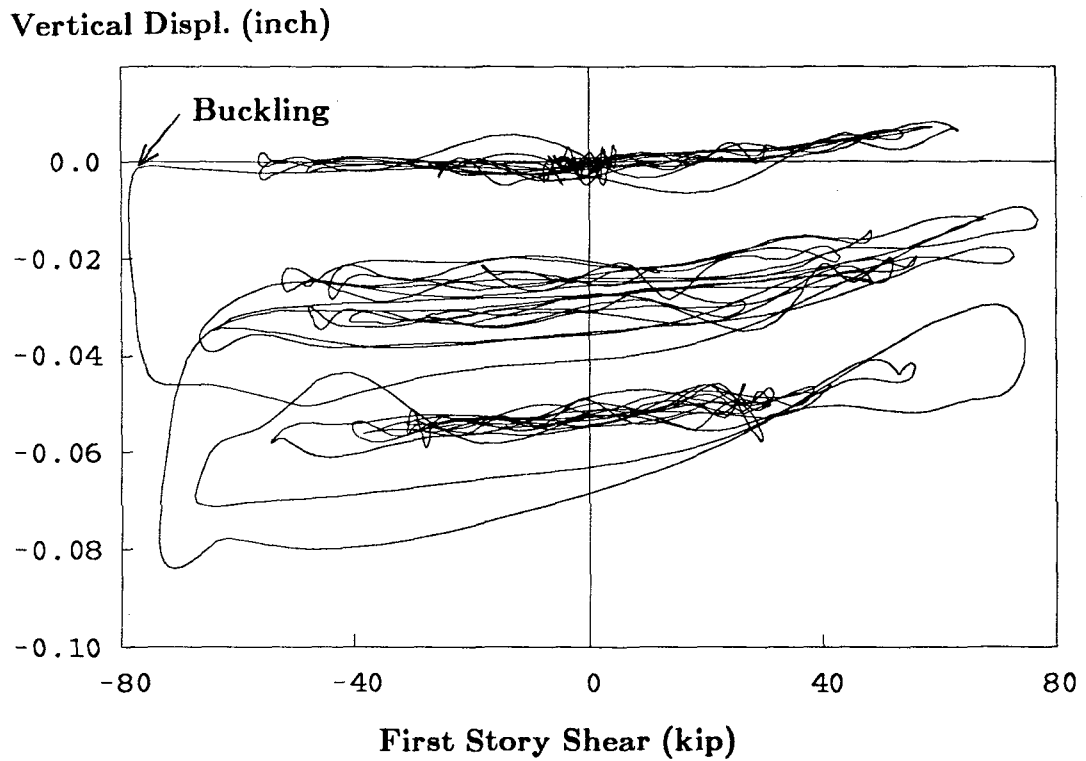


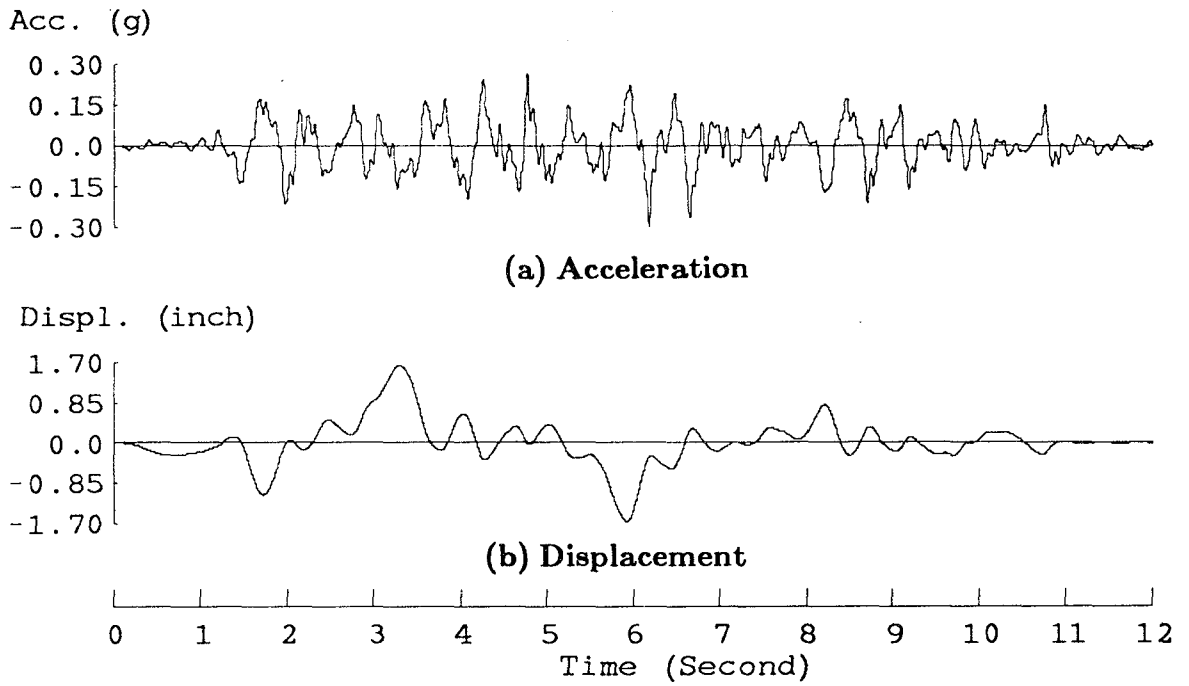
FIG. 7.52 MO-65 TEST HYSTERETIC DISSIPATED ENERGY DISTRIBUTION



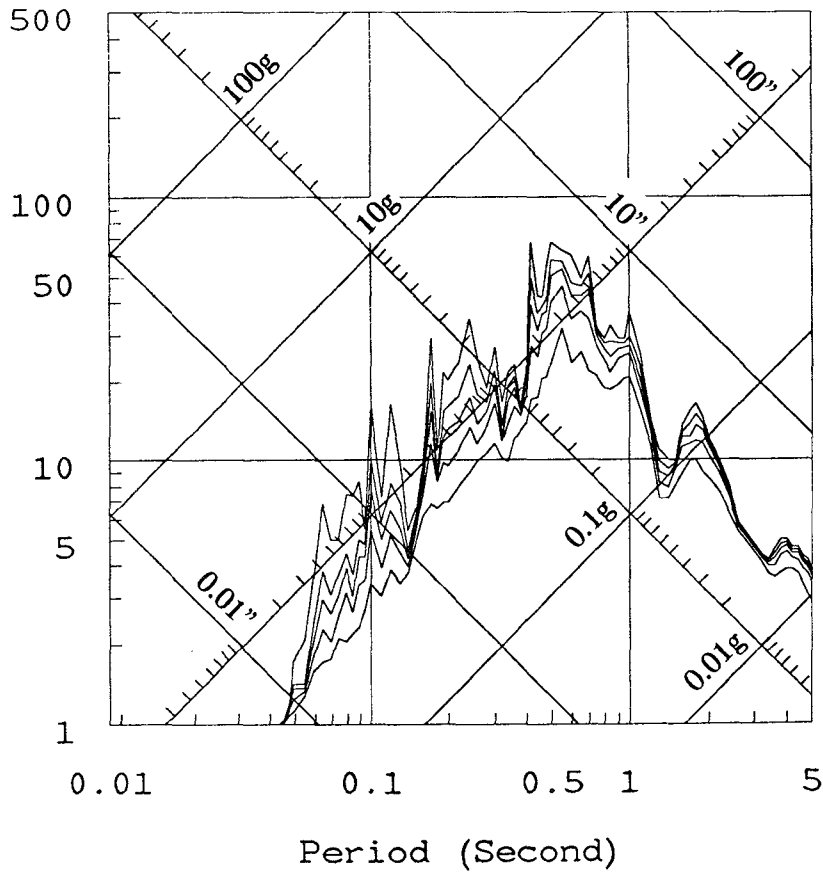
**FIG. 7.53 MO-65 TEST SECOND FLOOR BRACE-GIRDER JOINT
VERTICAL DISPLACEMENT TIME HISTORY**



**FIG. 7.54 MO-65 TEST SECOND FLOOR BRACE-GIRDER JOINT
VERTICAL DISPLACEMENT - FIRST STORY SHEAR CURVE**



Pseudo-Velocity (in/sec)



(c) Linear Elastic Response Spectra (0,0.5,1,2,5% Damping)

FIG. 7.55 MEASURED SHAKING TABLE HORIZONTAL MOTIONS AND RESPONSE SPECTRA (MO-POST1 TEST)

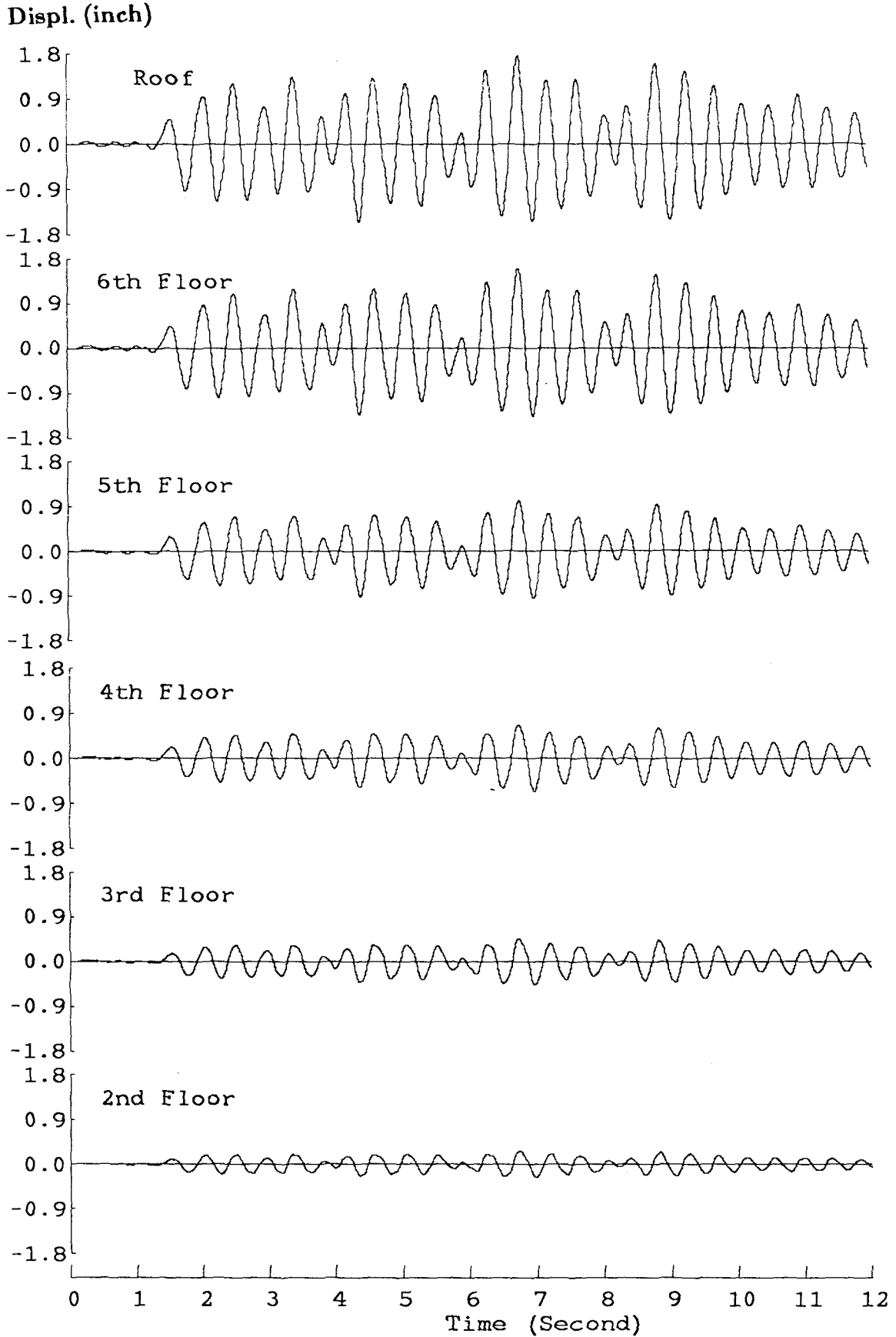


FIG. 7.56 MO-POST1 TEST RELATIVE DISPLACEMENT TIME HISTORIES

Inter-story drift (inch)

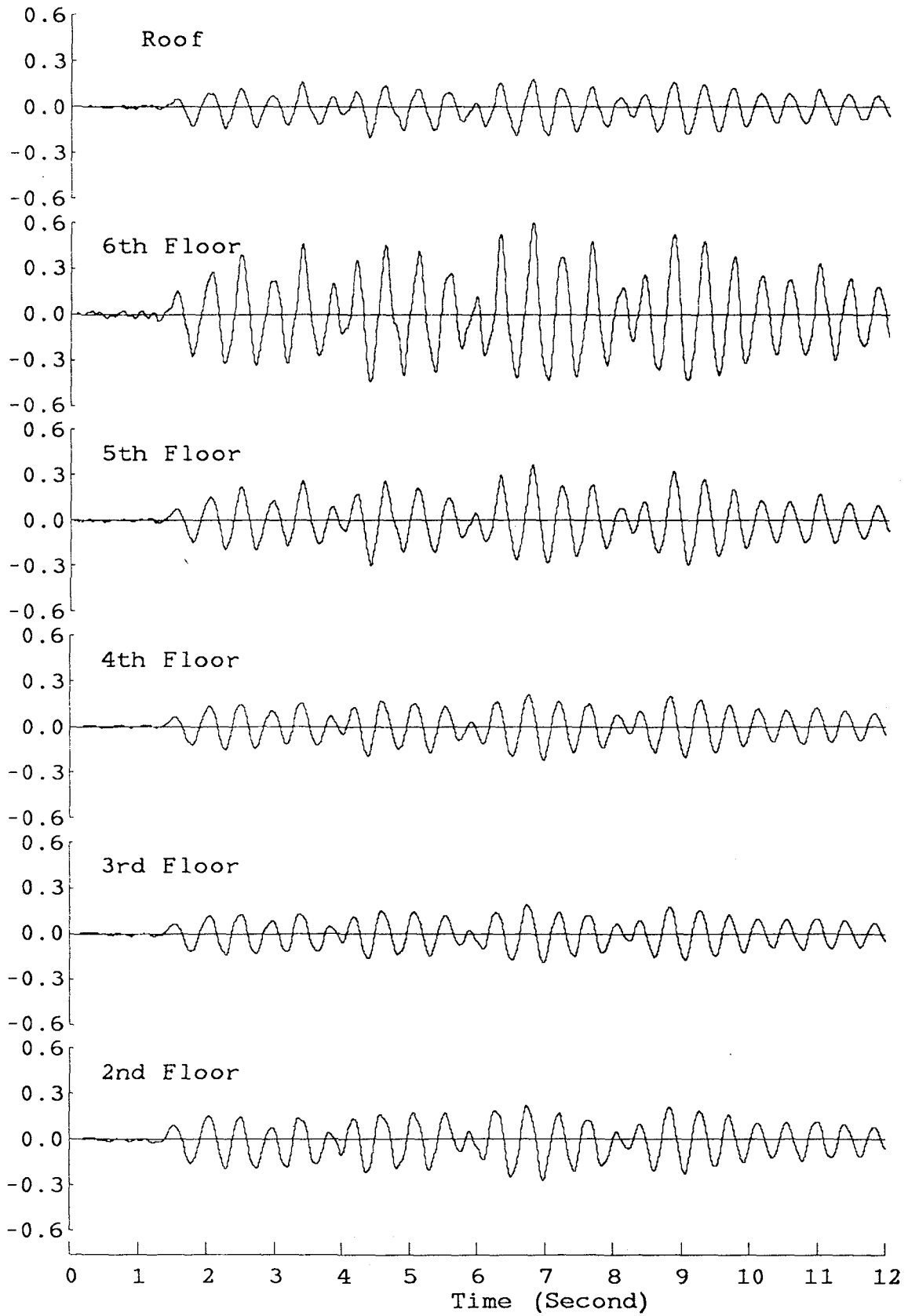
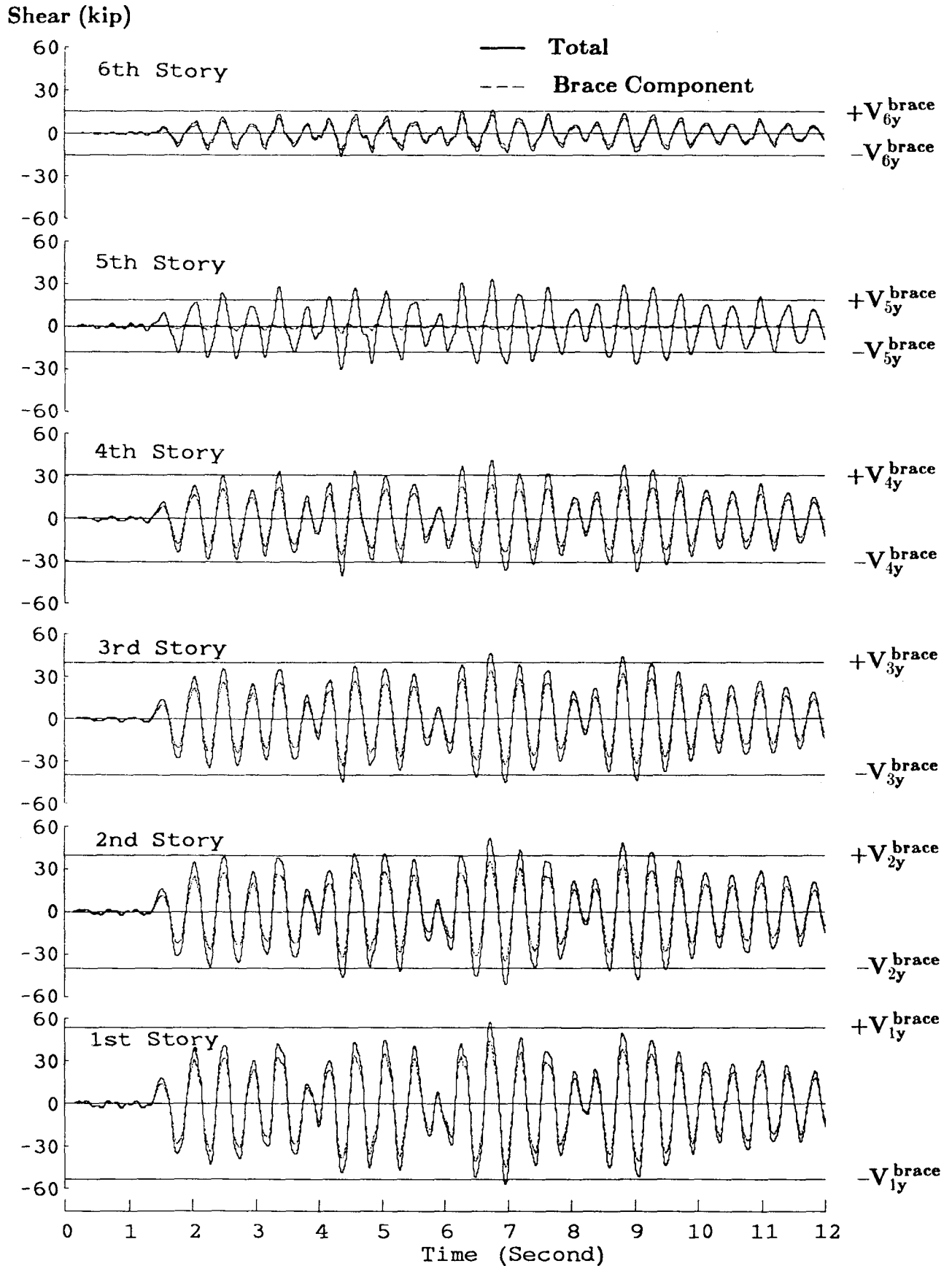


FIG. 7.57 MO-POST1 TEST INTER-STORY DRIFT TIME HISTORIES



**FIG. 7.58 STORY SHEAR (TOTAL AND BRACE COMPONENT)
TIME HISTORIES OF MO-POST1 TEST**

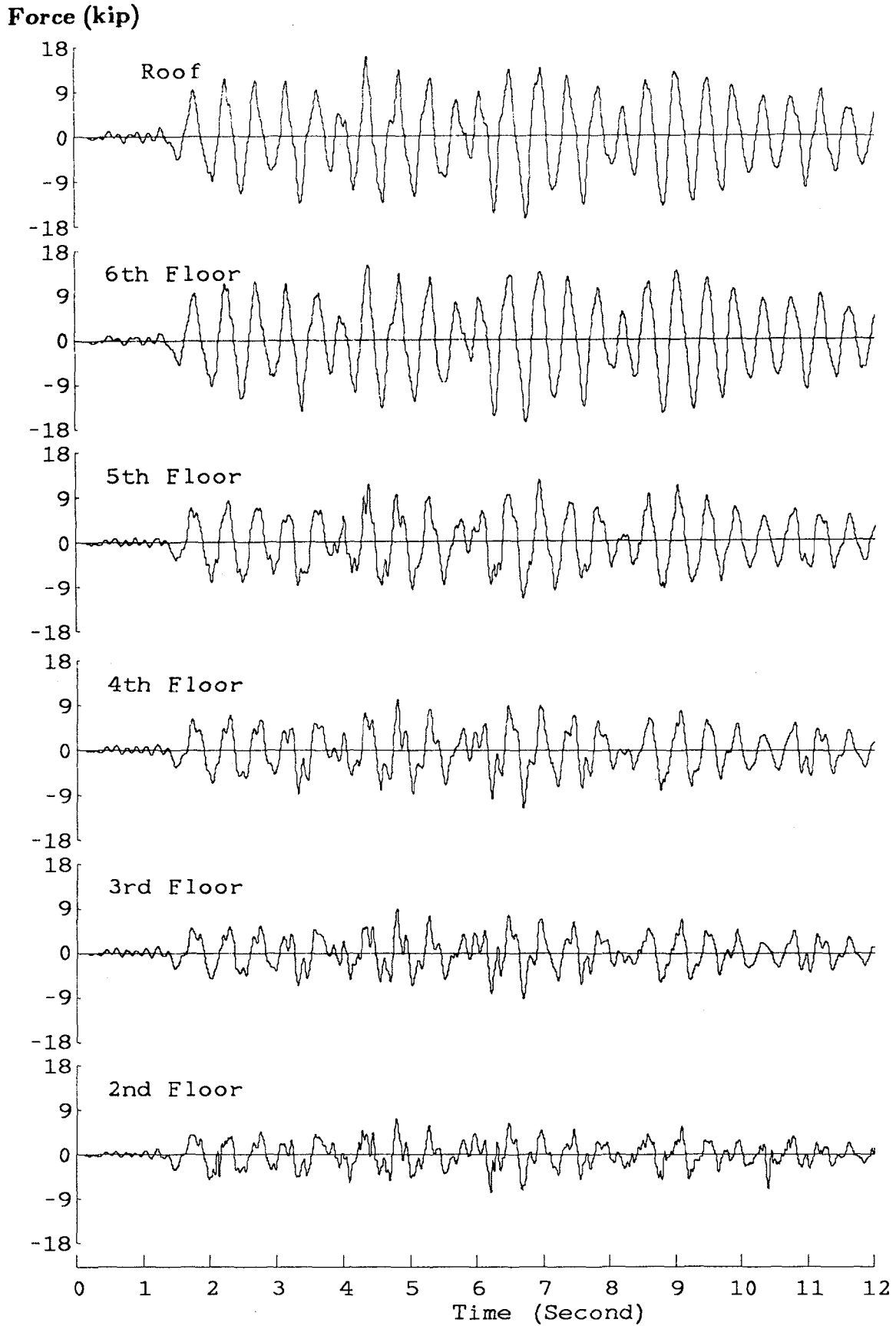
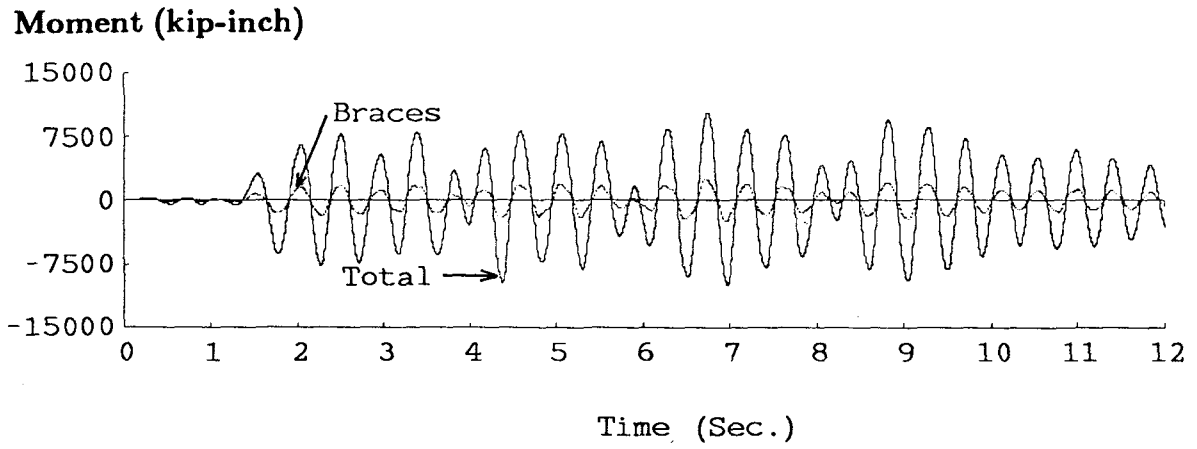


FIG. 7.59 MO-POST1 TEST LATERAL INERTIA FORCE TIME HISTORIES



**FIG. 7.60 MO-POST1 TEST BASE OVERTURNING MOMENT
TIME HISTORIES**

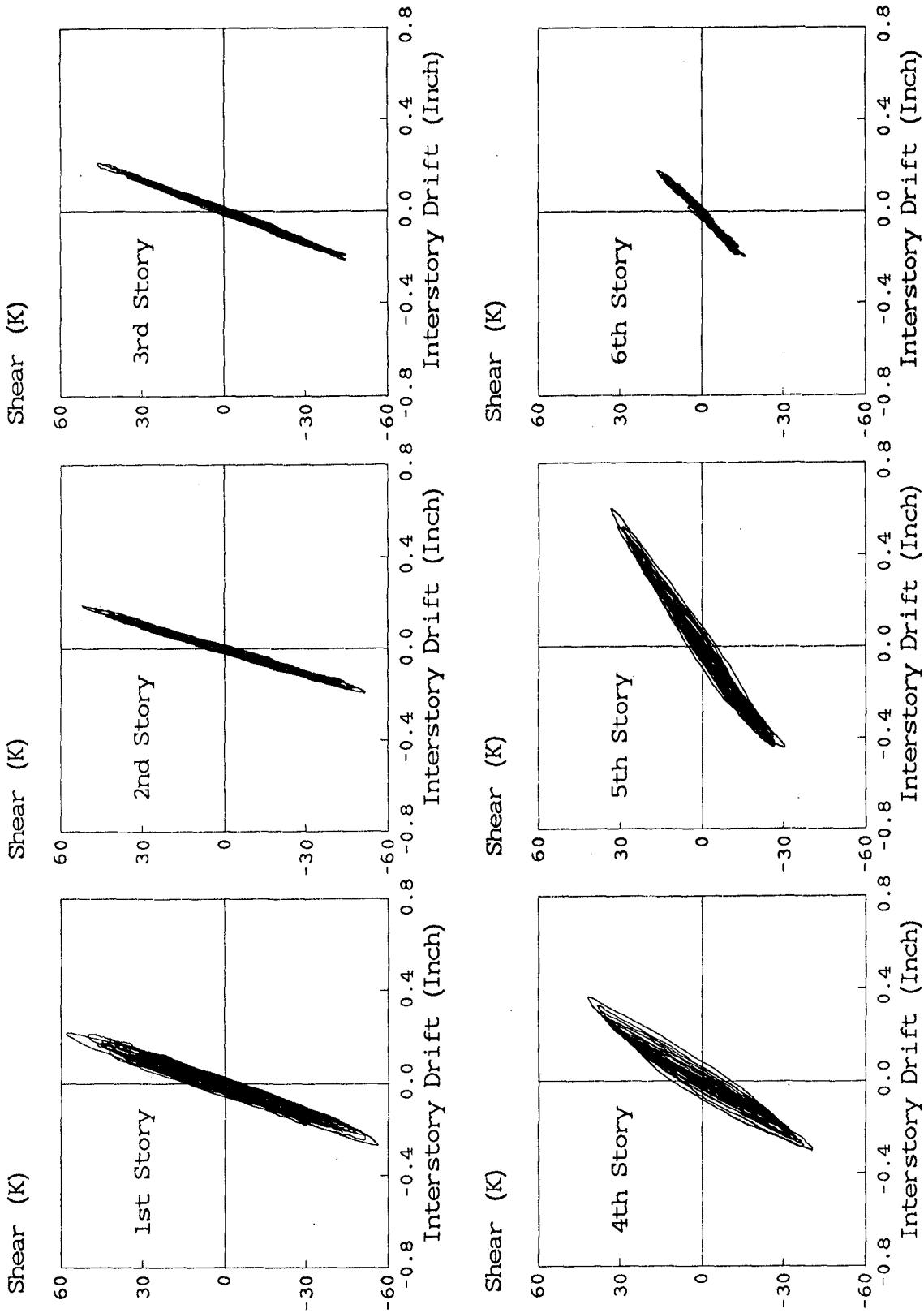


FIG. 7.61 MO-POST1 TEST INTER-STORY DRIFT VERSUS TOTAL STORY SHEAR (V^{TOTAL}) CURVES

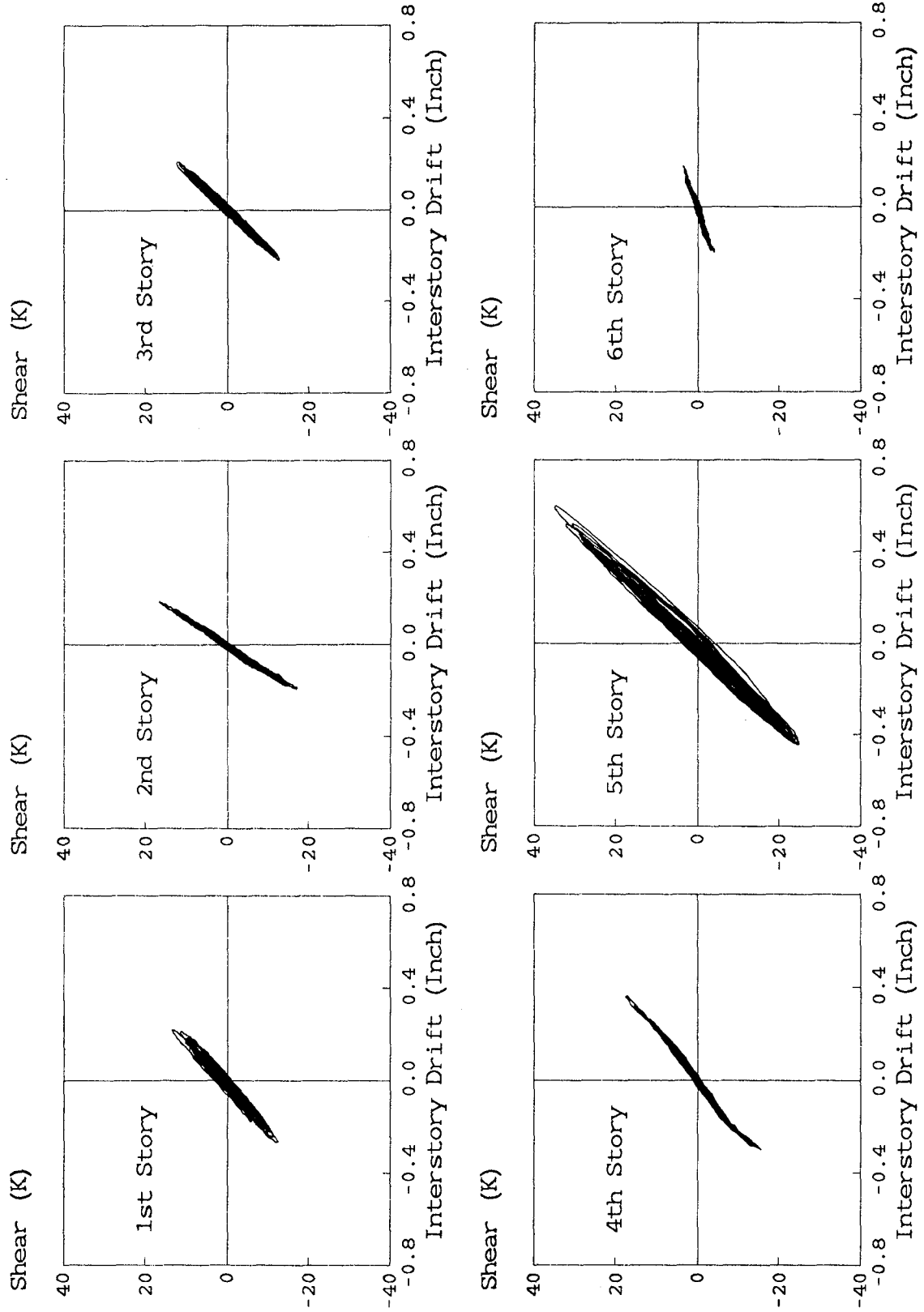


FIG. 7.62 MO-POST1 TEST INTER-STORY DRIFT VERSUS
STORY COLUMN SHEAR (V_{MRSF}) CURVES

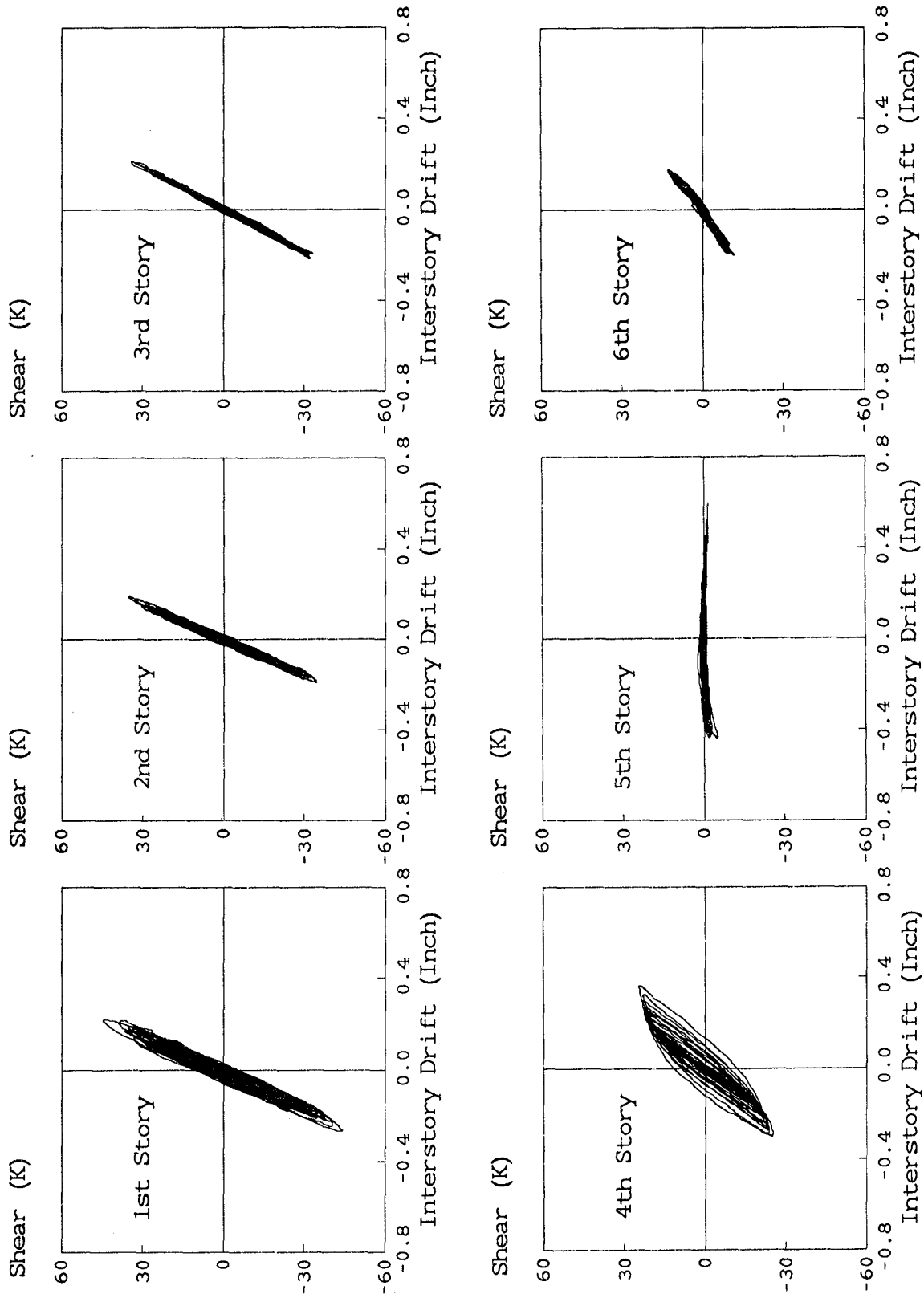


FIG. 7.63 MO-POST1 TEST INTER-STORY DRIFT VERSUS
STORY BRACE SHEAR (V_{BRACE}) CURVES

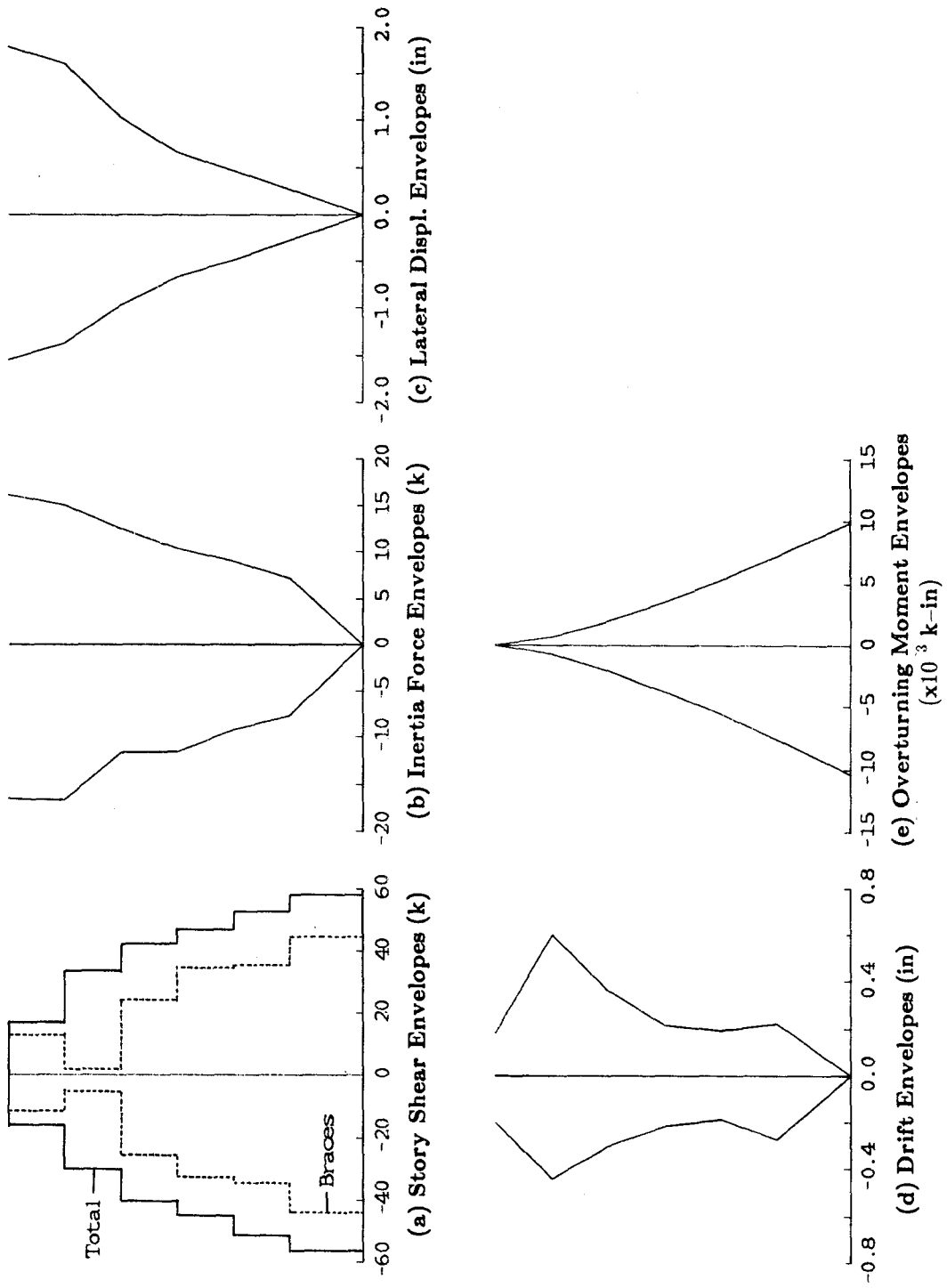


FIG. 7.64 MO-POST1 TEST RESPONSE ENVELOPES

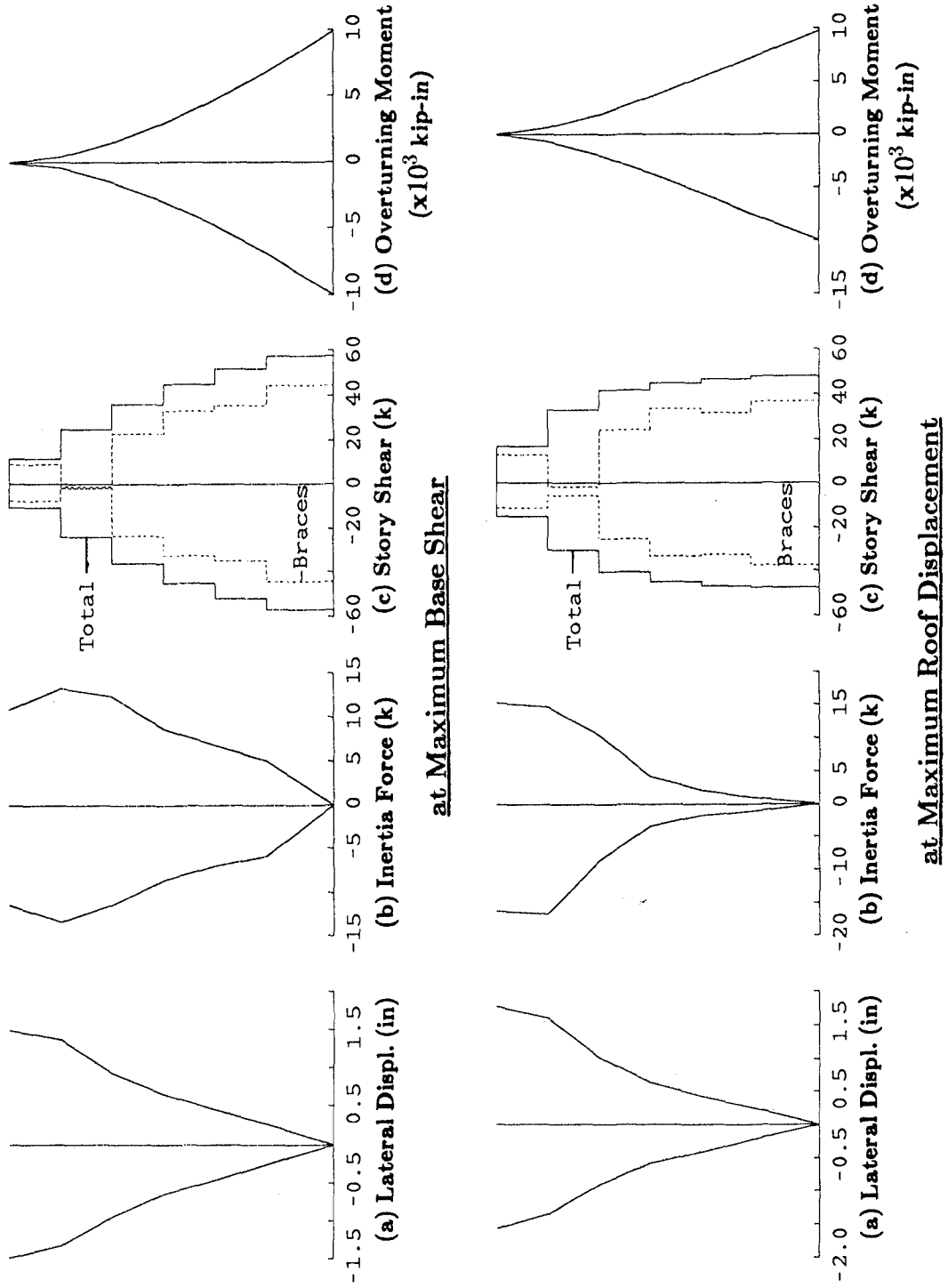


FIG. 7.65 MO-POSTI TEST RESPONSE PROFILES AT MAXIMUM RESPONSES

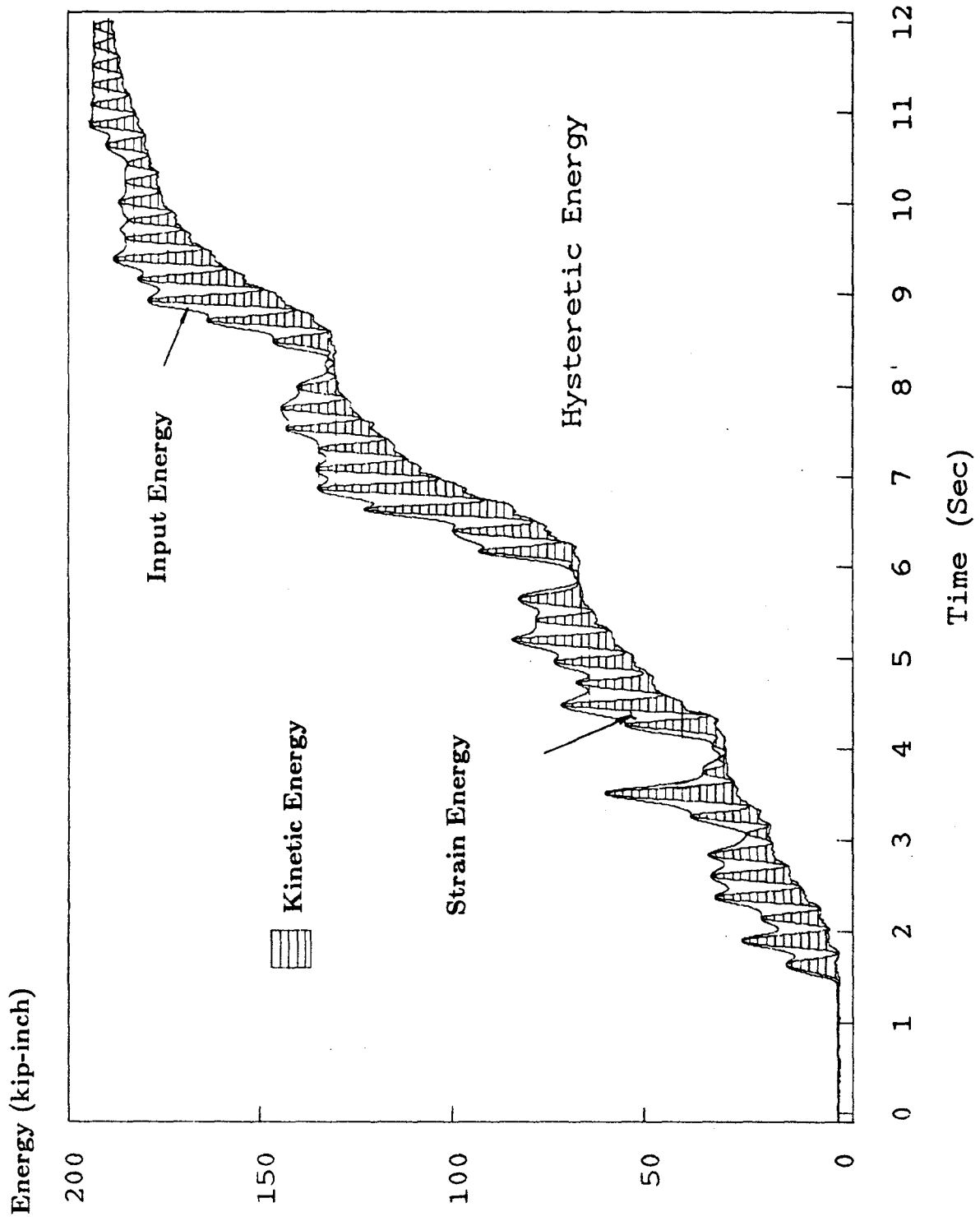


FIG. 7.66 MO-POST1 TEST ENERGY TIME HISTORIES

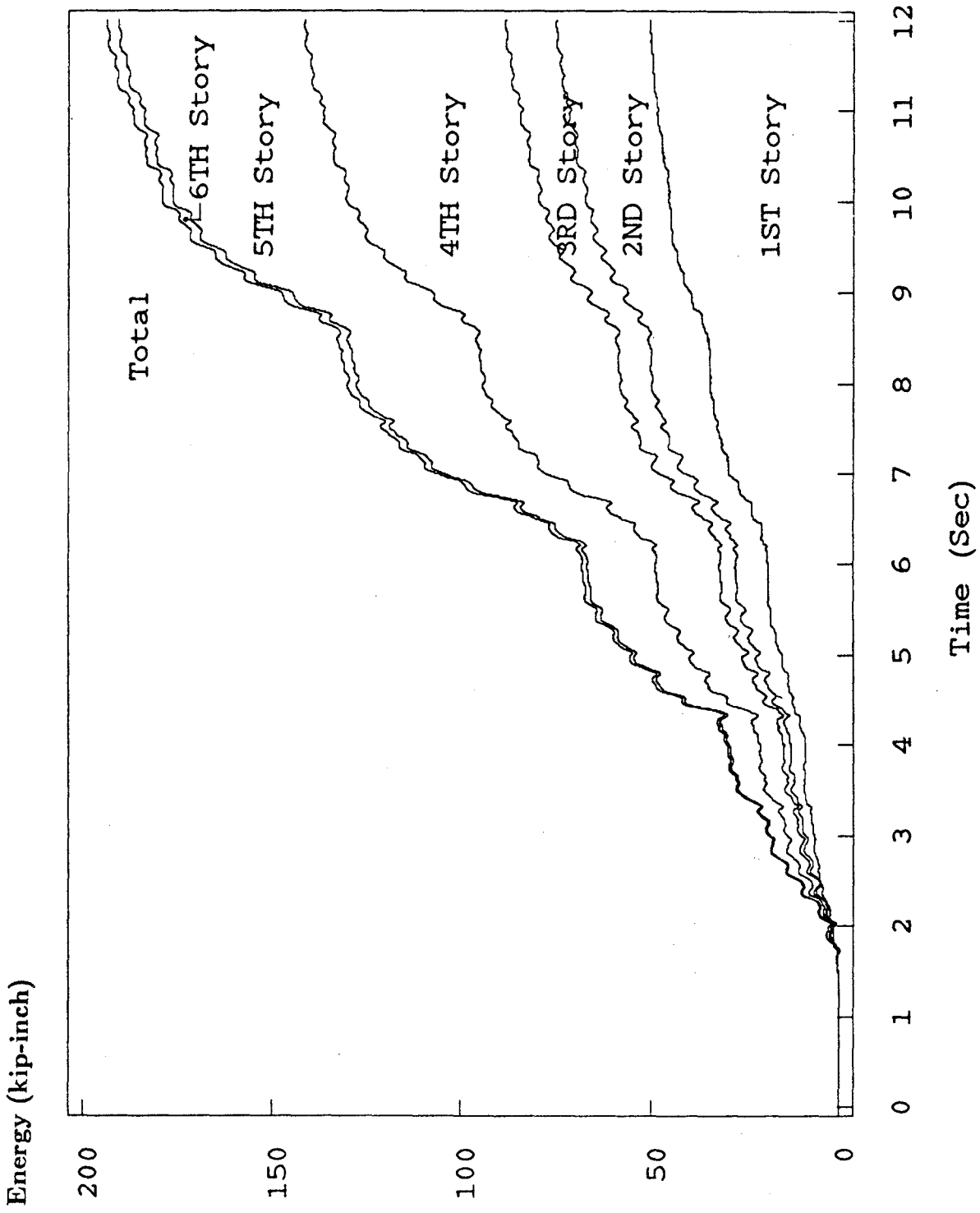
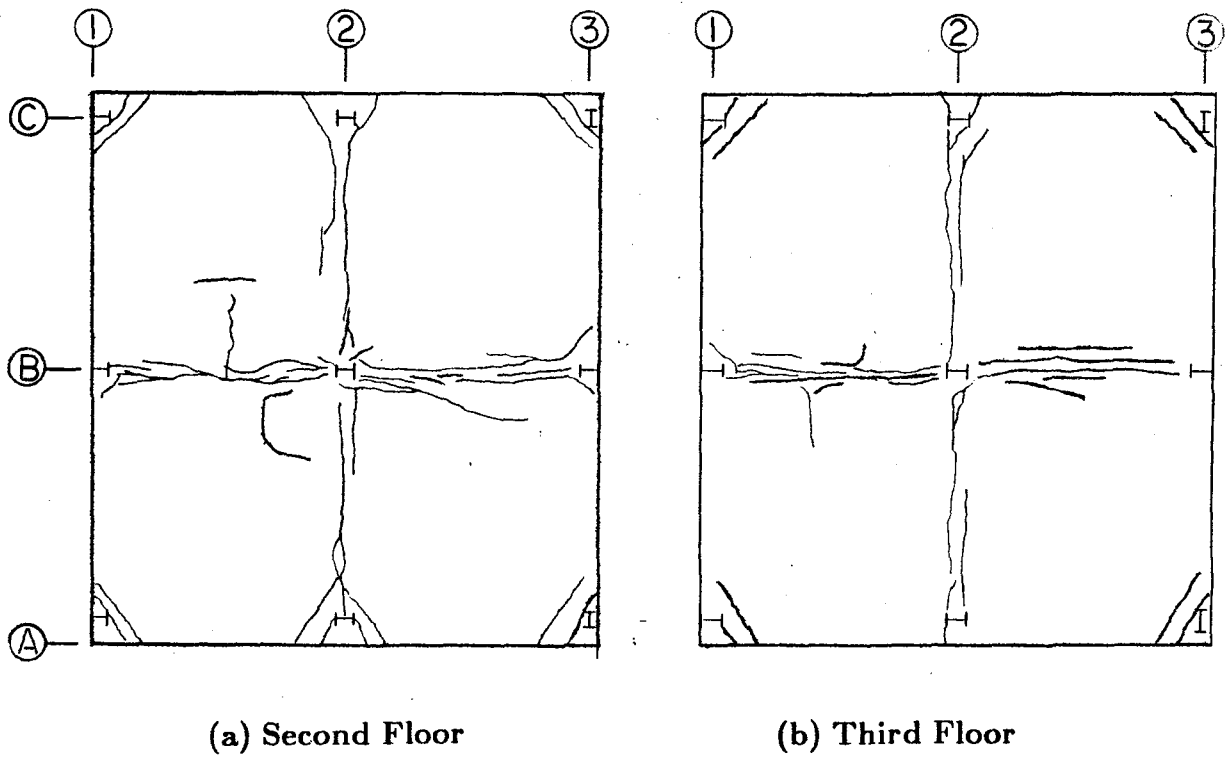


FIG. 7.67 MO-POST1 TEST HYSTERETIC DISSIPATED ENERGY DISTRIBUTION



maximum crack width = 0.015 inches

FIG. 7.68 CONCRETE SLAB CRACK PATTERN AFTER SHAKING TABLE TESTS

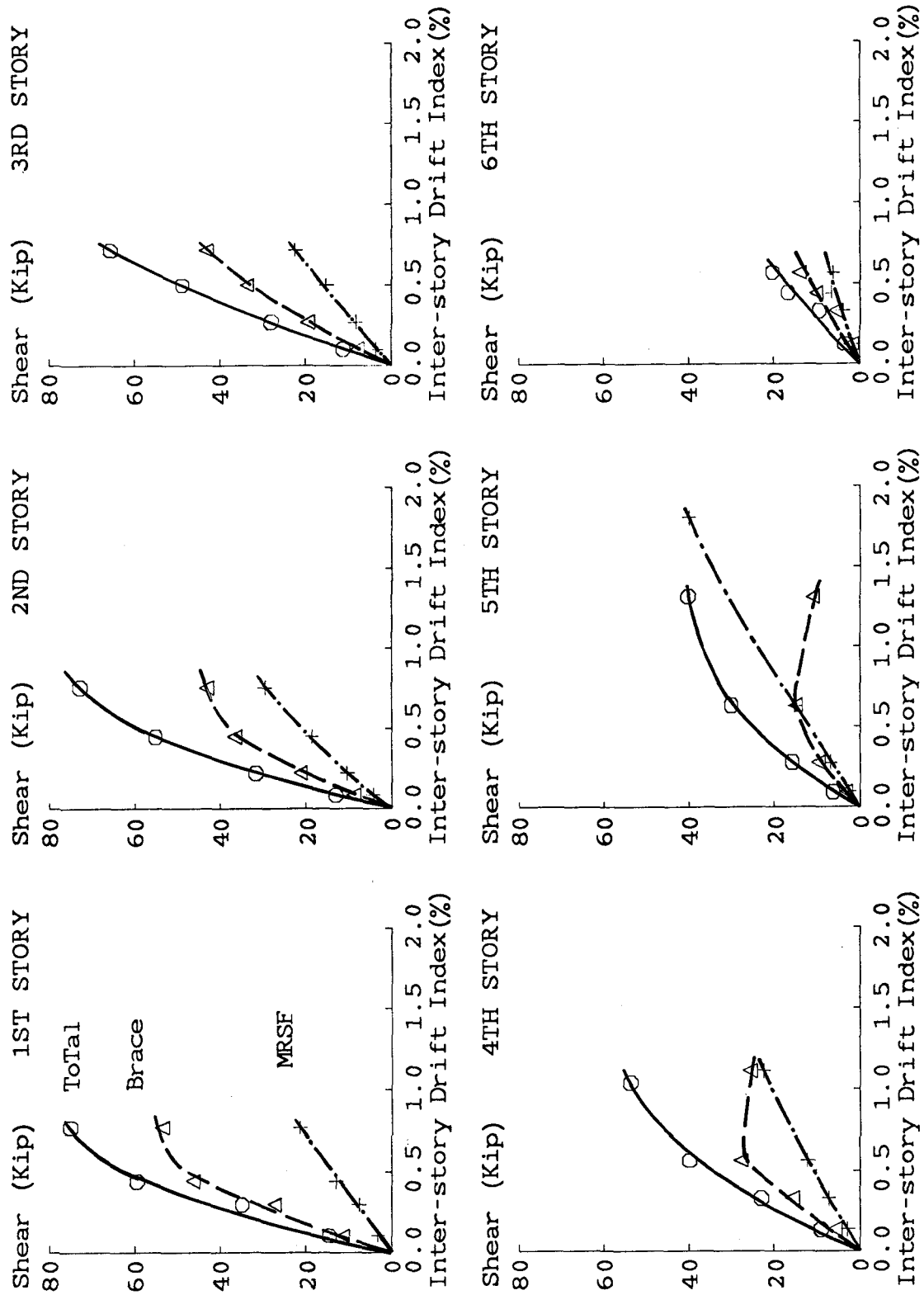


FIG. 8.1 ENVELOPES OF INTER-STORY DRIFT INDEX VERSUS STORY SHEAR

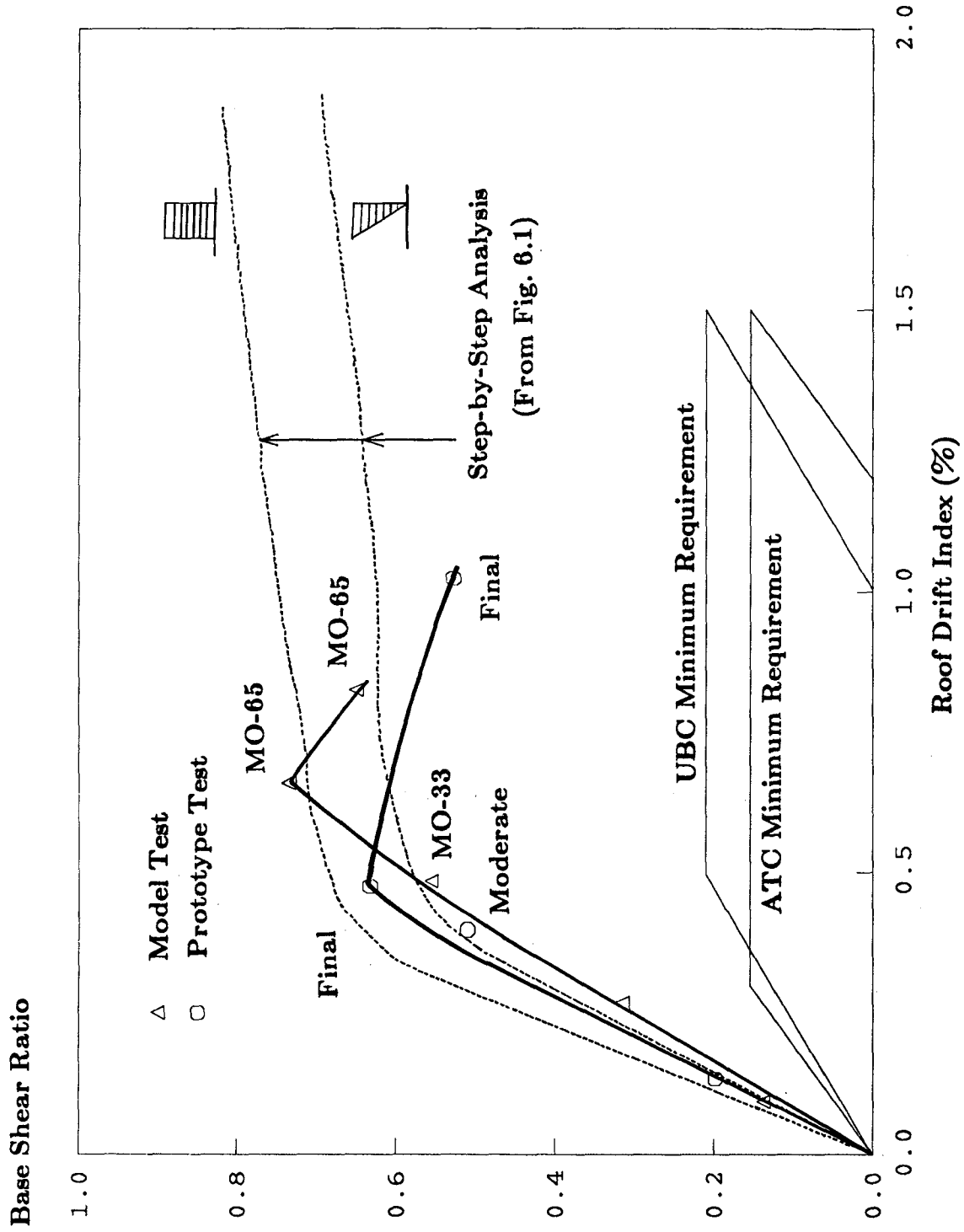


FIG. 8.2 ENVELOPES OF ROOF DRIFT INDEX VERSUS BASE SHEAR RATIO

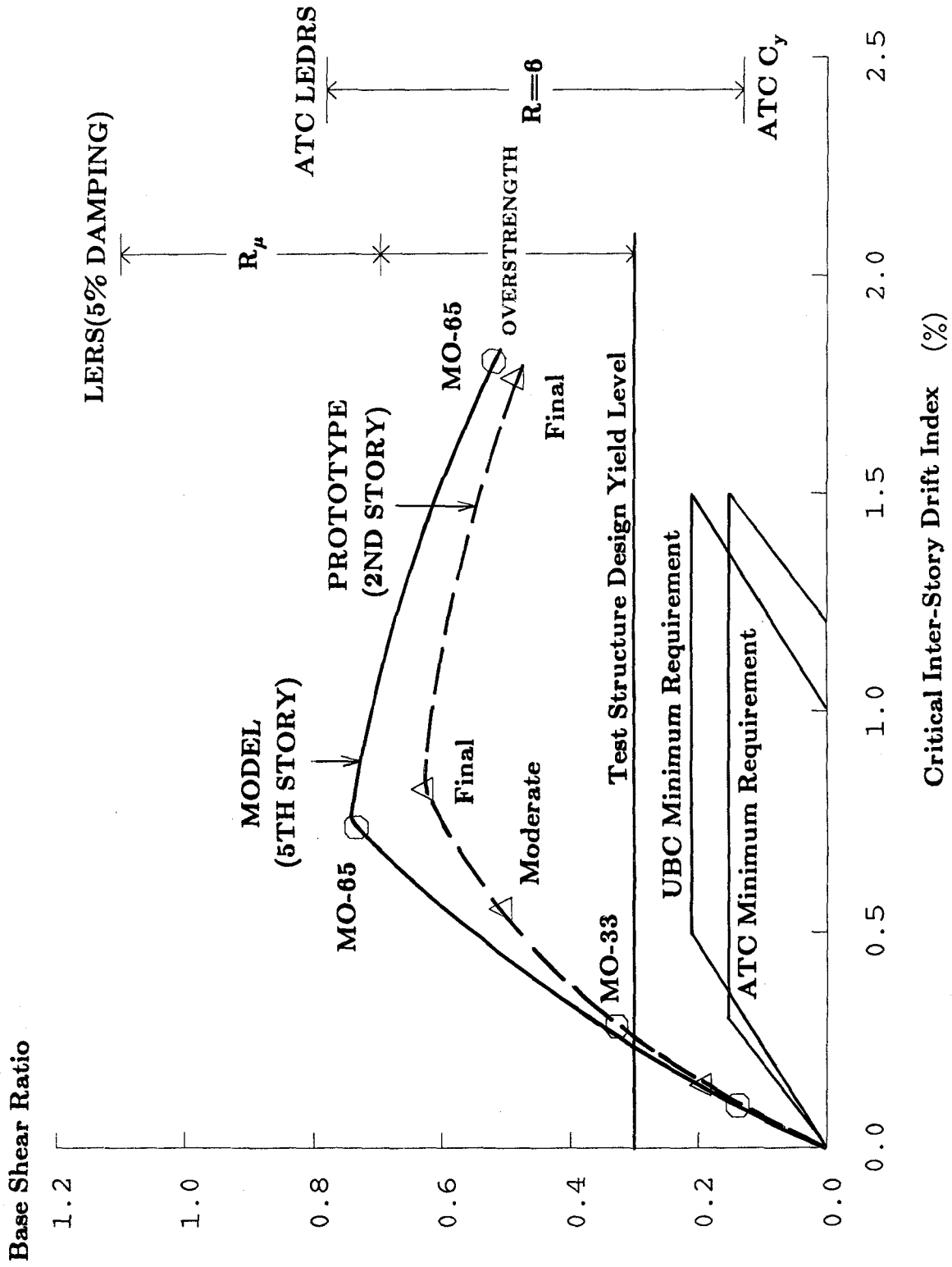


FIG. 8.3 ENVELOPES OF CRITICAL INTER-STORY DRIFT INDEX VERSUS BASE SHEAR RATIO

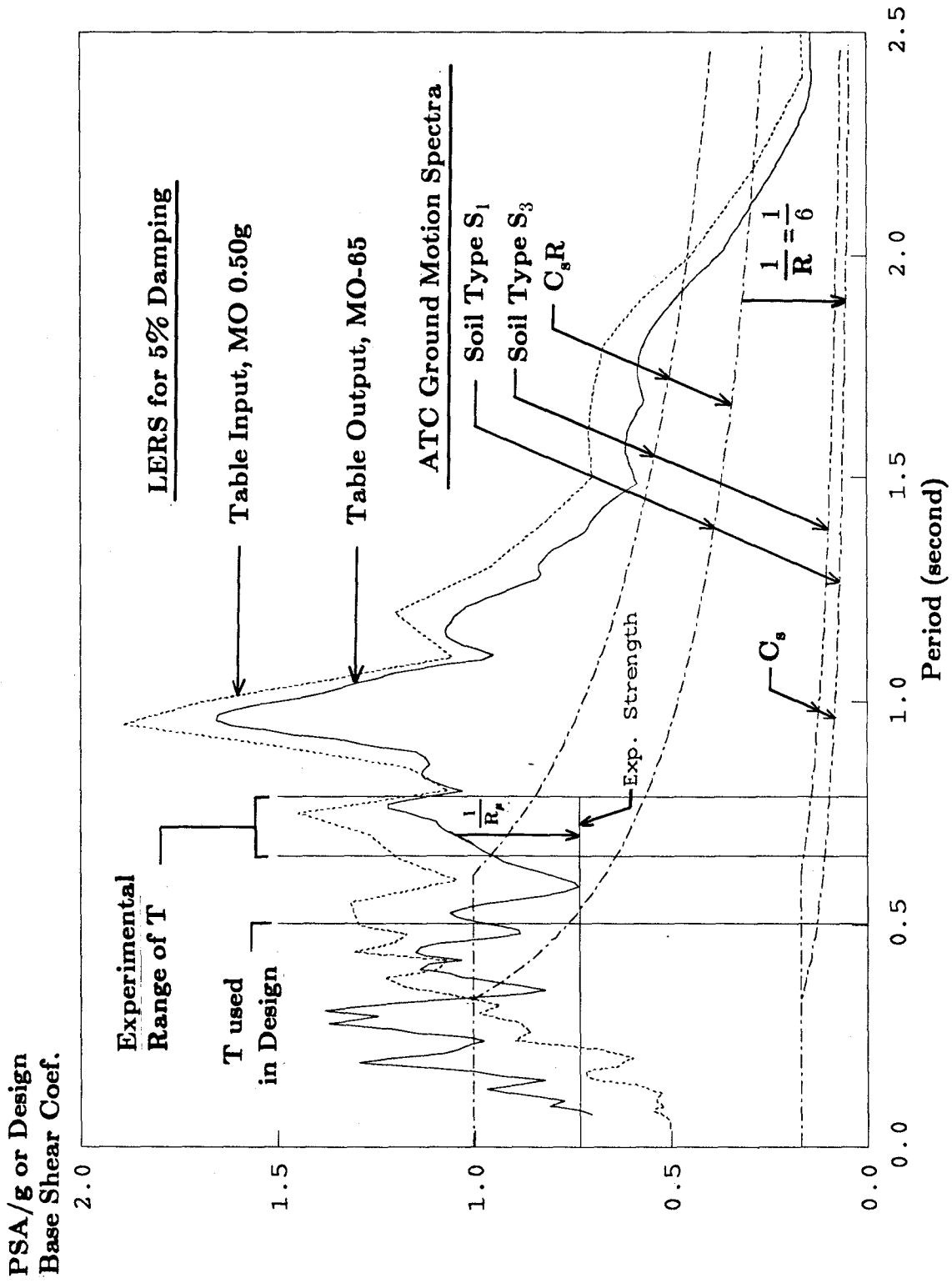


FIG. 8.4 COMPARISON OF 5% DAMPED LEERS, ATC LEERS AND
MEASURED MODEL STRENGTH

PSA/g or LEDRS

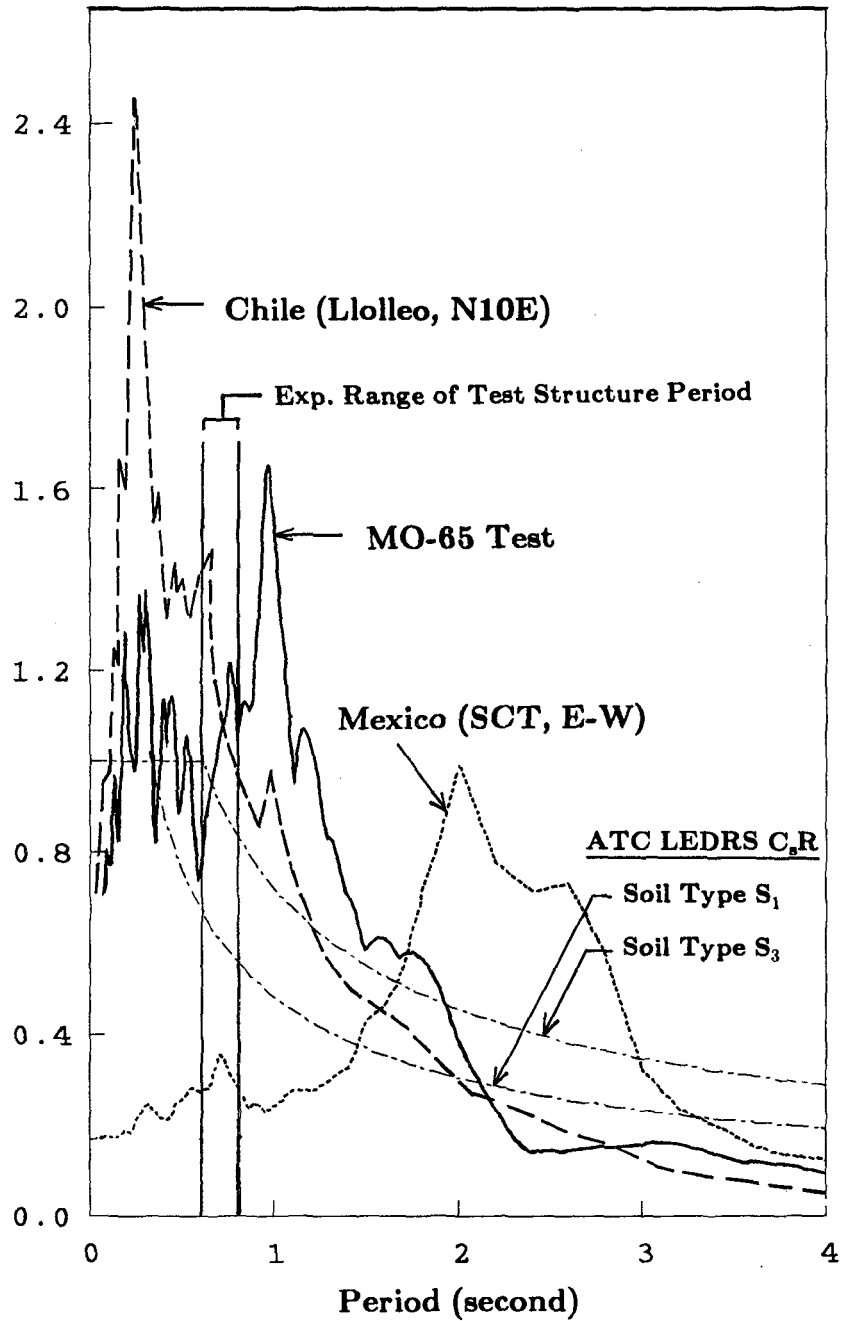
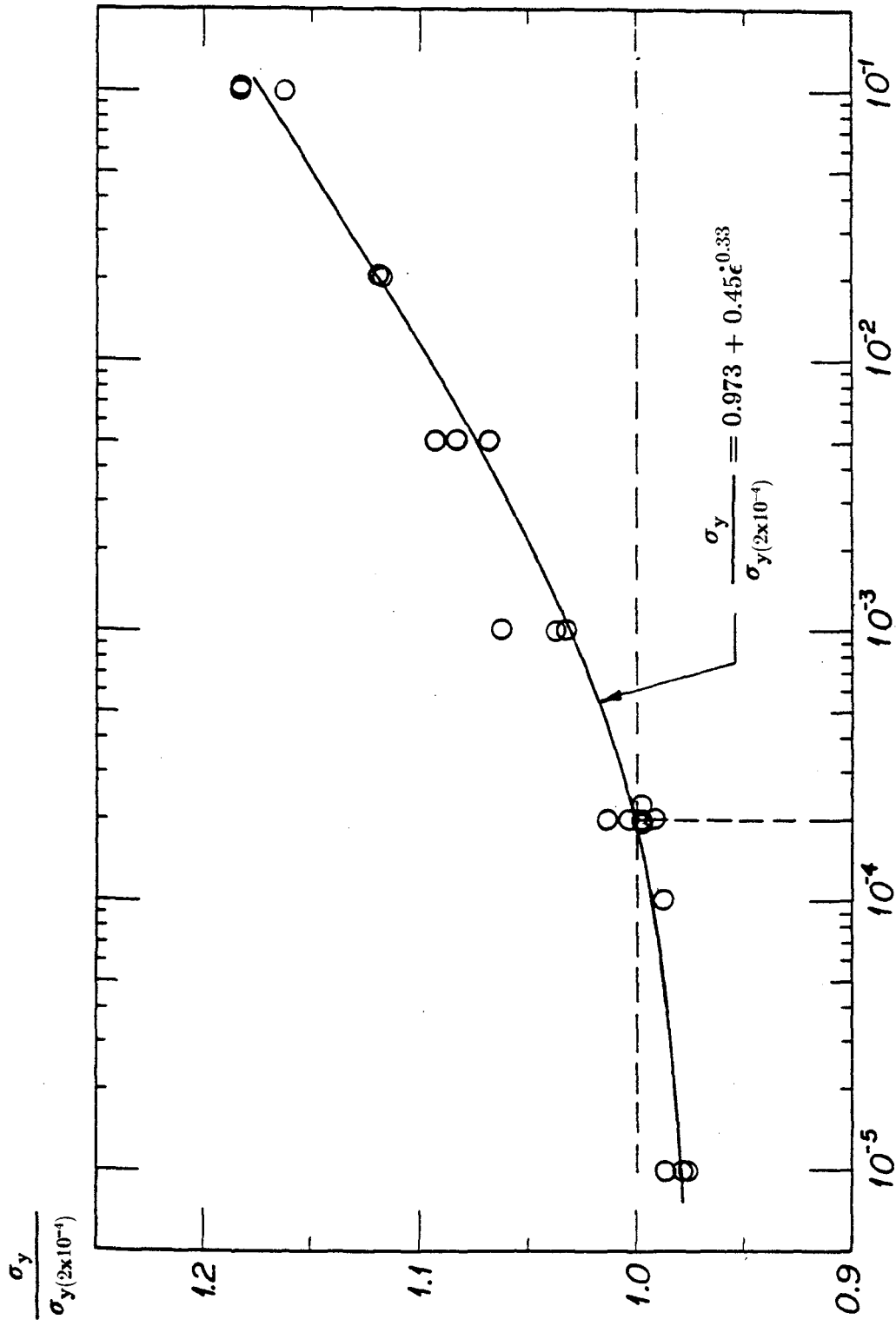


FIG. 8.5 COMPARISON OF LINEAR ELASTIC RESPONSE SPECTRA OF THE MO-65 TEST, 1985 MEXICO AND CHILEAN EQARTHQUAKES AND THE ATC LINEAR ELASTIC DESIGN RESPONSE SPECTRA



Strain Rate (1/second)

FIG. 8.6 STRAIN RATE EFFECT ON THE LOWER YIELD STRESS OF STRUCTURAL STEEL [26]

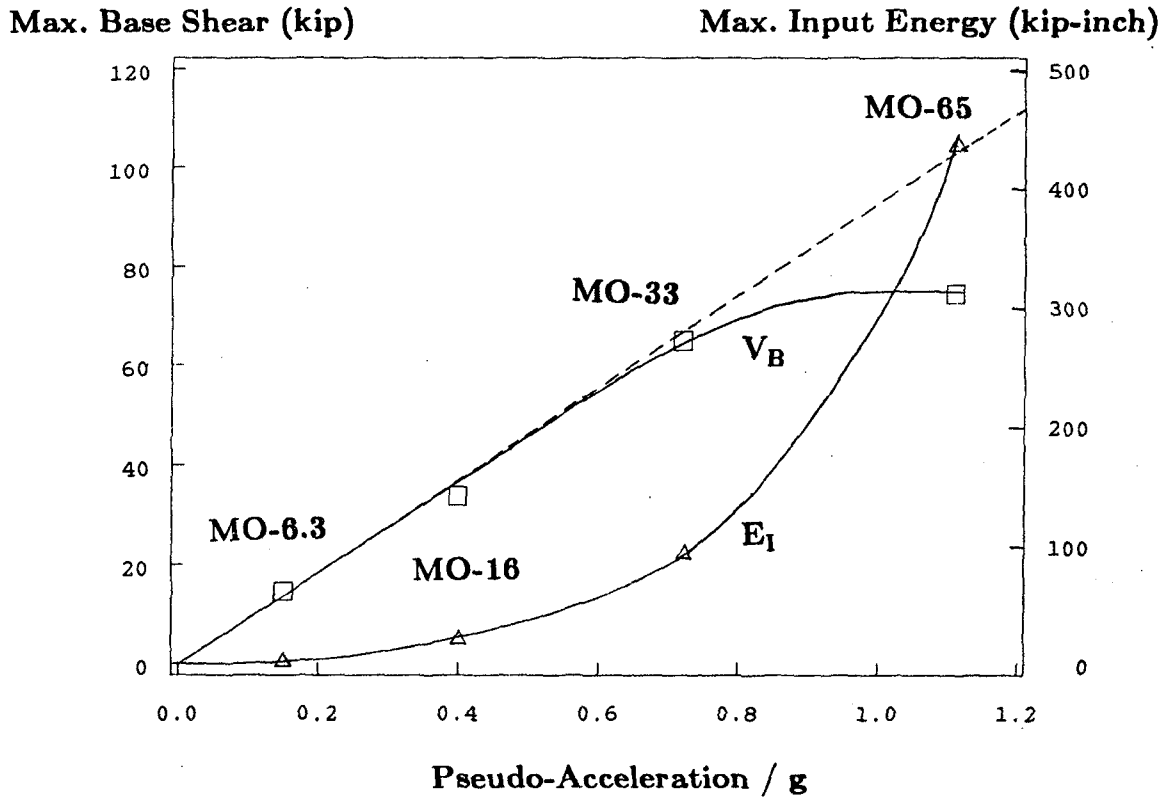


FIG. 8.7 ENVELOPES OF PSA/G VERSUS MAXIMUM BASE SHEAR AND MAXIMUM INPUT ENERGY

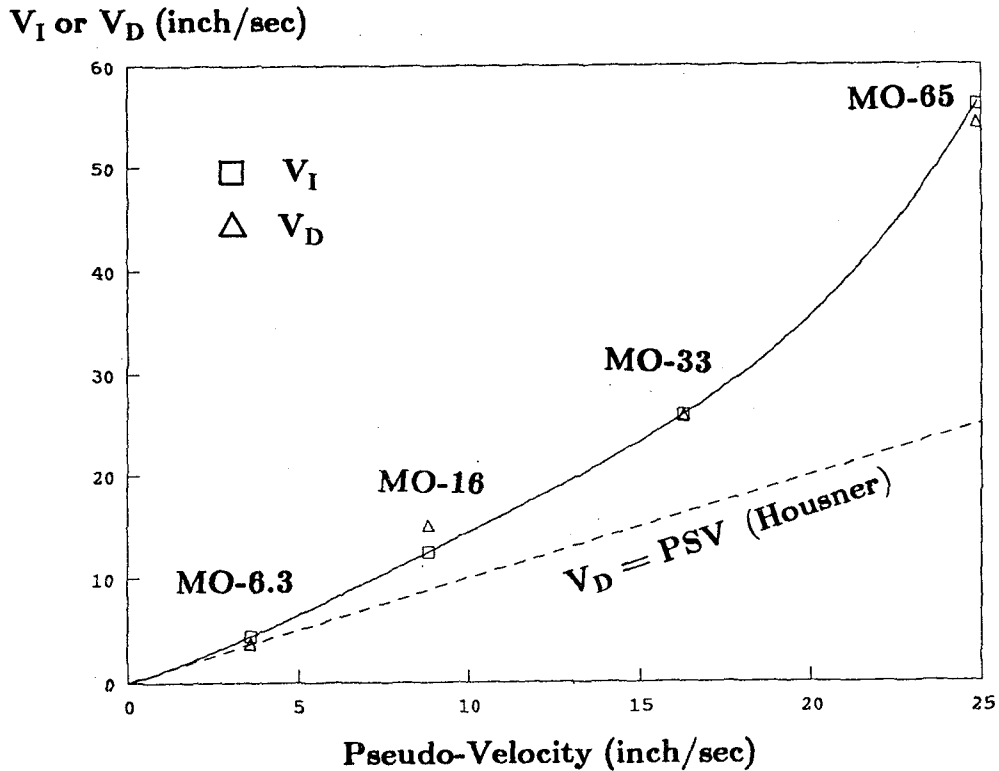
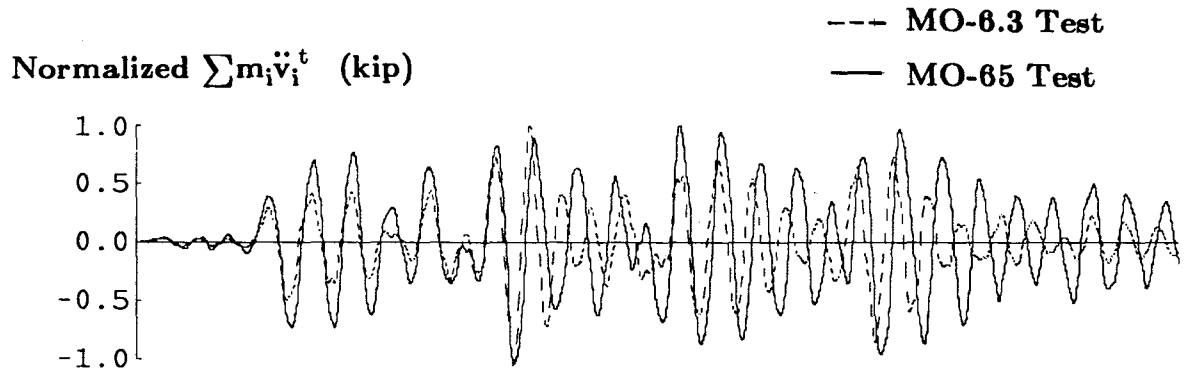
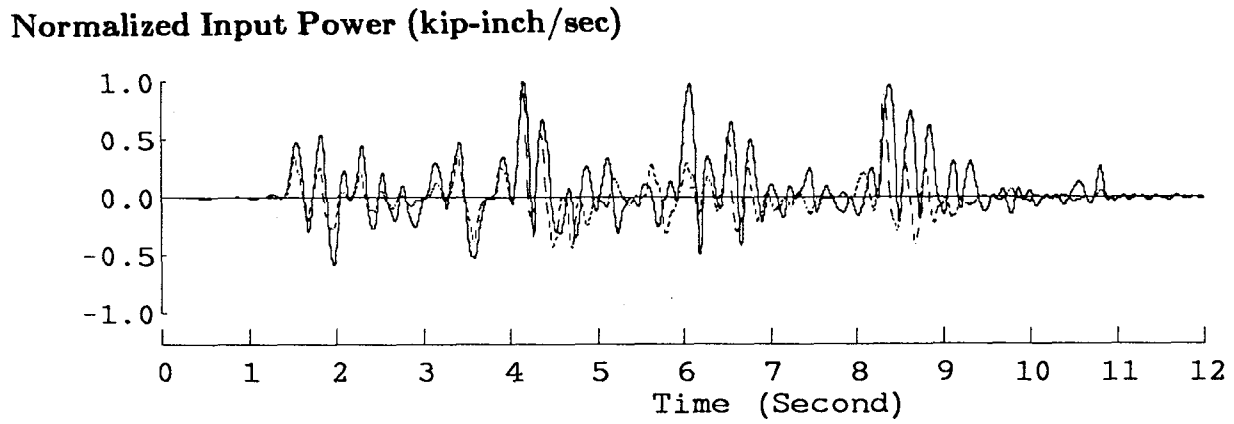


FIG. 8.8 ENVELOPES OF PSV VERSUS INPUT ENERGY EQUIVALENT VELOCITY



(a) Normalized $\sum m_i \ddot{v}_i^t$ Time History



(b) Normalized Input Power Time History

FIG. 8.9 NORMALIZED $\sum m_i \ddot{v}_i^t$ AND INPUT POWER TIME HISTORIES

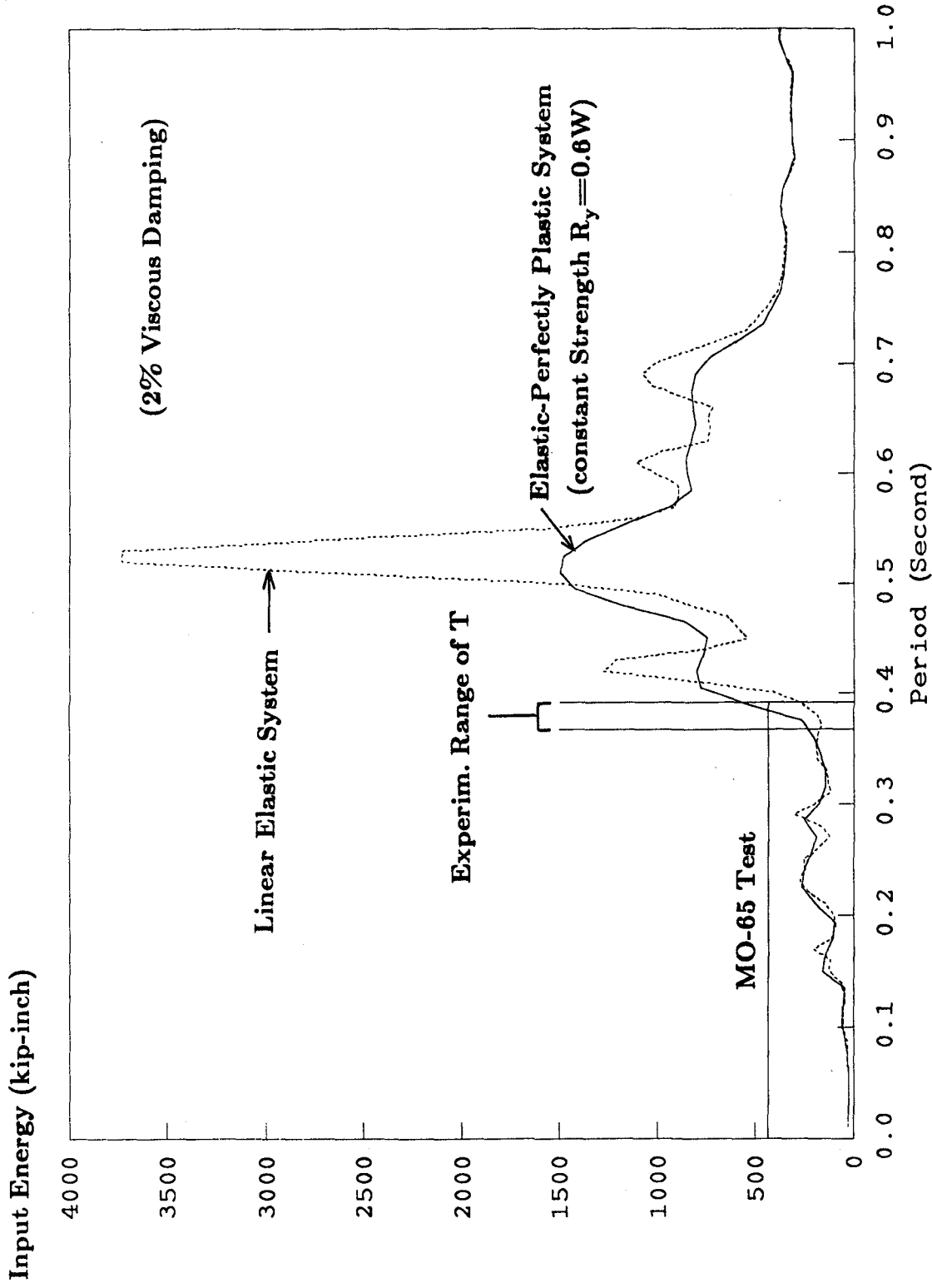


FIG. 8.10 TOTAL INPUT ENERGY SPECTRA FOR 2% DAMPED
SINGLE-DEGREE-OF-FREEDOM SYSTEM SUBJECTED TO
MEASURED MO-65 TEST TABLE HORIZONTAL ACCELERATION

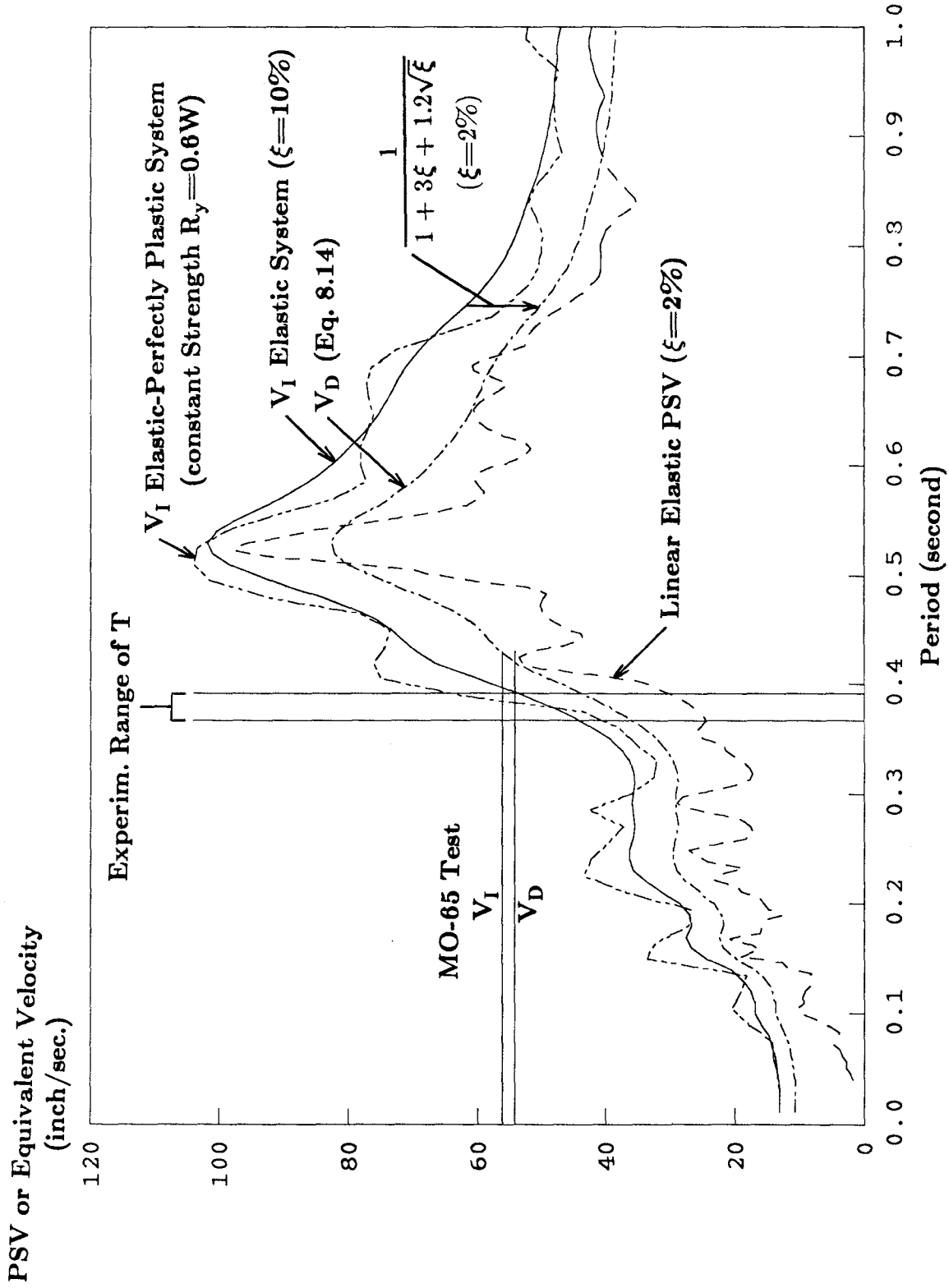


FIG. 8.11 INPUT ENERGY EQUIVALENT VELOCITY AND PSV SPECTRA FOR THE MEASURED MO-65 TEST TABLE HORIZONTAL ACCELERATION

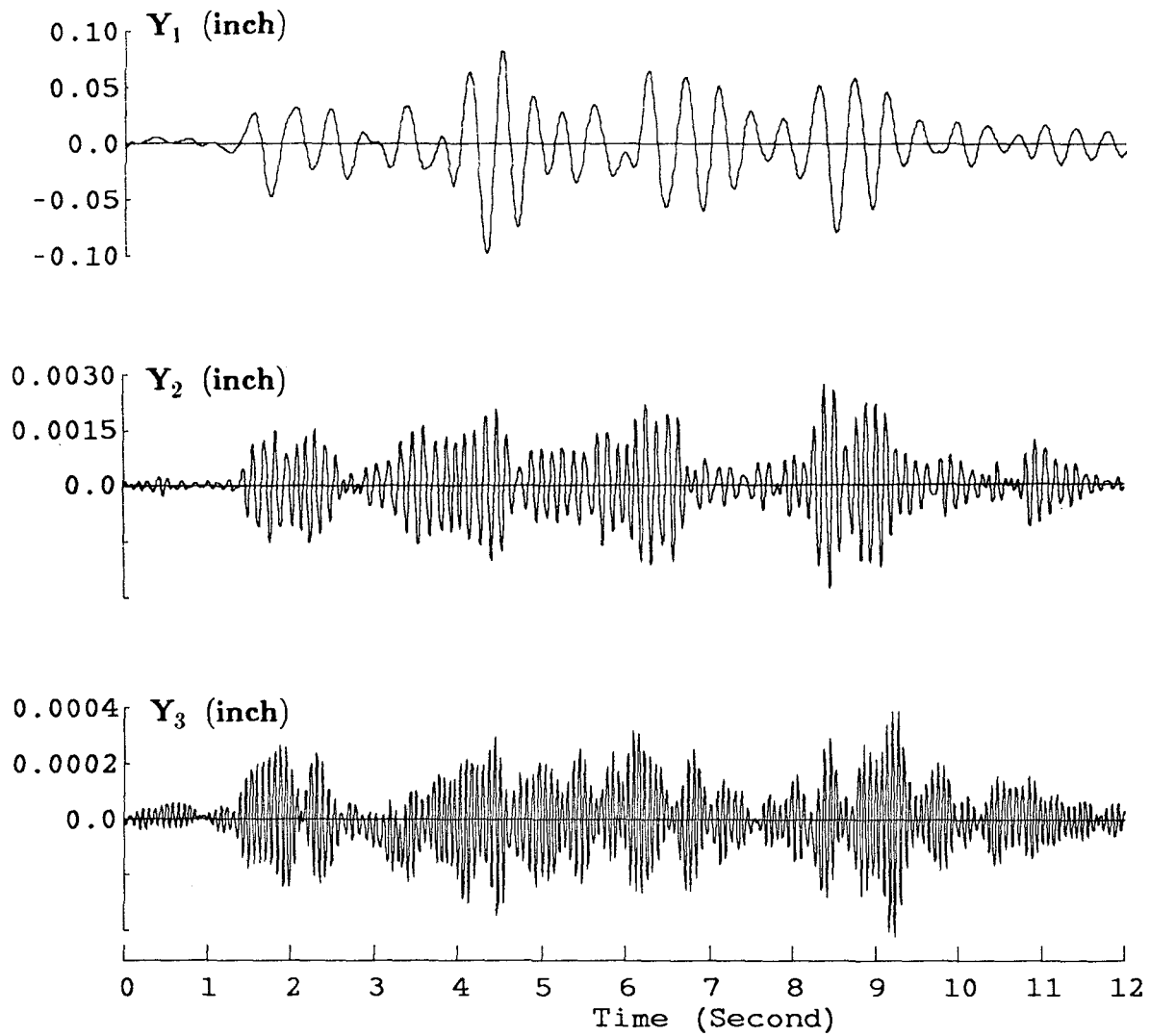


FIG. 8.12 MODAL DISPLACEMENT ($Y_i(t)$) TIME HISTORIES (MO-6.3 TEST)

Energy (kip-inch)

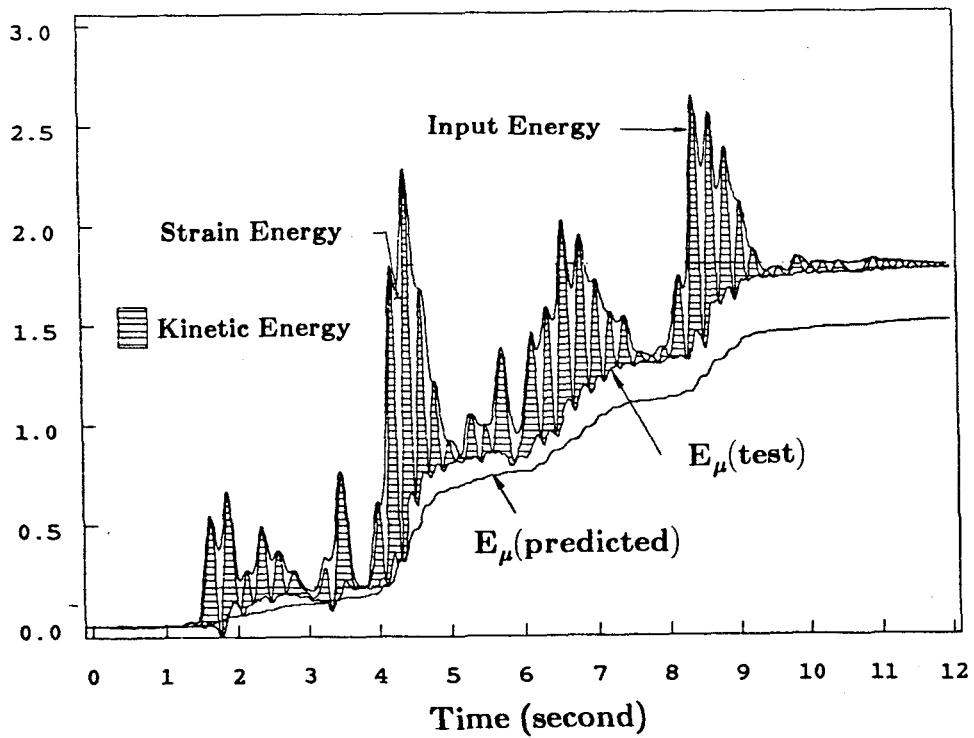


FIG. 8.13 COMPARISON OF VISCOUS DAMPED ENERGY (MO-6.3 TEST)

Energy (kip-inch)

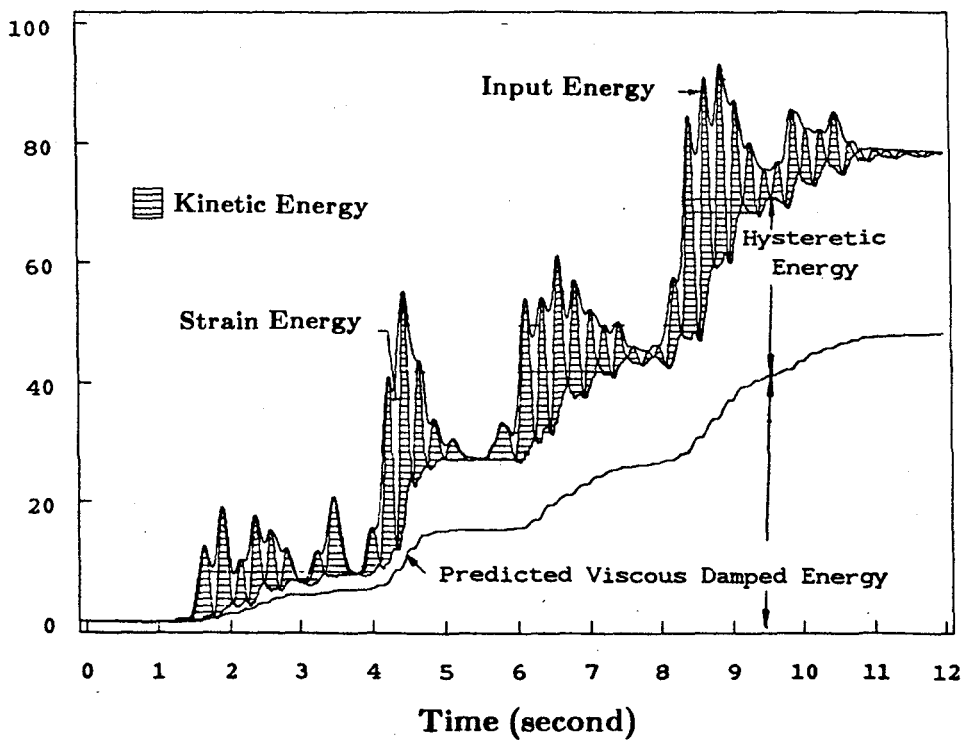


FIG. 8.14 COMPARISON OF VISCOUS DAMPED ENERGY (MO-33 TEST)

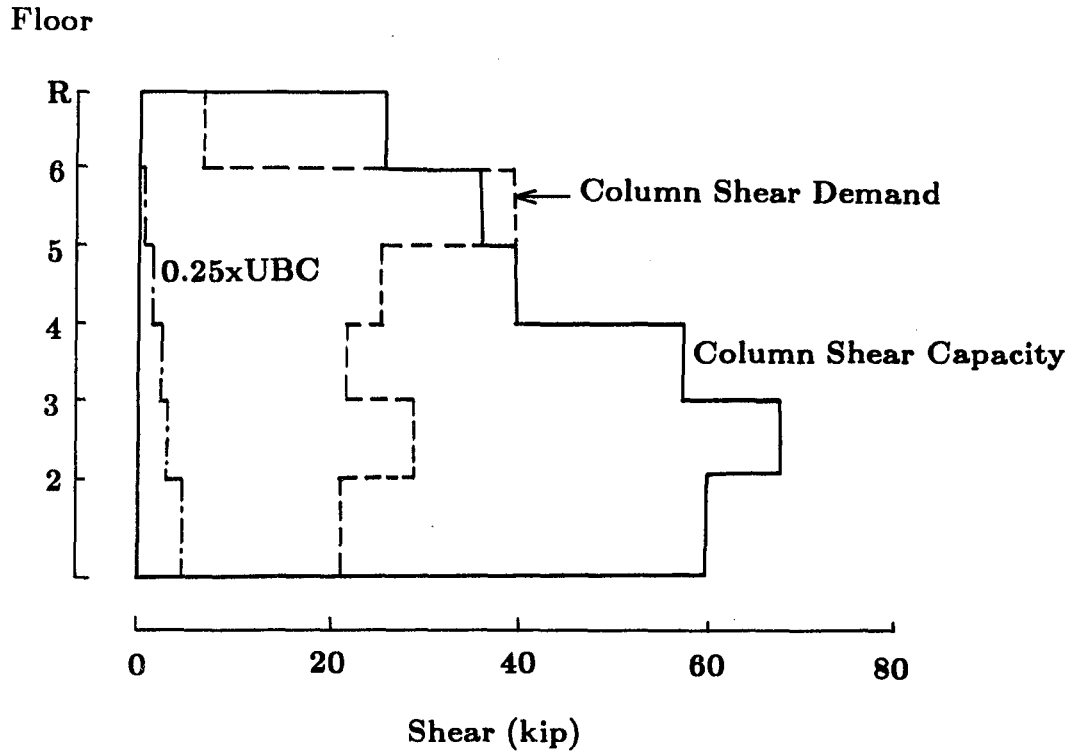


FIG. 8.15 MO-65 TEST STORY COLUMN SHEAR (V^{MRSF}) ENVELOPES

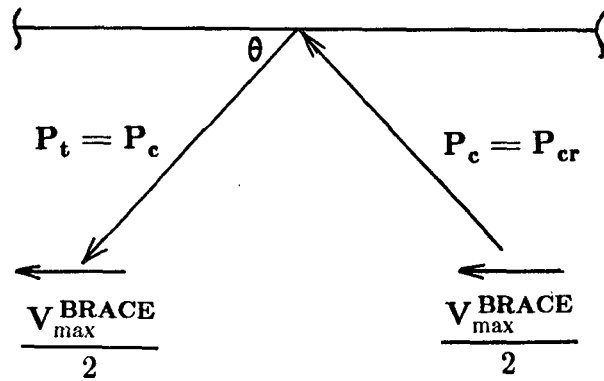


FIG. 8.16 SHEAR FORCE DISTRIBUTION AT MAXIMUM V^{BRACE}

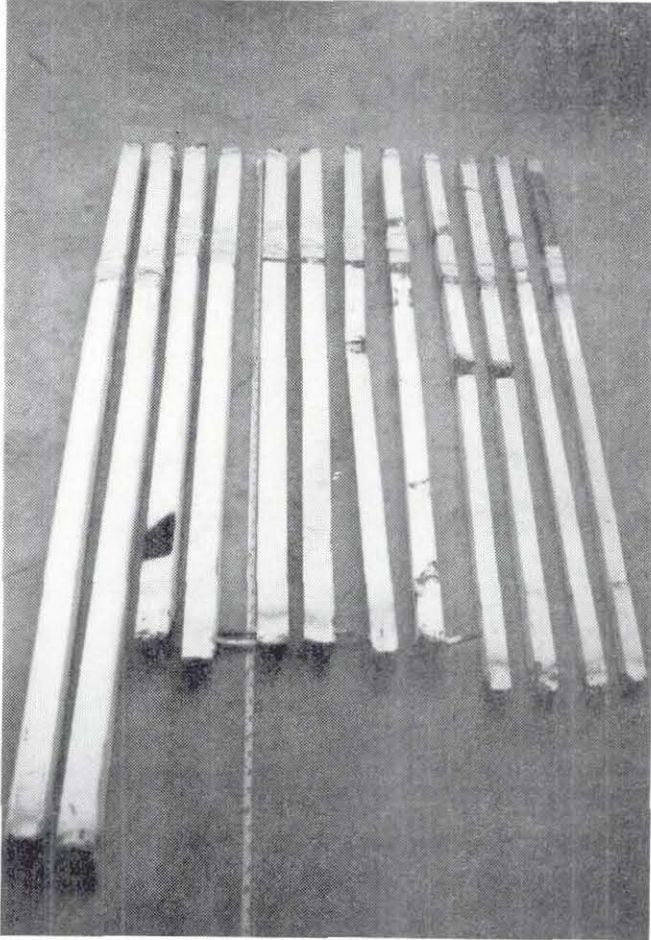


FIG. 8.17 DAMAGED BRACES AFTER THE SHAKING TABLE TESTS

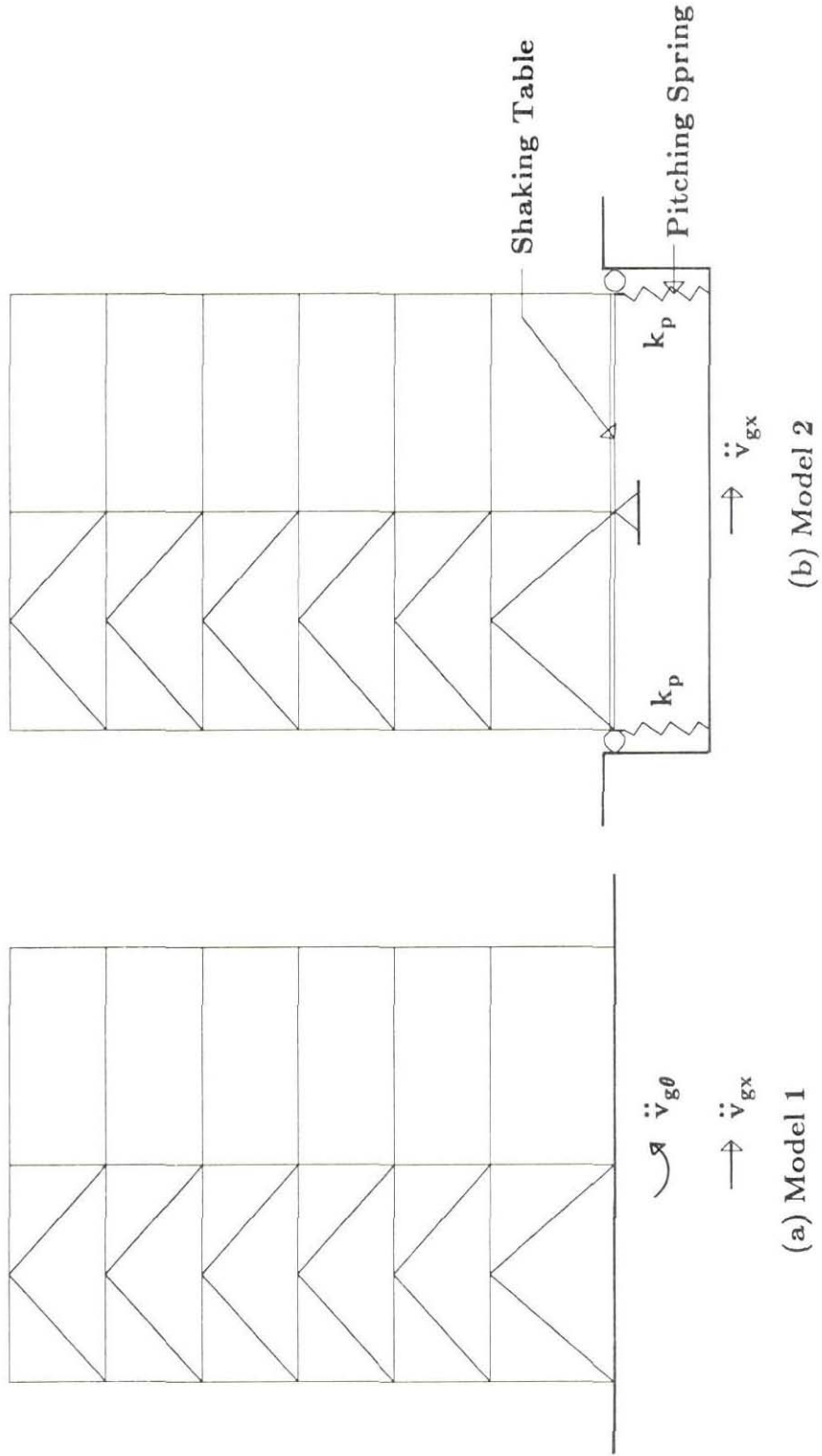


FIG. 9.1 MATHEMATICAL MODELS OF THE TEST STRUCTURE
(FRAME A AND FRAME C NOT SHOWN)

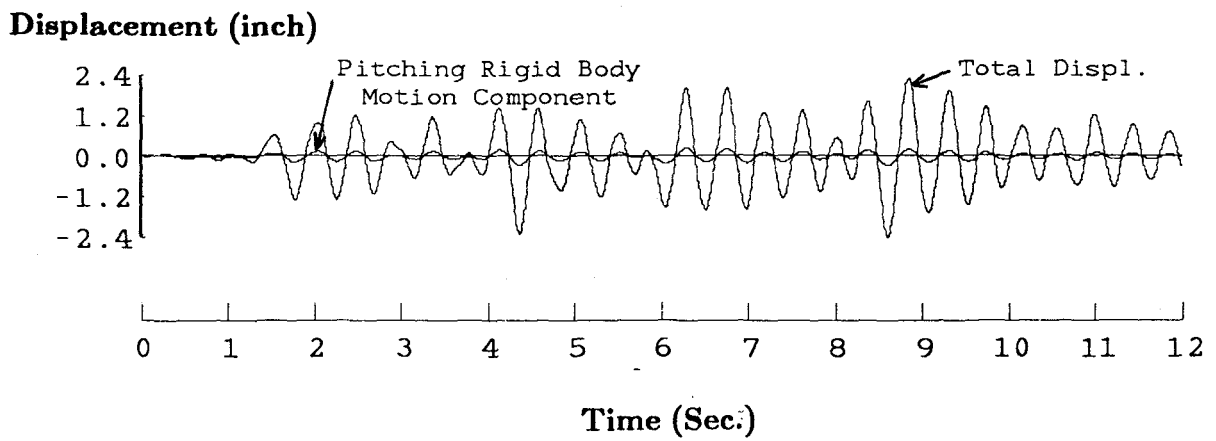
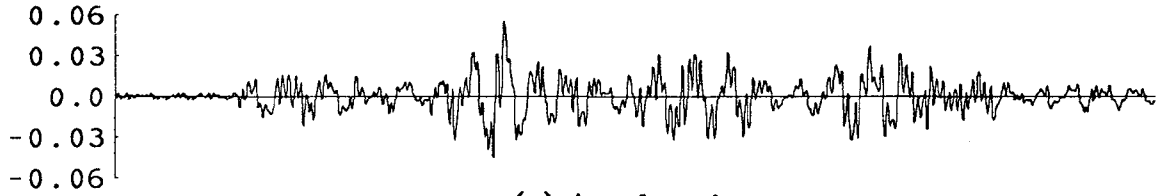


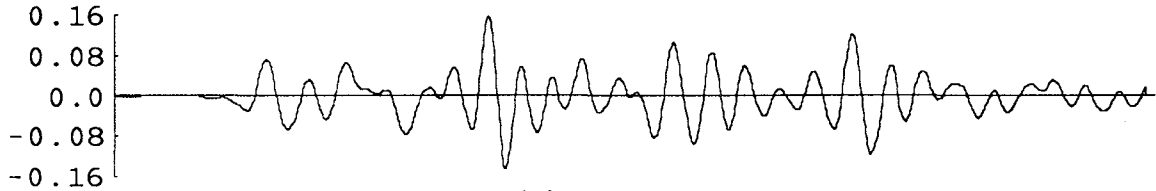
FIG. 9.2 CORRECTION OF TABLE PITCHING RIGID BODY MOTION COMPONENT FROM THE LATERAL DISPLACEMENT

Pitching Acc. (rad/sec²)

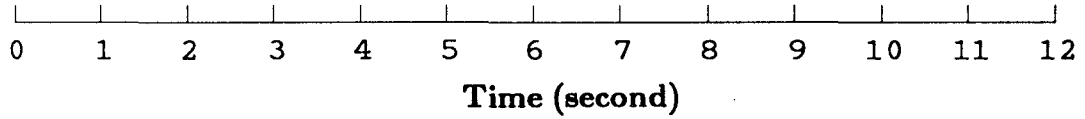


(a) Acceleration

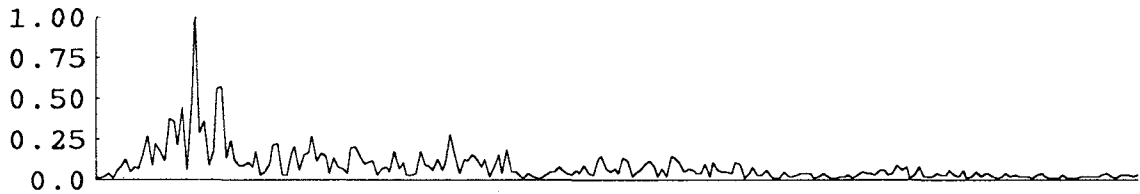
Pitching Displ. (x10⁻³rad)



(b) Displacement

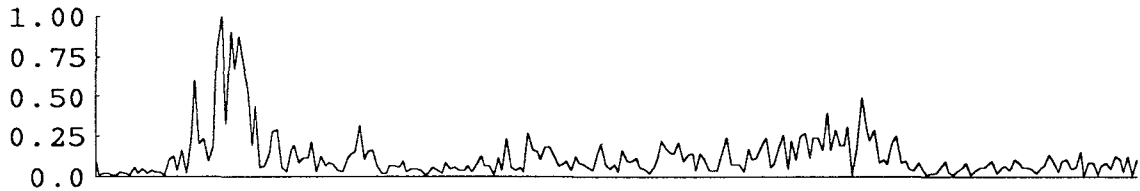


Normalized Amplitude



(c) Fourier Amplitude Spectrum of Horizontal Acceleration

Normalized Amplitude



(d) Fourier Amplitude Spectrum of Pitching Acceleration

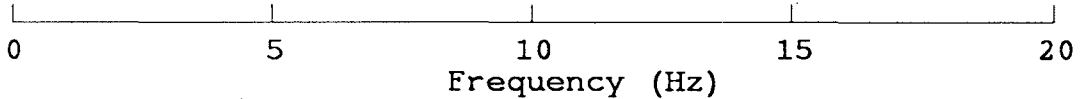


FIG. 9.3 MEASURED TABLE PITCHING MOTION AND FOURIER AMPLITUDE SPECTRA OF MEASURED TABLE ACCELERATIONS (MO-6.3 TEST)

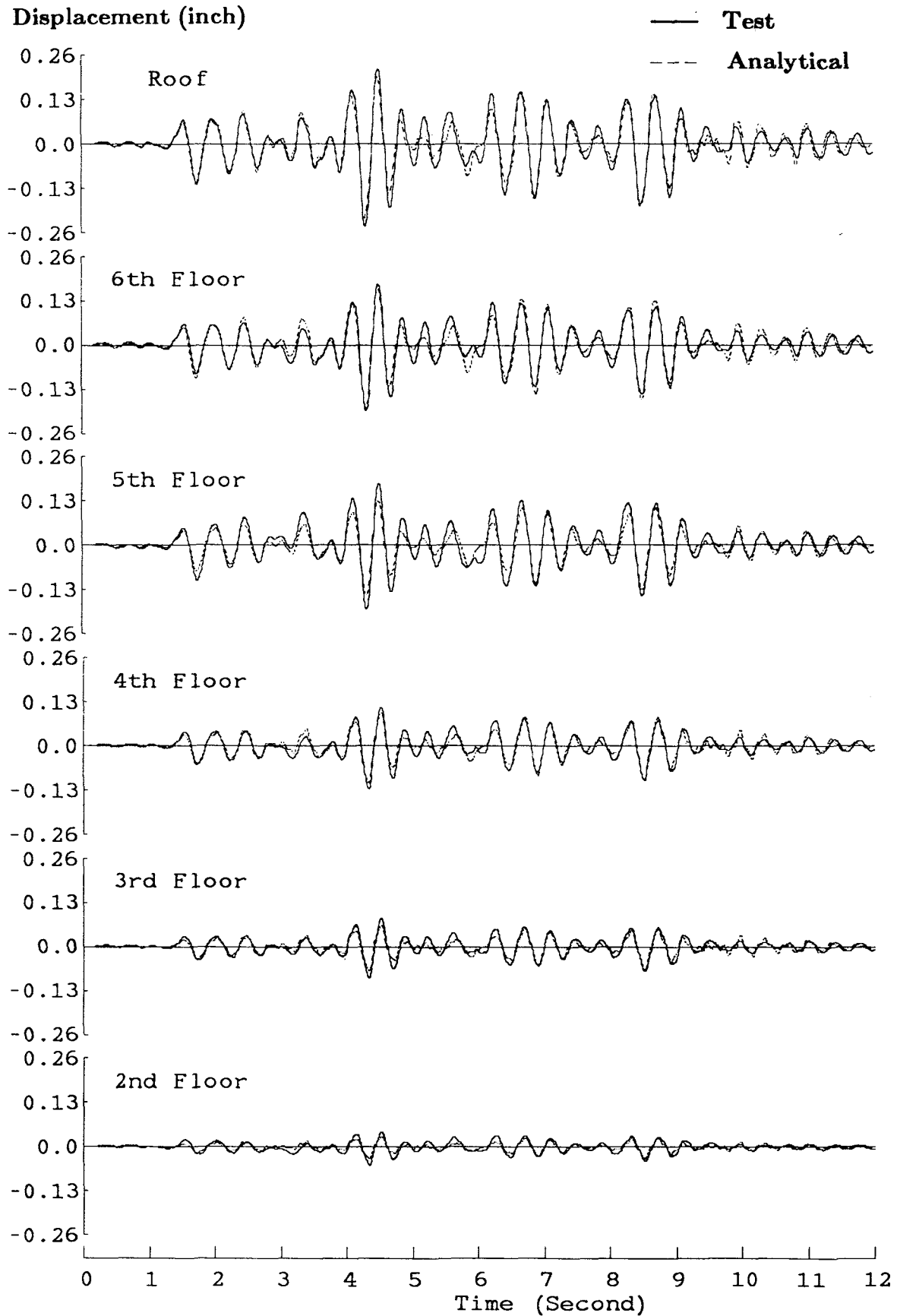


FIG. 9.4 COMPARISON OF 0.3-SCALE MODEL TEST AND ANALYTICAL LATERAL DISPLACEMENT RESPONSES (MO-6.3 TEST)

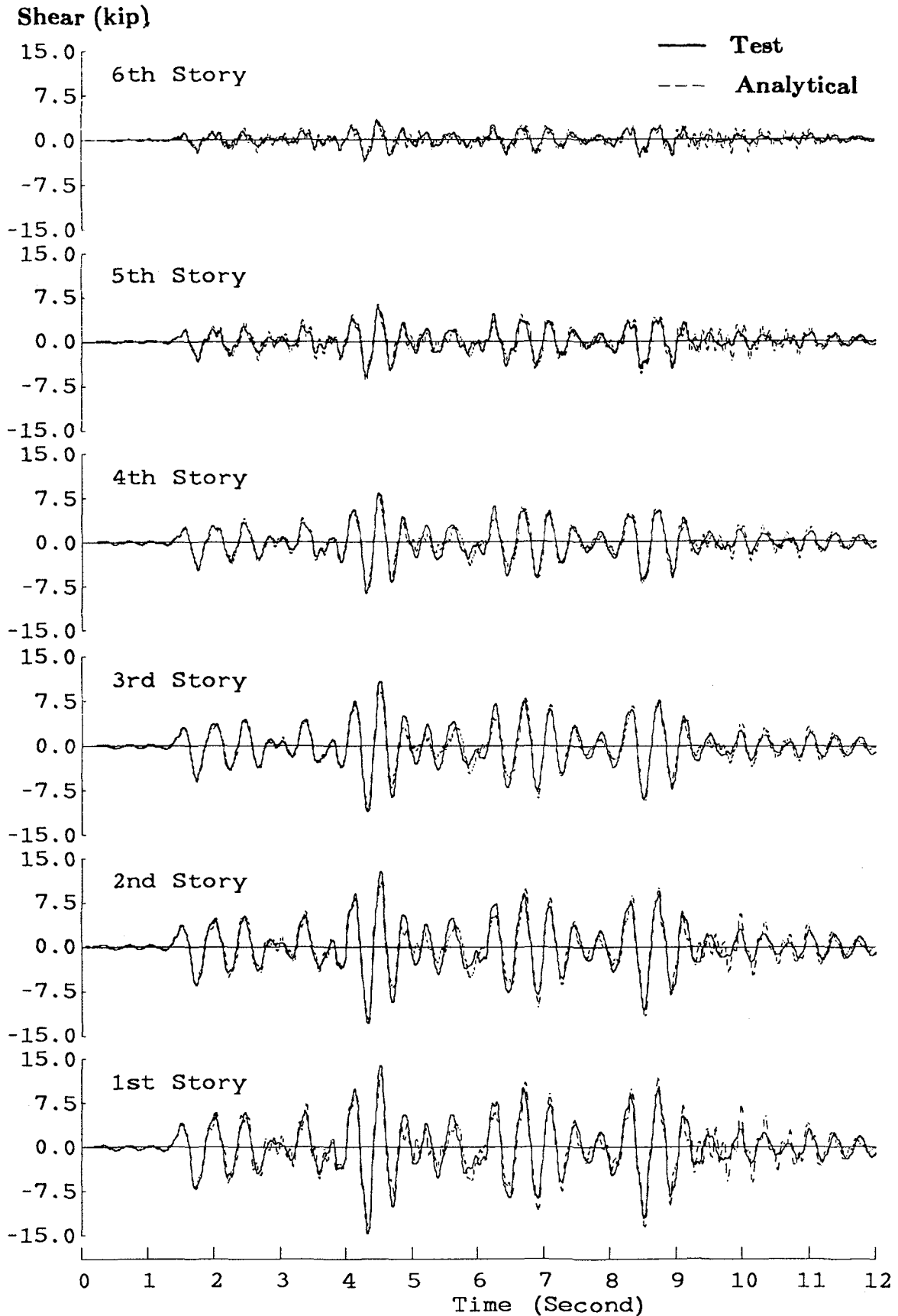


FIG. 9.5 COMPARISON OF 0.3-SCALE MODEL TEST AND ANALYTICAL STORY SHEAR RESPONSES (MO-6.3 TEST)

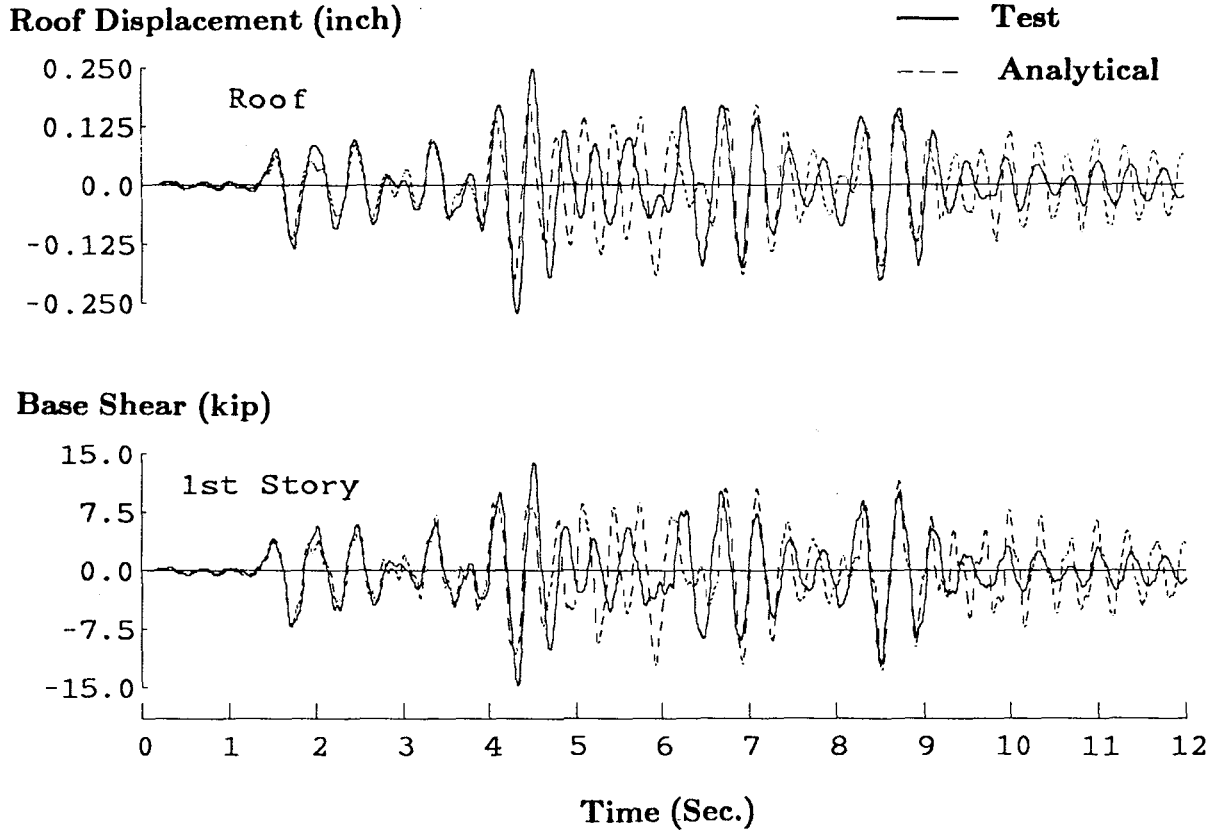


FIG. 9.6 COMPARISON OF 0.3-SCALE MODEL TEST AND ANALYTICAL RESPONSE BY IGNORING TABLE PITCHING MOTION (MO-6.3 TEST)

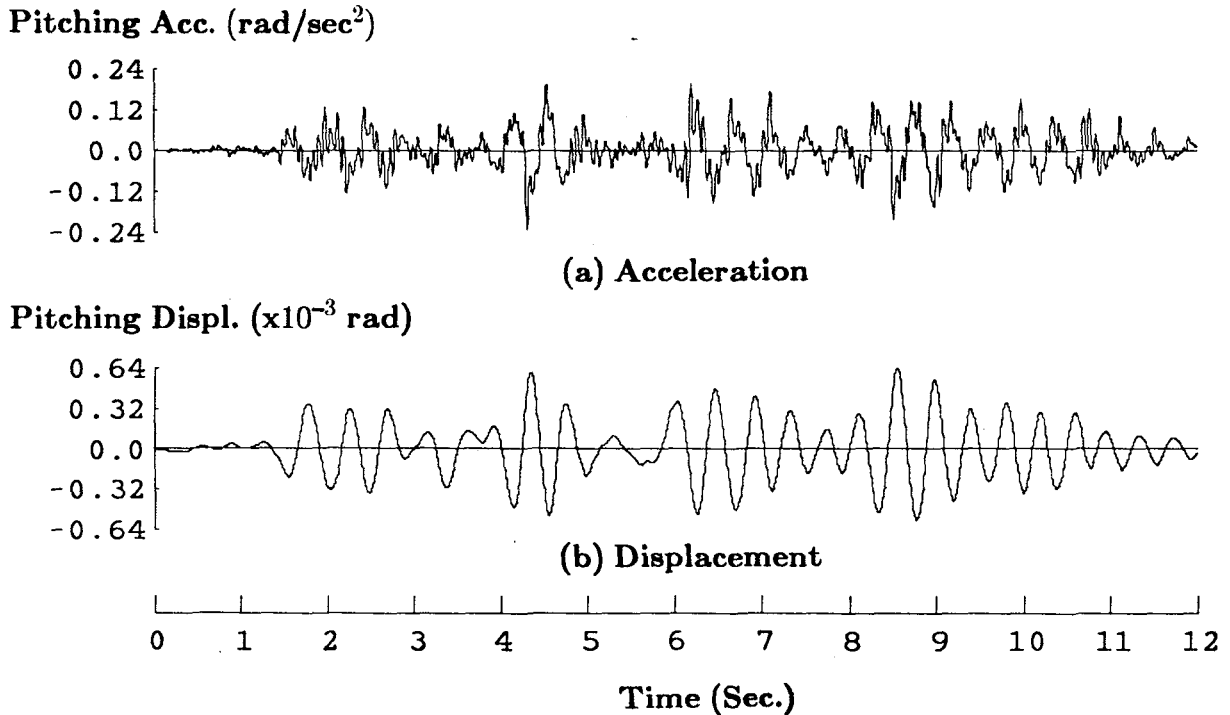


FIG. 9.7 MEASURED TABLE PITCHING MOTIONS (MO-33 TEST)

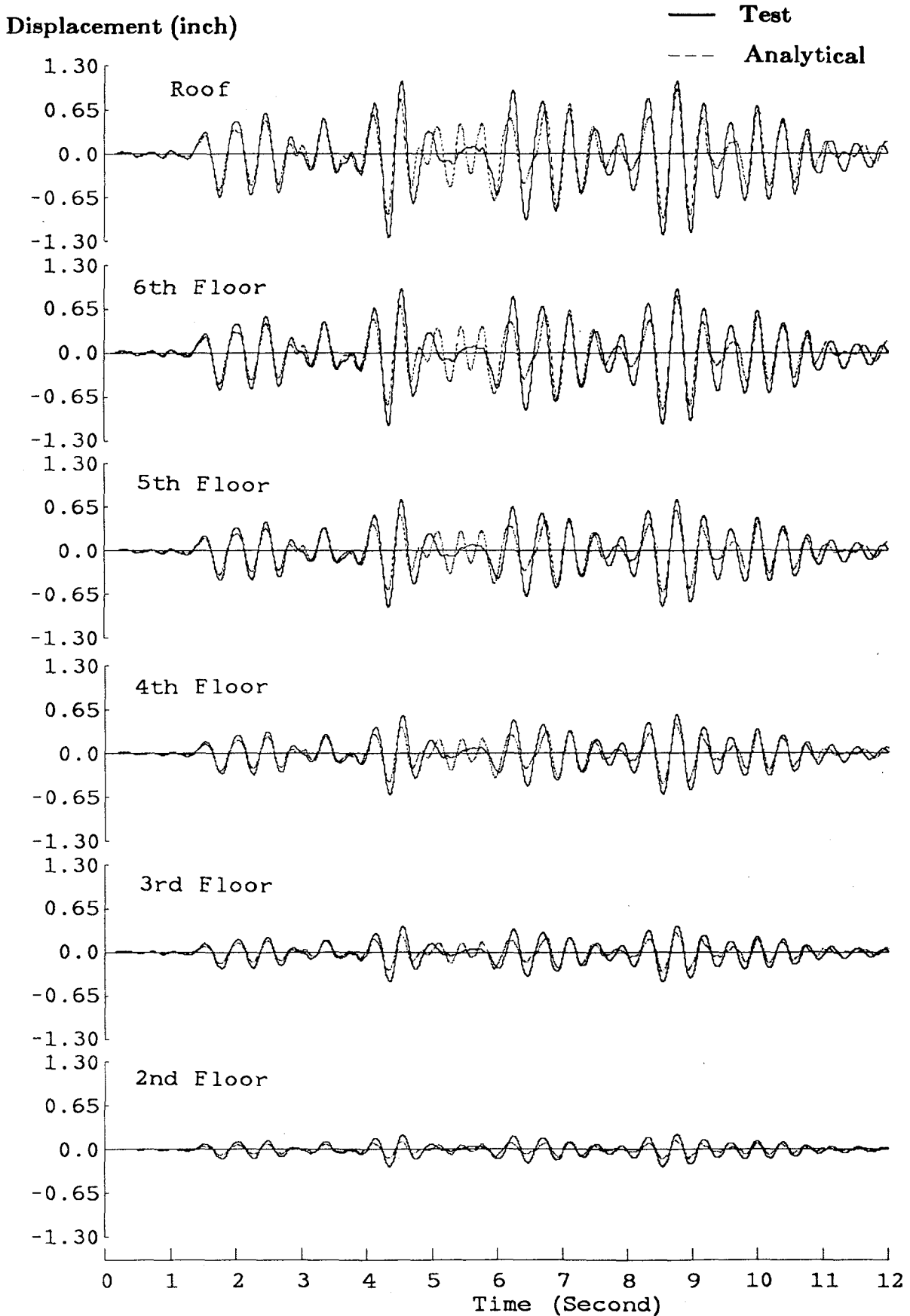


FIG. 9.8 COMPARISON OF 0.3-SCALE MODEL TEST AND ANALYTICAL LATERAL DISPLACEMENT RESPONSES (MO-33 TEST)

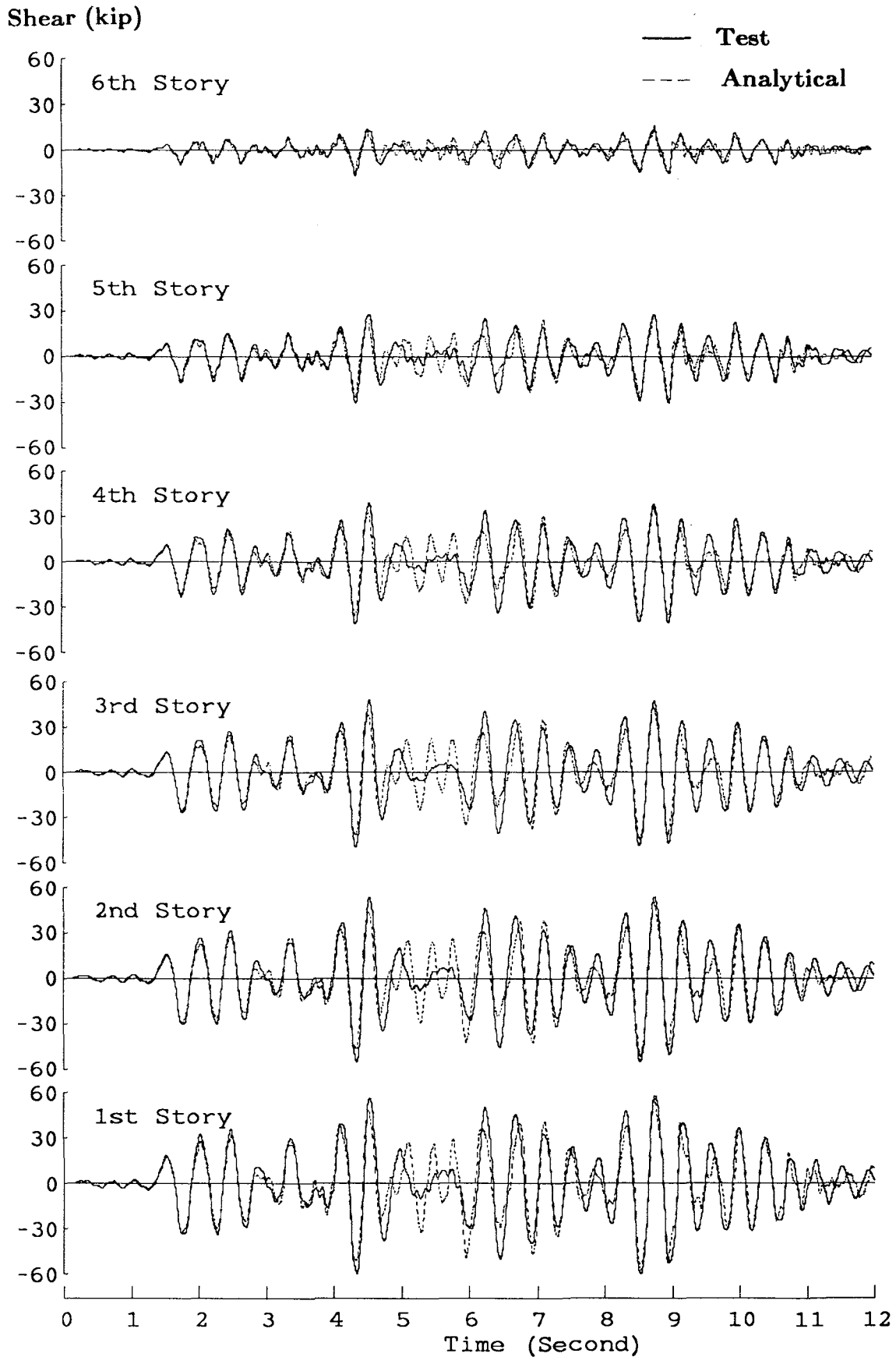


FIG. 9.9 COMPARISON OF 0.3-SCALE MODEL TEST AND ANALYTICAL STORY SHEAR RESPONSES (MO-33 TEST)

Displacement ($\times 10^{-3}$ inch)

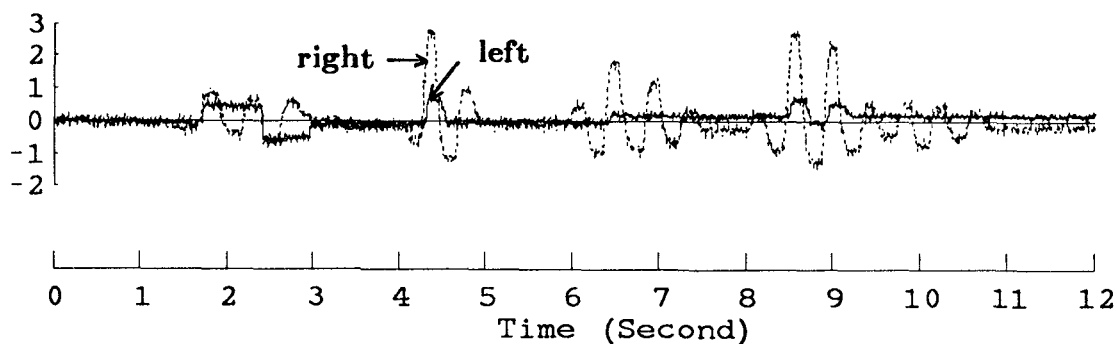
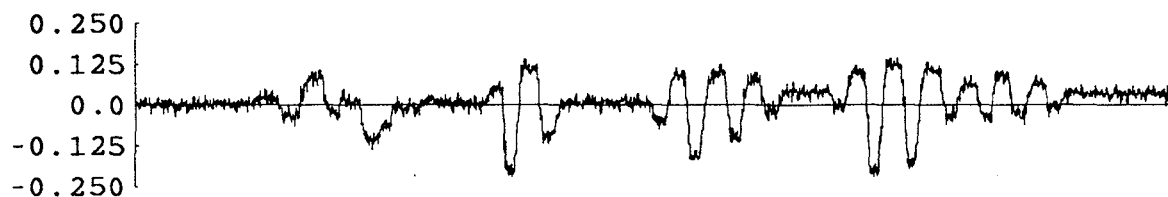


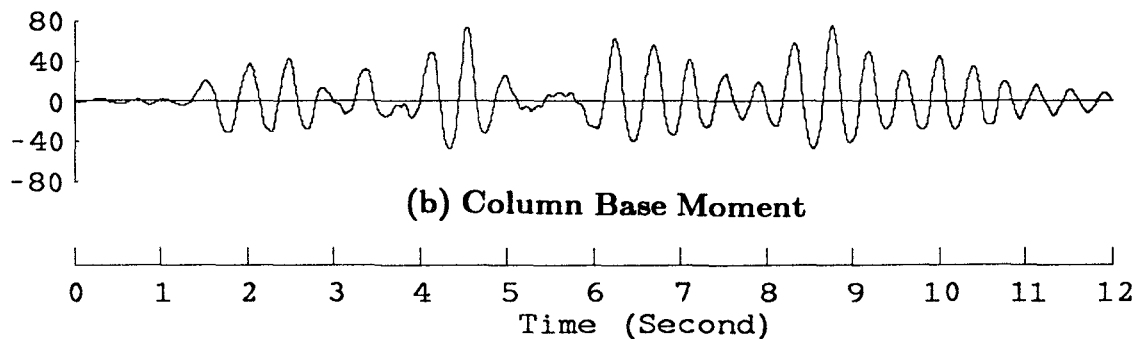
FIG. 9.10 MEASURED FOUNDATION VERTICAL MOVEMENTS
AT COLUMN 1C_{B2}

Rotation ($\times 10^{-3}$ radian)



(a) Foundation Rotation

Moment (kip-inch)



(b) Column Base Moment

FIG. 9.11 COLUMN 1C_{B2} BASE MOMENT AND FOUNDATION ROTATION
(MO-33 TEST)

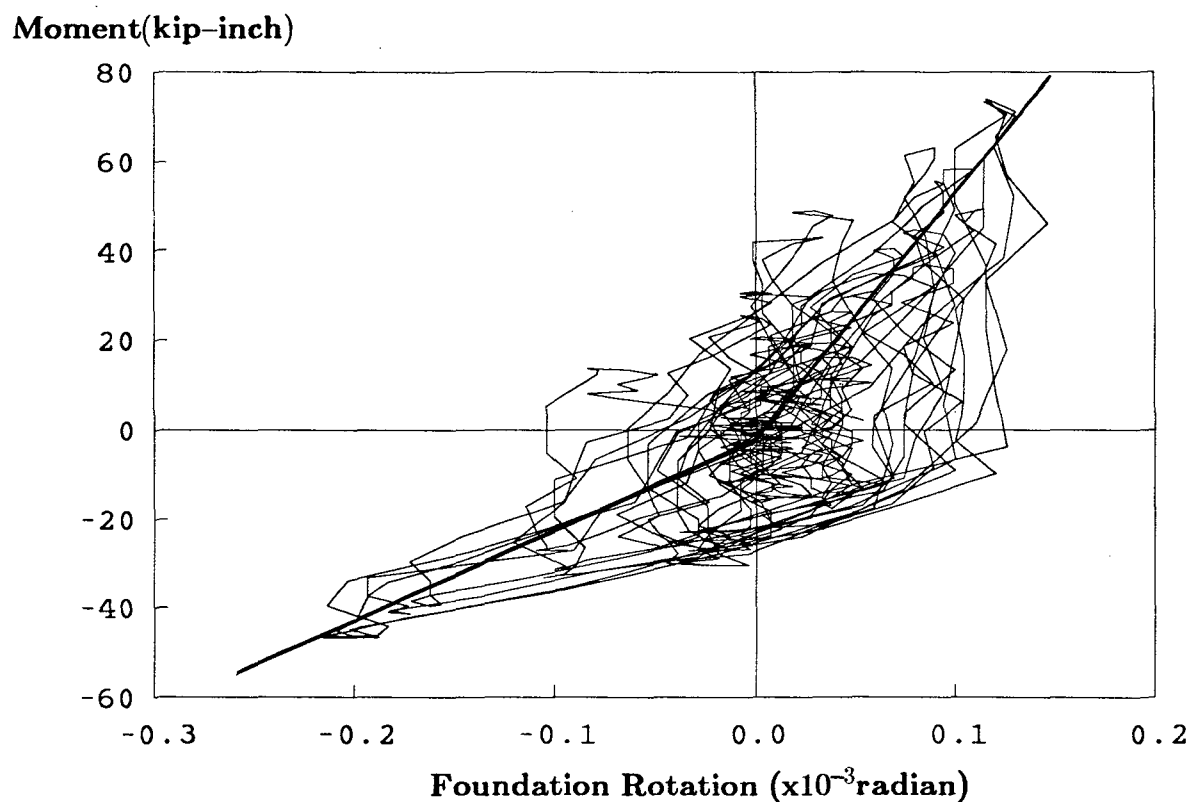


FIG. 9.12 COLUMN 1C_{B2} : MEASURED FOUNDATION ROTATION VERSUS COLUMN END MOMENT CURVE (MO-33 TEST)

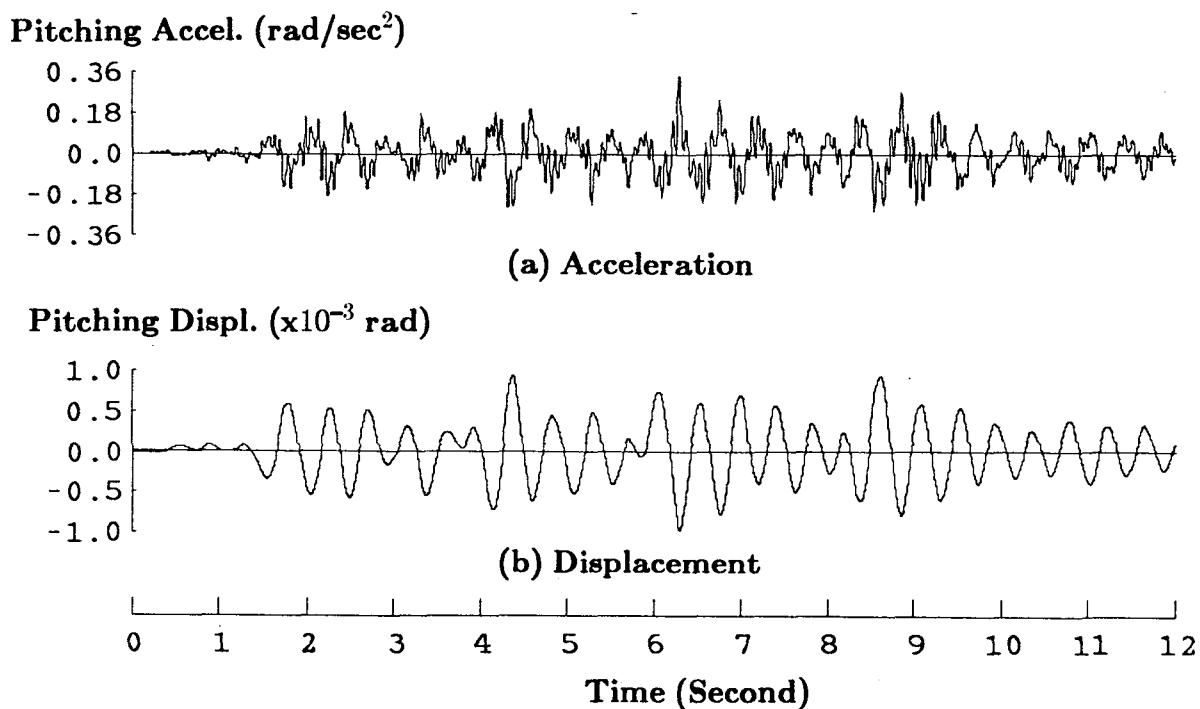


FIG. 9.13 MEASURED TABLE PITCHING MOTIONS (MO-65 TEST)

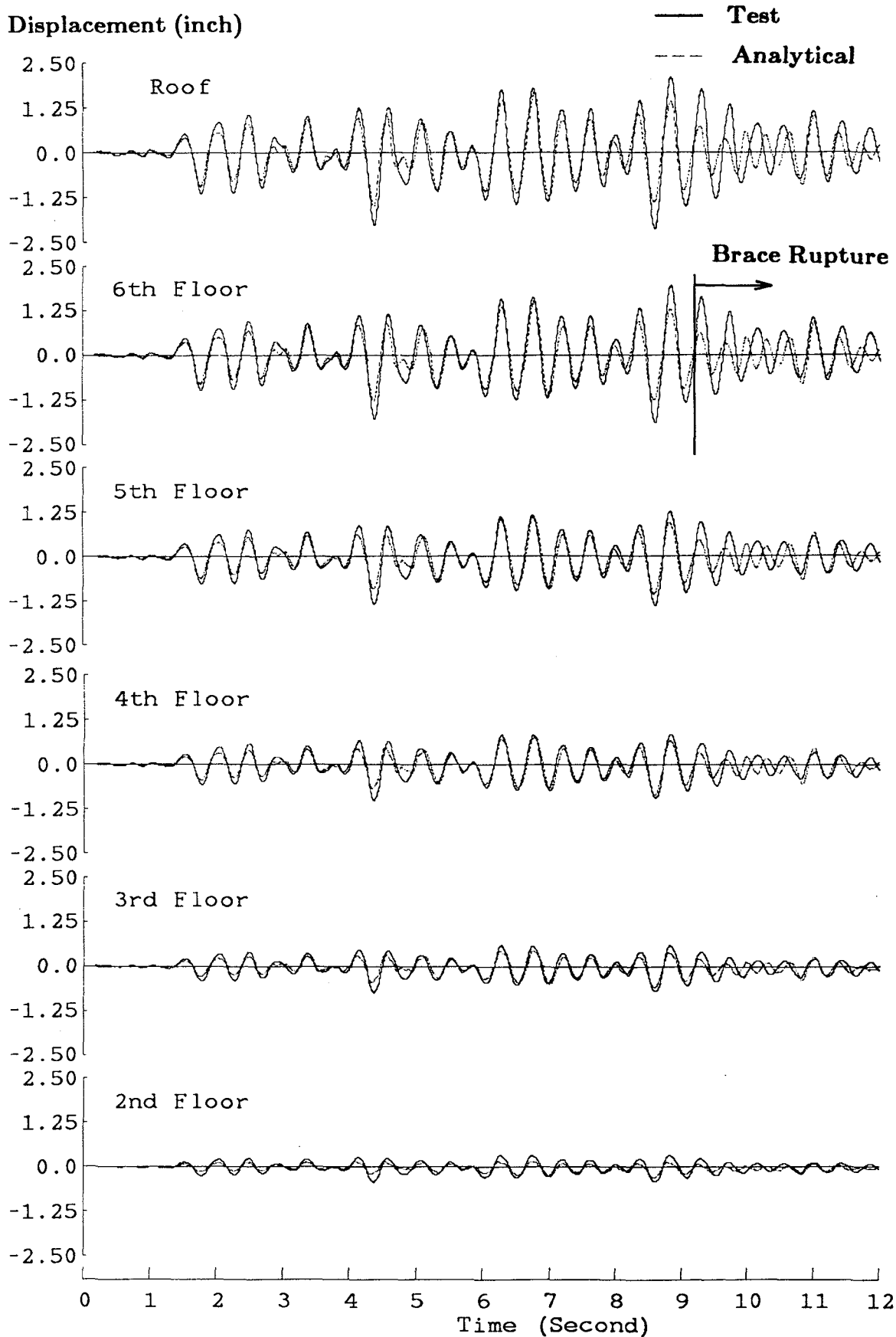


FIG. 9.14 COMPARISON OF 0.3-SCALE MODEL TEST AND ANALYTICAL LATERAL DISPLACEMENT RESPONSES (MO-65 TEST)

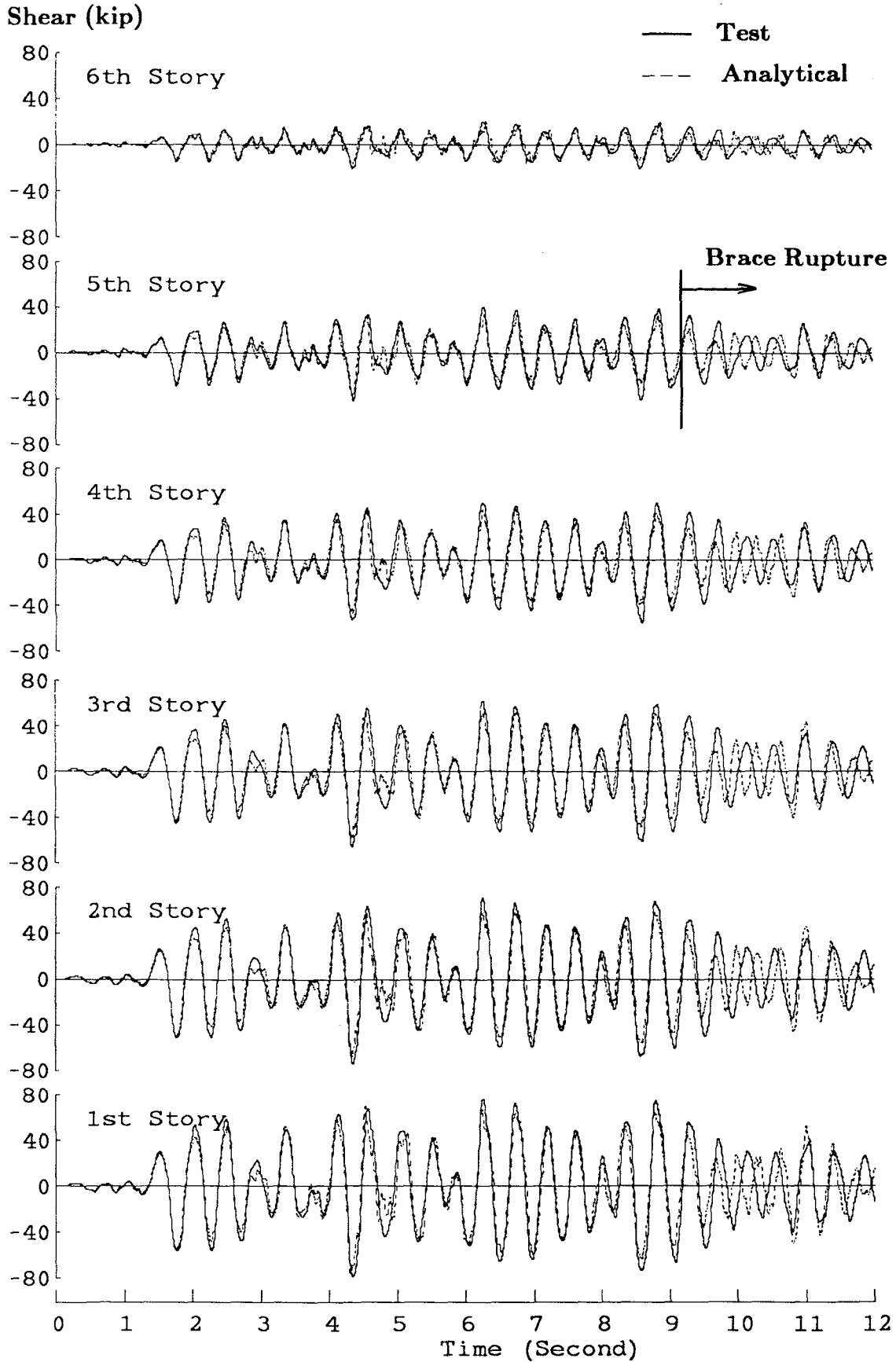
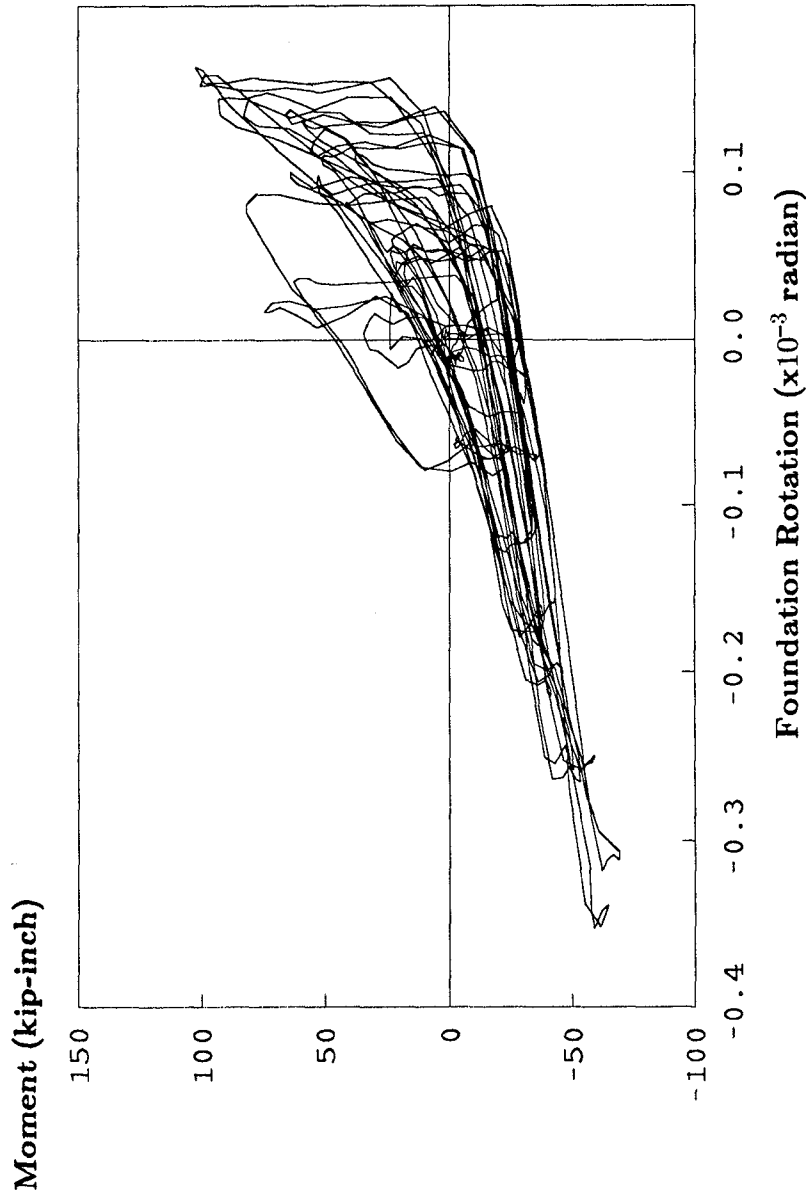


FIG. 9.15 COMPARISON OF 0.3-SCALE MODEL TEST AND ANALYTICAL STORY SHEAR FORCE RESPONSES (M/O-66-2517)



**FIG. 9.16 COLUMN 1C_{B2} : MEASURED FOUNDATION ROTATION
VERSUS COLUMN END MOMENT CURVE (MO-65 TEST)**

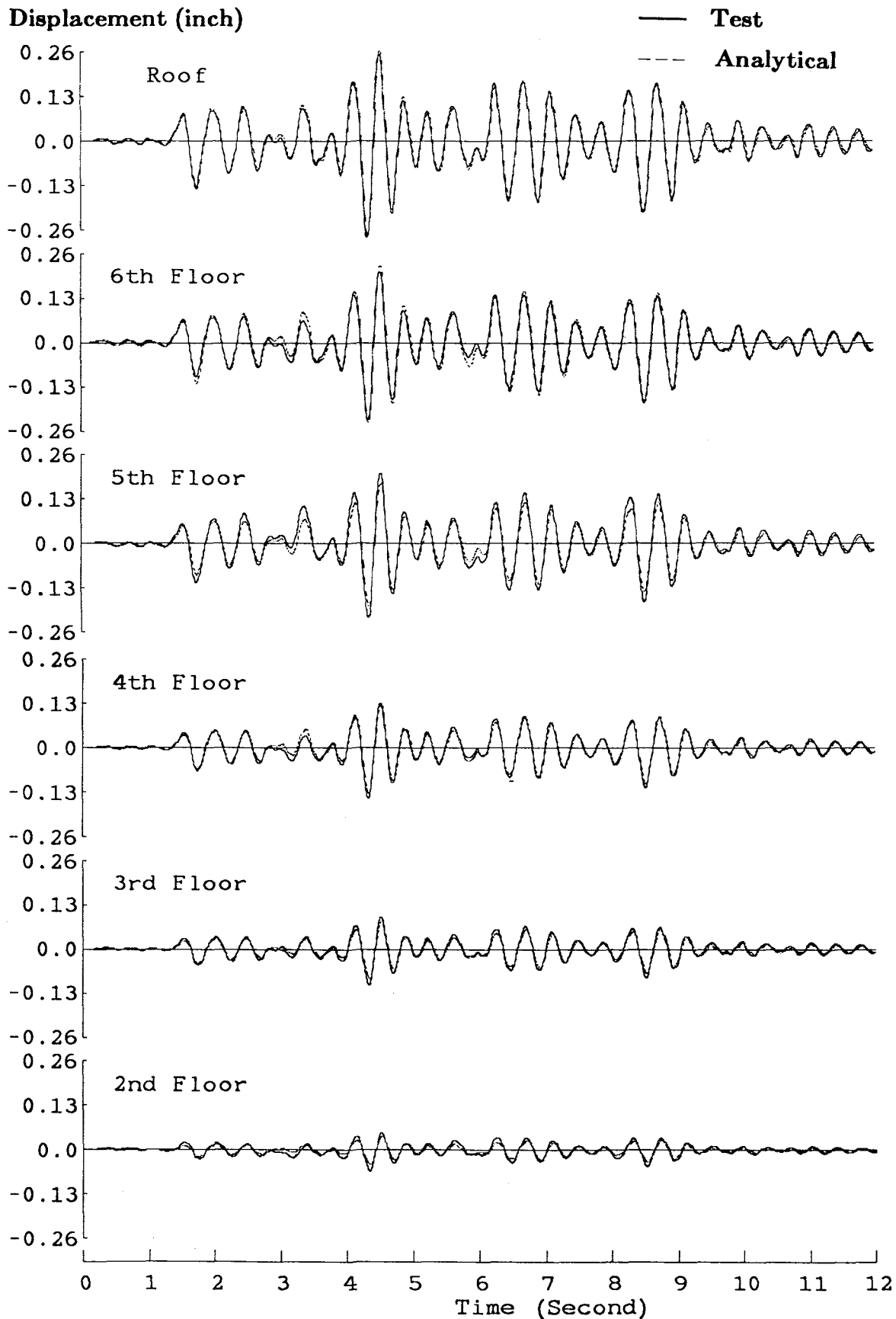


FIG. 9.17 MODEL 2 METHOD: COMPARISON OF 0.3-SCALE MODEL TEST AND ANALYTICAL LATERAL DISPLACEMENT RESPONSE (MO-6.3 TEST)

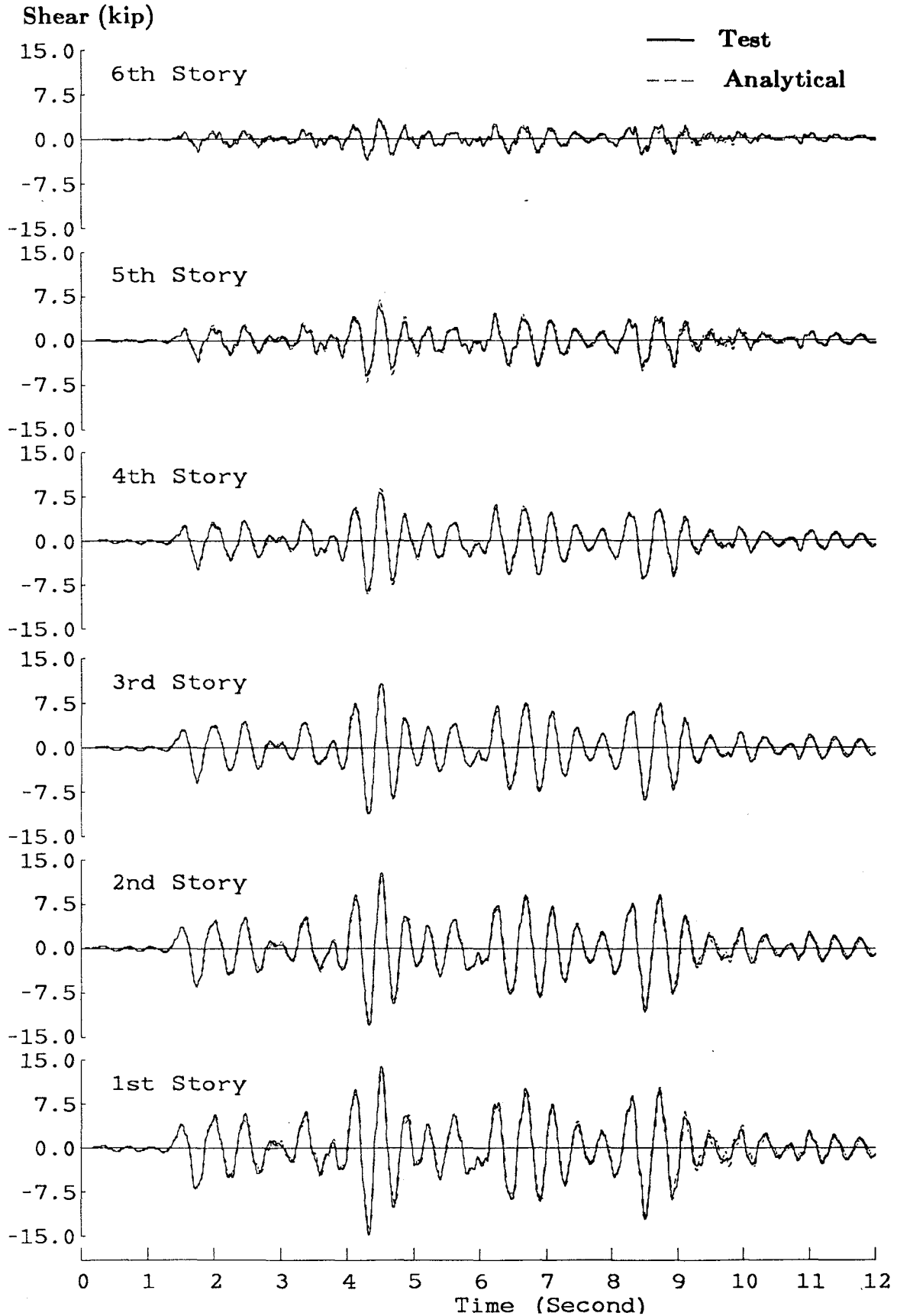


FIG. 9.18 MODEL 2 METHOD: COMPARISON OF MODEL TEST AND ANALYTICAL STORY SHEAR RESPONSE (MO-6.3 TEST)

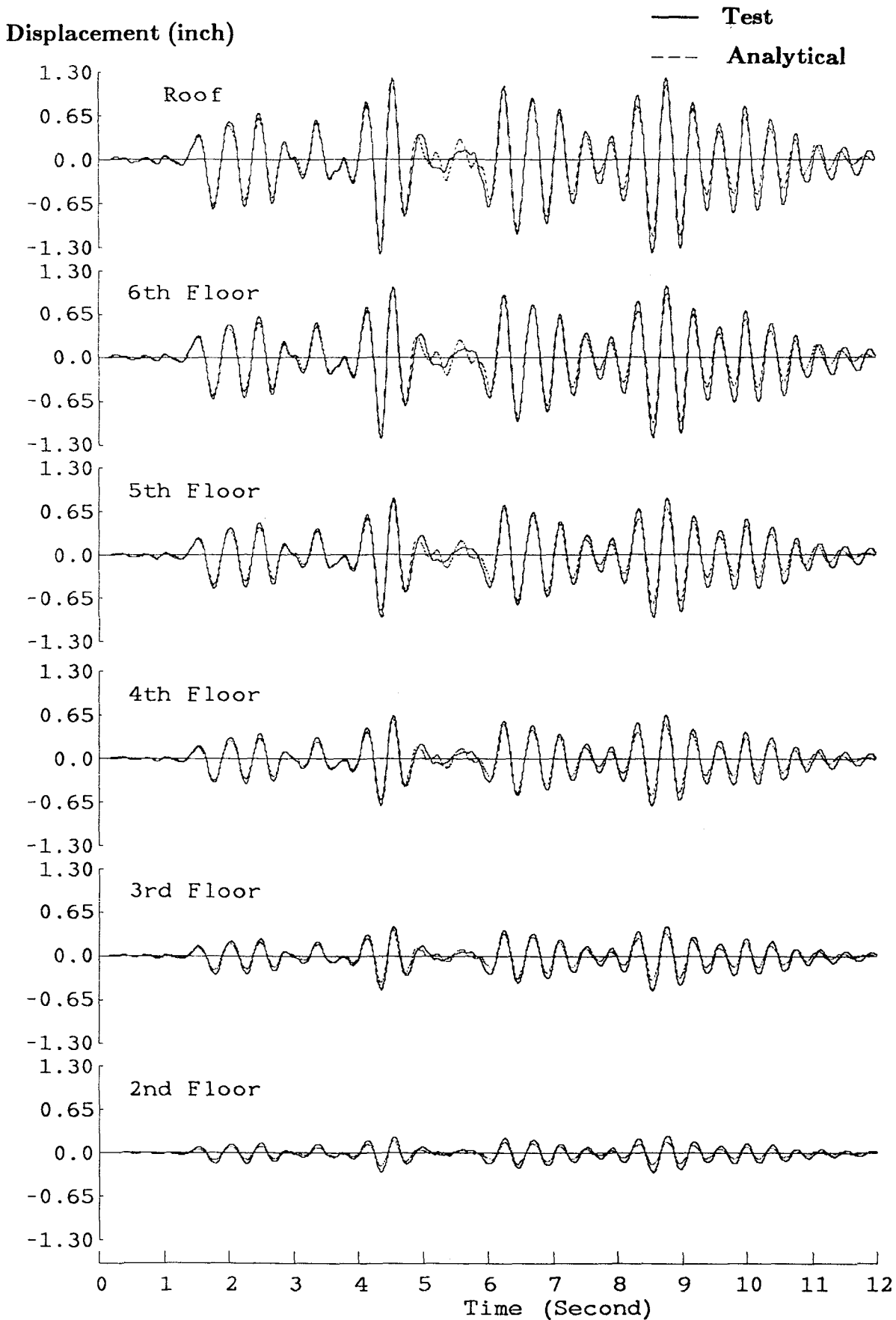


FIG. 9.19 MODEL 2 METHOD: COMPARISON OF MODEL TEST AND ANALYTICAL LATERAL DISPLACEMENT RESPONSE (MO-33 TEST)

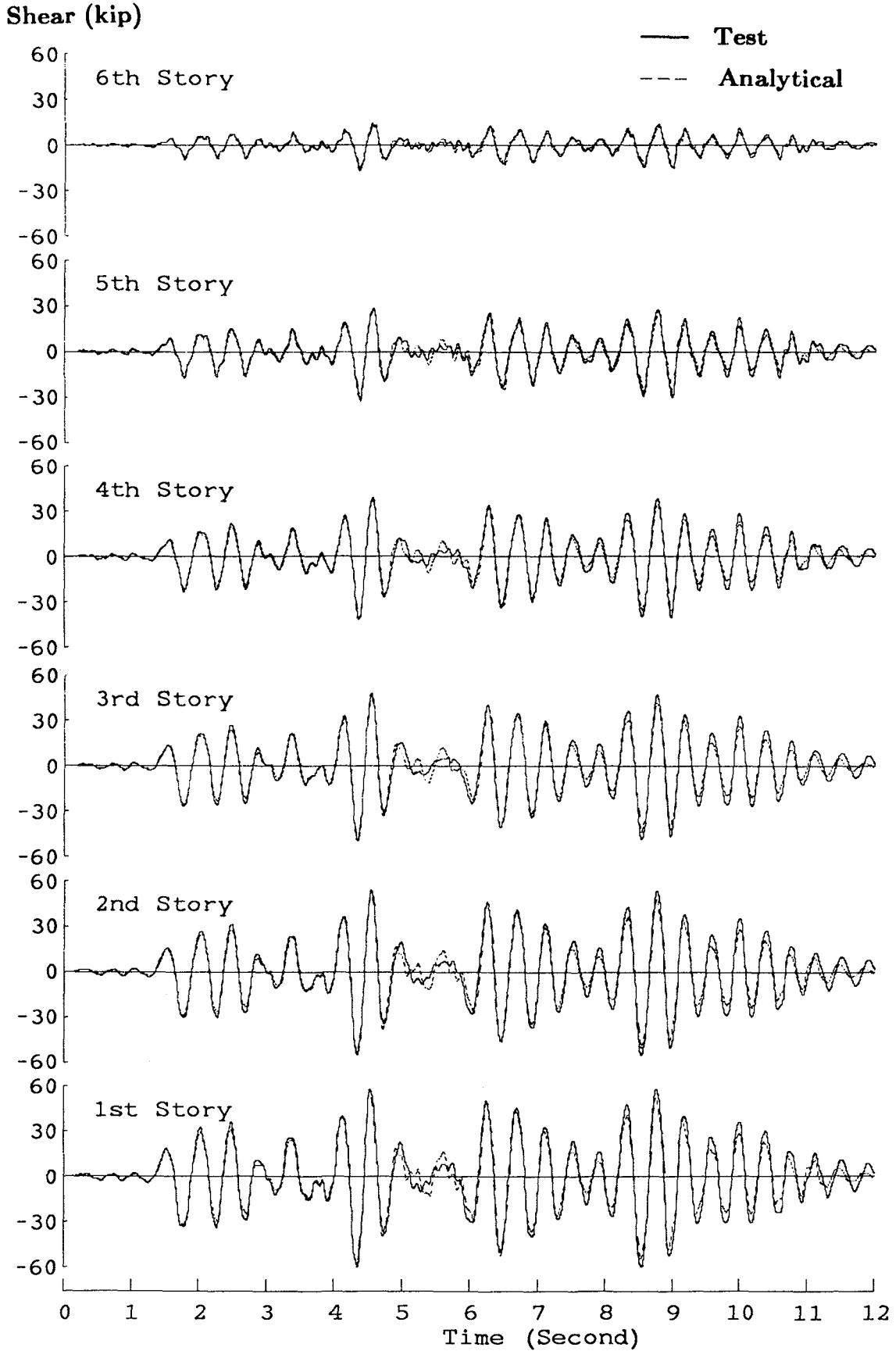


FIG. 9.20 MODEL 2 METHOD: COMPARISON OF MODEL TEST AND ANALYTICAL STORY SHEAR RESPONSE (MO-33 TEST)

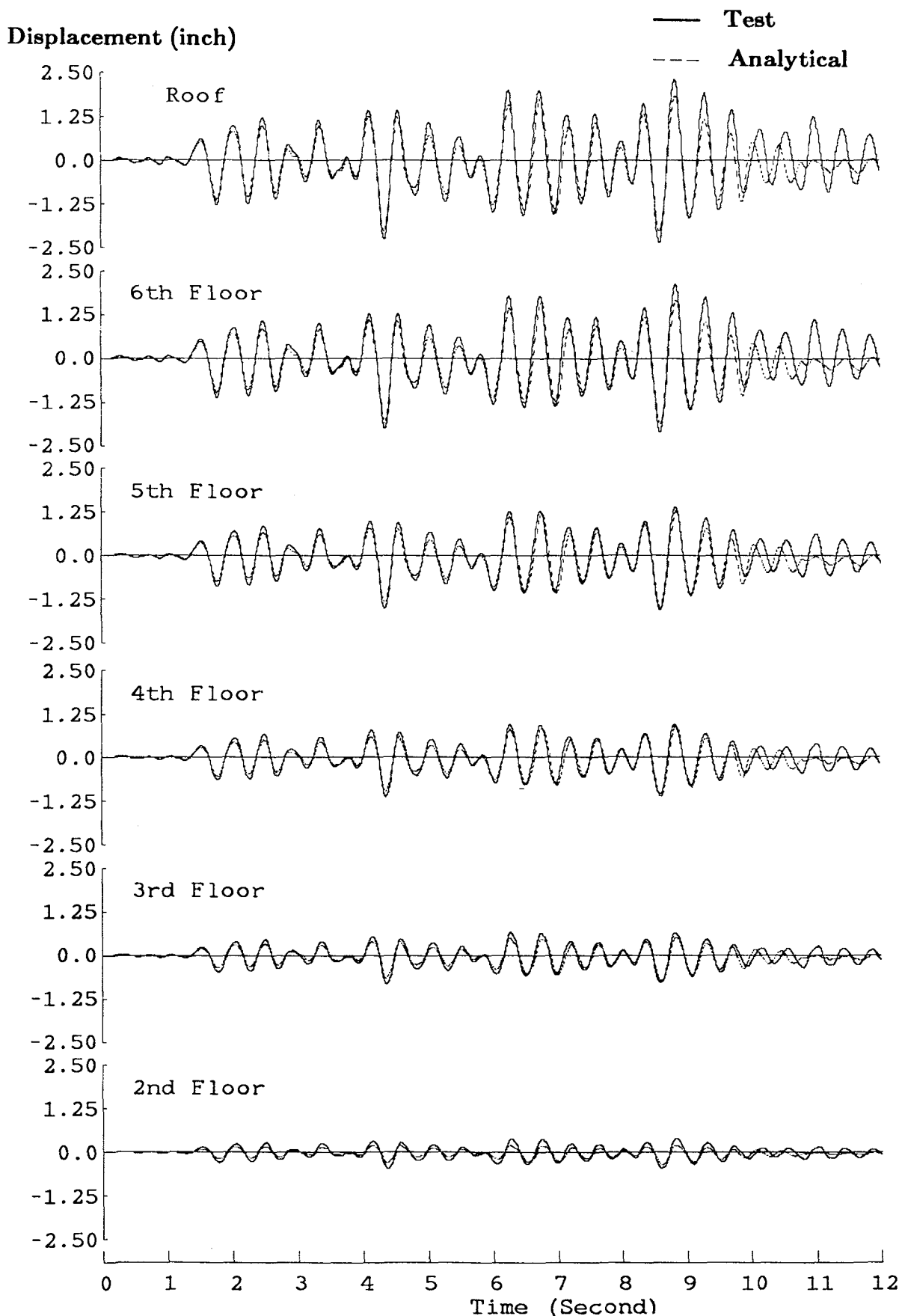


FIG. 9.21 MODEL 2 METHOD: COMPARISON OF MODEL TEST AND ANALYTICAL LATERAL DISPLACEMENT RESPONSE (MO-65 TEST)

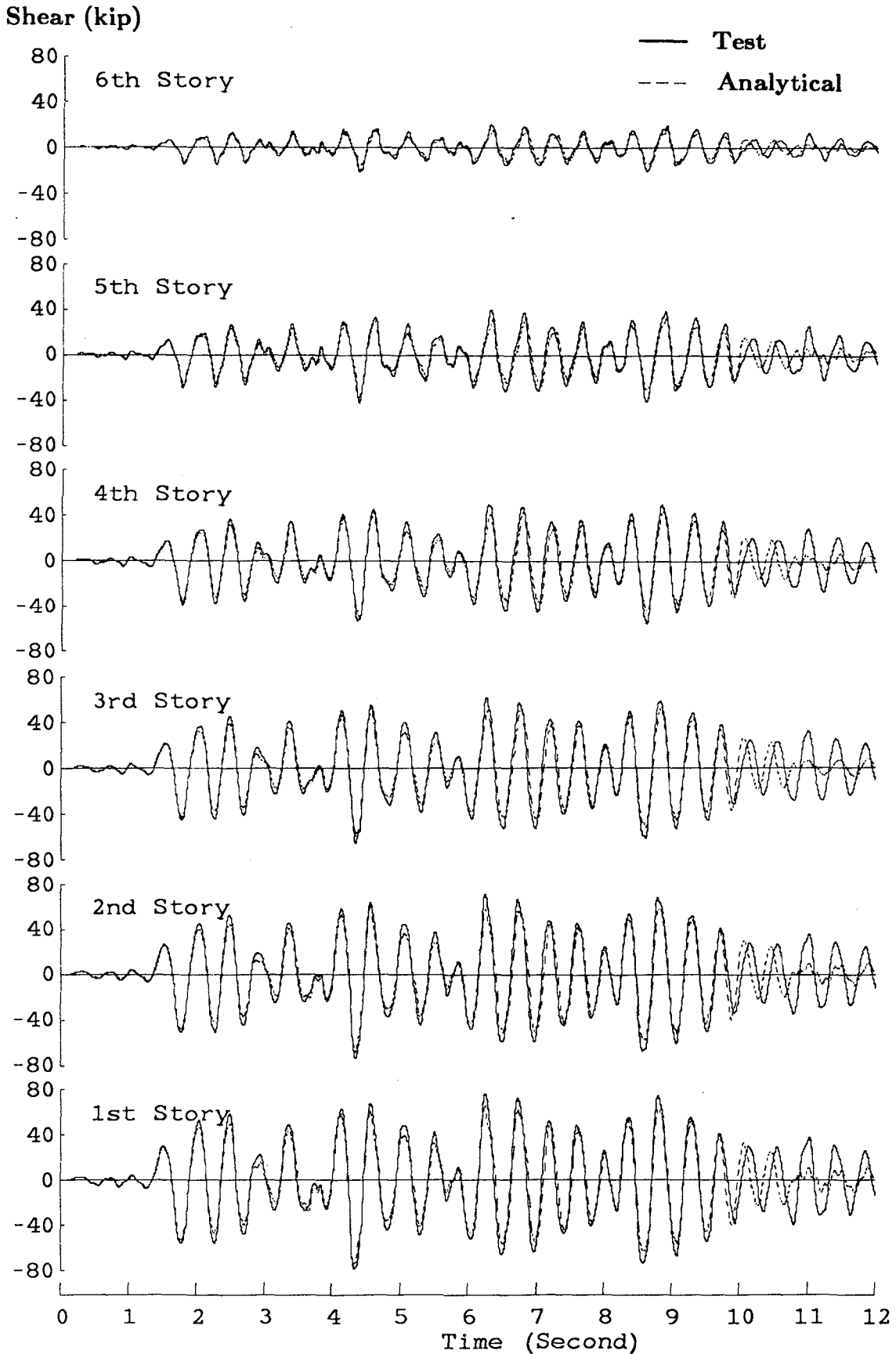
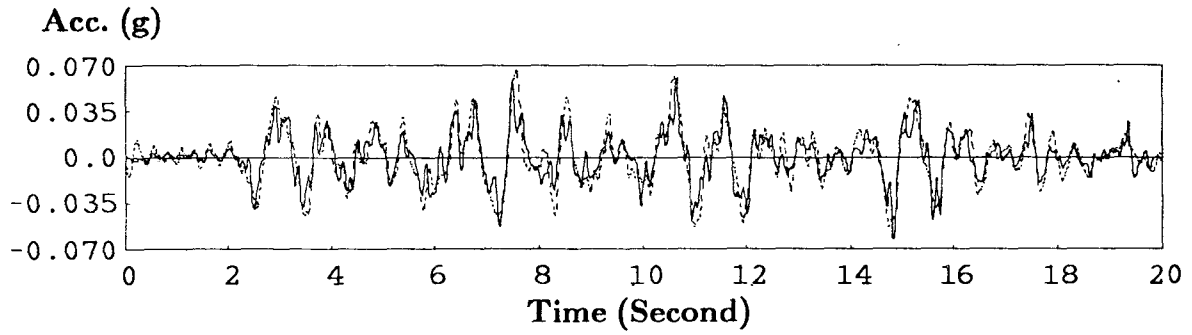
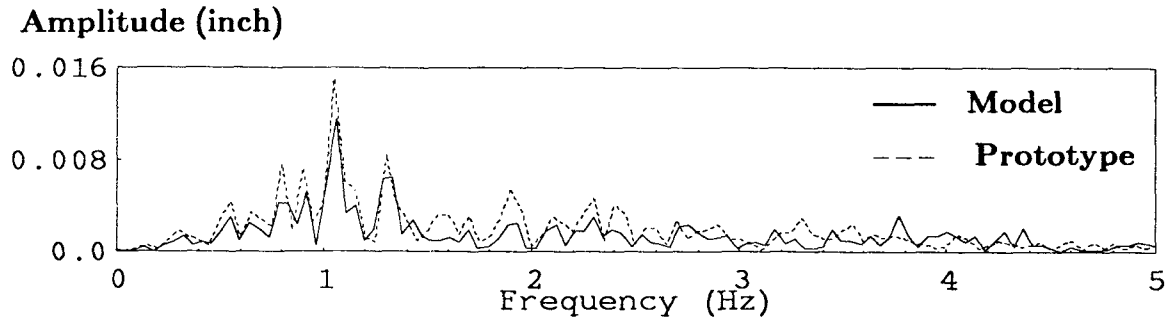


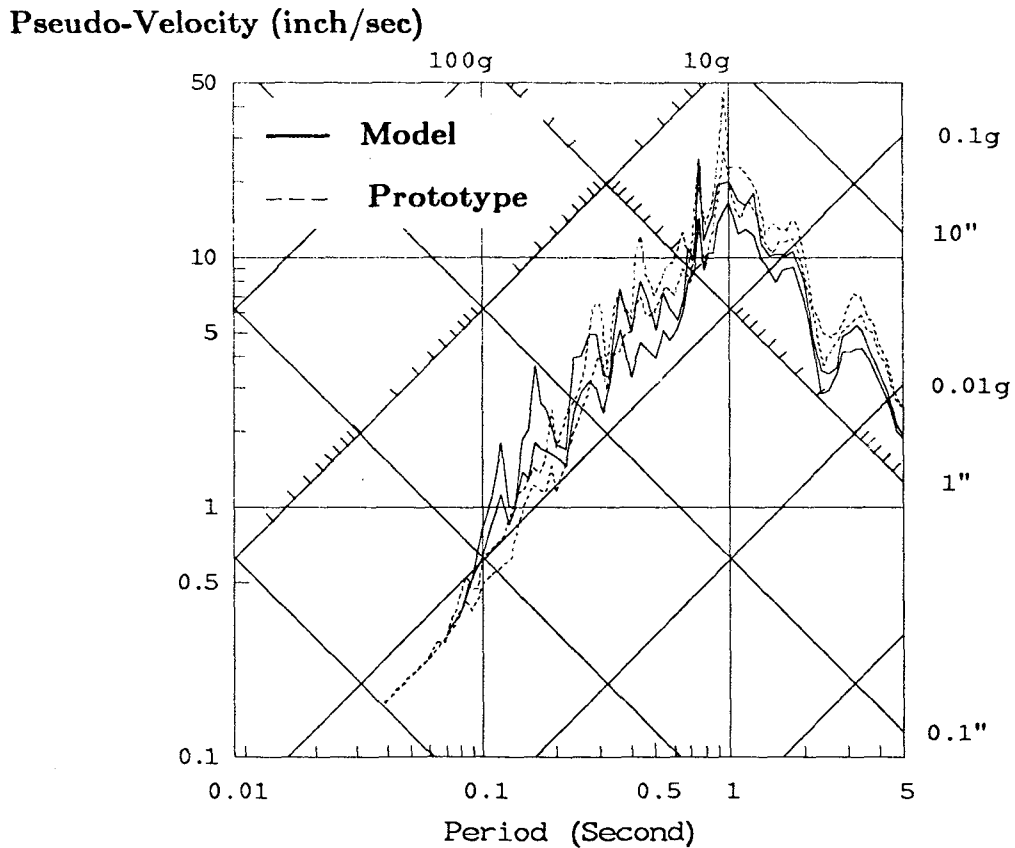
FIG. 9.22 MODEL 2 METHOD: COMPARISON OF MODEL TEST AND ANALYTICAL STORY SHEAR RESPONSE (MO-65 TEST)



(a) Acceleration



(b) Fourier Amplitude Spectra



(c) Linear Elastic Response Spectra (0.5 and 2% damping)

FIG. 9.23 PROTOTYPE AND MODEL COMPARISON OF GROUND MOTION USED IN SERVICEABILITY LIMIT STATE TESTS

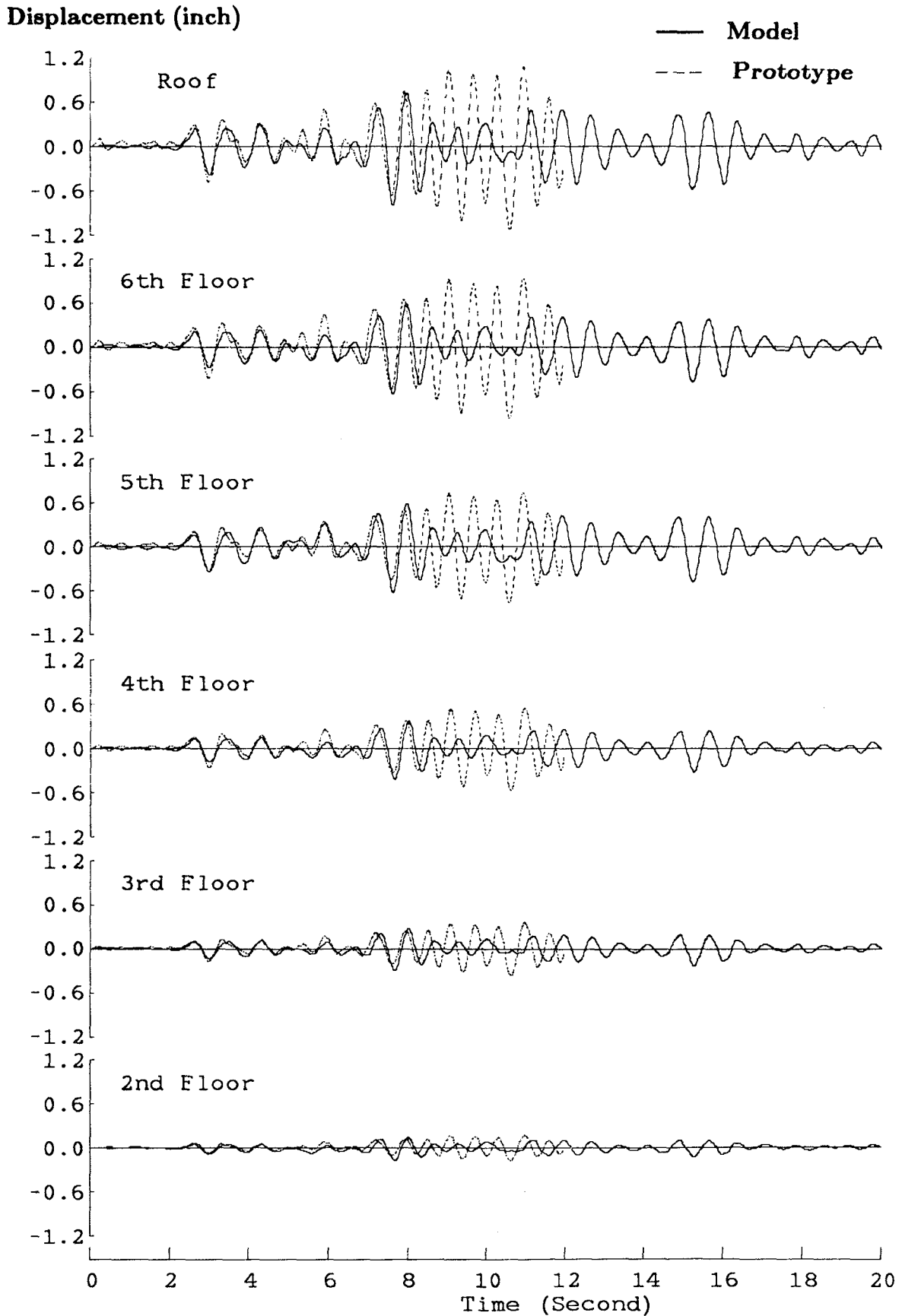


FIG. 9.24 COMPARISON OF PROTOTYPE AND MODEL LATERAL RESPONSES IN SERVICEABILITY LIMIT STATE TESTS

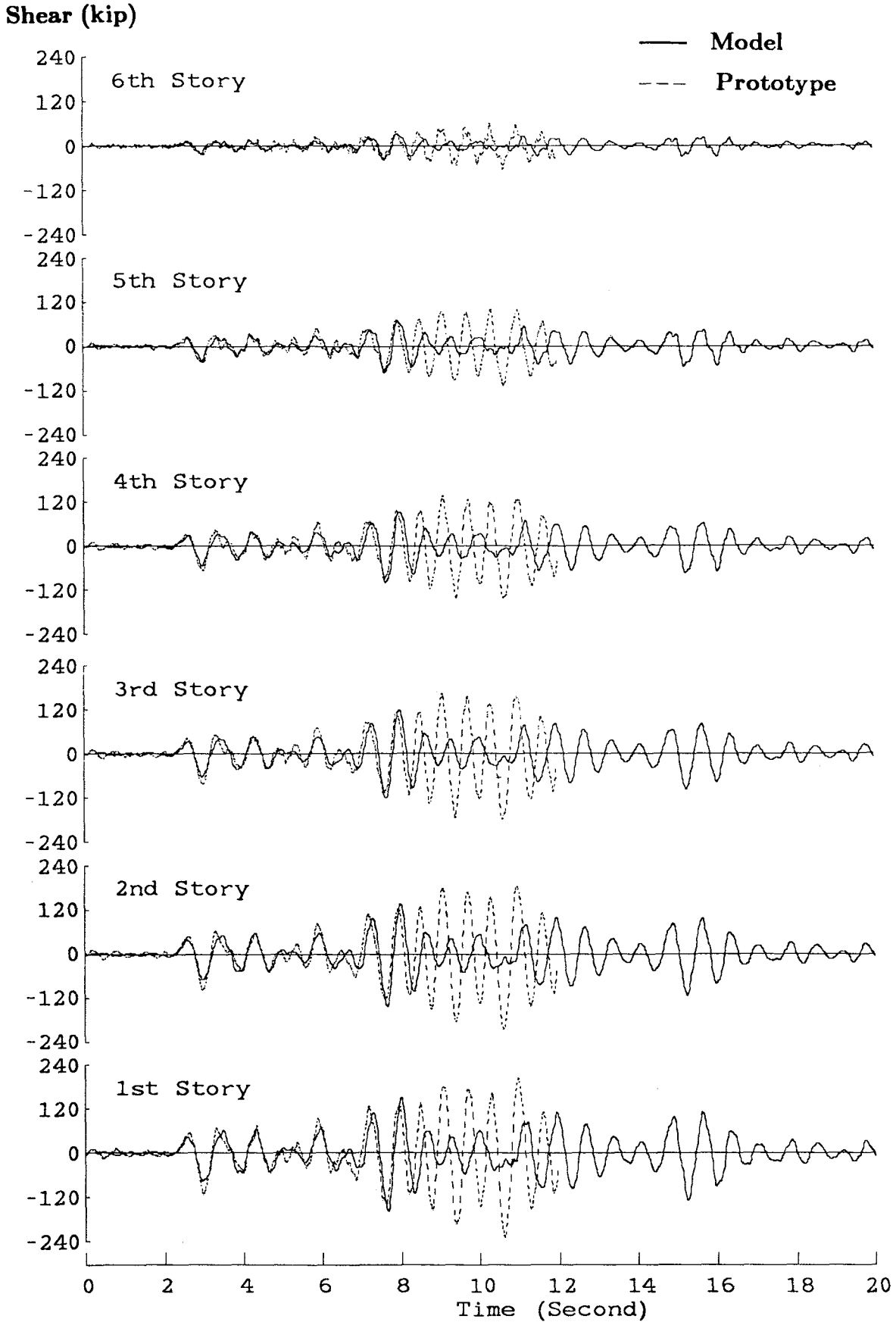
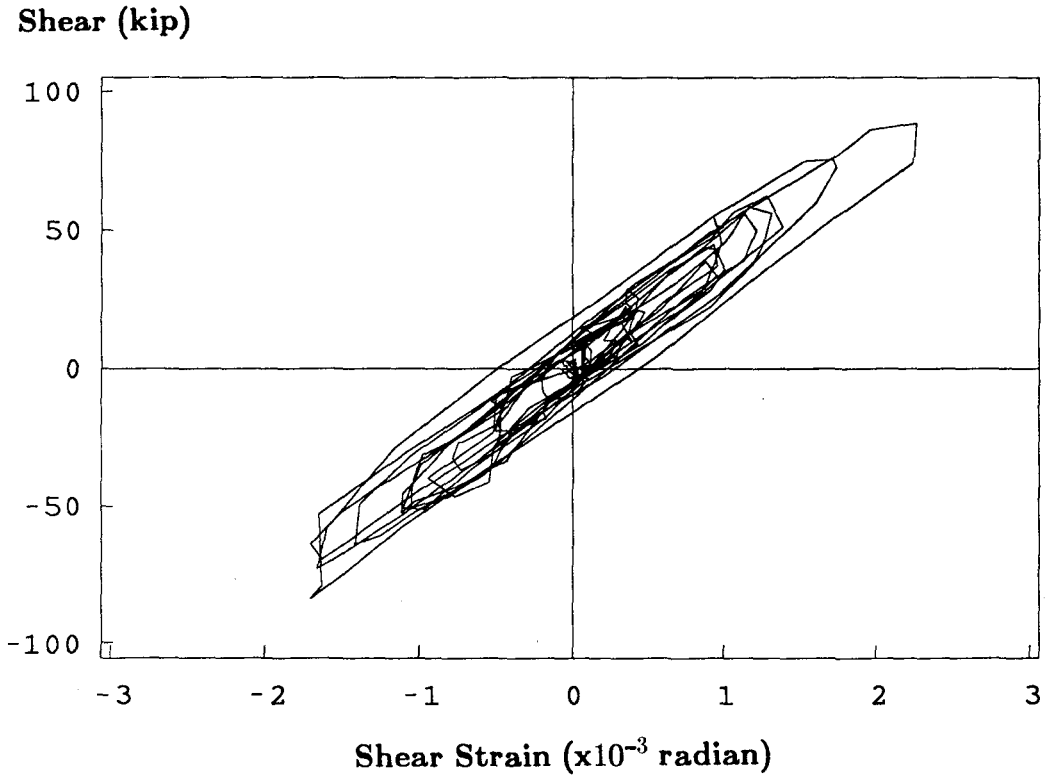


FIG. 9.25 COMPARISON OF PROTOTYPE AND MODEL STORY SHEAR RESPONSES IN SERVICEABILITY LIMIT STATE TESTS



**FIG. 9.26 PROTOTYPE ELASTIC-3 TEST SECOND FLOOR
BRACE-GIRDER JOINT PANEL ZONE RESPONSE**

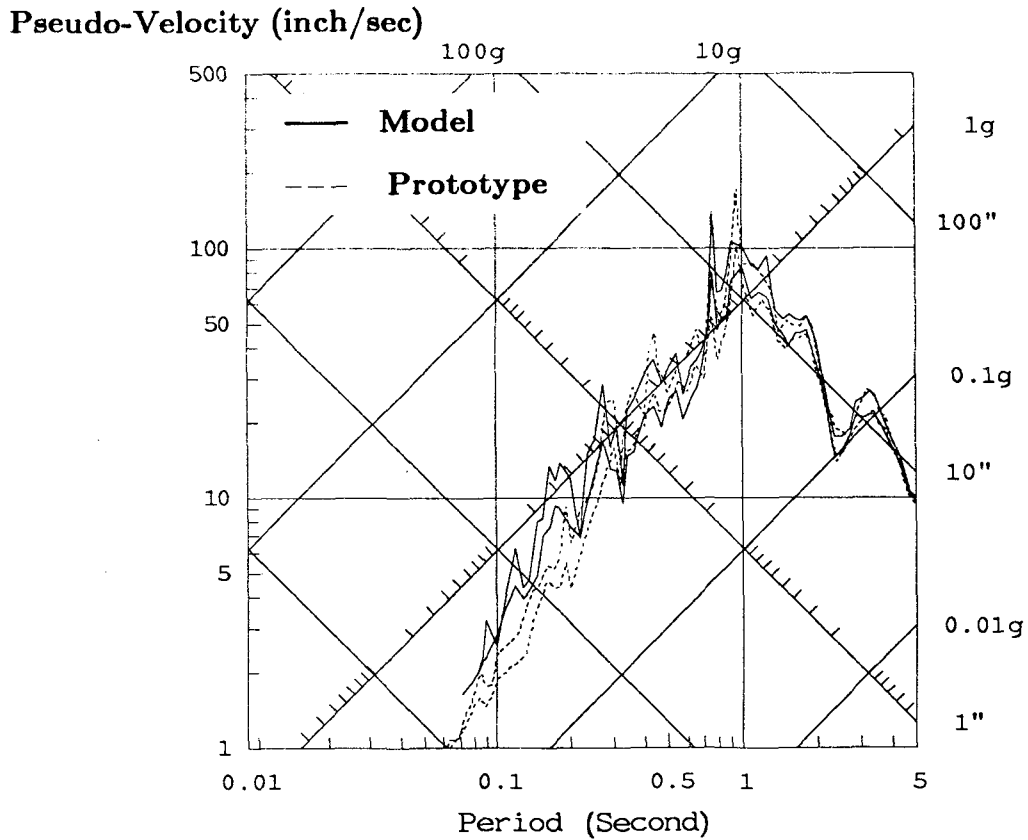
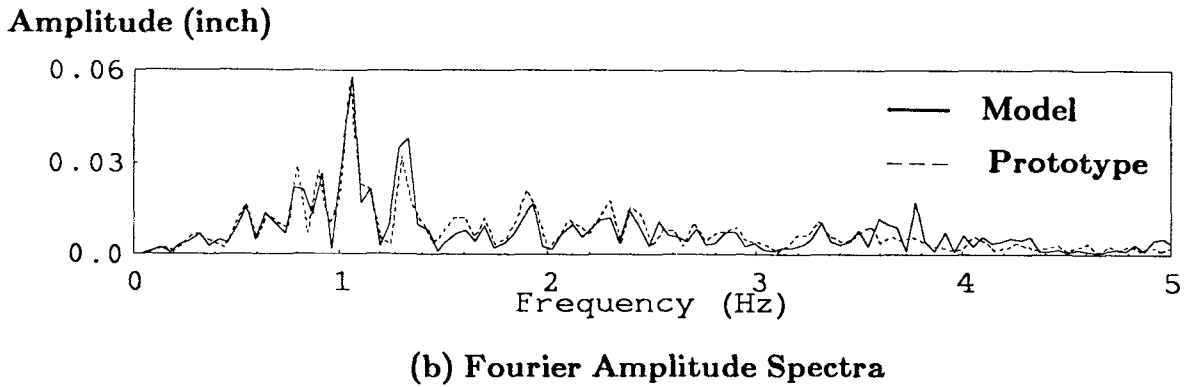
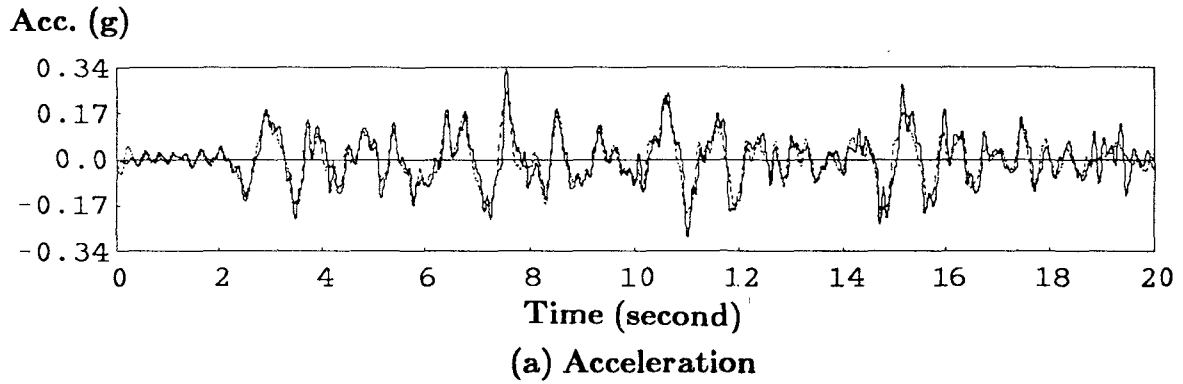


FIG. 9.27 PROTOTYPE AND MODEL COMPARISON OF GROUND MOTION USED IN DAMAGEABILITY LIMIT STATE TESTS

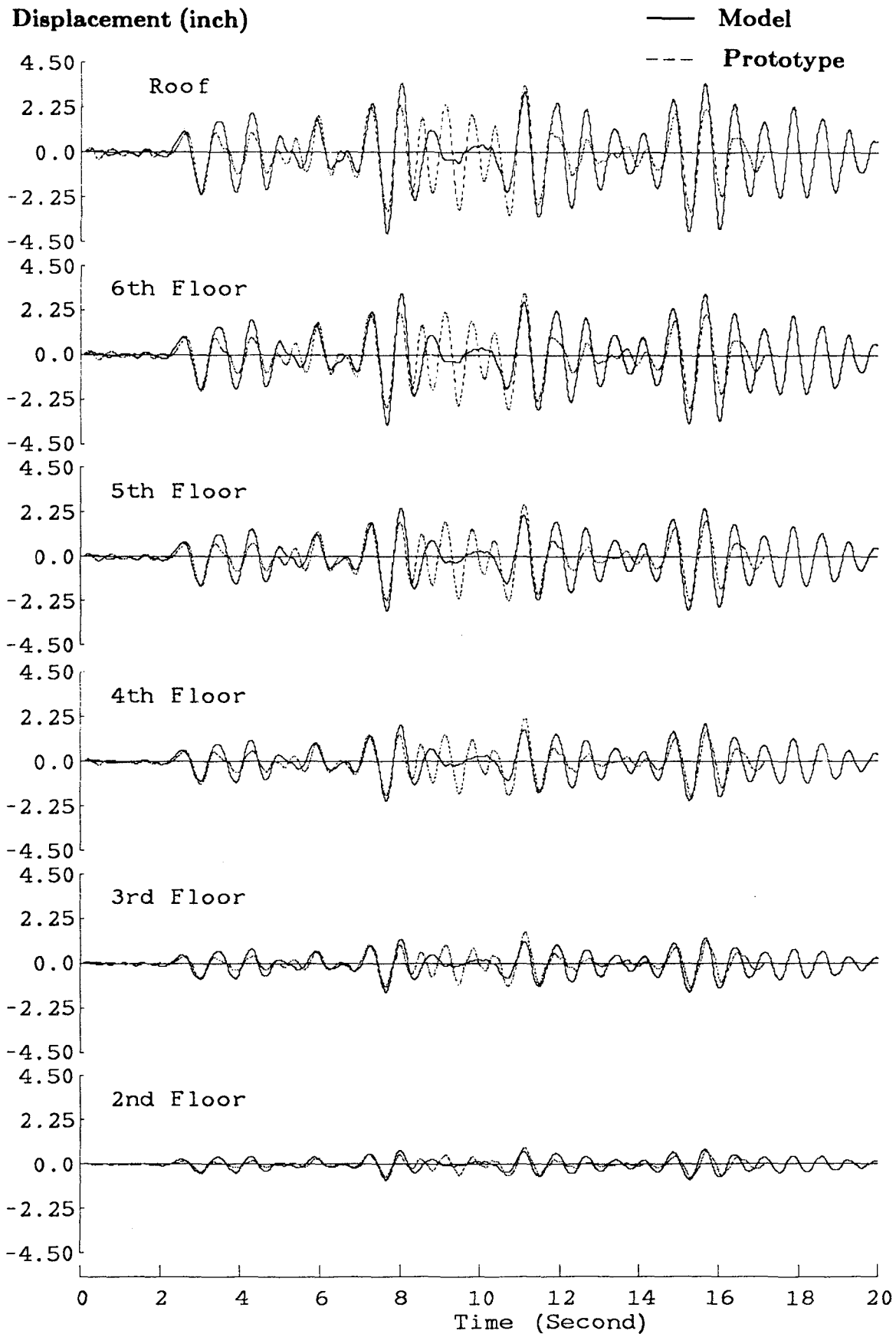


FIG. 9.28 COMPARISON OF PROTOTYPE AND MODEL LATERAL DISPLACEMENT RESPONSES IN DAMAGEABILITY LIMIT STATE TESTS

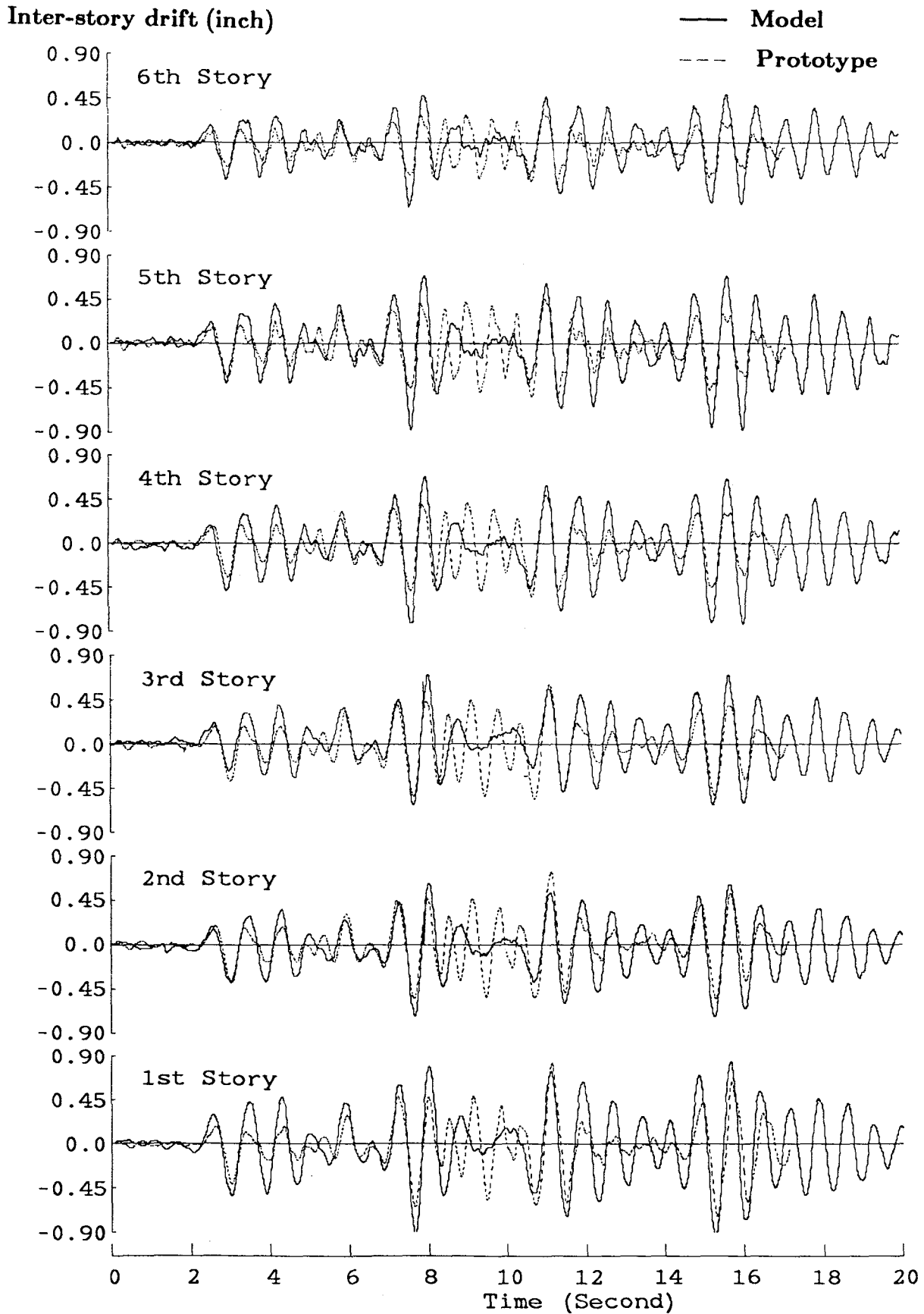


FIG. 9.29 COMPARISON OF PROTOTYPE AND MODEL INTER-STORY DRIFT RESPONSES IN DAMAGEABILITY LIMIT STATE TESTS

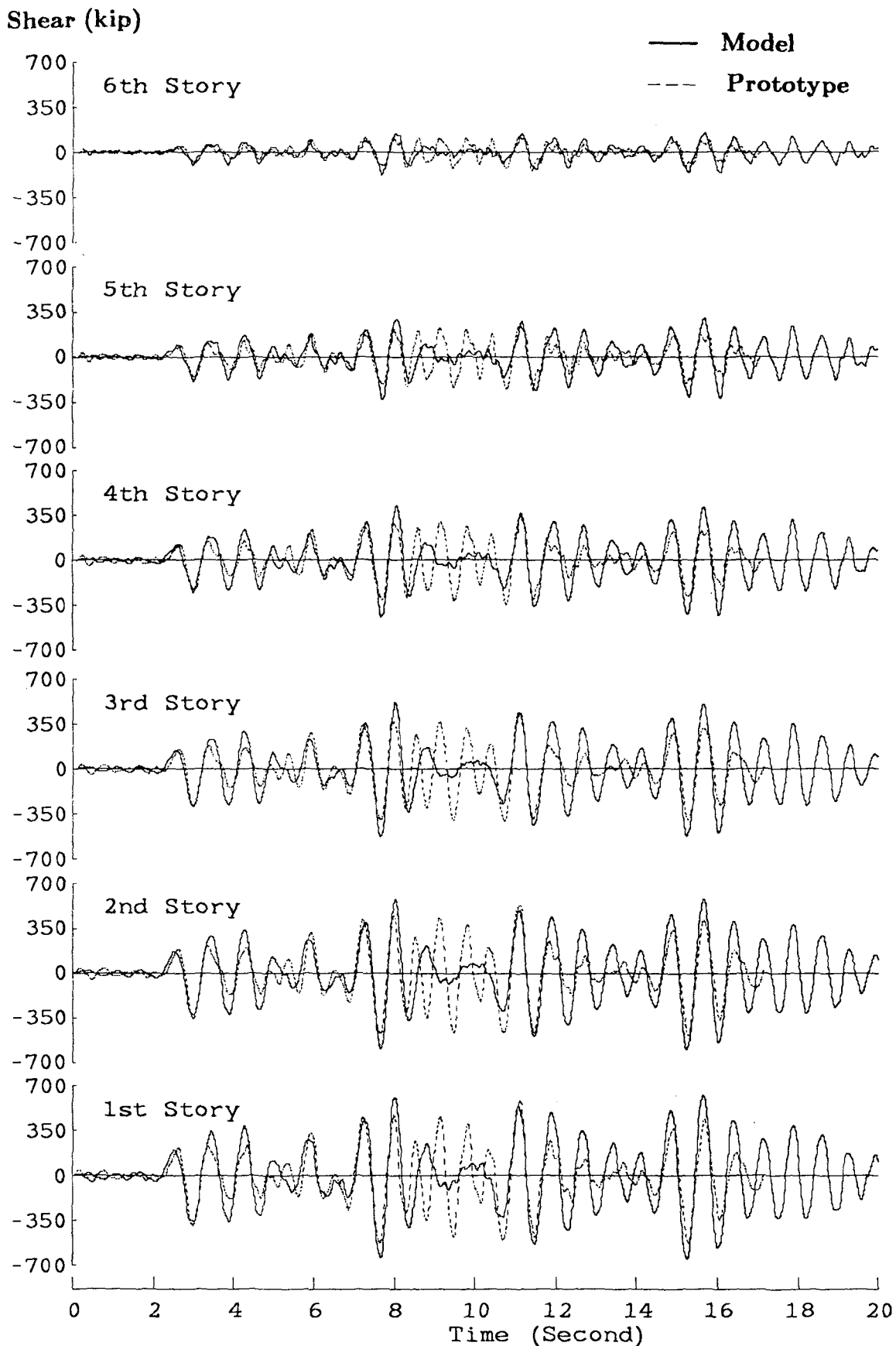


FIG. 9.30 COMPARISON OF PROTOTYPE AND MODEL STORY SHEAR RESPONSES IN DAMAGEABILITY LIMIT STATE TESTS

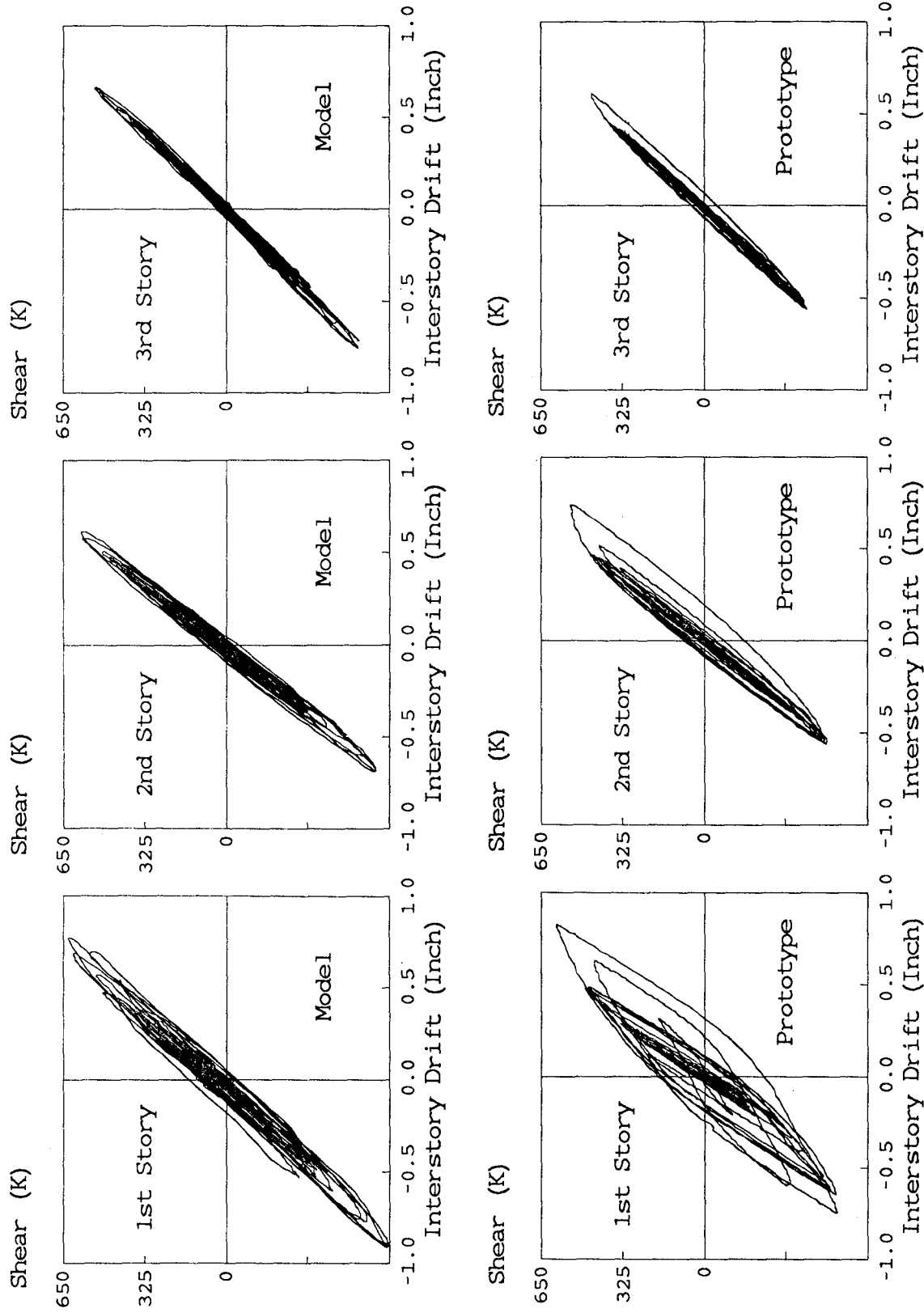
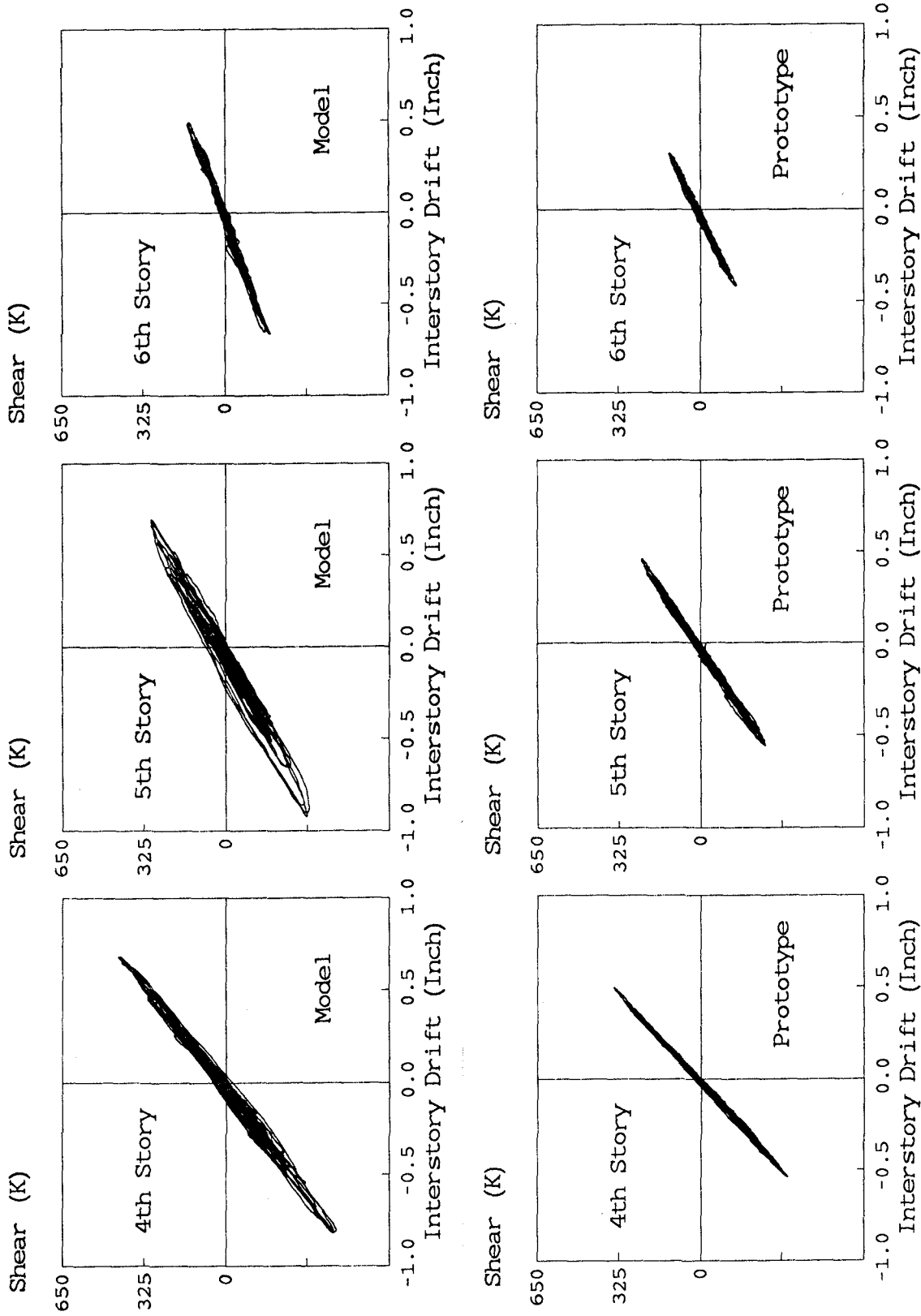


FIG. 9.31 DAMAGEABILITY LEVEL TEST INTER-STORY DRIFT

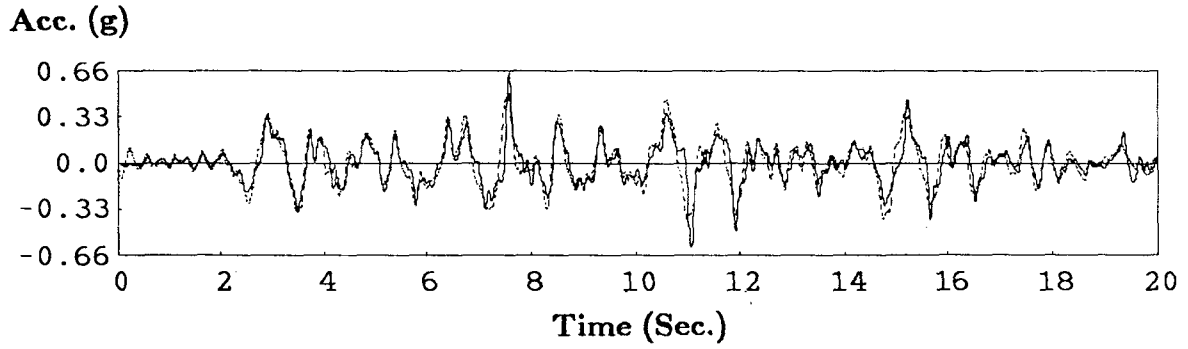
VERSUS TOTAL STORY SHEAR CURVES

(MODEL: MO-33 TEST; PROTOTYPE: MODERATE TEST)

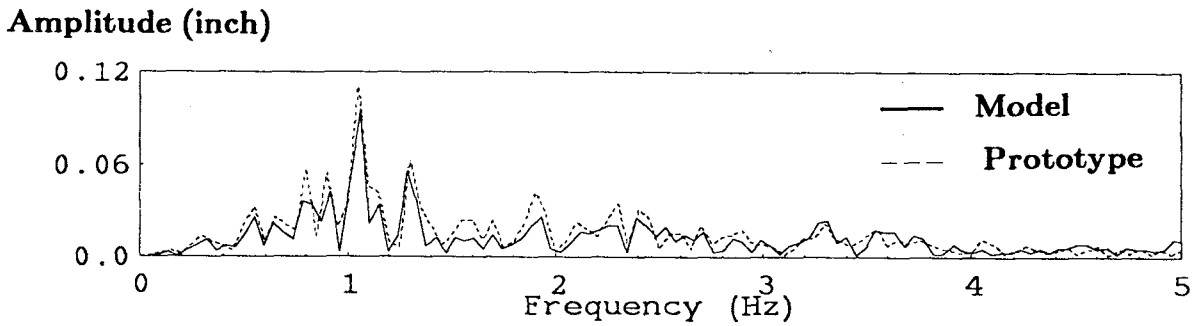


**FIG. 9.31 DAMAGEABILITY LEVEL TEST INTER-STORY DRIFT
VERSUS TOTAL STORY SHEAR CURVES (CONTINUED)**

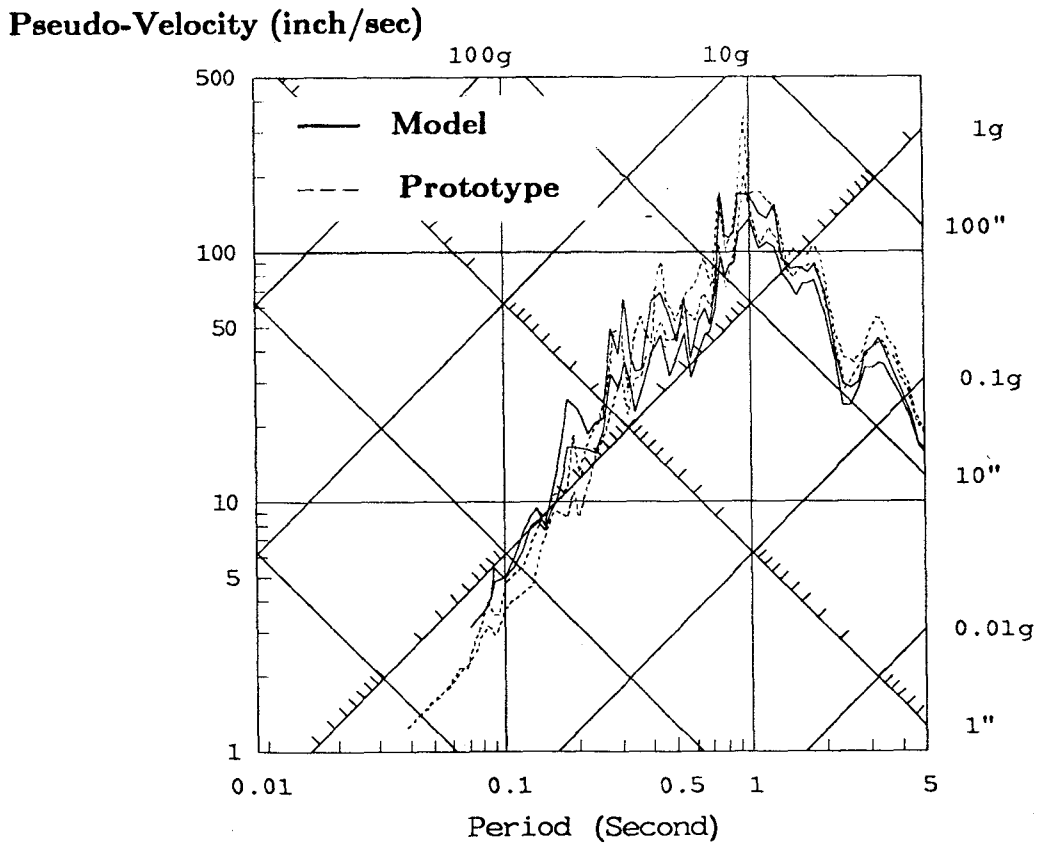
(Model: MO-33 Test; Prototype: Moderate Test)



(a) Acceleration



(b) Fourier Amplitude Spectra



(c) Linear Elastic Response Spectra (0.5 and 2% damping)

FIG. 9.32 PROTOTYPE AND MODEL COMPARISON OF GROUND MOTION USED IN COLLAPSE LIMIT STATE TESTS

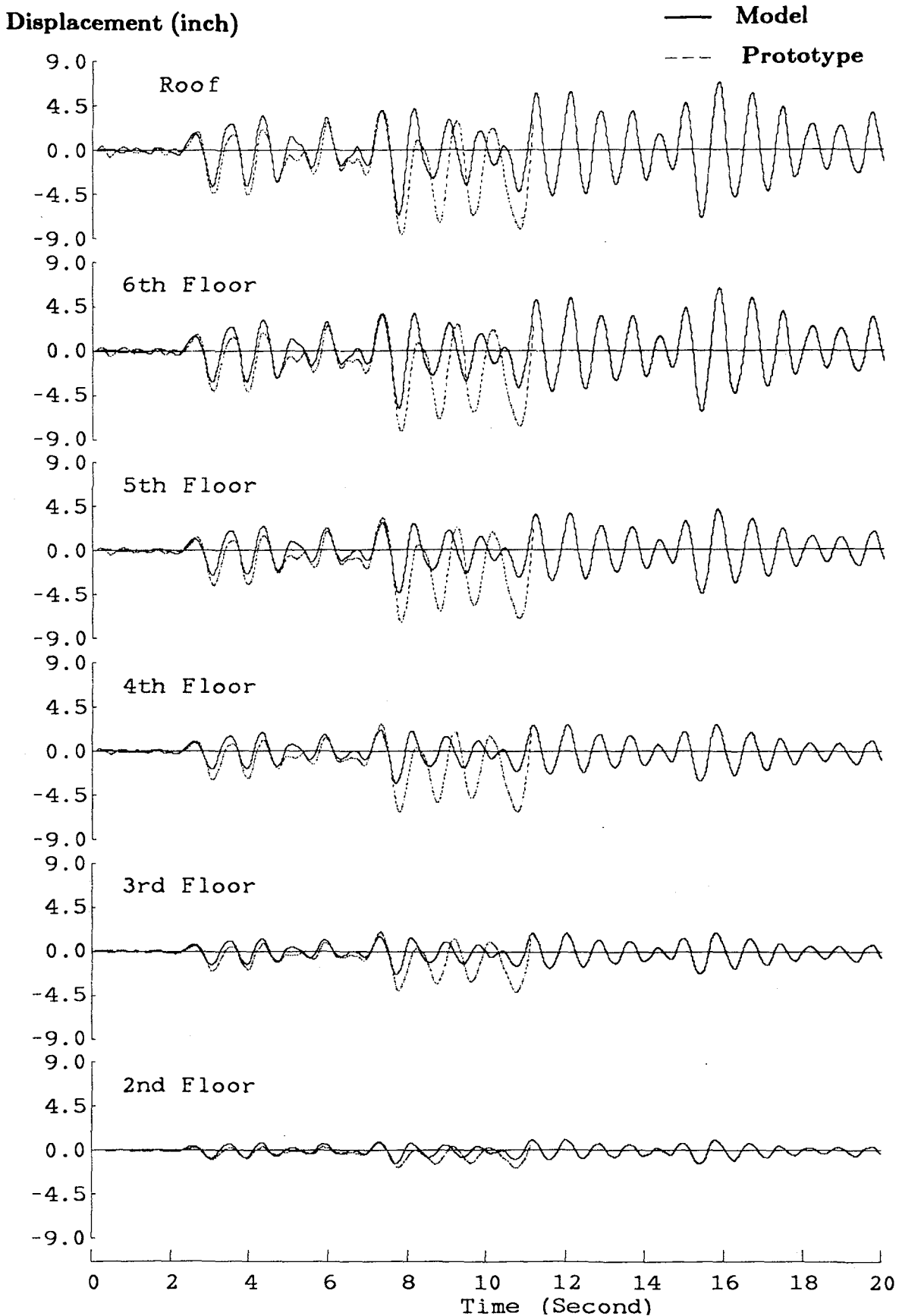


FIG. 9.33 COMPARISON OF PROTOTYPE AND MODEL LATERAL DISPLACEMENT RESPONSES IN COLLAPSE LIMIT STATE TESTS

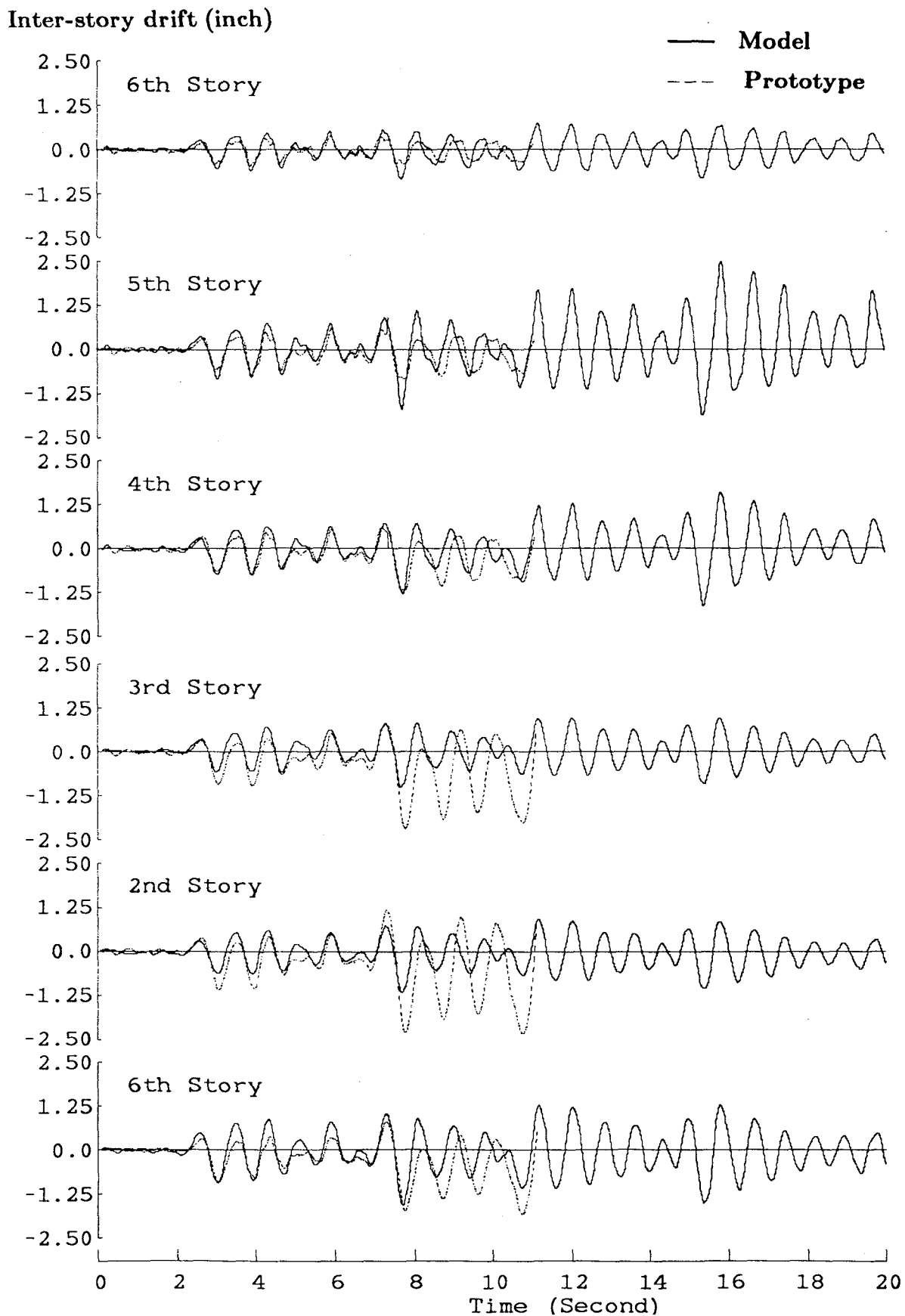


FIG. 9.34 COMPARISON OF PROTOTYPE AND MODEL INTER-STORY DRIFT RESPONSES IN COLLAPSE LIMIT STATE TESTS

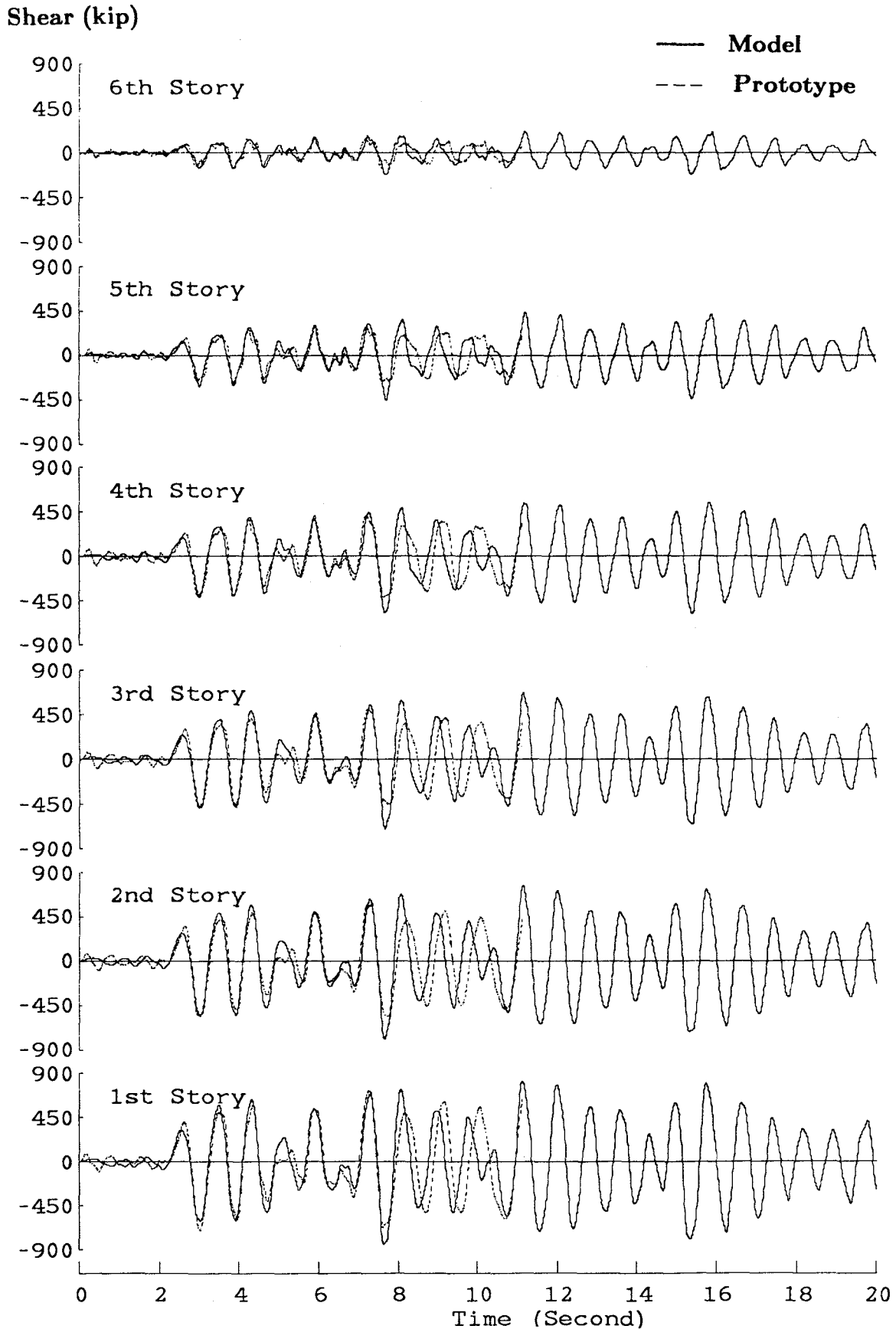
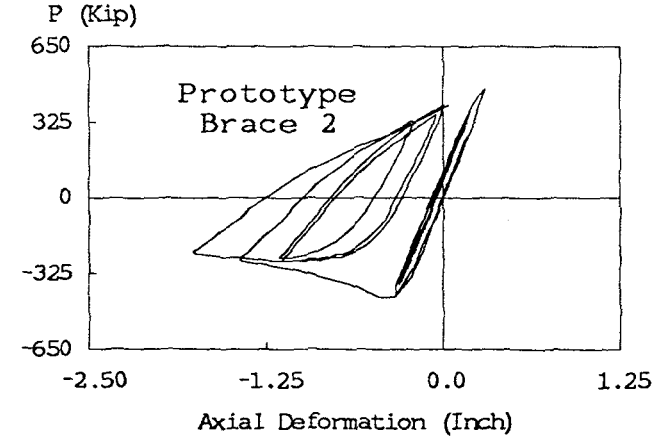
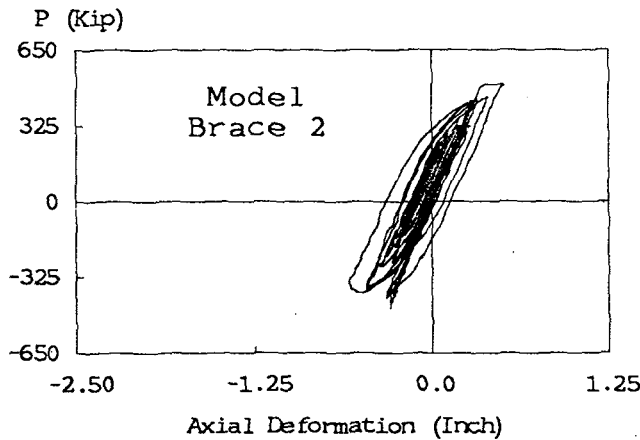
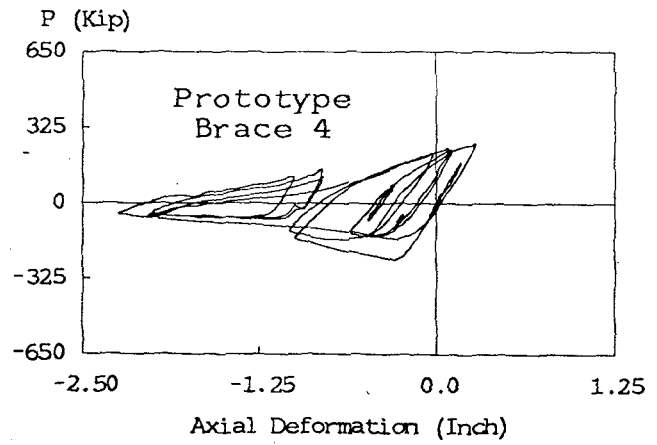
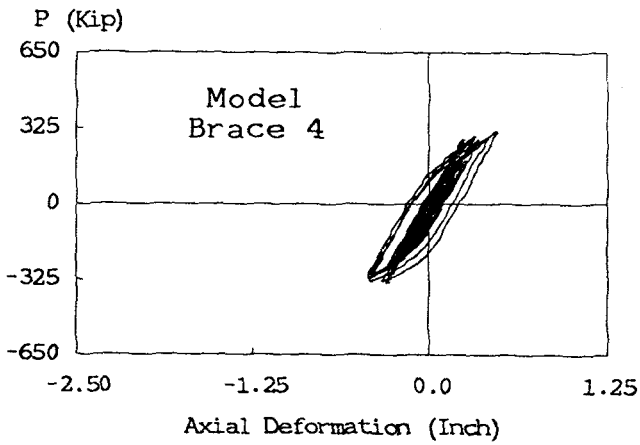
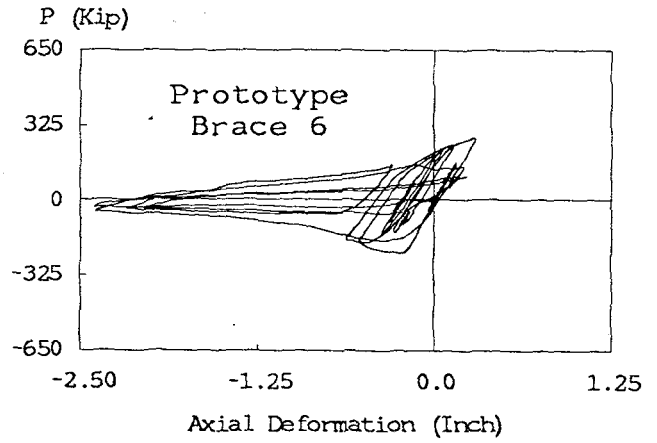
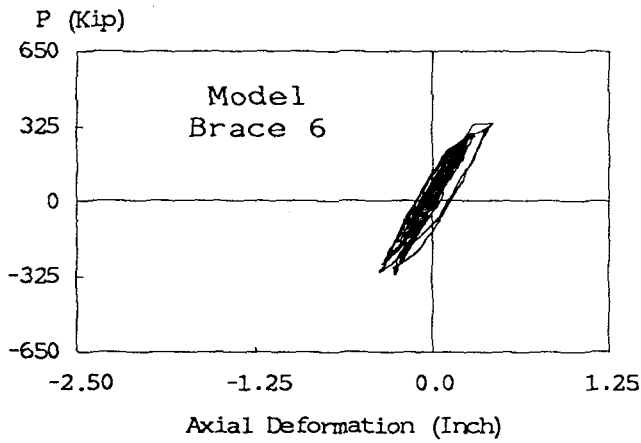
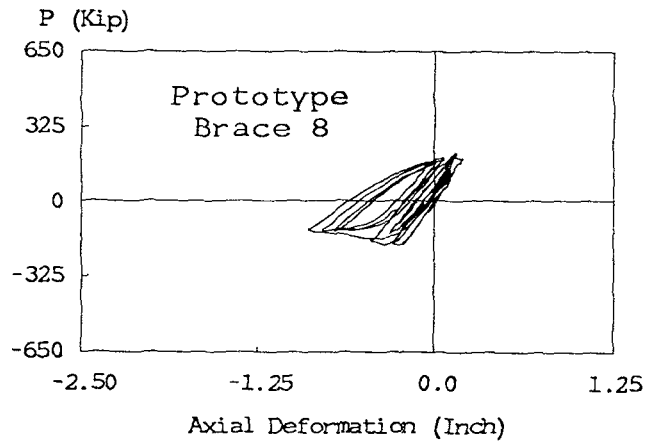
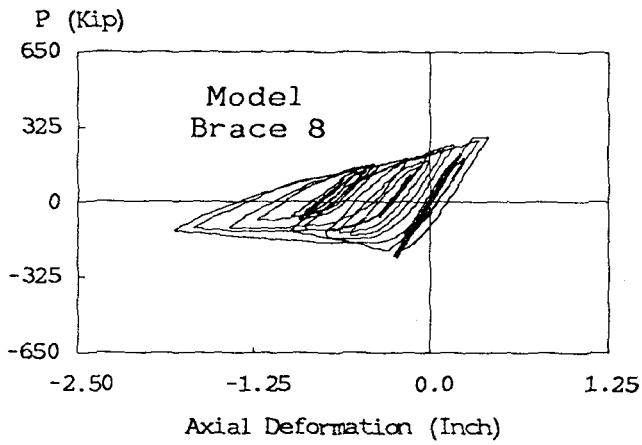
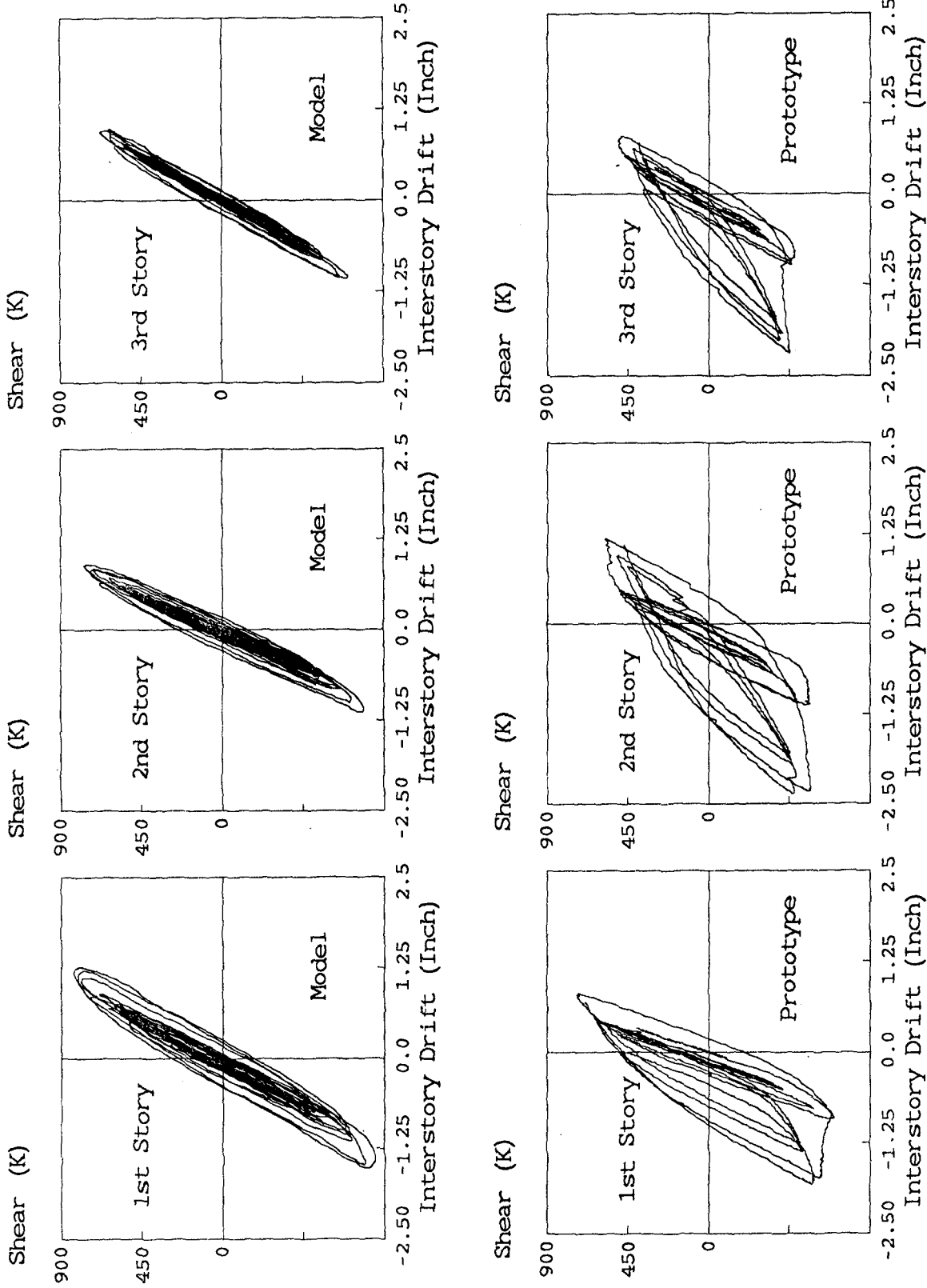


FIG. 9.35 COMPARISON OF PROTOTYPE AND MODEL STORY SHEAR RESPONSES IN COLLAPSE LIMIT STATE TESTS



**FIG. 9.38 COMPARISON OF PROTOTYPE AND MODEL BRACE
ENERGETIC RESPONSES IN COLLAPSE LIMIT STATE TESTS**



**FIG. 9.37 COMPARISON OF PROTOTYPE AND MODEL COLLAPSE LIMIT STATE TESTS
INTER-STORY DRIFT VERSUS TOTAL STORY SHEAR CURVES
(MODEL: MO-65 TEST; PROTOTYPE: FINAL TEST)**

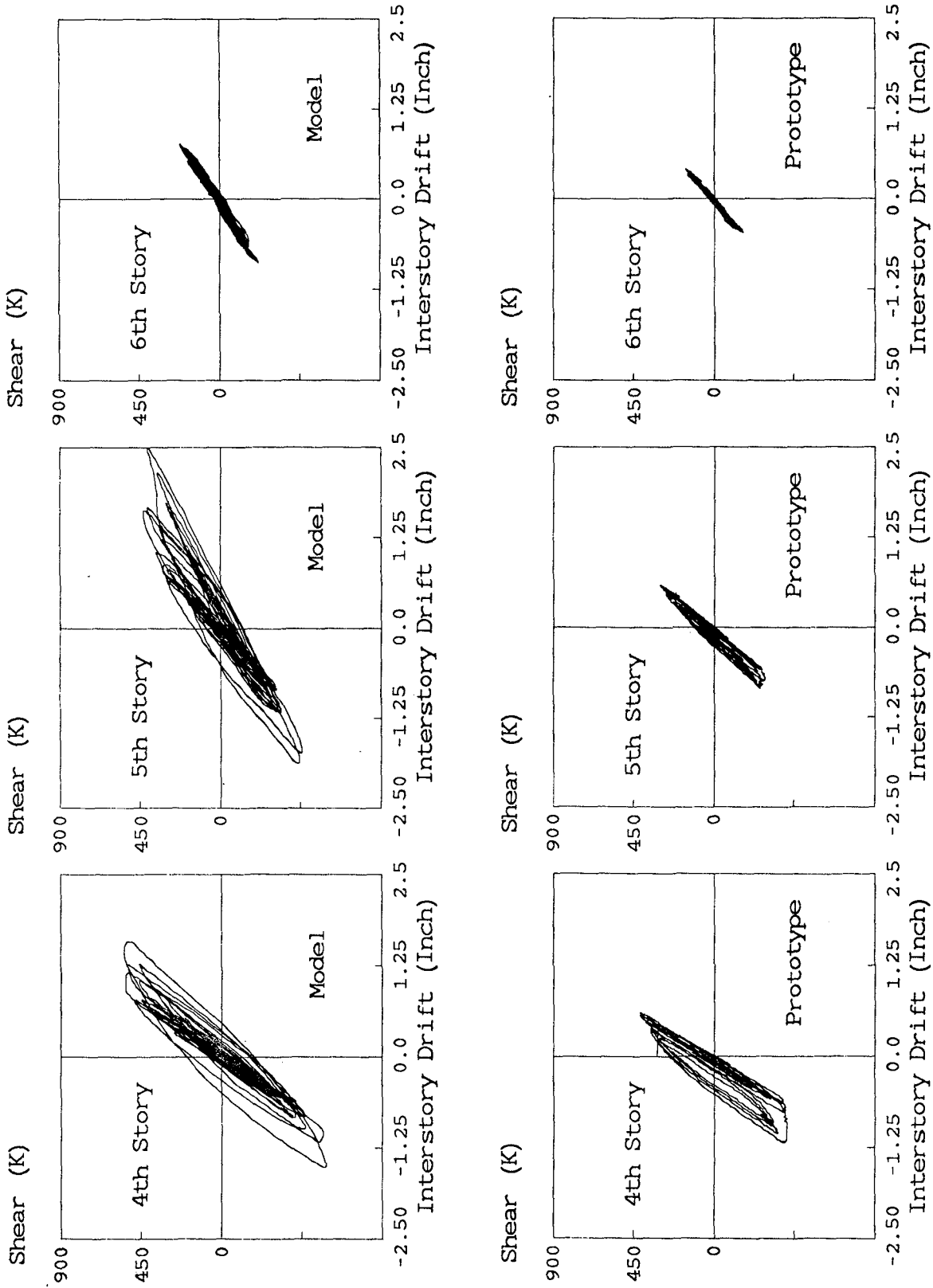


**FIG. 9.37 COMPARISON OF PROTOTYPE AND MODEL COLLAPSE LIMIT STATE TESTS
INTER-STORY DRIFT VERSUS TOTAL STORY SHEAR CURVES (CONTINUED)**

(MODEL: MO-65 TEST; PROTOTYPE: FINAL TEST)

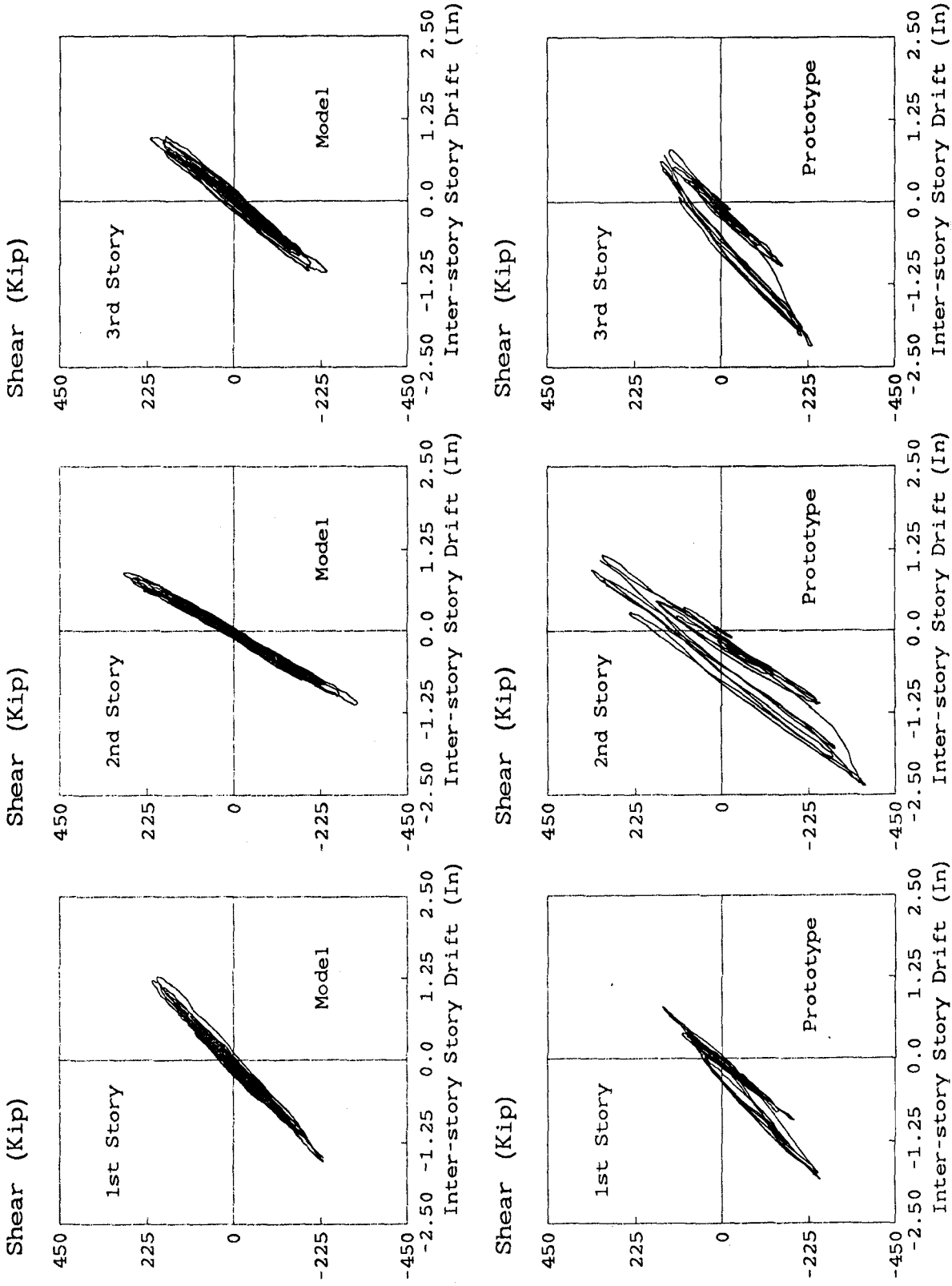
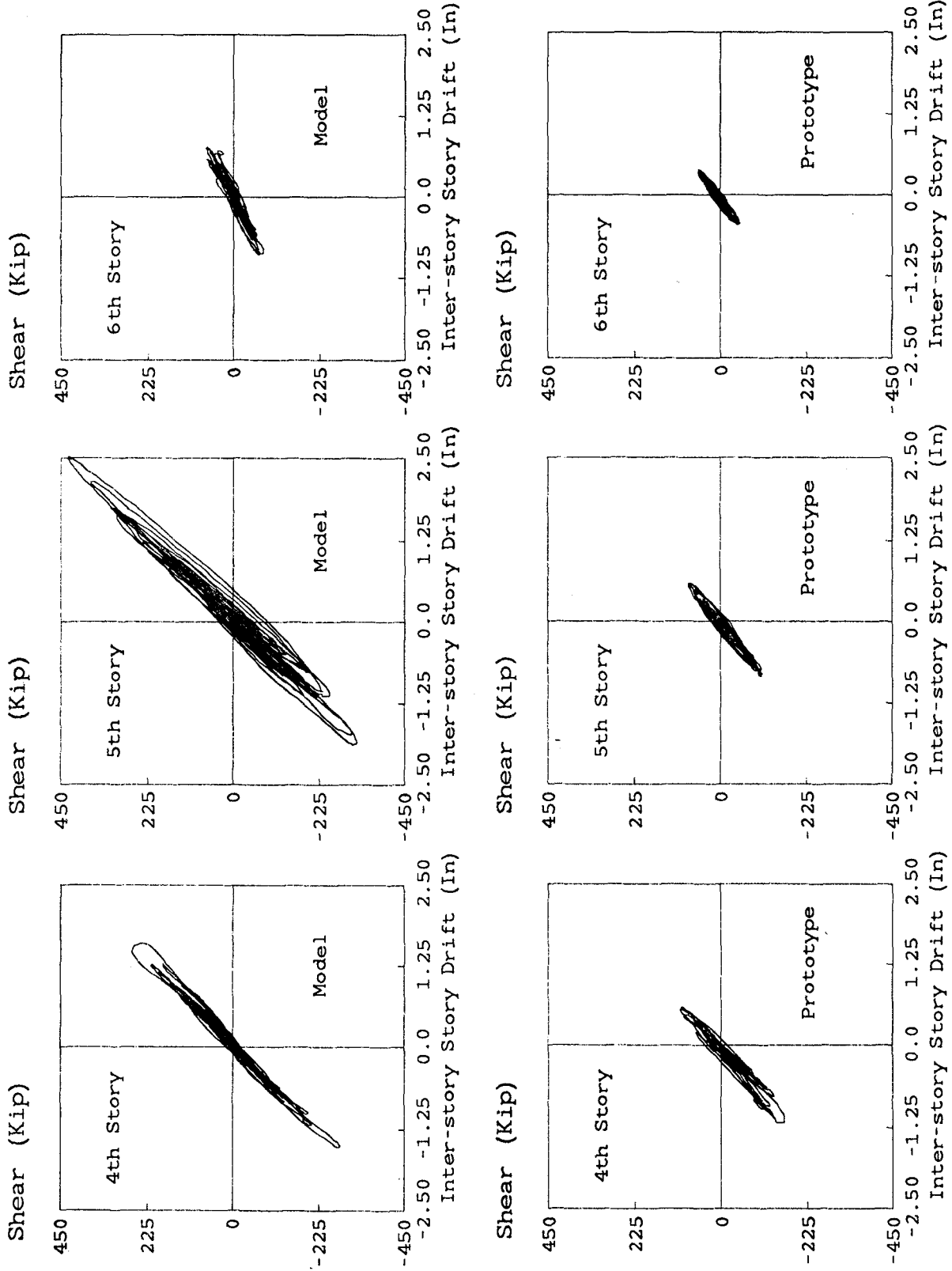
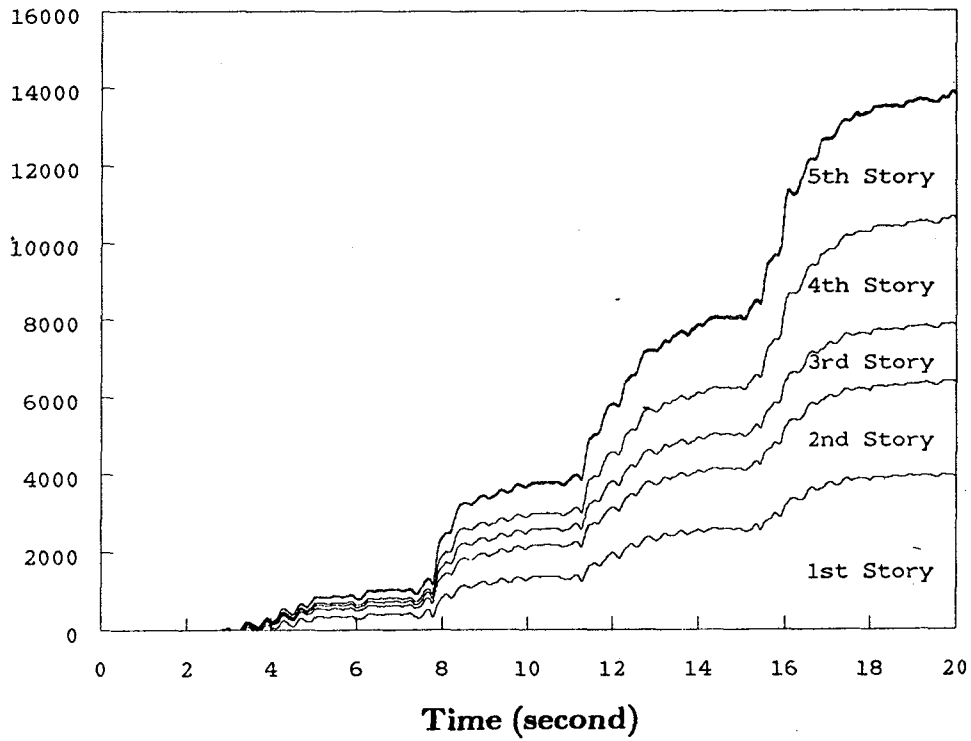


FIG. 9.38 COMPARISON OF PROTOTYPE AND MODEL COLLAPSE LIMIT STATE TESTS
INTER-STORY DRIFT VERSUS STORY COLUMN SHEAR CURVES
(MODEL: MO-65 TEST; PROTOTYPE: FINAL TEST)



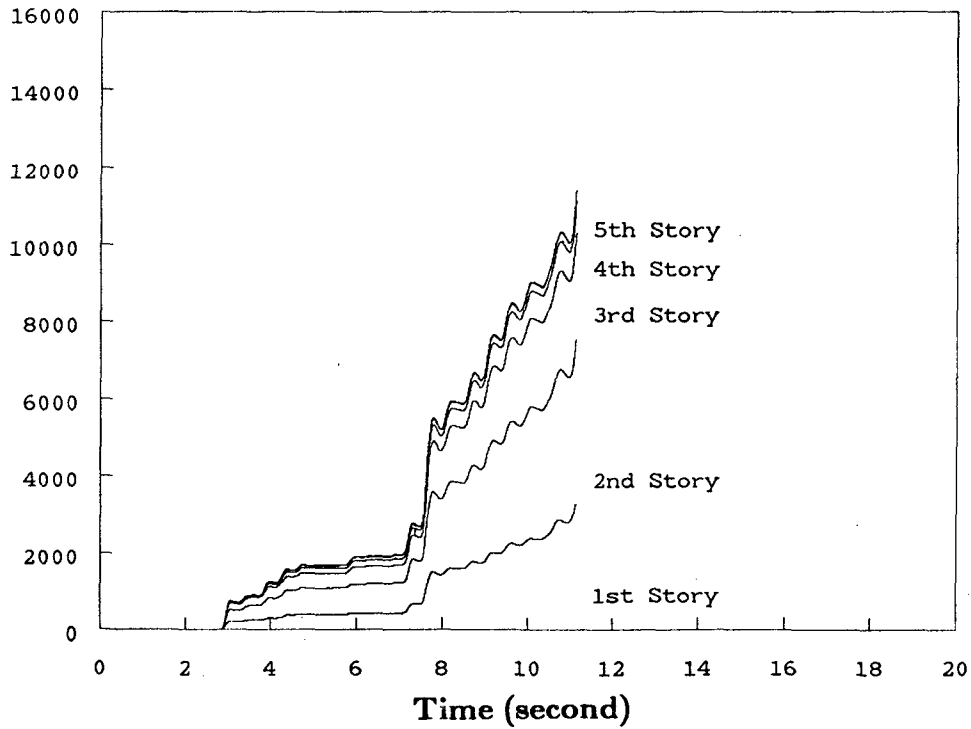
**FIG. 9.38 COMPARISON OF PROTOTYPE AND MODEL COLLAPSE LIMIT STATE TESTS
INTER-STORY DRIFT VERSUS STORY COLUMN SHEAR CURVES (CONTINUED)
(MODEL: MO-65 TEST; PROTOTYPE: FINAL TEST)**

Energy (kip-inch)



(a) 0.3-scale Model (MO-65 Test)

Energy (kip-inch)



(b) Prototype (Final Test)

FIG. 9.39 COMPARISON OF PROTOTYPE AND MODEL COLLAPSE

LIMIT STATE TESTS HYSTERETIC ENERGY DISTRIBUTION

EARTHQUAKE ENGINEERING RESEARCH CENTER REPORTS

NOTE: Numbers in parentheses are Accession Numbers assigned by the National Technical Information Service; these are followed by a price code. Copies of the reports may be ordered from the National Technical Information Service, 5285 Port Royal Road, Springfield, Virginia, 22161. Accession Numbers should be quoted on orders for reports (PB --- ---) and remittance must accompany each order. Reports without this information were not available at time of printing. The complete list of EERC reports (from EERC 67-1) is available upon request from the Earthquake Engineering Research Center, University of California, Berkeley, 47th Street and Hoffman Boulevard, Richmond, California 94804.

- UCB/EERC-79/01 "Hysteretic Behavior of Lightweight Reinforced Concrete Beam-Column Subassemblages," by B. Forzani, E.P. Popov and V.V. Bertero - April 1979 (PB 298 267)A06
- UCB/EERC-79/02 "The Development of a Mathematical Model to Predict the Flexural Response of Reinforced Concrete Beams to Cyclic Loads, Using System Identification," by J. Stanton & H. McNiven - Jan. 1979 (PB 295 875)A10
- UCB/EERC-79/03 "Linear and Nonlinear Earthquake Response of Simple Torsionally Coupled Systems," by C.L. Kan and A.K. Chopra - Feb. 1979 (PB 298 262)A06
- UCB/EERC-79/04 "A Mathematical Model of Masonry for Predicting its Linear Seismic Response Characteristics," by Y. Mengi and H.D. McNiven - Feb. 1979 (PB 298 266)A06
- UCB/EERC-79/05 "Mechanical Behavior of Lightweight Concrete Confined by Different Types of Lateral Reinforcement," by M.A. Manrique, V.V. Bertero and E.P. Popov - May 1979 (PB 301 114)A06
- UCB/EERC-79/06 "Static Tilt Tests of a Tall Cylindrical Liquid Storage Tank," by R.W. Clough and A. Niwa - Feb. 1979 (PB 301 167)A06
- UCB/EERC-79/07 "The Design of Steel Energy Absorbing Restrainers and Their Incorporation into Nuclear Power Plants for Enhanced Safety: Volume 1 - Summary Report," by P.N. Spencer, V.F. Zackay, and E.R. Parker - Feb. 1979 (UCB/EERC-79/07)A09
- UCB/EERC-79/08 "The Design of Steel Energy Absorbing Restrainers and Their Incorporation into Nuclear Power Plants for Enhanced Safety: Volume 2 - The Development of Analyses for Reactor System Piping," "Simple Systems" by M.C. Lee, J. Penzien, A.K. Chopra and K. Suzuki "Complex Systems" by G.H. Powell, E.L. Wilson, R.W. Clough and D.G. Row - Feb. 1979 (UCB/EERC-79/08)A10
- UCB/EERC-79/09 "The Design of Steel Energy Absorbing Restrainers and Their Incorporation into Nuclear Power Plants for Enhanced Safety: Volume 3 - Evaluation of Commercial Steels," by W.S. Owen, R.M.N. Pelloux, R.O. Ritchie, M. Faral, T. Ohhashi, J. Toplosky, S.J. Hartman, V.F. Zackay and E.R. Parker - Feb. 1979 (UCB/EERC-79/09)A04
- UCB/EERC-79/10 "The Design of Steel Energy Absorbing Restrainers and Their Incorporation into Nuclear Power Plants for Enhanced Safety: Volume 4 - A Review of Energy-Absorbing Devices," by J.M. Kelly and M.S. Skinner - Feb. 1979 (UCB/EERC-79/10)A04
- UCB/EERC-79/11 "Conservatism In Summation Rules for Closely Spaced Modes," by J.M. Kelly and J.L. Sackman - May 1979 (PB 301 328)A03
- UCB/EERC-79/12 "Cyclic Loading Tests of Masonry Single Piers; Volume 3 - Height to Width Ratio of 0.5," by P.A. Hidalgo, R.L. Mayes, H.D. McNiven and R.W. Clough - May 1979 (PB 301 321)A08
- UCB/EERC-79/13 "Cyclic Behavior of Dense Course-Grained Materials in Relation to the Seismic Stability of Dams," by N.G. Banerjee, H.B. Seed and C.K. Chan - June 1979 (PB 301 373)A13
- UCB/EERC-79/14 "Seismic Behavior of Reinforced Concrete Interior Beam-Column Subassemblages," by S. Viathanatepa, E.P. Popov and V.V. Bertero - June 1979 (PB 301 326)A10
- UCB/EERC-79/15 "Optimal Design of Localized Nonlinear Systems with Dual Performance Criteria Under Earthquake Excitations," by M.A. Bhatti - July 1979 (PB 80 167 109)A06
- UCB/EERC-79/16 "OPTDYN - A General Purpose Optimization Program for Problems with or without Dynamic Constraints," by M.A. Bhatti, E. Polak and K.S. Pister - July 1979 (PB 80 167 091)A05
- UCB/EERC-79/17 "ANSR-II, Analysis of Nonlinear Structural Response, Users Manual," by D.P. Mondkar and G.H. Powell July 1979 (PB 80 113 301)A05
- UCB/EERC-79/18 "Soil Structure Interaction in Different Seismic Environments," A. Gomez-Masso, J. Lysmer, J.-C. Chen and H.B. Seed - August 1979 (PB 80 101 520)A04
- UCB/EERC-79/19 "ARMA Models for Earthquake Ground Motions," by M.K. Chang, J.W. Kwiatkowski, R.F. Nau, R.M. Oliver and K.S. Pister - July 1979 (PB 301 166)A05
- UCB/EERC-79/20 "Hysteretic Behavior of Reinforced Concrete Structural Walls," by J.M. Vallenias, V.V. Bertero and E.P. Popov - August 1979 (PB 80 165 905)A12
- UCB/EERC-79/21 "Studies on High-Frequency Vibrations of Buildings - 1: The Column Effect," by J. Lubliner - August 1979 (PB 80 158 553)A03
- UCB/EERC-79/22 "Effects of Generalized Loadings on Bond Reinforcing Bars Embedded in Confined Concrete Blocks," by S. Viathanatepa, E.P. Popov and V.V. Bertero - August 1979 (PB 81 124 018)A14
- UCB/EERC-79/23 "Shaking Table Study of Single-Story Masonry Houses, Volume 1: Test Structures 1 and 2," by P. Gülkan, R.L. Mayes and R.W. Clough - Sept. 1979 (HUD-000 1763)A12
- UCB/EERC-79/24 "Shaking Table Study of Single-Story Masonry Houses, Volume 2: Test Structures 3 and 4," by P. Gülkan, R.L. Mayes and R.W. Clough - Sept. 1979 (HUD-000 1836)A12
- UCB/EERC-79/25 "Shaking Table Study of Single-Story Masonry Houses, Volume 3: Summary, Conclusions and Recommendations," by R.W. Clough, R.L. Mayes and P. Gülkan - Sept. 1979 (HUD-000 1837)A06

- UCB/EERC-79/26 "Recommendations for a U.S.-Japan Cooperative Research Program Utilizing Large-Scale Testing Facilities," by U.S.-Japan Planning Group - Sept. 1979(PB 301 407)A06
- UCB/EERC-79/27 "Earthquake-Induced Liquefaction Near Lake Amatitlan, Guatemala," by H.B. Seed, I. Arango, C.K. Chan, A. Gomez-Masso and R. Grant de Ascoli - Sept. 1979(NUREG-CRL341)A03
- UCB/EERC-79/28 "Infill Panels: Their Influence on Seismic Response of Buildings," by J.W. Axley and V.V. Bertero Sept. 1979(PB 80 163 371)A10
- UCB/EERC-79/29 "3D Truss Bar Element (Type 1) for the ANSR-II Program," by D.P. Mondkar and G.H. Powell - Nov. 1979 (PB 80 169 709)A02
- UCB/EERC-79/30 "2D Beam-Column Element (Type 5 - Parallel Element Theory) for the ANSR-II Program," by D.G. Row, G.H. Powell and D.P. Mondkar - Dec. 1979(PB 80 167 224)A03
- UCB/EERC-79/31 "3D Beam-Column Element (Type 2 - Parallel Element Theory) for the ANSR-II Program," by A. Riahi, G.H. Powell and D.P. Mondkar - Dec. 1979(PB 80 167 216)A03
- UCB/EERC-79/32 "On Response of Structures to Stationary Excitation," by A. Der Kiureghian - Dec. 1979(PB 80 166 929)A03
- UCB/EERC-79/33 "Undisturbed Sampling and Cyclic Load Testing of Sands," by S. Singh, H.B. Seed and C.K. Chan Dec. 1979(ADA 087 298)A07
- UCB/EERC-79/34 "Interaction Effects of Simultaneous Torsional and Compressional Cyclic Loading of Sand," by P.M. Griffin and W.N. Houston - Dec. 1979(ADA 092 352)A15
- UCB/EERC-80/01 "Earthquake Response of Concrete Gravity Dams Including Hydrodynamic and Foundation Interaction Effects," by A.K. Chopra, P. Chakrabarti and S. Gupta - Jan. 1980(AD-A087297)A10
- UCB/EERC-80/02 "Rocking Response of Rigid Blocks to Earthquakes," by C.S. Yim, A.K. Chopra and J. Penzien - Jan. 1980 (PB80 166 002)A04
- UCB/EERC-80/03 "Optimum Inelastic Design of Seismic-Resistant Reinforced Concrete Frame Structures," by S.W. Zagajeski and V.V. Bertero - Jan. 1980(PB80 164 635)A06
- UCB/EERC-80/04 "Effects of Amount and Arrangement of Wall-Panel Reinforcement on Hysteretic Behavior of Reinforced Concrete Walls," by R. Iliya and V.V. Bertero - Feb. 1980(PB81 122 525)A09
- UCB/EERC-80/05 "Shaking Table Research on Concrete Dam Models," by A. Niwa and R.W. Clough - Sept. 1980(PB81 122 368)A06
- UCB/EERC-80/06 "The Design of Steel Energy-Absorbing Restrainers and their Incorporation into Nuclear Power Plants for Enhanced Safety (Vol 1A): Piping with Energy Absorbing Restrainers: Parameter Study on Small Systems," by G.H. Powell, C. Oughourlian and J. Simons - June 1980
- UCB/EERC-80/07 "Inelastic Torsional Response of Structures Subjected to Earthquake Ground Motions," by Y. Yamazaki April 1980(PB81 122 327)A08
- UCB/EERC-80/08 "Study of X-Braced Steel Frame Structures Under Earthquake Simulation," by Y. Ghanaat - April 1980 (PB81 122 335)A11
- UCB/EERC-80/09 "Hybrid Modelling of Soil-Structure Interaction," by S. Gupta, T.W. Lin, J. Penzien and C.S. Yeh May 1980(PB81 122 319)A07
- UCB/EERC-80/10 "General Applicability of a Nonlinear Model of a One Story Steel Frame," by B.I. Sveinsson and H.D. McNiven - May 1980(PB81 124 877)A06
- UCB/EERC-80/11 "A Green-Function Method for Wave Interaction with a Submerged Body," by W. Kioka - April 1980 (PB81 122 269)A07
- UCB/EERC-80/12 "Hydrodynamic Pressure and Added Mass for Axisymmetric Bodies," by F. Nilrat - May 1980(PB81 122 343)A08
- UCB/EERC-80/13 "Treatment of Non-Linear Drag Forces Acting on Offshore Platforms," by B.V. Dao and J. Penzien May 1980(PB81 153 413)A07
- UCB/EERC-80/14 "2D Plane/Axisymmetric Solid Element (Type 3 - Elastic or Elastic-Perfectly Plastic) for the ANSR-II Program," by D.P. Mondkar and G.H. Powell - July 1980(PB81 122 350)A03
- UCB/EERC-80/15 "A Response Spectrum Method for Random Vibrations," by A. Der Kiureghian - June 1980(PB81 122 301)A03
- UCB/EERC-80/16 "Cyclic Inelastic Buckling of Tubular Steel Braces," by V.A. Zayas, E.P. Popov and S.A. Mahin June 1980(PB81 124 885)A10
- UCB/EERC-80/17 "Dynamic Response of Simple Arch Dams Including Hydrodynamic Interaction," by C.S. Porter and A.K. Chopra - July 1980(PB81 124 000)A13
- UCB/EERC-80/18 "Experimental Testing of a Friction Damped Aseismic Base Isolation System with Fail-Safe Characteristics," by J.M. Kelly, K.E. Beucke and M.S. Skinner - July 1980(PB81 148 595)A04
- UCB/EERC-80/19 "The Design of Steel Energy-Absorbing Restrainers and their Incorporation into Nuclear Power Plants for Enhanced Safety (Vol 1B): Stochastic Seismic Analyses of Nuclear Power Plant Structures and Piping Systems Subjected to Multiple Support Excitations," by M.C. Lee and J. Penzien - June 1980
- UCB/EERC-80/20 "The Design of Steel Energy-Absorbing Restrainers and their Incorporation into Nuclear Power Plants for Enhanced Safety (Vol 1C): Numerical Method for Dynamic Substructure Analysis," by J.M. Dickens and E.L. Wilson - June 1980
- UCB/EERC-80/21 "The Design of Steel Energy-Absorbing Restrainers and their Incorporation into Nuclear Power Plants for Enhanced Safety (Vol 2): Development and Testing of Restraints for Nuclear Piping Systems," by J.M. Kelly and M.S. Skinner - June 1980
- UCB/EERC-80/22 "3D Solid Element (Type 4-Elastic or Elastic-Perfectly-Plastic) for the ANSR-II Program," by D.P. Mondkar and G.H. Powell - July 1980(PB81 123 242)A03
- UCB/EERC-80/23 "Gap-Friction Element (Type 5) for the ANSR-II Program," by D.P. Mondkar and G.H. Powell - July 1980 (PB81 122 285)A03

- UCB/EERC-80/24 "U-Bar Restraint Element (Type 11) for the ANSR-II Program," by C. Oughourlian and G.H. Powell July 1980(PB81 122 293)A03
- UCB/EERC-80/25 "Testing of a Natural Rubber Base Isolation System by an Explosively Simulated Earthquake," by J.M. Kelly - August 1980(PB81 201 360)A04
- UCB/EERC-80/26 "Input Identification from Structural Vibrational Response," by Y. Hu - August 1980(PB81 152 308)A05
- UCB/EERC-80/27 "Cyclic Inelastic Behavior of Steel Offshore Structures," by V.A. Zayas, S.A. Mahin and E.P. Popov August 1980(PB81 196 180)A15
- UCB/EERC-80/28 "Shaking Table Testing of a Reinforced Concrete Frame with Biaxial Response," by M.G. Oliva October 1980(PB81 154 304)A10
- UCB/EERC-80/29 "Dynamic Properties of a Twelve-Story Prefabricated Panel Building," by J.G. Bouwkamp, J.P. Kollegger and R.M. Stephen - October 1980(PB82 117 128)A06
- UCB/EERC-80/30 "Dynamic Properties of an Eight-Story Prefabricated Panel Building," by J.G. Bouwkamp, J.P. Kollegger and R.M. Stephen - October 1980(PB81 200 313)A05
- UCB/EERC-80/31 "Predictive Dynamic Response of Panel Type Structures Under Earthquakes," by J.P. Kollegger and J.G. Bouwkamp - October 1980(PB81 152 316)A04
- UCB/EERC-80/32 "The Design of Steel Energy-Absorbing Restrainers and their Incorporation into Nuclear Power Plants for Enhanced Safety (Vol 3): Testing of Commercial Steels in Low-Cycle Torsional Fatigue," by P. Spencer, E.R. Parker, E. Jongewaard and M. Drory
- UCB/EERC-80/33 "The Design of Steel Energy-Absorbing Restrainers and their Incorporation into Nuclear Power Plants for Enhanced Safety (Vol 4): Shaking Table Tests of Piping Systems with Energy-Absorbing Restrainers," by S.F. Stiemer and W.G. Godden - Sept. 1980
- UCB/EERC-80/34 "The Design of Steel Energy-Absorbing Restrainers and their Incorporation into Nuclear Power Plants for Enhanced Safety (Vol 5): Summary Report," by P. Spencer
- UCB/EERC-80/35 "Experimental Testing of an Energy-Absorbing Base Isolation System," by J.M. Kelly, M.S. Skinner and K.E. Beucke - October 1980(PB81 154 072)A04
- UCB/EERC-80/36 "Simulating and Analyzing Artificial Non-Stationary Earthquake Ground Motions," by R.F. Nau, R.M. Oliver and K.S. Pister - October 1980(PB81 153 397)A04
- UCB/EERC-80/37 "Earthquake Engineering at Berkeley - 1980," - Sept. 1980(PB81 205 874)A09
- UCB/EERC-80/38 "Inelastic Seismic Analysis of Large Panel Buildings," by V. Schricker and G.H. Powell - Sept. 1980 (PB81 154 338)A13
- UCB/EERC-80/39 "Dynamic Response of Embankment, Concrete-Gravity and Arch Dams Including Hydrodynamic Interaction," by J.F. Hall and A.K. Chopra - October 1980(PB81 152 324)A11
- UCB/EERC-80/40 "Inelastic Buckling of Steel Struts Under Cyclic Load Reversal," by R.G. Black, W.A. Wenger and E.P. Popov - October 1980(PB81 154 312)A08
- UCB/EERC-80/41 "Influence of Site Characteristics on Building Damage During the October 3, 1974 Lima Earthquake," by P. Repetto, I. Arango and H.B. Seed - Sept. 1980(PB81 161 739)A05
- UCB/EERC-80/42 "Evaluation of a Shaking Table Test Program on Response Behavior of a Two Story Reinforced Concrete Frame," by J.M. Blondet, R.W. Clough and S.A. Mahin
- UCB/EERC-80/43 "Modelling of Soil-Structure Interaction by Finite and Infinite Elements," by F. Medina - December 1980(PB81 229 270)A04
- UCB/EERC-81/01 "Control of Seismic Response of Piping Systems and Other Structures by Base Isolation," edited by J.M. Kelly - January 1981 (PB81 200 735)A05
- UCB/EERC-81/02 "OPTNSR - An Interactive Software System for Optimal Design of Statically and Dynamically Loaded Structures with Nonlinear Response," by M.A. Bhatti, V. Ciampi and K.S. Pister - January 1981 (PB81 218 851)A09
- UCB/EERC-81/03 "Analysis of Local Variations in Free Field Seismic Ground Motions," by J.-C. Chen, J. Lysmer and H.B. Seed - January 1981 (AD-A099508)A13
- UCB/EERC-81/04 "Inelastic Structural Modeling of Braced Offshore Platforms for Seismic Loading," by V.A. Zayas, P.-S.B. Shing, S.A. Mahin and E.P. Popov - January 1981(PB82 138 777)A07
- UCB/EERC-81/05 "Dynamic Response of Light Equipment in Structures," by A. Der Kiureghian, J.L. Sackman and B. Nour-Omid - April 1981 (PB81 218 497)A04
- UCB/EERC-81/06 "Preliminary Experimental Investigation of a Broad Base Liquid Storage Tank," by J.G. Bouwkamp, J.P. Kollegger and R.M. Stephen - May 1981(PB82 140 385)A03
- UCB/EERC-81/07 "The Seismic Resistant Design of Reinforced Concrete Coupled Structural Walls," by A.E. Aktan and V.V. Bertero - June 1981(PB82 113 358)A11
- UCB/EERC-81/08 "The Undrained Shearing Resistance of Cohesive Soils at Large Deformations," by M.R. Pyles and H.B. Seed - August 1981
- UCB/EERC-81/09 "Experimental Behavior of a Spatial Piping System with Steel Energy Absorbers Subjected to a Simulated Differential Seismic Input," by S.F. Stiemer, W.G. Godden and J.M. Kelly - July 1981

- UCB/EERC-81/10 "Evaluation of Seismic Design Provisions for Masonry in the United States," by B.I. Sveinsson, R.L. Mayes and H.D. McNiven - August 1981 (PB82 166 075)A08
- UCB/EERC-81/11 "Two-Dimensional Hybrid Modelling of Soil-Structure Interaction," by T.-J. Tzong, S. Gupta and J. Penzien - August 1981 (PB82 142 118)A04
- UCB/EERC-81/12 "Studies on Effects of Infills in Seismic Resistant R/C Construction," by S. Brokken and V.V. Bertero - September 1981 (PB82 166 190)A09
- UCB/EERC-81/13 "Linear Models to Predict the Nonlinear Seismic Behavior of a One-Story Steel Frame," by H. Valdimarsson, A.H. Shah and H.D. McNiven - September 1981 (PB82 138 793)A07
- UCB/EERC-81/14 "TLUSH: A Computer Program for the Three-Dimensional Dynamic Analysis of Earth Dams," by T. Kagawa, L.H. Mejia, H.B. Seed and J. Lysmer - September 1981 (PB82 139 940)A06
- UCB/EERC-81/15 "Three Dimensional Dynamic Response Analysis of Earth Dams," by L.H. Mejia and H.B. Seed - September 1981 (PB82 137 274)A12
- UCB/EERC-81/16 "Experimental Study of Lead and Elastomeric Dampers for Base Isolation Systems," by J.M. Kelly and S.B. Hodder - October 1981 (PB82 166 182)A05
- UCB/EERC-81/17 "The Influence of Base Isolation on the Seismic Response of Light Secondary Equipment," by J.M. Kelly - April 1981 (PB82 255 266)A04
- UCB/EERC-81/18 "Studies on Evaluation of Shaking Table Response Analysis Procedures," by J. Marcial Blondet - November 1981 (PB82 197 278)A10
- UCB/EERC-81/19 "DELIGHT.STRUCT: A Computer-Aided Design Environment for Structural Engineering," by R.J. Balling, K.S. Pister and E. Polak - December 1981 (PB82 218 496)A07
- UCB/EERC-81/20 "Optimal Design of Seismic-Resistant Planar Steel Frames," by R.J. Balling, V. Ciampi, K.S. Pister and E. Polak - December 1981 (PB82 220 179)A07
- UCB/EERC-82/01 "Dynamic Behavior of Ground for Seismic Analysis of Lifeline Systems," by T. Sato and A. Der Kiureghian - January 1982 (PB82 218 926)A05
- UCB/EERC-82/02 "Shaking Table Tests of a Tubular Steel Frame Model," by Y. Ghanaat and R. W. Clough - January 1982 (PB82 220 161)A07
- UCB/EERC-82/03 "Behavior of a Piping System under Seismic Excitation: Experimental Investigations of a Spatial Piping System supported by Mechanical Shock Arrestors and Steel Energy Absorbing Devices under Seismic Excitation," by S. Schneider, H.-M. Lee and W. G. Godden - May 1982 (PB83 172 544)A09
- UCB/EERC-82/04 "New Approaches for the Dynamic Analysis of Large Structural Systems," by E. L. Wilson - June 1982 (PB83 148 080)A05
- UCB/EERC-82/05 "Model Study of Effects of Damage on the Vibration Properties of Steel Offshore Platforms," by F. Shahrivar and J. G. Bouwkamp - June 1982 (PB83 148 742)A10
- UCB/EERC-82/06 "States of the Art and Practice in the Optimum Seismic Design and Analytical Response Prediction of R/C Frame-Wall Structures," by A. E. Aktan and V. V. Bertero - July 1982 (PB83 147 736)A05
- UCB/EERC-82/07 "Further Study of the Earthquake Response of a Broad Cylindrical Liquid-Storage Tank Model," by G. C. Manos and R. W. Clough - July 1982 (PB83 147 744)A11
- UCB/EERC-82/08 "An Evaluation of the Design and Analytical Seismic Response of a Seven Story Reinforced Concrete Frame - Wall Structure," by F. A. Charney and V. V. Bertero - July 1982 (PB83 157 628)A09
- UCB/EERC-82/09 "Fluid-Structure Interactions: Added Mass Computations for Incompressible Fluid," by J. S.-H. Kuo - August 1982 (PB83 156 281)A07
- UCB/EERC-82/10 "Joint-Opening Nonlinear Mechanism: Interface Smeared Crack Model," by J. S.-H. Kuo - August 1982 (PB83 149 195)A05
- UCB/EERC-82/11 "Dynamic Response Analysis of Tchi Dam," by R. W. Clough, R. M. Stephen and J. S.-H. Kuo - August 1982 (PB83 147 496)A06
- UCB/EERC-82/12 "Prediction of the Seismic Responses of R/C Frame-Coupled Wall Structures," by A. E. Aktan, V. V. Bertero and M. Piazza - August 1982 (PB83 149 203)A09
- UCB/EERC-82/13 "Preliminary Report on the SMART 1 Strong Motion Array in Taiwan," by B. A. Bolt, C. H. Loh, J. Penzien, Y. B. Tsai and Y. T. Yeh - August 1982 (PB83 159 400)A10
- UCB/EERC-82/14 "Shaking-Table Studies of an Eccentrically X-Braced Steel Structure," by M. S. Yang - September 1982 (PB83 260 778)A12
- UCB/EERC-82/15 "The Performance of Stairways in Earthquakes," by C. Roha, J. W. Axley and V. V. Bertero - September 1982 (PB83 157 693)A07
- UCB/EERC-82/16 "The Behavior of Submerged Multiple Bodies in Earthquakes," by W.-G. Liao - Sept. 1982 (PB83 158 709)A07
- UCB/EERC-82/17 "Effects of Concrete Types and Loading Conditions on Local Bond-Slip Relationships," by A. D. Cowell, E. P. Popov and V. V. Bertero - September 1982 (PB83 153 577)A04

- UCB/EERC-82/18 "Mechanical Behavior of Shear Wall Vertical Boundary Members: An Experimental Investigation," by M. T. Wagner and V. V. Bertero - October 1982 (PB83 159 764)A05
- UCB/EERC-82/19 "Experimental Studies of Multi-support Seismic Loading on Piping Systems," by J. M. Kelly and A. D. Cowell - November 1982
- UCB/EERC-82/20 "Generalized Plastic Hinge Concepts for 3D Beam-Column Elements," by P. F.-S. Chen and G. H. Powell - November 1982 (PB03 247 981)A13
- UCB/EERC-82/21 "ANSR-III: General Purpose Computer Program for Nonlinear Structural Analysis," by C. V. Oughourlian and G. H. Powell - November 1982 (PB83 251 330)A12
- UCB/EERC-82/22 "Solution Strategies for Statically Loaded Nonlinear Structures," by J. W. Simons and G. H. Powell - November 1982 (PB83 197 970)A06
- UCB/EERC-82/23 "Analytical Model of Deformed Bar Anchorages under Generalized Excitations," by V. Ciampi, R. Elgehausen, V. V. Bertero and E. P. Popov - November 1982 (PB83 169 532)A06
- UCB/EERC-82/24 "A Mathematical Model for the Response of Masonry Walls to Dynamic Excitations," by H. Sucuoğlu, Y. Mengi and H. D. McNiven - November 1982 (PB83 169 011)A07
- UCB/EERC-82/25 "Earthquake Response Considerations of Broad Liquid Storage Tanks," by F. J. Cambra - November 1982 (PB83 251 215)A09
- UCB/EERC-82/26 "Computational Models for Cyclic Plasticity, Rate Dependence and Creep," by B. Mosaddad and G. H. Powell - November 1982 (PB83 245 829)A08
- UCB/EERC-82/27 "Inelastic Analysis of Piping and Tubular Structures," by M. Mahasuverachai and G. H. Powell - November 1982 (PB83 249 987)A07
- UCB/EERC-83/01 "The Economic Feasibility of Seismic Rehabilitation of Buildings by Base Isolation," by J. M. Kelly - January 1983 (PB83 197 988)A05
- UCB/EERC-83/02 "Seismic Moment Connections for Moment-Resisting Steel Frames," by E. P. Popov - January 1983 (PB83 195 412)A04
- UCB/EERC-83/03 "Design of Links and Beam-to-Column Connections for Eccentrically Braced Steel Frames," by E. P. Popov and J. O. Malley - January 1983 (PB83 194 811)A04
- UCB/EERC-83/04 "Numerical Techniques for the Evaluation of Soil-Structure Interaction Effects in the Time Domain," by E. Bayo and E. L. Wilson - February 1983 (PB83 245 605)A09
- UCB/EERC-83/05 "A Transducer for Measuring the Internal Forces in the Columns of a Frame-Wall Reinforced Concrete Structure," by R. Sause and V. V. Bertero - May 1983 (PB84 119 494)A06
- UCB/EERC-83/06 "Dynamic Interactions between Floating Ice and Offshore Structures," by P. Croteau - May 1983 (PB84 119 486)A16
- UCB/EERC-83/07 "Dynamic Analysis of Multiply Tuned and Arbitrarily Supported Secondary Systems," by T. Igusa and A. Der Kiureghian - June 1983 (PB84 118 272)A11
- UCB/EERC-83/08 "A Laboratory Study of Submerged Multi-body Systems in Earthquakes," by G. R. Ansari - June 1983 (PB83 261 842)A17
- UCB/EERC-83/09 "Effects of Transient Foundation Uplift on Earthquake Response of Structures," by C.-S. Yim and A. K. Chopra - June 1983 (PB83 261 396)A07
- UCB/EERC-83/10 "Optimal Design of Friction-Braced Frames under Seismic Loading," by M. A. Austin and K. S. Pister - June 1983 (PB84 119 288)A06
- UCB/EERC-83/11 "Shaking Table Study of Single-Story Masonry Houses: Dynamic Performance under Three Component Seismic Input and Recommendations," by G. C. Manos, R. W. Clough and R. L. Mayes - June 1983
- UCB/EERC-83/12 "Experimental Error Propagation in Pseudodynamic Testing," by P. B. Shing and S. A. Mahin - June 1983 (PB84 119 270)A09
- UCB/EERC-83/13 "Experimental and Analytical Predictions of the Mechanical Characteristics of a 1/5-scale Model of a 7-story R/C Frame-Wall Building Structure," by A. E. Aktan, V. V. Bertero, A. A. Chowdhury and T. Nagashima - August 1983 (PB84 119 213)A07
- UCB/EERC-83/14 "Shaking Table Tests of Large-Panel Precast Concrete Building System Assemblages," by M. G. Oliva and R. W. Clough - August 1983
- UCB/EERC-83/15 "Seismic Behavior of Active Beam Links in Eccentrically Braced Frames," by K. D. Hjelmstad and E. P. Popov - July 1983 (PB84 119 676)A09
- UCB/EERC-83/16 "System Identification of Structures with Joint Rotation," by J. S. Dimsdale and H. D. McNiven - July 1983
- UCB/EERC-83/17 "Construction of Inelastic Response Spectra for Single-Degree-of-Freedom Systems," by S. Mahin and J. Lin - July 1983

- NA UCB/EERC-83/18 "Interactive Computer Analysis Methods for Predicting the Inelastic Cyclic Behaviour of Structural Sections," by S. Kaba and S. Mahin - July 1983 (PB84 192 012)A06
- UCB/EERC-83/19 "Effects of Bond Deterioration on Hysteretic Behavior of Reinforced Concrete Joints," by F.C. Filippou, E.P. Popov and V.V. Bertero - Aug. 1983 (PB84 192 020)A10
- UCB/EERC-83/20 "Analytical and Experimental Correlation of Large-Panel Precast Building System Performance," by M.G. Oliva, R.W. Clough, M. Velkov, P. Gavrilovic and J. Petrovski - Nov. 1983
- UCB/EERC-83/21 "Mechanical Characteristics of Materials Used in a 1/5 Scale Model of a 7-Story Reinforced Concrete Test Structure," by V.V. Bertero, A.E. Aktan, H.G. Harris and A.A. Chowdhury - Sept. 1983 (PB84 193 697)A05
- NA UCB/EERC-83/22 "Hybrid Modelling of Soil-Structure Interaction in Layered Media," by T.-J. Tzong and J. Penzien - Oct. 1983 (PB84 192 178)A08
- UCB/EERC-83/23 "Local Bond Stress-Slip Relationships of Deformed Bars under Generalized Excitations," by R. Eligehausen, E.P. Popov and V.V. Bertero - Oct. 1983 (PB84 192 848)A09
- UCB/EERC-83/24 "Design Considerations for Shear Links in Eccentrically Braced Frames," by J.O. Malley and E.P. Popov - Nov. 1983 (PB84 192 186)A07
- NA UCB/EERC-84/01 "Pseudodynamic Test Method for Seismic Performance Evaluation: Theory and Implementation," by P.-S. B. Shing and S.A. Mahin - Jan. 1984 (PB84 190 644)A08
- UCB/EERC-84/02 "Dynamic Response Behavior of Xiang Hong Dian Dam," by R.W. Clough, K.-T. Chang, H.-Q. Chen, R.M. Stephen, G.-L. Wang and Y. Ghanaat - April 1984 (PB84 209 402)A08
- UCB/EERC-84/03 "Refined Modelling of Reinforced Concrete Columns for Seismic Analysis," by S.A. Kaba and S.A. Mahin - April 1984 (PB84 234 384)A06
- NA UCB/EERC-84/04 "A New Floor Response Spectrum Method for Seismic Analysis of Multiply Supported Secondary Systems," by A. Asfura and A. Der Kiureghian - June 1984 (PB84 239 417)A06
- NA UCB/EERC-84/05 "Earthquake Simulation Tests and Associated Studies of a 1/5th-scale Model of a 7-Story R/C Frame-Wall Test Structure," by V.V. Bertero, A.E. Aktan, F.A. Charney and R. Sause - June 1984 (PB84 239 409)A09
- UCB/EERC-84/06 "R/C Structural Walls: Seismic Design for Shear," by A.E. Aktan and V.V. Bertero
- UCB/EERC-84/07 "Behavior of Interior and Exterior Flat-Plate Connections subjected to Inelastic Load Reversals," by H.L. Zee and J.P. Moehle - August 1984 (PB86 117 629/AS) A07
- UCB/EERC-84/08 "Experimental Study of the Seismic Response of a Two-story Flat-Plate Structure," by J. P. Moehle and J.W. Diebold - August 1984 (PB86 122 553/AS) A12
- UCB/EERC-84/09 "Phenomenological Modeling of Steel Braces under Cyclic Loading," by K. Ikeda, S.A. Mahin and S.N. Dermizakis - May 1984 (PB86 132 198/AS) A08
- UCB/EERC-84/10 "Earthquake Analysis and Response of Concrete Gravity Dams," by G. Fenves and A.K. Chopra - Aug. 1984 (PB85 193 902/AS)A11
- UCB/EERC-84/11 "EAGD-84: A Computer Program for Earthquake Analysis of Concrete Gravity Dams," by G. Fenves and A.K. Chopra - Aug. 1984 (PB85 193 613/AS)A05
- UCB/EERC-84/12 "A Refined Physical Theory Model for Predicting the Seismic Behavior of Braced Steel Frames," by K. Ikeda and S.A. Mahin - July 1984 (PB85 191 450/AS)A09
- UCB/EERC-84/13 "Earthquake Engineering Research at Berkeley - 1984" - Aug. 1984 (PB85 197 341/AS)A10
- NA UCB/EERC-84/14 "Moduli and Damping Factors for Dynamic Analyses of Cohesionless Soils," by H.B. Seed, R.T. Wong, I.M. Idriss and K. Tokimatsu - Sept. 1984 (PB85 191 468/AS)A04
- NA UCB/EERC-84/15 "The Influence of SPT Procedures in Soil Liquefaction Resistance Evaluations," by H.B. Seed, K. Tokimatsu, L.F. Harder and R.M. Chung - Oct. 1984 (PB85 191 732/AS)A04
- NA UCB/EERC-84/16 "Simplified Procedures for the Evaluation of Settlements in Sands Due to Earthquake Shaking," by K. Tokimatsu and H.B. Seed - Oct. 1984 (PB85 197 887/AS)A03
- UCB/EERC-84/17 "Evaluation of Energy Absorption Characteristics of Bridge under Seismic Conditions," by R.A. Imbsen and J. Penzien - Nov. 1984
- UCB/EERC-84/18 "Structure-Foundation Interactions under Dynamic Loads," by W.D. Liu and J. Penzien - Nov. 1984
- UCB/EERC-84/19 "Seismic Modelling of Deep Foundations," by C.-H. Chen and J. Penzien - Nov. 1984
- UCB/EERC-84/20 "Dynamic Response Behavior of Quan Shui Dam," by R.W. Clough, K.-T. Chang, H.-Q. Chen, R.M. Stephen, Y. Ghanaat and J.-H. Qi - Nov. 1984 (PB86 115177/AS) A07

- NA UCB/EERC-85/01 "Simplified Methods of Analysis for Earthquake Resistant Design of Buildings," by E.F. Cruz and A.K. Chopra - Feb. 1985 (PB86 112299/AS) A12
- UCB/EERC-85/02 "Estimation of Seismic Wave Coherency and Rupture Velocity using the SMART 1 Strong-Motion Array Recordings," by N.A. Abrahamson - March 1985
- UCB/EERC-85/03 "Dynamic Properties of a Thirty Story Condominium Tower Building," by R.M. Stephen, E.L. Wilson and N. Stander - April 1985 (PB86 118965/AS) A06
- UCB/EERC-85/04 "Development of Substructuring Techniques for On-Line Computer Controlled Seismic Performance Testing," by S. Dermitzakis and S. Mahin - February 1985 (PB86 132941/AS) A08
- UCB/EERC-85/05 "A Simple Model for Reinforcing Bar Anchorages under Cyclic Excitations," by F.C. Filippou - March 1985 (PB86 112919/AS) A05
- UCB/EERC-85/06 "Racking Behavior of Wood-Framed Gypsum Panels under Dynamic Load," by M.G. Oliva - June 1985
- UCB/EERC-85/07 "Earthquake Analysis and Response of Concrete Arch Dams," by K.-L. Fok and A.K. Chopra - June 1985 (PB86 139672/AS) A10
- UCB/EERC-85/08 "Effect of Inelastic Behavior on the Analysis and Design of Earthquake Resistant Structures," by J.P. Lin and S.A. Mahin - June 1985 (PB86 135340/AS) A08
- UCB/EERC-85/09 "Earthquake Simulator Testing of a Base-Isolated Bridge Deck," by J.M. Kelly, I.G. Buckle and H.-C. Tsai - January 1986
- UCB/EERC-85/10 "Simplified Analysis for Earthquake Resistant Design of Concrete Gravity Dams," by G. Fenves and A.K. Chopra - September 1985
- UCB/EERC-85/11 "Dynamic Interaction Effects in Arch Dams," by R.W. Clough, K.-T. Chang, H.-Q. Chen and Y. Ghanaat - October 1985 (PB86 135027/AS) A05
- UCB/EERC-85/12 "Dynamic Response of Long Valley Dam in the Mammoth Lake Earthquake Series of May 25-27, 1980," by S. Lai and H.B. Seed - November 1985 (PB86 142304/AS) A05
- UCB/EERC-85/13 "A Methodology for Computer-Aided Design of Earthquake-Resistant Steel Structures," by M.A. Austin, K.S. Pister and S.A. Mahin - December 1985 (PB86 159480/AS) A10
- UCB/EERC-85/14 "Response of Tension-Leg Platforms to Vertical Seismic Excitations," by G.-S. Liou, J. Penzien and R.W. Yeung - December 1985
- UCB/EERC-85/15 "Cyclic Loading Tests of Masonry Single Piers: Volume 4 - Additional Tests with Height to Width Ratio of 1," by H. Sucuoglu, H.D. McNiven and B. Sveinsson - December 1985
- UCB/EERC-85/16 "An Experimental Program for Studying the Dynamic Response of a Steel Frame with a Variety of Infill Partitions," by B. Yanev and H.D. McNiven - December 1985
- UCB/EERC-86/01 "A Study of Seismically Resistant Eccentrically Braced Steel Frame Systems," by K. Kasai and E.P. Popov - January 1986
- UCB/EERC-86/02 "Design Problems in Soil Liquefaction," by H.B. Seed - February 1986
- UCB/EERC-86/03 "Implications of Recent Earthquakes and Research on Earthquake-Resistant Design and Construction of Buildings," by V.V. Bertero - March 1986
- UCB/EERC-86/04 "The Use of Load Dependent Vectors for Dynamic and Earthquake Analyses," by P. Leger, E.L. Wilson and R.W. Clough - March 1986
- UCB/EERC-86/05 "Two Beam-To-Column Web Connections," by K.-C. Tsai and E.P. Popov - April 1986
- UCB/EERC-86/06 "Determination of Penetration Resistance for Coarse-Grained Soils using the Becker Hammer Drill," by L.F. Harder and H.B. Seed - May 1986
- UCB/EERC-86/07 "A Mathematical Model for Predicting the Nonlinear Response of Unreinforced Masonry Walls to In-Plane Earthquake Excitations," by Y. Mengi and H.D. McNiven - May 1986
- UCB/EERC-86/08 "The 19 September 1985 Mexico Earthquake: Building Behavior," by V.V. Bertero - July 1986
- UCB/EERC-86/09 "EACD-3D: A computer program for three-dimensional earthquake analysis of concrete dams," by K.-L. Fok, J.F. Hall and A.K. Chopra - July 1986
- UCB/EERC-86/10 "Earthquake simulation tests and associated studies of a 0.3-scale model of a six-story concentrically braced steel structure," by C.-M. Uang and V.V. Bertero - December 1986

